

**AN EXPERIMENTAL INVESTIGATION OF UNSTEADY SURFACE PRESSURE ON
SINGLE AND MULTIPLE AIRFOILS**

by

Patrick F. Mish

Dissertation submitted to the Faculty of the
Virginia Polytechnic Institute and State University in
partial fulfillment of the requirements for the degree of

DOCTOR OF PHILOSPHY

in

Aerospace Engineering

APPROVED:

William J. Devenport, Chair

Ricardo A. Burdisso

Stewart A. Glegg

Saad A. Ragab

Joseph A. Schetz

Roger L. Simpson

March 31, 2003

Blacksburg, Virginia

Keywords: unsteady surface pressure, inviscid response, airfoil in turbulence, unsteady loading,
cascade response, aeroacoustic

Copyright © 2003 by Patrick F. Mish

AN EXPERIMENTAL INVESTIGATION OF UNSTEADY SURFACE PRESSURE ON SINGLE AND MULTIPLE AIRFOILS

by

Patrick F. Mish

William J. Devenport, Chairman

Aerospace and Ocean Engineering Department

(ABSTRACT)

This dissertation presents measurements of unsteady surface pressure on airfoils encountering flow disturbances. Analysis of measurements made on an airfoil immersed in turbulence and comparisons with inviscid theory are presented with the goal of determining the effect of angle of attack on an airfoils inviscid response. Unsteady measurements made on the surface of a linear cascade immersed in periodic flow are presented and analyzed to determine the relationship between the blades inviscid response and tip leakage vortex strength.

Measurements of fluctuating surface pressure were made on a NACA 0015 airfoil immersed in grid generated turbulence. The airfoil model has a 2' chord and spans the 6' Virginia Tech Stability Wind Tunnel test section. Two grids were used to investigate the effects of turbulence length scale on the surface pressure response. A large grid which produced turbulence with an integral scale 13% of the chord and a smaller grid which produced turbulence with an integral scale 1.3% of the chord. Measurements were performed at angles of attack, α from 0° to 20° . An array of microphones mounted subsurface was used to measure the unsteady surface pressure. The goal of this measurement was to characterize the effects of angle of attack on the inviscid response.

Lift spectra calculated from pressure measurements at each angle of attack revealed two distinct interaction regions; for $\omega_r = \frac{\omega b}{U_\infty} < 10$ a reduction in unsteady lift of up to 7 decibels (dB) occurs while an increase occurs for $\omega_r > 10$ as the angle of attack is increased. The reduction in unsteady lift at low ω_r with increasing angle of attack is a result that has never before been shown either experimentally or theoretically. The source of the reduction in lift spectral level appears to be closely related to the distortion of inflow turbulence based on analysis of surface pressure spanwise correlation length scales. Furthermore, while the distortion of the inflow appears to be critical in this experiment, this effect does not seem to be significant

in larger integral scale (relative to the chord) flows based on the previous experimental work of McKeough (1976) suggesting the airfoils size relative to the inflow integral scale is critical in defining how the airfoil will respond under variation of angle of attack.

A prediction scheme is developed that correctly accounts for the effects of distortion when the inflow integral scale is small relative to the airfoil chord. This scheme utilizes Rapid Distortion Theory to account for the distortion of the inflow with the distortion field modeled using a circular cylinder.

Measurement of the unsteady surface pressure response of a linear cascade in periodic disturbance is presented. Unsteady pressure was measured on the suction and pressure side of two cascade blades with an array of 24 microphones (12 per blade side) mounted subsurface. The periodic disturbance was generated using a pair of vortex generators attached to a moving end wall. Measurements were made for 8 tip gaps ($t_g/c = 0.00825, 0.0165, 0.022, 0.033, 0.045, 0.057, 0.079, 0.129$) and phased averaged with respect to the vortex generator pair position. This measurement was motivated by the results presented by Ma (2003). The work of Ma (2003) suggested that tip leakage vortex shedding in the presence of a periodic disturbance is heavily influenced by the inviscid response of the cascade blade. This conclusion was arrived at by Ma's (2003) observation that as the tip gap is increased the amount of fluctuation in the tip leakage vortex circulation increases dramatically, in fact, many times the circulation in the inflow vortices.

Unsteady pressure measurements reveal that the blade response involves a complex interaction of both inviscid response and viscous phenomena. However, a close relationship between unsteady tip loading and tip leakage vortex circulation is revealed suggesting the inviscid response is significant in determining the tip leakage vortex circulation. Additionally, predictions using inviscid theory agree well with measured levels of unsteady tip loading. As such, inviscid theory may be useful for predicting the tip leakage circulation and perhaps, pressure fluctuations in the tip leakage vortex.

Such works as this rarely, if ever, come to fruition without immense support, guidance, and understanding from many. As such, I must acknowledge those who were vital during its development.

Foremost, I must thank my parents, Bill and Dolores Mish. You created an environment that fostered free and creative thinking, and provided the encouragement and gentle shoves often required as one advances towards momentous goals. My success here is mirrored by your aptitude as parents, making this as much your achievement as my own. I also thank my two brothers, Bill and Kevin, and sister Donna for creating a family support network possessed by few and beloved by many. Ms. Patti Rothgeb is also thanked for the pivotal role she played during the crucial years of my youth. I credit my being here in large part to your compassionate nature and ability to inspire all those around you.

In many decisions in life a measure of serendipity is hoped for, although seldom realized; however, in the selection of advisor I met luck, and a windfall of it. Dr. William Devenport, a man as brilliant as he is selfless has been my advisor and mentor during the development of this work. Dr. Devenport, you showed me that good research is a commingling of objectivity, insight, and diligence, each of which you display with cleverness and skill I only hope one day to possess. You taught me far more, though, than how to undertake research; you taught me a way of thinking, an approach for solving problems, and you did so with kindness and patience that is unmatched. I have been fortunate to have had the opportunity to work under your supervision and, although I may be eager to leave the nest, I will dearly miss working with you, good friend.

I must also express my gratitude to my committee members, Dr. Ricardo Burdisso, Dr. Stewart Glegg, Dr. Sadd Ragab, Dr. Joe Schetz, and Dr. Roger Simpson. Each of you has provided a measure of technical insight and support which helped to advance this research from good to excellent. I would particularly like to thank Dr. Stewart Glegg, Department Head at Florida Atlantic University, for his involvement despite hundreds of miles of separation and leagues of other pressing matters. Also, Dr. Ricardo Burdisso is thanked not only for his assistance in developing a complete acoustic treatment system for the Virginia Tech Stability Wind Tunnel, but for his belief in my ability to fully manage this project from conception to implementation.

During this work I had the pleasure of mentoring both Aurelien Borgoltz and Josh Staubs as they pursued undergraduate research. Mr. Borgoltz worked with me during analysis of unsteady lift calculations and his work in this area is greatly appreciated. While working with me Mr. Borgoltz displayed a level of talent and independence that will surely serve him well through his remaining graduate student years. Mr. Staubs worked relentlessly, and often on a restrictive timeline, to develop several data acquisition codes. Mr. Staubs did a remarkable job developing cascade blade modifications and overseeing this work. Through all his work, Mr. Staubs displayed a level of maturity rarely found in undergraduates. I am thankful to have worked with you both.

I am also indebted to Shigeo Hayashibara for his design, construction, and assembly of some 130+ microphone circuits. Semere Bereketab and Hongwei Wang are thanked for their assistance with hotwire measurements and the analysis thereof. I owe a special thanks to my colleague, Ruolong Ma for his assistance in preparing the cascade tunnel for unsteady pressure

measurements. He trained me in the operation of this often finicky wind tunnel, showed me how to properly manufacture the moving belt, and spent countless hours providing valuable insight and assistance.

Greg Dudding is thanked for his expert craftsmanship and machining skills that transformed an extruded NACA 0015 section into a sophisticated unsteady pressure measurement system. I thank Bruce Stanger for his professional machining skills and ability to carefully manipulate, not one, but two cascade blades, transforming these into so called smart blades. His opinionated views and forward thinking are also appreciated and will not soon be forgotten, nor will his genuine kindness and continued thoughtfulness towards the entire AOE graduate student body. I thank Mike Vaught for the shop assistance he provided and for his skill and care in all projects he is involved with. I thank Steve Edwards for his excellent electronics work that made it possible to squeeze 12 properly working microphones in a relatively small cascade blade. Bill Oetjens is thanked for his careful guidance in running the Virginia Tech Stability Wind Tunnel and his assistance in installing and removing over 3500LBS of acoustic treatment.

The AOE main office staff is also thanked. Ms. Gail Coe is an Administrative and Program Specialist whose work is both efficient and creative. She displays dependability that is matched only by her kindness. A labyrinth of transactions was worked through by Departmental Administrator Ms. Wanda Foushee who I gratefully thank. The work of Ms. Betty Williams, Enrollment Services Assistant, in ensuring the timely arrival of my pay each month I acknowledge and thank.

I wish to thank my colleagues and friends, Dr. Chittiappa Muthanna, Master Diego de la Riva, Mr. Nicolas Spitz, Mr. Derek Gieger, Ms. Nanayporn Intaratep, Mr. Jon Vegard Larssen, Mr. Jim Ward, and Mr. Brandon S. Rowe. You dealt with me. For this I am immensely appreciative. Also, I thank Ms. Anne Sommers for her support and encouragement during much of this work and for teaching me the importance of effective organization and creative planning. Ms. Megan McKeel is thanked for teaching me to appreciate today, and to always say what I mean and mean what I say.

This work would not have been possible were it not for the kind support of Casey Burley and Tom Brooks of NASA Langley under grant NAG-1-2272 and Ki-Han Kim of the Office of Naval Research under grant N00014-99-1-0294. Their insight and feedback on my analysis of this substantial data set is also appreciated. Jay Casper and Feri Farassat, also of NASA Langley are thanked for their support as well.

Patrick F. Mish

March, 2003
Blacksburg, Virginia

LIST OF TABLES IX

LIST OF FIGURES X

LIST OF SYMBOLS XVIII

1. INTRODUCTION..... 1

 1.1 BACKGROUND 1

 1.1.1 *Pressure Fluctuations* 1

 1.1.2 *Unsteady Thin Airfoil Theory* 3

 1.2 THEORETICAL UNSTEADY RESPONSE OF AN AIRFOIL 6

 1.2.1 *The Exact Solution to Unsteady Thin Airfoil Theory* 6

 1.2.2 *Approximate Analytic and Numeric Models* 7

 1.3 EFFECTS OF ANGLE OF ATTACK AND THICKNESS ON THE AIRFOIL RESPONSE 10

 1.3.1 *Effects of Distortion: Rapid Distortion Theory* 11

 1.4 EXPERIMENTAL STUDIES OF THE AIRFOIL RESPONSE 12

 1.5 UNSTEADY RESPONSE OF A CASCADE 14

 1.5.1 *Theoretical Cascade Work* 14

 1.5.2 *Experimental Cascade Work* 16

 1.6 BOUNDARY LAYER PRESSURE FLUCTUATIONS 17

 1.7 MOTIVATION FOR CURRENT STUDY 20

 1.8 OUTLINE OF DISSERTATION 22

2. APPARATUS AND INSTRUMENTATION 23

 2.1 SINGLE AIRFOIL IN TURBULENCE 23

 2.1.1 *Wind Tunnel* 23

 2.1.2 *Wind Tunnel Walls* 23

 2.1.3 *Turbulence Generating Grid* 28

 2.1.4 *Airfoil Model* 33

 2.1.5 *Microphone System* 37

 2.1.6 *Reference Acoustic System* 44

 2.1.7 *Hot-wire Anemometry* 45

 2.1.8 *Boundary Layer Trip and Leading Edge Bump* 46

 2.1.9 *Modified trailing edge* 47

 2.1.10 *Flow Visualization* 48

3. SINGLE AIRFOIL IN TURBULENCE PREDICTIONS 50

 3.1 ZERO MEAN LOADING PREDICTIONS 50

 3.2 INCORPORATING THE EFFECTS OF TURBULENCE DISTORTION 52

 3.2.1 *Rapid Distortion Theory Background* 52

 3.2.2 *Derivation of Cross-spectral Density of Surface Pressure Fluctuations* 54

 3.2.3 *Application of Reba and Kerschen Surface Pressure Prediction Code* 56

4. SINGLE AIRFOIL IN TURBULENCE: EXPERIMENTAL DETAILS AND DATA QUALITY 59

 4.1 MEASUREMENT CONDITIONS AND DATA SAMPLING 59

4.1.1 Solid Test Section Wall Test.....	59
4.1.2 Acoustically Treated Wall Test.....	60
4.1.3 Coordinate System.....	61
4.2 MEASUREMENT UNCERTAINTY.....	61
4.2.1 Uncertainty in Pressure Spectra.....	61
4.2.2 Uncertainty in RMS Pressure.....	62
4.3 BASIC FLOW DEFINITION.....	63
4.3.1 Mean and Unsteady Blockage Effects.....	63
4.3.2 Mean Pressure.....	63
4.3.3 Stagnation, Transition, and Separation Points.....	64
4.3.4 Large Grid Flow Visualization.....	64
4.4 QUALITY OF UNSTEADY PRESSURE DATA.....	66
4.4.1 Spanwise Homogeneity.....	66
4.4.2 Effects of Acoustic Treatment and Data Repeatability.....	68
4.4.3 Data Symmetry.....	70
4.4.4 Contamination and Dominance of Various Pressure Fluctuation Sources.....	74
4.5 SUMMARY OF EXPERIMENTAL DETAILS AND DATA QUALITY.....	81
5. SINGLE AIRFOIL IN TURBULENCE: ANALYSIS OF UNSTEADY PRESSURE DATA.....	144
5.1 PRESSURE SPECTRA AND MEAN SQUARE PRESSURE.....	144
5.1.1 Pressure Difference Spectra at Zero Angle of Attack.....	144
5.1.2 Pressure Difference Spectra at Non-Zero Angle of Attack.....	145
5.1.3 Mean Square Pressure at Zero Angle of Attack.....	146
5.1.4 Mean Square Pressure at non-Zero Angle of Attack.....	147
5.2 LIFT SPECTRA AND MEAN SQUARE LIFT.....	147
5.2.1 Motivation for Forming Unsteady Lift.....	147
5.2.2 Unsteady Lift Formulation.....	148
5.2.3 Verification of Lift Formulation.....	149
5.2.4 Lift Spectra at Zero Angle of Attack.....	154
5.2.5 Comparison of Predicted and Measured Unsteady Lift at Angle of Attack.....	154
5.2.6 Mean Square Lift at non-Zero Angle of Attack.....	155
5.3 ADMITTANCE FUNCTION.....	156
5.4 SURFACE PRESSURE CORRELATION LENGTH SCALES.....	157
5.4.1 Spanwise Correlation Length Scale.....	157
5.4.2 Chordwise Correlation Length Scale.....	159
5.5 CORRELATION OF VELOCITY AND PRESSURE.....	161
5.6 EFFECTS OF A MODIFIED TRAILING EDGE.....	162
5.6.1 Correlation of Pressure in Space and Time.....	162
5.6.2 Unsteady Lift.....	163
5.7 SOURCES OF LOW FREQUENCY ANGLE OF ATTACK EFFECT.....	163
5.7.1 Laminar Separation Bubble.....	164
5.7.2 Distortion of Inflow.....	164
5.8 A MODEL FOR PREDICTING ANGLE OF ATTACK EFFECTS.....	165
5.9 HIGH FREQUENCY ANGLE OF ATTACK EFFECTS.....	169
5.10 COMPUTING FAR-FIELD NOISE FROM SURFACE PRESSURE.....	170
5.11 SUMMARY.....	172

6. CASCADE IN PERIODIC DISTURBANCE.....	210
6.1 BACKGROUND	210
7. CASCADE INSTRUMENTATION AND APPARATUS	212
7.1 LINEAR CASCADE WIND TUNNEL	212
7.2 MICROPHONE SYSTEM	217
8. CASCADE RESPONSE PREDICTION.....	220
8.1 LINEAR CASCADE OF FLAT PLATES.....	220
9. CASCADE IN PERIODIC DISTURBANCE: ANALYSIS OF UNSTEADY PRESSURE DATA	223
9.1 COORDINATE SYSTEM, TEST CONFIGURATION, AND DATA SAMPLING	223
9.2 FORMULATION OF PHASE AVERAGED DATA	224
9.2.1 <i>Phased Averaged Data</i>	224
9.3 MEASUREMENT UNCERTAINTIES.....	225
9.4 BASIC FLOW DEFINITION	225
9.4.1 <i>Contribution of Noise Sources</i>	225
9.5 UNSTEADY LOADING	229
9.5.1 <i>Chordwise Surface Pressure Distribution</i>	229
9.5.2 <i>Spanwise Surface Pressure Distribution</i>	231
9.5.3 <i>Tip Section Unsteady Lift</i>	233
9.5.4 <i>Tip Section Lift Compared with Inviscid Theory</i>	235
9.6 COMPARISON OF MEASURED LIFT WITH TIP LEAKAGE CIRCULATION	236
9.7 HIGHER ORDER MOMENTS AND SPECTRA	236
9.8 SUMMARY	236
10. CONCLUSIONS	299
10.1 SINGLE AIRFOIL IN TURBULENCE.....	299
10.1.1 <i>Primary Contributions</i>	299
10.1.2 <i>Suggestions for Future Work</i>	300
10.2 CASCADE IN PERIODIC DISTURBANCE.....	301
10.2.1 <i>Primary Contributions</i>	301
10.2.2 <i>Suggestions for Future Work</i>	302
REFERENCES.....	303
APPENDIX A.....	311
A.1 FORMULATION OF PRESSURE CROSS-SPECTRAL DENSITY FROM MEASURED PRESSURE ...	311
A.2 FORMULATION OF COHERENCE AND PRESSURE PHASING.....	312
VITA.....	313

Table 2.1: Flow speed and Reynolds number	29
Table 2.2: Longitudinal integral scales (λ) and velocity scales (u) that best describe the 2 grid turbulence flows.	32
Table 2.3: Turbulence length scales normalized on chord and leading edge radius	36
Table 3.1: Summary of unsteady pressure prediction code input parameters	52
Table 3.2: Parameters used in Reba and Kerschen (1996) airfoil response theory	53
Table 3.3: Parameters used in Kerschen/Amiet comparison	56
Table 4.1: Solid Wall Test Configuration Details	60
Table 4.2: Uncertainties in unsteady pressure spectra	61
Table 4.3: Stagnation point and laminar separation bubble locations for large grid measurement	66
Table 4.4: Measured chordwise location of microphones	72
Table 5.1: Location of microphones used in unsteady lift calculation	148
Table 5.2: Ratio of distortion location to cylinder radius	168
Table 7.1: Locations of microphones in blade 4 and 5	217
Table 8.1: Variable definitions for equation (8.1); see also figure 8.1	220
Table 8.2: Definition of figure 8.1 notation	221
Table 9.1: Microphones used in unsteady lift calculation and corresponding resolution	234

Figure 1.1: Unsteady Thin Airfoil Theory	4
Figure 2.1: Virginia Tech Stability Wind Tunnel	23
Figure 2.2: Pressure sound level at 30 m/s in solid wall configuration	24
Figure 2.3: Wind tunnel acoustic treatment schematic	25
Figure 2.4: Expected level and frequency range of attenuation	25
Figure 2.5: Cross-section of typical acoustic box	26
Figure 2.6: Pressure sound level at 30m/s with and without acoustic treatment	27
Figure 2.7: Downstream view of large grid	28
Figure 2.8: View of small grid	29
Figure 2.9: Cross-sectional averaged turbulence intensities for large grid flow	30
Figure 2.10: Cross-sectional averaged turbulence intensities for small grid flow	30
Figure 2.11 (a): Large grid flow contours of u -component turbulence normal stress normalized on U_∞^2	31
Figure 2.11 (b): Large grid flow contours of v -component turbulence normal stress normalized on U_∞^2	31
Figure 2.11 (c): Large grid flow contours of w -component turbulence normal stress normalized on U_∞^2	31
Figure 2.12 (a): Small grid flow contours of u -component turbulence normal stress normalized on U_∞^2	32
Figure 2.12 (b): Small grid flow contours of v -component turbulence normal stress normalized on U_∞^2	32
Figure 2.12 (c): Small grid flow contours of w -component turbulence normal stress normalized on U_∞^2	32
Figure 2.13: NACA 0015 measured and calculated geometry	33
Figure 2.14: Wing with hatch removed	34
Figure 2.15: Chordwise distribution of mean pressure taps	35
Figure 2.16: Roof mounting block	35
Figure 2.17: Roof mounting structure	36
Figure 2.18: Schematic of the wind tunnel contraction and test section showing the location of the grid and airfoil model.	36
Figure 2.19: Schematic of microphone system	37
Figure 2.20: Ninety-six microphone layout	38
Figure 2.21: Forty microphone layout	38
Figure 2.22: Effective microphone array	40
Figure 2.23: Microphone Calibrator	40
Figure 2.24: Microphone calibration schematic	41
Figure 2.25: Typical magnitude and phase calibrations	42
Figure 2.26: Cross-section through typical microphone and microphone mounting hole	43
Figure 2.27: Microphone lying beside mounting hole on interior of wing	43
Figure 2.28: Data and power cabling configuration	44
Figure 2.29: Bruel and Kjaer model 4138 reference microphone	45
Figure 2.30: Overview of reference microphone mounted on stand next to wing	45
Figure 2.31: Diagram of hot-wire probe	46

Figure 2.32: View looking down on mounted hot-wire	46
Figure 2.33: Close-up of boundary layer trip strip	47
Figure 2.34: Airfoil with modified trailing edge	48
Figure 2.35: Cross section showing trailing edge extension	48
Figure 2.36: Cross section showing dimensioned trailing edge extension	48
Figure 2.37: Example of flow visualization at 0° angle of attack	49
<hr/>	
Figure 3.1: Comparison of Amiet (1976a, b) and Reba and Kerschen (1996) theories	57
<hr/>	
Figure 4.1: Top down view of airfoil in wind tunnel test section defining positive angles of attack	83
Figure 4.2: Single airfoil in turbulence coordinate system	83
Figure 4.3: Mean pressure calculated lift coefficient shown with McKeough's (1976) data	84
Figure 4.4: Stagnation and separation locations of <i>small</i> scale turbulence flow	85
Figure 4.5: Stagnation, transition, and separation locations of <i>large</i> scale turbulence flow	85
Figure 4.6: $\alpha = 0^\circ$ oil flow visualization on the hatch- <i>pressure</i> -(a) and solid- <i>suction</i> -(b) side of airfoil. The numbers in black correspond to the location of microphones in percent chord	86
Figure 4.7: $\alpha = 4^\circ$ oil flow visualization on the hatch- <i>pressure</i> -(a) and solid- <i>suction</i> -(b) side of airfoil. The numbers in black correspond to the location of microphones in percent chord	87
Figure 4.8: $\alpha = 8^\circ$ oil flow visualization on the hatch- <i>pressure</i> -(a) and solid- <i>suction</i> -(b) side of airfoil. The numbers in black correspond to the location of microphones in percent chord	88
Figure 4.9: $\alpha = 12^\circ$ oil flow visualization on the hatch- <i>pressure</i> -(a) and solid- <i>suction</i> -(b) side of airfoil. The numbers in black correspond to the location of microphones in percent chord	89
Figure 4.10: $\alpha = 16^\circ$ oil flow visualization on the hatch- <i>pressure</i> -(a) and solid- <i>suction</i> -(b) side of airfoil. The numbers in black correspond to the location of microphones in percent chord	90
Figure 4.11: $\alpha = 20^\circ$ oil flow visualization on the hatch- <i>pressure</i> -(a) and solid- <i>suction</i> -(b) side of airfoil. The numbers in black correspond to the location of microphones in percent chord	91
Figure 4.12: Spanwise homogeneity of <i>small</i> grid unsteady pressure data at $\alpha = 0^\circ$ on the <i>suction side</i> of airfoil for chordwise positions $x/c = 1, 2.5, 4, 6, 9\%$. First column of numbers in legend indicates spanwise position and second column is unique number given to each microphone.	92-94
Figure 4.13: Spanwise homogeneity of <i>small</i> grid unsteady pressure data at $\alpha = 0^\circ$ on the <i>pressure side</i> of airfoil for chordwise positions $x/c = 1, 2.5, 4, 6, 9\%$. First column of numbers in legend indicates spanwise position and second column is unique number given to each microphone.	95-97
Figure 4.14: Spanwise homogeneity of <i>large</i> grid unsteady pressure data at $\alpha = 0^\circ$ on the <i>suction side</i> of airfoil for chordwise positions $x/c = 1, 2.5, 4, 6, 9\%$. First	98-100

column of numbers in legend indicates spanwise position and second column is unique number given to each microphone.	
Figure 4.15: Spanwise homogeneity of <i>large</i> grid unsteady pressure data at $\alpha = 0^\circ$ on the <i>pressure</i> side of airfoil for chordwise positions $x/c = 1, 2.5, 4, 6, 9\%$. First column of numbers in legend indicates spanwise position and second column is unique number given to each microphone.	101-103
Figure 4.16: Comparison of <i>large</i> grid p' spectra measured with solid and acoustically treated wind tunnel test section walls. Spectra are from <i>suction</i> side of airfoil ($x/c = 1, 2.5, 4, 6, 9, 14\%$) at $\alpha = 0^\circ$ and are normalized on the free-stream dynamic pressure.	104-106
Figure 4.17: Comparison of <i>large</i> grid p' spectra measured with solid and acoustically treated wind tunnel test section walls. Spectra are from <i>pressure</i> side of airfoil ($x/c = 1, 2.5, 4, 6, 9, 14\%$) at $\alpha = 0^\circ$ and are normalized on the free-stream dynamic pressure.	107-109
Figure 4.18: Comparison of <i>large</i> grid p' spectra measured with solid and acoustically treated wind tunnel test section walls. Spectra are from <i>suction</i> side of airfoil ($x/c = 1, 2.5\%$) at $\alpha = 8^\circ$ and are normalized on the free-stream dynamic pressure.	110
Figure 4.19: Comparison of <i>large</i> grid p' spectra measured with solid and acoustically treated wind tunnel test section walls. Spectra are from <i>pressure</i> side of airfoil ($x/c = 1, 2.5\%$) at $\alpha = 8^\circ$ and are normalized on the free-stream dynamic pressure.	111
Figure 4.20: Comparison of p' spectra on the pressure and suction side of airfoil at $\alpha = 0^\circ$. Comparison made at $x/c = 1, 2.5, 4, 6, 9, 14\%$.	112-114
Figure 4.21: Comparison of pressure and suction side p' spectra at $\alpha = 8^\circ$ and -8° for $x/c = 0.01, 0.025, 0.04, \text{ and } 0.06$	115-116
Figure 4.22: Measured geometry at each microphone location versus actual wing geometry	117
Figure 4.23: Pressure spectra comparison at $\alpha = 8^\circ$ and -8° for $x/c = 0.01$. Data at $\alpha = -8^\circ$ is taken with <i>leading edge bump</i> installed.	118
Figure 4.24: Pressure difference smooth flow data plotted at all angles of attack with matched RPM data at $\alpha = 0^\circ$ and reference (B&K) microphone data at $x/c = 0.01, 0.025, 0.04, 0.06$	119
Figure 4.25: Pressure difference matched flow speed data plotted at all angles of attack with matched RPM data at $\alpha = 0^\circ$ and reference (B&K) microphone data at $x/c = 0.09, 0.14, 0.2, 0.3$	120
Figure 4.26: Coherence and phase of matched flow speed data plotted at all angles of attack with matched RPM data at $\alpha = 0^\circ$ and reference (B&K) microphone data at $x/c = 0.01, 0.025, 0.04, 0.06$	121
Figure 4.27: Coherence and phase of matched flow speed data plotted at all angles of attack with matched RPM data at $\alpha = 0^\circ$ and reference (B&K) microphone data at $x/c = 0.09, 0.14, 0.2, 0.3$	122
Figure 4.28: Large grid auto-spectra plotted with COP (Burley-Brooks) at $\alpha = 0^\circ$ for $x/c = 0.025, 0.04, 0.06, 0.09, \text{ and } 0.14$	123
Figure 4. 29: Small grid auto-spectra plotted with COP (Burley-Brooks) at $\alpha = 0^\circ$ for	124

$x/c = 0.025, 0.04, 0.06, 0.09, \text{ and } 0.14$	
Figure 4.30: Pressure difference cross-spectra at $x/c = 0.01$, $\alpha = 0^\circ$ measured in smooth flow and in large and small grid turbulence	125
Figure 4.31: Pressure difference cross-spectra at $x/c = 0.06$, $\alpha = 0^\circ$ measured in smooth flow and in large and small grid turbulence	126
Figure 4.32: Pressure difference cross-spectra at $x/c = 0.14$, $\alpha = 0^\circ$ measured in smooth flow and in large and small grid turbulence	127
Figure 4.33: Dominant features expected in a contour plot of R_{pp}	128
Figure 4.34: Contour plots of pressure-pressure correlation, $R_{pp}(x=1\%,x',\tau)$ for <i>large</i> grid flow. The correlation is formed with the 1% chord microphone on the suction side of the airfoil	129-134
Figure 4.35: Contour plots of pressure-pressure correlation, $R_{pp}(x=1\%,x',\tau)$ for <i>large</i> grid flow. The correlation is formed with the 1% chord microphone on the <i>pressure</i> side of the airfoil	135-140
Figure 4.36: Contour plots of $R_{pp}(x=1\%,x',\tau)$ for <i>small</i> grid flow. The correlation is formed with the 1% chord microphone on the suction side of the airfoil	141-142
Figure 4.37: Comparison of measured and predicted pressure-pressure correlation, $R_{pp}(x=1\%,x',\tau)$ for <i>large</i> grid flow. The correlation is formed with the 1% chord microphone on the suction side of the airfoil.	143
<hr/>	
Figure 5.1: Comparison of measured and predicted pressure difference spectra for $\alpha = 0^\circ$ at $x/c = 1, 2.5, 4, 6, 9, \text{ and } 14\%$. Prediction is Amiet's (1976a, b) unsteady thin airfoil theory.	173-175
Figure 5.2: Predictions of pressure difference spectra from the Rapid Distortion Theory of Reba and Kerschen (1996) plotted with measured data for $\alpha = 0^\circ, 2^\circ, \text{ and } 6^\circ$ at chordwise locations, $x/c = 1, 2.5, 4, 6, 9, \text{ and } 14\%$	176-178
Figure 5.3: Pressure and suction side root mean squared of p as a function of x/c at $\alpha = 0^\circ$, formed from integrating pressure spectrum over $\omega_r = 0.4 - 100$. Comparison made with Amiet (1976a, b).	179
Figure 5.4: Pressure and suction side root mean squared of p as a function of angle of attack for $x/c = 0.01, 0.025, 0.04, 0.06, 0.09, \text{ and } 0.14$.	180
Figure 5.5: <i>Large</i> grid root mean square p computed from pressure difference spectra as a function of angle of attack for $x/c = 0.01, 0.025, 0.04, 0.06, 0.09, \text{ and } 0.14$	180
Figure 5.6: Microphones used in unsteady lift calculation indicated by triangle symbol	181
Figure 5.7: Resolving unsteady pressure into lift	181
Figure 5.8: $G_{\Delta P \Delta P}(\omega_r, x, x') = G_{\Delta P \Delta P}(3, x, x')$ showing the variation of the pressure difference cross-spectra in x	182
Figure 5.9: Depiction illustrating how Amiet's Thin Airfoil Theory is used to assess errors related to discretizing lift spectra equations	182
Figure 5.10: Continuous and discrete calculations of unsteady lift using Amiet's theory	183
Figure 5.11: $G_{\Delta P \Delta P}$ at $x/c = 2.5\%$, $\omega_r = 10$ from Amiet's theory computed	183

continuously and discretely, plotted against all other chordwise locations	
Figure 5.12a: Depiction of coordinate transformation used to form unsteady lift	184
Figure 5.12b: Depiction of coordinate transformation used to form unsteady lift	184
Figure 5.13: Projection of microphone locations into flow aligned coordinate system for Amiet thin airfoil theory simulation	185
Figure 5.14: Unsteady lift computed from Amiet simulation shown for each angle of attack	186
Figure 5.15: Drawing showing phase shift in pressure when airfoil is at non-zero angle of attack	187
Figure 5.16: Geometry of phasing model	188
Figure 5.17: Ratio of unsteady lift at non-zero angle of attack to zero angle of attack unsteady lift based on phasing model	188
Figure 5.18: Unsteady lift calculate from measured unsteady pressure in large grid turbulence	189
Figure 5.19: Large grid unsteady lift calculated using pressure measurements from the first 14% and the first 85% chord	190
Figure 5.20: Unsteady lift calculated from high angle of attack resolution data for <i>large</i> grid turbulence at $\alpha = 0^\circ$ compared with that predicted from Amiet's (1976a, b) theory.	191
Figure 5.21: Unsteady lift calculated from pressure measurements compared with lift computed from Reba and Kerschens (1996) unsteady response theory.	192
Figure 5.22: Measured L'^2 as a function of angle of attack compared with a curve representing α^2	193
Figure 5.23: Upwash velocity spectrum for <i>large</i> grid turbulence	194
Figure 5.24: Admittance function calculated from unsteady pressure measurements compared with McKeough's (1976) measurements	194
Figure 5.25: Comparison of measured and predicted <i>spanwise</i> correlation length scales, $\alpha = 0^\circ$	195
Figure 5.26: Effects of angle of attack on <i>spanwise</i> correlation length scales at $x/c = 1$ and 2.5% chord	196
Figure 5.27a: Top down view of airfoil at $\alpha = 0^\circ$ showing the reduction in cross-sectional area of an eddy encountering an airfoil as a result of eddy stretching by the mean potential field.	197
Figure 5.27b: Top down view of airfoil at $\alpha > 0^\circ$ showing the significant reduction in cross-sectional area of an eddy encountering an airfoil as a result of eddy stretching by the mean potential field.	197
Figure 5.28: Comparison of measured and predicted <i>chordwise</i> correlation length scales, $\alpha = 0^\circ$	198
Figure 5.29: Effects of angle of attack on <i>chordwise</i> correlation length scales at $x/c = 1$ and 2.5% chord	199
Figure 5.30: Contour plots of pressure-velocity correlation function, $R_{pv}(x=14\%, x', \tau)$	200
Figure 5.31: Contour plots of $R_{pp}(x=1\%, x', \tau)$ with trailing edge modification installed	201
Figure 5.32: Unsteady lift calculate with and without the modified trailing edge	202

Figure 5.33: Diagram showing a circular cylinder fit to the airfoils radius of curvature at the $\alpha = 4^\circ$ stagnation point location	203
Figure 5.34: Diagram showing the streamline along which the turbulence distortion is calculated	204
Figure 5.35: Unsteady lift spectra calculated using the distorted inflow turbulence energy spectra with Amiet's (1976a, b) solution. Distorted turbulence energy spectra are computed using the distortion tensor calculated along the stagnation streamline of a circular cylinder.	205
Figure 5.36: Unsteady lift spectra calculated using the distorted inflow turbulence energy spectra with Amiet's (1976a, b) solution for McKeough's (1976) flow conditions. Distorted turbulence energy spectra are computed using the distortion tensor calculated along the stagnation streamline of a circular cylinder.	206
Figure 5.37: Lift spectra scaled on the mean lift squared	207
Figure 5.38: Convective derivative of <i>pressure difference</i> cross-spectral density for $\alpha = 0^\circ$ at chordwise locations, $x/c = 1, 2.5, 4, 6, 9,$ and 14%	208-209
<hr/>	
Figure 7.1: Linear Cascade Wind Tunnel (courtesy of Ma 2003)	212
Figure 7.2: Cascade tunnel cross-section AA (courtesy of Ma 2003)	214
Figure 7.3: Delta wing vortex generator pair (courtesy of Ma 2003)	215
Figure 7.4: Planform view of the microphone distribution	218
Figure 7.5a: Cross-section of blade measuring unsteady pressure on suction side (blade 5)	219
Figure 7.5b: Cross-section of blade measuring unsteady pressure on pressure side (blade 4)	219
<hr/>	
Figure 8.1: Geometry used in Glegg's (1999) cascade response theory	221
<hr/>	
Figure 9.1: Schematic of blade/disturbance interaction showing coordinate system	238
Figure 9.2: Schematic showing position of vortex generators relative to blades as phase number varies from 0 to 256	239
Figure 9.3: Time averaged pressure spectra on <i>suction</i> side of blade at different spanwise stations for $t_g/c = 3.3\%$. Comparison of spectra measured for belt in motion and no vortex generators attached with spectra measured with vortex generators attached.	240
Figure 9.4: Spanwise RMS pressure on <i>suction</i> side of blade for $t_g/c = 3.3\%$ with belt in motion and no vortex generators attached compared with measurements made with vortex generators attached.	241
Figure 9.5: Time averaged pressure spectra on <i>suction</i> side of blade at different chordwise stations for $t_g/c = 3.3\%$. Comparison of spectra measured for belt in motion and no vortex generators attached with spectra measured with vortex generators attached.	242
Figure 9.6: Chordwise RMS pressure on <i>pressure</i> side of blade for $t_g/c = 3.3\%$ with belt in motion and no vortex generators attached compared with measurements made with vortex generators attached.	243

Figure 9.7: Time averaged pressure spectra on <i>pressure</i> side of blade at different spanwise stations for $t_g/c = 3.3\%$. Comparison of spectra measured for belt in motion and no vortex generators attached with spectra measured with vortex generators attached.	244
Figure 9.8: Spanwise RMS pressure on <i>pressure</i> side of blade for $t_g/c = 3.3\%$ with belt in motion and no vortex generators attached compared with measurements made with vortex generators attached.	245
Figure 9.9: Time averaged pressure spectra on <i>pressure</i> side of blade at different chordwise stations for $t_g/c = 3.3\%$. Comparison of spectra measured for belt in motion and no vortex generators attached with spectra measured with vortex generators attached.	246
Figure 9.10: Chordwise RMS pressure on <i>pressure</i> side of blade for $t_g/c = 3.3\%$ with belt in motion and no vortex generators attached compared with measurements made with vortex generators attached.	247
Figure 9.11: Comparison of chordwise p'^2 calculated from spectra and from phase averaged data. Such a comparison serves as an independent check of the two processing codes used. Plots presented for the suction and pressure side of blade for $t_g/c = 3.3\%$.	248
Figure 9.12: Ratio of RMS voltages calculated without and with vortex generators compared to ratio of RMS pressures calculated without and with vortex generators. Such comparisons ensure the proper application of microphone calibrations in both processing codes. Data presented for the pressure and suction side of blade as a function of chordwise location for $t_g/c = 3.3\%$.	249
Figure 9.13: Ratio of RMS voltages calculated without and with vortex generators compared to ratio of RMS pressures calculated without and with vortex generators. Such comparisons ensure the proper application of microphone calibrations in both processing codes. Data presented for the pressure and suction side of blade as a function of spanwise location for $t_g/c = 3.3\%$.	250
Figure 9.14: Measurement of acoustic field produced by radio tuned to static. Data on left was taken with the acquisition code used to make pressure measurements without vortex generators present. Data on right was taken with the acquisition code used to make pressure measurements when vortex generators are present. Comparison of both sets of data assists in ensuring data acquisition and processing is consistent between both measurements.	251
Figure 9.15: Suction side C_p as a function of phase number plotted for each tip gap along the chord at $x/c = 13, 18, 24, 30, 40, 55, 75$	252-255
Figure 9.16: Pressure side C_p as a function of phase number plotted for each tip gap along the chord at $x/c = 17.5, 23.125, 29.375, 39.375, 55, 76.25\%$	256-258
Figure 9.17: Pressure and suction side C_p movies as a function of chordwise location plotted for each tip gap, $t_g/c = 0.00825, 0.0165, 0.022, 0.033, 0.045, 0.057, 0.079, 0.129$	259-262
Figure 9.18: Suction side C_p as a function of phase number plotted for each tip gap along the span at $y/c = 1.875, 5, 7.5, 15, 55, 25, 45\%$	263-265
Figure 9.19: Pressure side C_p as a function of phase number plotted for each tip gap along the span at $y/c = 1.875, 5, 7.5, 15, 55, 25, 45\%$	266-268

Figure 9.20: Pressure and suction side C_p movies as a function of spanwise location plotted for each tip gap, $t_g/c = 0.00825, 0.0165, 0.022, 0.033, 0.045, 0.057, 0.079, 0.129$	269-272
Figure 9.21: Schematic showing typical Δx 's used in unsteady lift calculation	273
Figure 9.22: Unsteady Lift coefficient, C_L as a function of phase number plotted for tip gaps, $t_g/c = 0.00825, 0.0165, 0.022, 0.033$	274
Figure 9.23: Unsteady Lift coefficient, C_L as a function of phase number plotted for each tip gap, $t_g/c = 0.045, 0.057, 0.079, 0.129$	274
Figure 9.24: Theoretical and measured unsteady lift coefficient, C_L as a function of phase number plotted for $t_g/c = 0.00825, 0.0165, 0.022, 0.033, 0.045, 0.057, 0.079, 0.129$	275-278
Figure 9.25: Comparison of phase averaged C_L (upper plot) with phased averaged circulation (lower plot—courtesy of Ma, 2003) measured in the tip leakage vortex by Ma (2003).	279
Figure 9.26: Suction side C_p^2 as a function of phase number plotted for each tip gap along the chord at $x/c = 13, 18, 24, 30, 40, 55, 75\%$	280-283
Figure 9.27: Pressure side C_p^2 as a function of phase number plotted for each tip gap along the chord at $x/c = 17.5, 23.125, 29.375, 39.375, 55, 76.25\%$	284-286
Figure 9.28: Chordwise unsteady pressure spectra on the <i>suction</i> side plotted for each tip gap, $t_g/c = 0.00825, 0.0165, 0.022, 0.033, 0.045, 0.057, 0.079, 0.129$.	287-289
Figure 9.29: Spanwise unsteady pressure spectra on the <i>suction</i> side plotted for each tip gap, $t_g/c = 0.00825, 0.0165, 0.022, 0.033, 0.045, 0.057, 0.079, 0.129$.	290-292
Figure 9.30: Pressure spectra on the <i>pressure</i> side at each chordwise station plotted for each tip gap, $t_g/c = 0.00825, 0.0165, 0.022, 0.033, 0.045, 0.057, 0.079, 0.129$.	293-295
Figure 9.31: Spanwise unsteady pressure spectra on the <i>suction</i> side plotted for each tip gap, $t_g/c = 0.00825, 0.0165, 0.022, 0.033, 0.045, 0.057, 0.079, 0.129$.	296-298

$E[]$	Expected value
$\text{Re}[]$	Real part of complex number
$\langle \rangle$	Phased average quantities
∇^2	Laplacian operator
$ A(\omega) $	Admittance function defined such that, $\Phi_{c_L}(\omega) = \left(\frac{2\pi}{U_\infty}\right)^2 A(\omega) ^2 \Phi_{w_w}(\omega)$
A, B	Non-dimensional coefficients of equation describing the variation in $\overline{L^2}$
A_1	Non-dimensional constant in Kings law
A_2	Non-dimensional constant
a_j	Position of fluid particle prior to undergoing distortion in tensor form
b	Half chord, $c/2$, [m]
B_1	Constant in Kings law
bk	Response of Bruel and Kjaer reference microphone, [V/Pa]
c	Airfoil chord, [m]
C_L	Mean lift coefficient per unit span, L/qc
c_o	Speed of sound, [m/s]
$\langle C_p'^2 \rangle$	Phase averaged variance of fluctuating pressure coefficient
d_s	Distance along airfoil surface to pressure measurement location, [m]
E	Energy spectrum of the inflow turbulence, [m/sec ²]
E_{hw}	Output voltage produced by hot-wire in jet flow, [V]
f	Frequency, $\omega / 2\pi$, [Hz]
g	Airfoil response function (also referred to as blade response function and transfer function)

G_{Dt}	Convective derivative power spectral density, [Pa ² /sec ² Hz]
G_{dt}	Temporal derivative spectrum, [Pa ² /sec ² Hz]
G_{dx}	Spatial derivative spectrum, [Pa ² /sec ² Hz]
G_{LL}	Power spectral density of lift such that $\overline{L^2}(\alpha) = \int_0^\infty G_{LL}(\alpha, \omega) d\omega$, [Pa ² /m ² Hz ²]
G_{LL}^*	Normalized lift spectrum, $\frac{G_{LL}(\alpha, f)}{\overline{L^2}(\alpha)}$, [Hz ⁻²]
G_{NN}	Normal-to-airfoil chord force spectrum, [Pa ² /m ² Hz ²]
G_{pp}	Surface pressure auto-spectrum such that $\overline{p'^2} = \int_0^\infty G_{pp}(\omega) d\omega$, [Pa ² /Hz] see also Appendix A
$G_{P_u P_u'}$	Surface pressure cross-spectrum on upper surface of airfoil and equivalent to S_{qq} , [Pa ² /Hz]
$G_{P_l P_l'}$	Surface pressure cross-spectrum on lower surface of airfoil and equivalent to S_{qq} , [Pa ² /Hz]
$G_{P_u P_l'}$	Surface pressure cross-spectrum between pressure measured on upper and lower surface, [Pa ² /Hz]
G_{TN}	Cross spectrum between normal-to-airfoil chord force and tangent-to-airfoil chord force, [Pa ² /m ² Hz ²]
G_{TT}	Tangent-to-airfoil chord force spectrum, [Pa ² /m ² Hz ²]
$G_{p_1}^a$	Cross spectrum of calibrated B & K microphone signal and white noise signal
$G_{v_1}^a$	Auto-spectrum of white noise signal
$G_{V_2 V_1}^b$	Cross spectrum of Sennheiser microphone signal and white noise signal
$G_{v_1}^b$	Auto-spectrum of white noise signal
$G_{\Delta P \Delta P}$	Pressure difference auto-spectrum, [Pa ² /Hz], see also Appendix A
$G_{\Delta P_x \Delta P_x} _{Inviscid}$	Coherent output power, $\frac{G_{\Delta P_1 \Delta P_x}^2}{G_{\Delta P_1 \Delta P_1}}$, [Pa ² /Hz]
$G_{\Delta P_1 \Delta P_x}$	Pressure difference cross-spectra between microphones located at 1% chord and position x , [Pa ² /Hz]

$G_{\Delta P_1 \Delta P_1}$	Pressure difference auto-spectrum at 1% chord, [Pa ² /Hz]
h	Wind tunnel height, [m]
h_b	Cascade blade spacing, [m]
i	$\sqrt{-1}$ or, if subscripted, tensor notation index corresponding to 1, 2, 3
k	Magnitude of wavenumber vector, [m ⁻¹]
k_a	Acoustic frequency, ω_a
k_d	Inverse of the Kolmogorov length scale, $(\varepsilon/\nu^3)^{0.25}$
k_e	Characteristic wavenumber, $\frac{\sqrt{\pi}}{\lambda} \frac{\Gamma(\frac{5}{6})}{\Gamma(\frac{1}{3})}$, [m ⁻¹]
\hat{K}_x	Normalized wavenumber, $\frac{\omega/U}{k_e}$
K_x	Wavenumber in x direction, $2\pi f/U$, [m ⁻¹]
k_x, k_y, k_z	Wavenumber vector components in the x, y, z direction, [m ⁻¹]
L	Mean lift per unit span, [N/m]
L'	Unsteady lift per unit span, [N/m]
$\overline{L^2}$	Mean square lift, $\overline{L^2}(\alpha) = \int_0^\infty G_{LL}(\alpha, \omega) d\omega$, [Pa ² /m ²]
L_c	Chordwise pressure correlation length scale, $\int_0^{x_{\max}} \frac{S_{qq}(x_i, x_j, \eta = 0, f)}{S_{qq}(x_i, x_i, \eta = 0, f)} dx_j, [\text{m}]$
L_t	Normalized spanwise correlation length scale of inflow turbulence, $\frac{8\lambda \left[\Gamma(1/3) \right]^2}{3 \left[\Gamma(5/6) \right]^2} \frac{\hat{K}_x^2}{(3 + 8\hat{K}_x^2) \sqrt{1 + \hat{K}_x^2}}$
L_η	Spanwise pressure correlation length scale, $\int_0^{\eta_{\max}} \frac{S_{qq}(x_i, x_j, \eta, f)}{S_{qq}(x_i, x_i, \eta = 0, f)} d\eta, [\text{m}]$

m_n	Unique number given to each microphone
M	Mach number
M_∞	Free-stream Mach number
M_s	Sennhieser microphone calibration
n	Exponent in Kings law, 0.45
n_i	Unit outward normal on s in tensor notation
N	Number of ensemble averages
N_a	Normal-to-airfoil chord unsteady force, [N/m]
N_s	Record length
P	Magnitude of fluctuating surface pressure, [Pa]
p	Fluctuating pressure in far-field, [Pa]
p'	Fluctuating surface pressure, [Pa]
p'_{ij}	Compressive stress tensor, [Pa]
P_L, p_L	Fluctuating surface pressure on lower surface of airfoil, [Pa]
p_o	Pressure at infinity, [Pa]
P_s	Fluctuating pressure produced by calibration speaker, [Pa]
P_U, p_U	Fluctuating surface pressure on upper surface of airfoil, [Pa]
$\overline{p^2}$	Mean square pressure, $\int_0^\infty S_{qq}(x = x', \eta = 0, \omega) d\omega$, [Pa ²]
$\dot{p}(x, y, t)$	Substantial derivative of surface pressure, $\frac{\partial p(x, y, t)}{\partial t} - U_\infty \frac{\partial p(x, y, t)}{\partial x}$, [Pa/sec]
q	Free-stream dynamic pressure, $1/2\rho U_\infty^2$, [Pa]

\vec{q}	Perturbation velocity vector, $u\hat{i} + v\hat{j}$
r	Cylinder radius, [m]
\vec{r}	Position vector
Re	Reynolds number based on airfoil chord, $U_\infty c / \nu$
Re_θ	Reynolds number based on momentum thickness, $U_\infty \theta / \nu$
$R_{\dot{p}\dot{p}}$	Correlation coefficient of substantial derivative of surface pressure and itself, $\overline{\dot{p}(x, y, t) \dot{p}(x', y', t + \tau)}$
R_{pp}	Correlation coefficient of surface pressure with itself, $\frac{\overline{p(x, t) p(x', t + \tau)}}{\sqrt{\overline{p^2(x)} \overline{p^2(x')}}}$
R_{pu}	Correlation coefficient of surface pressure with fluctuating u -component of velocity, $\frac{\overline{p(x, t) u(t + \tau)}}{\sqrt{\overline{p^2(x)} \overline{u^2}}}$
$R_{\Delta\dot{p}\Delta\dot{p}}$	Correlation coefficient of differenced substantial derivative of pressure and itself, $\overline{\Delta\dot{p}(x, y, t) \Delta\dot{p}(x', y', t + \tau)}$
r_s	Distance between a point where the surface pressure fluctuations are measured and the point in the flow that is the source of the surface pressure fluctuations, [m]
s	Boundary defined by surface
s, n	Curvi-linear coordinate system with s directed along a streamline and n perpendicular
S_e	Sears function
S_{ij}	Distortion tensor
S_p	Response of calibration speaker, [Pa/V]
S_{qq}	Cross-spectral density of surface pressure fluctuations, [Pa ² /Hz], see also Appendix A
S_{qq}^Δ	Cross-spectral density of pressure difference fluctuations, [Pa ² /Hz], see also Appendix A
S_R	Sampling rate, [Hz]

t	Time, [sec]
T_a	Tangential-to-airfoil chord unsteady force, [N/m]
t_g	Blade tip gap, [m]
T_{ij}	Lighthill stress tensor, [Pa]
u, v, w	Fluctuating velocity components in $x, y,$ and z direction, [m/sec]
\bar{U}	Total inflow velocity, [m/sec]
\bar{U}_∞	Mean free-stream inflow velocity vector, [m/sec]
U_∞	Mean free-stream velocity in x direction, [m/sec]
U_e	Velocity at the edge of boundary layer, [m/sec]
U_{eff}	Cooling velocity in Kings law, [m/sec]
\bar{U}_i	Time averaged mean velocity, [m/sec]
$\overline{u_i u_j}$	Time averaged Reynolds stresses, [m ² /sec ²]
u_i	Fluctuating velocity components in tensor notation, [m/sec]
u_L	Perturbation velocity in x direction on lower surface of flat plat airfoil, [m/sec]
u_U	Perturbation velocity in x direction on upper surface of flat plat airfoil, [m/sec]
u_τ	Friction velocity, $\sqrt{\tau_w/\rho}$, [m/sec]
V_1	White noise voltage signal, [V]
V_2	Voltage signal generated by microphone during calibration, [V]
v_m	Microphone output voltage, [V]
Vol	Volume
w_a	$\sqrt{\left(\frac{M_\infty}{\beta^2}\right)^2 - \left(\frac{k_y}{\beta}\right)^2}$

w_o	Upwash amplitude, [m/s]
X_1	$\frac{X_1}{U_\infty} = \frac{x_1}{U_\infty} + \int_{-\infty}^{x_1} \left[\frac{1}{U'(x_1, X_3)} - \frac{1}{U_\infty} \right] dx_1$
X_3	Proportional to stream-function
x_o	Distance between a measurement location on the airfoil surface at zero angle of attack and the same measurement location when at some angle of attack, [m]
z	Complex number, $x + iy$
z_o	Complex number, $x_o + iy_o$
ΔP	Pressure difference, $P_L - P_U$, [Pa]
Δp_t	Temporal derivative of pressure difference, $\int_0^\infty \frac{\partial}{\partial t} [p_L(x, t) - p_U(x, t)] e^{-i2\pi ft} dt$, [Pa/sec]
Δp_x	Spatial derivative of pressure difference, $\int_0^\infty \frac{\partial}{\partial x} [p_L(x, t) - p_U(x, t)] e^{-i2\pi ft} dt$, [Pa/m]
$\Delta \dot{p}$	$\frac{D}{Dt} (P_U - P_L)$, [Pa/sec]
Φ_{ij}	Non-dimensional undistorted turbulence energy spectrum
Φ_{C_L}	Normalized lift spectrum, $G_{LL}(\alpha, \omega) \frac{4}{\rho U_\infty^2 b}$, [Pa/m ³ Hz ²]
Φ_{ij}^*	Non-dimensional distorted turbulence energy spectrum
$\Gamma()$	Gamma function
Γ	Circulation, [m ² /sec]
Ω_i	Vorticity tensor, [sec ⁻¹]
α	Angle of attack, [deg]
β	$\sqrt{1 - M^2}$
δ	Boundary layer thickness, [m]

δ_{ij}	Kroneker delta, 0 if $i \neq j$, 1 if $i = j$
δ^*	Boundary layer displacement thickness, [m]
ε	Dissipation rate of turbulence kinetic energy, [m^2/sec^3]
ε_c	Uncertainty in pressure spectrum based on statistical convergence
ε_{ijk}	Unit alternating tensor
ε_{p^2}	Uncertainty in mean square pressure
$\varepsilon_{p'}$	Uncertainty in root mean square pressure
ε_r	Uncertainty in pressure spectrum based on repeated measurements
ϕ	Phase angle, [deg]
ϕ_L	Velocity potential on lower surface of flat plat airfoil
ϕ_U	Velocity potential on upper surface of flat plat airfoil
ϕ_{ww}	energy spectrum of the upwash turbulence, [m^2/sec^2]
γ	Vortex strength [sec^{-1}]
γ_p^2	Coherence between two pressure measurement locations
η	Spanwise separation between two points, $y - y'$, [m]
λ	Integral scale of turbulence, [m]
ν	Kinematic viscosity, [m^2/sec]
π	~ 3.14
θ	Angle between the outward normal and a vector which originates from the location of the outward normal and extents to the location where p is to be determined
ρ	Density, [kg/m^3]
ρ_o	Density at infinity, [kg/m^3]

σ_a	$\frac{Mk_x}{\beta k_y}$
σ_{ij}	Viscous stress tensor, [Pa]
τ	Time delay, [sec]
τ_R	Retarded time, [sec]
τ_w	Shear stress magnitude at the wall, [Pa]
ω	Angular frequency, [rad/sec]
ω_r	Reduced frequency, $2\pi fb/U$
χ_l	Non-dimensional distorted wavenumber vector, $k_i(S_{li})^{-1}$

1. INTRODUCTION

When a body moves through an unsteady fluid the interaction of the two produces unsteady pressure fluctuations on the surface of the body which may radiate to the far-field (i.e. generates noise). The study of fluid/body interaction is of particular interest due the resulting noise generation (aerodynamic noise) as well as the unsteady loading produced which may induce undesirable vibration.

A rather complex flow field develops as a body moves through an unsteady fluid. Near the surface of the body a boundary layer develops transitioning from laminar to turbulent. Associated with the turbulent boundary layer are tiny eddies which vary spatially and temporally and thus produce pressure fluctuations on the surface of the body. The airfoil also experiences fluctuating pressure as a result of the unsteadiness in the incoming fluid. These pressure fluctuations are associated with the inviscid response of the airfoil, or in other words, the imposition of the non-penetration condition. Both types of pressure fluctuations, those arising from the boundary layer and those from the inviscid response, are sources of noise and vibration. If the body is aerodynamic (such as an airfoil) and the characteristic scale of the unsteady motion (i.e. turbulence) on the order of the body dimensions the dominant source of noise arises from the inviscid response.

The noise generated from turbo-machinery, helicopters, aircraft, and marine vehicles has made the study of fluid/body interaction quite important. However, understanding this complex interaction mathematically or experimentally has proven to be quite difficult.

1.1 Background

1.1.1 Pressure Fluctuations

The study of aerodynamic sound amounts to understanding how rotational kinetic energy is converted to acoustic waves involving longitudinal vibration¹. Lighthill (1952, 1954) developed the theory of aerodynamic sound through the acoustic analogy. Lighthill (1952, 1954) considers a region of fluctuating or turbulent fluid which occupies a larger volume of fluid at rest. He proposes that the equations describing the density variation in this fluid are equivalent to equations describing a uniform acoustic medium subject to an external fluctuating forcing

¹ Howe, M. S., *Acoustics of Fluid Structure Interactions*, Cambridge Press, 1998

function. Using this analysis Lighthill (1952, 1954) derives an inhomogeneous, exact wave equation for the propagation of sound generated aerodynamically and is given as,

$$\frac{\partial^2 \rho}{\partial t^2} - c_o^2 \nabla^2 \rho = \frac{\partial^2 T_{ij}}{\partial x_i \partial x_j} \quad (1.1)$$

where, T_{ij} is the Lighthill stress tensor defined as,

$$T_{ij} = \rho u_i u_j + \tau_{ij} + (p - c_o^2 \rho) \delta_{ij}. \quad (1.2)$$

The term $\rho u_i u_j$ is the Reynolds stress tensor, τ_{ij} is the viscous stress tensor, and $p - c_o^2 \rho$ is the thermal stress. The Lighthill stress tensor represents the external stress system acting on the uniform acoustic medium and is the difference in the effective stresses in the flow and the stresses in the uniform acoustic medium at rest.

The most general solution of an exact, inhomogeneous wave equation was first given by Stratton (1941) in his book *Electromagnetic Theory* and makes concessions for a control surface, S . If the surface is stationary and rigid, as in the case of an airfoil immersed in turbulent flow, the sound generated can be determined by implementing Curle's (1955) solution to Lighthill's equation. Here the time domain Greens function is used to derive the outgoing wave solution in integral form. In doing so, the notion of retarded time is developed to mean the time for a disturbance at location \bar{y} to propagate to location \bar{x} external to a boundary defined by surface s . Curle's equation is given as

$$c_o^2 (\rho - \rho_o) = \frac{\partial^2}{\partial x_i \partial x_j} \int_{Vol} [T_{ij}] \frac{dVol}{4\pi |\bar{x} - \bar{y}|} - \frac{\partial}{\partial x_i} \oint_s [p'_{ij}] \frac{ds_j(\bar{y})}{4\pi |\bar{x} - \bar{y}|}. \quad (1.3)$$

where quantities in $[]$ brackets are evaluated at the retarded time $\tau_R = t - \frac{|\bar{x} - \bar{y}|}{c_o}$ and $p'_{ij} = (p - p_o) \delta_{ij} - \sigma_{ij}$ is the compressive stress tensor. Also, δ is the Kroneker delta-function. Rearranging equation (1.3) allows the pressure in the far-field to be approximated as

$$p(\bar{x}, t) \approx \frac{x_i x_j}{4\pi c_o^2 |\bar{x}|^3} \frac{\partial^2}{\partial t^2} \int_{Vol} [\rho_o u_i u_j] dVol + \frac{x_i}{4\pi c_o |\bar{x}|^2} \frac{\partial}{\partial t} \oint_s [n_j p'_{ij}] ds \quad (1.4)$$

where n is the unit normal on s directed into the fluid. In doing so, the aerodynamic sound is represented with sound produced by quadrupole (first term, volume integration) and dipole (second term, surface integration) sources. Dipole sources result from the net unsteady force exerted on the fluid by the airfoil or the inviscid response. Quadrupole sources result from the

turbulence stress distribution and are typically associated with the turbulent boundary layer. Under certain circumstances equation (1.4) can be simplified to include only the dipole term. This is evident through comparison of the order of sound power of each source. The dipole term generates sound power on the order $\sim \lambda^2 \rho_o u^3 M^3$, where λ is the characteristic length of the turbulence. A quadrupole term produces sound power on the order $\sim \lambda^2 \rho_o u^3 M^5$. Evaluating the ratio of sound power of each, a factor of $1/M^2$ persists. Therefore, the acoustic power in the dipole term exceeds that from the quadrupole by a factor of $1/M^2$. The radiation of sound is thus dominated by the dipole term when the Mach number is small ($U_\infty/c_o \ll 1$). This interaction situation is defined as acoustically compact and as such can be represented solely by dipole-sources. Equation (1.4) then becomes

$$p(\bar{x}, t) \approx \frac{x_i}{4\pi c_o |\bar{x}|^2} \frac{\partial}{\partial t} \oint_s [n_j p'_{ij}] ds \quad (1.5)$$

If the shear stress components of p'_{ij} are small compared to the local surface pressure fluctuation p' , equation (1.5) can be further simplified to give a simple relation between the acoustic and surface pressure

$$p(\bar{x}, t) \approx \frac{\cos \theta}{4\pi c_o x} \frac{\partial}{\partial t} \oint_s [p'] ds \quad (1.6)$$

where θ is the angle between the outward normal and a vector which originates from the location of the outward normal and extends to the location where p is to be determined.

1.1.2 Unsteady Thin Airfoil Theory

Equation (1.6) clearly demonstrates if one wishes to obtain the acoustic pressure (far-field noise) an accurate estimate of the surface pressure is required. Thus, researchers embarked on a mission to develop techniques for computing the unsteady surface pressure of an airfoil interacting with turbulence. However, this is a forbidding task determining the unsteady surface pressure of an airfoil with thickness, at angle of attack, and immersed in a complex flow. Consequently, researchers worked to simplify the problem to a tractable nature. In doing so they developed unsteady thin airfoil theory. As the name suggests the airfoil is assumed to be thin, in fact having no actual thickness. Also, the airfoil is not at angle of attack and viscous effects are neglected (an implicit assumption in moving from equation 1.5 to equation 1.6). The airfoil can then be modeled as a vortex sheet with strength $\gamma(x, t)$ subject to a sinusoidal inflow with a wake

extending to infinity, $\gamma(x + tU_\infty)$ (as shown in figure 1.1). The fluid motion is irrotational everywhere else with a perturbation velocity defined by a velocity potential which vanishes at infinity. Other conditions imposed include the Kutta condition on the trailing edge, a kinematic boundary condition on the airfoil surface and a dynamic boundary condition on the vortex wake. Lastly, since the airfoil was once at rest the total circulation about the airfoil and its wake must vanish.

Consider figure 1.1;

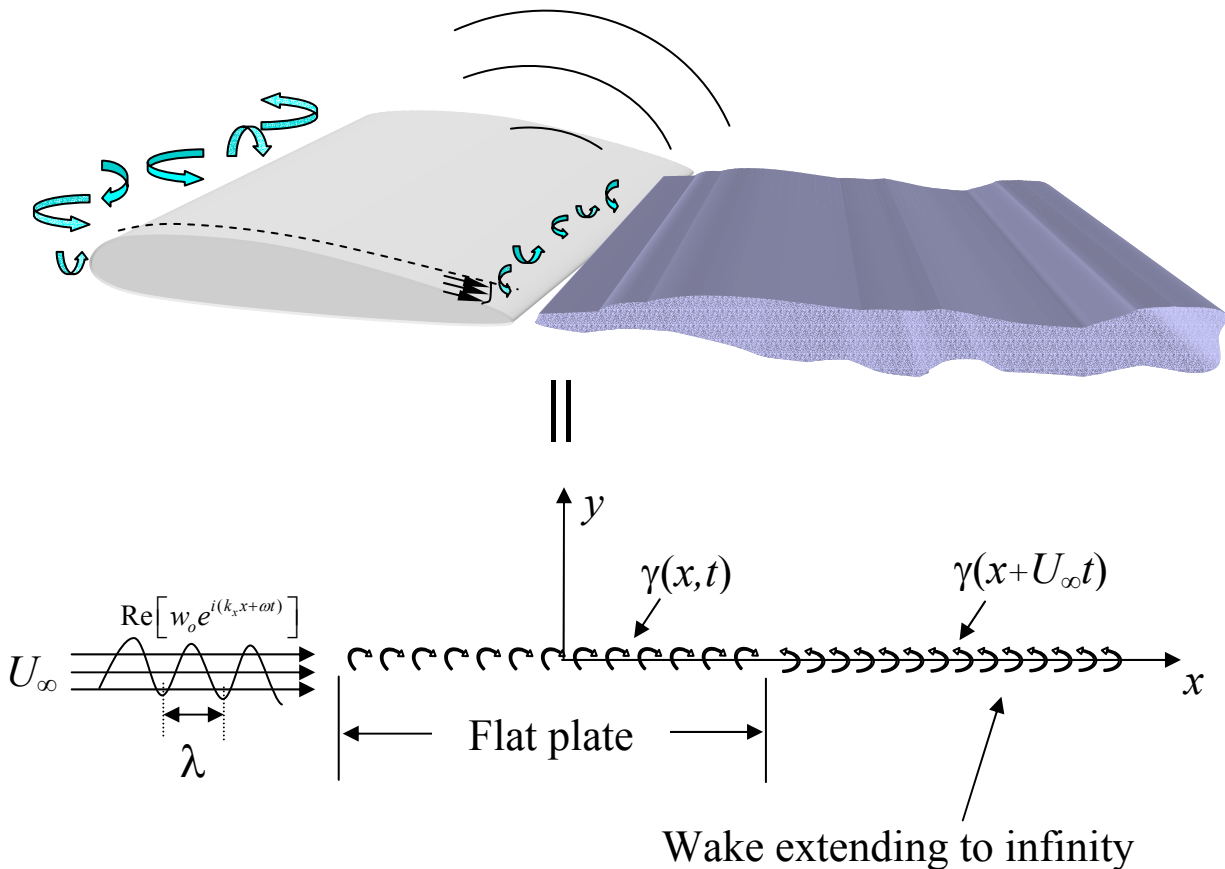


Figure 1.1: Unsteady Thin Airfoil Theory

the total flow (a sinusoidal gust with wave front parallel to the airfoil leading edge) is written as

$$\begin{aligned} \vec{U}(\vec{r}, t) &= \vec{U}_\infty + \vec{q}(\vec{r}, t) \\ &= (u + U_\infty)\hat{i} + v\hat{j} \end{aligned} \tag{1.7}$$

where $\vec{q}(\vec{r}, t) = u\hat{i} + v\hat{j}$ is the perturbation velocity and $\vec{r} = x\hat{i} + y\hat{j}$ is the position vector. It is convenient to write the v velocity component (or upwash) as $w_0 \sin(k_x x + \omega t)$ or similarly as

$\text{Re}\left[w_o e^{i(k_x x + \omega t)}\right]$ where w_o is the upwash amplitude; in doing so any form of homogeneous turbulent upwash (in the 2-dimensional sense) can be built using Fourier analysis. Note that the frequency, ω is related to the velocity as $\omega = k_x U_\infty$. Using this form of the upwash the perturbation velocity becomes

$$\vec{q} = u\hat{i} + w_o \sin(k_x x + \omega t) \hat{j} \quad (1.8)$$

Now, the flat plate with circulation is represented by a distribution of vorticity with strength γ . As such, potential flow theory gives the following relationship between the perturbation velocity and vorticity, in complex number form

$$u(z, t) - iv(z, t) = \frac{i}{2\pi} \int_{-c/2}^{\infty} \frac{\gamma(\xi, y, t)}{(z - z_o)} dz_o \quad (1.9)$$

where $i = \sqrt{-1}$, $z = x + iy$ and $z_o = x_o + iy_o$. Applying the dynamic boundary condition on the wake gives

$$\gamma(x, t) = \gamma(z_o + U_\infty t) \quad c/2 < x < \infty \quad (1.10)$$

and decomposing equation (1.9) into its real and imaginary parts produces the velocity components in terms of vorticity

$$u(\vec{r}, t) = \frac{1}{2\pi} \int_{-c/2}^{\infty} \frac{\gamma(\xi, y, t)y}{(x - \xi)^2 + y^2} d\xi \quad (1.11)$$

and

$$v(\vec{r}, t) = \frac{-1}{2\pi} \int_{-c/2}^{c/2} \frac{\gamma(\xi, y, t)(x - \xi)}{(x - \xi)^2 + y^2} d\xi + \frac{-1}{2\pi} \int_{c/2}^{\infty} \frac{\gamma(\xi + U_\infty t)(x - \xi)}{(x - \xi)^2 + y^2} d\xi \quad (1.12)$$

The complete solution can now be constructed by imposing the kinematic boundary condition (no flow through the surface) on the vertical velocity (1.12) which gives

$$-w_o \sin(k_x x + \omega t) = \frac{-1}{2\pi} \int_{-c/2}^{c/2} \frac{\gamma(\xi, y, t)(x - \xi)}{(x - \xi)^2 + y^2} d\xi + \frac{-1}{2\pi} \int_{c/2}^{\infty} \frac{\gamma(\xi + U_\infty t)(x - \xi)}{(x - \xi)^2 + y^2} d\xi \quad (1.13)$$

Equation (1.13) governs the relationship between the inflow and the vorticity under the assumption prescribed above. Through inversion of (1.13) the vorticity can be obtained and utilized to compute the unsteady pressure on the airfoil surface. With the surface pressure known equation (1.6) can be used to determine the pressure in the far-field.

The relationship between the pressure and vorticity is now presented. First, defining the pressure difference between the upper and lower side of the airfoil

$$\Delta P = P_U - P_L \quad (1.14)$$

where P_U is the pressure on the upper side of the airfoil and P_L the lower side. By unsteady Bernoulli's equation the velocity around the airfoil can be related to the surface pressure as

$$\Delta P = P_U - P_L = -\rho \frac{\partial \phi_U}{\partial t} - \frac{\rho}{2} (U_\infty + u_U)^2 + \rho \frac{\partial \phi_L}{\partial t} + \frac{\rho}{2} (U_\infty + u_L)^2 \quad (1.15)$$

with ϕ_U and ϕ_L are the velocity potential on the upper and lower surface and u_U and u_L the perturbation velocity in the \hat{i} direction on the upper and lower surface. Upon linearization of equation (1.15) the following relationship between unsteady pressure and velocity is obtained

$$\Delta P = \rho \frac{\partial (\phi_L - \phi_U)}{\partial t} + \rho U_\infty (u_L - u_U) \quad (1.16)$$

This equation can now be cast in terms of the vorticity by noting that equation (1.11) can be simplified when evaluated on the upper and lower surface of the flat plate to give

$$u(x, y = 0^\pm, t) = \pm \frac{1}{2} \gamma(x, t) \quad (1.17)$$

where $y = 0^\pm$ indicates the upper and lower surface of the flat plate. Equation (1.16) can then be recast as

$$\Delta P = -\rho U_\infty \gamma(x, t) - \frac{\partial}{\partial t} \int_{-\infty}^x \gamma(x, t) dx \quad (1.18)$$

A relationship has now been established (equation 1.13 with 1.18) between a sinusoidal inflow and the surface pressure. The crucial step in this solution is the ability to solve for the vorticity in (1.13). Considerable effort has been spent on extracting a solution to (1.13) in addition to extending Unsteady Thin Airfoil theory to the more realistic 3-dimensional case. The focus is now shifted to solutions to (1.13) and the search for rational representations of the airfoil response.

1.2 Theoretical Unsteady Response of an Airfoil

1.2.1 The Exact Solution to Unsteady Thin Airfoil Theory

Von Karman and Sears (1938) followed by Sears (1941) were some of the first to pioneer the theory of turbulence/airfoil interaction. Using the Unsteady Thin Airfoil approach Sears

derived an explicit expression for lift and moment that involve a combination of Bessel functions which have become known as the Sears function.

Liepmann (1952) extends Sears theory to consider the case of airfoil encountering turbulence of scale much greater than the span and utilizes statistical concepts in development of the lift response. He formulates the mean C_L squared in terms of an admittance function (Sears functions) and the power spectrum of a sinusoidal gust. This method is extended by Liepmann (1955) to allow the usage of the frequency spectrum of the incoming turbulence. Specifically, he introduces a two-wavenumber spectrum (spanwise and streamwise) to describe the turbulence which allows consideration of the more practical situation wherein turbulence scale is smaller than the span. The sinusoidal variation in angle of attack along the span is accounted for by taking the section lift at each spanwise location to be given by the local angle of attack and the two-dimensional Sears function. Ribner (1956) furthers this statistical approach to allow consideration of the full, 3-wavenumber turbulence spectrum and three dimensional response function.

1.2.2 Approximate Analytic and Numeric Models

Unsteady Thin Airfoil Theory is a 2-dimensional theory and therefore does not easily allow for the more realistic case of a sinusoidal gust with wave front skewed relative to the airfoil leading edge. Additionally, Unsteady Thin Airfoil Theory does not account for compressibility which is quite important in the production of aerodynamic sound. Therefore several approximate closed form and numerical solutions have been developed to address these cases.

1.2.2.1 Skewed Incompressible Gust

The skewed gust case was first considered by Filotas (1969) who found a closed form expression for the problem of an infinite, thin airfoil encountering a skewed, incompressible gust at zero angle of attack and derived approximate expressions for the lift and pressure distribution. His solution is based on Unsteady Thin Airfoil theory and utilizes an interpolation scheme to solve for the vorticity. His results were later demonstrated to be rather crude. Graham (1970a) also considered the skewed gust case and formulated a solution for the vorticity based on a Chebyshev series. The analysis is rather cumbersome in nature based on the consideration of both streamwise and spanwise shedding of vorticity due to the varying angle of attack along the

span. Graham provides the equations to numerically compute unsteady lift, chordwise pressure, and moment.

Mugridge (1970) provides a closed form expression for the lift response of a thin airfoil of finite span immersed in a convected skewed sinusoidal upwash. He also showed the interesting effect that as spanwise wavelength of the gust becomes small compared to the span cancellation of surface pressure fluctuations occurs everywhere except at the extreme edges of the airfoil span.

Amiet (1976a) developed a skewed gust incompressible solution valid at high reduced frequencies and large spanwise wave numbers from which the full compressible, skewed gust response can be derived. This work is extended by Amiet (1976b) to small spanwise wavenumbers utilizing Graham's (1970b) similarity rules with Amiet's (1974) compressible gust solution thus providing a solution to the complete spanwise wavenumber range.

1.2.2.2 Compressible Parallel Gust

The interaction of turbulence with a lifting body and the noise produced are tied closely to the compressible nature of the free stream fluid. It is therefore critical to consider the effects of compressibility in the turbulence/airfoil interaction problem. Early consideration of this important effect has been given by Possio (1938) and Reissner (1951). Reissner (1951) builds on Possio's (1938) work deriving a solution in terms of the velocity potential using Mathieu functions. From this solution he formulates expressions for unsteady lift and moment. Amiet (1974) modifies Miles (1950) solution to consider the case of a compressible two-dimensional gust problem and develops a closed form expression valid at low frequencies. Amiet (1976a) later derived a closed form expression for the two-dimensional, compressible upwash problem valid at high reduced frequency. He employed the first two steps of an iterative procedure given by Landahl in which the leading and trailing edge boundary conditions are alternately applied. For this reason the theory only applies to high frequencies when the acoustic wavelengths are not large compared to the chord.

Amiet (1975) also developed a relationship between the lift response function and turbulence spectrum which allowed prediction of far field acoustic radiation. In addition, he showed acoustic predictions can be made under certain conditions using only the unskewed gust response and limited information about the spanwise wavenumber content of the turbulence.

1.2.2.3 Skewed Compressible Gust

Having developed solutions for the parallel, compressible and skewed, incompressible gusts researchers began to formulate approximate solutions to the more realistic case of a skewed, compressible gust. Graham (1970b) extends his work (although still computational in nature) to the case of a skewed, compressible gust encountering a flat plate at zero incidences. He transforms this problem into two sub-problems via a Prandtl-Glauert transformation depending on the spanwise trace speed of the gust along the airfoil leading edge. In the case of a subsonic trace speed the plate response is expressed in terms of the incompressible skewed gust problem which has been solved by Graham (1970a). For a supersonic trace speed the response is recast in terms of the unskewed, compressible gust which has been solved by Possio (1938).

Adamczyk and Brand (1972) formulated a closed form solution for the skewed compressible gust which allows calculation of far field noise. Adamczyk (1974) wishing to more clearly define the unsteady pressure, lift and moment response developed an approximate theory for the compressible, skewed gust which compared favorably to the exact theory of Graham (1970b).

Chu and Widnall (1974) extend Amiet and Sears' (1970) approximation to derive a similarity rule for the three-dimensional interaction of a two-dimensional wing and convected oblique sinusoidal gust in compressible flow valid at low reduced frequency. Osborne (1971) employed the GASP approximation to transform the Sears' two-dimensional, incompressible solution into one for compressible flow in a straightforward analytic form. Although, as pointed out by Amiet (1974) this method cannot be utilized for the case of a two-dimensional airfoil since the solution involves integration over the infinite span. Therefore, Sing and Widnall develop a similarity rule which is valid in the presence of an infinite span wing. This method coupled with either Sears' (1941) two-dimensional or Filotas' (1969) three-dimensional incompressible flow solutions can be used as the bases for construction of analytic expressions for unsteady lift.

A second order theory for the three-dimensional, compressible case was developed by Graham and Kullar (1977). These researchers used a general perturbation series to derive a second order solution for lift coefficient and compared their results with those of Amiet (1974) and other approximate solutions. They demonstrated insufficiencies in Amiet's solution as spanwise wavenumber tends to zero.

Martinez and Widnall (1980) unified aerodynamic/acoustic theory through the derivation of a closed form expression which couples the airfoil response with the acoustic field. Building on the work of Amiet (1976a) and Adamczyk (1974) they give a high frequency approximation to the airfoil response for a skewed, compressible gust from which both surface pressure fluctuations and far field noise can be determined. Their solution agrees with Adamczyk's (1974) for the case of zero sweep and collapses to Amiet (1976a) for the case of a parallel gust.

1.3 Effects of Angle of Attack and Thickness on the Airfoil Response

Unsteady Thin Airfoil theory provides well as a tool for understanding critical aspects of turbulence-airfoil interaction. However, real airfoils have thickness and are typically at non-zero angles of attack. If one is to produce superior aerodynamic devices (in terms of reducing aerodynamic noise) an improved representation of the airfoil and interaction is mandatory. Therefore, researchers aware of the deficiencies of Unsteady Thin Airfoil Theory began to investigate possible avenues for the incorporation of thickness and mean loading (i.e. angle of attack) effects.

Perhaps the earliest attempt to consider angle of attack was that of Horlock (1968) and later extended by Morfey (1970). These researchers present a method for determining the lift fluctuation of an airfoil at angle of attack due to a gust parallel to the uniform flow field. Combining this method with established theory for transverse gusts (perpendicular to undisturbed flow) Horlock arrives at the fluctuating lift produced by both gust types. In his formulation Horlock argues that unsteady lift fluctuations arise not just by upwash fluctuations (producing an instantaneous change in angle of attack) but also by the streamwise velocity fluctuations changing the scaling of the lift coefficient.

Atassi (1984) develops a theory for computing the unsteady lift of a thin airfoil with small camber and at small angle of attack. The unsteady lift is constructed by linear superposition to the Sears lift accounting separately for airfoil thickness, camber, and angle of attack. By developing a solution built on the Sears function Atassi's (1984) theory is constricted to the case of a parallel gust and thus does not well represent actual fluid/body interaction. However, being a closed form solution does make this theory desirable and convenient for comparison with experimental data.

1.3.1 Effects of Distortion: Rapid Distortion Theory

Goldstein and Atassi (1976) were conceivably the first to consider the distortion of incoming turbulence in development of the airfoil response function. They employed the technique of Rapid Distortion Theory (RDT) which considers the distortion of an incoming vortical gust (tilting and stretching of vorticity vector) by the steady-state potential flow around the airfoil. They formulate a solution for the case of a two-dimensional, incompressible gust providing separate methods for calculating the effects of angle of attack, camber, and thickness on the unsteady lift response in terms of a correction to the Sears formula. Interestingly, they show the effect modeled by Horlock's theory is completely cancelled through a term arising from the distortion.

McKeough and Graham (1980) extended the RDT based prediction to the case of a skewed gust which they found to be consistent with Goldstein and Atassi's result for zero spanwise wavenumber. They determined that first order corrections to the zero angle of attack case arise from both distortion and the streamwise component of the velocity fluctuation. They also show that in the case of an airfoil immersed in homogenous isotropic turbulence these corrections cancel.

Atassi and Grzedzinski (1989) furthered the capability of RDT as an airfoil response prediction tool through the elimination of a key singularity arising from the infinite distortion of incoming vortical disturbances at the stagnation point. This singularity forms when applying RDT around a closed body, such as an airfoil and extends itself along the surface of the body at the exact location where the airfoil response is desired. Atassi and Grzedzinski showed that the irrotational field generated by the response of the airfoil must contain a canceling singular behavior and thus proposed a three way split of the fluctuating velocity field that accomplished this. Although greatly extending the capabilities of RDT in prediction of the airfoil response Atassi and Grzedzinski's method is a numerical procedure and their solution only considers the response at a few discrete frequencies.

Meyers and Kerschen (1995) develop a theoretical model for the noise generated when a convected gust encounters an airfoil at non-zero angle of attack. The analysis uses RDT to consider high frequency gusts (i.e. noncompact--gust wavelength is small compared to the airfoil chord). They show the level of noise generated is increased by mean loading and the mean

loading effects scale on the airfoil total lift. Their analysis is somewhat limited, however, due to the high frequency nature of the theory.

Scott and Atassi (1995) building on Scott (1990) extended the Atassi and Grezedzinski (1989) approach to a numerical method for solving subsonic flows with convected, three-dimensional vortical waves around a lifting airfoil. Their approach offers the computational efficiency of potential flow methods while accounting for the convection and distortion of incoming vortical disturbances by the mean flow field surrounding the airfoil. They compare their numerical solution of lift response to the Sears function and solutions of Possio's integral equation investigating the effects of thickness, camber and angle of attack at particular wavenumber frequencies. In general, they find that thickness becomes important at higher frequencies. They also showed that for small angles of attack ($\sim 1^\circ$) a reduction in unsteady lift occurs at low frequencies.

Reba and Kerschen (1996) develop a theory for the influence of angle of attack on the unsteady pressure distribution for a flat plate interacting with a high frequency gust. This work is extended in Reba and Kerschen (1997) to include the effects of airfoil camber. Their analysis utilizes RDT to consider the distortion of small amplitude vortical disturbances. The case of high aerodynamic reduced frequency, k is considered. The analysis shows that moderate levels of steady loading can significantly increase the amplitude of unsteady pressure fluctuations on the airfoil surface.

1.4 Experimental Studies of the Airfoil Response

Comparatively few experimental studies have complimented the development of airfoil response theories. Those that have been performed usually consist of measurements at a few discrete frequencies or measurement locations providing a crude representation of the airfoil response function.

Jackson, Graham and Maull (1973) measured the lift spectrum on a NACA 0015 in grid generated turbulence ($\lambda/c = 0.417$) at a Reynolds number (based on chord) of 16000 and compared the admittance function with two-dimensional Sears based on Liepmann's (1952, 1955) two-dimensional theory and his strip theory. They found good agreement with Graham's (1970a) three-dimensional theory while two-dimensional and strip theory overpredicted by an order of magnitude and 50% respectively. Also, the measured admittance increases above the

three-dimensional theory at low frequencies the reason for which the authors believe is related to the distortion of incoming turbulence which acts to enhance lift.

Commerford and Carta (1970, 1973) investigated unsteady pressure at 5 chordwise locations on a 5% thick circular arc airfoil immersed in a circular cylinder wake at a chord Reynolds number of 400000. The cylinder wake produced a sinusoidal, two-dimensional upwash gust with a reduced frequency of 3.9. They found reasonable agreement at low angles of attack with the Sears function although noted that the phase angle variation of chordwise pressure was not well predicted.

An experimental study of a circular arc airfoil immersed in a periodic wake generated by a pinwheel was performed by Fujita and Kovasznay (1974). Pressure measurements were made and compared to Meyer's theory (thin airfoil theory) for varying angles of attack in the time domain. They show reasonable agreement between experiment and theory for unstalled angles of attack.

Patterson and Amiet (1976a, 1976b) performed one of the few systematic unsteady pressure measurements which allow unambiguous comparison with theoretical developments. A NACA 0012 was immersed in grid generated turbulence of von Karman like spectrum ($L/c = 0.13$) and the unsteady pressure measured between 15 and 70% chord through embedded transducers. They also measured radiated noise level with microphones located outside of the wind tunnel jet. One transducer on the airfoil could be moved in the spanwise direction allowing measurement of the spanwise correlation. Measurements were performed at 4 speeds between 40 and 120m/s. They showed reasonable agreement between measured surface pressure spectra and correlations and Amiet's (1976a) high frequency prediction at zero angle of attack. Amiet's (1975) far field predictions also agreed well with far field measurements. These researchers also show an increase in radiated noise when the angle of attack is set to 8° and report (although do not show) an increase in surface pressure fluctuations which is small but measurable.

McKeough and Graham (1980), using a configuration similar to Jackson *et al.* complimented their RDT prediction with unsteady lift measurements on a NACA 0015 at 0° and 10° angle of attack immersed in grid generated turbulence ($\lambda/c = 0.4$, turbulence intensity = 5.8%). Unsteady lift measurements were also made at 0° angle of attack in lower turbulence intensity flow ($\lambda/c = 0.38$, turbulence intensity = 3.7%). They showed as much as a factor of 2 increase in mean-squared lift fluctuation at low reduced frequencies (<1) and argued that this

must be a second order effect due to the canceling of first order effects arising from the distortion and the streamwise component of the velocity fluctuation in the case of isotropic, homogenous turbulence.

Williams and Harris (1984) measured far field noise radiated by a helicopter rotor operating in grid and wake generated turbulence. These researchers uncovered an increase in peak SPL of broadband radiated noise with increasing mean loading. Also demonstrated was a greater rate of increase when the rotor is subject to lower turbulence levels which Williams and Harris feel is related to the distortion of the turbulence encountering the lifting airfoil.

1.5 Unsteady Response of a Cascade

The work presented above, both experimental and theoretical deals strictly with the case of a single airfoil encountering a turbulent flow wherein the inflow can be described by a Fourier sum over many sinusoidal waves (i.e. homogenous turbulence). However, significant fluid/body interaction noise is also generated when an airfoil or multiple airfoils are immersed in a turbulent flow which may or may not be homogenous. Such scenarios arise in turbo-fan machinery and sophisticated marine propulser systems wherein in a series of airfoils, or blades distributed circumferentially interact with the wake of a stator row to generate flow induced noise.

Several variations arise under this new scenario which require alternate modeling techniques. First, this interaction requires not just modeling a single airfoil but multiple airfoils to account for the effect each has on the other. Second, a gap often exists between the tip of each airfoil and housing in which it rotates necessitating the use of a 3-dimensional theory. Lastly, the inflow, depending on the configuration conditions may be inhomogeneous requiring additional modeling considerations. As such, research has been underway to investigate the response of a cascade of blades with and without tip gaps and in both homogeneous and inhomogeneous turbulence.

1.5.1 Theoretical Cascade Work

Kaji and Okazaki (1970) develop a theory for a cascade of airfoils in 2-dimensions. Their method uses a distribution of dipole sources along the surface of the blade. The source strength and velocity disturbance are related through an integral equation which is solved using a collocation technique. The 2-dimensional nature of this theory limits its usefulness. Kaji and Okazaki (1970a) in a later publication use their theory for the case of a rotor/stator interaction.

A theory for the unsteady loading, vortical field, and acoustic field upstream or downstream of a 2-dimensional blade row for any type of incoming gust is given by Smith (1973). However, the theory is numerical and becomes computationally intensive when the gust wave length is small compared to the blade chord.

Envia and Kerschen (1986) develop a theory for estimating noise from interaction of rotor wakes with a cascade of blades. The cascade is 3-dimensional with leading edges swept back in the direction of the flow. Their analysis assumes one blade does not influence any of the others and the blade chord is semi-infinite.

Kullar and Graham (1986) utilize a modified form of Unsteady Thin Airfoil theory which incorporates compressibility, the cascade effect, and makes concessions for a 3-dimensional inflow gust to analyze the unsteady loading on a cascade of staggered blades. They investigate the possibility of resonance's associated with transverse propagation of sound waves, in addition to coupling between acoustic fields upstream and downstream of the cascade which are associated with vortex shedding from the blade trailing edge.

Rapid Distortion Theory is used by Hall and Verdon (1991) in their development of a numerical solution for the gust response of a staggered cascade. The authors use their formulation to perform a study of blade thickness effects on the unsteady surface pressure at a reduced frequency ($\omega c/U_\infty$) of 5. They show that thickness has a limited effect with thicker blades having higher unsteady pressure levels over the first quarter chord.

A frequency domain linearized unsteady aerodynamic analysis, incorporating Rapid Distortion Theory is presented by Fang and Atassi (1993) for the case of 3-dimensional, vortical flow around a cascade. Their analysis computes the entire flow field in response to upstream 3-dimensional harmonic disturbances. They present results for two standard cascade configurations representing turbine and compressor blading for reduced frequencies from 0.1 to 5. Blade sweep and upstream gust conditions are found to strongly influence the unsteady blade response.

Glegg (1999) offers a closed form expression for the unsteady loading, acoustic mode amplitude, and sound power output of a 3-dimensional cascade immersed in a 3-dimensional gust. Building on the work of Envia and Kerschen (1986) a theory is developed which accounts for the effects of the spanwise unsteady loading in addition to considering the effects of blade coupling and taking the blades to have finite chord. Glegg (1999) shows the unsteady loading to

be a strong function of spanwise wavenumber and/or blade sweep. The closed form nature of this analysis makes it especially desirable for comparison with experimental data.

1.5.2 Experimental Cascade Work

Satyanarayana, Henderson, and Gostelow (1974) measured unsteady pressure on a cascade of blades immersed in a transverse gust flow at reduced frequencies between 0.01 and 0.102. These researchers note a strong dependence of the airfoil response on Reynolds number and boundary layer behavior. Fleeter, Capece, and Chiang (1989) investigated the unsteady aerodynamic response using an axial compressor configuration with varying angle of attack. They show a significant effect on the unsteady response with increasing mean loading.

Manwaring and Fleeter (1993) investigate the unsteady loading of a rotor blade instrumented with pressure transducers downstream of inlet guide vanes. The inflow is characterized by a reduced frequency (fc/U_∞) near 2. These researchers show a fairly large effect of angle of attack on the individual pressure and suction side of the blade. However, less of an effect is shown on the pressure difference, ΔP . The effect of angle of attack is strongest in the leading edge region where the loading is increased with angle of attack. This effect reverses around 10% chord where the unsteady loading is decreased by angle of attack.

Henderson and Fleeter (1993a) immerse a low solidity (0.17) axial flow rotor in two turbulent flows, one produced by stator vanes the other by perforated plates and surface pressure measurements are performed. They found when the inflow is produced by perforated plates, generating turbulence nearing a vortical gust the response of the rotor agrees well with linear theory. However, when the inflow turbulence is generated by stator vanes agreement with linear theory is found to be quite poor.

Henderson and Fleeter (1997) use their axial flow rotor (solidity = 0.17) to measure the unsteady response of rotor blades immersed in an idealized upwash disturbance at a reduced frequency ($\omega c/2U_\infty$) of 1.35. Their measurements of unsteady pressure at angles of attack from -22.5° to 22.5° show that the suction side is greatly affected by mean loading with the pressure side relatively unaffected.

Ma (2003) presents phase averaged measurements of unsteady pressure and velocity in a linear cascade. The cascade is configured to represent the interaction of a stator horseshoe vortex with a rotor blade. The tunnel consists of 8 blades forming 7 passages with a moving end wall which has small vortex generators attached to simulate the stator horseshoe vortex. One

interesting result from this work is the effect of tip gap on the circulation in the tip leakage vortex. As the tip gap is increased the amount of fluctuation in the tip leakage vortex circulation increases dramatically, in fact, many times the circulation in the inflow vortices. Ma (2003) has suggested this effect (at large tip gaps) may be a consequence of the inflow vortices interfering with the shedding of circulation from the tip gap. Although no measurements of the blade response were made calculations using Glegg's (1999) theory were performed and support this conclusion.

1.6 Boundary Layer Pressure Fluctuations

Pressure fluctuations arising from a turbulent boundary layer, although not typically a dominant noise source in fluid/body interaction are none the less important due to their contribution to the surface pressure. The fluctuating pressure at any point in a turbulent fluid can be derived simply by considering the divergence of the Navier-Stokes equations and performing a Reynolds decomposition yielding Poisson's equation for the pressure

$$\nabla^2 p = -\rho \left[2 \frac{\partial \bar{U}_i}{\partial x_j} \frac{\partial u_j}{\partial x_i} + \frac{\partial^2 (u_i u_j - \overline{u_i u_j})}{\partial x_i \partial x_j} \right] \quad (1.19)$$

The pressure on a surface is obtained by integrating over the space above the surface through the use of Green's theorem (symmetric form) to give

$$P = \frac{\rho}{\pi} \oint_s \left[\frac{\partial \bar{U}_i}{\partial x_j} \frac{\partial u_j}{\partial x_i} \right] \frac{ds}{r_s} + \frac{\rho}{2\pi} \oint_s \left[\frac{\partial^2 (u_i u_j - \overline{u_i u_j})}{\partial x_i \partial x_j} \right] \frac{ds}{r_s} \quad (1.20)$$

Equation (1.20) is referred to as the Poisson Integral.

Since the main thrust of this work is related to the inviscid response of an airfoil in turbulence only a brief review of the most important work related to boundary layer pressure fluctuations is given. Considerable attention has been given to pressure fluctuations arising from turbulent flow in the past 50 years. In fact, Lighthill (1952, 1954) performed some of the earliest research on turbulent pressure fluctuations. The acoustic analogy (as presented above, equation 1.1) was intended to address such pressure fluctuations.

High quality measurements of surface pressure were perhaps first performed by Willmarth and Woolridge (1962). These researchers measured the mean square and power spectrum of surface pressure fluctuations, as well as the space-time correlation of pressure in the streamwise direction and the spatial correlation of pressure in the lateral direction.

Measurements were performed under thick boundary layers of $Re_\theta = 29000$ and 38000 . Their measurements showed that pressure-producing turbulent structures are convected at speeds which vary with wavelength, with those having long wavelengths convected faster than those having short wavelengths. They also demonstrated that pressure producing turbulent structures decay and then vanish after convecting a distance of approximately six wavelengths. Length scales of fluctuating pressure were found to be the same in the lateral and streamwise directions and on the order of the boundary layer thickness.

A method for correcting high frequency attenuation due to the finite size of pressure measurement transducers was developed by Corcos (1963). His method assumes that the cross-spectrum of surface pressure fluctuations can be decomposed into streamwise and lateral directions. As such, Corcos (1963) numerically integrated the spatial correlation data of Willmarth and Woolridge (1962)

Measurements of power spectra and the magnitude of the streamwise and lateral cross-spectrum of surface pressure fluctuations were made by Schloemer (1967) in a mild adverse, mild favorable, and zero pressure gradient flows. His results showed an increase in low frequency spectral levels in the presence of an adverse pressure gradient while a decrease in high frequency spectral levels occurred in favorable pressure gradient flow. The adverse pressure gradient also causes turbulent structures to decay more rapidly.

Bradshaw (1967), building on the notions presented by Townsend (1961) presents measurements in the context of an active shear stress producing motion and an inactive irrotational motion that contributes little to shear stress production. Measurements of power spectrum and surface pressure-velocity correlations in an equilibrium, adverse pressure gradient were made. Bradshaw (1967) also employed dimensional analysis to demonstrate the contribution of active motions to the wavenumber spectrum of surface pressure decays as $\frac{\tau_w^2}{k_x}$ up to a wavenumber that is proportional to the viscous sublayer thickness. He argued the existence of an overlap region based on inner and outer boundary layer scalings in the surface pressure spectrum beneath 2-dimensional, turbulent boundary layers at high Reynolds number. The pressure spectrum in the overlap region should collapse when scaled on both inner and outer boundary layer variables and the spectrum should decay as ω^{-1} .

Measurements of the power spectrum and convective wave speed of surface pressure fluctuations at several locations beneath a 2-dimensional separating boundary layer were made by Simpson *et al.* (1987). They show a monotonic increase in root-mean-square (RMS) pressure fluctuations through the adverse pressure gradient attached flow region. RMS pressure in the detached flow region was shown to be proportional to the ratio of streamwise length scale to length scales in other directions. Spectra in the region of boundary layer separation collapse when the time scale is normalized with δ^*/U_∞ and pressure normalized with the maximum shear stress. Pressure spectra in the separating region fall off as ω^{-3} at high frequencies which is in agreement with the work of Bradshaw (1967) and Schloemer (1967). As a consequence of intermittent backflow the convective wave speed of surface pressure fluctuations at high frequencies decreases downstream of the onset of separation.

McGrath and Simpson (1987) measured surface pressure spectra, coherence, and convective wave speed beneath turbulent boundary layers with zero and favorable pressure gradients over a range of momentum thickness Reynolds numbers ($Re_\theta = 3000 - 18800$). Low frequency spectra were found to collapse when the time scale is normalized by δ^*/U_e and the pressure by τ_w . Additionally, at high frequencies a similar effect is observed when the time scale is normalized by ν/u_τ^2 and the pressure scale normalized with τ_w . An overlap region was also found in which the high and low frequency scalings collapsed spectra in the case of zero pressure gradient boundary layers for $Re_\theta > 5000$. The decay of spectra in the overlap region was found to go as $\omega^{-0.7}$ rather than ω^{-1} as proposed by Bradshaw (1967). Lateral coherence decayed faster in the presence of zero pressure gradient as compared to favorable pressure gradient which is in agreement with the results of Schloemer (1967). Lastly, the convective wave speed (normalized on freestream velocity) was found to be faster in favorable pressure gradients which is consistent with the findings of Schloemer (1967).

Goody and Simpson (2000) measure surface pressure spectra beneath 2-dimensional ($7300 < Re_\theta < 23400$) and pressure driven 3-dimensional ($Re_\theta = 5940$ and 23200) turbulent boundary layers. Pressure spectra from the 2-D measurement are shown to collapse at middle and high frequencies when scaled on inner boundary layer variables ($\nu / u_\tau, u_\tau, \tau_w$) and over middle frequencies when scaled on outer variables (δ, u_τ, τ_w). Also shown is an increase in RMS pressure with increasing Re_δ . These scaling parameters do not collapse spectra beneath 3-D

turbulent boundary layers which have a nearly constant mid-frequency level. Furthermore, spectral levels within the constant level frequency range are independent of Reynolds number. Based on their analysis with the Poisson equation the relationship between the variation of high frequency spectral levels and the variation in near wall mean velocity gradient along with $\overline{v^2}$ structure is reasoned to result from the spanwise pressure gradient.

An empirical model of surface pressure spectra and mean square pressure beneath a 2-dimensional, zero pressure gradient boundary layer is presented by Goody (2002). Using the experimental results of 7 research groups ($1400 < Re_\theta < 23400$) the model of Chase (1980) and Howe (1998) is modified to capture the appropriate level of low frequency pressure fluctuations and the correct decay rate at high frequencies. Goody's (2002) model also incorporates the effects of Reynolds number on surface pressure spectra. The model shows good agreement with experimental data across the frequency range and can be reliably used to extrapolate to higher Reynolds numbers.

1.7 Motivation for Current Study

The noise and vibration which result from fluid/body interaction is of great importance and has received considerable attention in the past 60 years. A wealth of theoretical models have been developed addressing the interaction of a single airfoil or multiple airfoils with various representations of the inflow turbulence. However, relatively few experiments have been performed to validate the many theories which exist. In real life airfoils have thickness, camber, and often operate at varying angles of attack. Theories which consider these effects and are not rigorously validated against experimental data are as useful to design as flipping a coin. Thus, a significant need exists for comprehensive experimental data which can validate (or invalidate) the many theories in use today.

Of particular interest in recent years has been the effect of angle of attack on the airfoil response. Having been postulated through various theoretical analyses, angle of attack effects have only recently been systematically documented. The author presented a study of airfoil response to inflow turbulence in his Masters thesis (Mish 2001). Surface pressure measurements were made on a 2 ft chord NACA 0015 at angles of attack varying from 0° to 20° in 4° increments. The airfoil was instrumented with 96 Sennheiser microphones mounted sub-surface (48 per side). Two inflows were considered each generated by a static grid; one with integral

scale $1/70^{\text{th}}$ of the chord and the other with integral scale $1/8^{\text{th}}$ of the chord. Measurement of mean pressure was also performed which indicated the onset of significant separation at $\alpha = 16^\circ$ and complete stall at $\alpha = 20^\circ$. One of the interesting results shown in this work was the variation in unsteady lift with angle of attack. In the presence of large scale turbulence ($\lambda/c = 1/8$) unsteady lift was found to decrease at low reduced frequencies ($\omega_r < 10$) while increasing at high reduced frequencies as the angle of attack increased. This result is surprising based on the previous experimental work of Patterson and Amiet (1976a, b) and McKeough and Graham (1980) and is not supported by the previous theoretical work of Reba and Kerschen (1996, 1997). However, in small scale turbulence ($\lambda/c = 1/70$) the unsteady lift increased across a similar reduced frequency range with increasing angle of attack.

This work further investigates the effects of angle of attack on the airfoil response. New measurements of unsteady pressure in large grid flow made in an acoustically treated wind tunnel facility are presented. The quality of this data and Mish (2001) data is further examined and the calculation of lift from unsteady pressure measurements is validated. Comparisons with Reba and Kerschens's (1996) response theory, which incorporates angle of attack effects, are made, as well as additional comparisons with Amiet's (1976a, b) zero angle of attack theory. This work also presents an improved model for the prediction of unsteady surface pressure which correctly accounts for the effects of angle of attack. This work is intended to be all inclusive and as such, presents some results which were originally shown in the authors Masters thesis (Mish 2001).

This work also investigates the response of a cascade of airfoils subject to a periodic disturbance using the same unsteady pressure measurement system. This measurement system is shown to measure the airfoils inviscid response very effectively based analysis of a single airfoil in turbulence and, as such is used to address questions raised by Ma (2003). The work of Ma (2003) has raised interesting questions about the effect of tip gap on fluid/body interaction. As suggested by Ma (2003), tip leakage vortex shedding appears to be heavily influenced by the inviscid response for large tip gaps. Thus, this work sets out to determine the inviscid response of a cascade blade through surface pressure measurements. Furthermore, this measurement will be compared to the unsteady loading theory developed by Glegg (1999).

1.8 Outline of Dissertation

This work is presented in 10 chapters. Chapter 2 provides the background on measurement techniques and apparatus used to obtain unsteady surface pressure data for a single airfoil in turbulence. An overview of airfoil response theories developed by Amiet (1976a, b) and Reba and Kerschen (1996) is given in chapter 3. The single airfoil in turbulence set-up and data quality is discussed in chapter 4. Chapter 5 presents the analysis of single airfoil in turbulence surface pressure measurements made on a NACA 0015 airfoil. Background and motivation for measuring the unsteady response of a cascade is given in chapter 6. The instrumentation and apparatus used in the measurement of unsteady surface pressure on a cascade of blades is presented in chapter 7. Chapter 8 expounds on the cascade response theory of Glegg (1999). The results of cascade unsteady pressure measurements are discussed in chapter 9. Finally, conclusions and further considerations are given in chapter 10.

2. APPARATUS AND INSTRUMENTATION

2.1 Single Airfoil in Turbulence

2.1.1 Wind Tunnel

The effects of angle of attack on the airfoil response were examined using the Virginia Tech Stability Wind Tunnel. The tunnel is a continuous, closed jet, single return, subsonic wind tunnel with a 6' × 6' test section 24 feet in length. A planform view is shown in Figure 2.1.

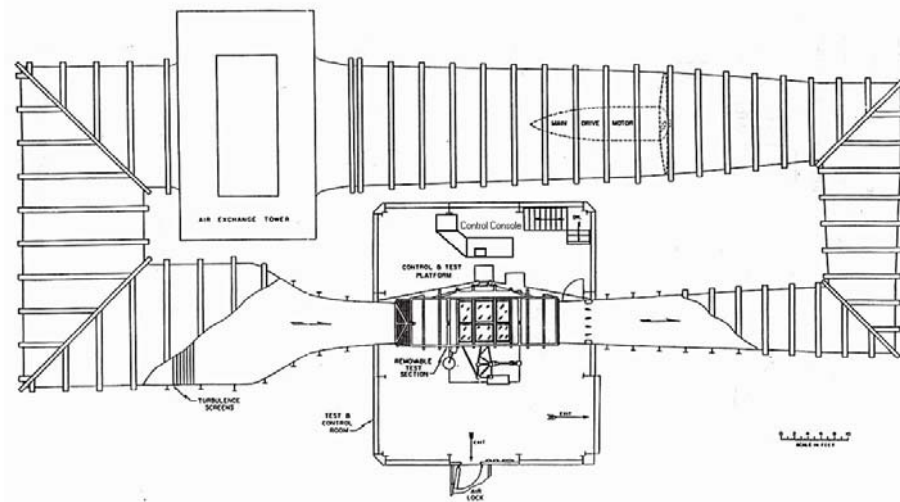


Figure 2.1: Virginia Tech Stability Wind Tunnel

The tunnel is powered by a 600hp DC motor driving a 14 foot propeller providing a maximum speed of about 60m/s. Tunnel speed is regulated by a custom designed Emerson VIP ES-6600 SCR Drive. Turbulence levels in the test section are extremely low, on the order of .05% or less, and flow in the empty test section is closely uniform (see Choi and Simpson, 1987). Although not originally designed as a low turbulence facility, the addition by the NACA of seven anti-turbulence screens, coupled with the other flow smoothing features of the tunnel, resulted in very low turbulence levels. The test section dynamic pressure is measured with a reference Pitot-static probe located 3.5" downstream of the test section entrance.

2.1.2 Wind Tunnel Walls

Measurements of unsteady surface pressure were made in two wind tunnel wall configurations; solid steel tunnel walls and acoustically treated walls.

The standard tunnel test section walls are made of steel plate on three sides with the fourth side made from Plexiglas (this configuration is referred to as solid walls). The acoustics in the

solid wall configuration are quite good as shown in figure 2.2 which is a plot of pressure sound level at a flow speed of 30m/s. The characteristics of this noise have been documented by Larssen and Devenport (1999). Acoustic noise levels were measured with a Bruel and Kjaer microphone fitted with a nose cone. The wind generated noise associated with this nose cone has not clearly been identified and therefore can not be subtracted out of the tunnel acoustic measurements. Thus, this measurement is a conservative estimate of the acoustic field within the test section and can be considered to represent the upper bound.

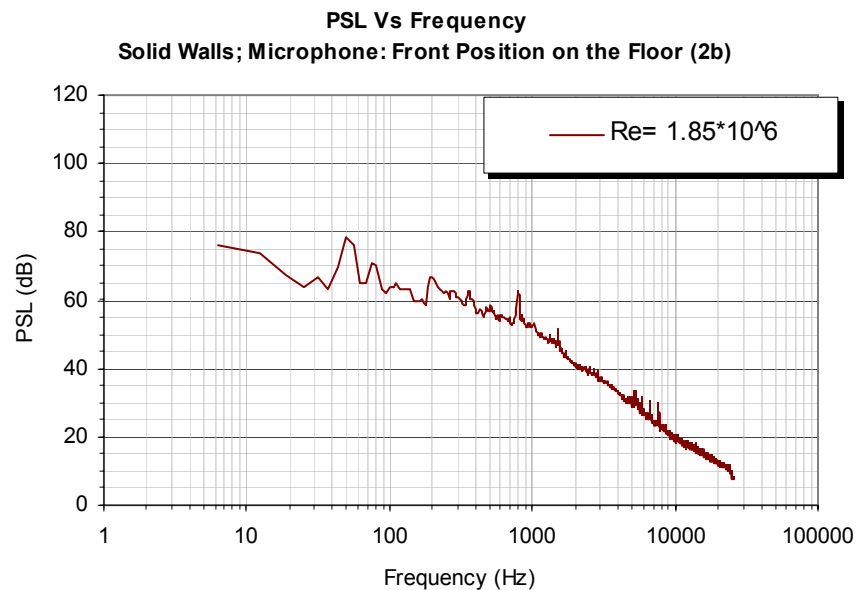


Figure 2.2: Pressure sound level at 30 m/s in solid wall configuration

Despite the relatively acoustically quiet environment offered by the solid wall configuration, wall treatment is developed to further reduce ambient noise levels. This treatment consists of a series of acoustic absorbers (boxes) replacing the solid walls of the wind tunnel test section. The wind tunnel test section with boxes attached is shown schematically in figure 2.3.

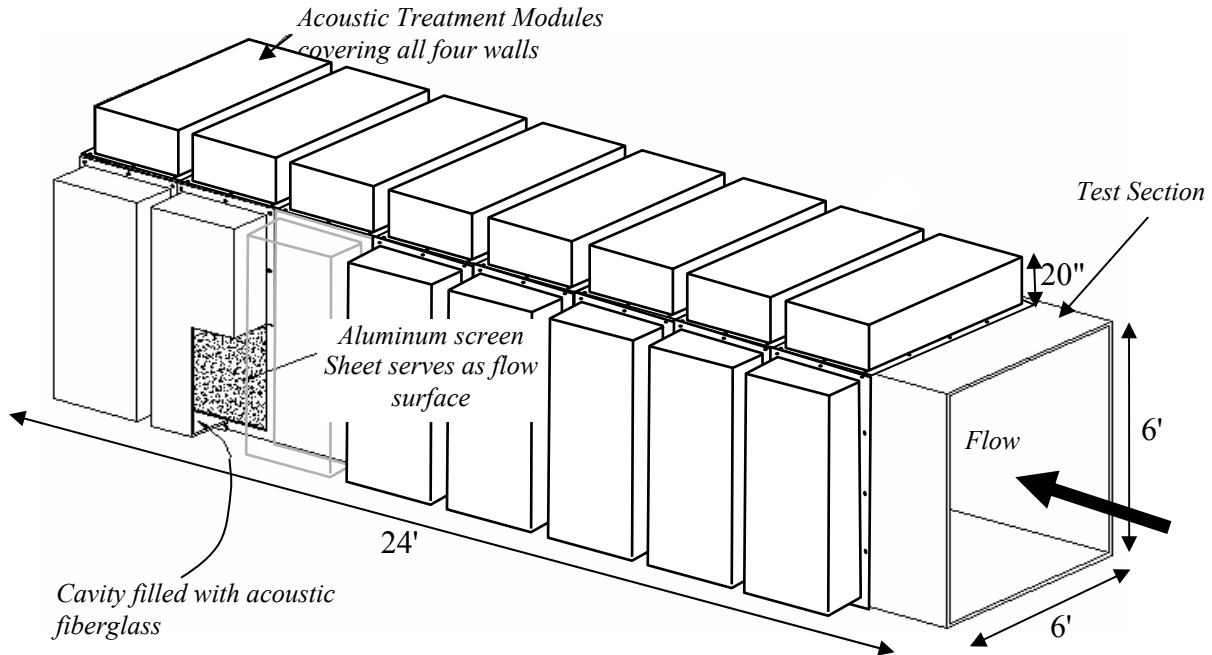


Figure 2.3: Wind tunnel acoustic treatment schematic

These boxes were designed to attenuate low frequency noise. The density of the material in the box and the box depth allow for control over the frequency range of attenuation. Thus, after analysis, a 20" nominal box depth is chosen which offers an expected attenuation as shown in figure 2.4.

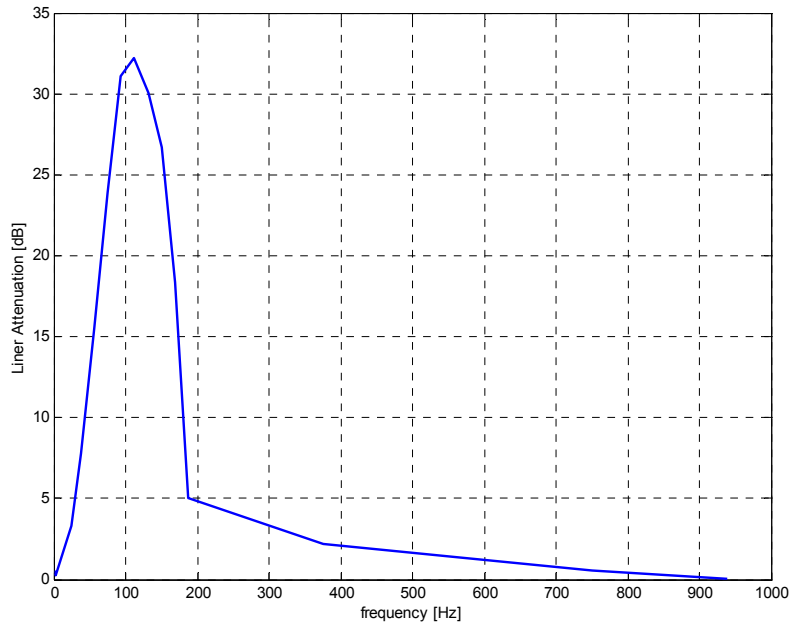


Figure 2.4: Expected level and frequency range of attenuation

The peak attenuation level of 33dB is expected to occur slightly above 100Hz with significant attenuation occurring from 10 to 200Hz.

The mounting locations and preexisting tunnel configuration dictated that nearly every box have custom dimension. The nominal dimensions are 20" deep, 6' long, and 3' wide however, some boxes are smaller in depth and width due to constraints from equipment surrounding the test section. A cross-section of a typical box is shown in figure 2.5.

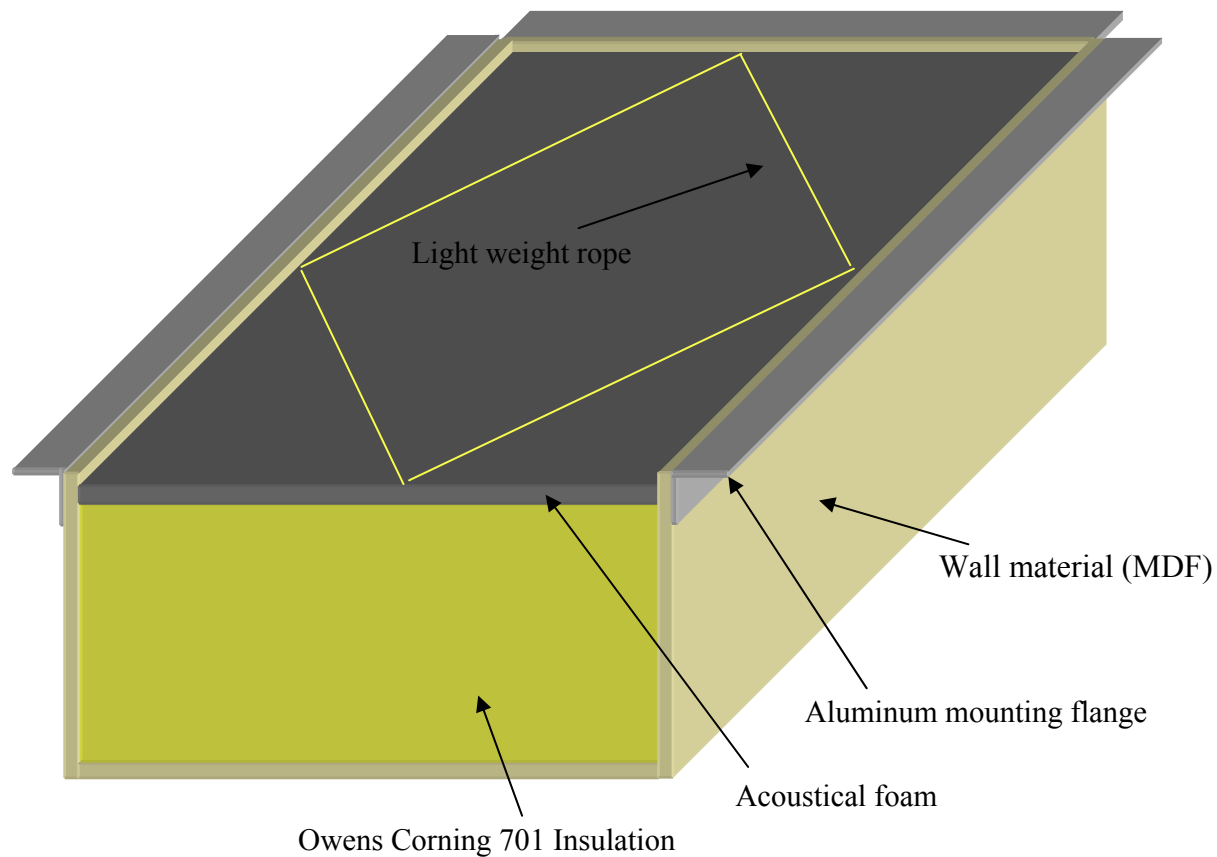


Figure 2.5: Cross-section of typical acoustic box

The box is made from 5/16" fiberboard, a material often referred to as MDF (medium density fiberboard). Each box is lightly stuffed with Owens Corning 701 insulation (1.5 lb/ft³) with a 3/4" sheet of acoustical foam placed on top of the insulation. The acoustical foam serves as a barrier between the insulation and flow thus minimizing the amount of airborne insulation particles. A lightweight rope is strung from side to side over the acoustical foam to keep the insulation and foam in place. The boxes are attached to the tunnel test section with 2" flange aluminum angle. After the boxes are mounted to the test section sheets of aluminum screen are

attached which serve as the test section wall and flow surface. The aluminum screen is 1/8" thick with a 40% open area ratio.

The effects of the acoustic treatment modules are documented through acoustic measurements with a Bruel and Kjaer microphone. The acoustic measurements of Larssen and Devenport (1999) made with the test section in solid wall configuration are compared with similar measurements in the acoustic treatment configuration. The pressure sound levels of both measurements are presented in figure 2.6 for a flow speed of 30m/s.

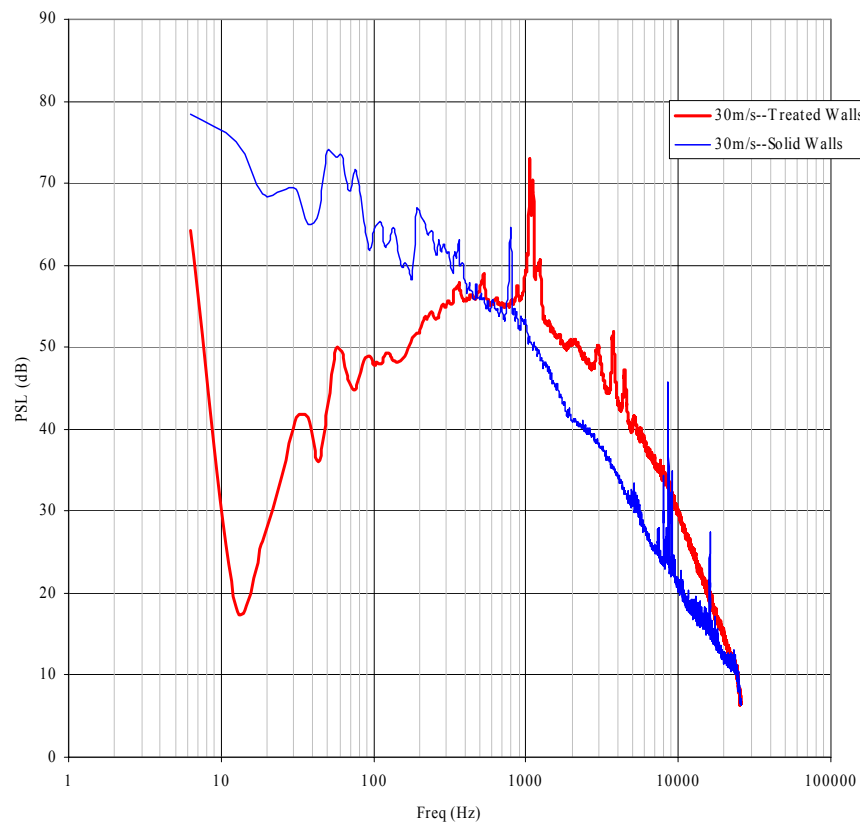


Figure 2.6: Pressure sound level at 30m/s with and without acoustic treatment

Considerable attenuation of the ambient sound field occurs between 10 and 500Hz with as much as 50dB of attenuation occurring between 10 and 20Hz. The spectra converge and crossover at 500Hz with the acoustically treated spectrum rising up to 10dB above the solid wall spectrum. The spectra appear to converge again at 20kHz. The increase in spectral level above 500Hz with the acoustic treatment in place is likely the result of flow interaction with the screen. Additionally, the boundary layer is thicker and produces more high frequency noise with the screen present.

2.1.3 Turbulence Generating Grid

Two grids have been developed for the Virginia Tech 6' x 6' Stability wind tunnel for the purpose of generating homogeneous isotropic turbulent flows for the study of unsteady airfoil response. The characteristics of each grid generated flow have been reported by Bereketab, *et al.* (2000) and are summarized here. The first, a square bi-planar grid with a 12" mesh size and an open area ratio of 69.4%, was mounted in the wind tunnel contraction 19.1 mesh sizes upstream of the location planned for the airfoil leading edge, at a point where the cross-sectional area was 32% larger than that of the test section (figure 2.7).

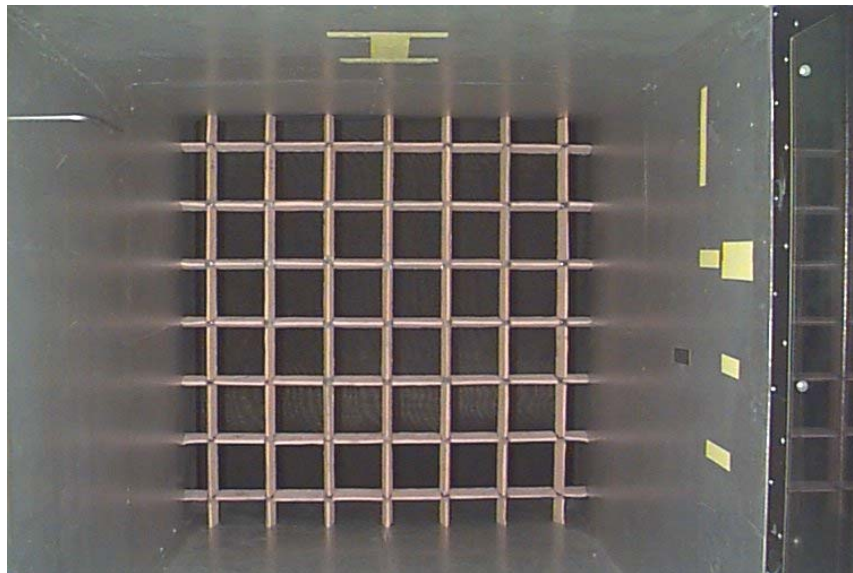


Figure 2.7: Downstream view of large grid

Acoustic foam wedges attached to the downstream side of the grid were used to minimize grid generated noise. The second grid, a metal weave with a 1.2" mesh size and an open area ratio of 68.2% was mounted in the tunnel test section at a position 16.1 mesh sizes upstream of the planned leading edge location (figure 2.8). It should be noted that the small grid is located downstream of the tunnel reference Pitot-static probe which requires a correction of the pressure loss across the grid when used as a reference for mean pressure measurements on the surface of the test airfoil.

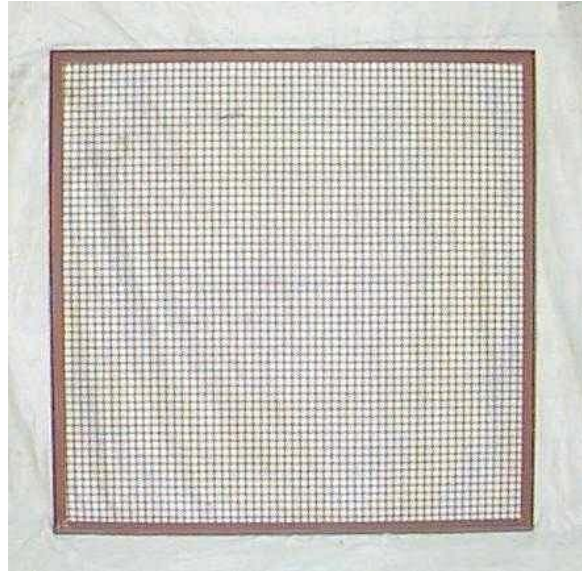


Figure 2.8: View of small grid

Table 2.1 summarizes flow speed and Reynolds number data for each grid as well as Reynolds number based on the chord of the NACA 0015 airfoil used in the subsequent surface pressure measurements.

Table 2.1: Flow speed and Reynolds number

Nominal Flow Speed (m/s)	Small Grid Re (based on cell size)	Large Grid Re (based on cell size)	Equivalent airfoil chord Re
30	63000	630000	980000

Three-component velocity and turbulence measurements were made with 4-sensor hot-wire probes over a 24"x24" cross section centered on the tunnel centerline in order to reveal the form of the grid generated flows. Velocity measurements were made in the plane of the airfoil leading edge (with airfoil removed). Turbulence intensities produced by the large grid are between 3% and 4% at all speeds and in all components as shown in figure 2.9.

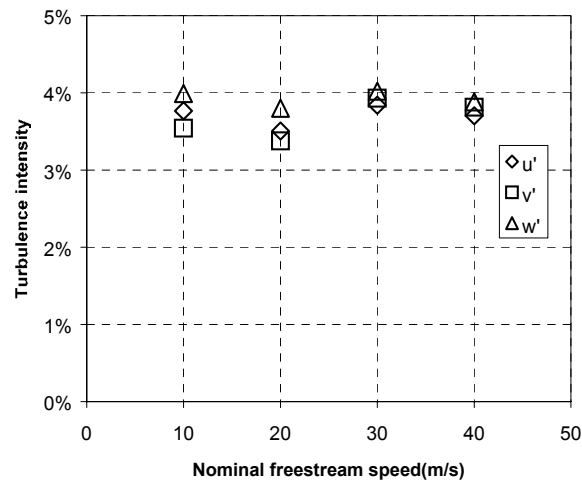


Figure 2.9: Cross-sectional averaged turbulence intensities for large grid flow

Turbulence intensities produced by the small grid are between 3.5% and 5% at all speeds and in all components as demonstrated in figure 2.10.

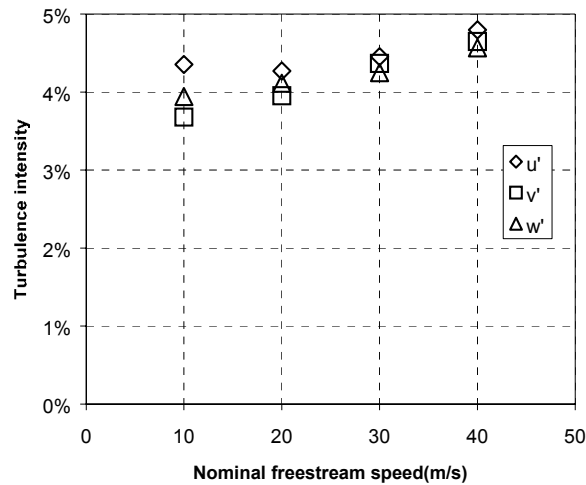


Figure 2.10: Cross-sectional averaged turbulence intensities for small grid flow

The isotropy of the turbulence components in the large grid flow appears best at 30m/s where the difference between the smallest and largest components is less than 5% of the measured intensity as revealed by turbulence stress contours in figure 2.11.

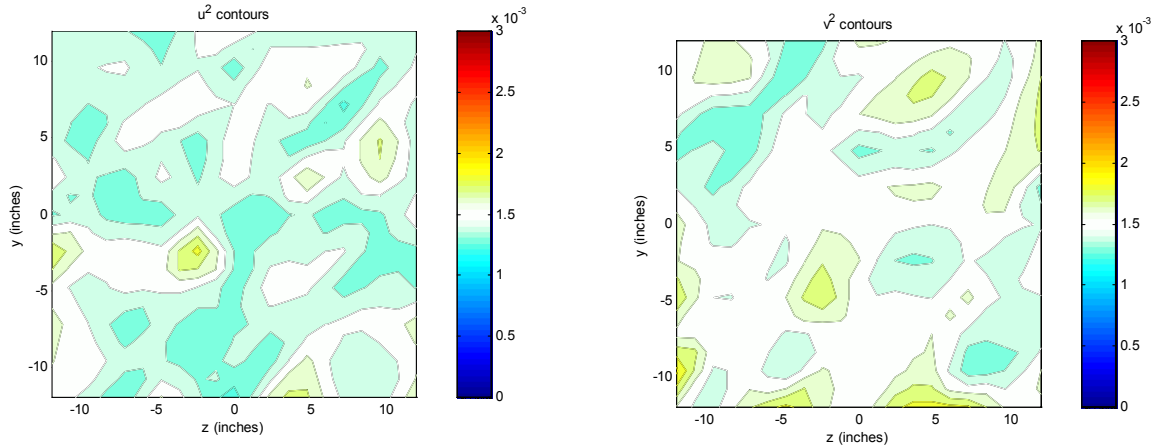


Figure 2.11 (a): Large grid flow contours of u -component turbulence normal stress normalized on U_∞^2

Figure 2.11 (b): Large grid flow contours of v -component turbulence normal stress normalized on U_∞^2

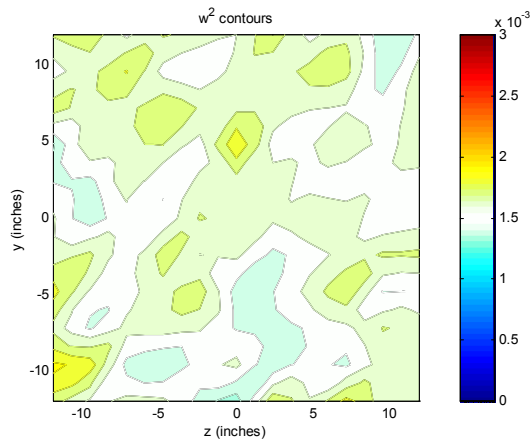


Figure 2.11 (c): Large grid flow contours of w -component turbulence normal stress normalized on U_∞^2

The variation in turbulence stress level appears to be random and within the uncertainty of the measurement. The turbulence stress field is closely homogeneous as well.

The isotropy of the turbulence, as shown in figure 2.12 appears very good at 30m/s in small grid flow, the difference between the smallest and largest components at 30m/s being less than 1 part in 20.

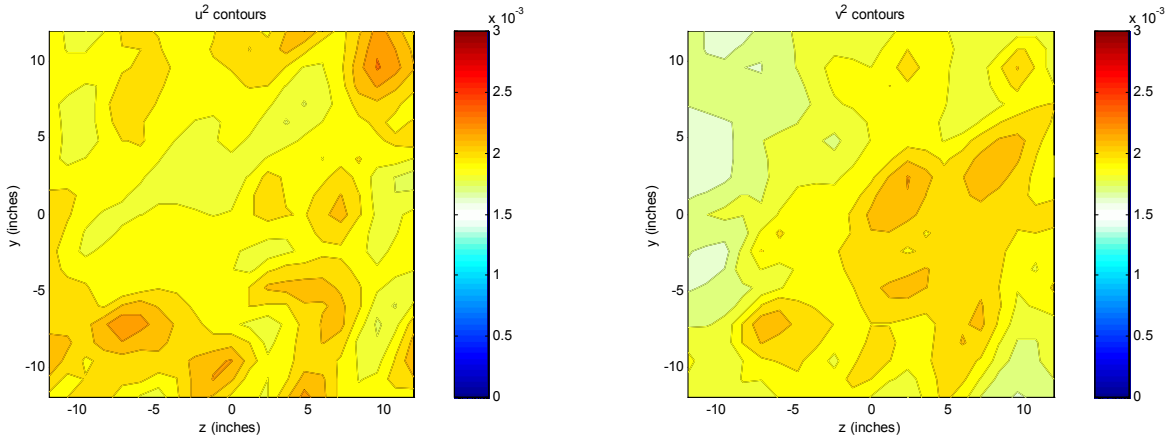


Figure 2.12 (a): Small grid flow contours of u -component turbulence normal stress normalized on U_∞^2

Figure 2.12 (b): Small grid flow contours of v -component turbulence normal stress normalized on U_∞^2

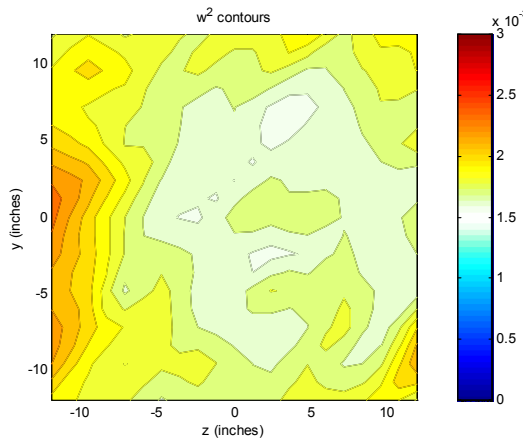


Figure 2.12 (c): Small grid flow contours of w -component turbulence normal stress normalized on U_∞^2

The turbulence stress field shows some slight in-homogeneities at all flow speeds, attributed to a slight bow in this grid (about 0.4" at the grid center in the downstream direction), and the blockage produced by the frame used to support it.

Table 2.2 presents the inferred integral length scale for each grid at 30m/s.

Table 2.2: Longitudinal integral scales (λ) and velocity scales (u) that best describe the 2 grid turbulence flows.

	Large grid	Small Grid
u/U_∞ (%)	3.93%	4.35%
λ (in.)	3.22	0.309

As reported in Bereketab, *et al* (2000) for wavenumbers below the upper limit of the inertial subrange, the spectra and correlations measured with both grids can be represented using the von

Karman interpolation formula with a single velocity and length scale. The spectra may be accurately represented over the entire wavenumber range by a modification of the von Karman interpolation formula that includes the effects of dissipation.

2.1.4 Airfoil Model

Surface pressure measurements are made on an instrumented NACA 0015 with chord length of 2-ft and 6-ft span manufactured by Sandia National Labs. The airfoil trailing edge is round with a radius of curvature of 0.1075". Measurement of the airfoil geometry confirms the 0015 shape which is calculated based on

$$\frac{z}{c} = \frac{0.15}{0.2} \cdot \left(0.2969 \cdot \left(\frac{x}{c} \right)^{1/2} - 0.126 \cdot \frac{x}{c} - 0.3516 \cdot \left(\frac{x}{c} \right)^2 + 0.2843 \cdot \left(\frac{x}{c} \right)^3 - 0.1015 \cdot \left(\frac{x}{c} \right)^4 \right). \quad (2.1)$$

Figure 2.13 presents the measured geometry plotted with the exact (analytically calculated) geometry.

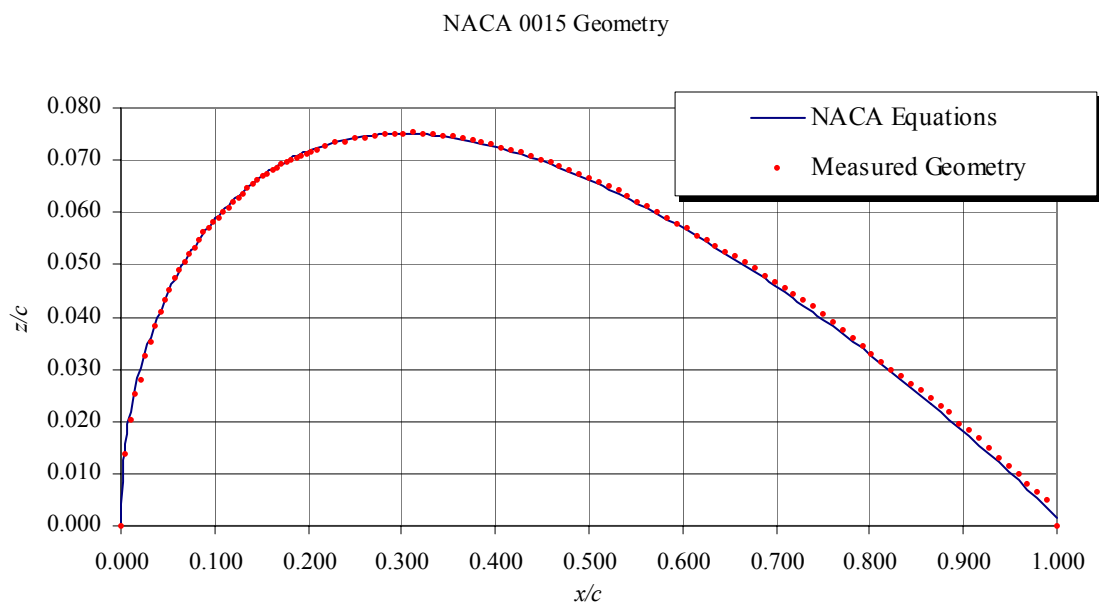


Figure 2.13: NACA 0015 measured and calculated geometry

The airfoil is manufactured as an extruded aluminum section. Minor imperfections are present on the surface of the airfoil consisting of scratches approximately 1/32" deep and 1/2" to 1" long. These imperfections are located primarily out of the measurement region and cover less than 0.1% of the total surface.

The airfoil model is equipped with a removable access hatch which is 2-ft in span, the length of the chord and half the thickness of the airfoil. The hatch is positioned mid-span. Figure 2.14 reveals the airfoil with hatch removed.



Figure 2.14: Wing with hatch removed

The hatch is placed over the access and shimmed internally to ensure a smooth transition from the hatch surface to the wing. Four bolts are used to fasten the hatch to the airfoil. The hatch is then sealed with 0.00275" clear tape along both sides and the leading and trailing edge. Wax is then used to blend the tape into the surface of the airfoil.

Mean pressure measurements are made with a 48 port scani-valve system. The scani-valve is connected and pressure measured with a Honeywell Model DRAL520GN pressure transducer interfaced with an IBM/AT computer through a data translation DT2801-A A/D converter. A Dwyer series 427 Mark III handheld digital manometer (range 0-10" of H₂O, accuracy ± 0.01 " of H₂O) was also used to make mean pressure measurements at 23% chord. Tygon tubing with 3mm outer diameter is used to traverse the distance between the manometer and the interior of the wing. 0.075" OD copper tubing is used to transition the Tygon tubing from the inner surface of the wing to the outer surface. Measurement points are located 2" down from the hatch in a chordwise plane exactly perpendicular to the leading edge. Figure 2.15 shows the chordwise location of the pressure ports.

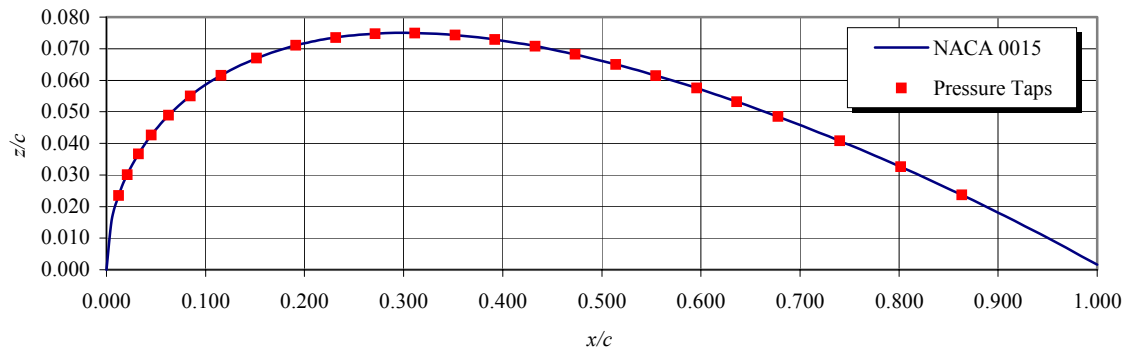


Figure 2.15: Chordwise distribution of mean pressure taps

Mounting of the airfoil model is done to allow rotation of the model about the quarter chord for angle of attack adjustment. Two 4.6" outer diameter (3.75" ID) aluminum pipes protrude from both ends of the airfoil and are bolted to the models internal structure centered at the quarter chord. The pipes then slip through holes in the tunnel roof and floor plating. The pipe protruding through the tunnel roof then slides through a mounting block (Figure 2.16) which allows adjustment of the yaw and rolling angle.

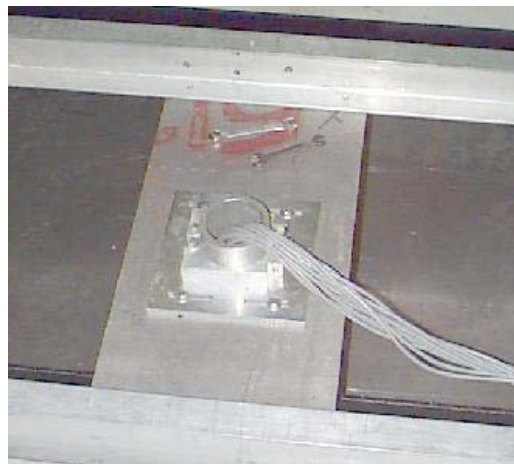


Figure 2.16: Roof mounting block

Finally, the roof pipe is clamped to the mounting block (Figure 2.17) and the floor pipe is clamped to the floor plate.



Figure 2.17: Roof mounting structure

Angle of attack adjustments are made by loosening the clamps and rotating the wing.

Angle of attack is determined by setting the trailing edge to angle of attack markings on the wind tunnel floor. The angle of attack setting is also verified using the mean pressure data plotted with the potential flow solution.

The airfoil model leading edge is located 229.2" (9.6 chords) downstream of the large grid as shown in figure 2.18.

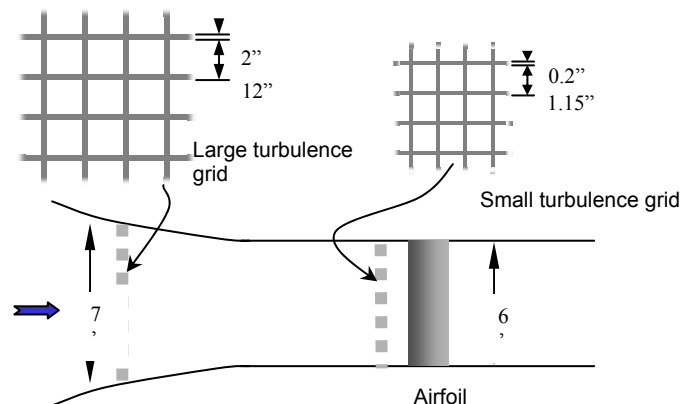


Figure 2.18: Schematic of the wind tunnel contraction and test section showing the location of the grid and airfoil model.

Turbulence length scales at this location (with the airfoil removed) normalized on chord and leading edge radius are presented in table 2.3.

Table 2.3: Turbulence length scales normalized on chord and leading edge radius

	Large grid	Small Grid
L/c	0.134	0.0129
L/r_c	5.41	0.519

2.1.5 Microphone System

The airfoil model is instrumented with a unique multiple-microphone system. The system, illustrated schematically in figure 2.19, can accommodate up to 96 Sennheiser KE 4-211-2 microphones.

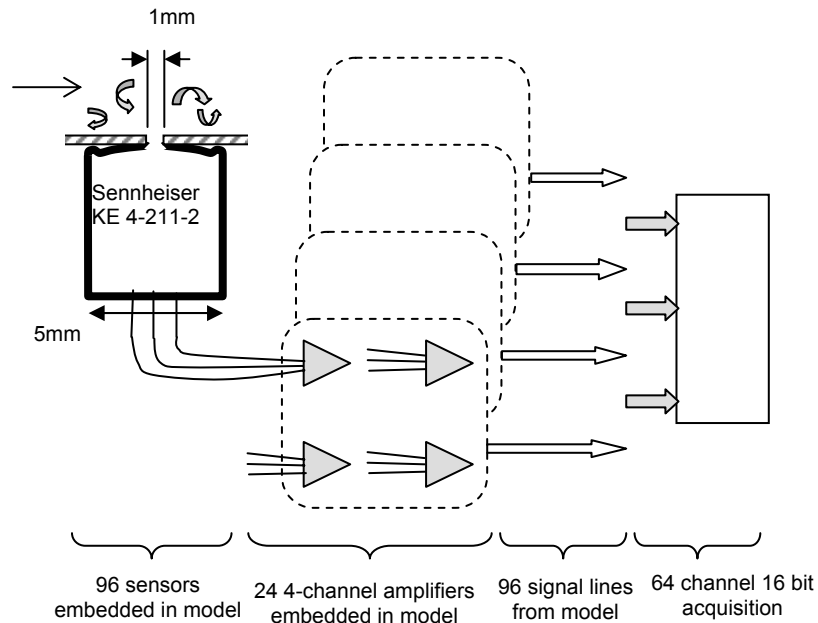


Figure 2.19: Schematic of microphone system

Measurements of unsteady surface pressure were made in the full 96 microphone configuration along with a complementary 40 microphone configuration. The 96 microphone configuration is shown in figure 2.20.

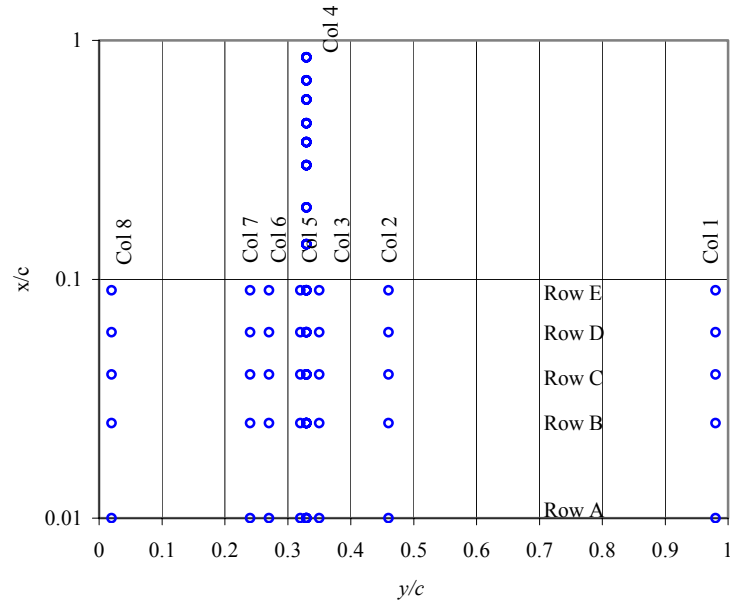


Figure 2.20: Ninety-six microphone layout

The 40 microphone configuration is shown in figure 2.21.

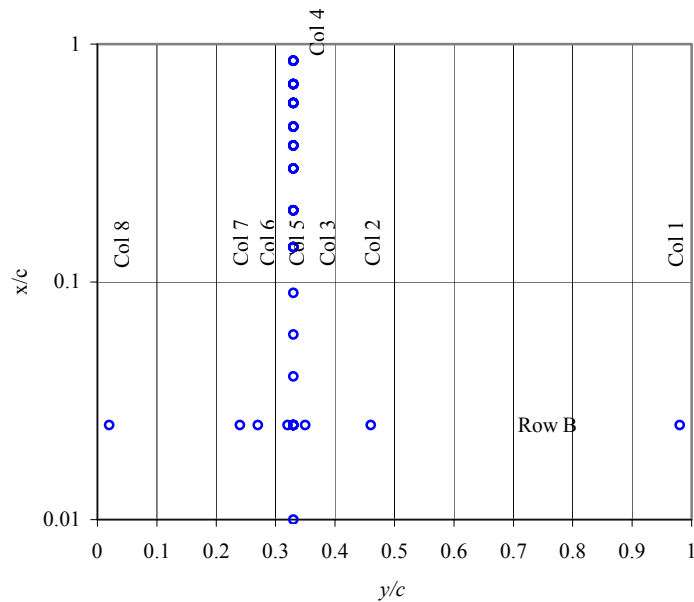


Figure 2.21: Forty microphone layout

The Sennheiser microphones are sensitive (10mV/Pa), provide low noise signals and a nominal response that is flat to within 1dB from 40Hz to 10000Hz, calibratable over a larger range. The microphones are built with a 1mm pinhole (providing reasonable spatial resolution) which can be recessed a short distance (typically 0.5mm) below the airfoil surface without

significantly degrading the response. They can measure signals up to an SPL of 125dB and are insensitive to vibration. Their small physical size allows a minimum sensor spacing of about 5mm (significantly less than the expected correlation length scales). We have built independent operating electronics and amplifier circuitry for each microphone using a compact modular approach that enables these systems to be embedded in the model close to the microphone locations. The system is powered by 6 custom-built quiet power supplies. It is operated, and measurements are made using a Hewlett Packard E1432 based data acquisition system. This system (which is expandable) provides simultaneous measurement of 64 channels with 16 bit accuracy at sampling rates up to 56kHz per channel, and has built in anti-alias filtering for each channel. It is important to note that this system is not limited to a 64-point measurement of the two-point surface pressure correlation function. Because of the spanwise homogeneity of a mean two-dimensional flow the 64-channel/96 microphone system can be positioned and manipulated to behave as a dense two dimensional array of 240 microphones. To understand how consider the full 96 microphone layout shown in figure 2.20. Coordinate x in this figure refers to distance downstream from the leading edge, and z to distance along the leading edge from the hatch edge. Microphones are located on *both* sides of the airfoil at the locations indicated. At first sight the microphone array appears very sparse in the spanwise direction, but this is deceptive. Since the flow is homogeneous in the z direction the absolute position of the sensors in this direction is irrelevant, and the two-point space-time correlation is only a function of their spanwise separation (the array defines many more spanwise separations than it does positions). The following is an example measurement strategy with this array

- Simultaneously measure signals from all microphones in column 4, A1-A8, and B1-B8
- Repeat measurement except with row C, D, E
- Because of spanwise homogeneity, this produces *at least* the same two-point correlation/spectral data as would be obtained from a simultaneous measurement using 240 microphones in the 2D array shown in figure 2.22 (i.e. correlation of every point pivoted about every point). Furthermore, the data set includes checks on the homogeneity assumed.

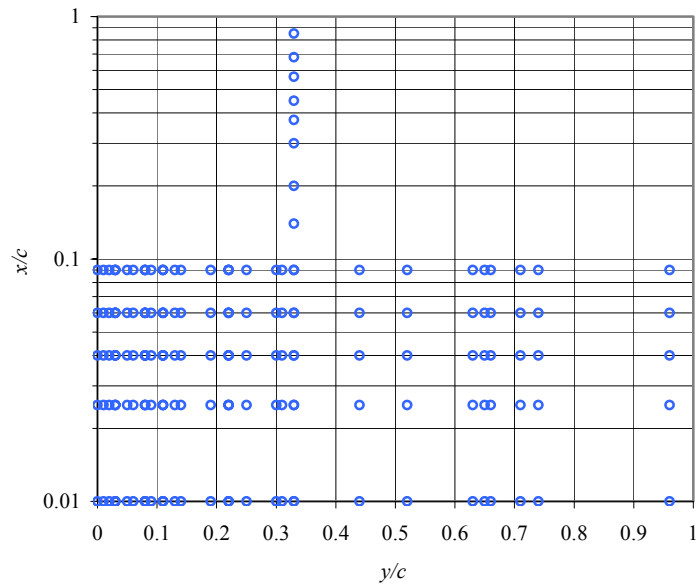


Figure 2.22: Effective microphone array

A central component of any such measurement system is a reliable means for calibrating the microphones. For accurate measurement of the space-time correlation one needs not just amplitude, but full phase vs. frequency calibrations for each microphone sensor. For this purpose a calibrator was built, adapted from a NASA design, and is shown schematically in figure 2.23.

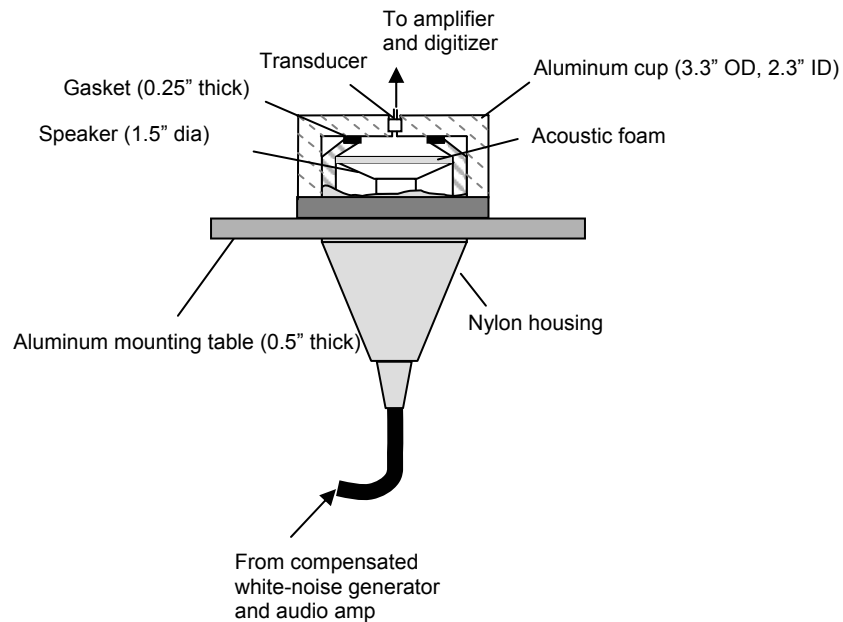


Figure 2.23: Microphone Calibrator

The calibrator consists of a small wide-range loudspeaker mounted on one side of a shallow cavity built into the end of a Nylon housing. The Nylon housing is fixed into a heavy aluminum plate with the open end of the housing extending 2 inches above the plate. The perimeter of the open end of the housing is lined with a rubber gasket that seals the cavity formed by an aluminum cup, which slides over the Nylon housing. Each microphone is placed in a recessed hole on the top of the aluminum cup, which is of similar dimension as those in the wing. The speaker system is driven from an audio amplifier using a white noise signal, compensated for the response of the speaker/amplifier system, generated by the HPE1432A. The cross spectrum between the input signal and microphone signal is then compared with a similar measurement made using the B&K reference microphone. The calibration is shown schematically in figure 2.24 where $V_1(t)$ is the white noise signal generated by the HP1432 (and also, simultaneously measured by the HP1432), $P_s(t)$ is the pressure signal produced by the speaker signal, and $V_2(t)$ is the voltage signal produced by the microphone which is feed back to the HP1432 for measurement.

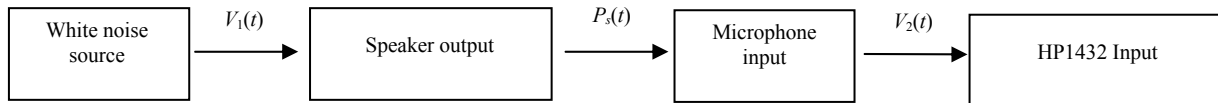


Figure 2.24: Microphone calibration schematic

The Sennheiser microphone response is obtained in the following manner: First, the speaker response, $S_p(\omega)$ [Pa/V] is determined using the Bruel and Kjaer reference microphone which has a known flat response, $bk(\omega)$ (0.803 V/Pa). This measurement is indicated as superscript *a*,

$$S_p(\omega) = E \left[\frac{V_2(\omega)}{bk(\omega)} \cdot V_1^*(\omega) \right] / E [V_1(\omega) \cdot V_1^*(\omega)] = \frac{G_{pv_1}^a}{G_{v_1v_1}^a} \text{ [Pa/V]} \quad (2.2)$$

where $E[\]$ is the expected value. The Sennheiser microphone calibration is then found in a subsequent measurement (indicated as superscript *b*) as

$$M_s(\omega) = \frac{E [V_2(\omega) \cdot V_1^*(\omega)]}{E [V_1(\omega) \cdot V_1(\omega)]} \cdot \frac{1}{S_p(\omega)} = \frac{G_{v_2v_1}^b}{G_{v_1v_1}^b} \cdot \frac{G_{v_1v_1}^a}{G_{pv_1}^a} \text{ [V/Pa]} \quad (2.3)$$

With this system a phase and amplitude calibration over the full frequency range of a microphone can be performed in less than 1 minute. A typical calibration performed in this manner is illustrated in figure 2.25.

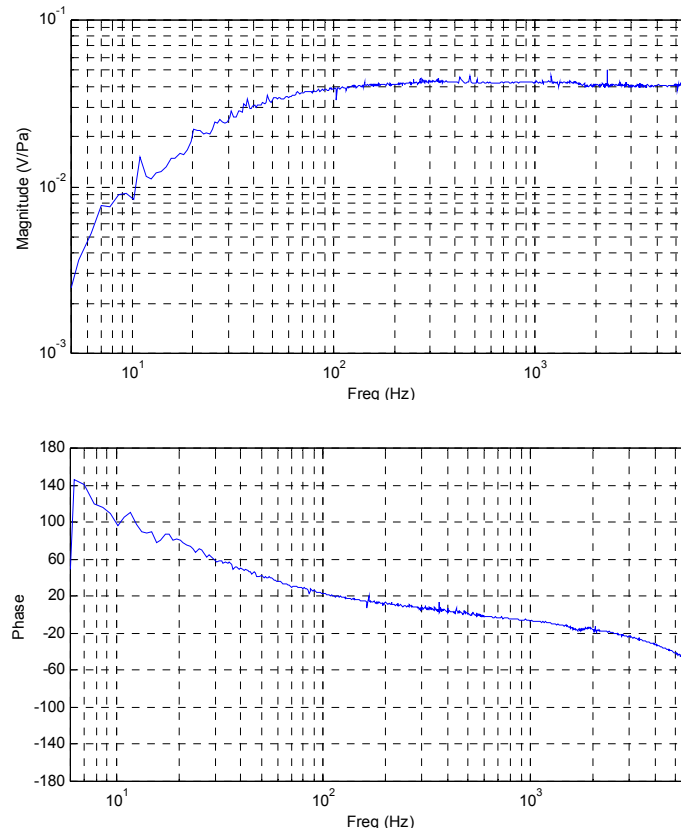


Figure 2.25: Typical magnitude and phase calibrations

The calibrator design was the result of an evolving process to achieve accurate and repeatable magnitude and phase calibrations. The initial calibrator design was handheld in nature allowing for calibration of each microphone while mounted in the wing. This design suffered from several flaws although primarily failing due to unreliable sealing between the calibrator and airfoil surface, particularly in the highly curved leading edge region, and the inability to consistently gather repeatable calibrations. Through further experimentation the Sennheiser microphone calibrations were shown to be unaffected by temperature variations within $70^{\circ}\text{F} \pm 5^{\circ}\text{F}$. Furthermore, the calibrations show little (within the uncertainty of the calibration) drift with time.

Each microphone is mounted from within the airfoil in a slightly larger diameter hole than the microphone. The hole is bored to within 0.5mm of the outer surface of the airfoil. A pin hole is drilled in the center of the bored hole and aligns with the microphone pin hole. A

typical cross-section through a microphone and microphone mounting hole is shown in figure 2.26.

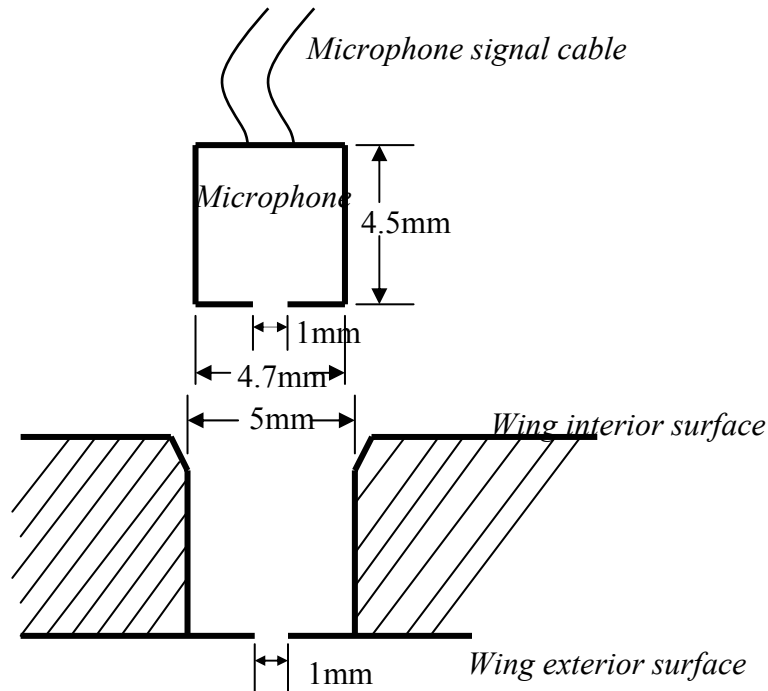


Figure 2.26: Cross-section through typical microphone and microphone mounting hole

Figure 2.27 shows a microphone lying beside a mounting hole on the interior of the wing.



Figure 2.27: Microphone lying beside mounting hole on interior of wing

The microphone is sealed and held in place with hot glue applied to the outer edge of the bored hole.

As stated above, operating electronics are embedded in the wing below and beside the access hatch. Power is supplied to the electronics through 3 power cables which exit the airfoil through the lower (tunnel floor) mounting pipe. Data from each microphone exits the wing on

10 data cables via the upper (tunnel roof) mounting pipe. This configuration which ensures minimal data contamination from the power supplies and cables is shown in figure 2.28.

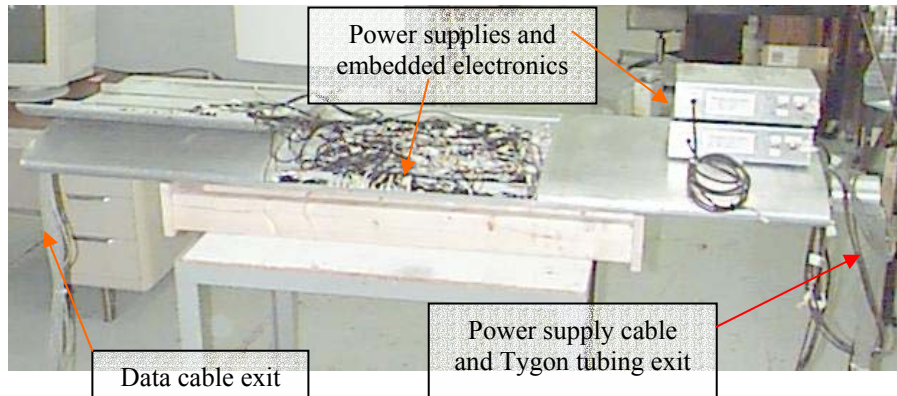


Figure 2.28: Data and power cabling configuration

2.1.6 Reference Acoustic System

Measurement of the tunnel test section acoustic field was performed simultaneously with some measurements of unsteady pressure. A Bruel and Kjaer model 4138 (figure 2.29) microphone mounted on an aerodynamic stand with microphone tip in the same plane as the wing leading edge was used (Figure 2.30).



Figure 2.29: Bruel and Kjaer model 4138 reference microphone

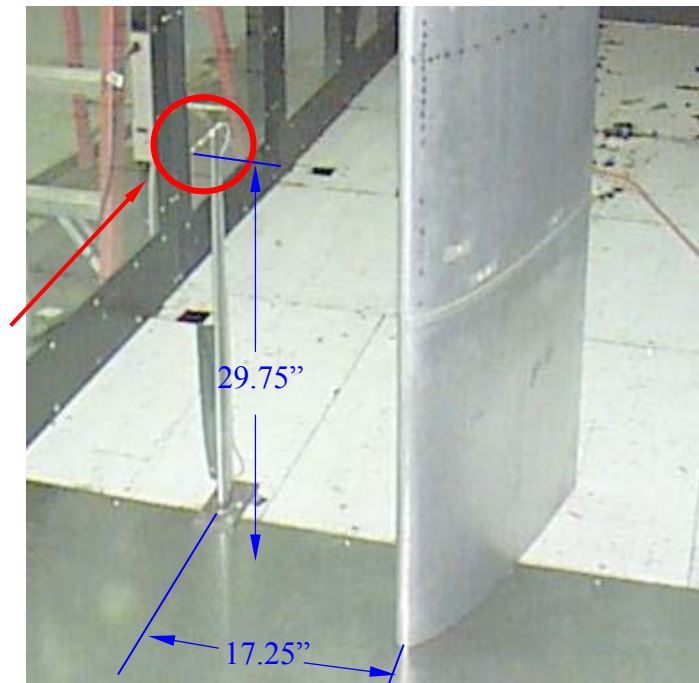


Figure 2.30: Overview of reference microphone mounted on stand next to wing

The microphone was located 17.25" to the starboard side of the airfoil chord line as measured at 0° angle of attack and 18.25" from the starboard test section wall at a height of 29.75".

The reference microphone signal is conditioned and amplified and data then recorded by the HP1432 while simultaneously recording unsteady pressure as measured by the Sennheiser microphones. As mentioned previously, this microphone is equipped with an aerodynamic wind screen which serves to protect the microphone diaphragm. The noise induced by this wind screen has not been undoubtedly identified and thus the acoustic levels measured will represent an upper threshold of the acoustic field present in the tunnel test section.

2.1.7 Hot-wire Anemometry

For some measurements a hot-wire probe was mounted just off the airfoil surface at the 14% chord location. The goal of such measurement was to reveal the velocity/pressure correlation of the flow occurring around the airfoil and through interpretation infer the nature of the eddy convection and deformation.

Velocity measurements were made using a single sensor hot-wire probe (figure 2.31).

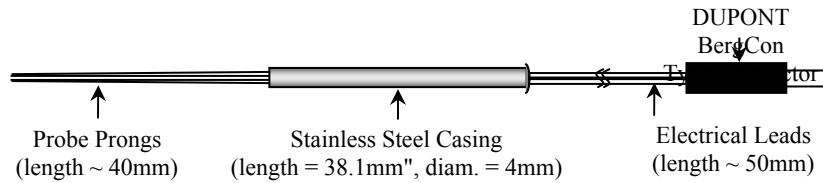


Figure 2.31: Diagram of hot-wire probe

The tip of the probe consists of two stainless steel tapered prongs that hold the sensor wire 40 mm upstream of the main body of the probe. The sensor wire is 0.8 mm in diameter and 5 mm in length. The hot-wire is operated with a Dantec 56C17 bridge and a Dantec 56C01 constant temperature anemometer unit. The amplified signal is then recorded simultaneously with pressure measurements by the HP1432E.

Velocity measurements were made 0.875 inches off the surface of the airfoil exactly above a microphone located at 14% chord and 33% span for all angles of attack including negative angles of attack. The mounting location was chosen to minimize interference associated with the probe and probe mount wake with unsteady pressure measurements. The hot-wire allows examination of pressure/velocity correlations on both the suction and pressure side of the blade. The probe is held with epoxy to a small aluminum mounting bracket. The mount bottom is bent at a 90° angle to form a flange which is then epoxied to the surface of the airfoil as displayed in figure 2.32.

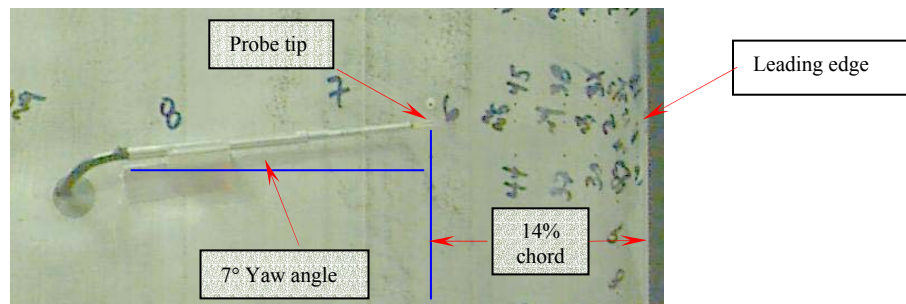


Figure 2.32: View looking down on mounted hot-wire

The mounted probe is yawed 7° to minimize the possibility of the mount wake contaminating the pressure field over the remaining chordwise microphones. The mounted probe tip is in a plane approximately parallel to a chordwise tangent line drawn at the 14% chord location.

The probe was operated at an overheat ratio of 1.7. Calibration is performed a short period prior to tunnel entry using a jet calibrator. The probe is placed in the jet calibrator and

through comparison of the output voltage (E_{hw}) produced by the hot-wire in the jet flow and the cooling velocity (U_{eff}) sensed by the jet calibrator the hot-wires calibration is obtained. Kings law

$$E_{hw}^2 = A_1 + B_1 U_{eff}^n \quad (2.4)$$

is used. The exponent n is taken as 0.45 and the constants A_1 and B_1 are determined via linear regression from 10 to 15 points. Flow temperatures within the test section were found to fluctuate $\pm 5^\circ\text{F}$. Hot-wire signals are temperature corrected using the method of Bearman.

2.1.8 Boundary Layer Trip and Leading Edge Bump

For some measurements of unsteady pressure a boundary layer trip strip is used. The trip is made from 1" wide electrical tape cut in half with pinking shears. Two layers of tape are used with the top layer set 1/8" downstream from the bottom layer. The total thickness of the trip is 0.08" with the bottom layer set 0.09% chord downstream from the leading edge. A close up picture of the trip strip attached to the airfoil is shown in figure 2.33.



Figure 2.33: Close-up of boundary layer trip strip

Measurement of unsteady pressure is also made with a small bump attached to the airfoil leading edge. The bump is made from yarn covered with electrical tape and has a diameter of 3/16" which extends the airfoil chord by 0.75%.

2.1.9 Modified trailing edge

Measurements of the unsteady pressure field were made with a modified sharp trailing edge to reveal trailing edge effects. This modification is incorporated using two 1-1/2" wide, 0.025" thick aluminum strips attached to the trailing edge along the entire span on both sides of the airfoil. The strips are attached to the airfoil with double sided tape and meet together to form a 0.050" thick trailing edge which extends the chord by 0.715". Figure 2.34 illustrates the airfoil

in test section after application of the trailing edge modification. A chordwise cross-section is shown in figure 2.35.

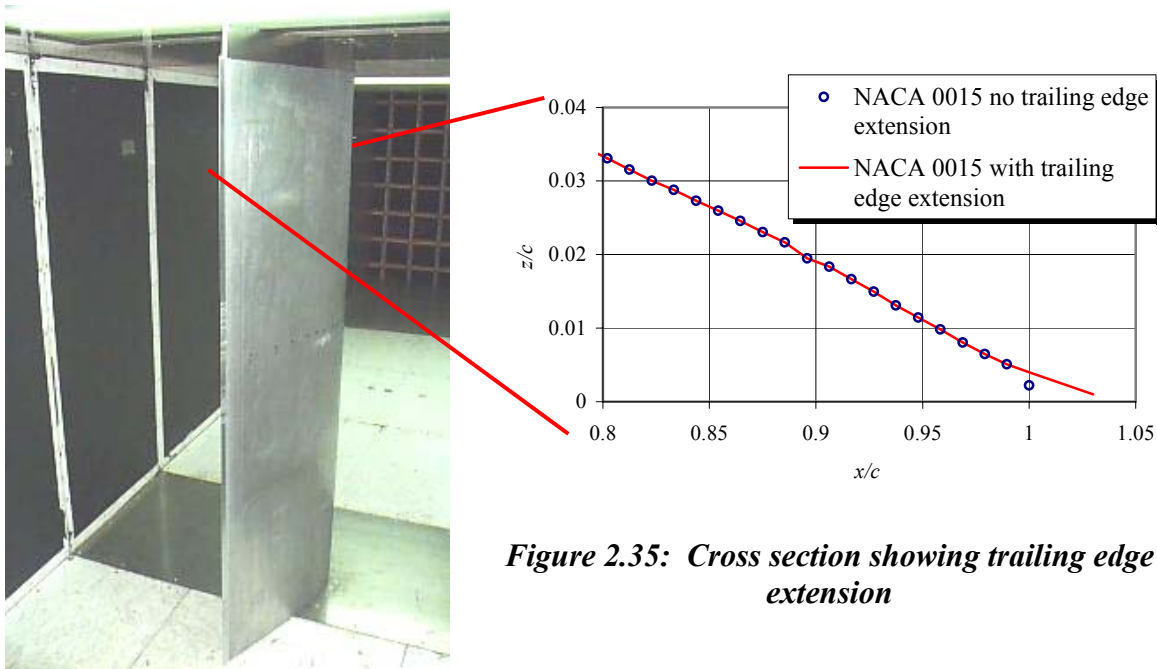


Figure 2.35: Cross section showing trailing edge extension

Figure 2.34: Airfoil with modified trailing edge

Figure 2.36 shows a dimensioned cross-section diagram of the airfoil with the trailing edge modification installed.

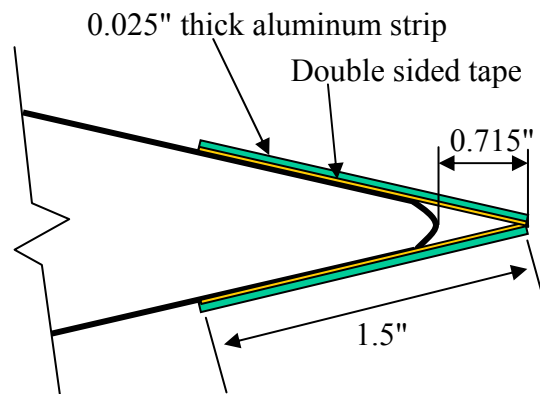


Figure 2.36: Cross section showing dimensioned trailing edge extension

2.1.10 Flow Visualization

Oil flow visualization is performed to document flow features on the airfoil surface at various angles of attack in large grid turbulence. Black construction paper covered with clear contact paper is wrapped around the airfoil over the region containing the microphones and attached to the airfoil with duct tape. Microphone locations are marked on the contact paper with a white paint pen. The oil mixture consists of 15 parts kerosene, 5 parts titanium dioxide (TiO_2), and 1 part oleic acid. Figure 2.37 shows a sample oil flow visualization taken at 0° angle of attack.

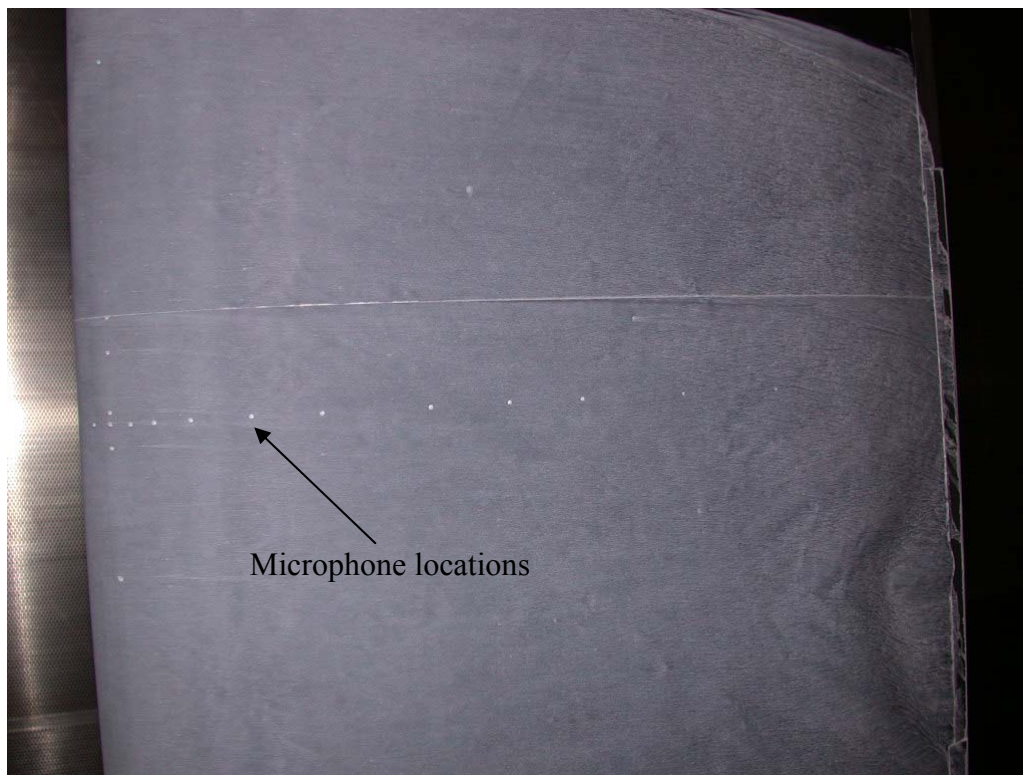


Figure 2.37: Example of flow visualization at 0° angle of attack

3. SINGLE AIRFOIL IN TURBULENCE PREDICTIONS

Two theoretical solutions to the problem of an airfoil encountering turbulence are presented in this chapter. A linearized, inviscid theory developed by Amiet (1976a, b) for a flat plate with no mean loading is presented. This theory is currently in use by engineers and will be directly compared with experimental results. A more sophisticated theory, which incorporates the effects airfoil angle of attack is also presented here. The formulation is from Reba and Kerschen (1996) and uses Rapid Distortion Theory to predict the response of a flat plate in turbulence. Direct comparison of this theory with measured data is not appropriate; however, predicted angle of attack trends are used for discussion.

3.1 Zero Mean Loading Predictions

For the relatively easier scenario of a flat plate at *zero angle of attack*, Amiet (1976a, b) derived one of the most commonly used (likely as a result of its closed form nature) solutions to the problem. Amiet, reworks Filotas' (1969) result into two solution regions, one which is valid at small spanwise wavenumbers (k_y) and the other at high spanwise wavenumbers. In doing so Amiet was able to improve the accuracy of the complete solution to order k_y . Amiet employed Graham's (1970b) similarity rules which relate the general case of a skewed compressible gust to either a parallel compressible gust or a skewed incompressible gust, both of which are much easier to solve, depending on the value of the parameter σ_a , where

$$\sigma_a = \frac{Mk_x}{\beta k_y} \quad (3.1)$$

and $\beta = \sqrt{1-M^2}$. If $\sigma_a \leq 1$ the similarity is to the skewed incompressible gust, whereas, if $\sigma_a \geq 1$ the similarity is to the parallel compressible gust case.

With the two solution regions defined Amiet (1976b), noting that each of the similarity rules are valid outside of the regime for which they are primarily applicable (Graham 1970b), presents a solution for $\sigma_a \leq 1$ derived from the parallel compressible gust case which is valid for small k_y (< 0.25). Patterson and Amiet (1976a, b), based on Amiet (1976b) give the *pressure difference* (see appendix A for definition), with coordinate system origin at mid-span, in this case as

$$\Delta P(x, y, t, k_x, k_y) = 2\pi\rho_o U w_o g(x, k_x, k_y) \cdot e^{i(k_x U t - k_y y)} \quad (3.2)$$

where $g(x, k_x, k_y)$ is the airfoil response function.

For large k_y , Amiet (1976a) derives the skewed incompressible gust solution using the procedure of Schwartzchild (1902) and Landahl (1961) from which the complete high frequency skewed compressible gust result can be obtained. The problem is formulated based on an infinitesimally thin airfoil representing a line discontinuity at zero angle of attack. The flow is assumed inviscid and incompressible with Kutta condition applied at the trailing edge. There is no condition specified at the leading edge. The airfoil response function can be derived (see Mish 2001) for the complete spanwise wavenumber range as

$$g(x, k_x, k_y) = -\frac{f(x, k_x, k_y)}{\pi\beta} \left\{ \pi x \left[\left(k_y^2 / \beta^2 - \mu^2 \right)^{1/2} + i(\mu M + k_x) \right] \right\}^{-1/2} e^{-x \left(k_y^2 / \beta^2 - \mu^2 \right)^{1/2} + i\mu M x} \quad (3.3)$$

where $f(x, k_x, k_y) = 1 - (x/2)^{1/2} \left\{ 1 - \operatorname{erf} \left[\left(2(2-x) \left(k_y^2 / \beta^2 - \mu^2 \right)^{1/2} \right)^{1/2} \right] \right\}$ when $k_y \geq \frac{M}{\sqrt{1-M^2}} k_x$, and

$f(x, k_x, k_y) = 1 - (x/2)^{1/2} \left\{ 1 - (1-i)E \left[2i \left(\frac{1}{\pi} (2-x) \left(\mu^2 - k_y^2 / \beta^2 \right)^{1/2} \right)^{1/2} \right] \right\}$ otherwise. In these

equations, $\mu = M k_x / \beta^2$ and $E[\]$ is the Fresnel integral function.

Due to the random nature of turbulence interacting with an airfoil it is necessary to work with statistical quantities such as the cross-power spectrum density of the pressure jump (S_{qq}^Δ) at two points on the airfoil surface rather than with ΔP itself. The final form of S_{qq}^Δ is obtained for a single sided spectrum (i.e. positive frequencies only) as a function of frequency f in Hertz as

$$S_{qq}^\Delta(x, x', \eta, f) = 16\pi U (\pi\rho b)^2 \int_0^\infty g^*(x', K_x, k_y) g(x, K_x, k_y) \Phi_{ww}(K_x, k_y) e^{ik_y \eta} dk_y \quad (3.4)$$

where $\eta = y - y'$, $K_x = 2\pi f / U$, and Φ_{ww} is the energy spectrum of the turbulence. It should be noted that a factor of π was left out of this expression in the authors masters thesis work (Mish 2001). This has been corrected in all Amiet predictions presented in subsequent chapters.

To compare with the measurements made using the microphone array a MATLAB code to predict the unsteady surface pressure field using the combined theoretical approach of Amiet (1976a, b) has been developed and utilizes the above formulations of S_{qq} . Amiets (1976a, b) prediction scheme requires inputs related to form of the turbulence spectrum, its length scale and turbulence intensity, and half chord of the modeled airfoil. All input parameters are summarized in table 3.1.

Table 3.1: Summary of unsteady pressure prediction code input parameters

Input Parameter	Value
<i>Turbulence spectral form</i> (Φ_{ww})	von Karman as given by Patterson and Amiet (1976a)
<i>Free-stream velocity</i> , U_∞	30m/s
<i>Large grid length scale</i> , λ :	0.0818m
<i>Small grid length scale</i> , λ :	0.0078m
<i>Large grid turbulence intensity</i> :	3.93%
<i>Small grid turbulence intensity</i> :	4.35%
<i>Airfoil half chord</i> , b	0.305m

3.2 Incorporating the Effects of Turbulence Distortion

3.2.1 Rapid Distortion Theory Background

A real airfoil with thickness and at some angle of attack will have a mean potential field associated with its presence in the flow. As such, turbulence encountering the airfoil will be modified as a consequence of the mean field velocity gradients. The modification of the turbulence takes place through stretching, compressing, and tilting of the vorticity vector. Such interaction can be described through the vorticity transport equation which is derived by considering the curl of the Eulers equation and given here as,

$$\frac{D\Omega_j}{Dt} = \Omega_i \frac{\partial U_j}{\partial x_i} \quad (3.5)$$

This equation is often referred to as the rapid distortion equation. This equation is, of course, an inviscid representation of the distortion. As such, it is valid only when the distortion occurs so rapidly that the interaction between turbulence and the influence of viscous dissipation can be neglected.

This method of modeling the evolution of turbulence is referred to as Rapid Distortion Theory (RDT). Batchelor and Proudman (1954) performed some of the pioneering work in the area of RDT, developing the appropriate conditions for its applications and the techniques required to apply this theory to a real flow. When considering the response of an airfoil to a turbulent inflow it is important to consider the effects of the mean field induced distortion of the inflow turbulence. Therefore, several researchers have developed theories for predicting the response of an airfoil to turbulence using the RDT approach.

The theory considered here was developed by Kerschen and Myers (1983), Myers and Kerschen (1995), and Reba and Kerschen (1996) for application to a flat plate airfoil subject to

some mean loading (i.e. at some angle of attack). A solution is derived for the unsteady pressure distribution on the airfoil surface due to interaction with a three dimensional time harmonic gust. The airfoil is assumed to be a zero thickness flat plate at some mean angle of attack to a subsonic inflow. The distortion of the inflow by the mean field velocity gradients is accounted for using RDT. Singular perturbation expansions are developed for the case of Mach number of order 1, wherein the acoustic wavelength is short compared to the airfoil chord and for the case of small Mach number, in which the acoustic wavelength is long compared to the airfoil chord. As such, the airfoil-gust interaction analysis is simplified in various asymptotic limits at high and low acoustic frequencies, where the acoustic frequency is given as

$$k_a = w_a \omega_r \quad (3.6)$$

with $w_a = \sqrt{\left(\frac{M_\infty}{\beta^2}\right)^2 - \left(\frac{k_3}{\beta}\right)^2}$, $\beta = \sqrt{1 - M_\infty^2}$, k_3 is the spanwise wavenumber.

Note, the notation used here is consistent with that presented by Reba and Kerschen (1996) and is used and defined *only* in this section. For the case of $M_\infty \ll 1$ (the case for the present experiment, $M_\infty = 0.087$), the low acoustic frequency limit is applied. In doing so the gust may be two or three dimensional; however, due to the relationship between the acoustic frequency and spanwise wavenumber a three dimensional gust is limited to only very small spanwise wavenumbers. Reba and Kerschen (1996) develop a FORTRAN computer routine the theory outlined above.

Reba and Kerschen (1996) give the inflow as

$$v'(\omega_r, k_n, k_3) = \varepsilon U_\infty (A_t, A_n, A_3) e^{i\omega_r(\phi + k_n y + k_3 x_3 - t)} \quad (3.7)$$

where $U_\infty \varepsilon$ is taken to be the upwash amplitude referred to as w_o . The parameters of equation 3.3 are given in table 3.2

Table 3.2: Parameters used in Reba and Kerschen (1996) airfoil response theory

Parameter	Comment	Non-dimensionalization
ε	Dimensionless small number	-
U_∞	Freestream velocity	-
(A_t, A_n, A_3)	Streamwise, normal to planform, and spanwise non-dimensional gust amplitudes	-
ω_r	Reduced frequency	$\omega b / U_\infty = k_t b$
b	Half chord, $c/2$	-
ϕ	Non-dimensional mean flow velocity potential	$\phi_p / U_\infty b$

ψ	Non-dimensional mean flow stream function	$\psi_p \beta_\infty / U_\infty b$
x_3	Non-dimensional spanwise coordinate	x_p / b
k	Non-dimensional streamwise wavenumber	$k_t b$
$\omega_r k_n$	Non-dimensional normal to planform wavenumber	-
$\omega_r k_3$	Non-dimensional spanwise wavenumber	-
t	Non-dimensional time	$t_p b / U_\infty$
β_∞	Prandtl-Glauert transformation	$(1-M^2)^{1/2}$

A modified pressure, p is calculated by the code for the pressure and suction side of the airfoil which, for a given set of gust amplitudes, is a function of the wavenumber vector, chordwise position, Mach number, and angle of attack. The modified pressure is related to the physical pressure, p' on the surface of the airfoil by

$$p'(x, k_n, k_3, t) = -p(x, \omega_r, k_n, k_3) \rho U_\infty w_o e^{i\omega_r(k_3 x_3 - t)} \quad (3.8)$$

where w_o is the upwash amplitude. The code also uses a FORTRAN IMSL library function for the evaluation of the complex error function. This function produces significant errors when the reduced frequency becomes large. Therefore, all analysis with this prediction scheme is limited to $1 < \omega_r < 10$ which seems to produce reasonable results.

3.2.2 Derivation of Cross-spectral Density of Surface Pressure Fluctuations

Reba and Kerschen (1996) do not present an explicit expression for the airfoil response function (i.e. transfer function). Additionally, their program is designed to compute the modified pressure for one set of inflow wave amplitudes and wavenumbers. Therefore, in order to estimate the surface pressure cross-spectral density using this code for the experimental inflows researched here it was necessary to implicitly determine the airfoil response function and integrate over all wavenumbers. This is accomplished by considering the response of the airfoil to a unit amplitude gust. As such, the transfer function is found in terms of the modified pressure, p_{ua} as (keeping with the notation of Reba and Kerschen)

$$g(x, \omega_r, k_n, k_3) = -p_{ua}(x, \omega_r, k_n, k_3) \rho U_\infty w_o \quad (3.9)$$

with $W_o = 1$. Summing over all wavenumbers, the relationship between the surface pressure, p' and the inflow can then be written in terms of the transfer function as

$$p'(x, x_3, t) = \int_{-\infty}^{\infty} \int_{-\infty}^{\infty} \int_{-\infty}^{\infty} g(x, \omega_r, k_n, k_3) w_o e^{i\omega_r(k_3 x_3 - t)} dk_n dk_3 d\omega_r \quad (3.10)$$

where W_o is the upwash amplitude. The Fourier transform with respect to time can now be performed to give the surface pressure in terms of frequency such that

$$p'(x, x_3, \omega_r) = \int_{-\infty}^{\infty} \int_{-\infty}^{\infty} \int_{-\infty}^{\infty} g(x, \omega_r, k_n, k_3) w_o e^{i\omega_r(k_3 x_3 - t)} e^{-i\omega_r t} dk_n dk_3 d\omega_r dt \quad (3.11)$$

Assuming the dependency of the spanwise wavenumber on reduced frequency is removedⁱ and substituting equation 3.9 for the transfer function, g , equation 3.11 becomes

$$p'(x, x_3, \omega_r) = U_{\infty} \rho \int_{-\infty}^{\infty} \int_{-\infty}^{\infty} -p_{ua}(x, \omega_r, k_n, k_3) w_o e^{ik_3 x_3} dk_n dk_3 \quad (3.12)$$

where $k_3 = \frac{\hat{k}_3}{\omega_r}$. The pressure jump (or difference), ΔP is now formed by considering the difference between the pressure on the upper and lower surface of the airfoil

$$\begin{aligned} \Delta P(x, x_3, \omega_r) &= p_U' - p_L' \\ &= U_{\infty} \rho \int_{-\infty}^{\infty} \int_{-\infty}^{\infty} -[p_{Uua}(x, \omega_r, k_n, k_3) - p_{Lua}(x, \omega_r, k_n, k_3)] w_o e^{ik_3 x_3} dk_n dk_3 \end{aligned} \quad (3.13)$$

where p_{Uua} and p_{Lua} are the modified pressures computed for a unit amplitude inflow on the upper and lower surfaces respectively. The cross-spectrum of pressure difference fluctuations can now be computed by taking the expected value of the pressure difference times its conjugate

$$S_{qq}^{\Delta}(x, x', x_3, x'_3, \omega_r) = \lim_{T \rightarrow \infty} \frac{\pi}{T} E \left[\Delta P(x, x_3, \omega_r) \Delta P(x', x'_3, \omega_r)^* \right]. \quad (3.14)$$

Noting that the only non-deterministic quantity of equation 3.13 is the upwash amplitude, w_o which can be related to the upwash velocity spectrum, ϕ_{ww} as

$$E \left[w_o(\omega_r, k_3) w_o(\omega_r, k'_3)^* \right] = \frac{R}{\pi} \delta(k_3 - k'_3) \phi_{ww}(\omega_r, k_3) \quad (3.15)$$

where $T = R/U_{\infty}$ and R is the spatial region over which the inflow is considered (both T and R are normalized with the free-stream velocity), the pressure difference cross-spectrum becomes

$$S_{qq}^{\Delta}(x, x', \eta, \omega_r) = (U_{\infty} \rho)^2 \int_{-\infty}^{\infty} \int_{-\infty}^{\infty} (p_{Uua} - p_{Lua})(p_{Uua}' - p_{Lua}')^* \phi_{ww}(\omega_r, k_3) e^{ik_3 \eta} dk_n dk_3 \quad (3.16)$$

where $\eta = x_3 - x'_3$. To avoid confusion it is worth noting, explicitly that equation 3.16 is for a double sided spectrum in frequency ($-\infty < \omega_r < \infty$) and therefore is multiplied by 2 when calculated to obtain a single sided spectrum for comparison purposes.

ⁱ The FORTRAN code developed by Reba and Kerschen (1996) was modified to remove the dependence of the spanwise and normal to planform wavenumber on frequency by dividing both parameters by the reduced frequency.

3.2.3 Application of Reba and Kerschen Surface Pressure Prediction Code

As a check to ensure the cross-spectral density, S_{qq} is calculated correctly a comparison with Amiet's (1976a, b) theory is performed. Both theories ideally should converge to the same solution at zero angle of attack. Since it is not possible to integrate over the same spanwise wavenumber range in both theories (i.e. Reba and Kerschen's theory is limited to low acoustic frequencies) a comparison at one set of wavenumbers is performed. The following are the input parameters for both theories;

Table 3.3: Parameters used in Kerschen/Amiet comparison

Parameter	Comment	Value
M_∞	Mach No.	0.087
k	Streamwise wavenumber	1
k_3	Spanwise wavenumber	1
k_n	Normal to planform wavenumber	1
η	Spanwise separation	0
u/U_∞	Turbulence intensity	3.98%
λ	Integral length scale of turbulence	0.08m
x/c	Chordwise locations	1, 2.5, 4, 6, 9, 14%

Figure 3.1 is a plot of the auto-spectral level for Amiet (1976a, b) and Reba and Kerschen's (1996) theories as a function of chordwise location. Note that in the y-axis label $G_{\Delta p \Delta p}$ is the auto-spectrum of the pressure difference calculated in Hertz and is related to S_{qq}^Δ as

$$G_{\Delta p \Delta p}(f) = \frac{2\pi b}{U_\infty} S_{qq}^\Delta(x = x', \eta, \omega_r) \quad (3.17)$$

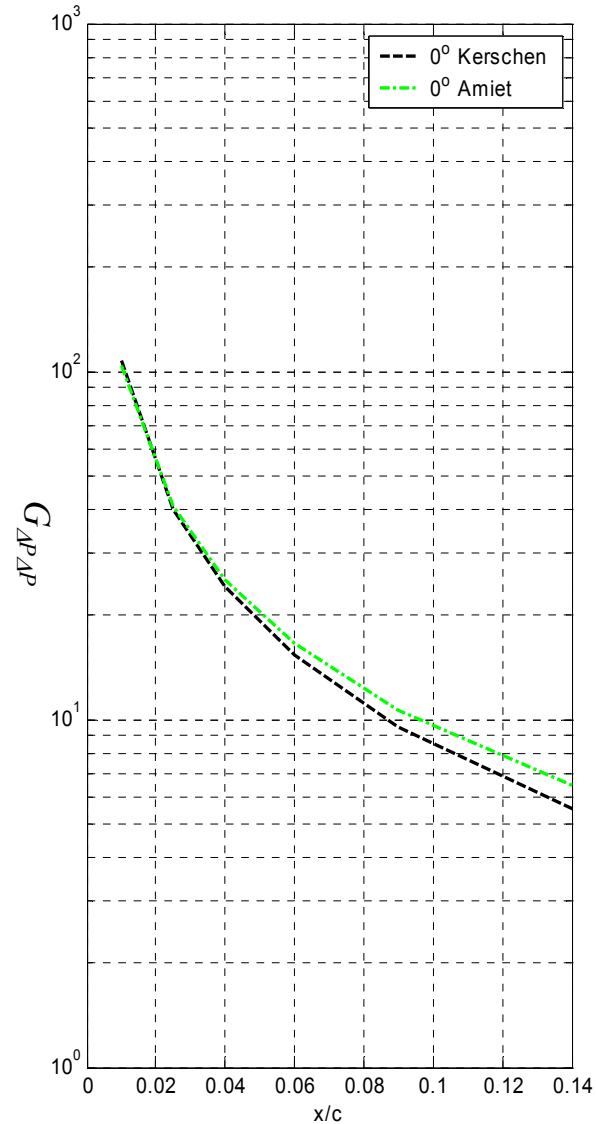


Figure 3.1: Comparison of Amiet (1976a, b) and Reba and Kerschen (1996) theories

Figure 3.1 shows excellent agreement between the two theories up to 4% chord at which point Reba and Kerschen's theory begins to diverge slightly. The divergence of the two theories beyond 4% chord is likely related to the numerical integration scheme employed in Reba and Kerschen's code.

Having confidence in the formulation of S_{qq} the above procedure is used to investigate the effects of turbulence distortion on unsteady pressure and lift. The following serve as input parameters to Reba and Kerschen's FORTRAN code;

$$M_{\infty} = 0.087$$

$$k = i, \text{ where } i = 1, 2, 3 \dots 10$$

$$k_3 = \frac{10^{[(j-1)\Delta k_3]}}{k}, \text{ where } j = 1, 2, 3 \dots 41 \text{ and } \Delta k_3 = 0.01$$

$$k_n = \frac{10^{[(l-1)\Delta k_n]}}{k}, \text{ where } l = 1, 2, 3 \dots 30 \text{ and } \Delta k_n = 0.06$$

$$\eta = 0$$

$$\alpha = 0^\circ, 2^\circ, 6^\circ$$

$$x/c = 1, 2.5, 4, 6, 9, 14\%$$

4. SINGLE AIRFOIL IN TURBULENCE: EXPERIMENTAL DETAILS AND DATA QUALITY

This experiment sets out to measure the inviscid response of an airfoil in turbulence using an array of microphones mounted sub-surface. In this chapter the experimental details are provided and the quality of the measured unsteady pressure data examined.

4.1 Measurement Conditions and Data Sampling

Measurements of unsteady pressure were made in two wind tunnel configurations. A set of measurements was made with the Virginia Tech Stability Wind Tunnel in its solid wall configuration (i.e. steel plates form test section walls). A complimentary set of measurements was made with the steel walls replaced by acoustically treated walls.

4.1.1 Solid Test Section Wall Test

Measurements of unsteady surface pressure were made in solid wall configuration using an array of ninety-six microphones (forty-eight per side with each side a mirror image of the other). Measurements were made at angles of attack, $\alpha = 0^\circ, 4^\circ, 8^\circ, 12^\circ, 16^\circ, 20^\circ$ (figure 4.1 defines positive angles of attack). The nominal flow velocity was 30 m/s corresponding to a chord Reynolds number of 1.17×10^6 . Measurements were made with the airfoil immersed in small and large grid turbulence. Two sampling rates were used to gather data in large grid turbulence; 1.6 kHz and 12.8 kHz. Data was sampled at 12.8 kHz in small grid turbulence. Five hundred records of data were taken with a record length of 2048.

Simultaneous measurement of all ninety-six microphones was not possible due to the data acquisition systems sixty-four channel capacity. Therefore, measurements were made in three microphone blocks with the longest chordwise row of microphones common to each as discussed in chapter 2 and shown in figure 2.22. Block one measured the first two spanwise rows (row A & B), block two the third and fourth spanwise rows (row C & D), and block three the fifth spanwise row (row E). Some measurements also used a fourth block of microphones which was composed of rows B & D.

Several subsets of unsteady pressure data were taken under alternate configurations. To aid in assessing noise in unsteady pressure measurements, data was taken with the turbulence generating grid removed. Two types of measurements were made in this configuration. One

matched the flow velocity of 30 m/s (nominally) which aids in assessing contamination associated with boundary layer pressure fluctuations. This measurement is referred to as ‘smooth flow’ in subsequent discussion. The other matched the tunnel fan speed (RPM) achieved when the grid is installed which aids in determining the extent of ambient acoustic field contamination. Additionally, as discussed in chapter 2, measurements of unsteady pressure were made with a modified trailing edge and simultaneous velocity/pressure measurements were also performed. Table 4.1 summarizes the angle of attacks, microphone configuration, sampling rates, and grids used in each solid wall measurement.

Table 4.1: Solid Wall Test Configuration Details

<i>Measurement</i>	<i>Angle of attack</i>	<i>No. of Mics</i>	<i>Microphones Used. Definitions refer to figure 2.20</i>	<i>Grid</i>	<i>Sampling Rate</i>
Unsteady pressure	0°, 4°, 8°, 12°, 16°, 20°	96	Column 4 Row A-E	Large	1.6kHz
				Small	12.8kHz
Velocity/Pressure	-16°, -8°, 0°, 8°, 16°	54	Column 4 Row B & D	Large	1.6kHz
				Small	12.8kHz
Modified trailing edge	0°, 4°, 8°, 12°, 16°, 20°	54	Column 4 Row B & D	Large	1.6kHz
				Small	12.8kHz
Matched flow speed	0°, 4°, 8°, 12°, 16°, 20°	54	Column 4 Row B & D	No grid	1.6kHz
Matched RPM	0°	54	Column 4 Row B & D	No grid	1.6kHz
				No grid	12.8kHz

Mean pressure measurements were also made using the forty-eight port scani-valve system described in chapter 2. These measurements were made at $\alpha = 0^\circ, 4^\circ, 8^\circ, 12^\circ, 16^\circ, 20^\circ$.

4.1.2 Acoustically Treated Wall Test

A complimentary set of unsteady pressure measurements were made with the Virginia Tech Stability Wind Tunnel solid walls replaced by acoustic treatment modules. These measurements were performed with an array of forty microphones configured as discussed in chapter 2 and shown in figure 2.21 (i.e. column 4 and row B). The instrumented airfoil was immersed in large grid turbulence only for this set of measurements with data taken over a range of angles of attack, α , from 0° to 20° in 2° increments. Two sampling rates were used for these measurements; 1.6 kHz and 25.6 kHz. One-thousand records were taken with a record length of 2048.

Additionally, measurements were performed at $\alpha = -4^\circ$ and -8° . A boundary layer trip was incorporated into a set of measurements covering $\alpha = -8^\circ, -4^\circ,$ and 4° . Lastly, a leading edge bump was installed and unsteady pressure measured at $\alpha = -8^\circ$. For this set of measurements a sampling rate of 1.6 kHz with a record length of 2048 was used to take 200 records of data. Mean pressure measurements were made at 20% chord to ensure correct angle of attack alignment.

4.1.3 Coordinate System

The coordinate system used in the description of all single airfoil in turbulence data is shown in figure 4.1 and 4.2. The origin is in the plane of the leading edge with x directed downstream at mid-span, y directed up along the leading edge, and z completing the system by the right-hand rule.

4.2 Measurement Uncertainty

4.2.1 Uncertainty in Pressure Spectra

An estimate of the uncertainty in unsteady pressure measurements is made based on repeated measurements. At any one angle of attack measurements were made with three microphone blocks with the longest chordwise row of microphones common to each block. By considering the three repeated measurements of the longest chordwise row the uncertainty in the pressure difference spectra can be obtained at each chordwise location. Table 4.2 presents the uncertainty in pressure difference spectra, ε_r for $x/c = 1$ and 4% (representative locations) in decibels (dB) based on repeated measurements at $\alpha = 0^\circ$ in large grid flow at 20 to 1 odds (95%).

Table 4.2: Uncertainties in unsteady pressure spectra

ω_r	ε_r at $x/c = 0.1$ (\pm dB)	ε_r at $x/c = 0.4$ (\pm dB)
<i>Large Grid</i>		
1	0.58	0.92
10	0.49	0.40
35	0.81	0.18
<i>Small Grid</i>		
10	0.58	0.46
100	0.50	0.57
300	0.36	0.38

The uncertainty in auto-spectra is further reduced through spanwise averaging. The reduction in uncertainty based on statistical convergence is given by Bendat and Piersol (1986) as

$$\varepsilon_c = \frac{\varepsilon_r}{\sqrt{N}} \quad (4.1)$$

where $N = 8$ (the number of microphones in a spanwise row). As such, spanwise averaging reduces spectral certainty sixty-five percent giving a maximum uncertainty of 0.35dB at $x/c = 4\%$ for $\omega_r = 1$.

4.2.2 Uncertainty in RMS Pressure

Mean-square pressure is calculated by integrating the pressure spectrum such that

$$\overline{p^2} = \int_0^{\infty} S_{qq}(x = x', \eta = 0, \omega) d\omega \quad (4.2)$$

where S_{qq} is the *surface pressure* cross-spectral density. Values of the RMS pressure, p' are calculated from the square root of $\overline{p^2}$. Using the analysis of Kline and McClintock (1953) the uncertainty in the $\overline{p^2}$ is estimated as

$$\varepsilon_{\overline{p^2}} = \varepsilon_{\text{spectrum}} \frac{\sqrt{\sum_{i=1}^N S_{qq}^2(\omega_i) \Delta\omega_i^2}}{\sum_{i=1}^N S_{qq}(\omega_i) \Delta\omega_i} \quad (4.3)$$

where $S_{qq}(\omega_i)$ and $\Delta\omega_i$ are the spectral value and bin width at the i th position. Here the error in the spectrum, $\varepsilon_{\text{spectrum}}$ is taken as ε_c from equation (4.1). The uncertainty of the RMS pressure is given by Kline and McClintock (1953) as

$$\varepsilon_{p'} = \sqrt{\frac{1}{2} \varepsilon_{\overline{p^2}}^2} \quad (4.4)$$

Root mean square pressure uncertainty, $\varepsilon_{p'}$, values at chordwise locations from 1% to 14% are evaluated at each angle of attack on the pressure and suction side of the airfoil. These values are found to be less than 3%.

4.3 Basic Flow Definition

4.3.1 Mean and Unsteady Blockage Effects

The combined effect of solid and wake blockage produce at most slightly more than 1% change in velocity in both grid flows which is expected to negligibly affect unsteady pressure measurements. Streamline curvature restriction produced up to a 0.38° increase in angle of attack occurring in the small grid flow at $\alpha = 16^\circ$ and as much as a 0.042 reduction in C_L occurring again in the small grid flow at $\alpha = 20^\circ$. The changes implied by the streamline curvature restriction correction are considered small and will not adversely affect unsteady pressure measurements. Additional details on mean blockage effects are available in Mish (2001)

The effects of unsteady blockage or, what is also referred to as unsteady wall interference, have been investigated by Karasoy (1990). Karasoy measures the unsteady surface pressure of an oscillating airfoil at several oscillation frequencies and at varying values of h/c , where h is the tunnel test section half height/width and c is the characteristic dimension of the body (taken to be the airfoil chord). These results show that for small values of h/c (< 0.5) a large rise in unsteady pressure occurs for $\omega_r < 1$. As h/c increases above 1 the unsteady surface pressure is minimally affected. In the case of the present experiment $h/c = 1.5$ and, as such the unsteady pressure measurements are believed to be largely unaffected.

4.3.2 Mean Pressure

Mean pressure measurements are summarized here (discussed in detail in Mish 2001) through the presentation of mean C_L versus angle of attack for both large and small grid measurements. Figure 4.3, adapted from Mish (2001), presents lift coefficients for $\alpha = 0^\circ, 4^\circ, 8^\circ, 12^\circ, 16^\circ$, and 20° calculated from integrating mean pressure measurements. Also shown on figure 4.3 are the mean C_L values for various measurements made by McKeough (1976) with a NACA 0015 in various scale and intensity turbulent flows. The theoretical lift curve, $2\pi\alpha$ is also plotted on figure 4.3. In both the large and small grid flows there is a region of unstalled flow which persists up to $\alpha = 16^\circ$. With the airfoil immersed in small grid flow complete stall does not occur at $\alpha = 20^\circ$. This is likely a result of the small scale grid generated turbulence interacting with the turbulent boundary layer. High levels of kinetic energy are brought into the

boundary layer since the scale of the grid generated turbulence is on the order of the turbulent boundary layer scale. In the large grid flow the airfoil stalls at $\alpha = 20^\circ$.

4.3.3 Stagnation, Transition, and Separation Points

The transition, stagnation, and separation locations are recapped here (discussed in detail in Mish 2001) through figure 4.4 (small grid) and 4.5 (large grid). These figures, which are adapted from Mish (2001), show a cross-section of the airfoil with the locations of transition, stagnation, and separation denoted by symbols along the edge of the airfoil. In the small grid turbulence transition, determined from high pass filtered pressure time series, was found to occur forward of the most leading edge microphone (1% chord) and is therefore taken to occur at the leading edge. Based on examination of mean pressure data, a small laminar separation bubble may develop over the leading edge region at $\alpha = 16^\circ$ and 20° . No independent verification of this bubble is offered. The large grid transition locations are shown to shift down the chord on the pressure side as the angle of attack is increased while moving towards the leading edge on the suction side. Mean pressure data also suggests the occurrence of a laminar separation bubble at $\alpha = 16^\circ$ in the large grid flow. Although not presented here, Mish (2001) shows a comparison of the mean pressure at $\alpha = 16^\circ$ angle with panel method calculations which show a loss of pressure over the first 5% chord. Oil flow visualization is used to provide additional evidence on the presence of this bubble.

4.3.4 Large Grid Flow Visualization

Oil flow visualization is performed over a range of angles of attack including, $\alpha = 0^\circ, \pm 4^\circ, \pm 8^\circ, \pm 12^\circ, 16^\circ, 20^\circ$ in *large* grid turbulence only. The oil flow visualization is performed by wrapping black contact paper around the airfoil as discussed in chapter 2. The contact paper will of course moderately alter the shape of the airfoil and smoothes out surface irregularities. Therefore, flow phenomena which are triggered by local airfoil geometry may not be present when oil flow visualization is in progress. Hence, oil flow visualization, as with many types of flow visualization requires cautious interpretation of results. As such, the conclusions drawn here are somewhat ambiguous and, where possible, are corroborated with independent data.

Figure 4.6 presents oil flow visualization results at $\alpha = 0^\circ$ on the access hatch side of the airfoil (4.6a) and solid side of the airfoil (4.6b). A thinning of particles is shown to occur, between 11% and 15% chord on the hatch (pressure side when angle of attack is positive) side of

the airfoil and between 8% and 12% chord on the solid side. This is likely a result of boundary layer transition. That is, as transition occurs there is a rise in skin friction which in turn carries additional particles out of the transition region. The transition points noted by Mish (2001) based on analysis of unsteady pressure data are near 6% chord on the hatch side and 8% chord on the solid side. The slight disagreement may be the result of the contact paper used during flow visualization. As mentioned above, the contact paper will tend to smooth out small imperfections on the surface of the airfoil. These imperfections would otherwise act to destabilize the flow and cause transition to occur closer to the airfoil leading edge.

As the angle of attack is increased from $\alpha = 4^\circ$ to 16° a darker colored region persists (i.e. thinning of particles in the oil mixture implying an increase in skin friction) over approximately 3% of the chord on the suction side of the airfoil that may be related to an unsteady laminar separation bubble (denoted in figures 4.7-4.11 by the two red lines). This region, staying nearly the same size moves towards the leading edge with increasing angle of attack. The laminar separation bubble, if truly present, likely develops as follows; first the laminar boundary layer separates just downstream of the suction peak where the pressure is strongly adverse. Next, the separated laminar shear layer quickly becomes turbulent and subsequently reattaches a short distance downstream. The turbulent reattachment is believed to cause the thinning of oil particles shown in figures 4.7-4.11. Analysis of mean pressure data also suggests the occurrence of a laminar separation bubble at $\alpha = 16^\circ$. Furthermore, the work of McKeough (1976) showed a similar phenomenon occurring on a NACA 0015 immersed in grid generated turbulence. McKeough immersed a 0.3m NACA 0015 in turbulence characterized by a length scale 40% of c and intensity of 6%. He observed, through tuft flow visualization, the development of a small leading edge laminar separation bubble as the angle of attack was increased, ultimately culminating in combined lead/trailing edge stall. The lack of a clear separation or reattachment line in the oil suggests that the laminar separation bubble is highly unsteady. This would be consistent with bubble formation in turbulent flow. That is, as the loading on the airfoil fluctuates as a consequence of interacting with the inflow, the size and position of the bubble will be altered blurring the separation and reattachment points. At $\alpha = 20^\circ$ (figure 4.11) the flow appears to separate just before 1% chord causing the airfoil to completely stall.

Figures 4.6-4.11 also show the approximate stagnation point location. These locations agree well with the mean pressure data presented in Mish (2001). Table 4.3 presents the

approximate locations of the stagnation point and turbulent reattachment of the conjectured laminar separation bubble at each angle of attack along with the theoretical stagnation point location (calculated based on inviscid theory using a vortex panel code). The location of turbulent reattachment of the speculated laminar separation bubble is approximated based on the observed oil thinning.

Table 4.3: Stagnation point and laminar separation bubble locations for large grid measurement

α (deg)	Stag Pt. Theory (% c)	Stag Pt. Flow Vis. (% c)	Turbulent reattachment of speculated laminar separation bubble location (% c)
0	0	0	No separation
4	0.4	No data	6-9
8	1.6	1.7	2.5-6
12	3.6	2.7	2.6-6
16	6.7	4.2	0.9-2.3
20	10.5	6.0	separation

4.4 Quality of Unsteady Pressure Data

4.4.1 Spanwise Homogeneity

It is important to verify that measured unsteady pressure fluctuations are indeed homogeneous across the span as would be expected based on the spanwise homogeneous inflow. The homogeneity is checked by comparing auto-spectra from each spanwise location for any given chordwise location. Such comparisons are possible for chordwise positions $x/c = 1, 2.5, 4, 6, 9\%$.

Small grid surface pressure auto-spectra (G_{pp}) from each spanwise location are presented in figure 4.12 at $\alpha = 0^\circ$ for chordwise positions $x/c = 1, 2.5, 4, 6, 9\%$ on the suction side of the airfoil. The spectra at $x/c = 1\%$ are banded together within ~ 3 decibels (dB) for all spanwise locations except $y/c = 33\%$. The calibration for the microphone at this location is incorrect and, as such, this microphone has been removed from subsequent analysis. Moving to $x/c = 2.5\%$, the spectra across the span fall agreeably on top of each other with ~ 2 dB of spread. Similar agreement is shown at $x/c = 4$ and 6% . The homogeneity of spectra at $x/c = 9\%$ is within 4dB however, microphones at locations $y/c = 24$ and 35% fall decades below the other locations as a result of bad microphone calibrations. These two microphones were also removed from additional analysis.

Small grid pressure side auto-spectra from each spanwise location are presented at $\alpha = 0^\circ$ for chordwise positions $x/c = 1, 2.5, 4, 6, 9\%$ in figure 4.13. The spectra from different spanwise stations compare to within 3dB at all locations except $y/c = 27\%$. The source of this spectrum's rise ($\sim 3\text{dB}$ relative to its spanwise companions) is not clear; however, it may be related to flow asymmetries produced by small asymmetries in the leading edge. The spectra agree well at $x/c = 2.5$ and 4% with $\sim 3\text{dB}$ of spread across the span. Moving to $x/c = 6\%$, spectra vary across the span by as much as 7dB. This poor agreement in spanwise spectra persists at $x/c = 9\%$ with $\sim 9\text{dB}$ of discrepancy. The source of this considerable variation at both $x/c = 6$ and 9% may be related to asymmetries in the flow. Inspection of microphone calibrations shows them to be consistent at each spanwise location. Flow asymmetries may arise from asymmetric boundary layer transition, wakes produced by microphone mounting holes, or leading edge asymmetries.

Comparisons of suction side spectra at different spanwise stations for the large grid turbulence are presented in figure 4.14 with the airfoil at $\alpha = 0^\circ$. Spanwise data comparisons are made for chordwise locations $x/c = 1, 2.5, 4, 6, 9\%$. Spectra at $x/c = 1\%$ are within 1dB across the span. Similar agreement is shown at $x/c = 2.5\%$ with exception to the spectrum at $y/c = 98\%$. The microphone here suffers from a bad calibration and is removed from remaining analysis. Spanwise spectra at $x/c = 4$ and 6% agree within $\sim 2\text{dB}$. This agreement continues at $x/c = 9\%$ however, two microphones at $y/c = 24$ and 27% suffer from bad calibrations and are also removed from further data analysis.

Large grid pressure side auto-spectra from each spanwise location are presented at $\alpha = 0^\circ$ for chordwise positions $x/c = 1, 2.5, 4, 6, 9\%$ in figure 4.15. Spectra at $x/c = 1\%$ agree within $\sim 3\text{dB}$ except for the spectrum at $y/c = 46\%$. A flow asymmetry, likely produced by the leading edge, seems to be the source of spectral level reduction at this location. The agreement of spanwise spectra improves slightly to within $\sim 2\text{dB}$ at $x/c = 2.5, 4,$ and 6% . At $x/c = 9\%$ spanwise spectra are within $\sim 3\text{dB}$ for $\omega_r < 10$. Above $\omega_r = 10$ the spectra spread out with as much as 10dB of difference occurring across the span. This high frequency variation is likely related to asymmetric boundary layer transition.

In summary, the homogeneity of spanwise unsteady pressure measurements is good with exception to several measurement locations corrupted by bad microphone calibrations. These locations have been removed from further data analysis. With spanwise consistency demonstrated, the data is averaged across the span to aid in reducing uncertainty (a full

explanation of the formation of cross-spectral density of pressure fluctuations and the inherent averaging utilized is presented in appendix A). The remaining analysis will employ this reduced uncertainty data set, where appropriate.

4.4.2 Effects of Acoustic Treatment and Data Repeatability

Recalling that two independent measurements (solid wall and acoustic walls) of unsteady pressure were performed only with the airfoil in large grid turbulence, this section discusses repeatability and acoustic treatment effects related to the large grid data only.

Zero Angle of Attack: Measurements of unsteady pressure were made in two wind tunnel test section configurations (solid and acoustically treated walls). Comparison of spectra from these measurements is useful for determining the repeatability of the measurement and assessing the effects of acoustic treatment. Of chief concern is the presence of local flow phenomena which may *not* be highly repeatable and therefore, produce differences in the data sets. The effect and repeatability of laminar separation bubbles is of particular interest given the evidence of such features in oil flow visualization. As such, comparisons of pressure spectra from both measurements are made in figure 4.16 and 4.17 for the suction and pressure sides of the airfoil respectively. Spectra are presented for $\alpha = 0^\circ$ at $x/c = 1, 2.5, 4, 6, 9, 14\%$.

The suction side comparison (figure 4.16) consistently shows the solid wall pressure spectra residing above the acoustic wall spectra. At $x/c = 1\%$ the agreement is within $\sim 1.75\text{dB}$ across the frequency range. However, the agreement deteriorates slight at $x/c = 2.5\%$ with $\sim 3\text{dB}$ of difference occurring over all frequencies. Chordwise positions, $x/c = 4, 6,$ and 9% show agreement within $\sim 2\text{dB}$ across all frequencies. Spectra at 14% chord are within $\sim 2\text{dB}$ for $\omega_r < 7$ and then diverge by as much as $\sim 7\text{dB}$ over higher frequencies. The divergence at high frequencies may result from transition occurring at slightly different chordwise locations in each measurement.

Spectra measured on the airfoil pressure side for each wall configuration are presented in figure 4.17. As with the suction side, the solid wall spectra are consistently situated above the acoustic wall spectra at all chordwise locations. The leading edge measurement location, $x/c = 1\%$ shows $\sim 3\text{dB}$ of difference for $\omega_r < 10$. The agreement improves to nearly perfect as the frequency increases. The poor agreement at this location may be the result of a local flow

phenomenon, such as a transient laminar separation bubble. Evidence of such a bubble is shown in oil flow visualization. The agreement improves to within ~ 1 dB at $x/c = 2.5$ and 4% over all frequencies. At $x/c = 6\%$ agreement is within ~ 2 dB for $\omega_r < 10$, however, deteriorates to ~ 4 dB with increasing frequency. Spectra are within 1dB for $\omega_r < 10$ at $x/c = 9\%$. Due, perhaps, to differences in chordwise transition location, the agreement gets worse with increasing frequency. Similar type agreement is shown at $x/c = 14\%$, however, for $\omega_r < 10$ nearly 3dB of difference in spectral level occurs.

Eight Degrees Angle of Attack: Comparisons of spectra measured in the presence of solid and acoustic walls are also made at $\alpha = 8^\circ$ for chordwise locations, $x/c = 1$ and 2.5%. Figure 4.18 and 4.19 present spectra measured on the suction and pressure side of the airfoil respectively. On the suction side (figure 4.18) the spectrum measured with solid walls resides above spectrum measured with acoustic walls. The difference is nearly 2dB at both chordwise locations, $x/c = 1$ and 2.5% across the frequency range and is similar to that shown at $\alpha = 0^\circ$. On the pressure side (figure 4.19) at $x/c = 1\%$ the solid wall spectrum is above the acoustic wall spectrum by as much as 3dB across the frequency range. The agreement improves at $x/c = 2.5\%$ with no more than 1dB of difference occurring; however, the acoustic wall spectrum has now shifted above the solid wall spectrum.

Discussion on Measurement Repeatability: The repeatability of this measurement is reasonable; however, differences are shown on both sides of the airfoil at $\alpha = 0^\circ$ and 8° . Because differences occur across the range of measured frequencies, it is unlikely such differences arise solely from the acoustically treated test section walls. The acoustic treatment was shown to produce significant attenuation at low frequencies and therefore, would be expect to impact unsteady pressure measurements in this range. The other possible sources for the observed differences are;

1. Airfoil location
2. Turbulence generating grid

It is possible that the airfoil was shifted upstream or downstream by nominally 5cm between the two measurements thereby, locating the airfoil a slightly different distance from the turbulence generating grid. As such, the energy in the inflow at the leading edge would change between the

two measurements producing pressure fluctuations of different magnitude. The data presented suggests (since solid wall spectra reside above acoustic wall spectra) the airfoil was located slightly further downstream during the acoustically treated test section measurement. The other possibility is the turbulence grid. The grid was removed and then reinstalled for the second measurement and in doing so may have been reinstalled slightly differently. These differences could alter the turbulence produced and cause the small differences in unsteady pressure measurements.

Lastly, the large difference observed at 1% chord on the pressure side of the airfoil for both $\alpha = 0^\circ$ and 8° at low frequency is particularly interesting. The source of this discrepancy may be a combined effect of that discussed above and a transient laminar separation bubble. Evidence of a laminar separation bubble is suggested by oil flow visualization and, if present and coupled with the inflow would tend to mask the pressure response over the region of occurrence. Such a bubble would likely not be a highly repeatable phenomenon, especially if triggered by some very local leading edge feature. As such, it is feasible that this bubble was present to a greater extent during the acoustically treated test section measurement causing a low frequency reduction in the pressure response at the 1% chord location. That being said, the agreement between the two data sets is reasonable and therefore, they will be used interchangeably throughout the remaining analysis.

4.4.3 Data Symmetry

The next step in confirming the quality of measured unsteady pressure data is a check of the data symmetry. Unsteady pressure spectra on the pressure and suction side of the airfoil should be comparable within the uncertainty of the data at $\alpha = 0^\circ$. Similarly, data should be comparable from both sides of the airfoil measured at positive and negative angles of attack. That is, pressure spectra measured on the pressure side of the foil should agree at both positive and negative angles of attack and similarly for the suction side.

Zero Angle of Attack: A comparison of spectra measured on both sides of the airfoil at $\alpha = 0^\circ$ is presented in figure 4.20. In this figure the sides of the airfoil are designated as suction and pressure even though the airfoil is at zero angle of attack. The agreement at $x/c = 1\%$ is marginal with the suction side spectrum nearly 4dB above the pressure side for low frequencies. The

agreement improves with increasing frequency to near perfect at $\omega_r = 100$. Chordwise locations, $x/c = 2.5, 4$, and 6% show nearly perfect agreement over the measured frequency range. Some difference is observed at very high frequencies ($\omega_r > 200$) which may be related to resonance in the microphone mounting hole. The agreement at $x/c = 9\%$ is very good for $1 < \omega_r < 10$. Below $\omega_r < 1$ the suction side spectrum rises $\sim 4\text{dB}$ above the pressure side spectrum. Differences above $\omega_r = 10$ are likely the result of asymmetric boundary layer transition. The agreement returns to very near perfect at $x/c = 14\%$ with exception to some disagreement at $\omega_r > 200$ due possibly to microphone mounting hole resonance.

Positive and Negative Eight Degrees Angle of Attack: A comparison of pressure spectra at $\alpha = \pm 8^\circ$ is presented in figure 4.21 for $x/c = 1, 2.5, 4$, and 6% chord. In these plots spectra at $\alpha = \pm 8^\circ$ on the pressure side (indicated by ‘Pressure’ in the figure) should be similar and likewise for the suction side (indicated by ‘Suction’). At 1% chord spectra measured on the pressure side of the airfoil fall nearly on top of each other. On the suction side at 1% the agreement between $\alpha = \pm 8^\circ p'$ spectra is poor with the $\alpha = -8^\circ$ spectra falling 6dB below the $\alpha = 8^\circ$ spectra. Spectra at 2.5% chord on the suction side are found to be within 2dB of agreement. On the pressure side the agreement is slightly worse with 3dB of difference shown. By 4% chord data on both sides of the airfoil are within 1dB over much of the low frequency range. For $\omega_r > 10$ asymmetric boundary layer transition likely produces the differences in pressure spectra observed at 4% chord. At 6% chord the agreement remains quite good at all frequencies with less than 1dB of asymmetry occurring across the frequency range.

Discussion on Sources of Asymmetries: Asymmetries are shown to occur primarily in the leading edge region ($x/c = 1$ and 2.5%) for $\alpha = 0^\circ$ and $\pm 8^\circ$. Several asymmetry sources are investigated, including

1. Airfoil angle of attack
2. Microphone calibrations
3. Airfoil leading edge geometry

Airfoil angle of attack

If the airfoil were at a very small angle of attack differences in the pressure spectra from one side of the airfoil to the other would be visible with the greatest difference showing up at the leading edge. However, the airfoil angle of attack was sighted to 0° and checked with mean pressure measurements which confirmed the angle of attack setting. Furthermore, since spectra at 4, 6, 9, and 14% chord are in near perfect agreement additional doubt is cast on this argument.

Microphone calibrations

Data used to form these plots are spanwise averaged where possible. That is, the auto-spectrum at each of the 8 spanwise locations is averaged to form the auto-spectrum for chordwise locations. This process assists in reducing the uncertainty associated with microphone calibrations. Additionally, microphone calibrations are consistent with each other at each chordwise location where spanwise averaging is not possible.

Airfoil Geometry

The airfoil thickness and chordwise location of microphones at $y/c = 0.33$ —up to 14% chord—was measured and is presented in figure 4.22 along with the theoretical NACA 0015 geometry. Variation in chordwise location of microphones in any spanwise row relative to each other is less than 0.1mm. The measured chordwise locations are presented in table 4.4.

Table 4.4: Measured chordwise location of microphones

Nominal x/c	Pressure side measured x/c	Suction side measured x/c
0.01	0.0115	0.0125
0.025	0.0255	0.0270
0.04	0.0410	0.0430
0.06	0.0610	0.0630
0.09	0.0900	0.0930
0.14	0.1400	0.1440

Microphones on the suction side tend to be located 0.1% to 0.3% chord further downstream than those on the pressure side. This result is unexpected based on the comparison of pressure spectra of adjacent microphones. That is, spectra decrease by approximately 1.25dB per 1% chord with increasing chordwise location. Therefore, if the suction side microphones are located slightly aft of the pressure side microphones then the measured spectra on the suction side of the airfoil should fall slightly below that on the pressure side of the airfoil. Just the opposite is shown to

occur in the spectra of figure 4.20 at low reduced frequencies. The measured thickness agrees well with the airfoils theoretical shape for the measured chordwise locations.

There are a few other clues which may help explain the leading edge asymmetries that tie in with the leading edge geometry. The poor repeatability combined with the asymmetries at the most leading edge locations suggests that some sort of local flow phenomena is present. Oil flow visualization implies the presence of a laminar separation bubble on the suction side of the airfoil (for positive angles of attack). Such a bubble would be quite sensitive to local geometry and configuration. Additionally, if this bubble were coupled with the inflow the unsteady loading could be affected locally. As such, it is possible that this bubble develops at a different location and possibly over a greater or less extent of the chord in each measurement (solid wall and acoustic wall) and, for this reason, the repeatability is poor in the leading edge region. If this is indeed the case, such a local flow phenomenon could produce the asymmetries shown in pressure spectra at $\alpha = \pm 8^\circ$ in both experiments. It is possible that the geometry at the leading edge is slightly different from one side to the other and this difference causes the laminar separation bubble to develop differently. If the laminar separation bubble on the suction side at $\alpha = -8^\circ$ is larger compared to that which occurs on the suction side at $\alpha = 8^\circ$, and well coupled with the inflow then a significant reduction of the unsteady pressure could occur on the suction side at $\alpha = -8^\circ$. That is, the larger bubble, if coupled to the inflow, could be shedding vorticity and as such, reducing the loading on the airfoil and consequently driving down the unsteady pressure spectral level.

No quantitative investigation of this theory through alternate flow visualization or other means was undertaken. However, a small side study was performed to test the effects of slight changes to the leading edge geometry. A small bump made of yarn and covered with electrical tape (as discussed in chapter 2) was attached to the leading edge and pressure measurements made at $\alpha = -8^\circ$. The results of these measurements are presented in figure 4.23 which compares the p' spectra measured at $\alpha = -8^\circ$ (with leading edge bump installed) with those measured at $\alpha = 8^\circ$ (with no leading edge bump present) for the 1% chord location. The agreement of pressure side data remains very good with less than 1dB of difference occurring. The suction side data remains out of agreement; however, the $\alpha = -8^\circ$ spectrum rises slightly so that the difference between the two is ~ 2.2 dB. This is substantial improvement from the 6dB of difference which occurs with no leading edge bump present. The leading edge bump may be suppressing, to some

extent, the formation of the leading edge laminar separation bubble and in doing so increases the unsteady loading on the airfoil since less vorticity is shed by the smaller bubble. Therefore, this result does offer additional circumstantial support for the local flow phenomenon theory presented above. Furthermore, it suggests that *viscous* effects may play a significant role in determining the surface pressure response. The surface pressure is assumed to be a result of the inviscid response of the airfoil (i.e. the non-penetration condition is imposed at the airfoil surface) and therefore, local geometry should not affect the response of the airfoil to the inflow turbulence. This leading edge bump experiment, through its influence of the 1% chord pressure response, suggests that local geometry does play an important role and as such, viscosity is significant to determining the airfoil response. Therefore, it stands to reason that the asymmetries shown in figure 4.20 and 4.21 are related to a local flow phenomenon which is influenced by leading edge geometry.

4.4.4 Contamination and Dominance of Various Pressure Fluctuation Sources

This experiment sets out to measure the inviscid response of an airfoil in turbulence using microphones. The expectation here is that the microphones will measure pressure fluctuations associated with the non-penetration condition. However, measurements of unsteady pressure made with microphones are subject to a variety of contamination sources. Contamination can result from the wind tunnel acoustic field, boundary layer, stall, convection of eddies, and electrical noise. This section sets out to determine the extent of contamination from these sources and reveal the dominance of the inviscid response in unsteady pressure measurements.

Acoustic Contamination: A somewhat qualitative estimate of the extent of acoustic field contamination is possible through comparison of smooth flow, matched RPM, and reference microphone measurements. The reference microphone is expected to provide an upper bound estimate of the acoustic field. Also, the reference microphone spectrum falls near 30dB below surface pressure spectra for leading edge chordwise locations ($1\% < x/c < 14\%$). As such, the extent of acoustic contamination can be estimated through a comparison of reference microphone data with that measured on the surface of the airfoil in smooth flow and matched RPM.

Auto-spectra of the across chord pressure difference are presented at eight chordwise locations (1, 2.5, 4, 6, 9, 14, 20, and 30%) for the cases of smooth flow at all angles of attack,

matched RPM at $\alpha = 0^\circ$, and reference microphone measurement in figures 4.24 and 4.25. Figures 4.26 and 4.27 present the corresponding coherence and phase of these signals. At the unstalled ($0^\circ, 4^\circ, 8^\circ, 12^\circ$) angles of attack the smooth flow and matched RPM spectra remain as much as 30dB below the reference microphone spectrum at all eight chordwise locations over much of the frequency range, varying from as high as 115dB at $\alpha = 12^\circ$ to as low as 65dB at $\alpha = 0^\circ$. The reference microphone, as discussed in chapter 2 may, by its existence in the flow, generate pressure fluctuations and thus the spectrum measured represents an upper bound on the tunnel acoustic field. Therefore, the fact that smooth flow data remains below the upper bound tunnel acoustic field indicates the low level of noise present at the airfoil surface. Also, across chord phasing (figures 4.26 and 4.27) remains at nearly 0° at each chordwise location for the unstalled angles of attack indicating the primary source of pressure fluctuation is the ambient acoustic field. Coherence, although reaching to 0.8 at some frequencies is quite ‘spiky’ and falls off at higher reduced frequencies (>10) beyond 9% chord demonstrating the weak nature of the dominant pressure fluctuation.

Stalled angle of attack spectra (16° and 20°) are well above the reference microphone spectrum, which is expected considering the unsteadiness associated with stall. The $\alpha = 16^\circ$ and 20° spectra remain within 8dB of each other at all eight chordwise locations with, interestingly the $\alpha = 16^\circ$ spectrum in general residing at a higher level than the $\alpha = 20^\circ$ spectrum. These spectra achieve between 120 and 130dB at the lowest reduced frequency and fall to as low as 80dB at the highest reduced frequency. Therefore, it can be concluded that at stalled angles of attack the large unsteady pressure fluctuations occurring in the presences of the separated flow will dominate the unsteady pressure measurement.

Therefore, based on the low smooth flow, matched RPM, and reference microphone spectral levels, ambient acoustic related pressure fluctuations are not expected to significantly contaminate the data set. However, at stalled angles of attack, the large pressure fluctuations associated with separated flow are expected to dominate the unsteady pressure measurement.

Turbulent Boundary Layer Contamination: To aid in assessing the extent of contamination from turbulent boundary layer pressure fluctuations a technique presented by Burley *et al.* (1997) is used. Burley *et al.* (1997) developed a method for extracting the desired pressure fluctuation—inviscid response pressure fluctuations—from microphone measurements. They

assume that the inviscid response will correlate across the chord of the airfoil. As such, the pressure fluctuations related to the inviscid response can be extracted by correlating with the airfoil leading edge (or at least the most forward pressure measurement location). The leading edge is used because it is assumed to be dominated by pressure fluctuations related to the inviscid response. In this way, the pressure fluctuations related to the turbulent boundary layer can be removed (since the boundary layer pressure fluctuations will not correlate of large distances) leaving the inviscid response auto-spectra. This method employs what is referred to as the Coherent Output Power (COP) and extracts what amounts to the inviscid response surface pressure auto-spectra. The COP is defined as

$$G_{\Delta P_x \Delta P_x} \Big|_{Inviscid} = \frac{G_{\Delta P_1 \Delta P_x}^2}{G_{\Delta P_1 \Delta P_1}} \quad (4.5)$$

where $G_{\Delta P_1 \Delta P_1}$ is the pressure difference auto-spectrum at 1% chord and $G_{\Delta P_1 \Delta P_x}$ is the pressure difference cross-spectra between microphones located at 1% chord and position x .

Figure 4.28 presents large grid pressure difference auto-spectra measured at 1, 2.5, 4, 6, 9, and 14% chord plotted with the inviscid response auto-spectra (COP—presented as *Burley-Brooks* in plots) at $\alpha = 0^\circ$. The measured auto-spectra compares well with COP at all chordwise location for $\omega_r < 10$ indicating that significant acoustic and boundary layer pressure fluctuations are not present. Above reduced frequencies of 10 COP begins to fall below measure auto-spectra signifying the onset of significant acoustic and/or boundary layer pressure fluctuations. Due to the comparatively low acoustic level in the tunnel the measured auto-spectra are believed to be primarily elevated as a consequence of small scale (higher frequency) boundary layer pressure fluctuations.

Now, consider the COP calculated for small grid unsteady pressure measurements. Auto-spectra measured in small grid turbulence are expected to contain some boundary layer pressure fluctuation contamination as a consequence of grid generated turbulence scale. This turbulence scale is on the same order as the boundary layer scale and thus the grid generated turbulence tends to add energy to the boundary layer. Additionally, the hydrodynamic pressure fluctuations associated with the convection of turbulence down the chord may contribute significantly to the overall pressure response. Figure 4.29 presents a comparison of small grid measured pressure difference auto-spectra with inviscid response auto-spectra (COP) at 1, 2.5, 4, 6, 9, and 14%

chord. Inviscid response auto-spectra (COP) fall below measured auto-spectra by as much as 1 order of magnitude in spectral level at 2.5% chord and continue to fall relative to measured auto-spectra at the remaining chordwise locations. The large difference between measured and inviscid response auto-spectra results from the lack of correlation of pressure fluctuations with the leading edge. The inviscid response of the airfoil is, of course, still present; however, pressure fluctuations associated with the turbulent boundary layer and the convection of the free-stream turbulence along the airfoil chord are significant enough to mask the inviscid response and cause the COP to fall considerably relative to measured auto-spectral levels.

Measurement System Noise: Measurement system noise is another source of contamination of particular concern since it will correlate across all microphones thereby, artificially driving up cross-spectral levels. The effects of measurement system noise can be assessed through comparison of large and small grid pressure spectra with pressure spectra measured in smooth flow. Surface pressure measurements made in smooth flow form a baseline measure of noise (as shown above), including measurement system noise. Comparing cross-spectra from the two measurements (airfoil in turbulence with smooth flow) will reveal which is more dominant. If cross-spectra measured with the airfoil in turbulence have a higher spectral level then they are not expected to be contaminated with measurement systems noise. Pressure difference cross-spectra are formed as

$$G_{\Delta P_i \Delta P_j} = E \left\langle \left[P_U(x_i) - P_L(x_i) \right]^* \left[P_U(x_j) - P_L(x_j) \right] \right\rangle. \quad (4.6)$$

Figure 4.30 through 4.32 presents a comparison of pressure difference cross-spectra measured in large and small grid turbulence and smooth flow pressure difference cross-spectra for chordwise locations (denoted by index i of above equation) of 1%, 6%, and 14% at $\alpha = 0^\circ$. The cross-spectra at each location i are taken with 6 other chordwise locations (denoted by index j in the above equation) at 1%, 2.5%, 4%, 6%, 9%, and 14%. This data has been presented in pressure difference form.

In the case of large grid turbulence, surface pressure cross-spectra are more than two decades in spectral level above cross-spectra measured with no grid turbulence and show distinctly different shape. These characteristics are visible at each chordwise location. Now, considering the small grid turbulence surface cross-spectra, it is shown that these spectral levels are as much as a decade in magnitude above smooth flow cross-spectra. These spectra also take

on a distinctive shape and this characteristic is present at each chordwise location. The difference in the shape and the increase in spectral level suggest the presence of correlated pressure fluctuations which are significantly more dominant than those measured in smooth flow. As such, this data does not appear to be contaminated by measurement system noise, boundary layer noise, or ambient acoustic noise.

Dominance of Inviscid Response and Hydrodynamic Pressure Fluctuations: The correlation of pressure fluctuations in space and time offers an effective technique for identifying dominant types of pressure fluctuations occurring on the airfoil surface. Such correlations are referred to as pressure-pressure space-time correlation, or cross-correlation $R_{pp'}(x, x', \tau)$. Investigating the pressure-pressure correlations will help assess the extent of viscous phenomena (or hydrodynamic pressure fluctuations) involved in the total airfoil response.

The pressure-pressure correlation, $R_{pp'}$ is defined as

$$R_{pp'}(x, x', \eta, \tau) = \frac{\overline{p(x, y, t) p(x', y', t + \tau)}}{\sqrt{\overline{p^2(x, y)} \overline{p^2(x', y')}}} \quad (4.7a)$$

where $\overline{p^2}$ is the mean-square pressure. The quantity can also be computed from the cross-power spectral density of surface pressure fluctuations as

$$R_{pp'}(x, x', \eta, \tau) = \frac{\int_{-\infty}^{\infty} S_{qq}(x, x', \eta, f) e^{i2\pi f\tau} df}{\sqrt{\overline{p^2(x)} \overline{p^2(x')}}} \quad (4.7b)$$

The space-time correlation is a three dimensional function (when $\eta = 0$) which, when contour plotted, can reveal the speeds that pressure fluctuations are moving along the airfoil chord. For example, consider the contour plot of $R_{pp'}$ shown in figure 4.33 with space on the vertical axis (x/c) and time on the horizontal axis ($\tau U_{\infty}/c$). Ridges in the correlation will have a slope associated with them that corresponds to a velocity. This is the velocity at which pressure fluctuations are moving along the airfoil chord. As such, pressure fluctuations that convect with the mean flow (such as eddies) have a slope of 1 ($x/\tau = U_{\infty}$) while propagating (i.e. at the speed of sound) pressure fluctuations will have slope of 12 (sound speed + mean free-stream, $x/\tau = 12U_{\infty}$).

Figure 4.34 presents the correlation of pressure with the suction side 1% chord measurement location in space and time at $\alpha = 0^\circ, 2^\circ, 4^\circ, 6^\circ, 8^\circ, 10^\circ, 12^\circ, 14^\circ, 16^\circ, 18^\circ, 20^\circ$ for the airfoil in large grid turbulence. On these plots, positive x/c indicates the pressure side of the airfoil and negative x/c the suction side. The measured correlation is formed from pressure data sampled at 25.6 kHz and is high pass filtered at 100Hz to remove uncertainties associated with microphone calibrations. Both sides of the airfoil are correlated with the same microphone (1% chord, on the suction side). At all angles of attack the correlations shows a ridge with a 12:1 slope occurring on the pressure side of the airfoil. This region of high correlation is the airfoils inviscid response and clearly dominates the unsteady pressure measurement at all angles of attack. All angles of attack (more so with increasing angle of attack) show a ridge in the correlation with a slope of 1:1 on the airfoils suction side which likely results from convection of turbulence by the free-stream. The suction side also shows a strong inviscid response with a ridge in the correlation occurring with a 12:1 slope. It is interesting to see the break in the correlation function on the suction side which is evident at all angles of attack and occurs around the 15% chord location. As the angle of attack is increased this region of no correlation tends to grow along the chord of the airfoil covering as much as 20% of the chord at the higher angles of attack. This region may be related to the formation of a laminar separation bubble (as suggested by flow visualization) which masks the response of microphones in this area from the response of the entire airfoil. When the airfoil stalls at $\alpha=20^\circ$ disturbances begin to convect at $U_\infty/2$ which is the characteristic convection speed in a separated flow region. In summary, figure 4.34 clearly demonstrates the dominance of the airfoils inviscid response when interacting with large grid turbulence.

For completeness sake, the correlation of pressure with the 1% chord measurement location on the *pressure* side of the airfoil in space and time is presented in figure 4.35 for large grid flow at $\alpha = 0^\circ, 2^\circ, 4^\circ, 6^\circ, 8^\circ, 10^\circ, 12^\circ, 14^\circ, 16^\circ, 18^\circ, 20^\circ$. The cross-correlation shows strong correlation of pressure on both sides of the airfoil along the chord for $\alpha < 8^\circ$ that appears to be related to the airfoils inviscid response. The correlation function also has a ridge with a slope near 12:1 (i.e. propagation of pressure waves). A break in the correlation function is also observed to occur near 15% chord and convected pressure fluctuations appear to be emerging from this area for $\alpha < 8^\circ$. Signs of eddy convection on the suction side of the airfoil (recalling the correlation function is formed with the 1% chord microphone on the pressure side) are

surprising and suggest the presence of a transient laminar separation bubble that is coupled with the inflow. Such coupling would alter the unsteady loading and therefore, result in correlation between convected disturbances on the suction side of the airfoil with measurements on the pressure side of the airfoil. For 8° , 10° , 12° , and 14° angle of attack, significant correlation related to propagating pressure waves is observed along the chord on the pressure side. Eddy convection appears to be present on the pressure side as well, indicated by the 1:1 slope of the correlation ridge. Convected pressure fluctuations with a slope less than 1:1 also become more significant on the suction side; however, significantly correlated propagated pressure fluctuations appear to vanish. Beyond $\alpha = 14^\circ$ propagated pressure fluctuations dominate the pressure side with significant convection occurring on the suction side. The convection on the suction side appears to occur at a speed close to have the mean flow velocity based on the slope of the correlation ridge.

Additional support for the dominance of the inviscid response is provided by the pressure correlation function formed with the 1% chord measurement location of the *pressure* side of the airfoil (figure 4.35). Furthermore, this analysis has helped to substantiate the possible presence of a transient laminar separation bubble coupled with the inflow and occurring on the suction side of the airfoil.

Figure 4.36 presents the pressure-pressure space-time correlation from small grid turbulence/airfoil interaction surface pressure measurements at $\alpha = 0^\circ$, 4° , 8° , 12° , 16° , and 20° . The most notable occurrence in figure 4.36 is the reduction in correlation level relative to the large grid data. The inviscid response is present up to $\alpha = 12^\circ$ on both sides of the airfoil indicated by the correlation ridge occurring along the airfoil chord at near a 12:1 slope. At all angles of attack pressure fluctuations convecting along the airfoil chord (1:1 slope) are also visible. A standing wave pattern also is visible in the correlation at $\alpha = 4^\circ$ and 8° which may be related to system noise. The wave has a period close to that which would correspond to 60Hz power system noise. The pressure-pressure correlation seems to indicate that the inviscid response is not particularly strong in the small grid flow. The inflow length scale being $1/80^{\text{th}}$ of the airfoil chord may explain why this turbulence/airfoil interaction does not excite a strong inviscid response. With little evidence of a significant inviscid response in these pressure measurements the aeroacoustic relevance of this turbulence/airfoil interaction is minimized.

That being said, the remaining portion of this dissertation will focus on analysis of large grid pressure fluctuations in which the inviscid response is significant and dominant.

Lastly, the theoretical form of the cross-correlation function, as predicted by Amiet's (1976a, b) unsteady loading theory is presented and compared with the large grid measured cross-correlation at $\alpha = 0^\circ$ in figure 4.37. The predicted correlation drops off slightly moving away from the leading edge; however, the slope of the peak correlation is infinite indicating that the entire airfoil responds instantaneously to the inflow upwash. This, of course is much different from the real interaction in which the airfoil pressure field must adjust at the speed of sound (hence the 12:1 slope of the correlation peak). Due to hydrodynamic pressure fluctuations the measured correlation drops off faster moving away from the leading edge when compared with the predicted. The prediction also does not account for the convection of eddies along the airfoil chord which occurs in the real flow. Consequently, the predicted correlation does not show a peak occurring with a 1 to 1 slope which would be indicative of eddy convection. In summary, the predicted pressure-pressure correlation captures the inviscid response of the airfoil well in the leading edge region; however, the prediction fails to drop off as quickly moving along the airfoil chord as shown to occur in the measurement.

4.5 Summary of Experimental Details and Data Quality

Unsteady pressure measurements on the surface of an airfoil in turbulence were made with the goal of measuring pressure fluctuations associated with the airfoils inviscid response. The airfoil was immersed in two grid generated flows to assess the effect of turbulence scale on the airfoil response. Measurements were made at angles of attack ranging from $\alpha = 0^\circ$ to 20° .

Two separate tests were conducted in large grid flow; one measuring unsteady pressure with solid steel test section walls, the other with acoustically treated walls present. Comparison of data from these two tests reveals poor repeatability in the leading edge region. Furthermore, asymmetries are shown in the leading edge region. It is believed repeatability and asymmetry issues arise from a local flow phenomenon, such as a transient laminar separation bubble. Oil flow visualization and investigation of the pressure-pressure space-time correlation supports the presence of such bubble. The repeatability and asymmetry issues appear to be representing real events on the airfoil surface which impact the airfoils inviscid response. As such, the repeatability and asymmetry issues are not looked at as corrupting features, but rather as

additional intimations which can aid in understanding the physics of turbulence-airfoil interaction.

Acoustic, boundary layer, and electrical noise contamination are investigated. Large grid unsteady pressure data is shown to be largely contamination free over much of the frequency range. Small grid data is shown to contain substantial hydrodynamic pressure fluctuations although, is largely free of acoustic and electrical noise contamination. Additional support is given to this conclusion based on analysis of the pressure-pressure space-time correlation. The space-time correlation shows the inviscid response is dominant in unsteady pressure measurements when the turbulence is large; however, the inviscid response is weak and pressure measurements contain significant hydrodynamic pressure fluctuations when the turbulence is small. Based on these results the remaining analysis of this data will focus on large grid turbulence-airfoil interaction.

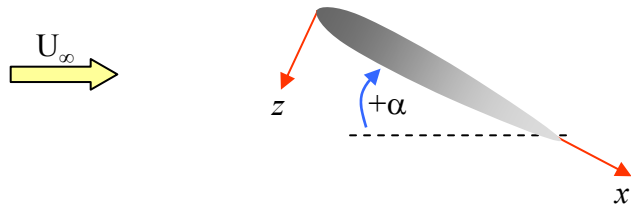


Figure 4.1: Top down view of airfoil in wind tunnel test section defining positive angles of attack

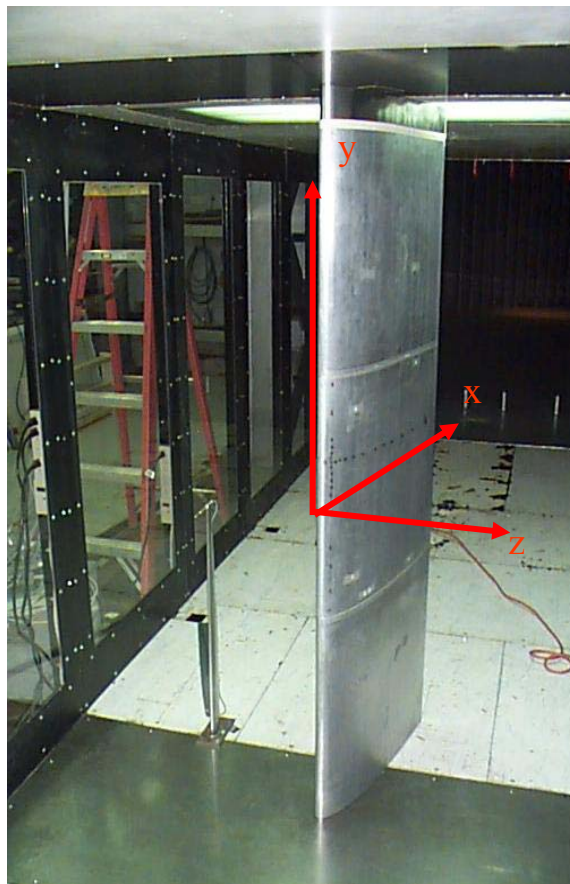


Figure 4.2: Single airfoil in turbulence coordinate system

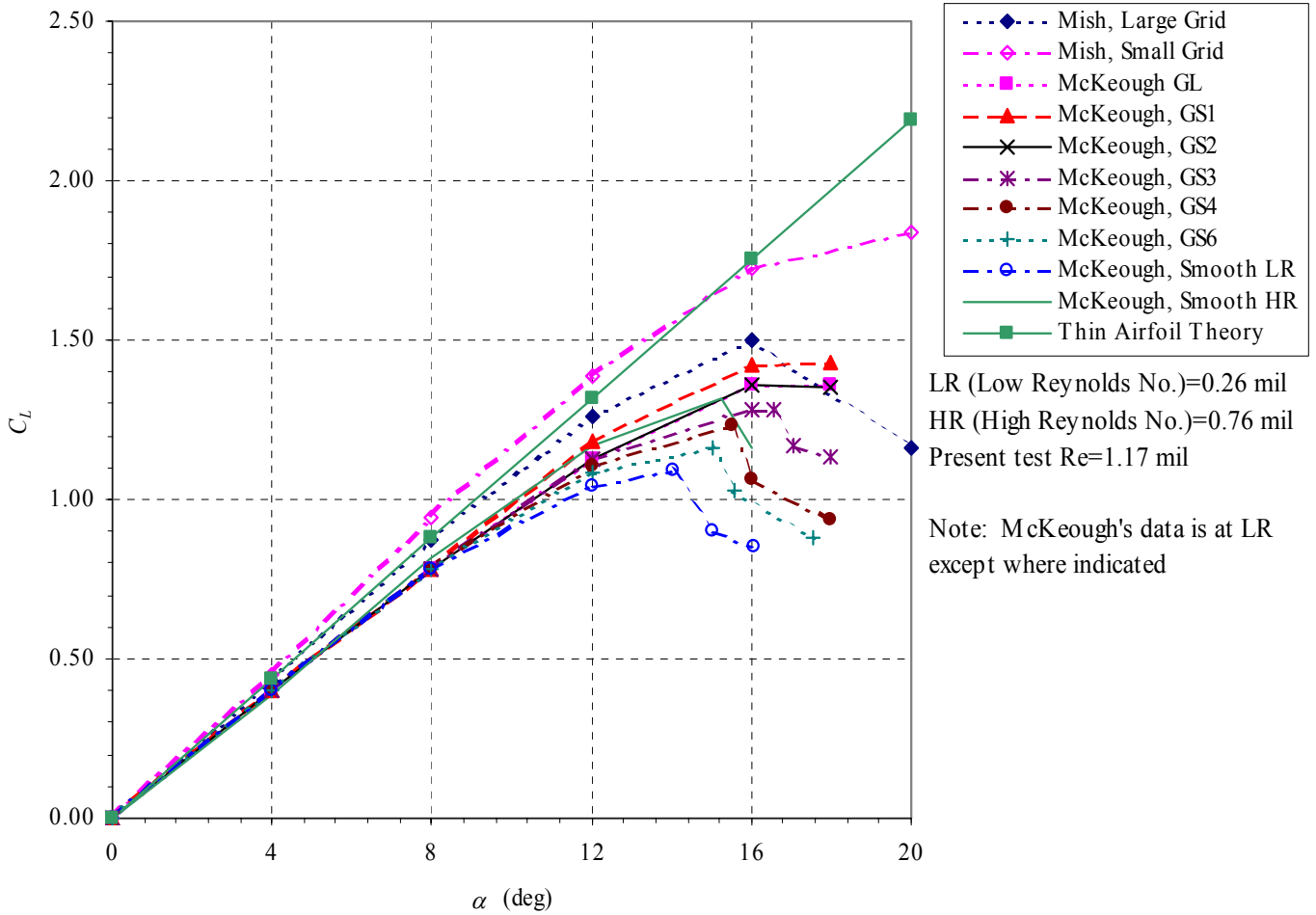


Figure 4.3: Mean pressure calculated lift coefficient shown with McKeough's (1976) data

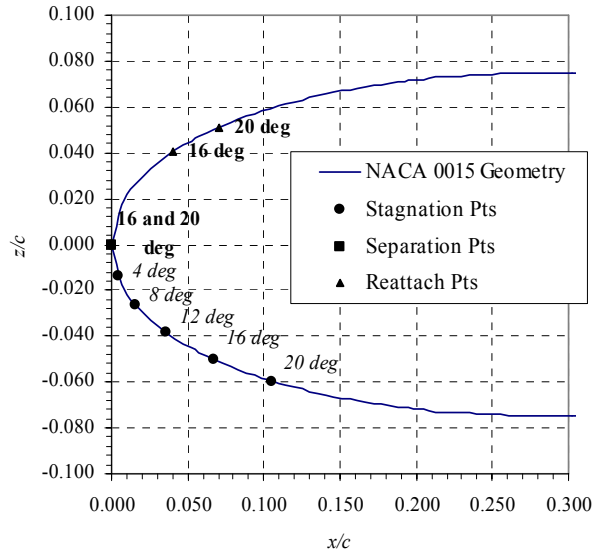


Figure 4.4: Stagnation and separation locations of *small scale turbulence flow*

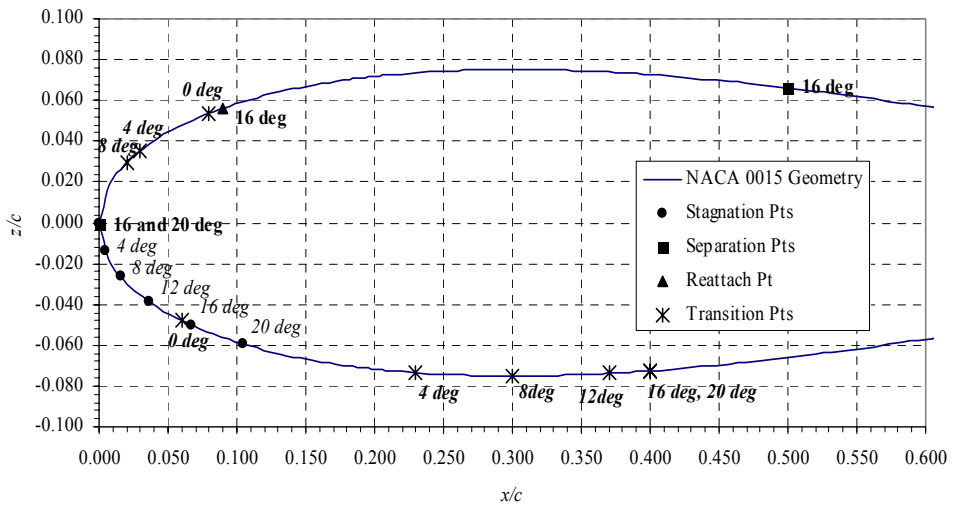
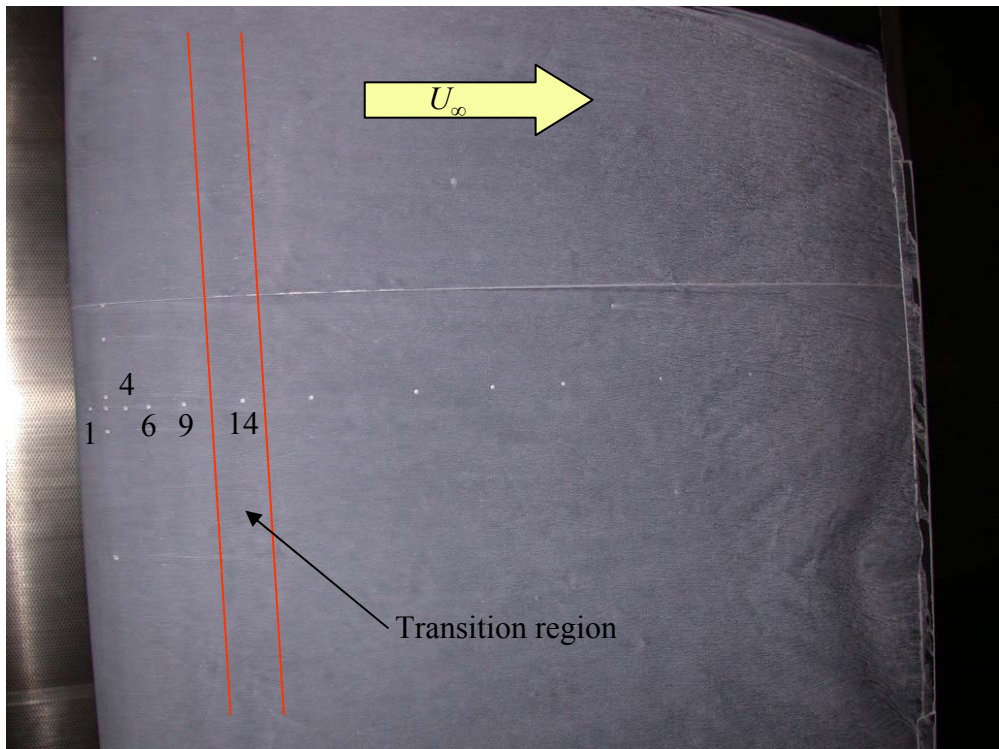
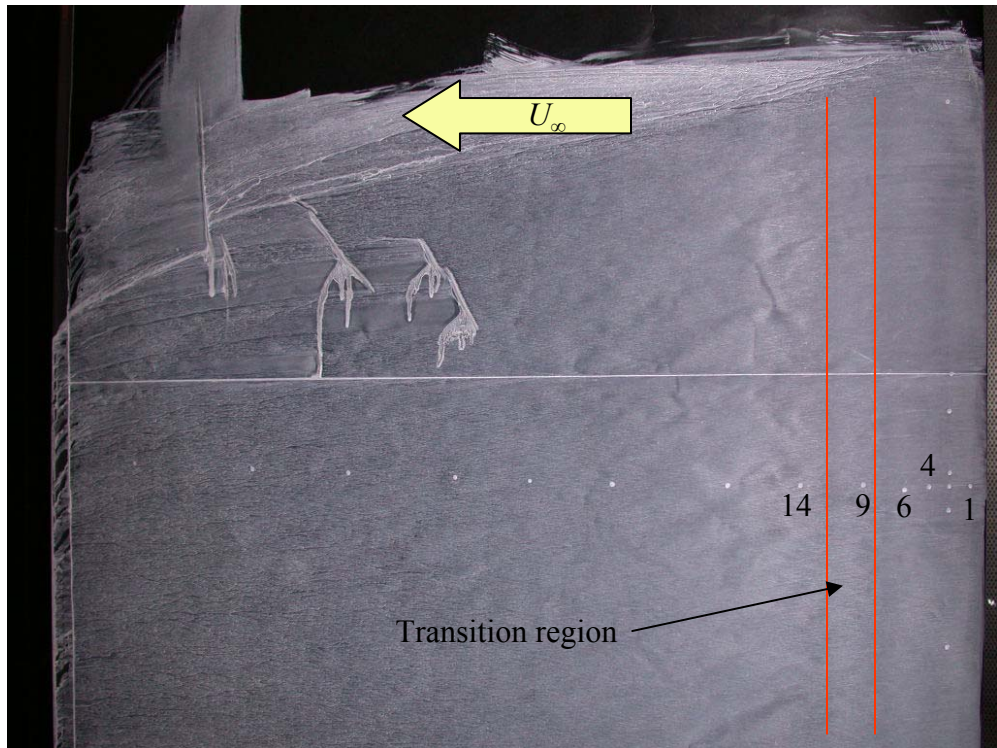


Figure 4.5: Stagnation, transition, and separation locations of *large scale turbulence flow*



(a)

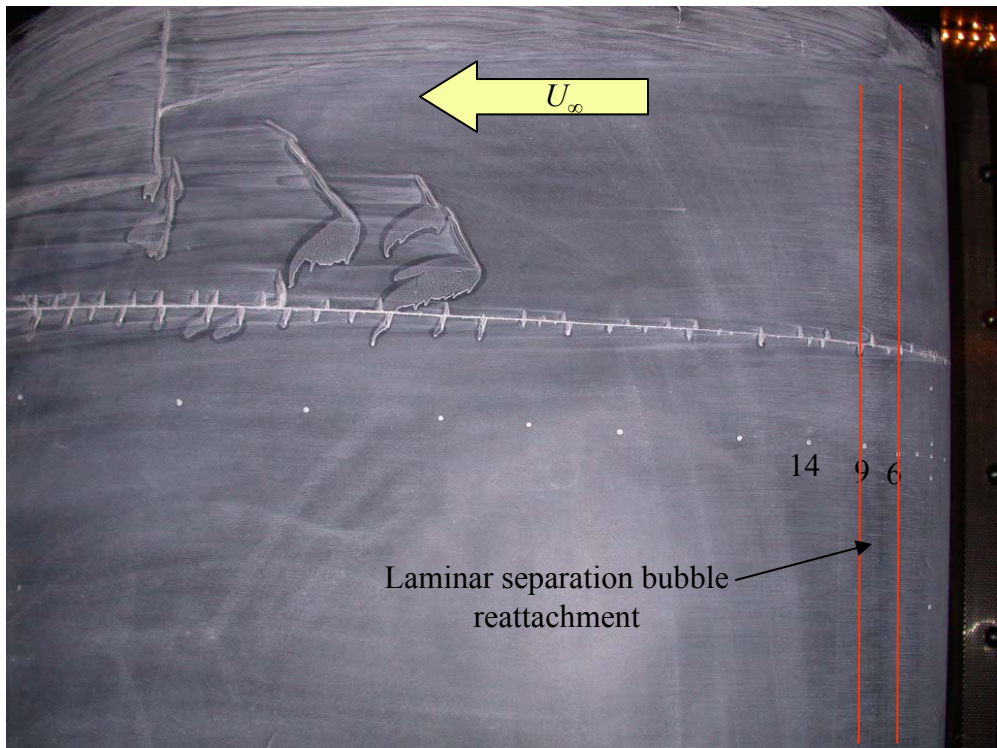


(b)

Figure 4.6: $\alpha = 0^\circ$ oil flow visualization on the hatch-pressure-(a) and solid-suction-(b) side of airfoil. The numbers in black correspond to the location of microphones in percent chord

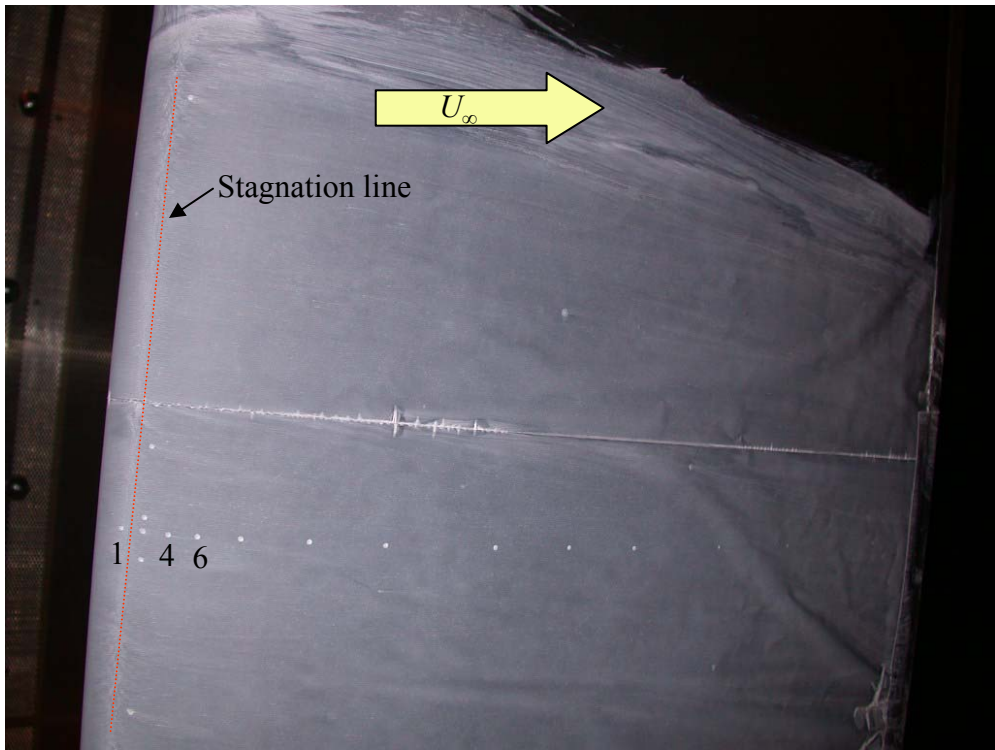


(a)

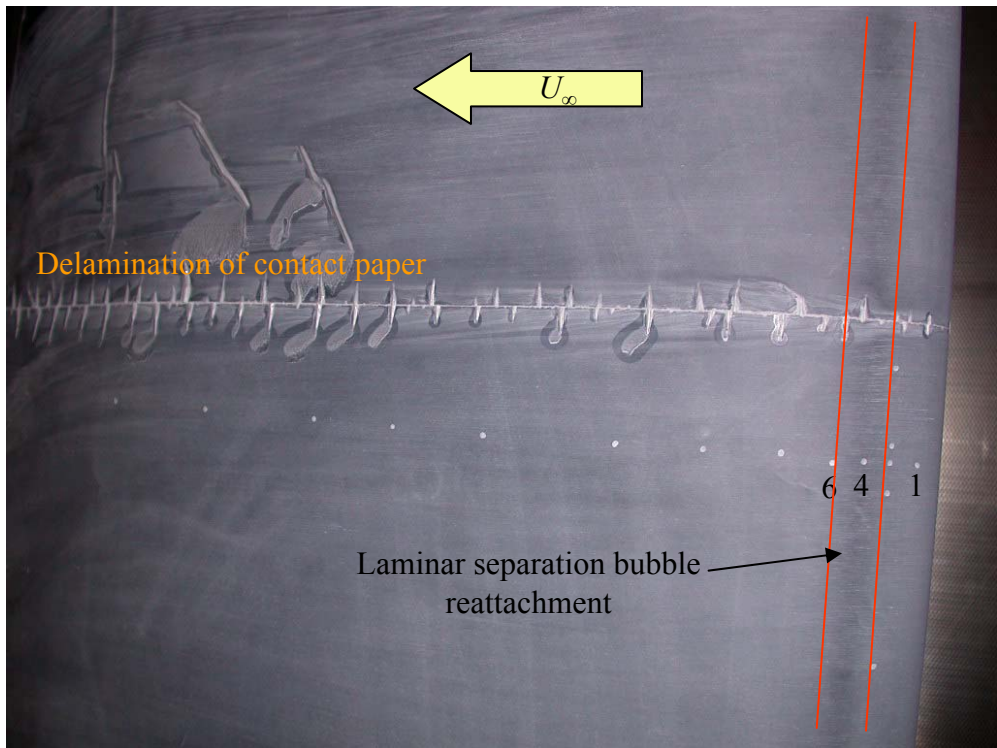


(b)

Figure 4.7: $\alpha = 4^\circ$ oil flow visualization on the hatch-pressure-(a) and solid-suction-(b) side of airfoil. The numbers in black correspond to the location of microphones in percent chord

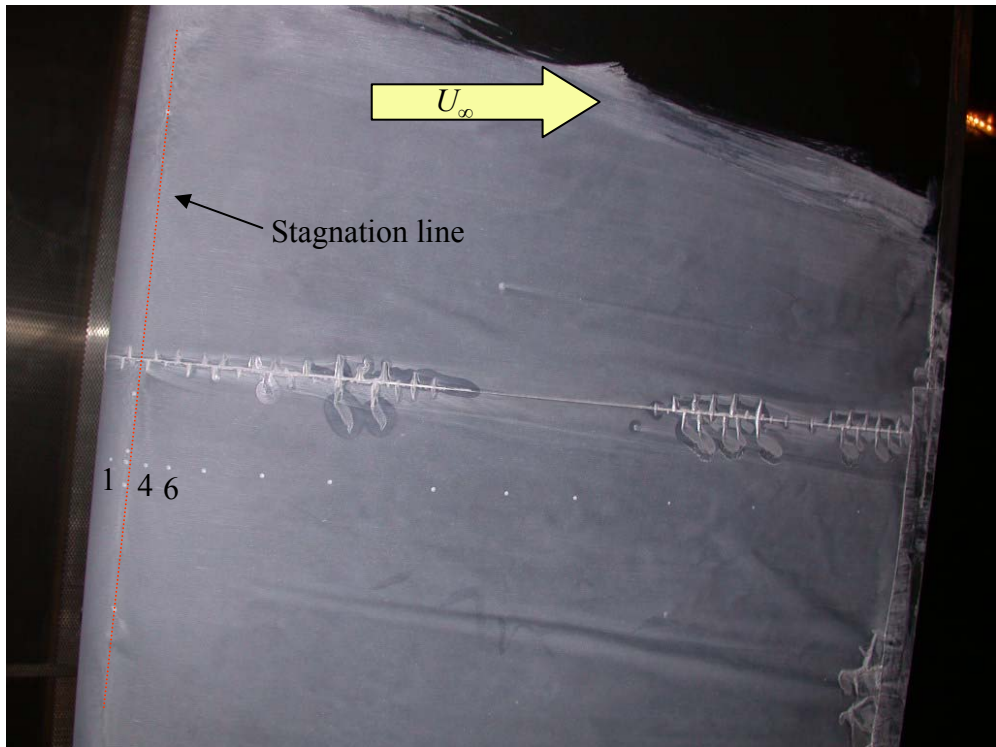


(a)

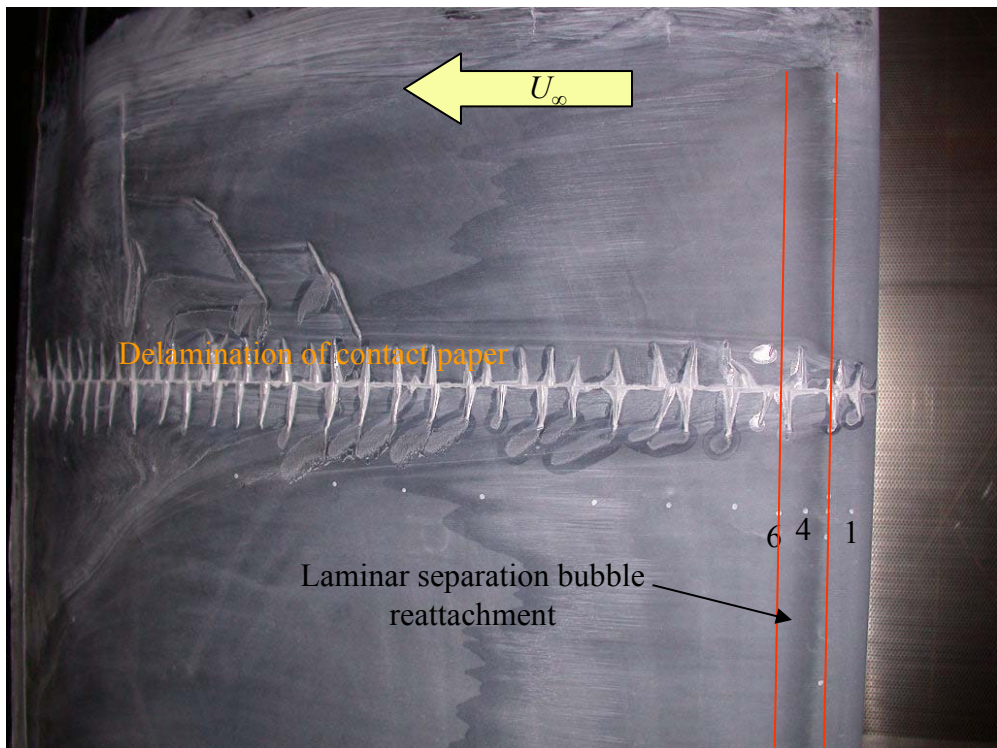


(b)

Figure 4.8: $\alpha = 8^\circ$ oil flow visualization on the hatch-pressure-(a) and solid-suction-(b) side of airfoil. The numbers in black correspond to the location of microphones in percent chord

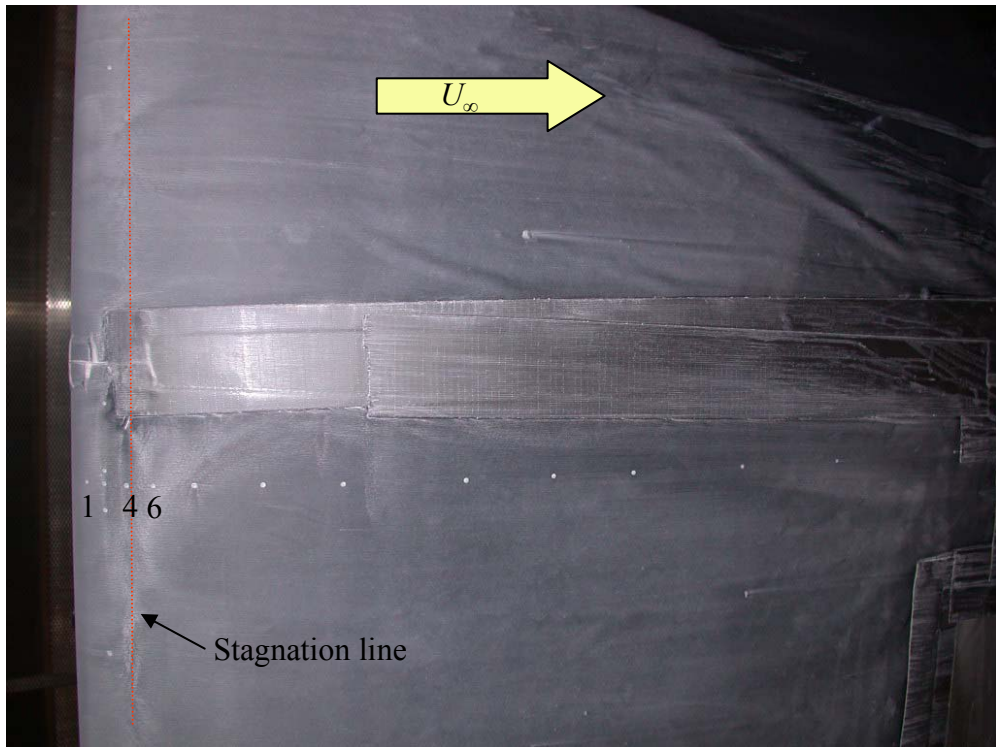


(a)

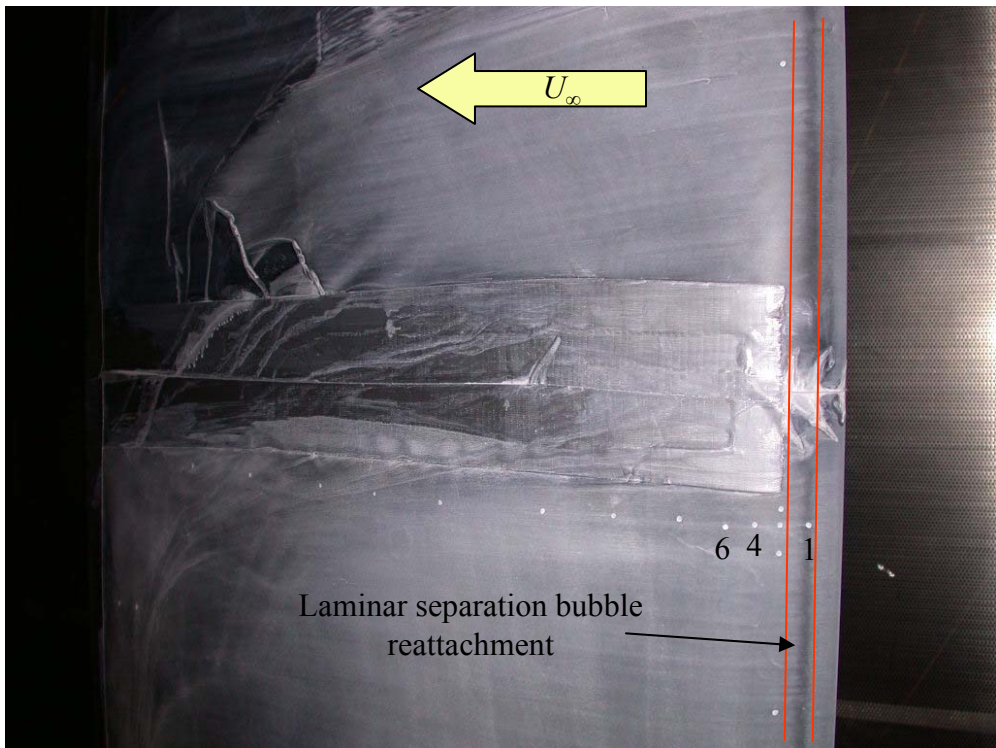


(b)

Figure 4.9: $\alpha = 12^\circ$ oil flow visualization on the hatch-pressure-(a) and solid-suction-(b) side of airfoil. The numbers in black correspond to the location of microphones in percent chord

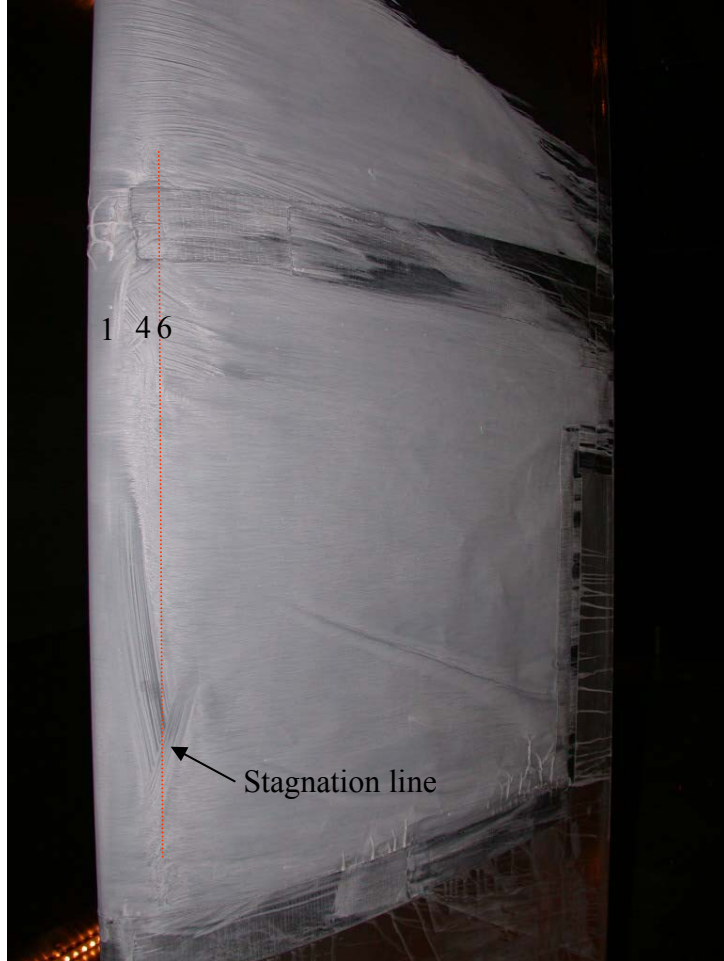


(a)



(b)

Figure 4.10: $\alpha = 16^\circ$ oil flow visualization on the hatch-pressure-(a) and solid-suction-(b) side of airfoil. The numbers in black correspond to the location of microphones in percent chord



a)



b)

Figure 4.11: $\alpha = 20^\circ$ oil flow visualization on the hatch-*pressure*-(a) and solid-*suction*-(b) side of airfoil. The numbers in black correspond to the location of microphones in percent chord

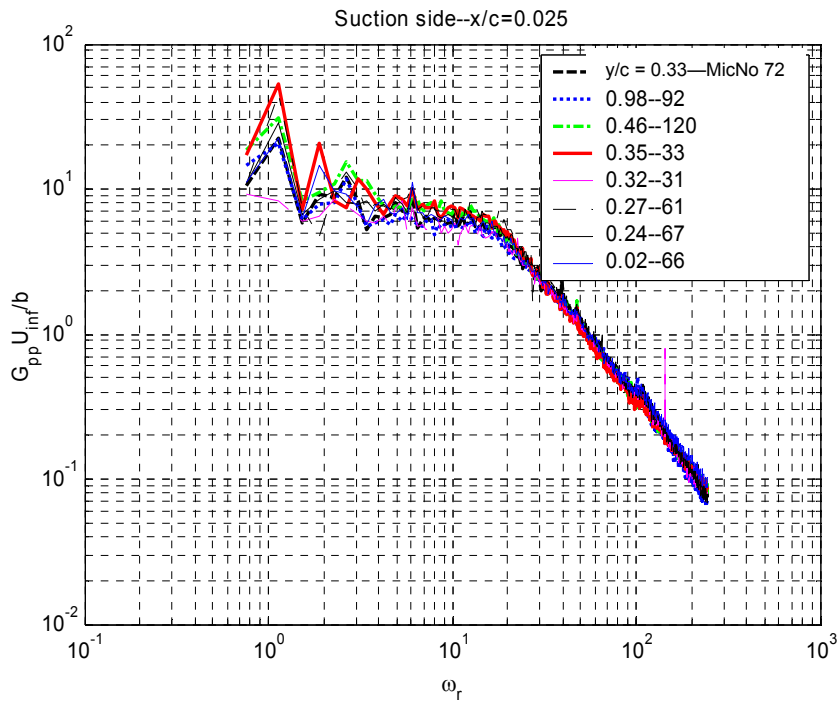
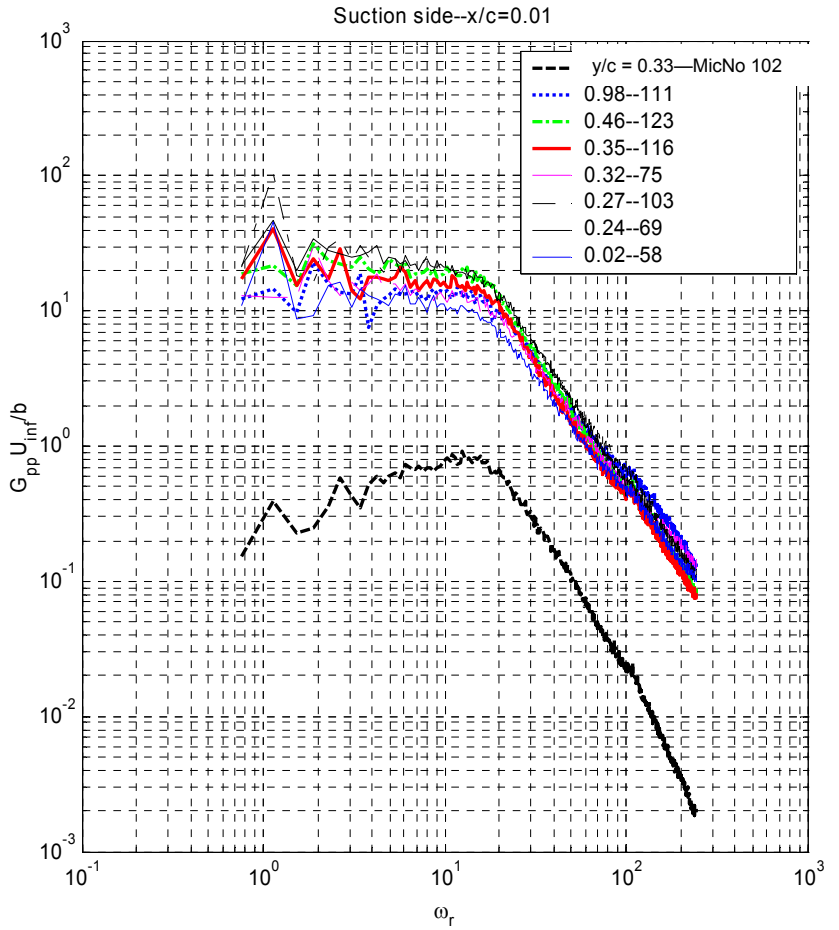


Figure 4.12: Spanwise homogeneity of *small* grid unsteady pressure data at $\alpha = 0^\circ$ on the *suction side* of airfoil for chordwise positions $x/c = 1, 2.5, 4, 6, 9\%$. First column of numbers in legend indicates spanwise position and second column is unique number given to each microphone.

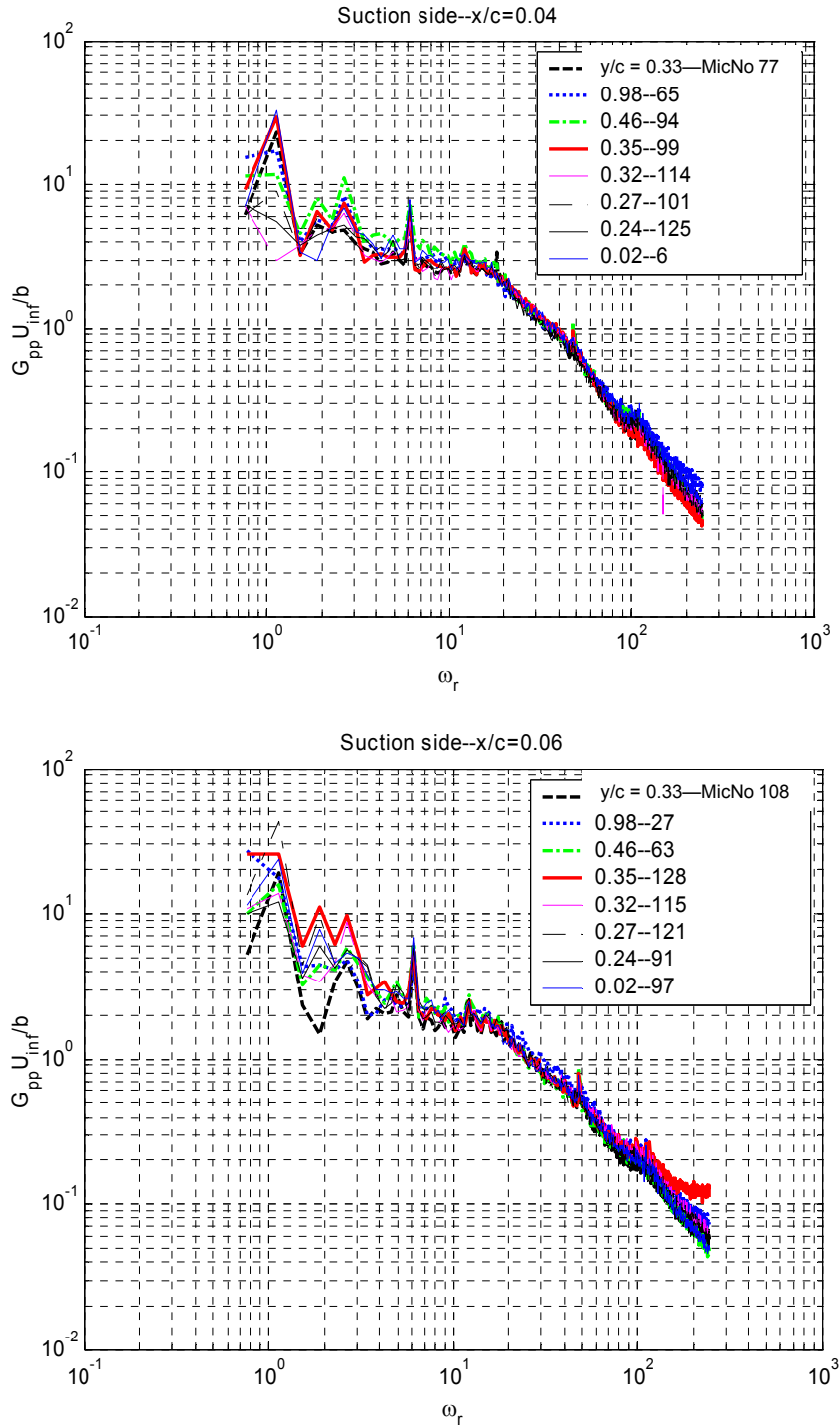


Figure 4.12 continued: Spanwise homogeneity of *small* grid unsteady pressure data at $\alpha = 0^\circ$ on the *suction side* of airfoil for chordwise positions $x/c = 1, 2.5, 4, 6, 9\%$. First column of numbers in legend indicates spanwise position and second column is unique number given to each microphone.

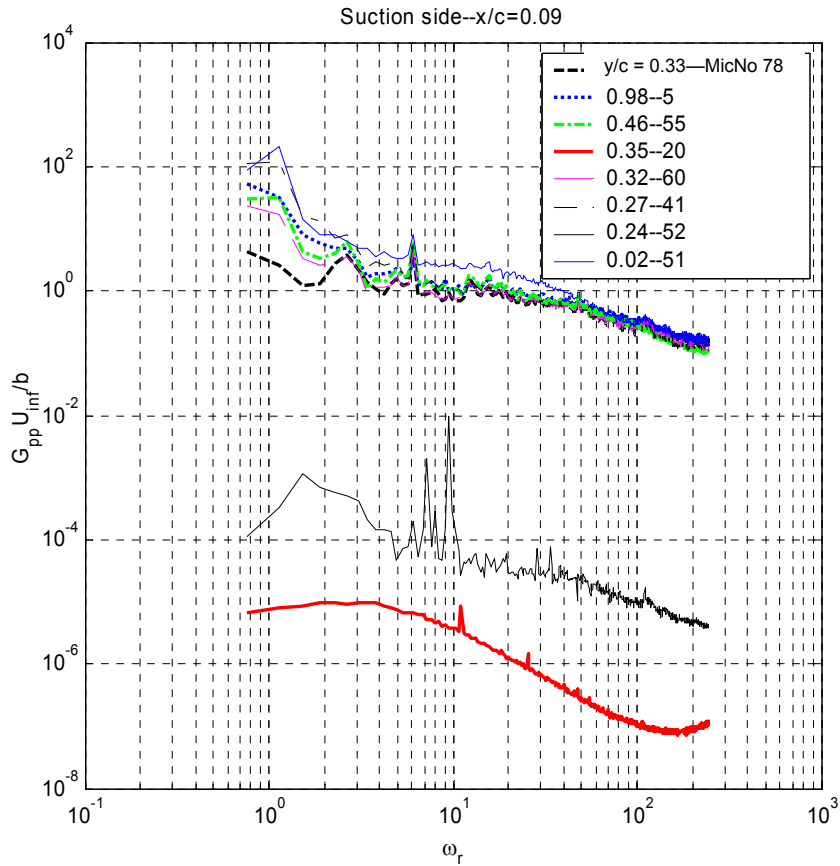


Figure 4.12 continued: Spanwise homogeneity of *small* grid unsteady pressure data at $\alpha = 0^\circ$ on the *suction side* of airfoil for chordwise positions $x/c = 1, 2.5, 4, 6, 9\%$. First column of numbers in legend indicates spanwise position and second column is unique number given to each microphone.

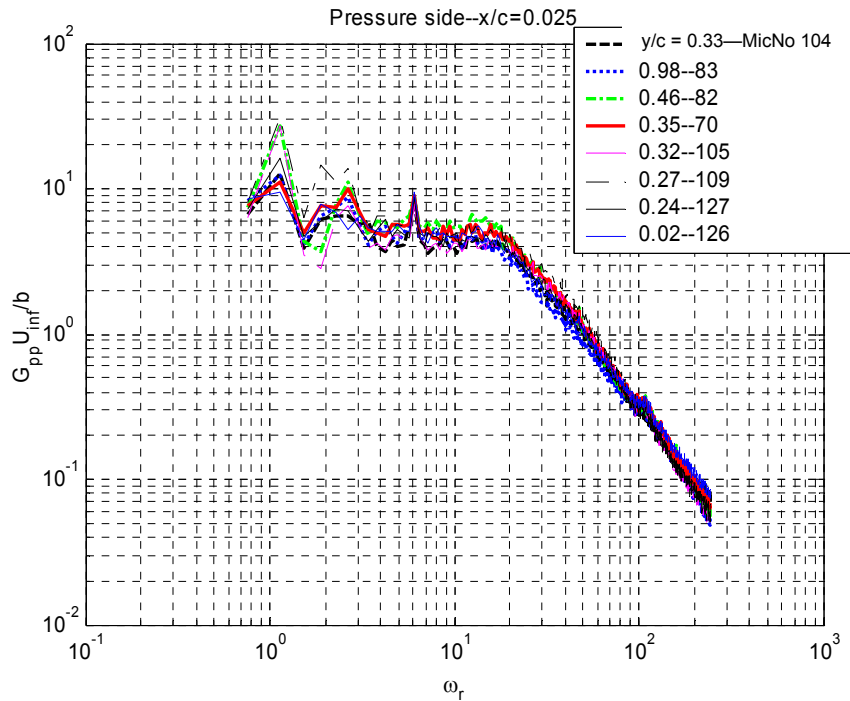
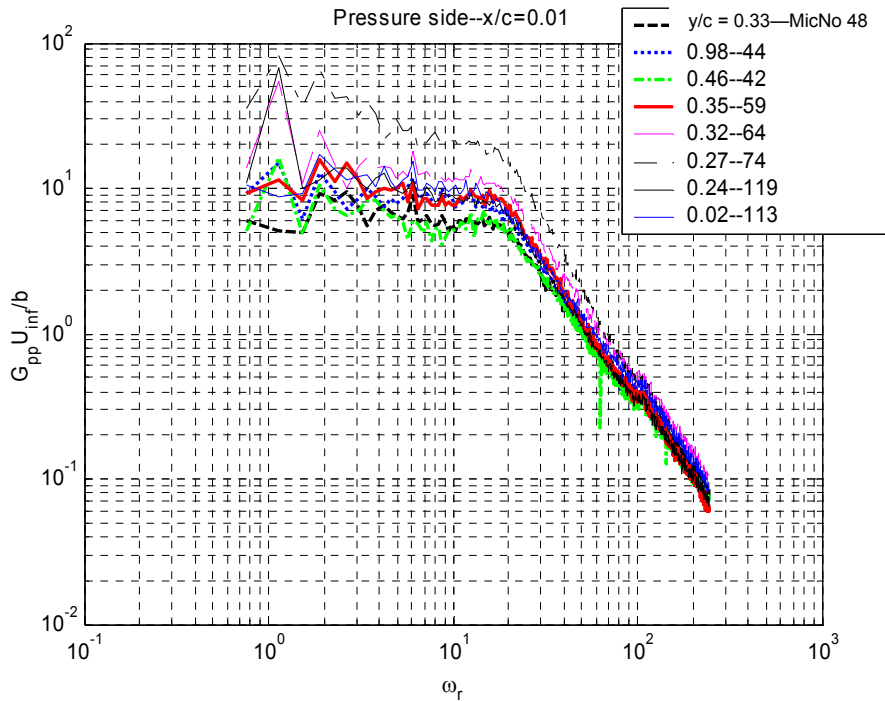


Figure 4.13: Spanwise homogeneity of *small grid* unsteady pressure data at $\alpha = 0^\circ$ on the *pressure side* of airfoil for chordwise positions $x/c = 1, 2.5, 4, 6, 9\%$. First column of numbers in legend indicates spanwise position and second column is unique number given to each microphone.

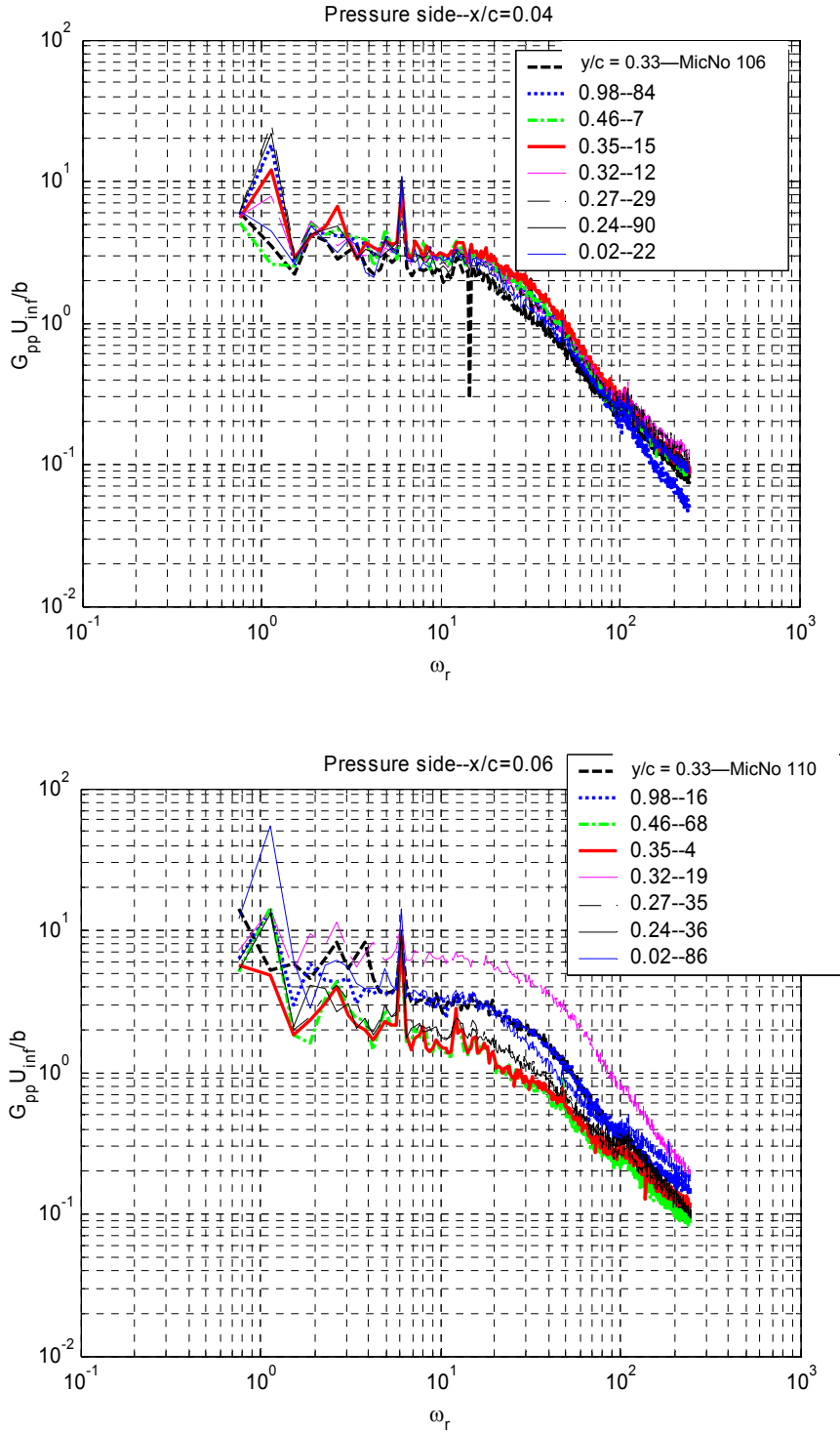


Figure 4.13 continued: Spanwise homogeneity of *small* grid unsteady pressure data at $\alpha = 0^\circ$ on the *pressure side* of airfoil for chordwise positions $x/c = 1, 2.5, 4, 6, 9\%$. First column of numbers in legend indicates spanwise position and second column is unique number given to each microphone.

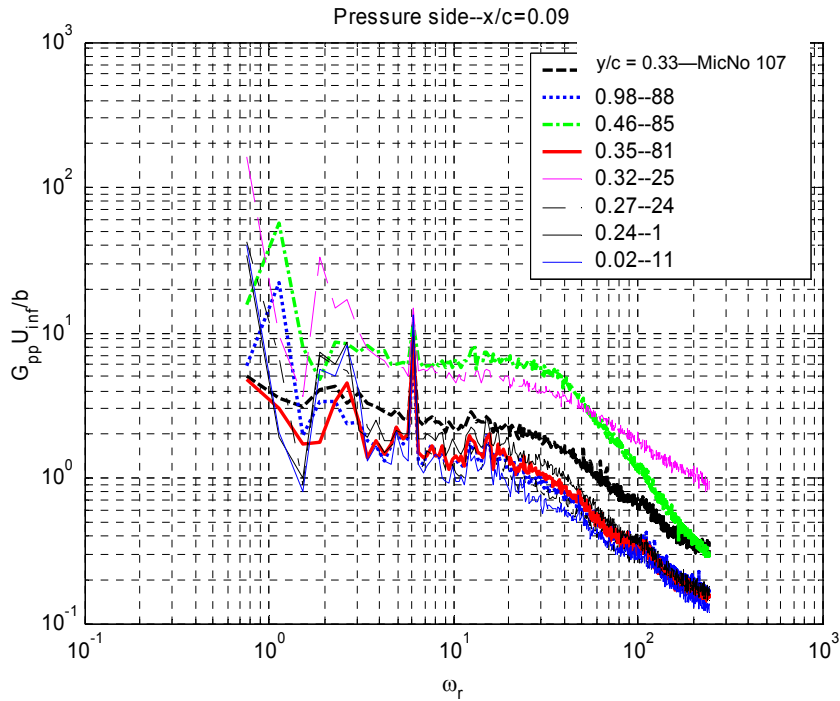


Figure 4.13 continued: Spanwise homogeneity of *small* grid unsteady pressure data at $\alpha = 0^\circ$ on the *pressure side* of airfoil for chordwise positions $x/c = 1, 2.5, 4, 6, 9\%$. First column of numbers in legend indicates spanwise position and second column is unique number given to each microphone.

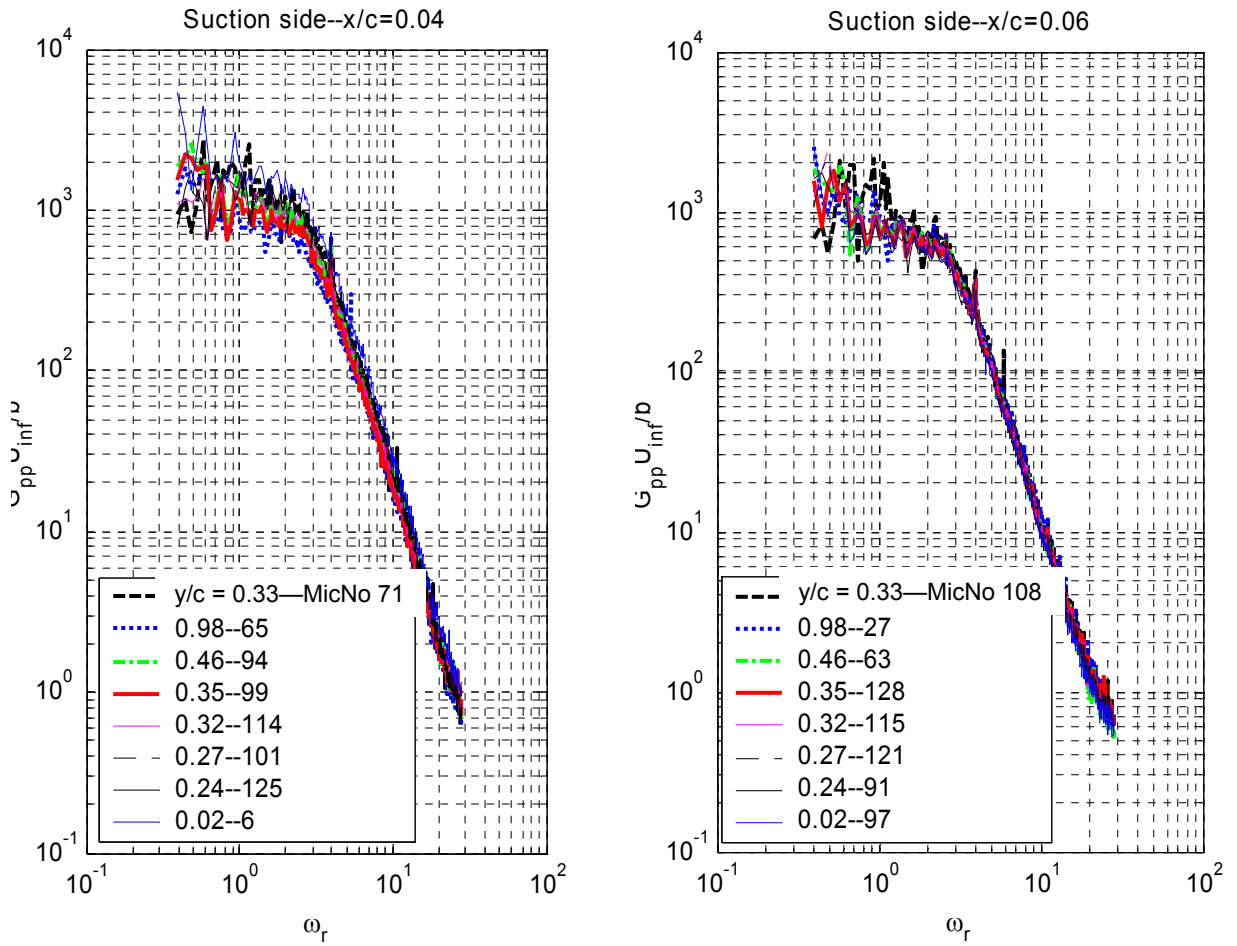


Figure 4.14 continued: Spanwise homogeneity of *large* grid unsteady pressure data at $\alpha = 0^\circ$ on the *suction side* of airfoil for chordwise positions $x/c = 1, 2.5, 4, 6, 9\%$. First column of numbers in legend indicates spanwise position and second column is unique number given to each microphone.

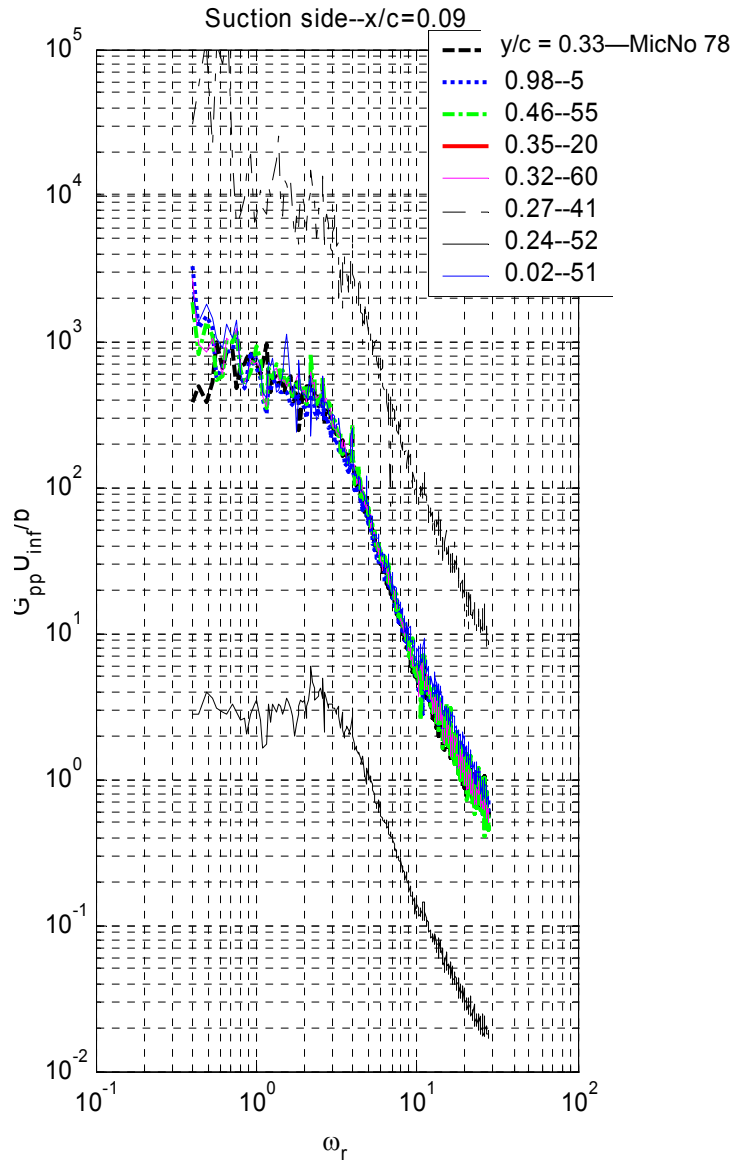


Figure 4.14 continued: Spanwise homogeneity of *large* grid unsteady pressure data at $\alpha = 0^\circ$ on the *suction side* of airfoil for chordwise positions $x/c = 1, 2.5, 4, 6, 9\%$. First column of numbers in legend indicates spanwise position and second column is unique number given to each microphone.

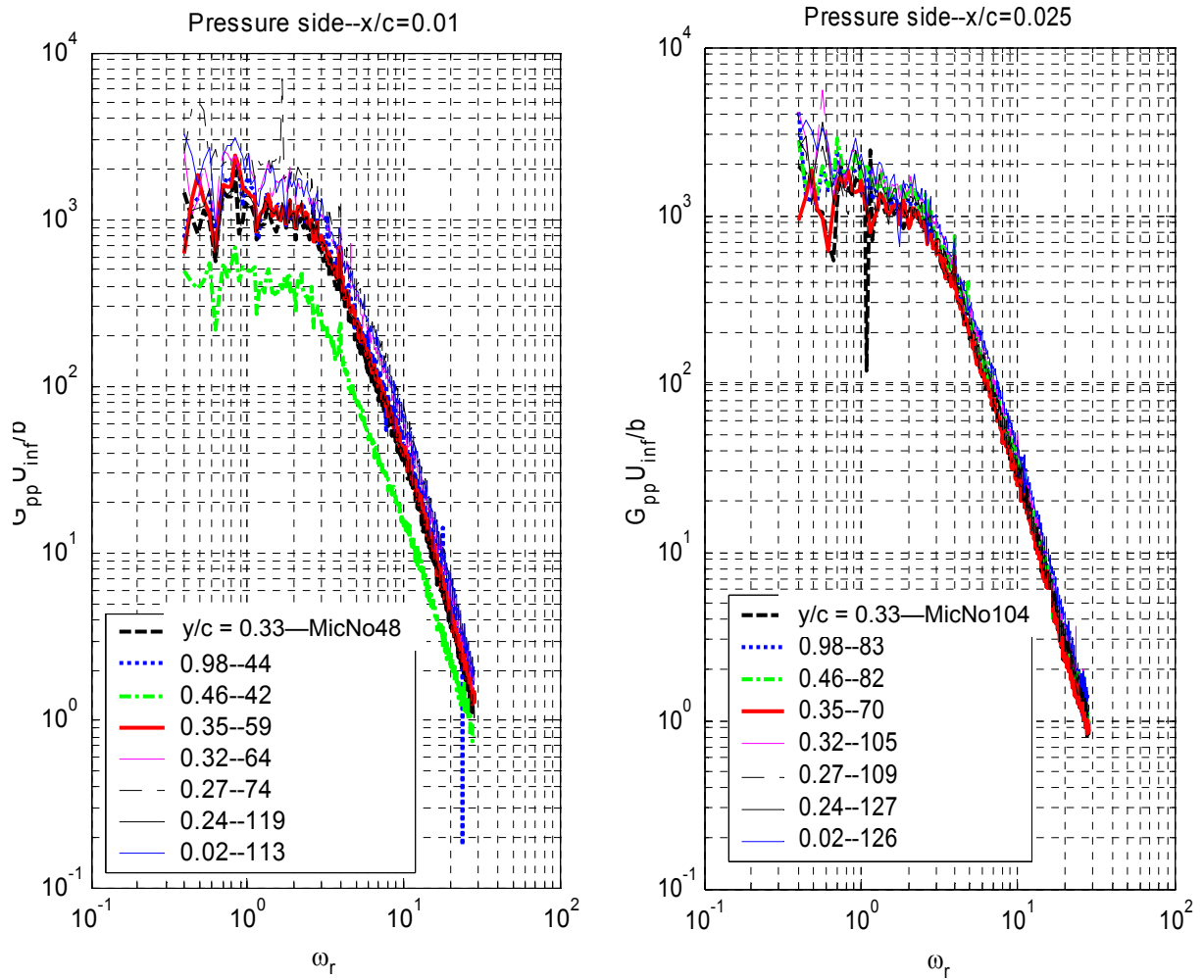


Figure 4.15: Spanwise homogeneity of *large grid* unsteady pressure data at $\alpha = 0^\circ$ on the *pressure side* of airfoil for chordwise positions $x/c = 1, 2.5, 4, 6, 9\%$. First column of numbers in legend indicates spanwise position and second column is unique number given to each microphone.

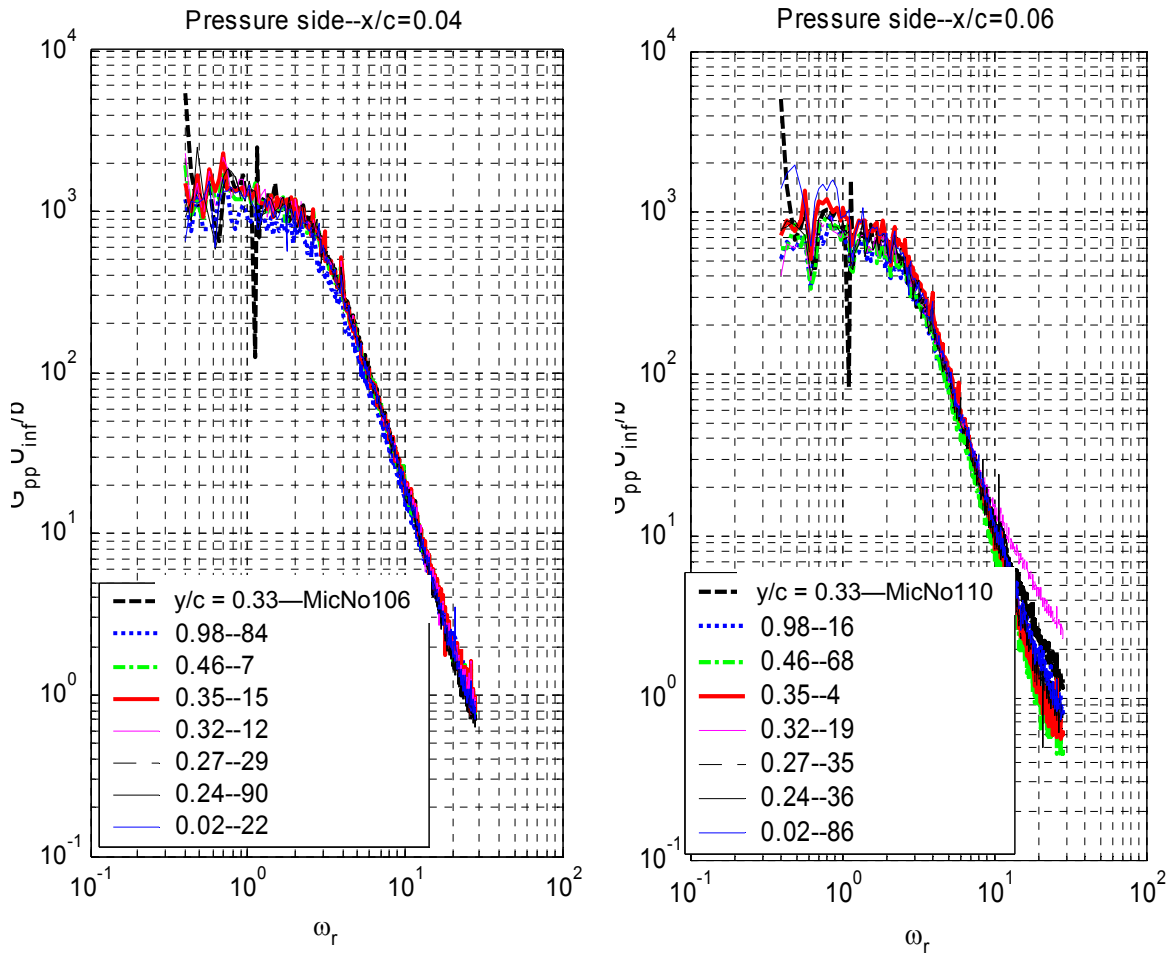


Figure 4.15 continued: Spanwise homogeneity of *large grid* unsteady pressure data at $\alpha = 0^\circ$ on the *pressure side* of airfoil for chordwise positions $x/c = 1, 2.5, 4, 6, 9\%$. First column of numbers in legend indicates spanwise position and second column is unique number given to each microphone.

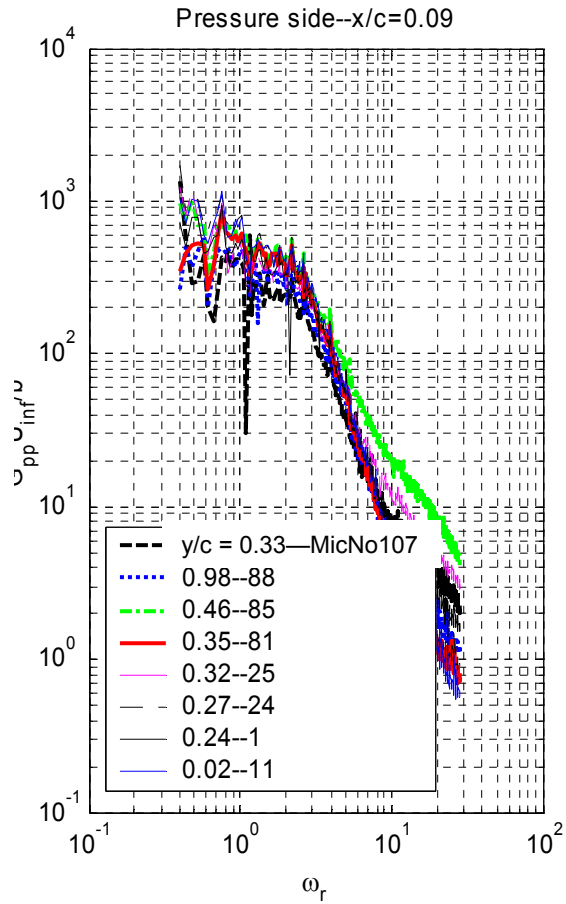


Figure 4.15 continued: Spanwise homogeneity of *large* grid unsteady pressure data at $\alpha = 0^\circ$ on the *pressure side* of airfoil for chordwise positions $x/c = 1, 2.5, 4, 6, 9\%$. First column of numbers in legend indicates spanwise position and second column is unique number given to each microphone.

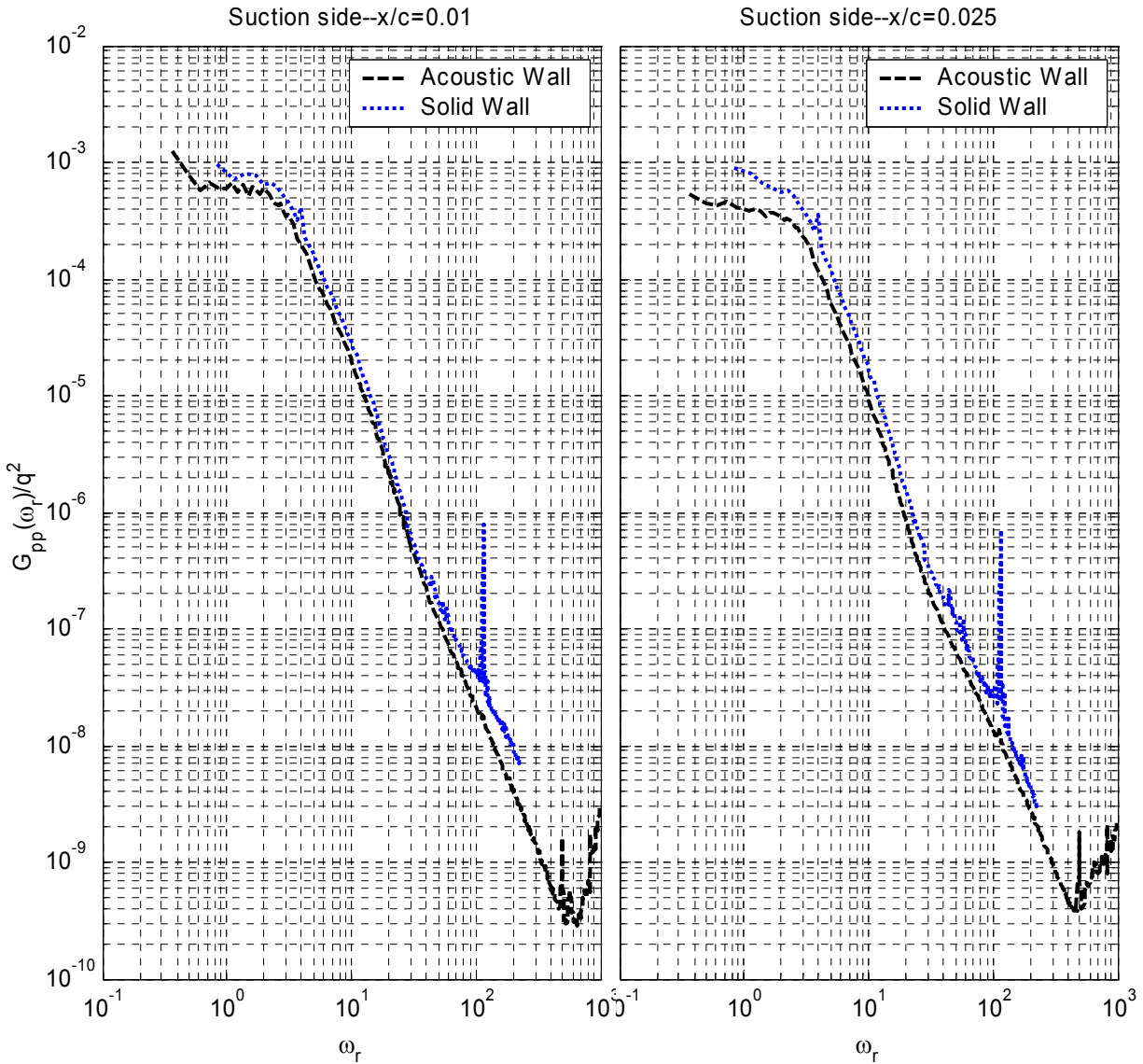


Figure 4.16: Comparison of *large grid* p' spectra measured with solid and acoustically treated wind tunnel test section walls. Spectra are from *suction* side of airfoil ($x/c = 1, 2.5, 4, 6, 9, 14\%$) at $\alpha = 0^\circ$ and are normalized on the free-stream dynamic pressure.

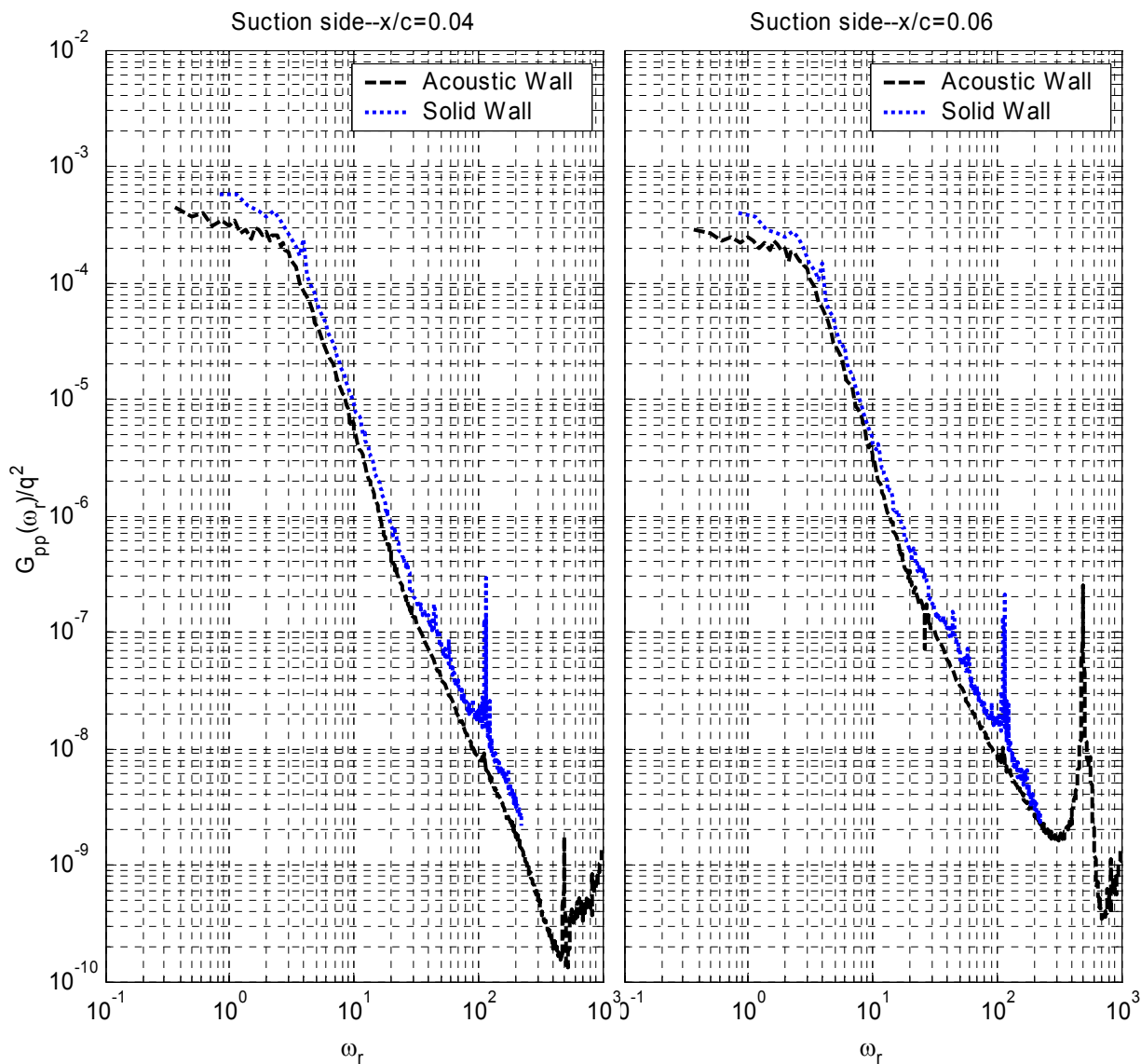


Figure 4.16 continued: Comparison of *large grid* p' spectra measured with solid and acoustically treated wind tunnel test section walls. Spectra are from *suction* side of airfoil ($x/c = 1, 2.5, 4, 6, 9, 14\%$) at $\alpha = 0^\circ$ and are normalized on the free-stream dynamic pressure.

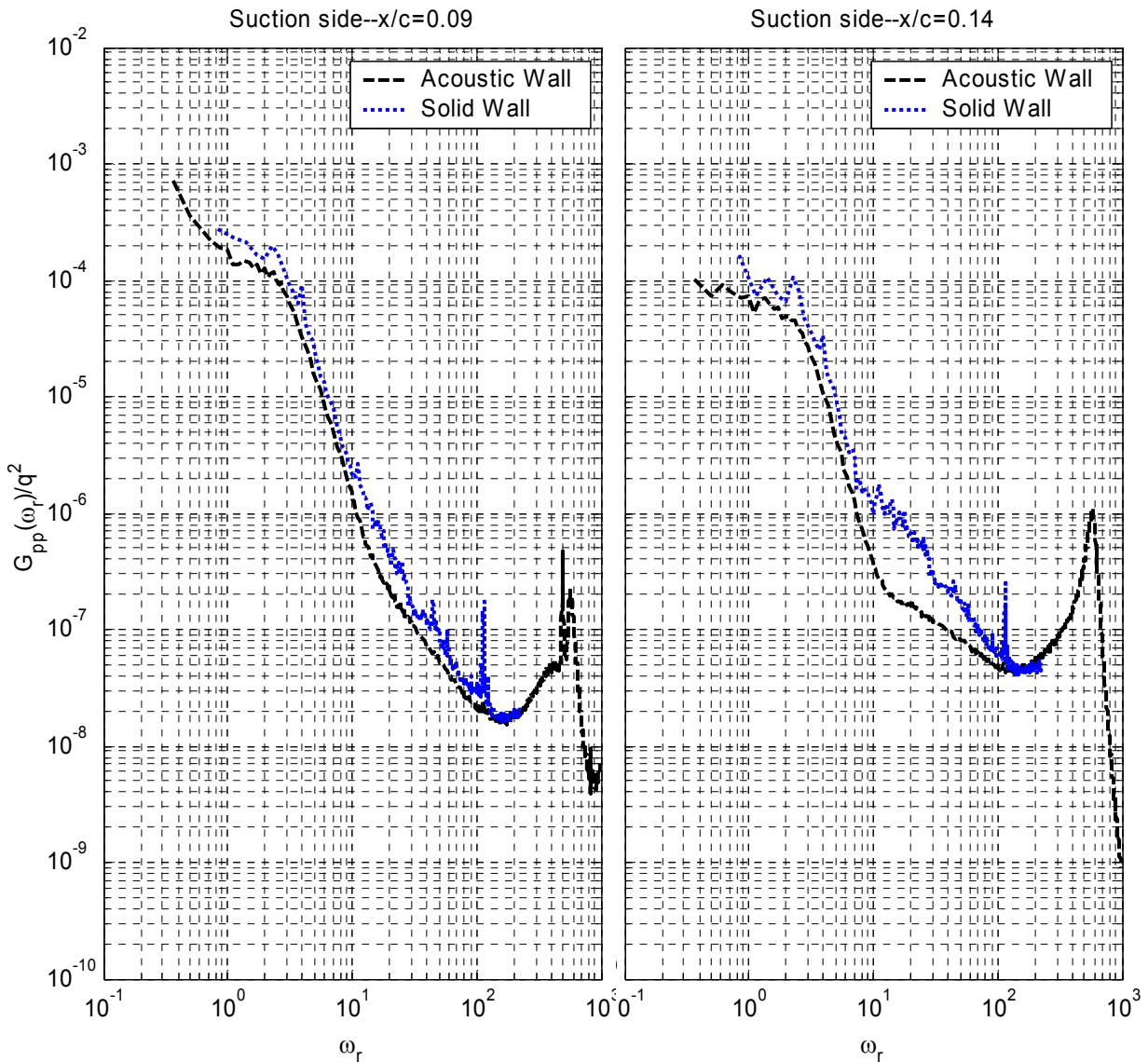


Figure 4.16 continued: Comparison of *large* grid p' spectra measured with solid and acoustically treated wind tunnel test section walls. Spectra are from *suction* side of airfoil ($x/c = 1, 2.5, 4, 6, 9, 14\%$) at $\alpha = 0^\circ$ and are normalized on the free-stream dynamic pressure.

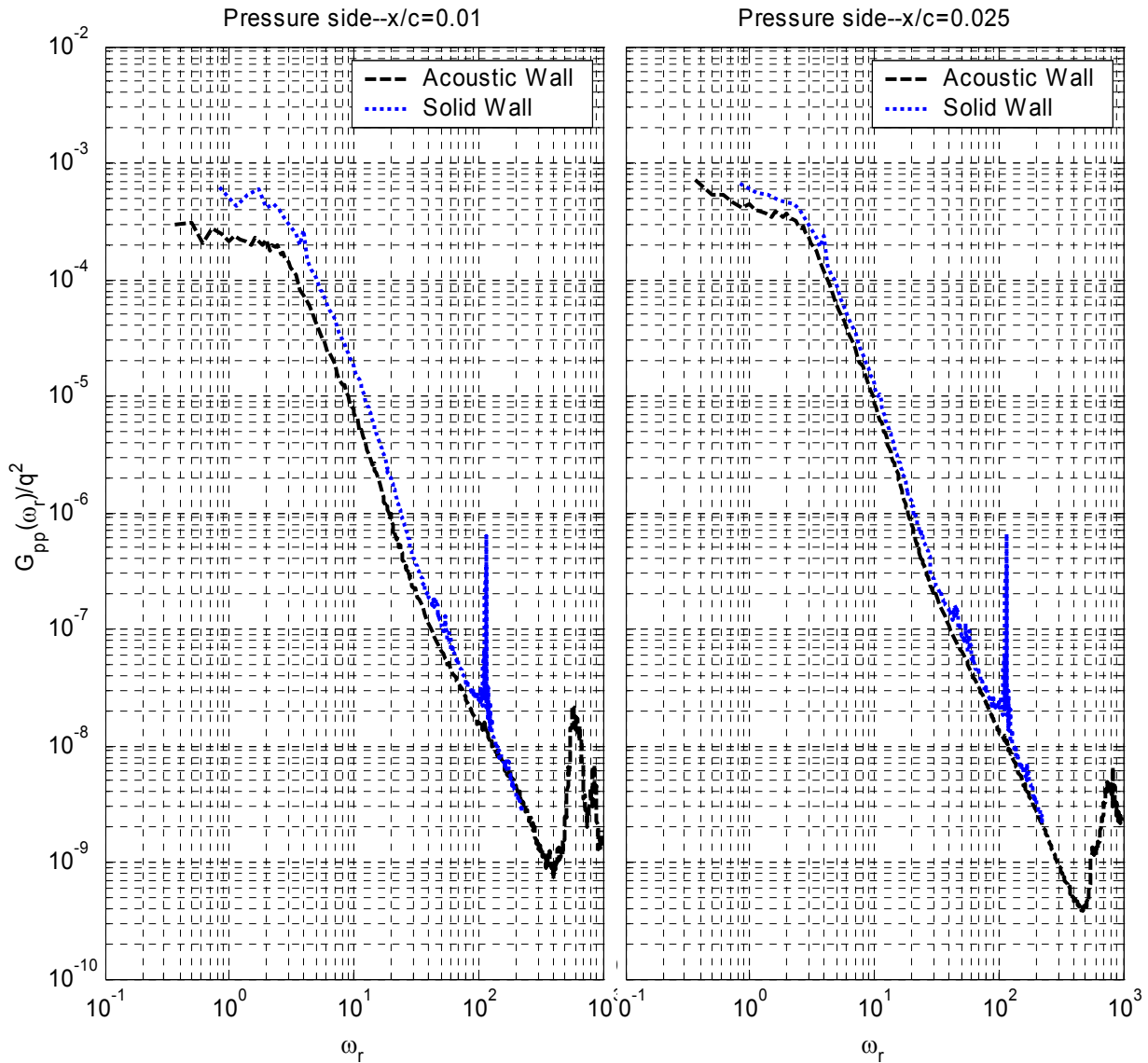


Figure 4.17: Comparison of *large grid* p' spectra measured with solid and acoustically treated wind tunnel test section walls. Spectra are from *pressure* side of airfoil ($x/c = 1, 2.5, 4, 6, 9, 14\%$) at $\alpha = 0^\circ$ and are normalized on the free-stream dynamic pressure.

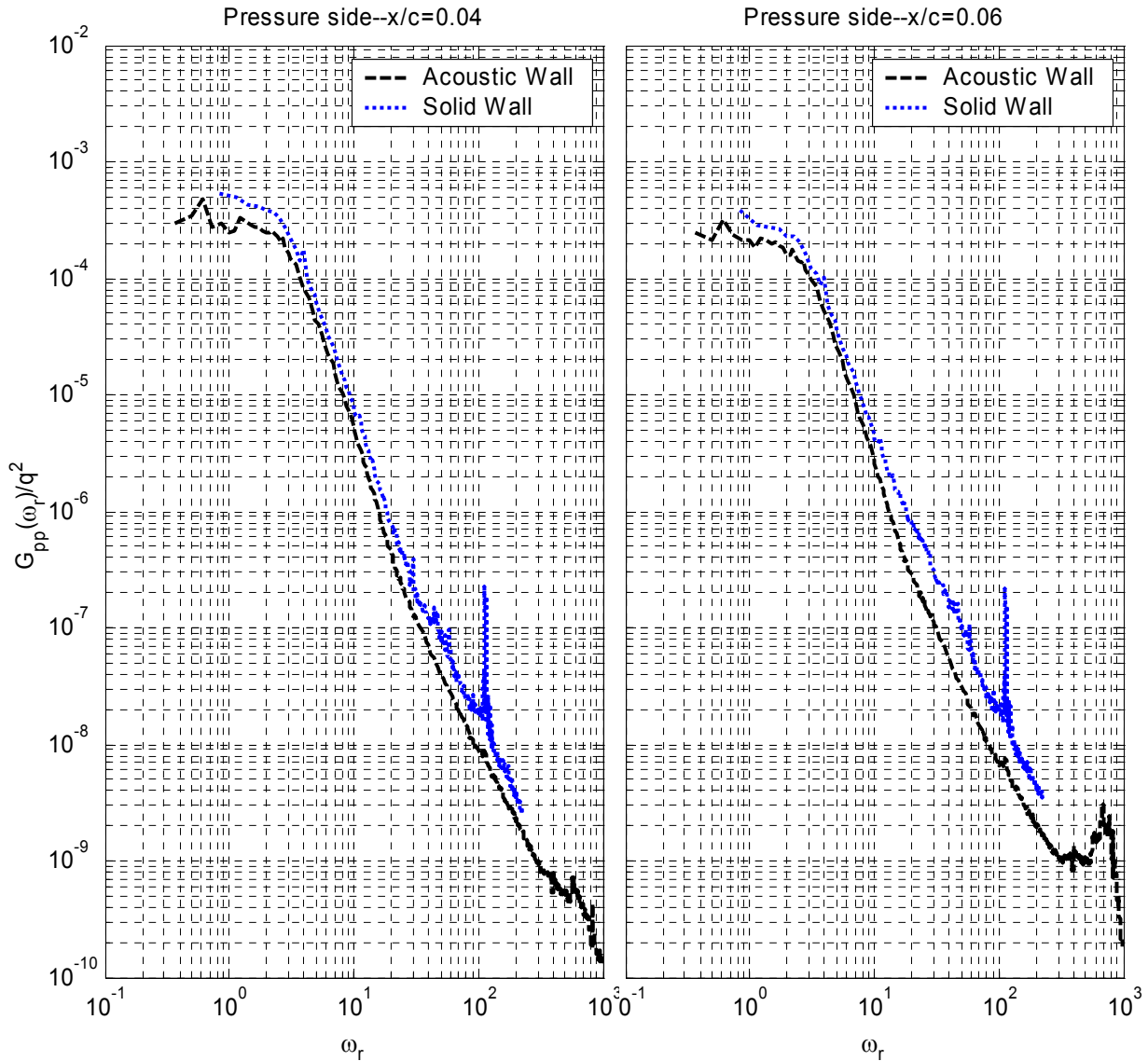


Figure 4.17 continued: Comparison of *large* grid p' spectra measured with solid and acoustically treated wind tunnel test section walls. Spectra are from *pressure* side of airfoil ($x/c = 1, 2.5, 4, 6, 9, 14\%$) at $\alpha = 0^\circ$ and are normalized on the free-stream dynamic pressure.

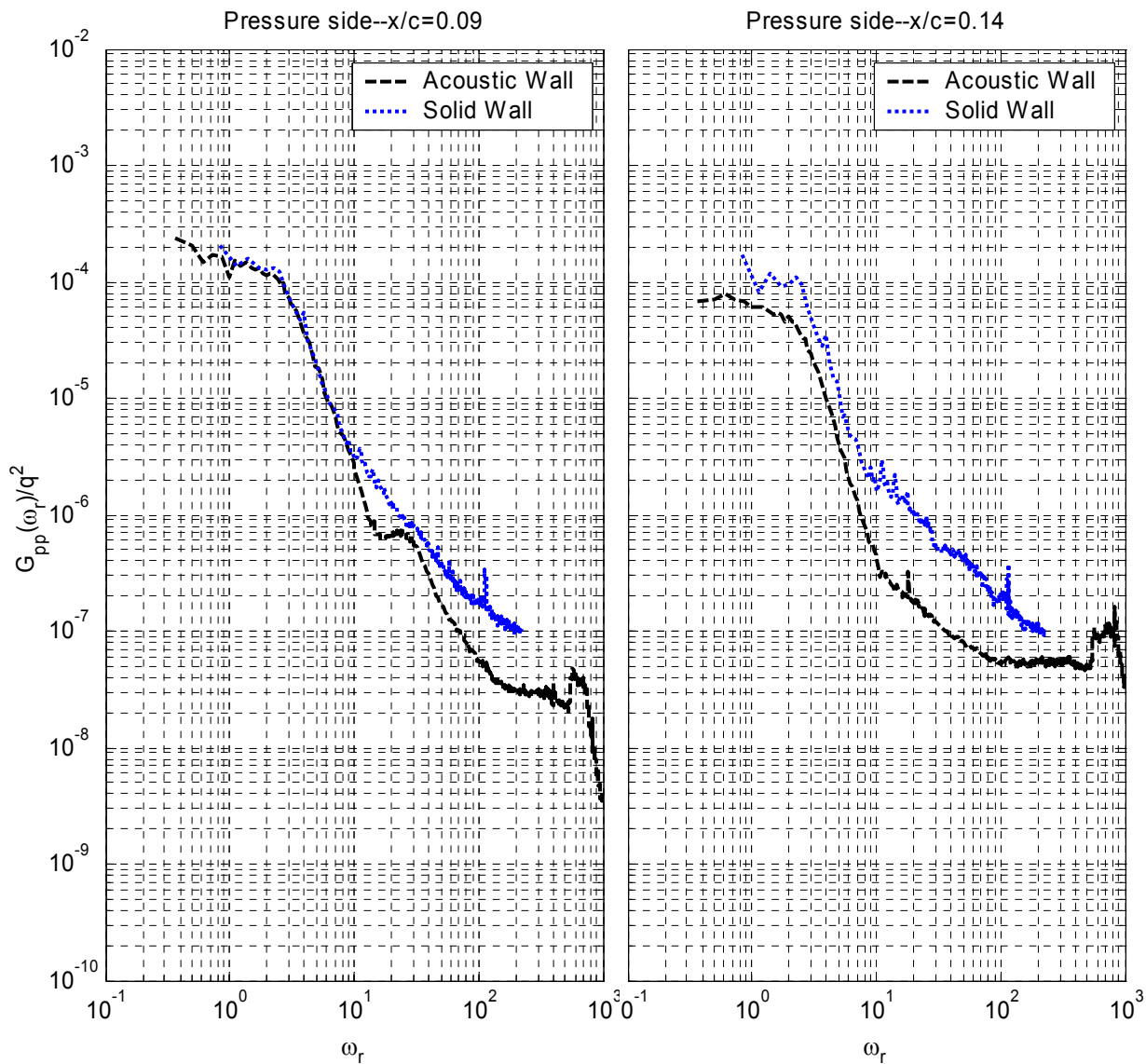


Figure 4.17 continued: Comparison of *large* grid p' spectra measured with solid and acoustically treated wind tunnel test section walls. Spectra are from *pressure* side of airfoil ($x/c = 1, 2.5, 4, 6, 9, 14\%$) at $\alpha = 0^\circ$ and are normalized on the free-stream dynamic pressure.

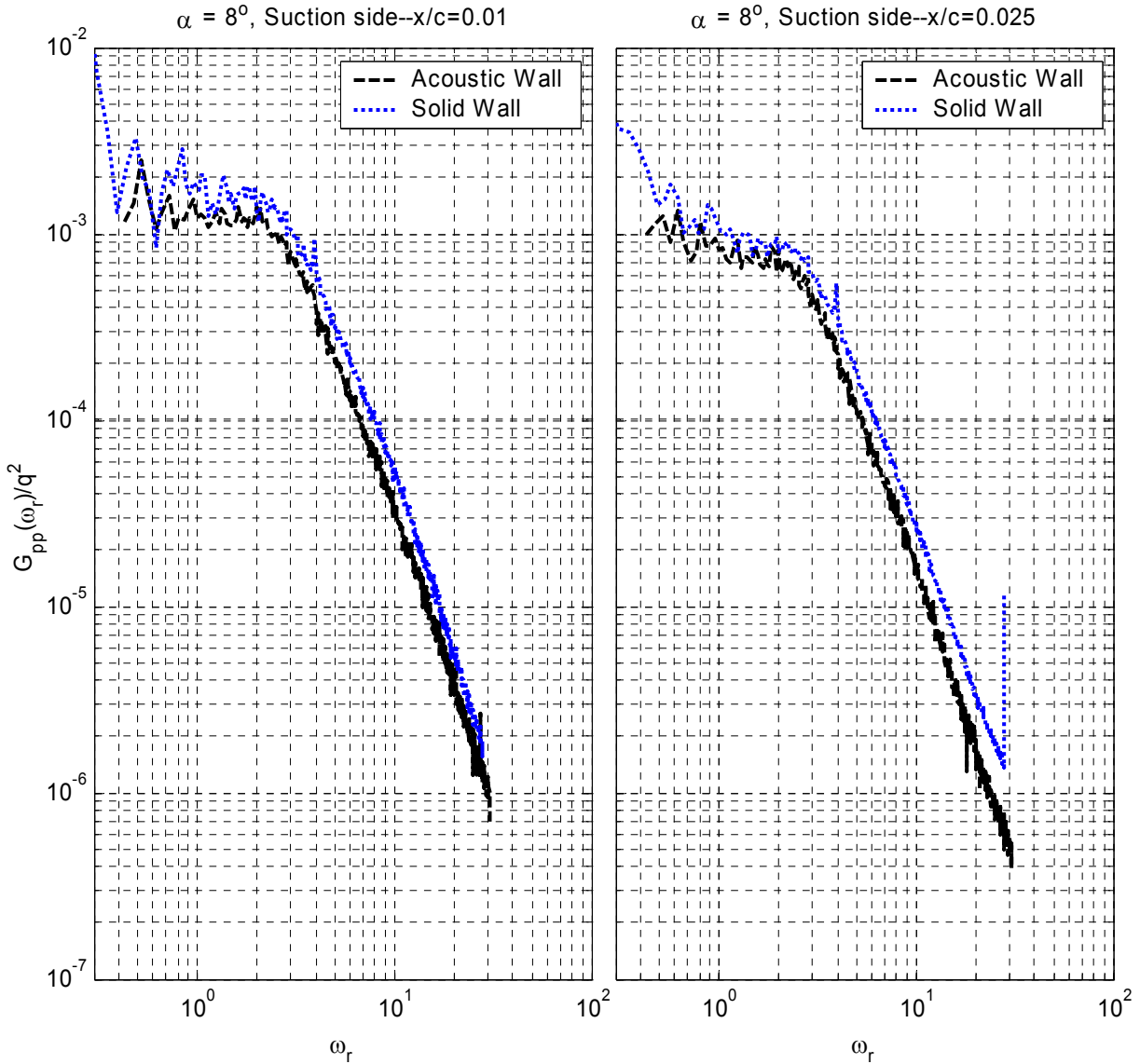


Figure 4.18: Comparison of *large grid* p' spectra measured with solid and acoustically treated wind tunnel test section walls. Spectra are from *suction* side of airfoil ($x/c = 1, 2.5\%$) at $\alpha = 8^\circ$ and are normalized on the free-stream dynamic pressure.

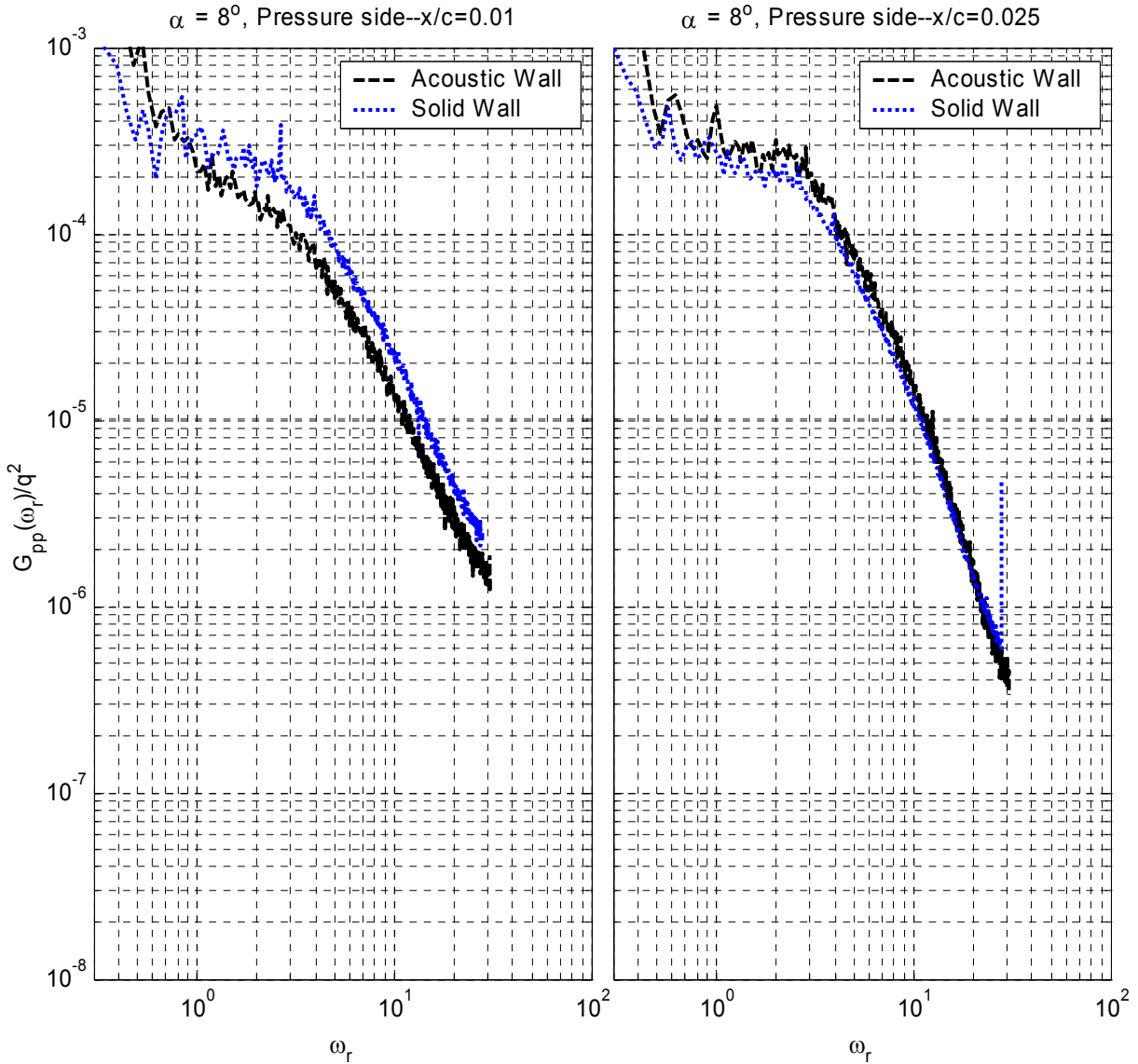


Figure 4.19: Comparison of *large grid* p' spectra measured with solid and acoustically treated wind tunnel test section walls. Spectra are from *pressure* side of airfoil ($x/c = 1, 2.5\%$) at $\alpha = 8^\circ$ and are normalized on the free-stream dynamic pressure.

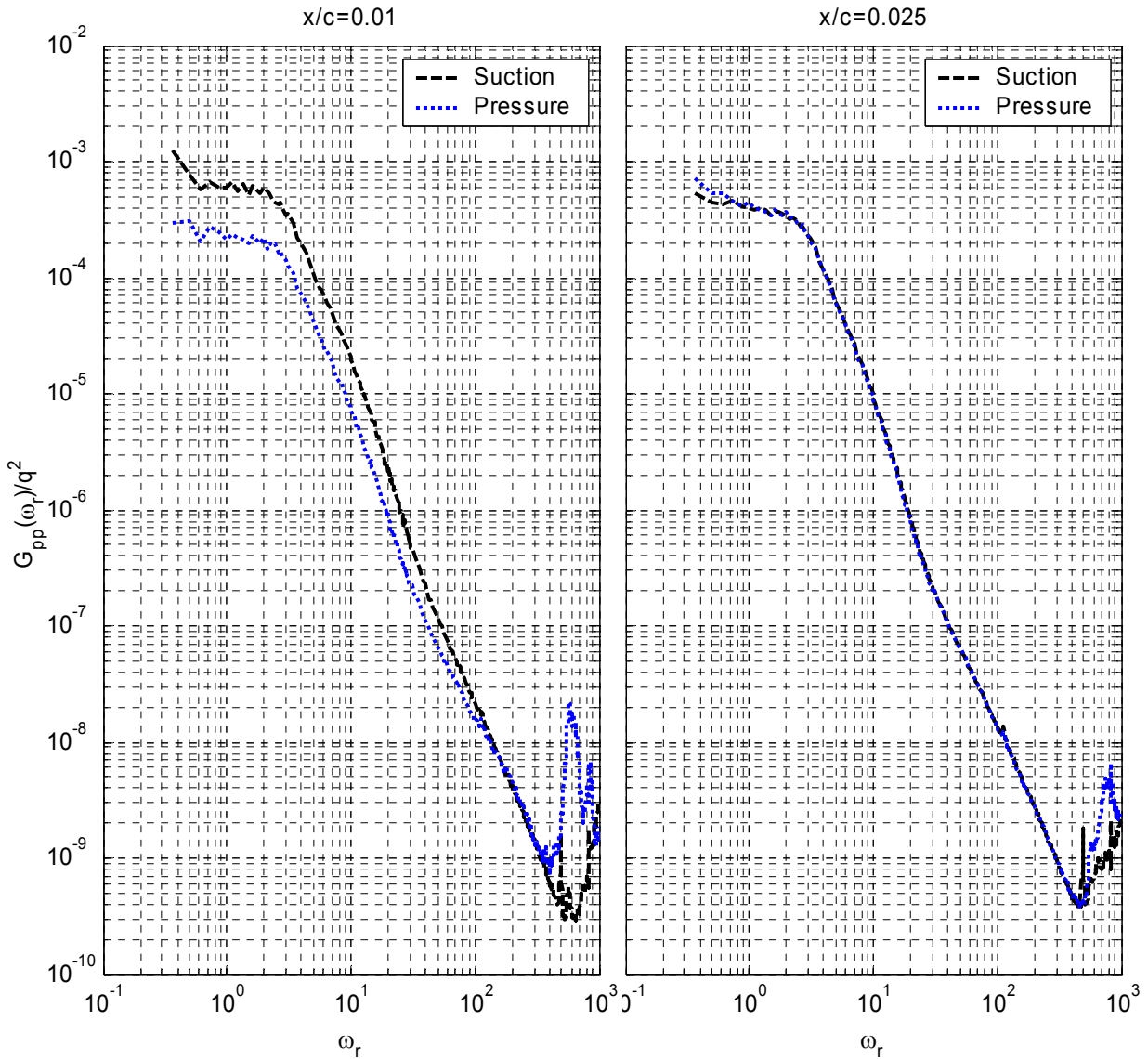


Figure 4.20: Comparison of p' spectra on the pressure and suction side of airfoil at $\alpha = 0^\circ$. Comparison made at $x/c = 1, 2.5, 4, 6, 9, 14\%$.

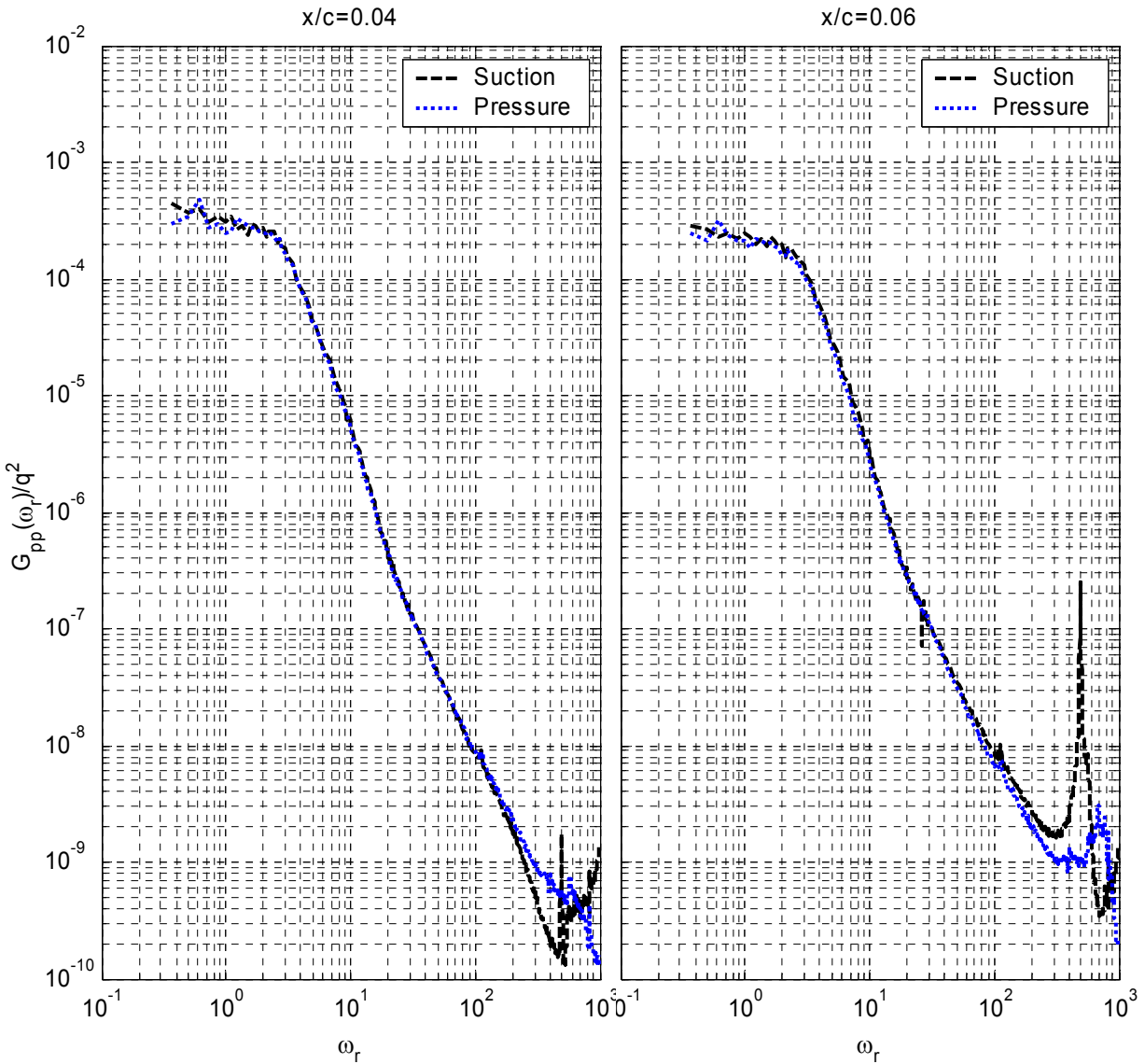


Figure 4.20 continued: Comparison of p' spectra on the pressure and suction side of airfoil at $\alpha = 0^\circ$. Comparison made at $x/c = 1, 2.5, 4, 6, 9, 14\%$.

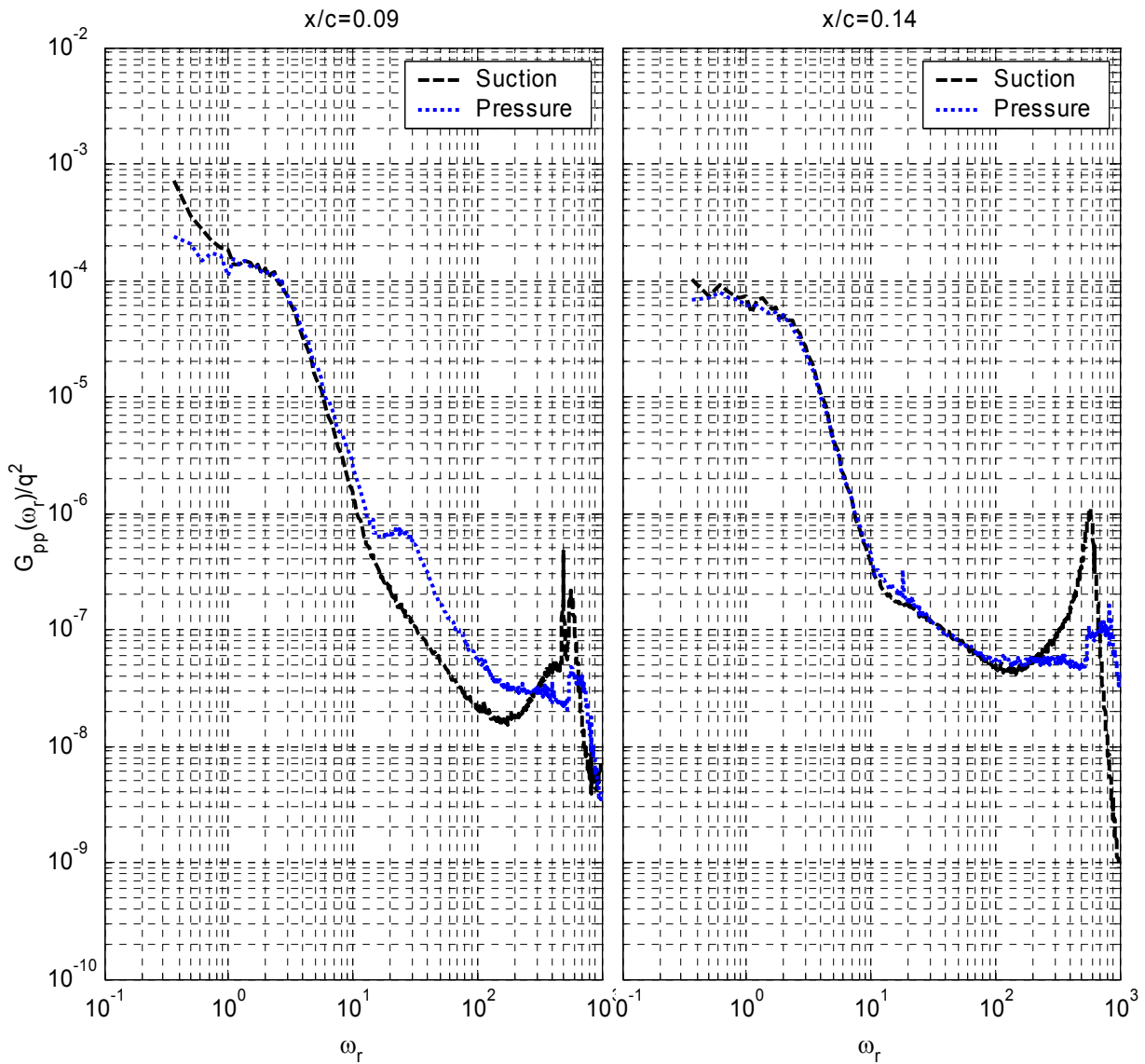


Figure 4.20 continued: Comparison of p' spectra on the pressure and suction side of airfoil at $\alpha = 0^\circ$. Comparison made at $x/c = 1, 2.5, 4, 6, 9, 14\%$.

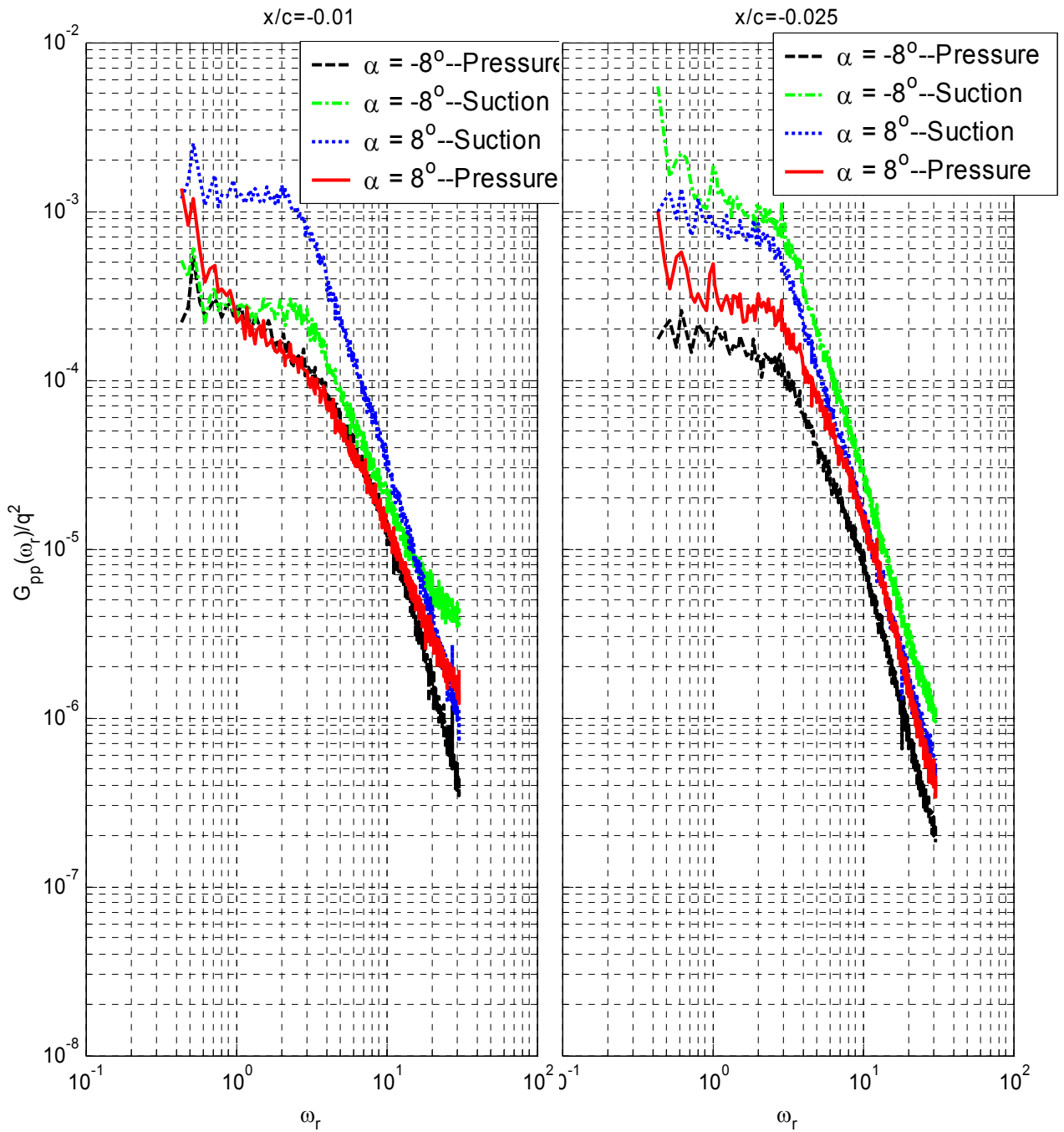


Figure 4.21: Comparison of pressure and suction side p' spectra at $\alpha = 8^\circ$ and -8° for $x/c = 0.01, 0.025, 0.04,$ and 0.06

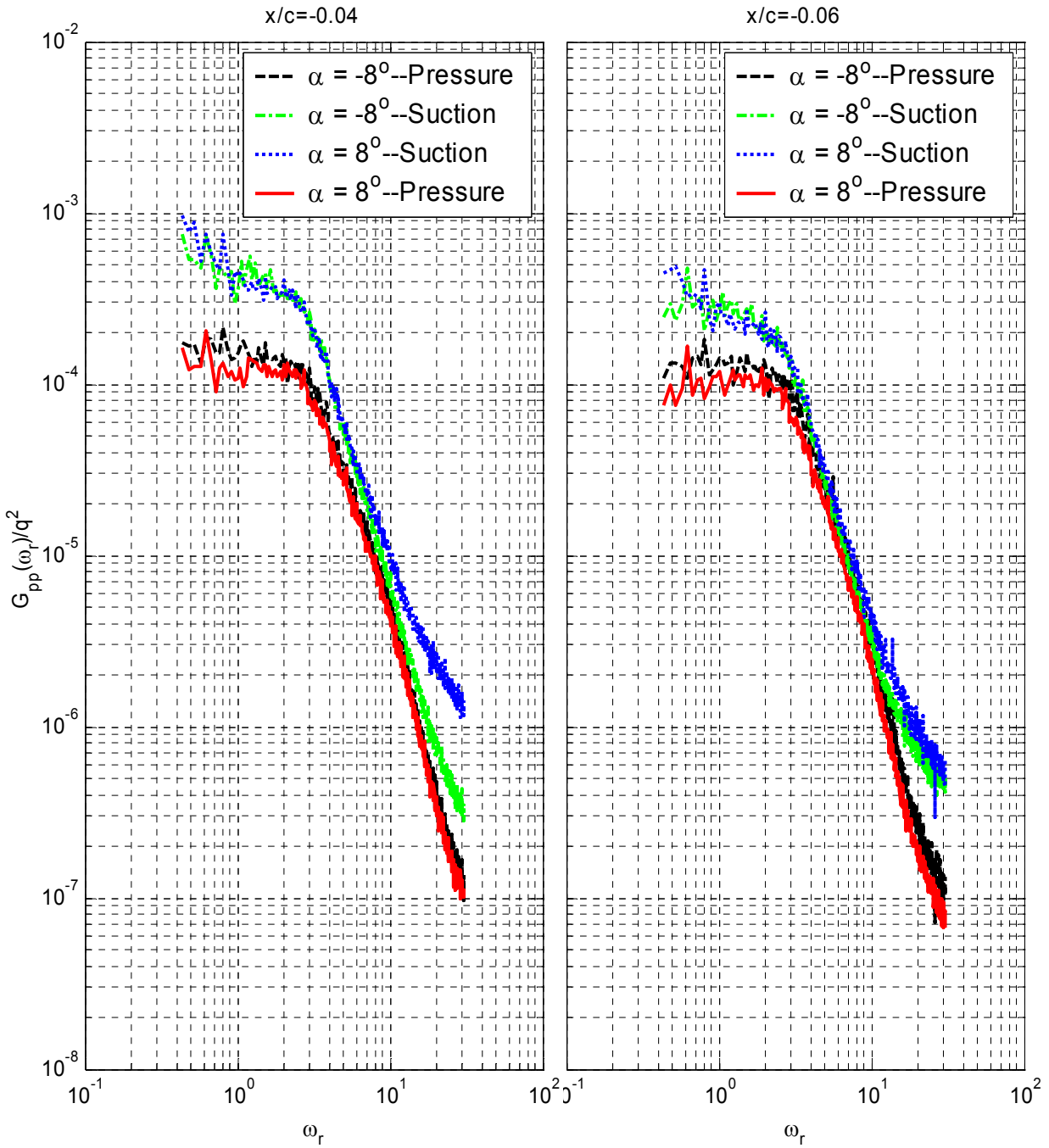


Figure 4.21 continued: Comparison of pressure and suction side p' spectra at $\alpha = 8^\circ$ and -8° for $x/c = 0.01, 0.025, 0.04,$ and 0.06

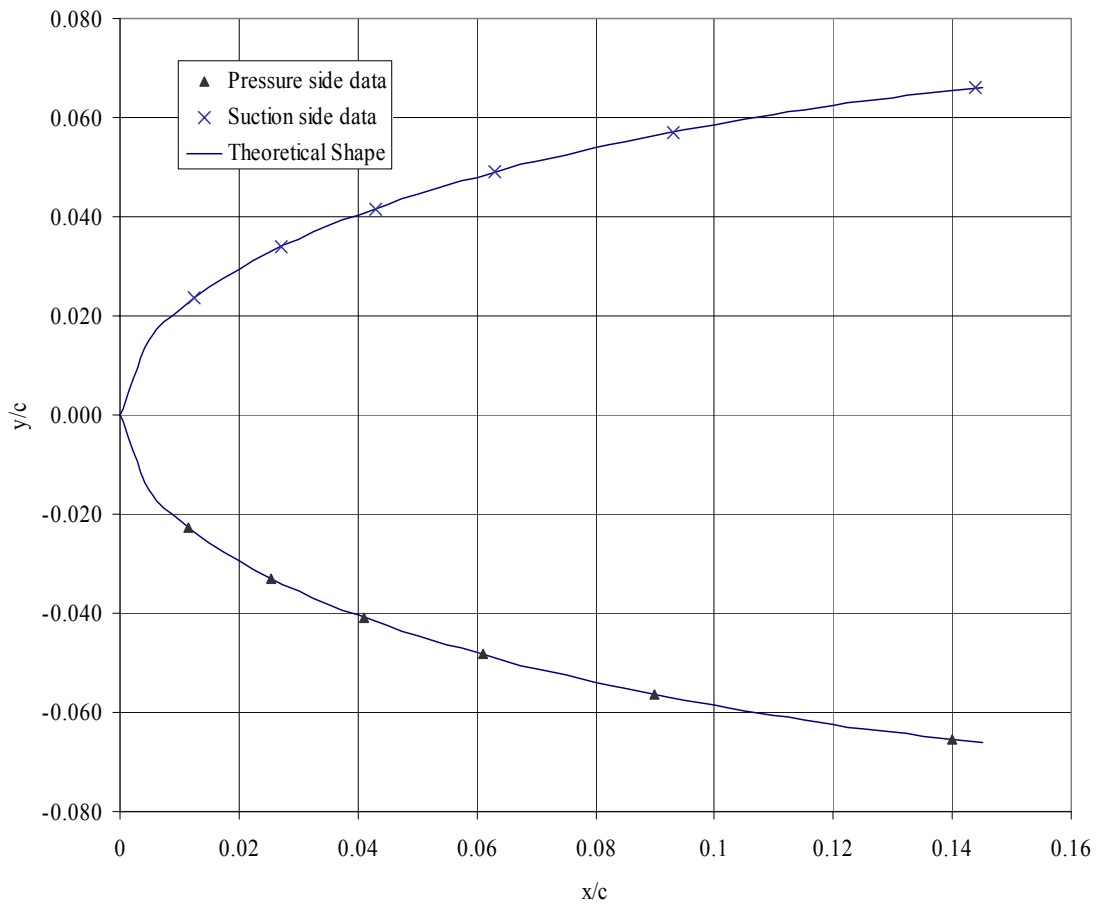


Figure 4.22: Measured geometry at each microphone location versus actual wing geometry

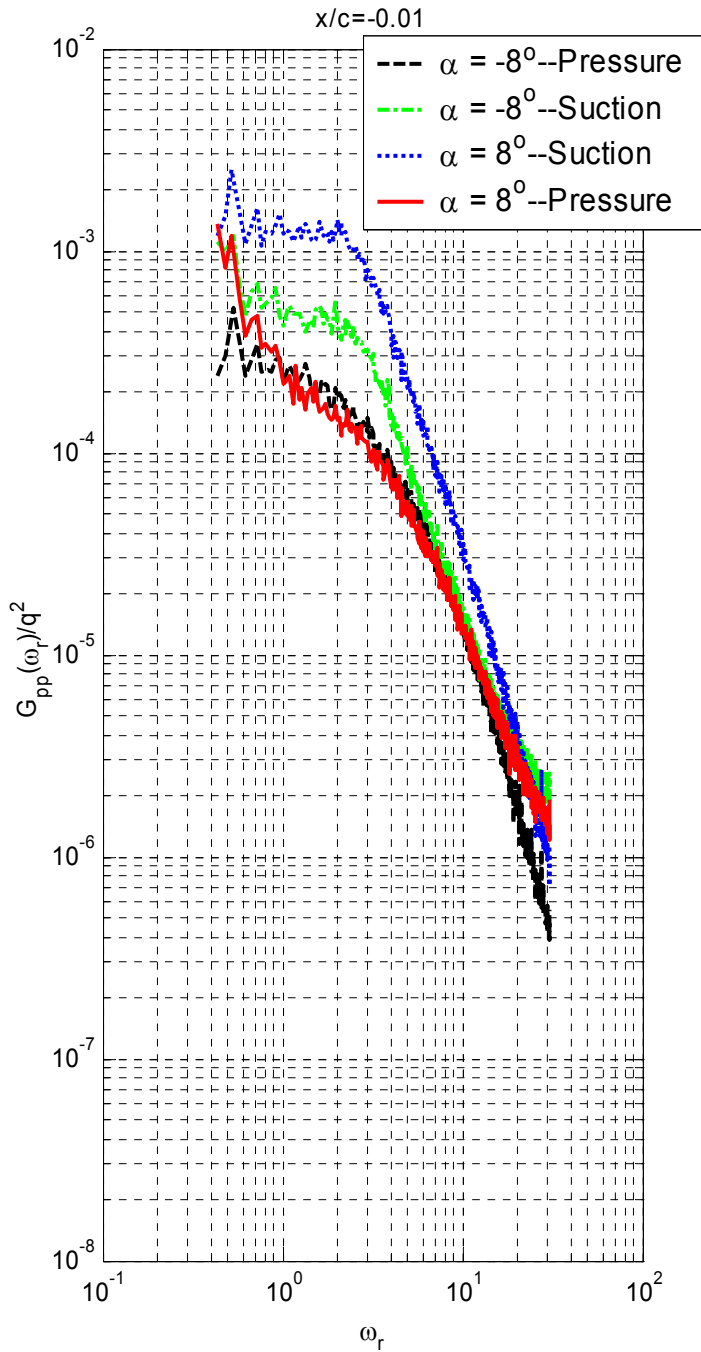


Figure 4.23: Pressure spectra comparison at $\alpha = 8^\circ$ and -8° for $x/c = 0.01$. Data at $\alpha = -8^\circ$ is taken with *leading edge bump* installed.

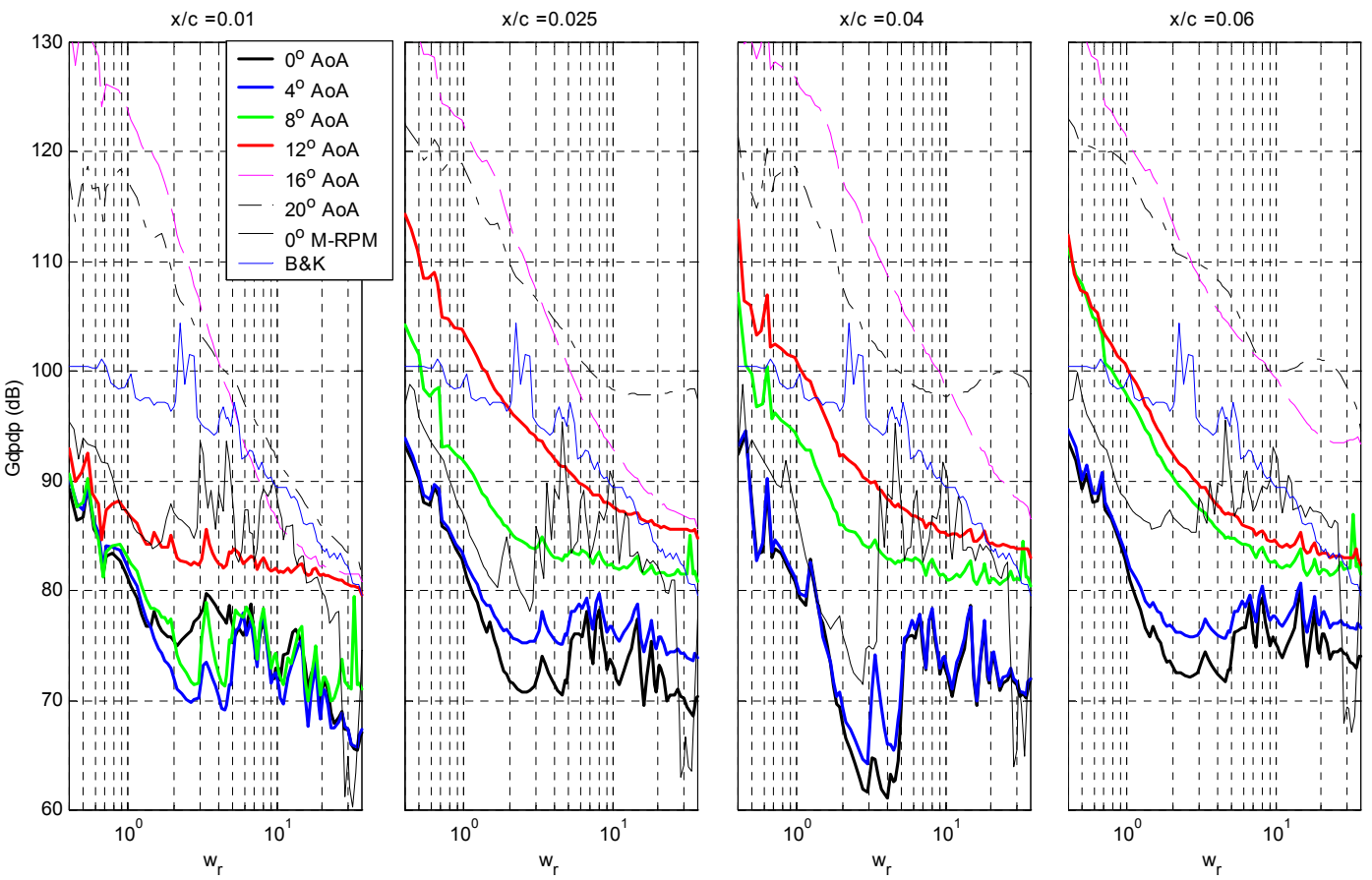


Figure 4.24: Pressure difference smooth flow data plotted at all angles of attack with matched RPM data at $\alpha = 0^\circ$ and reference (B&K) microphone data at $x/c = 0.01, 0.025, 0.04, 0.06$

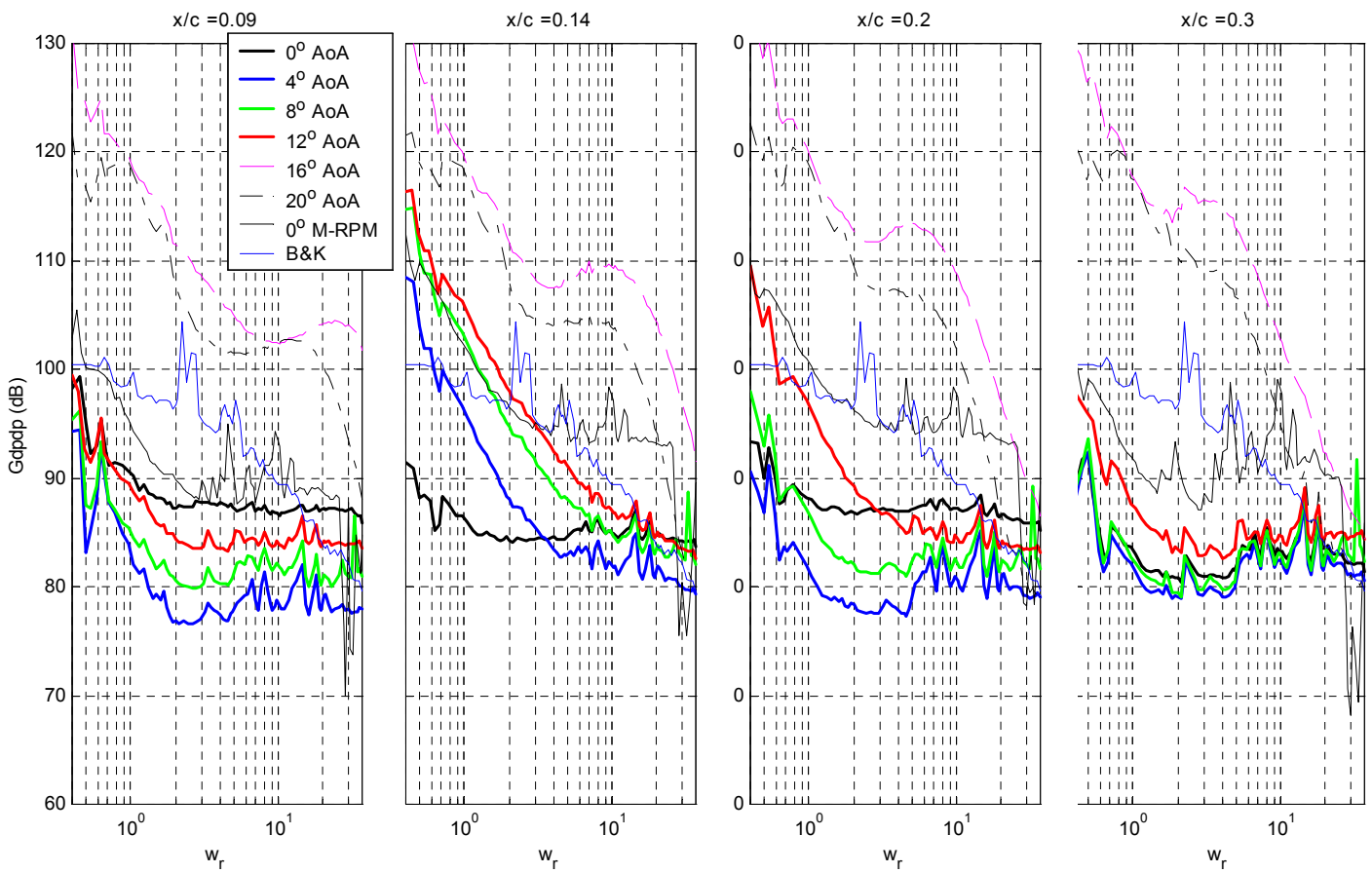


Figure 4.25: Pressure difference matched flow speed data plotted at all angles of attack with matched RPM data at $\alpha = 0^\circ$ and reference (B&K) microphone data at $x/c = 0.09, 0.14, 0.2, 0.3$

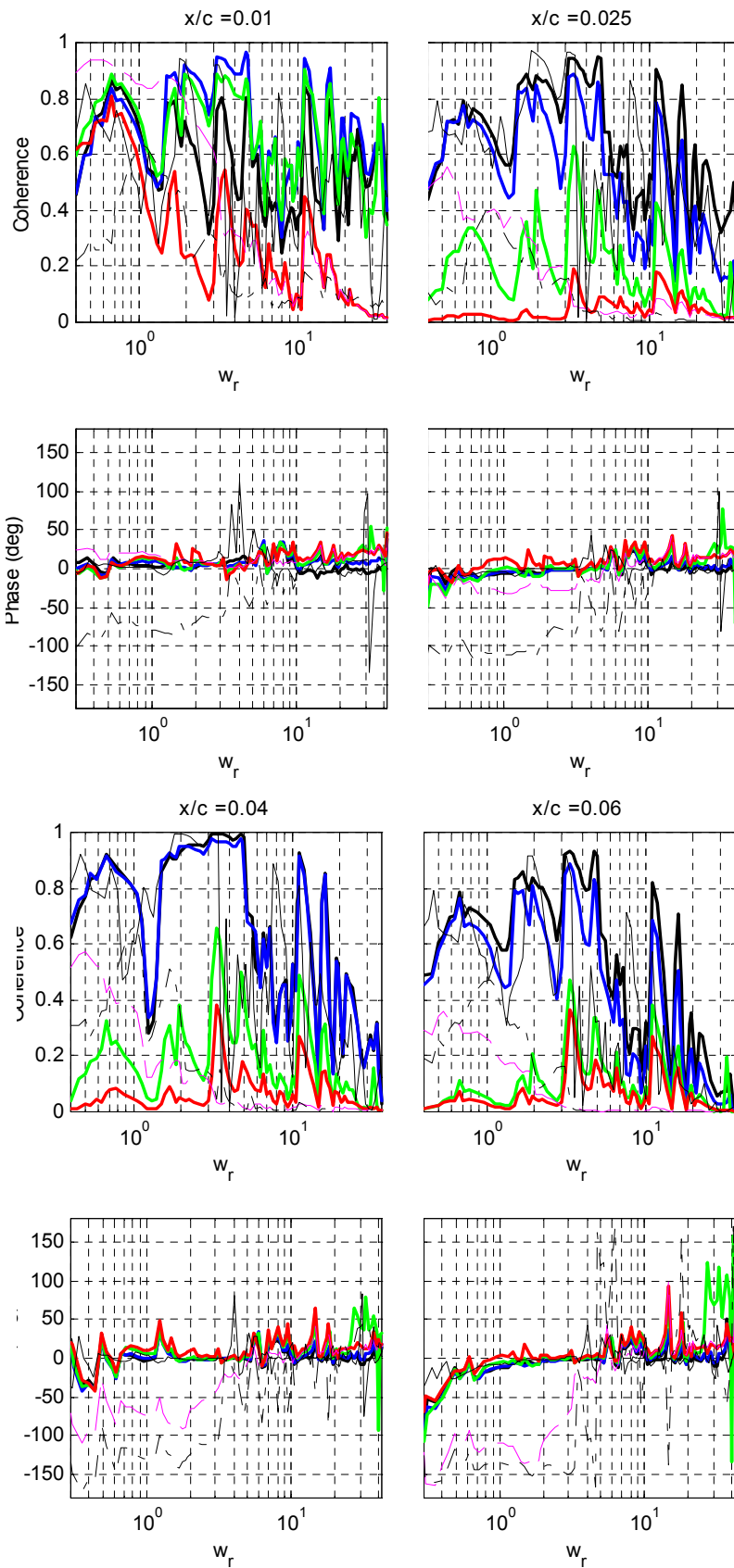


Figure 4.26: Coherence and phase of matched flow speed data plotted at all angles of attack with matched RPM data at $\alpha = 0^\circ$ and reference (B&K) microphone data at $x/c = 0.01, 0.025, 0.04, 0.06$

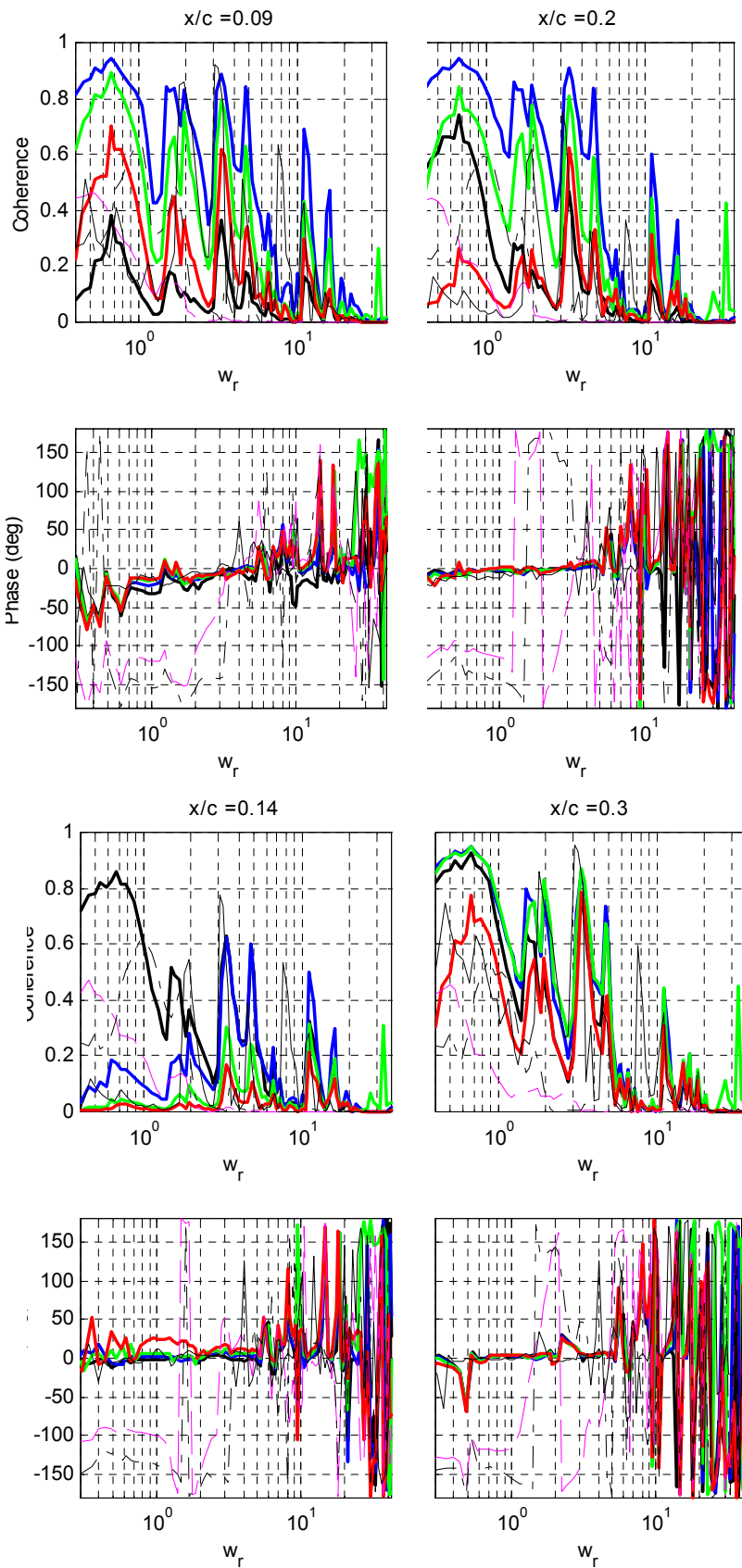


Figure 4.27: Coherence and phase of matched flow speed data plotted at all angles of attack with matched RPM data at $\alpha = 0^\circ$ and reference (B&K) microphone data at $x/c = 0.09, 0.14, 0.2, 0.3$

Moving down the airfoil chord

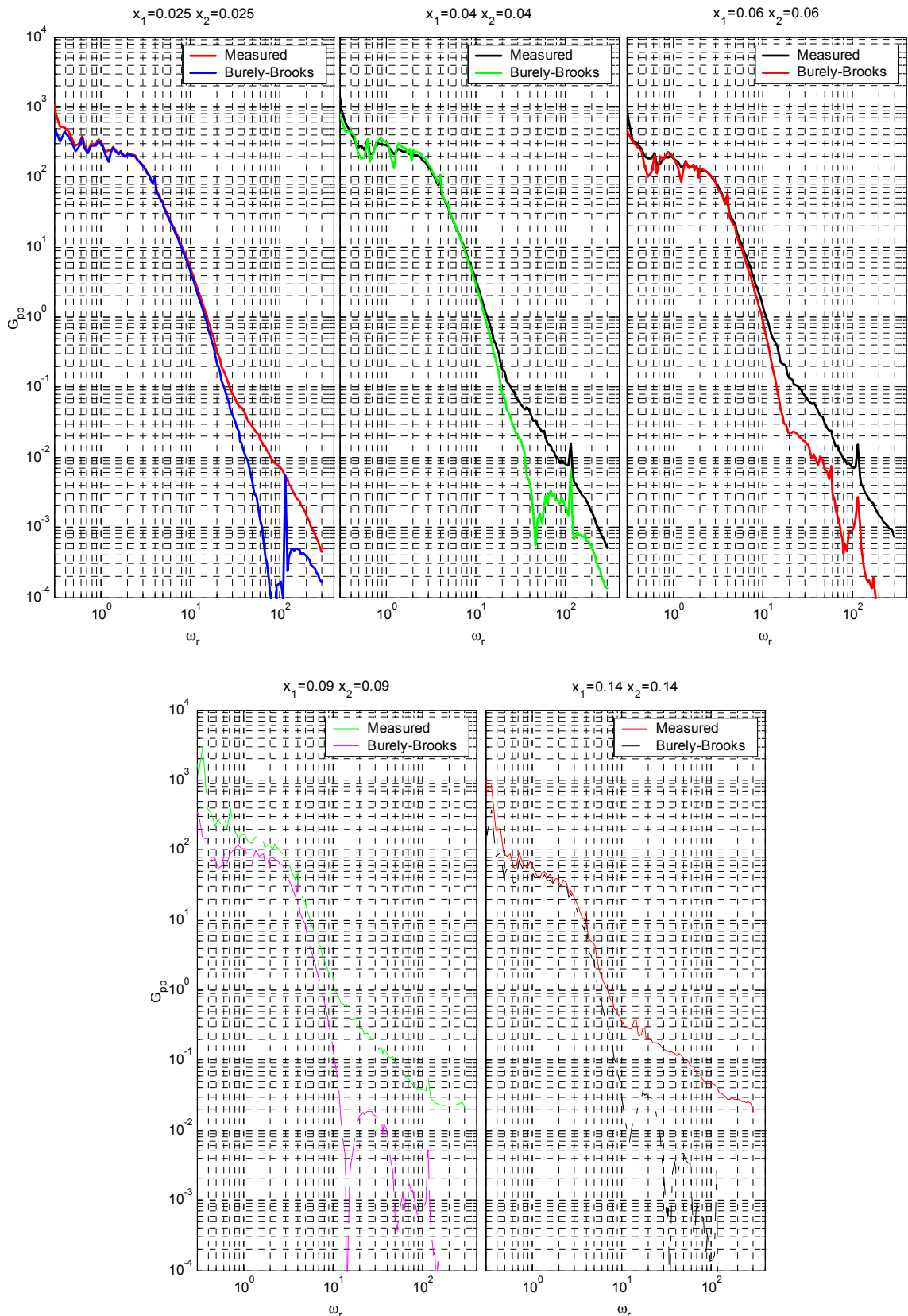


Figure 4.28: Large grid auto-spectra plotted with COP (Burley-Brooks) at $\alpha = 0^\circ$ for $x/c = 0.025, 0.04, 0.06, 0.09,$ and 0.14

Moving down the airfoil chord

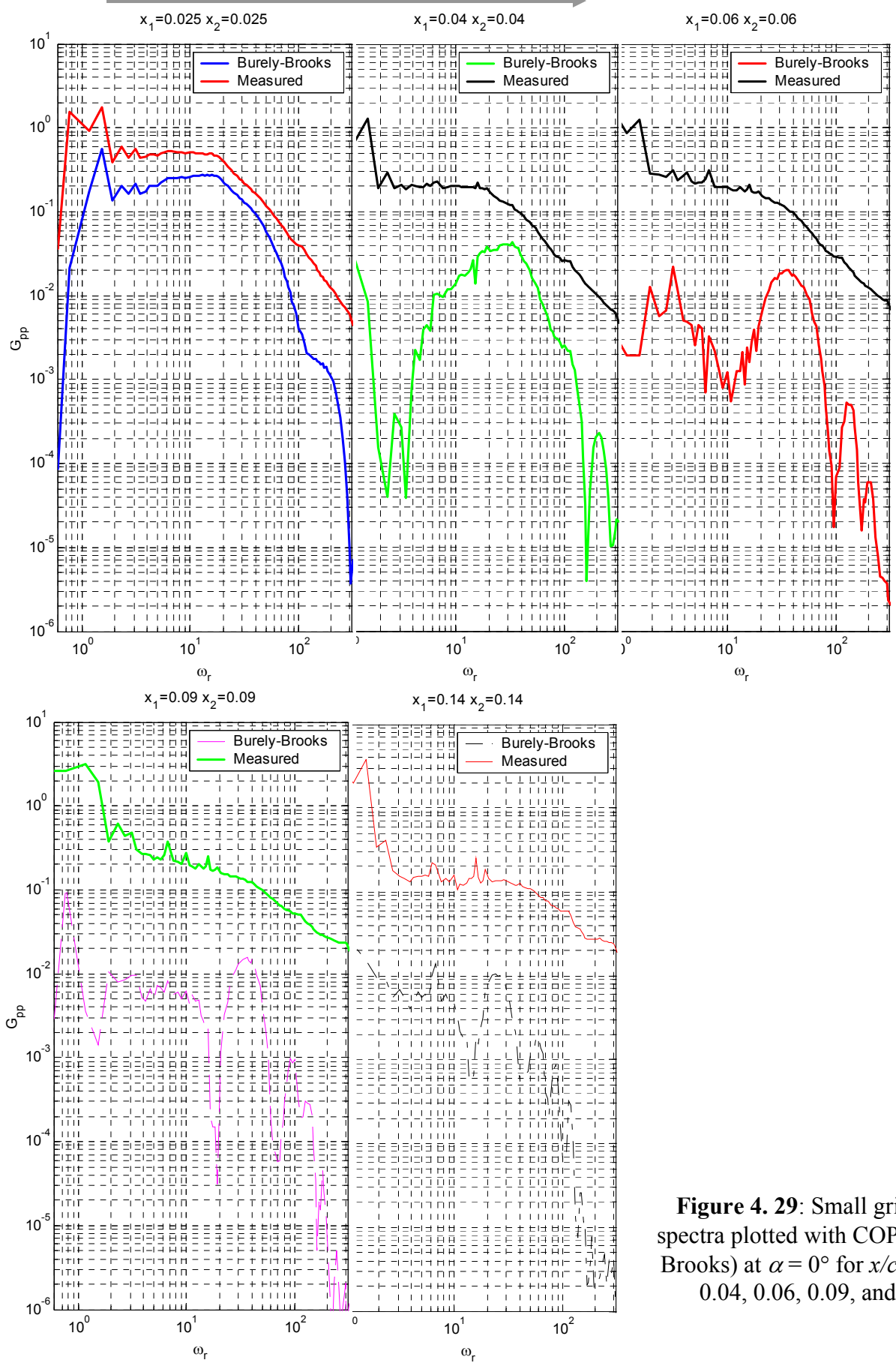


Figure 4. 29: Small grid auto-spectra plotted with COP (Burely-Brooks) at $\alpha = 0^\circ$ for $x/c = 0.025, 0.04, 0.06, 0.09,$ and 0.14

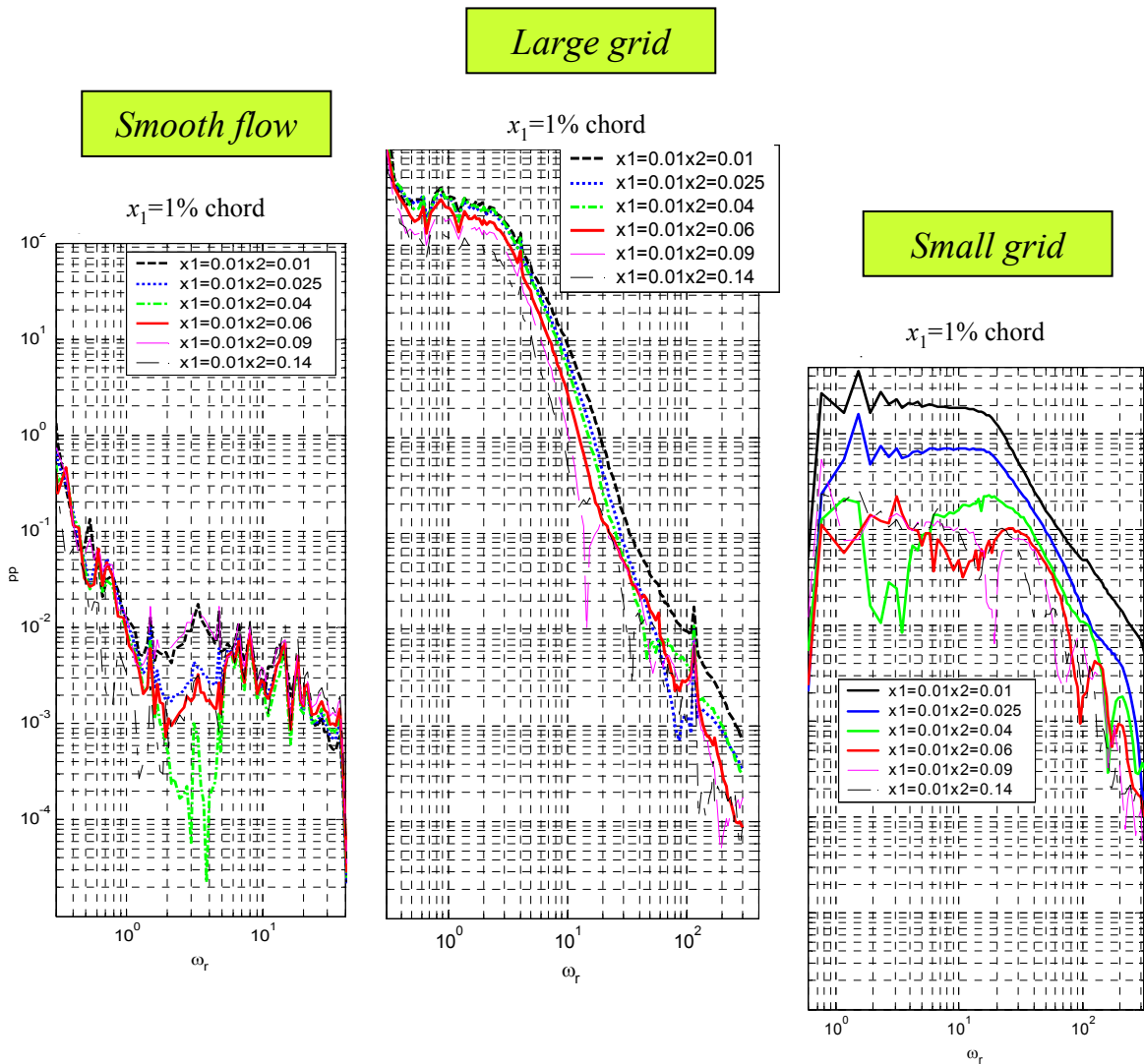


Figure 4.30: Pressure difference cross-spectra at $x/c = 0.01$, $\alpha = 0^\circ$ measured in smooth flow and in large and small grid turbulence

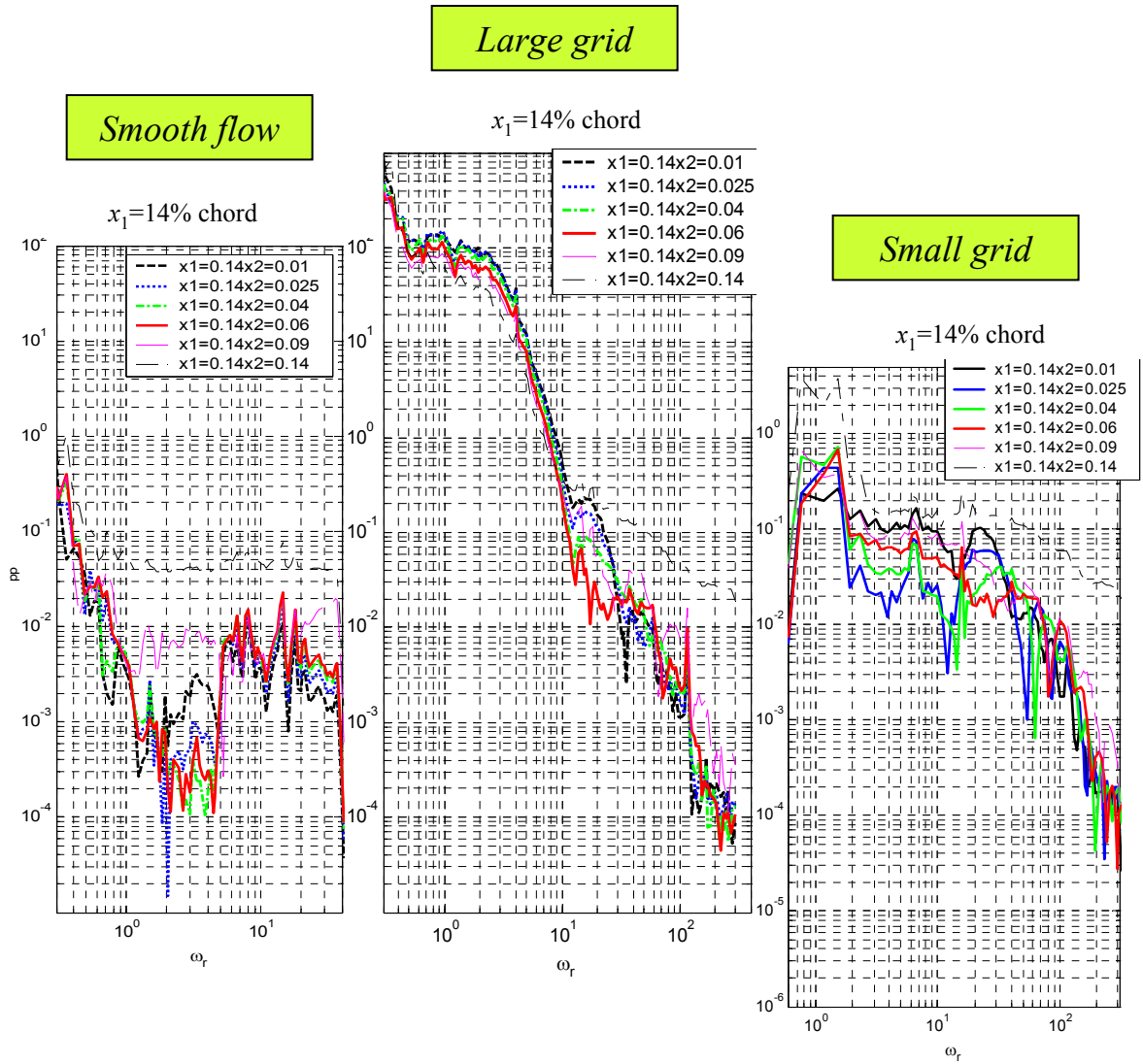


Figure 4.32: Pressure difference cross-spectra at $x/c = 0.14$, $\alpha = 0^\circ$ measured in smooth flow and in large and small grid turbulence

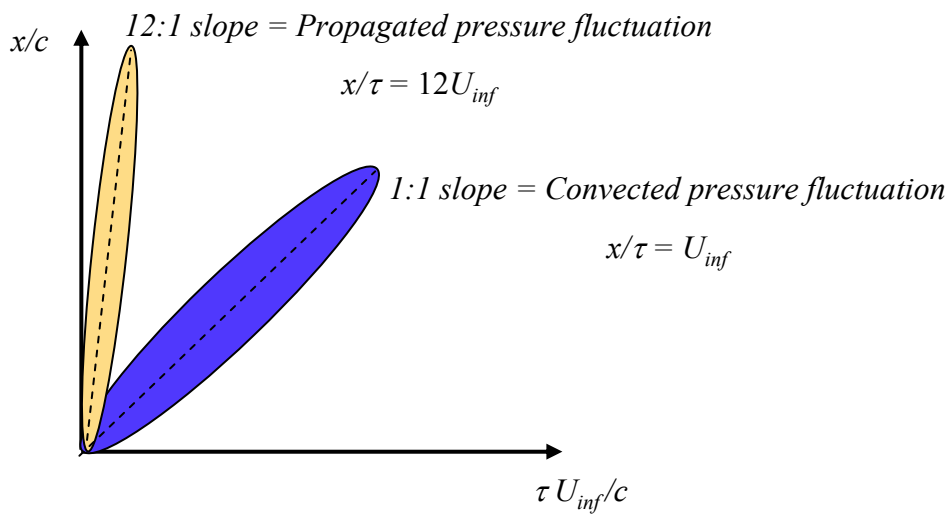


Figure 4.33: Dominant features expected in a contour plot of R_{pp} ,

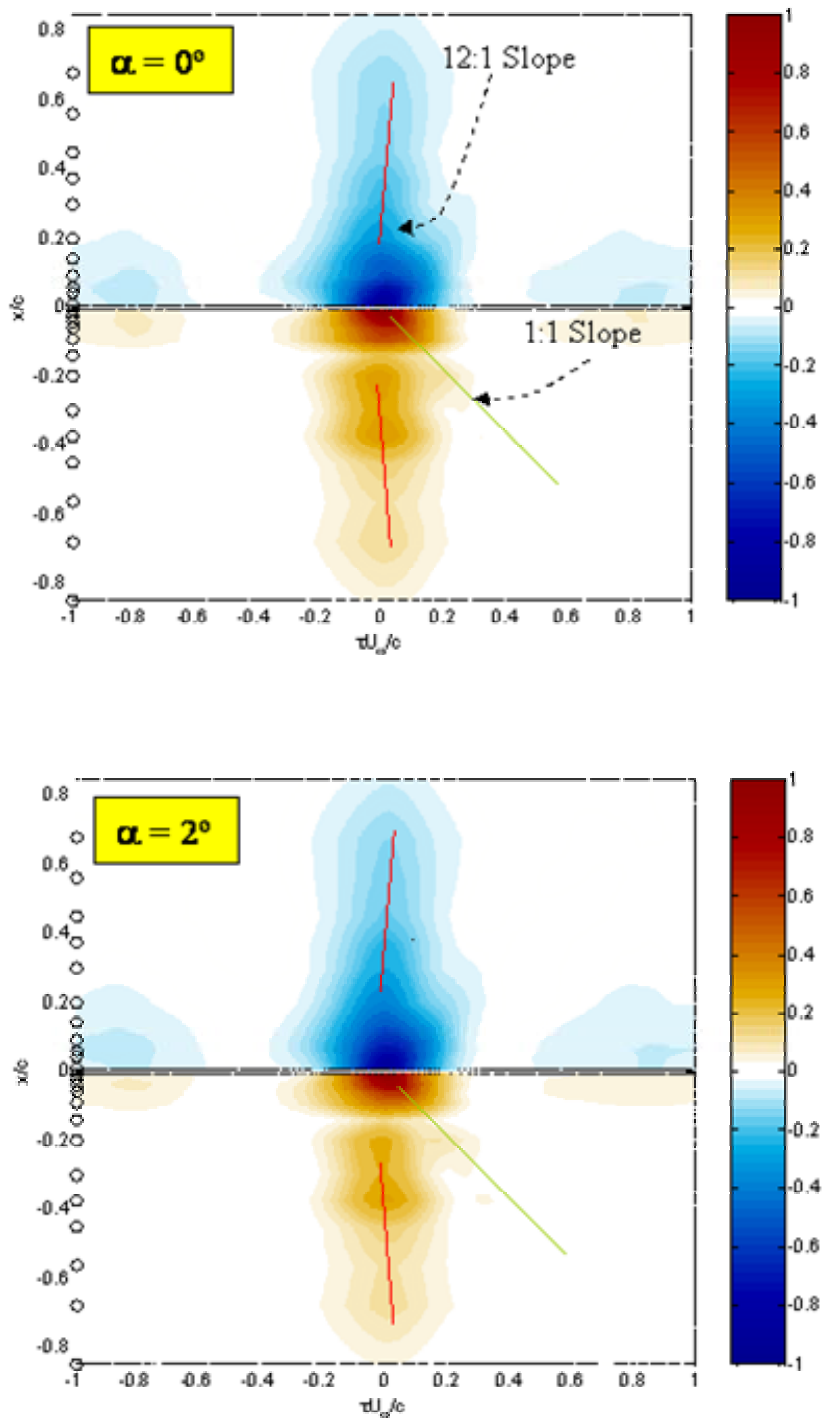


Figure 4.34: Contour plots of pressure-pressure correlation, $R_{pp}(x=1\%, x', \tau)$ for *large* grid flow. The correlation is formed with the 1% chord microphone on the suction side of the airfoil

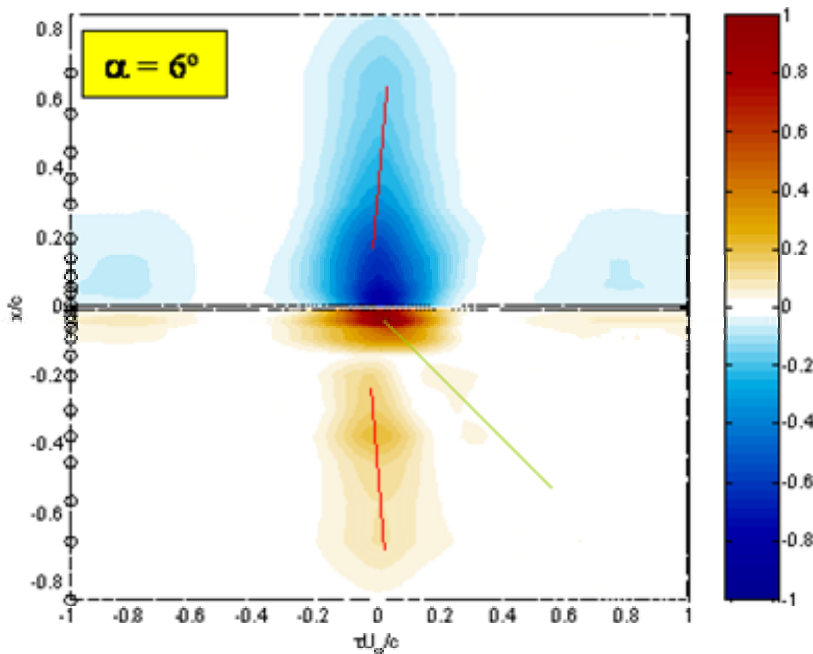
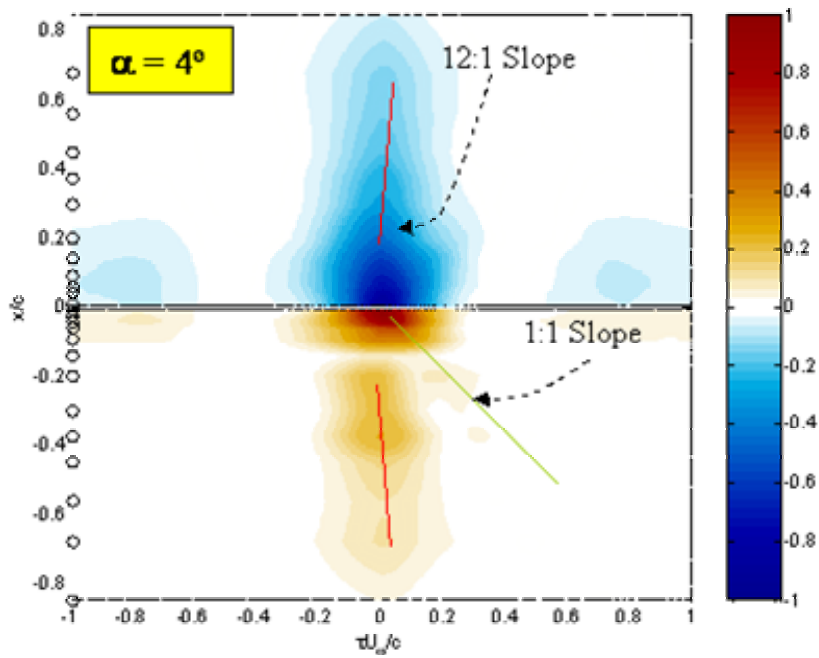


Figure 4.34 continued: Contour plots of pressure-pressure correlation, $R_{pp}(x=1\%, x', \tau)$ for *large* grid flow. The correlation is formed with the 1% chord microphone on the suction side of the airfoil

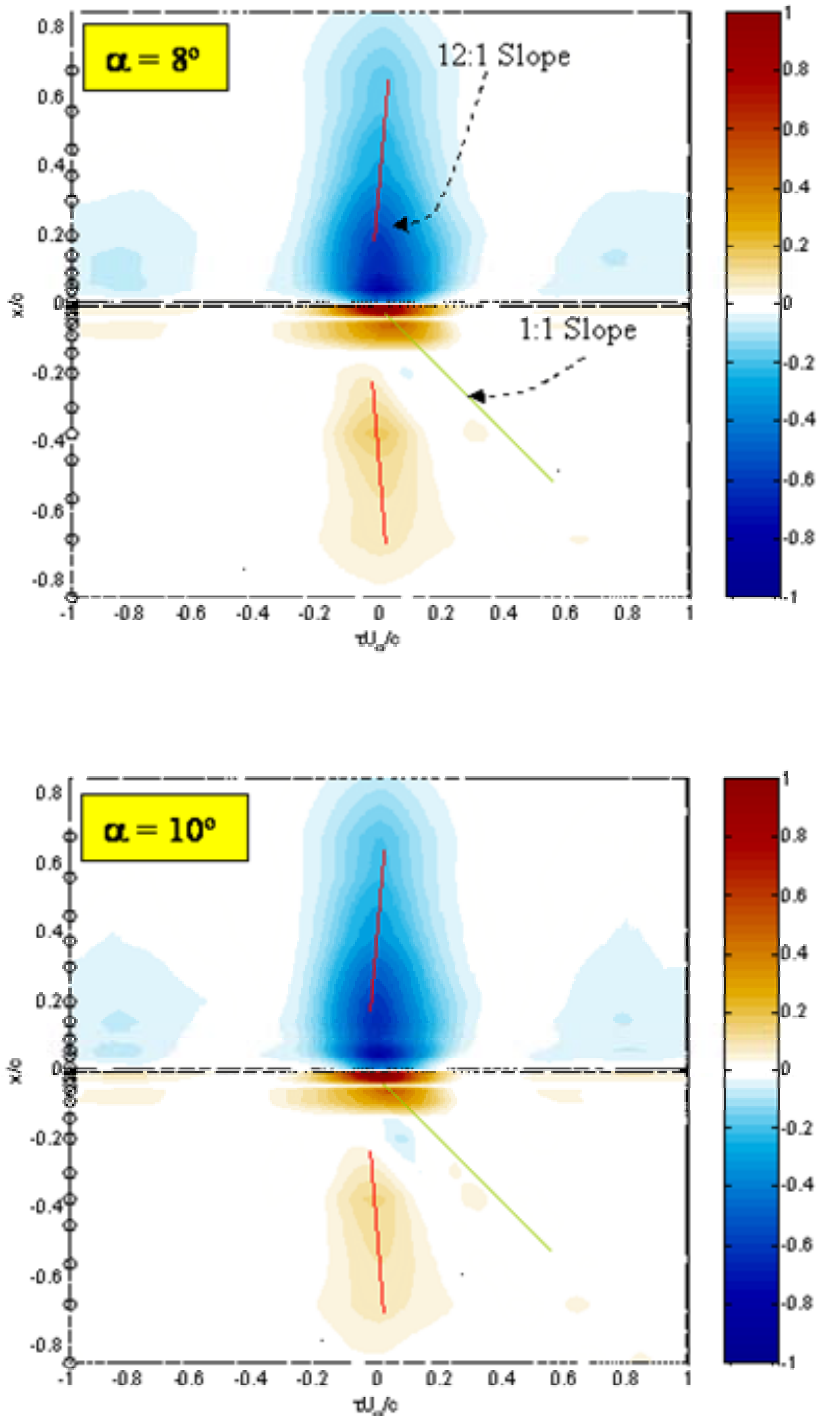


Figure 4.34 continued: Contour plots of pressure-pressure correlation, $R_{pp}(x=1\%, x', \tau)$ for *large* grid flow. The correlation is formed with the 1% chord microphone on the suction side of the airfoil

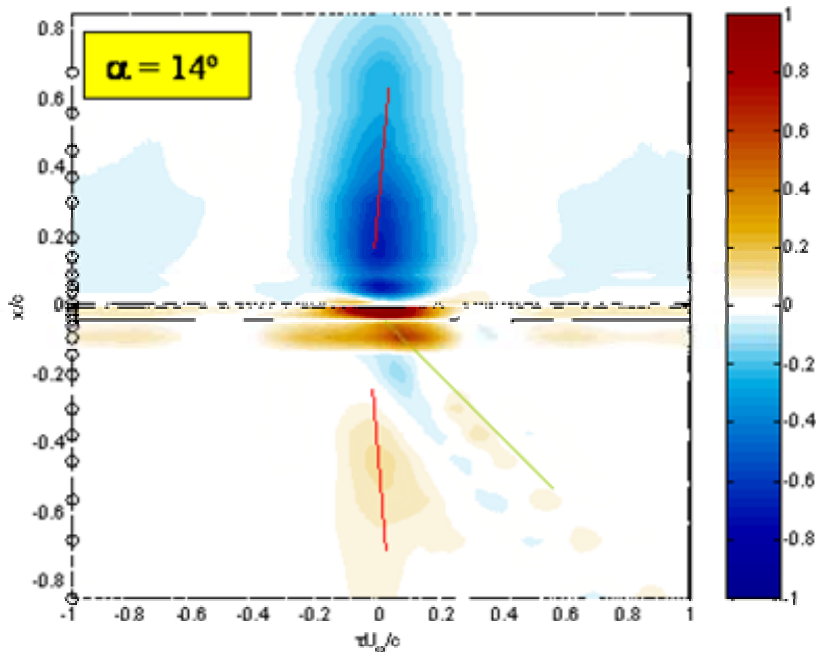
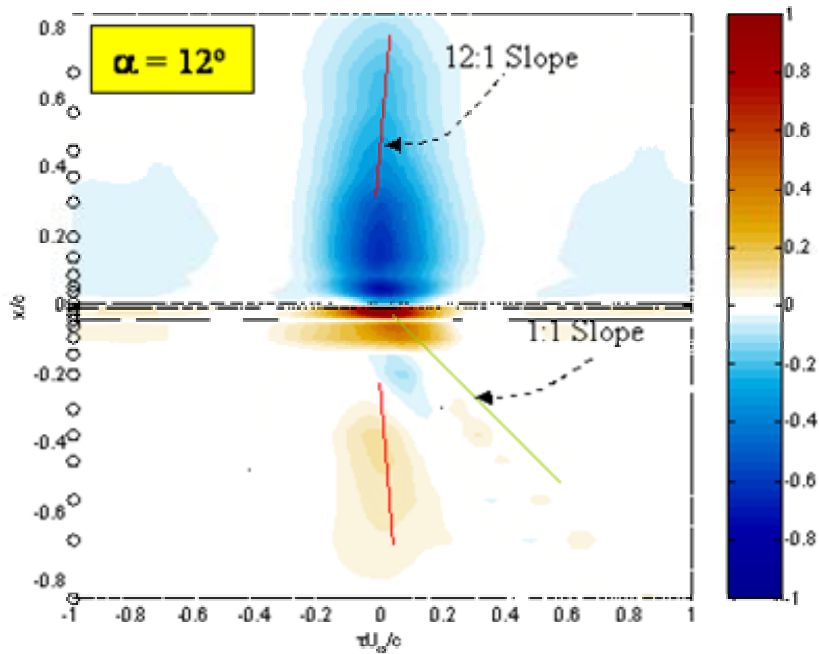


Figure 4.34 continued: Contour plots of pressure-pressure correlation, $R_{pp}(x=1\%, x', \tau)$ for *large* grid flow. The correlation is formed with the 1% chord microphone on the suction side of the airfoil

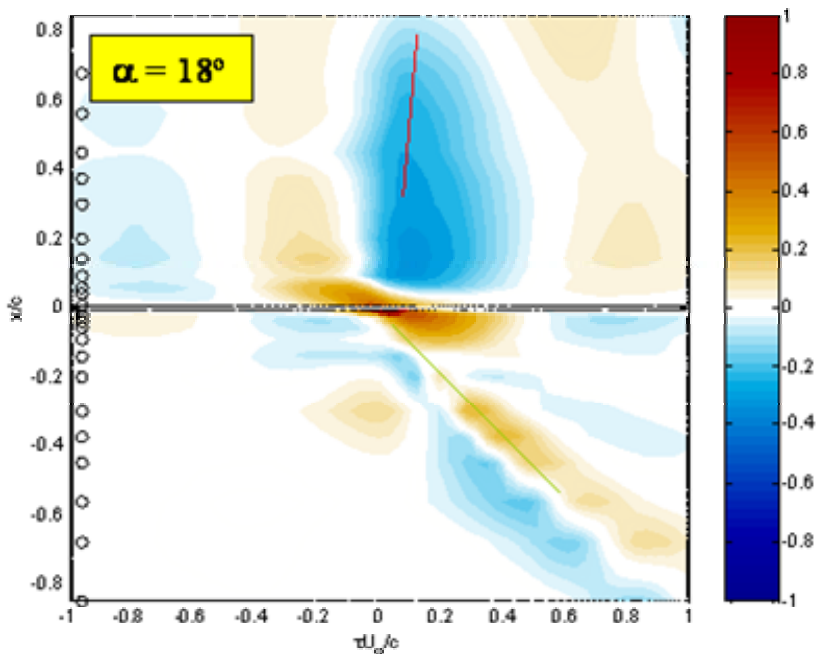
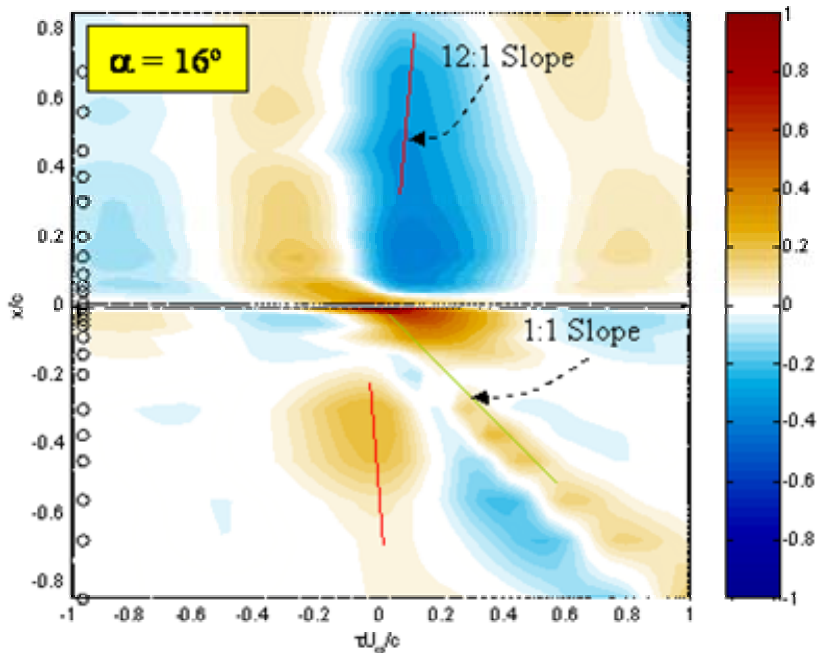


Figure 4.34 continued: Contour plots of pressure-pressure correlation, $R_{pp}(x=1\%, x', \tau)$ for *large* grid flow. The correlation is formed with the 1% chord microphone on the suction side of the airfoil

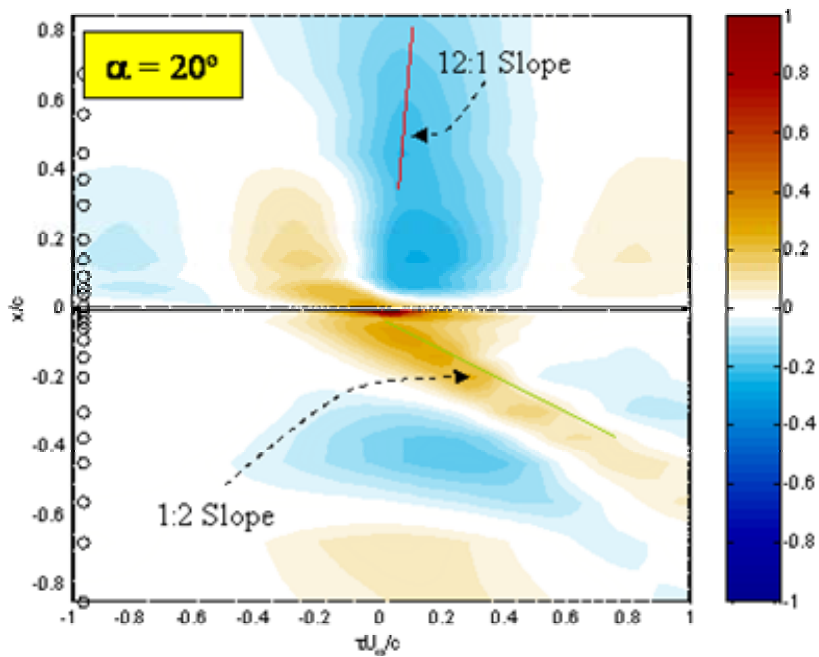


Figure 4.34 continued: Contour plots of pressure-pressure correlation, $R_{pp}(x=1\%, x', \tau)$ for *large* grid flow. The correlation is formed with the 1% chord microphone on the suction side of the airfoil

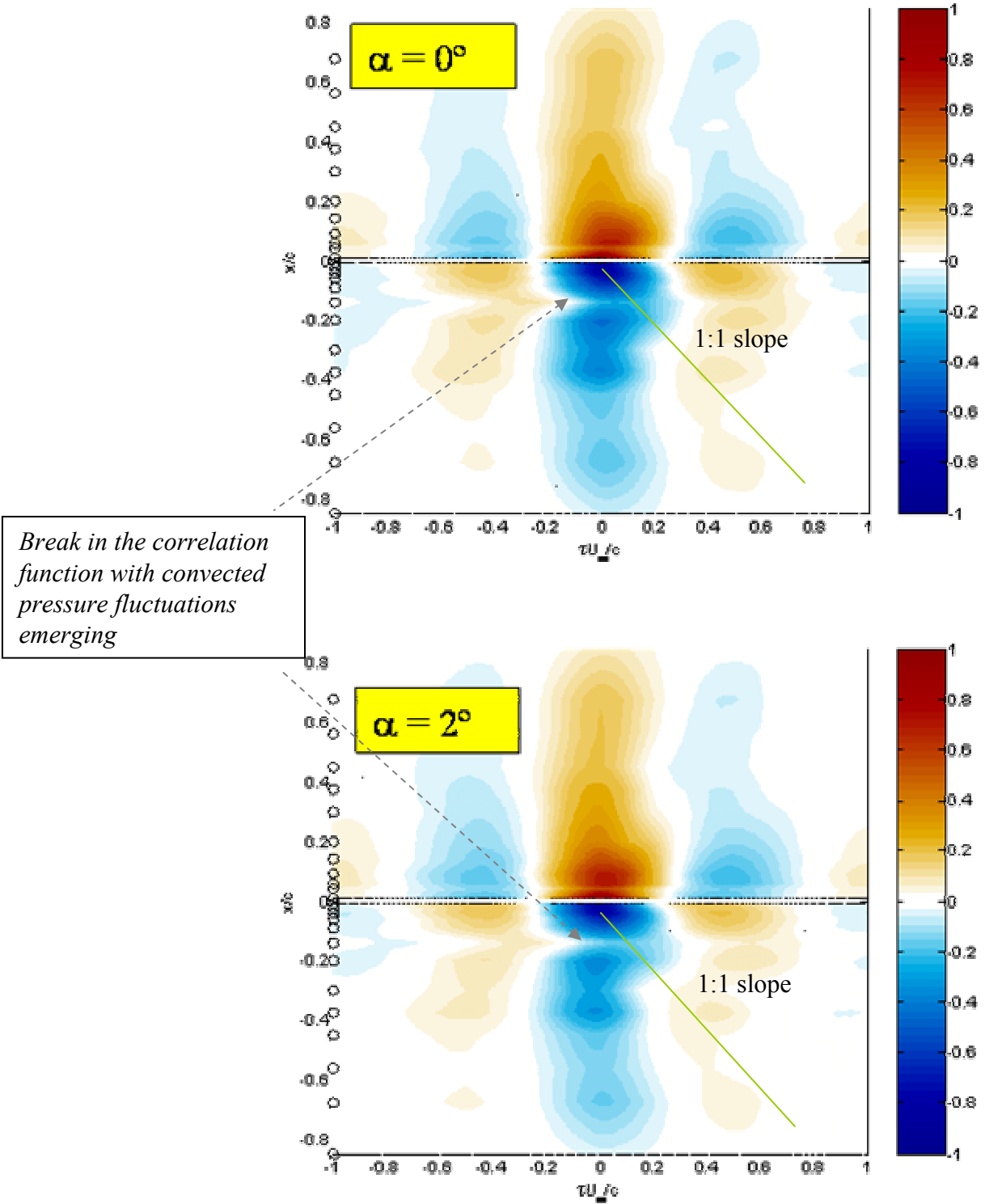
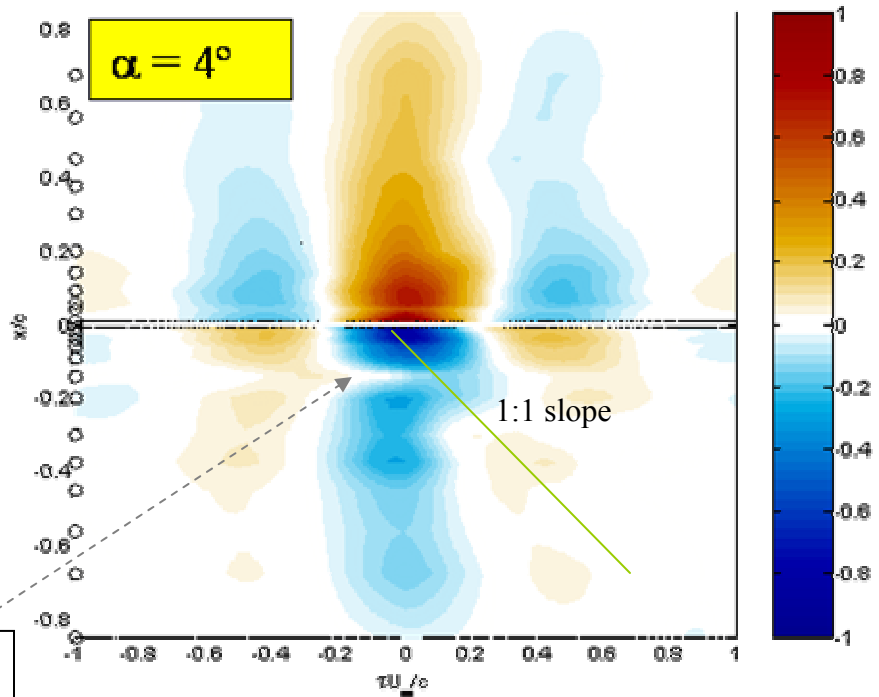


Figure 4.35: Contour plots of pressure-pressure correlation, $R_{pp}(x=1\%,x',\tau)$ for *large* grid flow. The correlation is formed with the 1% chord microphone on the *pressure* side of the airfoil



Break in the correlation function with convected pressure fluctuations emerging

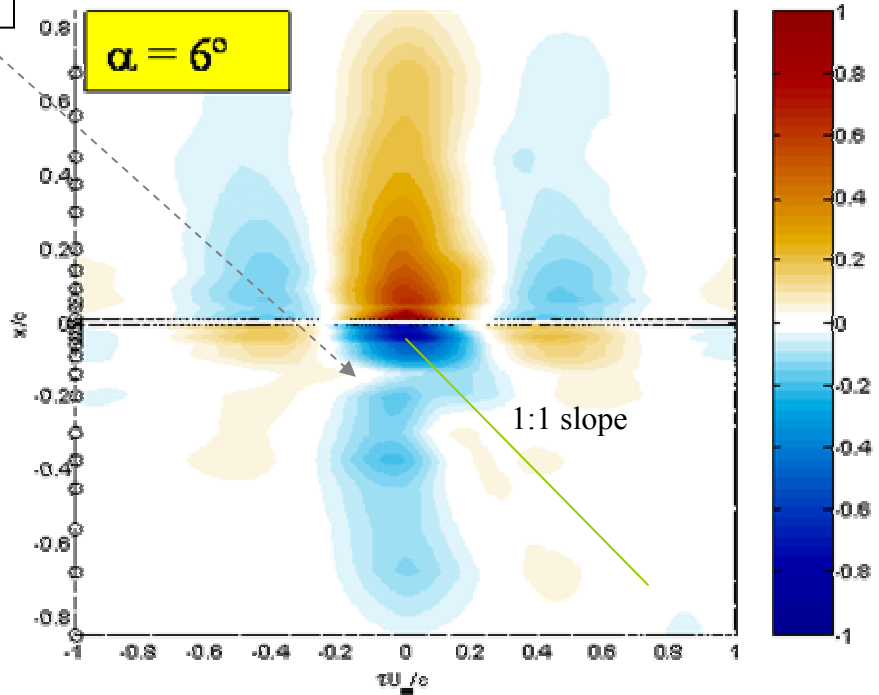


Figure 4.35 continued: Contour plots of pressure-pressure correlation, $R_{pp}(x=1\%,x',\tau)$ for large grid flow. The correlation is formed with the 1% chord microphone on the *pressure* side of the airfoil

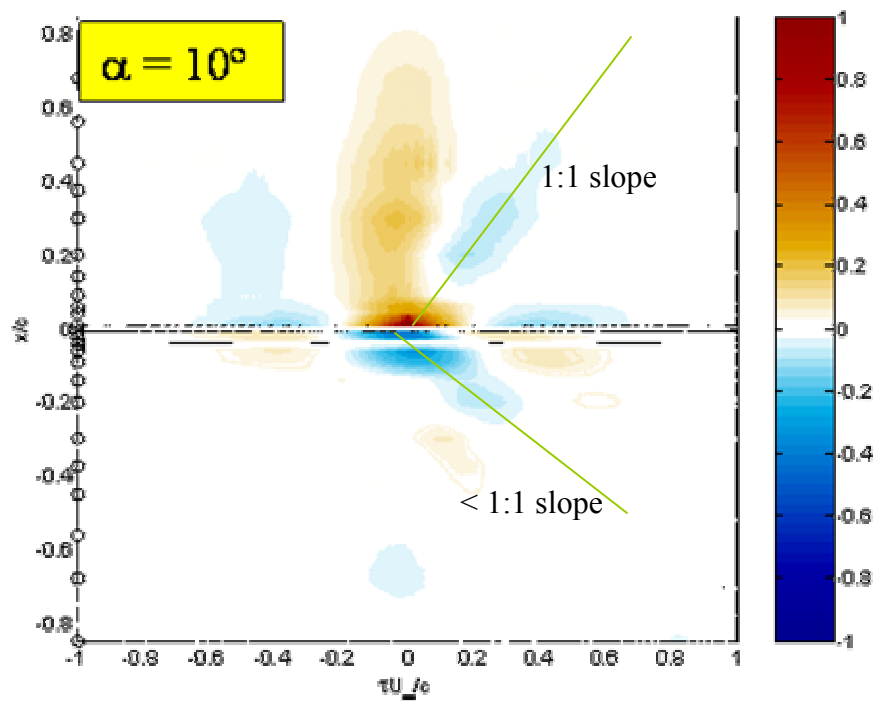
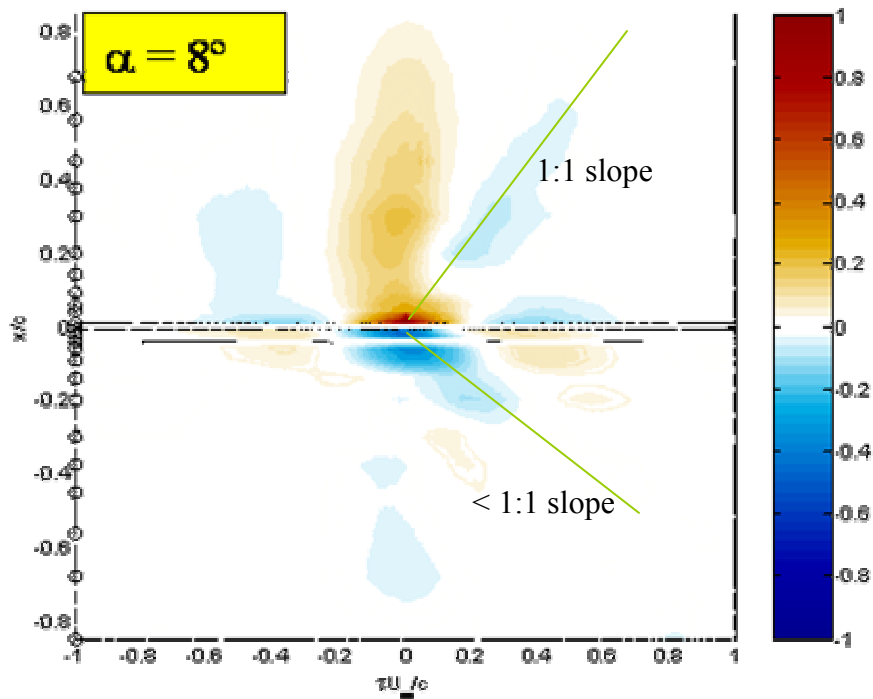


Figure 4.35 continued: Contour plots of pressure-pressure correlation, $R_{pp}(x=1\%, x', \tau)$ for large grid flow. The correlation is formed with the 1% chord microphone on the *pressure* side of the airfoil

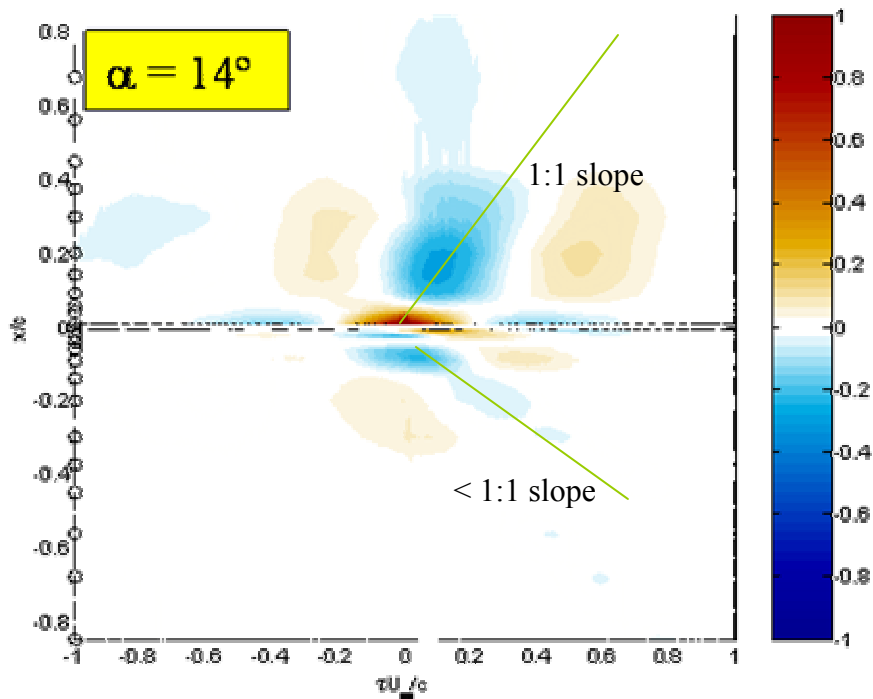
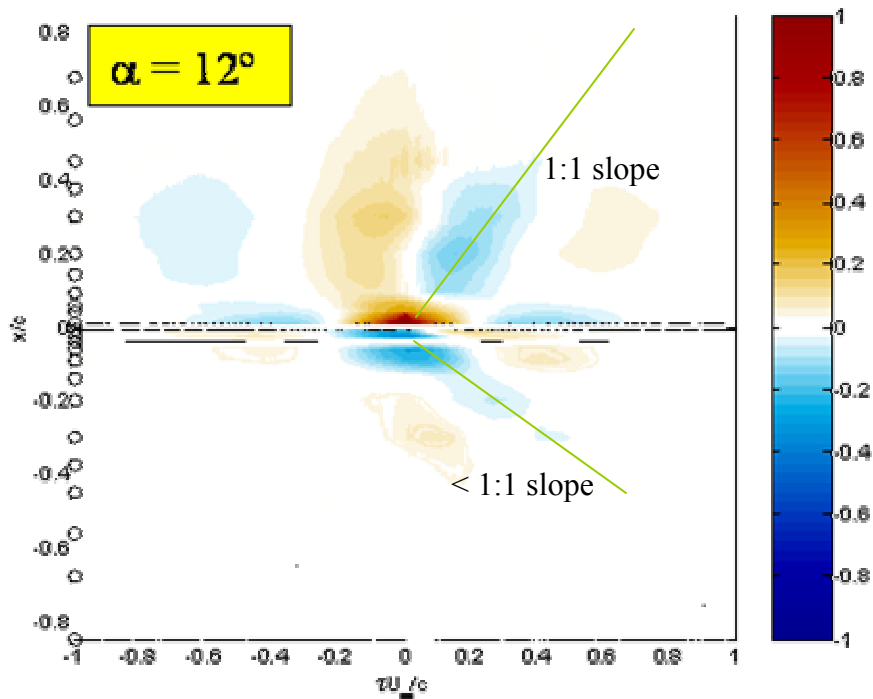


Figure 4.35 continued: Contour plots of pressure-pressure correlation, $R_{pp}(x=1\%,x',\tau)$ for large grid flow. The correlation is formed with the 1% chord microphone on the *pressure* side of the airfoil

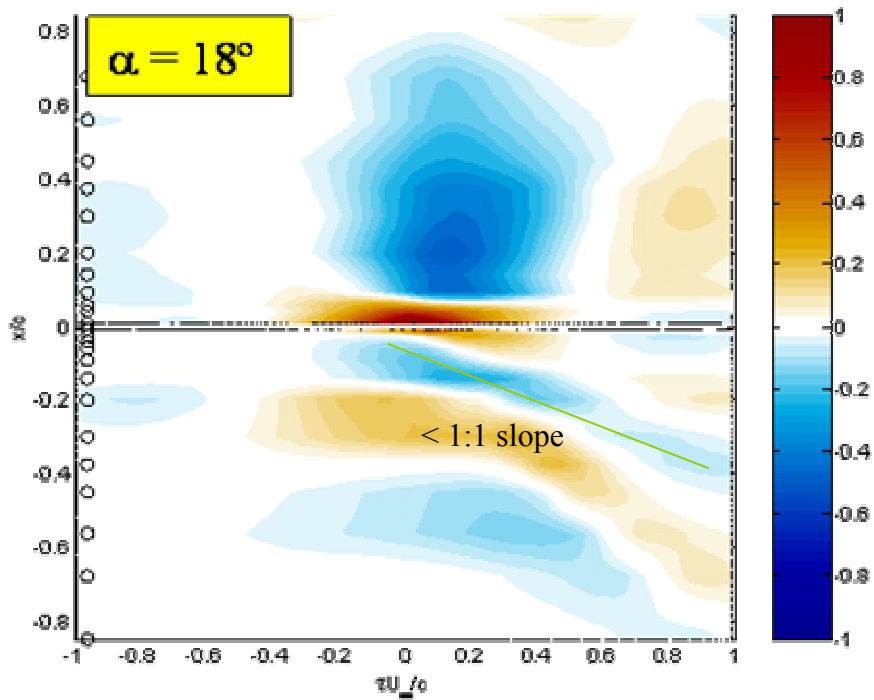
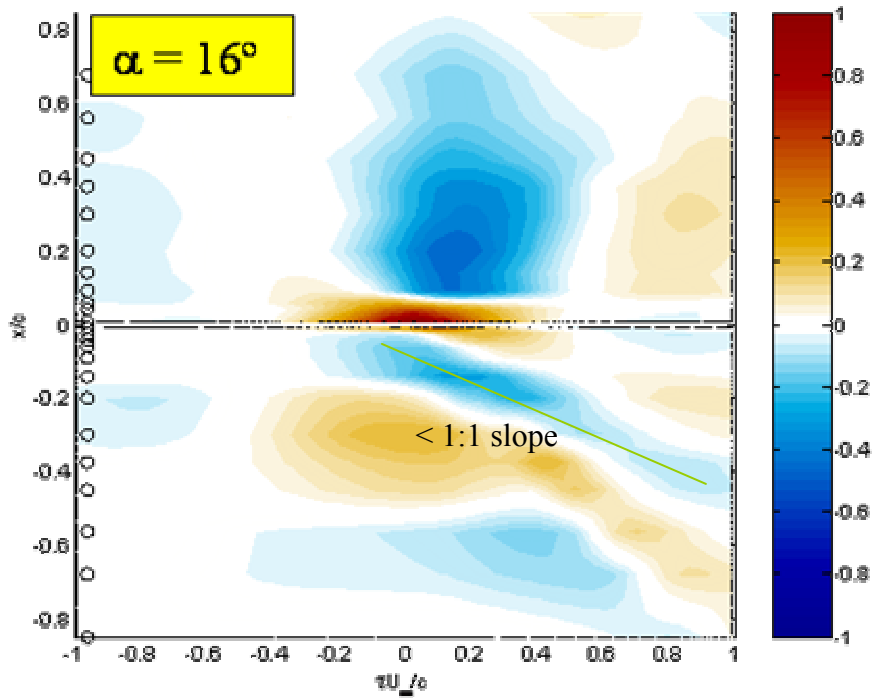


Figure 4.35 continued: Contour plots of pressure-pressure correlation, $R_{pp}(x=1\%, x', \tau)$ for large grid flow. The correlation is formed with the 1% chord microphone on the *pressure* side of the airfoil

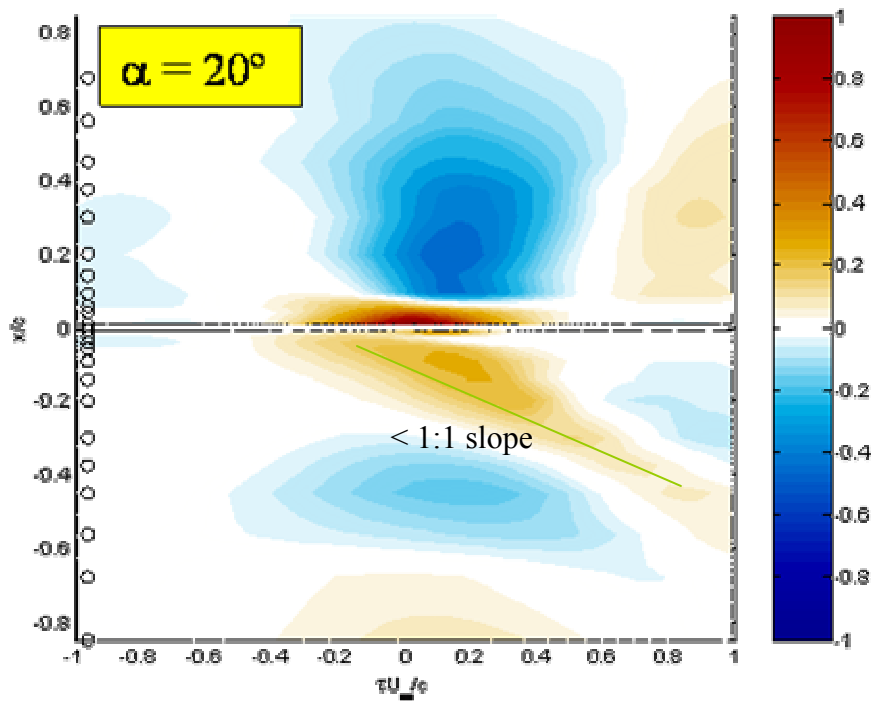


Figure 4.35 continued: Contour plots of pressure-pressure correlation, $R_{pp}(x=1\%, x', \tau)$ for large grid flow. The correlation is formed with the 1% chord microphone on the *pressure* side of the airfoil

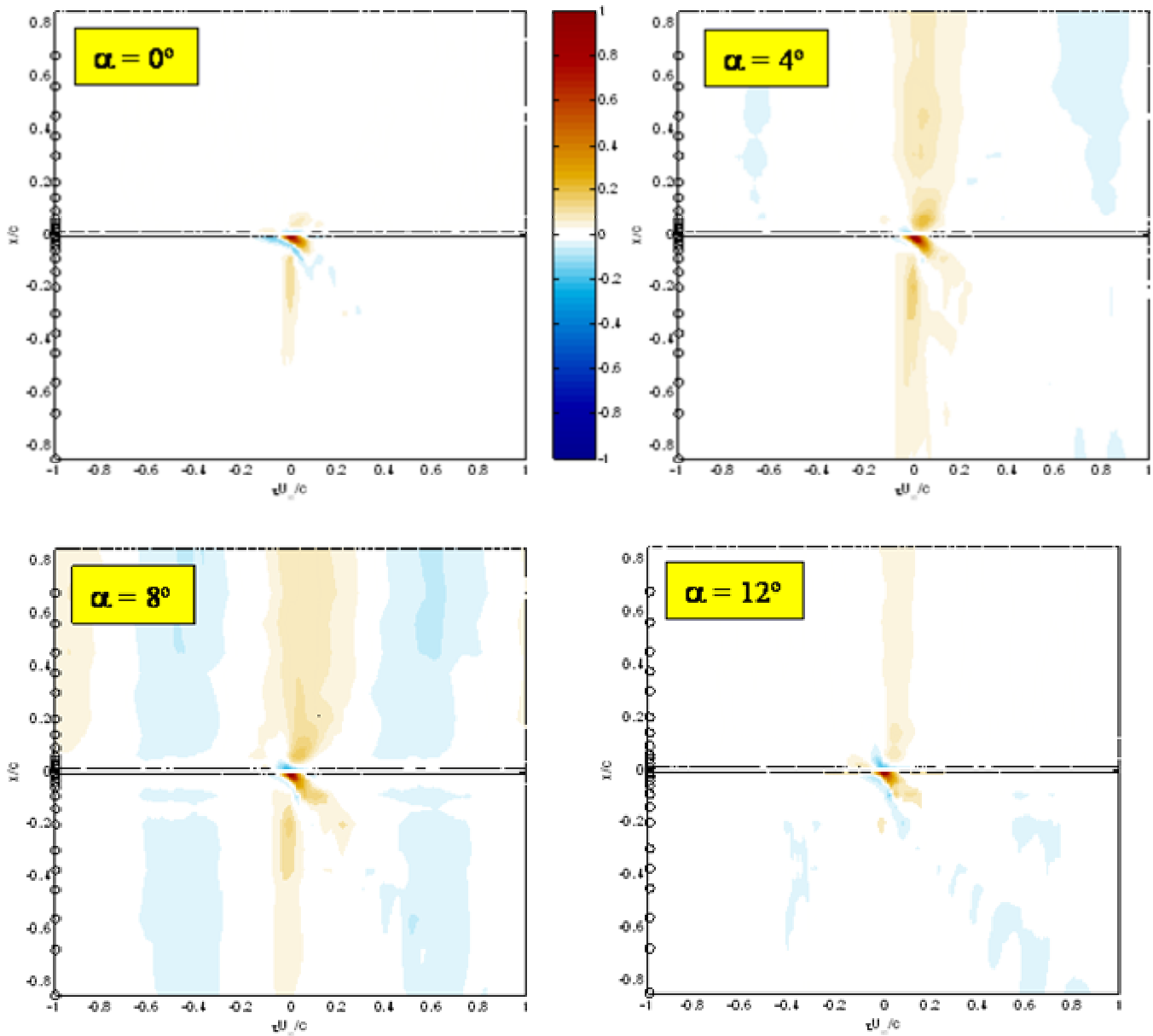


Figure 4.36: Contour plots of $R_{pp}(x=1\%, x', \tau)$ for *small* grid flow. The correlation is formed with the 1% chord microphone on the suction side of the airfoil

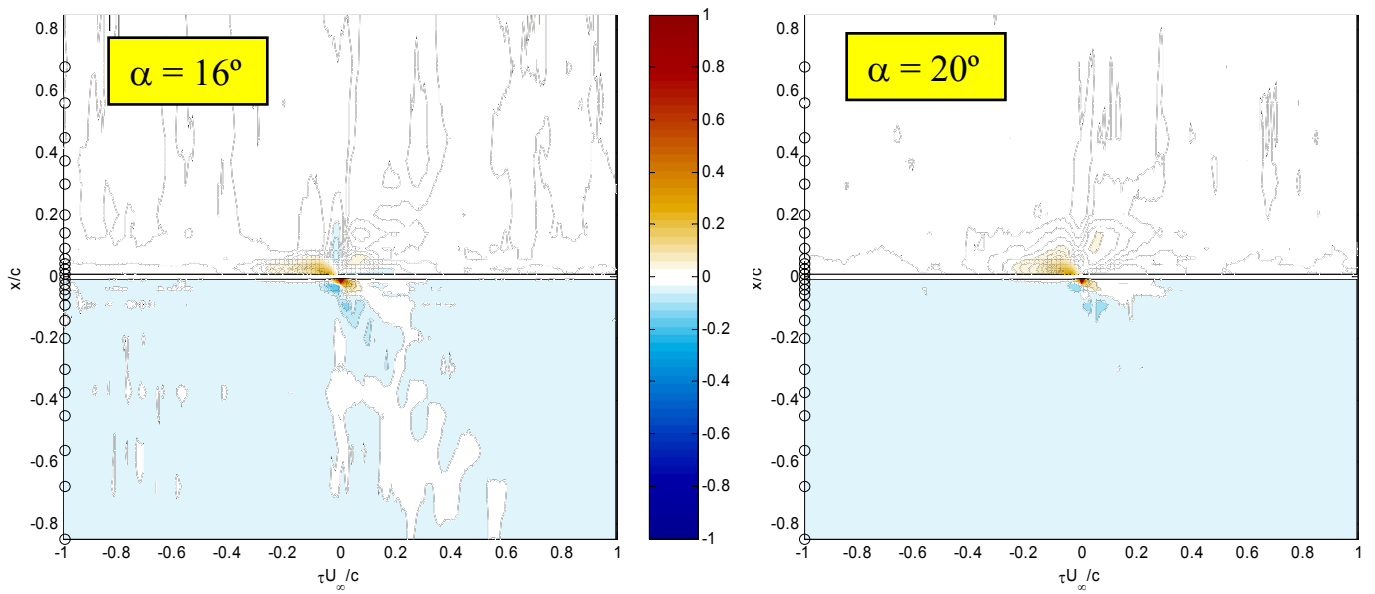


Figure 4.36 continued: Contour plots of $R_{pp}(x=1\%,x',\tau)$ for *small* grid flow. The correlation is formed with the 1% chord microphone on the suction side of the airfoil

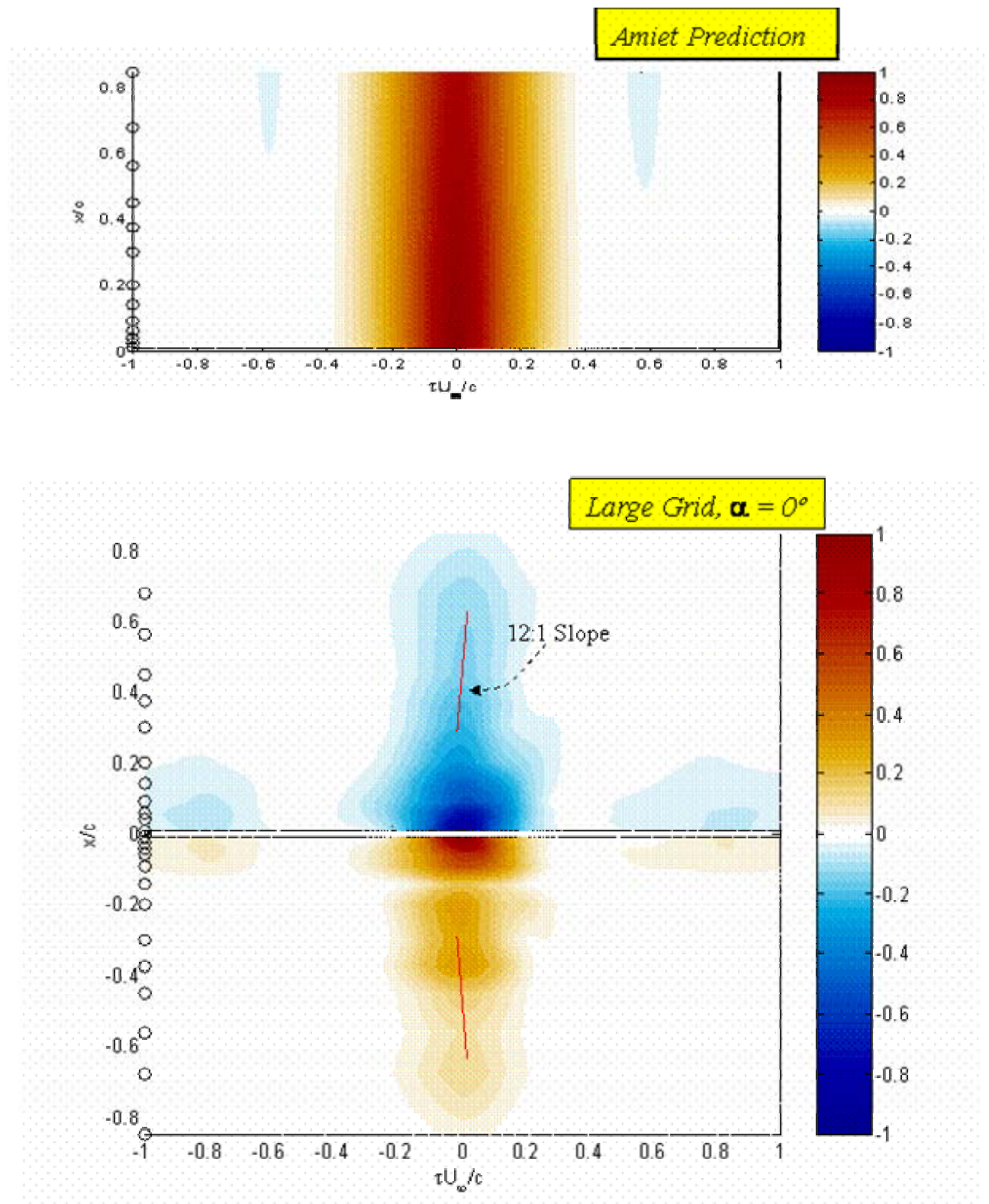


Figure 4.37: Comparison of measured and predicted pressure-pressure correlation, $R_{pv}(x=1\%, x', \tau)$ for *large grid* flow. The correlation is formed with the 1% chord microphone on the suction side of the airfoil.

5. SINGLE AIRFOIL IN TURBULENCE: ANALYSIS OF UNSTEADY PRESSURE DATA

This chapter presents analysis of unsteady surface pressure measured on the NACA 0015 airfoil in the large grid turbulence. Measurements of unsteady pressure were made at angles of attack, $\alpha = 0^\circ$ to 20° . Comparisons between Amiet's (1976a, b) flat plate, zero angle of attack theory and measured pressure spectra are presented. Effects of angle of attack on pressure spectra are examined and comparisons made with Reba and Kerschen's (1996) unsteady loading theory. Unsteady pressure measurements are then used to calculate lift and the effects of angle of attack examined. Measured lift spectra are compared with Amiet's (1976a, b) theory for $\alpha = 0^\circ$ and Reba and Kerschen's (1996) at non-zero angle of attack. The sources of observed angle of attack effect are examined through investigation of pressure correlation length scales, a modified trailing edge, and scaling of unsteady lift. Based on this analysis, a prediction scheme is presented which accurately captures the effects of angle of attack at low ω_r within the parameters of this experiment. Lastly, this chapter demonstrates how surface pressure measurements can be used to make estimates of far-field noise.

5.1 Pressure Spectra and Mean Square Pressure

5.1.1 Pressure Difference Spectra at Zero Angle of Attack

Measured pressure spectra are compared with Amiet's (1976a, b) theory in this section. Recall from chapter 3, Amiet (1976a, b) theoretically computes the unsteady response of a flat plate airfoil at zero angle of attack. Figure 5.1 presents a comparison of Amiet's predicted *pressure difference* spectra (see appendix A for definition of pressure difference) with measured *pressure difference* spectra at $\alpha = 0^\circ$ for chordwise locations, $x/c = 1, 2.5, 4, 6, 9,$ and 14% normalized on free-stream dynamic pressure, q . Both the measurement and prediction fall monotonically moving away from the leading edge. At all chordwise locations Amiet's theory agrees well with the measured shape of $G_{\Delta P \Delta P}$ spectra. However, the theory tends to over predict spectra levels, particularly at 1% chord with as much as 7dB of difference occurring here. The over prediction of surface pressure in the leading edge region is likely the consequence of the leading edge singularity which occurs in Amiet's theory. The agreement in spectral level improves to within 1dB moving away from the leading edge. The measured data tends to roll off slightly faster than the prediction over $5 < \omega_r < 20$. The disagreement in slope may be a result of

the airfoil thickness. Other researchers have shown similar results, although unpublished (private communication, Gershfeld 2002). The slope of the measured data decreases for $\omega_r > 20$. The change is subtle for the first 4 chordwise locations and may be related to convection of eddies by the free-stream. At $x/c = 9$ and 14% the slope changes substantially more for $\omega_r > 20$ as significant boundary layer pressure fluctuations begin to affect the high frequency response.

At some chordwise locations a high frequency spike is present in measured $G_{\Delta P \Delta P}$. This spike, occurring over a range of $300 < \omega_r < 800$ appears to be related to resonance within the microphone mounting hole that was not accounted for in the microphone calibration.

5.1.2 Pressure Difference Spectra at Non-Zero Angle of Attack

Measured pressure spectra are compared with Reba and Kerschen's (1996) linearized RDT predictions for similar chordwise locations and angles of attack. Such a comparison will aid in assessing the effects of turbulence distortion on surface pressures. Recall from chapter 3, Reba and Kerschen (1996) developed a solution for the response of a flat plate at small angle of attack using Rapid Distortion Theory (RDT). The FORTRAN code produced by Reba and Kerschen (1996) is used to calculate the airfoil response from which the pressure difference cross-spectral density is computed (equation 3.16). However, due to the restriction in Reba and Kerschen's theory of low acoustic wavenumber it is not possible to integrate over a large range of spanwise wavenumbers. Consequently, the absolute level of predictions from Reba and Kerschen's theory are somewhat questionable. As such, a direct comparison between predicted and measured unsteady pressure level is not appropriate, although a comparison of spectral shape and variation with angle of attack and chordwise position seems reasonable.

Figure 5.2 presents the *pressure difference* spectra as a function of frequency at six chordwise ($x/c = 1, 2.5, 4, 6, 9, 14\%$) locations and three angles of attack ($\alpha = 0^\circ, 2^\circ, 6^\circ$) normalized on free-stream dynamic pressure, q . This figure presents the RDT predictions of Reba and Kerschen (1996) and the measured *pressure difference* spectra. The predicted spectra of Reba and Kerschen fall monotonically moving away from the leading edge at all angles of attack, as shown to occur in measured data. Additionally, the spectra show a somewhat flat range for $\omega_r < 2$ and then begin to fall off with a slope similar to that shown in measured data. The agreement in level between the predicted $\alpha = 0^\circ$ spectrum and the measured $\alpha = 0^\circ$ spectrum at 1% chord is believed to be a coincidence for the reasons stated above.

The interesting occurrence shown in figure 5.2 is the significant rise in predicted spectral level with increasing angle of attack. This rise is particularly dominant at low reduced frequencies, with up to a 16dB increase and occurs at all chordwise locations. The spectral levels tend to converge at higher reduced frequencies. The measured data shows a slight increase (2.5dB) at 1% chord; however tends to show little variation as the angle of attack is increased. The reason for the large change in spectral level predicted by Reba and Kerschen (1996) with increasing angle of attack is likely related to the flat plate model they assume. The potential field associated with a flat plate at angle of attack will distort the inflow substantially more than an actual airfoil with thickness due to the very large velocity gradients that stretch and tilt the vorticity vectors of the inflow turbulence in the vicinity of the leading edge singularity. Clearly, though the main result shown here is that a *flat plate* RDT representation of turbulence-airfoil interaction is not sufficient for correctly predicting the effects of angle of attack on the surface pressure given the relative inflow scale and airfoil chord used in this experiment.

5.1.3 Mean Square Pressure at Zero Angle of Attack

It is now interesting to examine Amiet's prediction of the root mean square (RMS) pressure and its agreement with measured RMS pressures. The unsteady pressure spectrum at each chordwise location on the pressure and suction side of the airfoil is integrated to obtain root mean square p' values as

$$\overline{p^2}(x) = \int_{f_{\min}}^{f_{\max}} S_{qq}(x, x', \eta, f) df \quad (5.1)$$

where S_{qq} is the *surface pressure* cross-spectral density, $x = x'$, and $\eta = 0$. The integration is performed from a minimum frequency, $f_{\min} = 6\text{Hz}$ ($\omega_r = 0.4$) to a maximum frequency, $f_{\max} = 1570\text{Hz}$ ($\omega_r = 100$). These values are compared with those calculated from Amiet's (1976a, b) theory in figure 5.3 at $\alpha = 0^\circ$ as a function of chordwise position (up to 14% chord) and are normalized on the free-stream dynamic pressure, q . The pressure spectra presented in figure 5.1 show very good agreement with Amiet's theory at chordwise locations beyond 2.5%. Therefore, not surprisingly, the agreement of p' values compare within 3% across the chord. The 1% chord location shows a drop in measured p' on the pressure side which may be related to a local flow phenomenon as discussed in chapter 4. In the leading edge region Amiet's prediction begins to

rise rapidly as a consequence of the leading edge singularity in this theory, producing large differences between measured and predicted RMS pressure.

5.1.4 Mean Square Pressure at non-Zero Angle of Attack

The effects of angle of attack on p' values are investigated in figures 5.4 and 5.5. The spectrum from chordwise locations 1% to 14% are each integrated to obtain $\overline{p'^2}$ values for both pressure and suction sides of the airfoil at all angles of attack. The integration is performed over frequencies ranges $\omega_r = 0.4$ to 100. Root mean square pressures are normalized on free-stream dynamic pressure.

Figure 5.4 presents the root mean square pressure calculated from *surface pressure* spectra as a function of angle of attack for $x/c = 0.01, 0.025, 0.04, 0.06, 0.09,$ and 0.14 . The leading edge positions (1% to 6% chord) on the suction and pressure side are most affected by angle of attack. The pressure reaches a peak on the suction side (at the unstalled angles of attack) at $\alpha = 12^\circ$ at 1% chord. At $\alpha = 20^\circ$ the airfoil is stalled causing p' to rise substantially on the suction side at all locations. On the pressure side of the airfoil p' peaks at $\alpha = 18^\circ$. Again, the leading edge locations tend to most affected by angle of attack.

Root mean square pressures, $\sqrt{\Delta p'^2}$ calculated from *pressure difference* spectra are presented in figure 5.5. It is interesting to see that RMS $\Delta p'^2$ remain essentially flat up to $\alpha = 14^\circ$ at all chordwise locations. A slight rise occurs at $x/c = 1\%$ between 0° and 4° angle of attack. The $\sqrt{\Delta p'^2}$ lack of dependence on angle of attack suggests the increased eddy stretching (by the mean velocity field) that likely takes place with increasing angle of attack does not substantially increase the intensity of pressure fluctuations in the leading edge region.

5.2 Lift Spectra and Mean Square Lift

5.2.1 Motivation for Forming Unsteady Lift

The effects of angle of attack on the surface pressure response can be well summarized by investigating the unsteady lift calculated from unsteady pressure measurements. Such a calculation inherently contains surface pressure and pressure difference auto- and cross-spectra and provides an integrated view of the airfoil response.

5.2.2 Unsteady Lift Formulation

This section presents the equations for calculating lift from unsteady pressure measurements and addresses issues associated with such calculations. Integration of stochastic quantities is not a trivial matter and as such, considerable effort is spent in identifying sources of error and verifying results.

Unsteady lift is calculated from pressure measurements made over the first 14% of the airfoil chord. This corresponds to 6 microphones per airfoil side used in the calculation. The microphones used in the lift calculation are denoted in figure 5.6 by red triangles and their chordwise and spanwise location presented in table 5.1.

Table 5.1: Location of microphones used in unsteady lift calculation

y/c	x/c
0.33	0.01
0.33	0.025
0.33	0.04
0.33	0.06
0.33	0.09
0.33	0.14

The unsteady pressure measurements must first be resolved into normal-to-chord and tangential-to-chord force components as shown in figure 5.7. The relationship between these forces and lift is a simple coordinate transformation from the airfoil to flow aligned coordinates given as

$$L' = N_a \cos(\alpha) - T_a \sin(\alpha) \quad (5.2)$$

where L is lift and α is angle of attack. Since the lift is a random quantity the expected value is taken to give the lift spectrum

$$\begin{aligned} G_{LL} &= E[L' * L'] \\ &= E[N_a^* N_a \cos^2(\alpha) + T_a^* T_a \sin^2(\alpha) - T_a^* N_a \sin(\alpha) \cos(\alpha) - N_a^* T_a \sin(\alpha) \cos(\alpha)] \quad (5.3) \\ &= G_{NN} \cos^2(\alpha) + G_{TT} \sin^2(\alpha) - 2 \operatorname{Re}(G_{TN}) \sin(\alpha) \cos(\alpha) \end{aligned}$$

G_{NN} and G_{TT} are the normal and tangential force spectrum and G_{TN} is the cross-spectrum between these forces. These spectra can be computed from unsteady pressure measurements as

$$G_{NN}(\omega_r) = E \left[\int_0^{x_{\max}} \int_0^{x_{\max}} \Delta P(x, \omega_r)^* \Delta P(x', \omega_r) dx dx' \right] = \int_0^{x_{\max}} \int_0^{x_{\max}} G_{\Delta P \Delta P}(\omega_r, x, x') dx \cdot dx' \quad (5.4)$$

$$\begin{aligned}
 G_{TT}(\omega_r) &= E \left[\int_0^{z_{\max}(x)} \left[P_U(z(x), \omega_r)^* + P_L(z(x), \omega_r)^* \right] dz(x) \cdot \int_0^{z_{\max}(x')} \left[P_U(z(x'), \omega_r) + P_L(z(x'), \omega_r) \right] dz(x') \right] \\
 &= \int_0^{z(x)} \int_0^{z(x')} \left[G_{P_U P_U}(\omega_r, x, x') + G_{P_L P_L}(\omega_r, x, x') + 2\text{Re}(G_{P_U P_L}(\omega_r, x, x')) \right] dz(x) \cdot dz(x') \quad (5.5)
 \end{aligned}$$

$$\begin{aligned}
 G_{TN}(\omega_r) &= E \left[\int_0^{z_{\max}(x)} \left[P_U(z(x), \omega_r)^* + P_L(z(x), \omega_r)^* \right] dz(x) \cdot \int_0^{x_{\max}} \left[P_U(x', \omega_r) - P_L(x', \omega_r) \right] dx' \right] \\
 &= \int_0^{z(x)} \int_0^{x_{\max}} \left[G_{P_U P_U}(\omega_r, x, x') - G_{P_L P_L}(\omega_r, x, x') + G_{P_U P_L}(\omega_r, x, x') - G_{P_L P_U}(\omega_r, x, x') \right] dz(x) \cdot dx' \quad (5.6)
 \end{aligned}$$

where $G_{\Delta P \Delta P}$ is given as

$$\begin{aligned}
 G_{\Delta P \Delta P}(\omega_r, x, x') &= E \left[\left(P_U(x, \omega_r) - P_L(x, \omega_r) \right)^* \left(P_U(x', \omega_r) - P_L(x', \omega_r) \right) \right] \\
 &= E \left[\Delta P(x, \omega_r)^* \Delta P(x', \omega_r) \right] \quad (5.7)
 \end{aligned}$$

Of course the unsteady pressure measurements are not defined spatially in a continuous manner and therefore, the above equations must be discretized. The final discretized form of these equations is presented below.

$$G_{NN}(\omega_r) = \sum_{i=1}^6 \sum_{j=1}^6 G_{\Delta P \Delta P}(\omega_r, x_i, x_j) \Delta x_i \Delta x_j \quad (5.8)$$

$$G_{TT}(\omega_r) = \sum_{i=1}^6 \sum_{j=1}^6 \left[G_{P_U P_U}(\omega_r, x_i, x_j) + G_{P_L P_L}(\omega_r, x_i, x_j) + 2\text{Re}(G_{P_U P_L}(\omega_r, x_i, x_j)) \right] \Delta z(x_i) \Delta z(x_j) \quad (5.9)$$

$$G_{TN}(\omega_r) = \sum_{i=1}^6 \sum_{j=1}^6 \left[\begin{array}{l} G_{P_U P_U}(\omega_r, x_i, x_j) - G_{P_L P_L}(\omega_r, x_i, x_j) \\ G_{P_U P_L}(\omega_r, x_i, x_j) - G_{P_L P_U}(\omega_r, x_i, x_j) \end{array} \right] \Delta z(x_i) \Delta x_j \quad (5.10)$$

The indices i and j run from 1 to 6 and correspond to the six microphone locations used in the unsteady lift calculation.

5.2.3 Verification of Lift Formulation

The formulation of the unsteady lift in this manner raises two important questions which are addressed prior to presenting the calculated lift spectra:

1. What is the effect of the discrete microphone spacing used to form the unsteady lift spectra?

2. What is the effect of the airfoil to flow-aligned coordinate transformation?

Effects of Discrete Microphone Spacing on Lift: The equations used in the unsteady lift formulation are presented above in definite integral form. For practical implementation with a discrete measurement system these equations must be discretized. Consider, for example the discretization of the normal-to-chord force spectra G_{NN}

$$G_{NN}(\omega_r) = \int_0^{x_{\max}} \int_0^{x_{\max}} G_{\Delta P \Delta P'}(\omega_r, x, x') dx \cdot dx' \approx \sum_{i=1}^6 \sum_{j=1}^6 G_{\Delta P \Delta P'}(\omega_r, x_i, x_j) \Delta x_i \Delta x_j \quad (5.11)$$

$G_{\Delta P \Delta P}$ is defined only at microphone measurement locations and therefore must be approximated at all other locations. Error can result from this discrete computation if $G_{\Delta P \Delta P}$ is not adequately defined in rapidly changing regions. Consider figure 5.8 which is a contour plot of large grid $G_{\Delta P \Delta P}$ as a function of x/c and x'/c at $\omega_r = 3$ for $\alpha = 0^\circ$. In the leading edge region $G_{\Delta P \Delta P}$ reaches a peak and drops off quickly moving down the chord. This function must be defined with sufficient resolution for the lift computation to be accurate.

The effects of discretization can be assessed using Amiet's theory. The assessment can be done by computing the unsteady lift discretely and continuously from Amiet's theory. That is Amiet's theory can be used to compute the unsteady pressure at the same chordwise locations used in the experiment from which the unsteady lift can be computed. This lift spectrum can then be compared from a continuous integration of Amiet's solution. Figure 5.9 presents a visual depiction of the exact and discrete techniques used with Amiet's theory.

The continuous unsteady lift spectrum calculation is performed in a quasi-continuous manner by taking a very small Δx ($= 0.14\%$ chord). The discrete lift is calculated using the same chordwise microphone distribution shown in figure 5.6 (chordwise location presented in table 5.1). The von Karman turbulence spectrum is used in this calculation with the integral scale and turbulence intensity taken as the values in the large grid turbulence measurement.

Figure 5.10 presents a comparison of Amiet's continuous versus discrete lift calculations in large scale turbulence (the angle of attack is zero; i.e. Amiet's solution does not allow for airfoil mean loading). Notice the discrete lift falls below the continuous by 0.7dB. The decrease of the simulated discrete lift is a consequence of cutting off the pressure peak at the leading edge. That is, consider figure 5.11, a plot of Amiet's $G_{\Delta P \Delta P}$ at $x/c = 2.5\%$ chord for $\omega_r = 10$ as a function of $x/c - x'/c$ (where x'/c is every chordwise position) for both the discrete and continuous

case. In the leading edge region, $G_{\Delta P \Delta P}$ rises up at a high rate as a consequence of the singularity occurring there. This portion of the pressure distribution is not included in the discrete lift calculation causing the overall level to fall below the continuous calculation. Thus, it can be concluded that in the presence of a noise free measurement calculating lift discretely from pressure measurements will result in a slight reduction (< 1 dB) of unsteady lift.

Effect of Airfoil to Flow-Aligned Coordinate Transformation: The next item to consider is the effect of the coordinate transformation implemented in the calculation of unsteady lift to rotate from airfoil aligned to flow aligned coordinates. When calculated unsteady lift the pressure difference, ΔP is taken across the chord (as depicted in figure 5.12a and 5.12b) such that,

$$\Delta P(x_1) = P_U(x_1) - P_L(x_1) \quad (5.12)$$

where $P_U(x_1)$ and $P_L(x_1)$ are the pressure on the upper and lower side of the airfoil, respectively at chordwise location x_1 in airfoil aligned coordinates. However, it is desired to form the pressure difference in the direction of lift (also shown in figure 5.12b) such that,

$$\Delta P(x_1^a) = P_U(x_1^a) - P_L(x_1^a) \quad (5.13)$$

where $P_U(x_1^a)$ and $P_L(x_1^a)$ are the pressure on the upper and lower side of the airfoil, respectively at location x_1^a in flow aligned coordinates. Since the actual microphone distribution is fixed and thus, does not allow for pressure differencing in the direction of lift, a coordinate rotation must be implemented to obtain the unsteady lift. This transformation is taken as,

$$G_{LL}(\omega_r) = G_{NN} \cos^2(\alpha) + G_{TT} \sin^2(\alpha) - 2 \operatorname{Re}(G_{TN}) \sin(\alpha) \cos(\alpha) \quad (5.14)$$

and is derived above.

The effects of this coordinate transformation can be simulated using Amiet's thin airfoil theory. For some angle of attack, α the actual microphone locations (as denoted in table 5.1) on the top and bottom of the wing are projected into a flow aligned coordinate system as shown in figure 5.13. The pressure difference between these projected top and bottom points is then calculated. The lift spectrum, G_{LL} is then computed by numerically integrating these values for each angle of attack and compared with each other. G_{LL} is computed as follows (using the notation of figure 5.13),

$$\begin{aligned} G_{LL}(\omega_r) = & \sum \sum G_{P(x_{nU}^a)P(x_{mU}^a)} \Delta x_{nU}^a \Delta x_{mU}^a + \sum \sum G_{P(x_{nU}^a)P(x_{mL}^a)} \Delta x_{nU}^a \Delta x_{mL}^a \\ & + \sum \sum G_{P(x_{nL}^a)P(x_{mU}^a)} \Delta x_{nL}^a \Delta x_{mU}^a + \sum \sum G_{P(x_{nL}^a)P(x_{mL}^a)} \Delta x_{nL}^a \Delta x_{mL}^a \end{aligned} \quad (5.15)$$

Figure 5.14 presents unsteady lift calculated in this manner for each angle of attack. The lift spectra calculated using Amiet's simulation show little variation (<1 dB) as a consequence of the coordinate transformation. Therefore, it is concluded that lift spectra are not significantly effected by the transformation from airfoil to flow aligned coordinates.

Another perspective on the coordinate transformation can be taken which considers the phasing of the pressure response across the chord. When the airfoil is at angle of attack pressure sensors on the suction side of the airfoil are further away from the stagnation point than their companions on the pressure side. This results in a slight phase difference between the pressures measured on each side of the airfoil as shown in figure 5.15. The phase difference can be modeled by considering the pressure fluctuations to be harmonic. Referring to the notation of figure 5.16 the pressure at $\alpha = 0^\circ$ is given as

$$\Delta P(\alpha = 0) = 2Pe^{i\omega\left(t + \frac{d_s}{U_\infty}\right)} \quad (5.16)$$

and the pressure at non-zero angle of attack as

$$\Delta P(\alpha) = Pe^{i\omega\left(t + \frac{d_s + x_o}{U_\infty}\right)} + Pe^{i\omega\left(t + \frac{d_s - x_o}{U_\infty}\right)}. \quad (5.17)$$

Now, by taking the ratio of eq. 5.16 and eq. 5.17 the effect of the phasing difference is revealed as

$$\frac{\Delta P(\alpha)}{\Delta P(\alpha = 0)} = \frac{Pe^{i\omega\left(t + \frac{d_s + x_o}{U_\infty}\right)} + Pe^{i\omega\left(t + \frac{d_s - x_o}{U_\infty}\right)}}{2Pe^{i\omega\left(t + \frac{d_s}{U_\infty}\right)}} = \cos\left(\frac{\omega x_o}{U_\infty}\right) \quad (5.18)$$

In forming the power spectral density of pressure fluctuations the pressure difference is multiplied by its conjugate and, as such, the cosine term of eq. 5.18 is squared. If x_o is assumed constant then integrating along the chord (as performed to obtain unsteady lift) will not affect the result of equation 5.18. A plot of the phase shift model (equation 5.18 squared) as a function of frequency for each angle of attack is presented in figure 5.17. The phase shift model shows no reduction in unsteady lift for $\omega_r < 10$; however, reduction in unsteady lift above $\omega_r = 10$ is possible based on this model.

Unsteady Lift Spectra: Lift spectra, G_{LL} calculated from unsteady pressure measurements are presented in figure 5.18 with spectral level plotted against ω_r . The results are very surprising in

light of previous mathematical and experimental work on this problem. Two frequency dependent interaction regions are shown in this figure. At low frequencies ($\omega_r < 10$) a suppression of unsteady lift with increasing angle of attack occurs with a maximum lift reduction of 5dB. The opposite effect occurs at high frequencies ($\omega_r > 10$) with a rise in unsteady lift of up to 10dB occurring with increasing angle of attack. The reduction in unsteady lift at low ω_r is a never before shown result and unexpected based on previous experimental studies, in addition to not being predicted by theoretical formulations. McKeough (1976) showed, through unsteady lift measurements on a NACA 0015 in turbulence an increase in unsteady lift with an increase from $\alpha = 0^\circ$ to 10° . Patterson and Amiet (1976a) discussed, although did not present supporting data, an increase in surface pressure spectral magnitude with increasing angle of attack. This result is also not supported by theoretical formulations which account for airfoil mean loading, such as the theories developed by Reba and Kerschen (1997) and Atassi (1984). It should be noted, the lift spectrum at $\alpha = 20^\circ$ shows significant unsteadiness at low ω_r which results from large scale pressure fluctuations associated with stall. Airfoil stall at this angle of attack is corroborated by mean pressure measurements and flow visualization.

Effects of Forming the Spectra over the First Fourteen Percent Chord: With the unsteady lift presented one last issue remains to be examined. The effects of limiting the integration of unsteady pressure to the first 6 microphones (i.e. up to 14% chord) must be examined to ensure the trends with angle of attack are not influenced by this bounding. Effects which may result from this bounding are examined through comparison of unsteady lift spectra calculated using all thirteen chordwise microphones with lift calculated from the first 6 chordwise microphones. Using all thirteen microphones will result in integration along 85% of the airfoil chord.

Figure 5.19 shows lift spectra calculated from partial and full chord integration. Lift spectra calculated over 85% chord show the same angle of attack observations revealed in spectra formed with the first 14% chord. Lift spectra calculated over the first 85% chord are not as smooth as the 14% chord lift spectra due to turbulent boundary layer pressure fluctuations and trailing edge separation. Furthermore, the inclusion of more measurement locations into the 85% chord lift calculation causes the overall lift spectra level to rise. Large scale, low frequency pressure fluctuations associated with stall are clearly revealed by the increase in unsteady lift

level at low frequency at $\alpha = 20^\circ$ when the unsteady lift is calculated from all microphones (85% chord).

5.2.4 Lift Spectra at Zero Angle of Attack

The $\alpha = 0^\circ$ lift spectrum, G_{LL} is presented in figure 5.20 along with that calculated from Amiet's (1976a, b) theory. Over low ω_r (< 5) the measurement and prediction are within 3dB and the agreement in shape is very good. The measured G_{LL} begins to fall off with a greater slope than the predicted for $5 < \omega_r < 20$. The spectral levels are within 13dB in this region. The difference in slope of the predicted G_{LL} is likely related to the zero thickness flat plate model used in this theory. The predicted and measured G_{LL} crossover at $\omega_r = 120$ as a consequence of the change in slope of the measured G_{LL} . The change in slope which occurs at higher ω_r is related to turbulent boundary layer pressure fluctuations which become significant at higher frequencies and tend to dominant the unsteady lift over this frequency range. The peak in G_{LL} which occurs at $\omega_r = 600$ is related to resonance of the microphone-mounting hole system.

5.2.5 Comparison of Predicted and Measured Unsteady Lift at Angle of Attack

The lift spectra calculated from pressure measurements are compared with lift spectra computed from Reba and Kerschen's (1996) Rapid Distortion Theory in figure 5.21. Lift is calculated for $\alpha = 0^\circ, 2^\circ,$ and 6° using Reba and Kerschen's theory. A direct comparison of measured and theoretical unsteady lift levels is not appropriate given the spanwise wavenumber integration restriction (discussed in section above); however, a comparison of spectral shape and trends with angle of attack are still of substantial value. For small angles of attack ($\alpha < 6^\circ$), the measured G_{LL} falls by less than 1.5dB. Over the remaining angles of attack the lift falls up to 5dB (note, at $\alpha = 20^\circ$ the airfoil is stalled and, as such, a significant rise in unsteady lift occurs at low ω_r). The RDT prediction of Reba and Kerschen shows a substantial increase in unsteady lift over a similar range of ω_r . The large increase (as much as 14dB) appears to occur as a consequence of the flat plate model assumed in the theory. The velocity gradients associated with the leading edge singularity of a flat plate at some α in inviscid flow are much larger than those of an airfoil with thickness. As such, the inflow is not distorted as it would be when encountering a real airfoil with thickness.

The measured lift spectra begin to converge and show no effect of angle of attack over $5 < \omega_r < 10$. Over the remaining ω_r range G_{LL} remains unchanged for small α 's ($\alpha < 6^\circ$). The lift spectra's lack of dependence on angle of attack over this ω_r range agrees well with the measurements made by McKeough (1976). The G_{LL} predicted by Reba and Kerschen over this ω_r range increase with increasing angle of attack by as much as 6dB; however, the spectra appear to be converging at higher ω_r . Again, in the presence of an airfoil with thickness it is likely that the theory of Reba and Kerschen would not predict as large an increase in G_{LL} with increasing angle of attack. In fact, the convergence of the lift spectra over this ω_r range may be associated with the airfoils finite thickness.

For $\omega_r > 10$ the slope of the measured G_{LL} begins to decrease as pressure fluctuations associated with the turbulent boundary layer and hydrodynamic pressure fluctuations begin to affect the unsteady lift. Comparisons with Reba and Kerschen's theory were not possible over this frequency range due to an unreliable complex error routine used in their FOTRAN code.

5.2.6 Mean Square Lift at non-Zero Angle of Attack

The lift spectrum calculated from the first 14% chord is integrated at each angle of attack to obtain $\overline{L^2}$ values as

$$\overline{L^2}(\alpha) = \int G_{LL}(\alpha, f) df \quad (5.19)$$

The mean squared lift is obtained by integrating over $\omega_r = 0.35 - 10$. Mean square L values normalized on $(qc)^2$, where q is the dynamic pressure and c the chord are presented in figure 5.22 as a function of angle of attack. As pointed out by McKeough and Graham (1980) angle of attack effects should appear first in terms of order α^2 . Therefore, figure 5.22 also shows a curve representing an α^2 variation for comparison with the data. As the angle of attack is increased the mean square L decreases nearly as α^2 up to $\alpha = 14^\circ$. Agreement with the α^2 curve is within 6% up to $\alpha = 14^\circ$. The coefficients, A and B are calculated to be -0.00137 and 0.5045 respectively. Unsteady lift associated with separation becomes significant at $\alpha = 16^\circ$ causing the rate of decrease in $\overline{L^2}$ to fall. At $\alpha = 20^\circ$ the unsteadiness in the lift is due primarily to stall causing an apparent increase in $\overline{L^2}$.

5.3 Admittance Function

An airfoil interacting with turbulence can be treated as a linear system (as is done with most theoretical representations) and as such the response (unsteady lift) can be written in terms of the excitation (inflow turbulence) multiplying a transfer function (airfoil response). If the output is taken as the unsteady lift, the transfer function is often referred to as an admittance function and can be written as

$$\Phi_{C_L}(\omega) = \left(\frac{2\pi}{U_\infty} \right)^2 |A(\omega)|^2 \Phi_{ww}(\omega) \quad (5.20)$$

where $\Phi_{ww}(\omega)$ is the upwash velocity spectrum, $|A(\omega)|^2$ is the admittance function and $\Phi_{C_L}(\omega)$ is the normalized lift spectrum defined as

$$\Phi_{C_L}(\omega) = G_{LL}(\omega) \frac{4}{\rho U_\infty^2 b} \quad (5.21)$$

Based on velocity measurements presented in Bereketab *et al.* (2000) the energy spectrum of the inflow turbulence can be represented over the entire wavenumber range (including the inertial subrange) using the interpolation of Panchev and Kesich (Hinze, 1975, pp. 241) giving

$$E(k) = \frac{55}{9\sqrt{\pi}} \frac{\Gamma(\frac{5}{6})}{\Gamma(\frac{1}{3})} \frac{u^2}{k_e} \left(\frac{k}{k_e} \right)^4 \left[1 + \left(\frac{k}{k_e} \right)^2 \right]^{\frac{17}{6}} \left[1 + \frac{1}{f_\alpha} \left(\frac{k}{k_d} \right)^{\frac{2}{3}} \left(\frac{2}{3\alpha^2} \right)^{\frac{1}{3}} \right] \times \exp \left[-\frac{3}{2} \left(\frac{2}{3f_\alpha^2} \right)^{\frac{1}{3}} \left(\frac{k}{k_d} \right)^{\frac{4}{3}} - \frac{1}{f_\alpha} \left(\frac{k}{k_d} \right)^2 \right] \quad (5.22)$$

where f_α is given as

$$f_\alpha = \sqrt{\frac{18\sqrt{\pi}\Gamma(\frac{1}{3})}{165\Gamma(\frac{5}{6})}} \frac{\varepsilon}{k_e u^3} = 0.6774 \dots \frac{\varepsilon}{k_e u^3} \quad (5.23)$$

The upwash is then determined as (Hinze, 1975)

$$\Phi_{ww}(k_x, k_y, k_z) = \frac{E(k)}{4\pi k^2} \left(1 - \frac{k_z^2}{k^2} \right) \quad (5.24)$$

Integrating over k_z and k_y gives the one-dimensional velocity spectrum used in equation 5.20. The wavenumber, k_x can be related to angular frequency, ω by Taylors hypothesis, $k_x = U_\infty/\omega$. Figure 5.23 presents the von Karman and modified von Karman spectrum. Note the von

Karman spectrum is referred to as Amiets von Karman in figure 5.23 and is calculated from Patterson and Amiet (1976a, pp 57). The modified von Karman is calculated from equation 5.22.

The admittance is extracted using equation 5.20 and compared with the experimental results of McKeough (1976) for large scale turbulence interaction in figure 5.24. Recall, McKeough made unsteady lift measurements on a NACA 0015 in turbulence at $\alpha = 0^\circ$ and 10° . The scale of the turbulence was 40% of the chord with intensity of 5.8%. For all angles of attack the admittance forms a 'V' shape, dropping from $\omega_r = 10$ to $\omega_r = 25$ and then rising up. The rise in admittance at high frequency may be related to eddy convection or boundary layer pressure fluctuations. That is, the unsteady lift spectra slope decreases at the higher frequencies (as a result of eddy convection and boundary layer pressure fluctuations) while the turbulence spectrum continues to drop off at a constant slope as shown in figure 5.23.

The angle of attack variation is preserved in the admittance function with as much as 5dB of decrease observed at low reduced frequencies with increasing angle of attack. At $\alpha = 0^\circ$ the slope of the flat region ($\omega_r = 2$ to 20) is in agreement with McKeough's data; however, the data of the present measurement is shifted to the right as a consequence of the smaller scale turbulence ($\lambda/c = 13\%$). Surprisingly, the magnitude of the admittance of the present measurement is above McKeoughs. McKeoughs data also shows an increase in admittance magnitude with increasing angle of attack. At $\alpha = 10^\circ$ the slope of McKeoughs data agrees well with the present data at $\alpha = 8^\circ$.

5.4 Surface Pressure Correlation Length Scales

The spanwise and chordwise correlation length scales are presented to offer additional insight into the source of the angle of attack effect observed in unsteady lift spectra and admittance function. Furthermore, comparisons are made with Amiet's (1976a, b) theory to determine the ability of his solution to accurately predict correlation length scales at zero angle of attack.

5.4.1 Spanwise Correlation Length Scale

The spanwise correlation length scale is computed at the five most leading edge measurement chordwise locations ($x/c = 1, 2.5, 4, 6, 9\%$). The spanwise correlation length scales are computed from the pressure cross-spectrum as

$$L_\eta = \int_0^{\eta_{\max}} \frac{S_{qq}(x, x', \eta, f)}{S_{qq}(x, x', \eta = 0, f)} d\eta \quad (5.25)$$

where L_η is normalized on the airfoil chord, $\eta_{\max} = 96\%$ chord, and S_{qq} is the *pressure difference* cross-spectral density. This calculation is carried out at each chordwise location from 1% to 9% chord with $x = x'$ for all frequency.

Zero Angle of Attack: Figure 5.25 presents L_η calculated from measured unsteady pressure and as predicted by Amiet's (1976a, b) theory as a function of frequency at $x/c = 1, 2.5, 4, 6,$ and 9% for $\alpha = 0^\circ$ (note: high frequency data was only taken in spanwise rows at 1 and 2.5% chord). At 1% chord the spanwise correlation length of the inflow turbulence is also presented and calculated from the von Karman spectrum (Amiet, 1975) as

$$L_t(f) = \frac{8\lambda}{3} \left[\frac{\Gamma(1/3)}{\Gamma(5/6)} \right]^2 \frac{\hat{K}_x^2}{(3 + 8\hat{K}_x^2) \sqrt{1 + \hat{K}_x^2}} \quad (5.26)$$

where $\hat{K}_x = \frac{\omega/U}{k_e}$ with $k_e = \frac{\sqrt{\pi}}{\lambda} \frac{\Gamma(5/6)}{\Gamma(1/3)}$. Reasonable agreement between L_t and the measured

L_η at 1% chord occurs for $10 < \omega_r < 30$. This result seems logical since the surface pressure length scale in the leading edge arises from the turbulence-airfoil leading edge interaction. Moving away from the leading edge, the measured L_η is shown to increase over the entire frequency range. This is an expected result since the change in airfoil lift occurs by propagation of acoustic waves. That is, the acoustic wave that forms at the leading edge propagates in all directions with a spherical wave front. Amiet's theory under predicts the spanwise length scale below $\omega_r = 10$ for all chordwise positions which is likely related to the flat plate model used in this theory. At 1 and 2.5% chord agreement within 2% chord is shown to occur for $\omega_r > 20$. The data begins to fall below Amiet's prediction for $\omega_r > 20$ beyond 2.5% chord. At these higher frequencies boundary layer pressure fluctuations (high frequency), which correlate over very small spanwise separations ($< 1\%$ chord) begin to contaminate L_η by driving up S_{qq} at $\eta = 0$ and thus, causing L_η to fall. In summary, Amiet's (1976a, b) theory is limited in its ability to accurately predict the spanwise correlation when the airfoil is not well modeled by a flat plate.

Effects of Angle of Attack: Investigating the variation of the spanwise correlation with angle of attack offers additional hints on the source of the angle of attack effect. Figure 5.26 presents the spanwise correlation length scale as a function of reduced frequency for each angle of attack ($\alpha = 0^\circ, 4^\circ, 8^\circ, 12^\circ, 16^\circ, 20^\circ$) at $x/c = 1$ and 2.5% chord. At both chordwise locations a strong dependence on angle of attack is shown in L_η . As the angle of attack is increased L_η falls over much of the frequency range; however, most dramatically over $\omega_r < 10$. The reduction in the L_η in the leading edge region with increasing angle of attack suggests that eddies are being increasingly stretched by the mean field producing turbulence with a smaller spanwise length scale. This type of phenomenon may be the mechanism producing the reduction in unsteady loading at low reduced frequencies. Figure 5.27a, b depicts how such a process could reduce the unsteady loading. At small α 's the inflow eddy (labeled 'A') is convected towards the leading edge of the airfoil and moderately stretched by the mean field velocity gradients (eddy labeled 'B') as shown in figure 5.27a. Now, at a higher angle of attack, the same eddy 'A' is stretched considerably more as a consequence of the increased rate of strain in the mean field which reduces the spanwise length scale to that shown by eddy 'C' (figure 5.27b). Since the spanwise length scale of the inflow is related to the spanwise correlation length scale of the surface pressure, as suggested in figure 5.25, a reduction in the surface pressure L_η occurs with increasing angle of attack. The reduction in L_η means that the pressure has less of a correlated area to act over. Since the intensity of pressure fluctuations appears to remain largely unaffected by angle of attack, the overall unsteady loading decreases with increasing angle of attack as a consequence of the reduction in correlated area.

5.4.2 Chordwise Correlation Length Scale

Correlation length scales are typically defined for quantities which are homogeneous (i.e. ergodic) in space and time. The cross-spectrum of surface pressure fluctuations is indeed homogeneous in the spanwise direction, and, as such the distance between two spanwise points (η) becomes the defining parameter. However, in the chordwise direction pressure fluctuations are inhomogeneous (for example, this is apparent through comparison of chordwise auto-spectra) and thus the absolute chordwise position relative to any other chordwise position must be considered. Therefore, it is not necessarily appropriate to compute the chordwise correlation

length scale. Nevertheless, this quantity is essential for computing far-field noise from surface pressure fluctuations and is thus presented here.

The chordwise correlation length scale is calculated much like the spanwise correlation as

$$L_c = \int_0^{x_{\max}} \frac{S_{qq}(x, x', \eta = 0, f)}{S_{qq}(x, x, \eta = 0, f)} dx' \quad (5.27)$$

with L_c normalized on the airfoil chord, $x = x'$, $x_{\max} = 85\%$ chord, and S_{qq} is the *pressure difference* cross-spectral density.

Zero Angle of Attack: Figure 5.28 presents L_c as function of frequency calculated from unsteady pressure measurements and that predicted by Amiet's theory at $x/c = 1, 2.5, 4, 6,$ and 9% for $\alpha = 0^\circ$. With increasing chordwise distance from the leading edge L_c increases nearly the same amount at all frequencies up to 6% chord. At 9 and 14% chord L_c continues to increase for $\omega_r < 10$ while beginning to decrease at higher frequencies. The increase in L_c is, as with the spanwise correlation length scales an expected phenomenon due to the propagation of acoustics waves as a consequence of lift adjustment. The reduction shown to occur over $\omega_r > 10$ at 9 and 14% chord is likely due to contamination from boundary layer pressure fluctuations much like that which affects the spanwise correlations. Recalling the length scale of the inflow turbulence, $\lambda/c = 0.13$, it is interesting to note that L_c is in close agreement with the inflow length scale at 1% chord for low reduced frequencies.

Amiet's theory predicts L_c to within $5\% c$ at all frequencies up to 6% chord. The theory begins to over predict L_c for frequencies above 10 at 9 and 14% chord. This may be a combined result of the flat plate model assumed in Amiet's theory and contamination of the data through boundary layer pressure fluctuations.

Effects of Angle of Attack: Angle of attack effects on the chordwise correlation length scale are presented in figure 5.29. It is interesting to see that variation in the airfoils mean loading does not affect L_c nearly as significantly as shown in the spanwise correlation. Furthermore, at 1% chord L_c increases slightly for $\omega_r < 10$. At 2.5% chord slight reduction in L_c does occur as the angle of attack is increased to $\alpha = 16^\circ$. When $\alpha = 20^\circ$ L_c rise up significantly since the airfoil is stalled and large scale pressure fluctuations develop at low frequencies.

5.5 Correlation of Velocity and Pressure

Examining the correlation of pressure and velocity will aid in identifying both hydrodynamic and acoustic pressure fluctuations and may offer additional insight into the laminar separation bubble theory presented in chapter 4. Recalling that for some angle of attack simultaneous measurements of velocity and pressure were performed, correlation of these two quantities is presented here. Details on the instrumentation associated with the velocity-pressure measurement can be found in chapter 2; although briefly, hotwire measurements were made (simultaneously with pressure measurements) at 14% chord on the suction side (suction side defined for positive α 's) of the airfoil. The hotwire was located $\frac{3}{4}$ " off the airfoil surface. The velocity-pressure space-time correlation is formed as

$$R_{pu}(x, \tau) = \frac{\overline{p(x, t)u(t + \tau)}}{\sqrt{\overline{p^2(x)}\overline{u^2}}} \quad (5.28)$$

where u is the fluctuating velocity measured by a single hotwire located at 14% chord. Investigating the correlation of velocity and pressure assists in determining whether pressure fluctuations arise from convected or propagated disturbances. In this way, the correlation function will help determine if vortex shedding is occurring as a consequence of an inflow coupled laminar separation bubble and thereby altering the airfoil loading.

The correlation function is presented in figure 5.18 for $\alpha = 0^\circ, \pm 8^\circ, \pm 16^\circ$. Superimposed on the pressure-velocity correlation contours are gradient vectors computed by taking the derivative of the correlation with respect to time and space. These vectors assist in identifying ridges in correlation. At $\alpha = 0^\circ$ on the pressure side of the airfoil a correlation ridge forms (indicated by the red dashed line) at a 12:1 slope with significant pressure-velocity correlation up to 85% chord indicating propagation of sound speed pressure fluctuations. Bearing in mind the location of the hotwire on the airfoil suction side, the correlation will not show convection on the pressure side. However, on the suction side of the airfoil *both* convected and propagated pressure fluctuations are shown in the correlation function. The convect disturbances appear to be moving at a velocity slightly less than the mean free-stream. At $\alpha = 8^\circ$ the correlation looks much like that at $\alpha = 0^\circ$. As the angle of attack is increased to 16° a significant inviscid response is shown on the pressure side of the airfoil with convection occurring near the mean free-stream

velocity on the suction side. The convection may be related to vorticity shedding from a leading edge transient laminar separation bubble.

The correlation is changed dramatically at $\alpha = -8^\circ$ and -16° with the hotwire now located on the pressure side of the airfoil. At these angles of attack the correlation shows little evidence of a strong inviscid response. Some possible convection is evident (indicated by the solid red line) and appears to be slightly faster than the mean free-stream velocity. Eddies impacting the leading edge and then convecting along the pressure side of the airfoil appear to either be 1) substantially distorted such that they pass below the $\frac{3}{4}$ " gap between the airfoil surface and hotwire or 2) have no significant component which survives after impacting the leading edge. If in fact there is no significant component of the eddy surviving, then a Rapid Distortion Theory (RDT) model could be quite simplified such that the distortion would only need to be considered in neighborhood of the leading edge.

5.6 Effects of a Modified Trailing Edge

To examine the effects of trailing edge geometry, measurements were performed with a modified trailing edge. The modification transforms the NACA 0015's rounded trailing edge to one that is sharp (see chapter 2 for geometry details) and extends the airfoil chord by 3%. The rounded trailing edge allows for infinite number of velocity solutions to the inviscid flow around the airfoil. Of course in steady, inviscid flow only one solution occurs in reality; however, in unsteady flow little evidence of the applicability of the classical Kutta condition is available. Furthermore, the experimental work of Poling and Telionis (1986) suggests that the "classical Kutta condition" is never satisfied in unsteady flow. Indeed, they show that in unsteady flow at low ω_r the shedding of vorticity results in a finite velocity at the trailing edge. As such, the unsteady circulation may be slightly altered relative to that which would occur if the "classical Kutta condition" were met and would clearly impact the unsteady loading of an airfoil encountering turbulence.

5.6.1 Correlation of Pressure in Space and Time

The space-time correlation is investigated with a modified trailing edge in Figure 5.31 for each angle of attack ($\alpha = 0^\circ, 4^\circ, 8^\circ, 12^\circ, 16^\circ, 20^\circ$). The correlation is formed by taking $x = 1\%$ chord on the suction side (negative x/c values) and varying x' with $\eta = 0$. The data is high pass

filtered at 100Hz to eliminate uncertainties associated with microphone calibrations below this range (i.e. this data is processed the same way as the data presented without modified trailing edge in chapter 4). The inviscid response dominates on the pressure side of the airfoil at all angles of attack with the ridge of the correlation nearing a 12:1 slope. On the suction side the inviscid response is dominant up to $\alpha = 8^\circ$; however, convection (1:1 slope) of eddies begins to become significant at higher angles of attack. Significant separation occurs at $\alpha = 16^\circ$ causing substantial convection on the suction side of the airfoil. The airfoil is stalled at $\alpha = 20^\circ$ and shows little correlation on the suction side.

The space-time correlation measured with the modified trailing edge compares very closely with that measured with an unmodified trailing edge (figure 4.34) at all angles of attack. This finding indicates that small changes in the chord length impact the inviscid response very little. This occurrence makes sense given that the dominant energy in the inflow turbulence is in wavenumbers much smaller than the chord length. Additionally, the sharpness of the trailing edge appears to impact the inviscid response minimally suggesting that the “classical Kutta condition” can be reliably applied in unsteady flow (as assumed in unsteady thin airfoil theory).

5.6.2 Unsteady Lift

A comparison of unsteady lift calculated from measurements with both types of trailing edges will assist in understanding the effects of trailing edge geometry. The unsteady lift spectra calculated from the modified trailing edge pressure measurements are compared with those calculated from unmodified trailing edge measurements in figure 5.32. Little variation (within the uncertainty of the data) between the spectra calculated with and without the modified trailing edge occurs across the frequency range. This result confirms that indeed, a rounded trailing edge (within the parameters of this experiment) behaves much like a sharp trailing edge in unsteady flow. Additionally, the slight increase in chord length associated with the sharp trailing edge seems to affect the airfoils response negligibly.

5.7 Sources of Low Frequency Angle of Attack Effect

The analysis of unsteady pressure measurements presented here and in chapter 4 seems to suggest two reasonable sources for the observed reduction in unsteady lift at low ω . The transient laminar separation bubble suggested by oil flow visualization and leading edge pressure asymmetries is one means for the relaxation in unsteady loading. Another possibility is the

reduction in spanwise correlation length scale as a result of inflow distortion. The likelihood of each is examined in this section.

5.7.1 Laminar Separation Bubble

A possible source of the reduction in unsteady lift at low reduced frequency may be the presence of a laminar separation bubble in the leading edge region of the airfoil. The flow visualization presented revealed the possibility of a laminar separation bubble occurring in the leading edge region. Some additional support of such a phenomenon is offered by the asymmetries shown in pressure spectra. Also, the reduction in the pressure-pressure correlation shown to occur on the suction side in the leading edge region may be related to the formation of such a bubble. This bubble, if indeed present could serve as an explanation for the reduction of unsteady lift with increasing angle of attack. At low reduced frequencies the bubble could be synchronizing with the unsteady lift such that the bubble sheds vorticity and thereby relaxes the unsteadiness in the lift. There is little evidence in the RMS pressure to indicate the presence of a laminar separation bubble; however, this alone is not evidence enough to eliminate such a possibility but, also does not aid in the support of this theory. Careful measurement of the velocity field surrounding the airfoil coupled with improved flow visualization (such as helium bubble flow visualization) would allow for unambiguous proof (or disproof) of such a scenario.

5.7.2 Distortion of Inflow

Analysis of the spanwise correlation length scale suggests distortion of turbulence as a consequence of the airfoils presence in the flow is a significant factor in reducing unsteady lift with increasing angle of attack. The spanwise extent of correlated pressure fluctuations in the leading edge region appears to be produced by the inflow turbulence as suggested through comparison of the undistorted inflow spanwise turbulence length scale (L_t) with the spanwise pressure correlation length scale (L_η). As such, with the airfoil at angle of attack, stretched eddies (consequently, with a reduced L_t) impact the leading edge thereby reducing L_η . The reduction in L_η reduces the correlated area over which the pressure acts. Since the intensity of pressure fluctuations appears to remain largely unaffected by angle of attack (as shown in figure 5.5), the overall unsteady loading decreases with increasing angle of attack as a consequence of the reduction in correlated area. This theory may be the most conceivable of the two presented

based on the observed variation of L_η and $\sqrt{\Delta p'^2}$ with angle of attack which offer particularly strong support.

Furthermore, while the distortion of the inflow appears to be critical in this experiment, wherein the integral scale (λ/c) is 13% of the chord, this effect does not seem to be significant in large integral scale (relative to the chord) flow. Recall McKeough's measurement of unsteady lift on a NACA 0015 which showed a 3dB (for $\omega_r < 1$) increase in lift with an increase from $\alpha = 0^\circ$ to 10° and had an inflow integral scale of 40% of the chord. As such, it appears the relative scale of the inflow to chord length is important in determining the airfoils response when subject to mean loading. Unsteady loading models like those developed by Graham (1970a), Atassi (1984), and Reba and Kerschen (1996) seem to encapsulate mean loading effects well for this large scale turbulence case. In fact, Graham's (1970a) theory agrees well with McKeough's unsteady lift measurements based on comparisons he presented. However, for the case of small scale turbulence (relative to the airfoil chord), these models do not depict the dominant physics of turbulence-airfoil interaction well. The reason seems to be related to the flat plate with leading edge stagnation point assumed in these models that does not account for the inflow distortion correctly.

5.8 A Model for Predicting Angle of Attack Effects

A new model is suggested here that will correctly account for the inflow distortion and therefore, the dominant factor impacting the airfoil response for the parameters of this experiment ($\lambda/c = 13\%$). This new model combines accurate modeling of the turbulence distortion using Rapid Distortion Theory (RDT) with Amiet's (1976a, b) flat plate unsteady loading theory. This type of modeling scheme will require as input the distorted turbulence energy spectrum to account for the effects of angle of attack.

Rapid Distortion Theory Background: Rapid Distortion Theory (RDT) is a scheme for predicting the evolution of turbulence as it is stretched and compressed by the mean velocity field. The foundation for this theory was laid by Batchelor and Proudman (1954) and uses the linearized form of the vorticity transport equation to predict distortion effects. This theory works under the assumption that

1. Distorting effects of turbulence on itself are negligible

2. The scale of the turbulence is small compared to the scale of the distortion
3. The duration of the distortion is small, such that the influence of viscous dissipation can be neglected.

In Lagrangian form the vorticity transport equation, or what is often referred to as Cauchy's equation is given as (in tensor notation)

$$\Omega_i = \frac{\partial x_i}{\partial a_j} \Omega'_j \quad (5.29)$$

where Ω'_j is the vorticity at the beginning of the distortion (time t') with position determined by a_j and Ω_i is the vorticity at the end of the distortion (time t) with position x_j . The term $\frac{\partial x_i}{\partial a_j}$ is

referred to as the distortion tensor and will depend on the mean velocity field. Batchelor and Proudman (1954) define the distortion tensor as

$$S_{ij} = \frac{\partial x_i}{\partial a_j} = \delta_{ij} + \int_{t'}^t \frac{\partial U_i}{\partial a_j} dt \quad (5.30)$$

where a_j is the initial position of the particle at time t' , x_i is the position at time t , U_i is the mean velocity component and δ_{ij} is the Kronecker delta. Using Goldstein's (1979) model the distortion tensor can be computed from a two dimensional mean velocity field as

$$S_{ij} = \begin{bmatrix} \frac{\partial X_1}{\partial s} & 0 & \frac{\partial X_1}{\partial n} \\ 0 & 1 & 0 \\ \frac{\partial X_3}{\partial s} & 0 & \frac{\partial X_3}{\partial n} \end{bmatrix}^{-1} \quad (5.31)$$

Note that in eq. 5.31, the mean field does not vary in the y direction (i.e. along the span of the airfoil) and hence the zero and unity terms. In this equation s and n form a curvilinear coordinate system with s along a streamline and n perpendicular to the streamline. The quantity X_3 is proportional to the stream function with X_1 defined as the drift function and given as

$$\frac{X_1}{U_\infty} = \frac{x_1}{U_\infty} + \int_{-\infty}^{x_1} \left[\frac{1}{U'(x_1, X_3)} - \frac{1}{U_\infty} \right] dx_1 \quad (5.32)$$

where here U' is the mean velocity component parallel to the free-stream velocity (U_∞) and x_1 is the component of the fluid particle position vector parallel to U_∞ . Through manipulation of the drift function, the distortion simplifies to

$$S_{ij} = \begin{bmatrix} \frac{\overline{U_\infty}}{U_\infty} & 0 & \frac{\partial X_1}{\partial n} \\ 0 & 1 & 0 \\ 0 & 0 & \frac{U_\infty}{|\overline{U_\infty}|} \end{bmatrix}^{-1} \quad (5.33)$$

where $|\overline{U_\infty}|$ is the magnitude of the mean velocity vector. The term $\frac{\partial X_1}{\partial n}$ is difficult to compute because it implies integration along a streamline (eq. 5.32) followed by differentiation perpendicular to the streamline; however, this calculation is feasible with careful application of numerical procedures.

Batchelor and Proudman (1954) show that the distorted turbulence energy spectrum can be calculated using the distortion tensor and the undistorted energy spectrum as

$$\Phi_{ij-dist}^*(\chi) d\chi = \varepsilon_{ikl} \varepsilon_{mnp} \varepsilon_{jab} \varepsilon_{uvw} \chi_l \chi_b \chi^{-4} k_n k_u S_{km} S_{au} \Phi_{pw}(k) dk \quad (5.34)$$

with $\chi_l = k_l (S_{li})^{-1}$ is the non-dimensional distorted wave number vector, S_{ij} is the distortion tensor, ε_{ijk} is the unit alternating tensor and $\Phi_{ij}(k)$ is the non-dimensional undistorted energy spectrum tensor.

New Airfoil Response Model: A new unsteady response model is developed which uses a circular cylinder to predict the inflow distortion. Ideally, the distortion tensor is calculated based on the actual mean field produced by the airfoil; however, using a cylinder has the distinct advantage of significantly simplifying the distortion tensor calculation. The circular cylinder radius is determined based on a fit to the airfoil curvature at the location of the mean stagnation point for any given angle of attack. Figure 5.33 shows a circular cylinder fit to the NACA 0015 at a location that corresponds to the $\alpha = 4^\circ$ stagnation point. The location of the mean stagnation point is easily calculated using a vortex panel method.

The stagnation streamline associated with this circular cylinder is then used to predict the distortion of the inflow via RDT (eq. 5.34) as depicted in figure 5.34. The first step in this calculation is determining the stagnation streamline velocity which is obtained for a circular cylinder from potential flow theory as

$$\frac{U(x)}{U_\infty} = 1 - \left(\frac{r}{x}\right)^2 \quad (5.35)$$

where r is the cylinder radius. The distortion tensor is then readily computed from the potential flow solution using eq. 5.33

$$S_{ij} = \begin{bmatrix} \frac{U(x)}{U_\infty} & 0 & 0 \\ 0 & 1 & 0 \\ 0 & 0 & \frac{U_\infty}{U(x)} \end{bmatrix}^{-1}. \quad (5.36)$$

Notice the most difficult term to compute in the distortion tensor, $\frac{\partial X_1}{\partial n}$ is zero when calculated along the stagnation streamline of a circular cylinder and hence, the real convenience of using the cylinder approximation.

This calculation is carried out for $\alpha = 0^\circ, 4^\circ, 8^\circ,$ and 12° . The distortion is compute at a location, x (referring to the notation of figure 5.34) that is some percentage of the integral scale ($\lambda/c = 13\%$) upstream of the cylinder such that

$$x = r + A_2 \lambda. \quad (5.37)$$

The constant, A_2 is taken as 1 for the present calculation resulting in calculation of the distorted turbulence spectrum one integral scale upstream from the circular cylinder. The ratio of distortion location, x to cylinder radius, r for each angle of attack is given in table 5.2.

Table 5.2: Ratio of distortion location to cylinder radius

Angle of Attack	x/r
0°	-9.81
4°	-3.14
8°	-2.11
12°	-1.71

With the distorted turbulence spectrum computed, Amiet's (1976a, b) theory is used to predict the airfoils response to the distorted inflow at each simulated angle of attack.

The results of this calculation are presented in figure 5.35 with lift spectra, G_{LL} plotted against ω_r for each angle of attack. The lift spectra are calculated discretely using the same six chordwise locations used to calculate lift from measured unsteady pressure. This new unsteady

loading prediction scheme shows a 6dB reduction in lift for $\omega_r < 10$ as α is increased from 0° to 12° . This is an excellent prediction of the angle of attack trend and surprisingly good prediction of amount of spectral level reduction. In light of the approximations used in the formulation (i.e. calculation of distortion one integral scale upstream of a circular cylinder), prediction of the correct change in spectral level with angle of attack was not expected. This model also predicts some reduction in unsteady lift for $\omega_r > 10$ which is not shown in the measurement. Clearly though, this model provides solid evidence that, in fact, the distortion of the inflow is crucial in producing the reduction of unsteady lift with increasing angle of attack.

To shed additional light on the relative importance of the inflow distortion for large scale turbulence (large relative to chord length), this model is used to predict the unsteady lift based on McKeough's flow conditions ($U_\infty = 15\text{m/s}$, $\lambda/c = 0.4$, $TI = 6.5\%$). This calculation is carried out as outlined above with $x/r = 3.1$ and 27.2 for $\alpha = 0^\circ$ and 12° respectively. Figure 5.36 presents the predicted unsteady lift spectra as a function of ω_r . Less than 1dB of reduction in lift spectral level is predicted for $\omega_r < 10$ with the spectra falling nearly on top of each other for higher frequencies. As expected, this theory does not predict the increase in unsteady lift shown to occur in McKeough's measurements. However, this prediction does prove the point that the inflow distortion is not an important factor in determining the unsteady loading (for $\lambda/c = 0.4$) and, in fact, those factors which are correctly modeled in Graham's (1970a) theory are likely dominant.

5.9 High Frequency Angle of Attack Effects

The unsteady lift calculated from pressure measurements (Figure 5.18) shows an increase in spectral with increasing angle of attack for $\omega_r > 10$. This increase in unsteady loading can be explained by scaling lift spectra. Lift spectra are scaled on the square of the mean lift as

$$G_{LL}^*(\alpha, f) = \frac{G_{LL}(\alpha, f)}{\bar{L}^2(\alpha)} \quad (5.38)$$

where G_{LL} is the unsteady lift as calculated from eq. (4.3) and \bar{L}^2 is the mean lift squared.

Figure 5.37 presents the scaled lift spectra (note, data for $\alpha = 0^\circ$ is not presented due to singularity which results from zero mean lift) as a function of reduced frequency. As expected, this scaling amplifies the angle of attack effect at low frequencies ($\omega_r < 10$) causing a greater reduction in unsteady lift with increasing angle of attack. However, above $\omega_r = 10$ the lift

spectra are collapsed to within 5dB by the mean lift scaling for $\alpha > 4^\circ$. This is a considerable reduction in the 10dB of variation with angle of attack shown over this frequency range to occur in the unscaled lift spectra. The collapsing of data over this frequency range suggests the variation in unsteady lift here is closely related to the mean loading on the airfoil.

Furthermore, this scaling suggests that effects of angle of attack are frequency dependent with the distortion of the inflow defining the low frequency effects and the airfoils mean loading producing the high frequency effect. In the present experiment the crossover appears to occur near $\omega_r = 10$.

5.10 Computing Far-field Noise from Surface Pressure

Lastly, because it is the ultimate goal of any surface response theory to generate predictions of the far-field noise produced during turbulence-airfoil interaction the usefulness of this data for such schemes is presented. Casper and Farassat (2002) present a technique for computing far-field loading noise (i.e. inviscid response noise) from the unsteady surface pressure distribution. The solution depends on the time derivative and surface gradient of the unsteady pressure. The required input for their formulation is obtained by expressing the surface pressure as the cross-correlation of the substantial derivative of p , such that

$$\dot{p}(x, y, t) = \frac{\partial p(x, y, t)}{\partial t} - U_\infty \frac{\partial p(x, y, t)}{\partial x} \quad (5.39)$$

and the cross-correlation is given as,

$$R_{\dot{p}\dot{p}}(x, x', \eta, \tau) = \overline{\dot{p}(x, y, t) \dot{p}(x', y', t + \tau)}. \quad (5.40)$$

The *pressure difference* inverse Fourier transform of eq. (5.38)—the convective derivative spectrum—is considered here for zero spanwise separation (i.e. $\eta = 0$) and is obtain as

$$G_{D_t}(x, x', \eta, f) = \int_0^\infty R_{\Delta\dot{p}\Delta\dot{p}}(x, x', \eta, \tau) e^{-i2\pi f\tau} d\tau \quad (5.41)$$

where the left hand side of eq. (5.39) is computed from time series data as

$$G_{D_t}(x, x', f) = \frac{2}{N \cdot S_R} E \left[\left\{ \Delta p_t(x, f) + U_\infty \Delta p_x(x', f) \right\} \left\{ \Delta p_t(x', f) + U_\infty \Delta p_x(x', f) \right\}^* \right] \quad (5.42)$$

with

$$\Delta p_x(x, f) = \int_0^{\infty} \frac{\partial}{\partial x} [p_L(x, t) - p_U(x, t)] e^{-i2\pi ft} dt$$

$$\Delta p_t(x, f) = \int_0^{\infty} \frac{\partial}{\partial t} [p_L(x, t) - p_U(x, t)] e^{-i2\pi ft} dt$$
(5.43)

The spatial and temporal derivatives of eq. (5.41) are evaluated numerically such that

$$\frac{\partial \Delta p(x, t)}{\partial x} \approx \frac{\Delta p(x_i, t) - \Delta p(x_{i+2}, t)}{x_{i+2} - x_i}$$

$$\frac{\partial \Delta p(x, t)}{\partial t} \approx \frac{\Delta p(x, t_i) - \Delta p(x, t_{i+2})}{t_{i+1} - t_i}$$
(5.44)

The time derivative, G_{dt} and space derivative, G_{dx} , both components of the convective derivative spectrum, are also considered and can be directly calculated from eq. (5.41) as

$$G_{dt}(x, x', f) = \frac{2}{N \cdot S_R} E \left[\Delta p_t(x, f) \Delta p_t(x', f)^* \right]$$
(5.45)

and

$$G_{dx}(x, x', f) = \frac{2}{N \cdot S_R} E \left[\Delta p_x(x, f) \Delta p_x(x', f)^* \right]$$
(5.46)

The above quantities are calculated for $\alpha = 0^\circ$ at $x/c = 1, 2.5, 4, 6, 9, 14\%$ chord and presented in figure 5.38 as a function of reduced frequency along with the *pressure difference* spectral density, $G_{\Delta P \Delta P}$. The spatial derivative spectrum, G_{dx} (eq. 5.46) closely resembles the pressure difference spectrum in shape for all chordwise positions. This indicates the acoustic wavelength is so large that the pressure field appears to be the same over very small chordwise separations. The time derivative, G_{dt} (eq. 5.45) rolls off with nearly the same slope as $G_{\Delta P \Delta P}$ for $\omega_r > 3$ at all chordwise locations. G_{dt} begins to fall off for $\omega_r < 3$ which is expected since the time derivative of a slowly varying signal will tend to zero. The convective derivative spectrum, G_{Dt} (eq. 5.42) bears close resemblance to the time derivative spectrum at all chordwise locations for $\omega_r > 3$. The rise in G_{dx} tends to offset the fall in G_{dt} resulting in leveling off of G_{Dt} at $\omega_r < 3$. Beyond 9% chord the accuracy of G_{dx} becomes questionable due to the large chordwise separations. In addition, boundary layer pressure fluctuations begin to contaminate the data for $\omega_r > 20$ at 9% chord and beyond.

5.11 Summary

Unsteady pressure measurements made on the surface of a NACA 0015 immersed in large grid turbulence ($\lambda/c = 13\%$) are presented and the effects of angle of attack examined. Pressure measurements are used to calculate unsteady lift. With increasing angle of attack, lift spectra show a decrease by as much as 5dB in spectral level for $\omega_r < 10$ and an increase of as much as 10dB in spectral level for $\omega_r > 10$.

The increase in unsteady lift observed for $\omega_r > 10$ is found to be related to the mean lift of the airfoil based on lift spectrum scaling using the mean lift squared. Based on analysis of the spanwise pressure correlation length scale, the reduction in unsteady lift is believed to result from distortion of the inflow by the mean velocity field. However, predictions of unsteady lift made with Reba and Kerschen's (1996) unsteady loading theory, which accounts for effects of mean loading through Rapid Distortion Theory, show a significant rise in lift spectra level with increasing angle of attack. Their theory does not capture the correct angle of attack effect at low ω_r because the distortion of the inflow is not accurately predicted with the flat plate model they assume.

As such, a model is developed that accurately predicts the effects of angle of attack on unsteady lift spectra. This model uses a circular cylinder fit to the airfoil to compute effects of distortion on the inflow turbulence. The distorted inflow velocity spectrum is then used with Amiet's (1976a, b) theory to predict the unsteady loading. This model successfully captures the reduction observed in unsteady lift spectra calculated from pressure measurements. Furthermore, it is shown that angle of attack effects arising from inflow distortion are significant only when the relative scale of the inflow turbulence to airfoil chord is sufficiently small ($\lambda/c = 13\%$ for present experiment). Factors which are well predicted by theories such as Graham (1970a), Atassi (1984), Reba and Kerschen (1996) become dominant when the scale of the inflow is large compared to the airfoil chord.

Lastly, it is shown that unsteady pressure measurements can likely be used to make far-field noise predictions using the method presented by Casper and Farassat (2002).

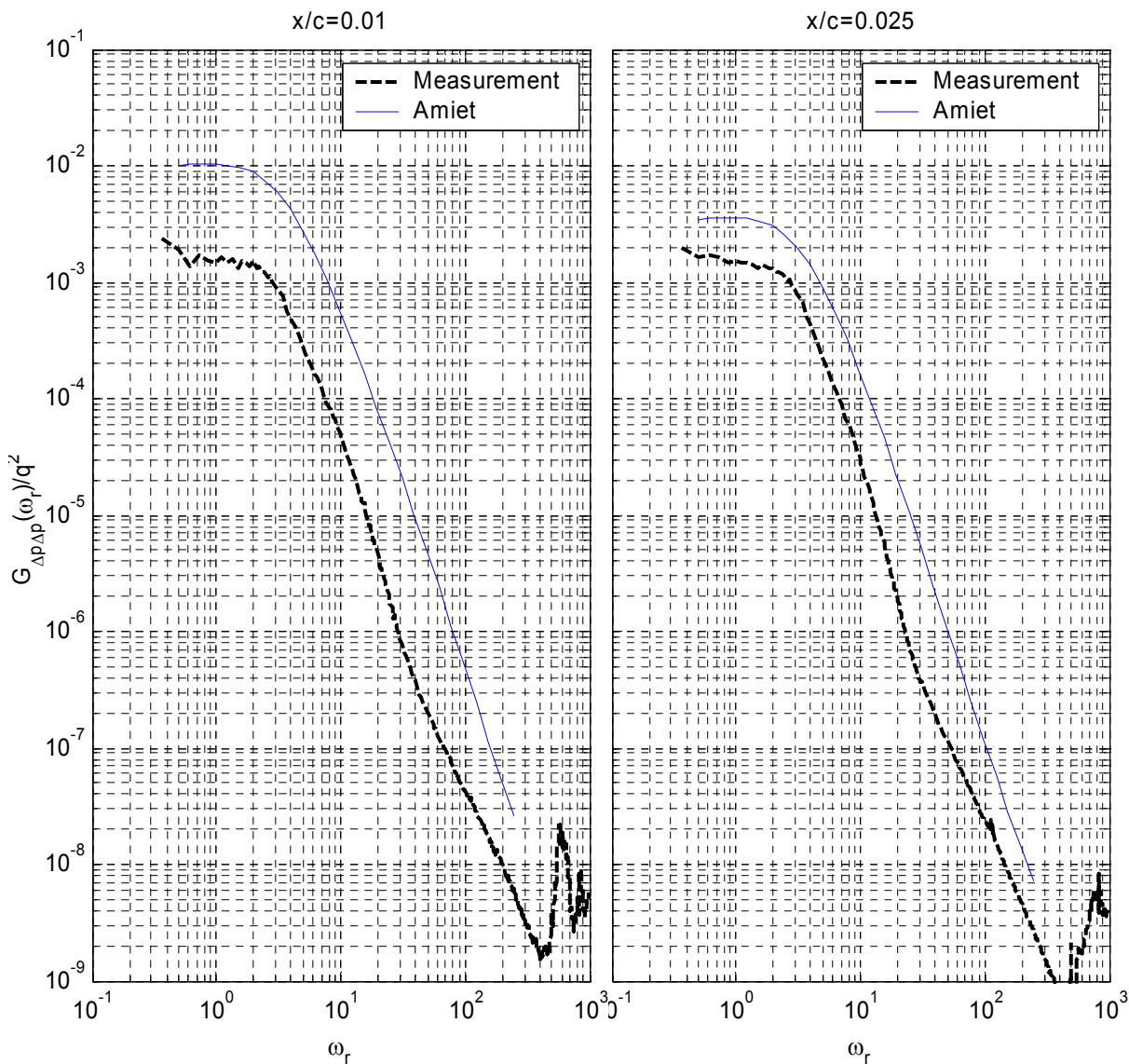


Figure 5.1: Comparison of measured and predicted pressure difference spectra for $\alpha = 0^\circ$ at $x/c = 1, 2.5, 4, 6, 9,$ and 14% . Prediction is Amiet's (1976a, b) unsteady thin airfoil theory.

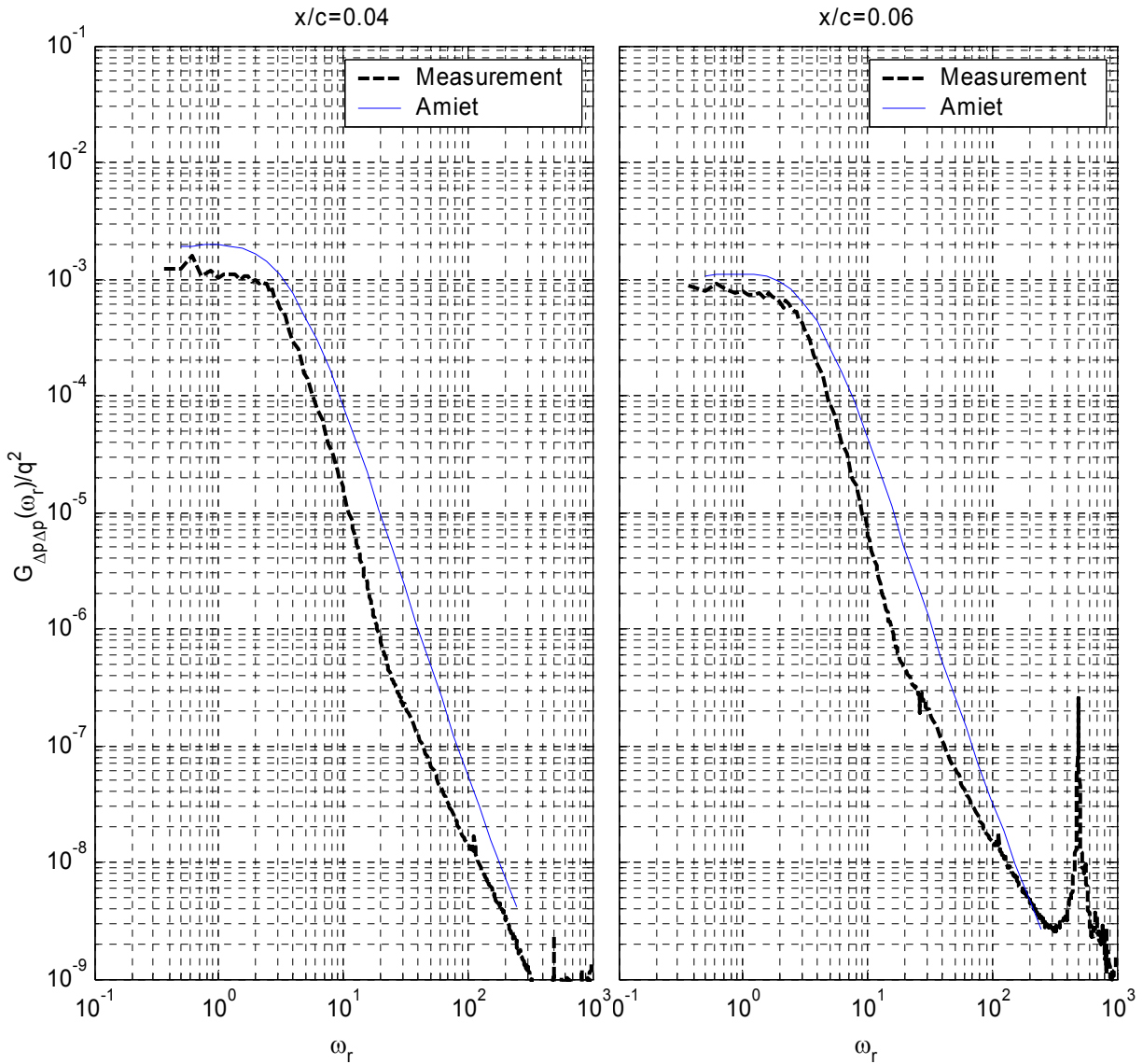


Figure 5.1 continued: Comparison of measured and predicted pressure difference spectra for $\alpha = 0^\circ$ at $x/c = 1, 2.5, 4, 6, 9,$ and 14% . Prediction is Amiet's (1976a, b) unsteady thin airfoil theory.

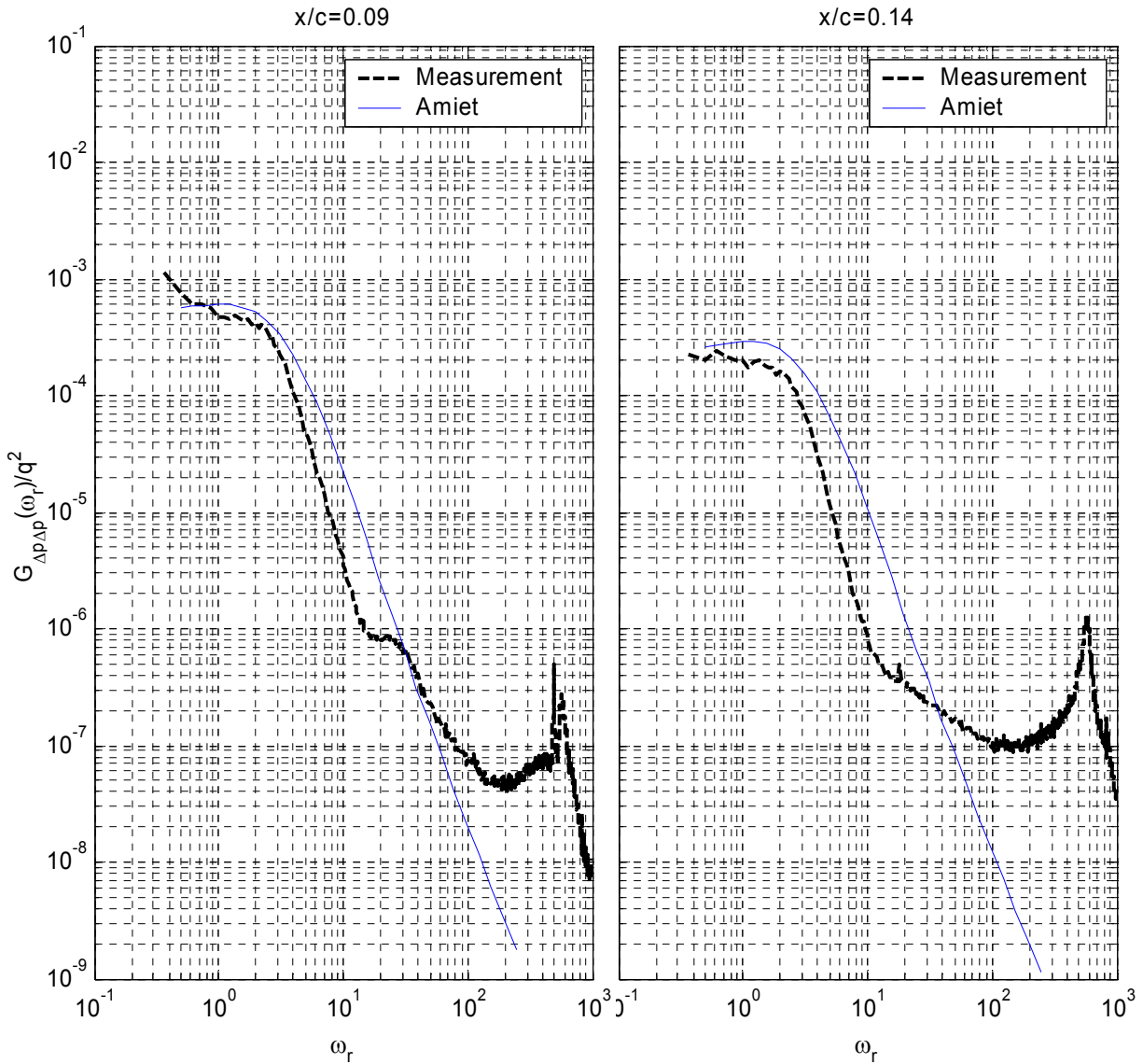


Figure 5.1 continued: Comparison of measured and predicted pressure difference spectra for $\alpha = 0^\circ$ at $x/c = 1, 2.5, 4, 6, 9,$ and 14% . Prediction is Amiet's (1976a, b) unsteady thin airfoil theory.

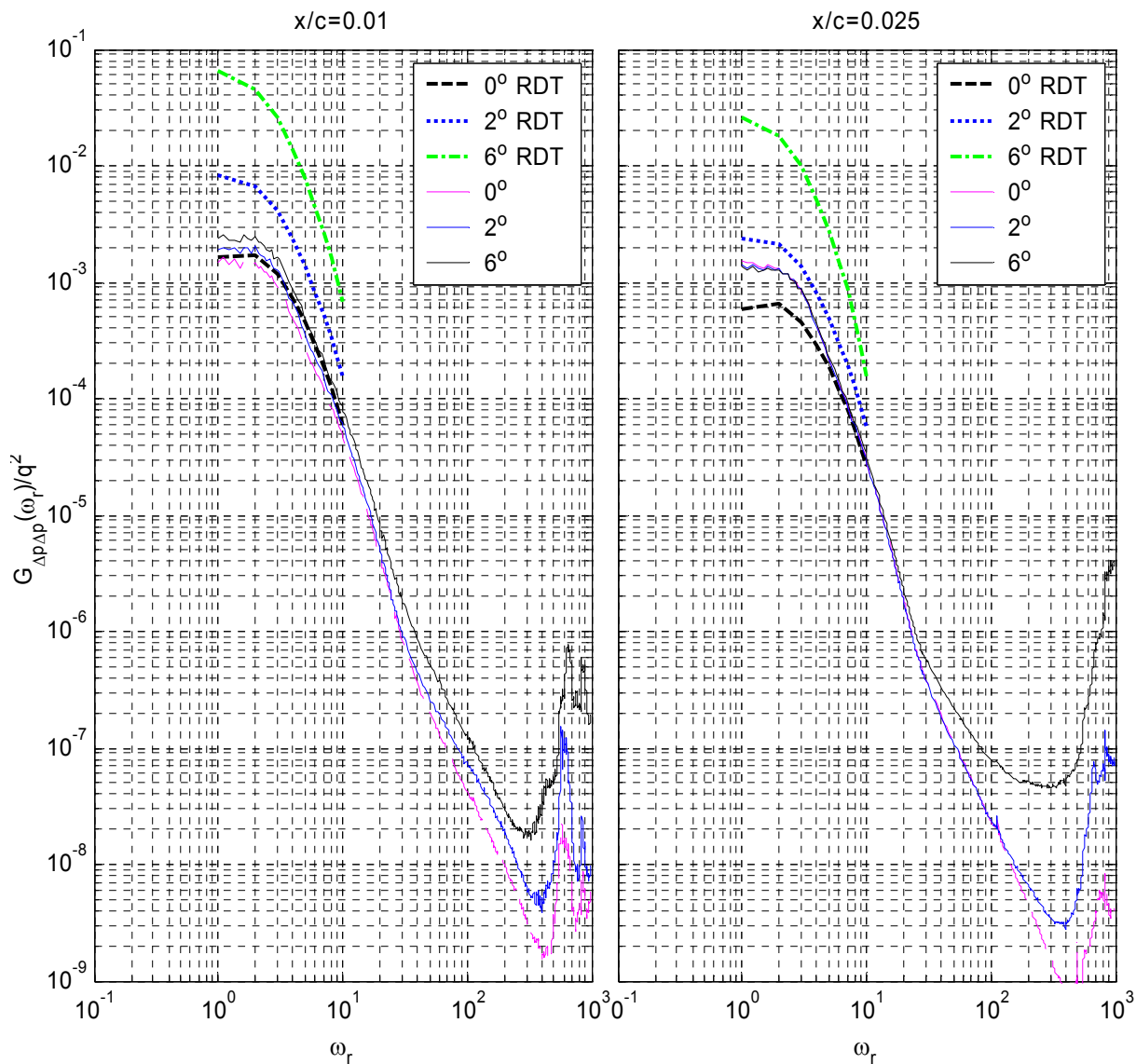


Figure 5.2: Predictions of pressure difference spectra from the Rapid Distortion Theory of Reba and Kerschen (1996) plotted with measured data for $\alpha = 0^\circ, 2^\circ,$ and 6° at chordwise locations, $x/c = 1, 2.5, 4, 6, 9,$ and 14%

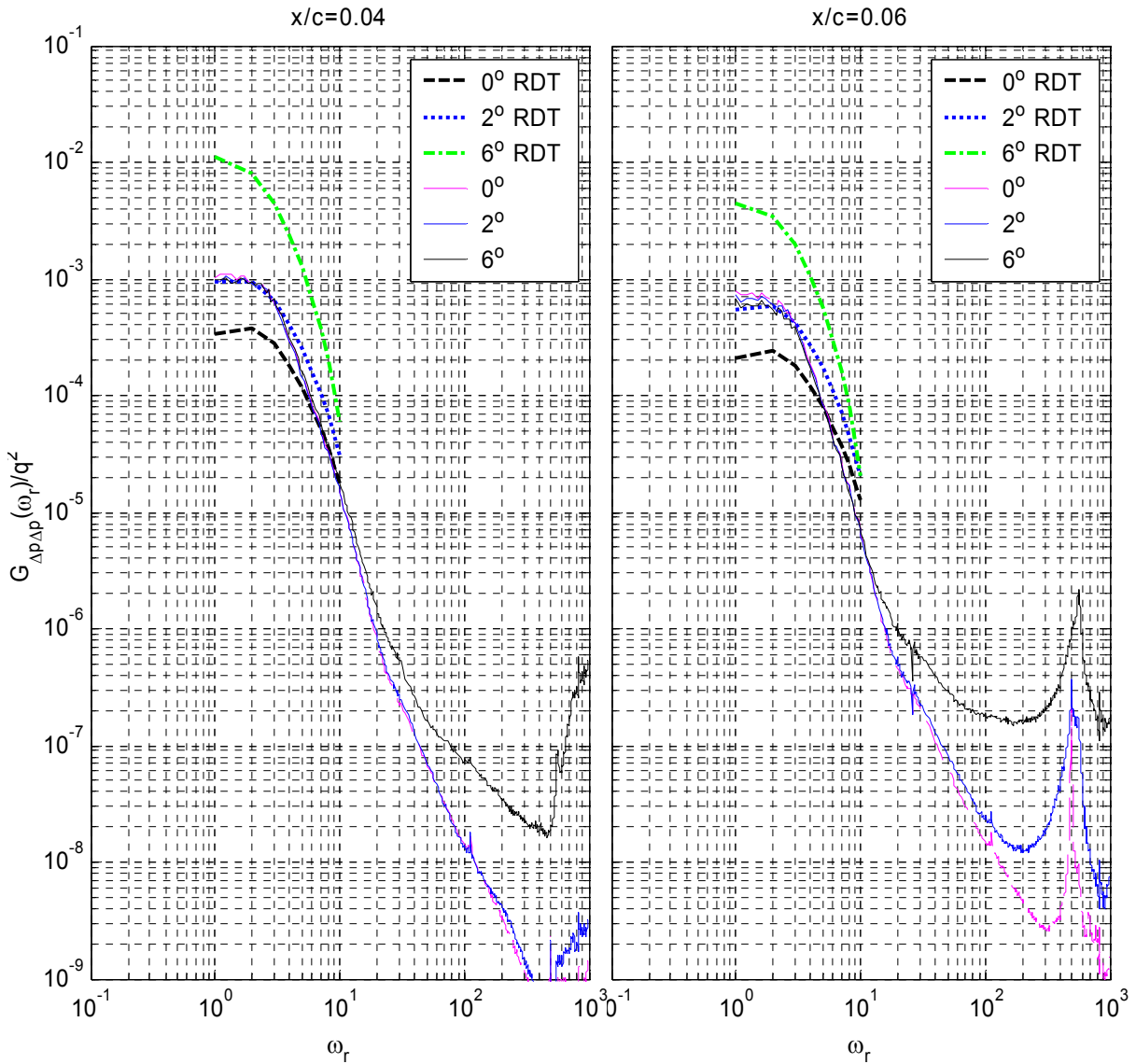


Figure 5.2 continued: Predictions of pressure difference spectra from the Rapid Distortion Theory of Reba and Kerschen (1996) plotted with measured data for $\alpha = 0^\circ, 2^\circ,$ and 6° at chordwise locations, $x/c = 1, 2.5, 4, 6, 9,$ and 14%

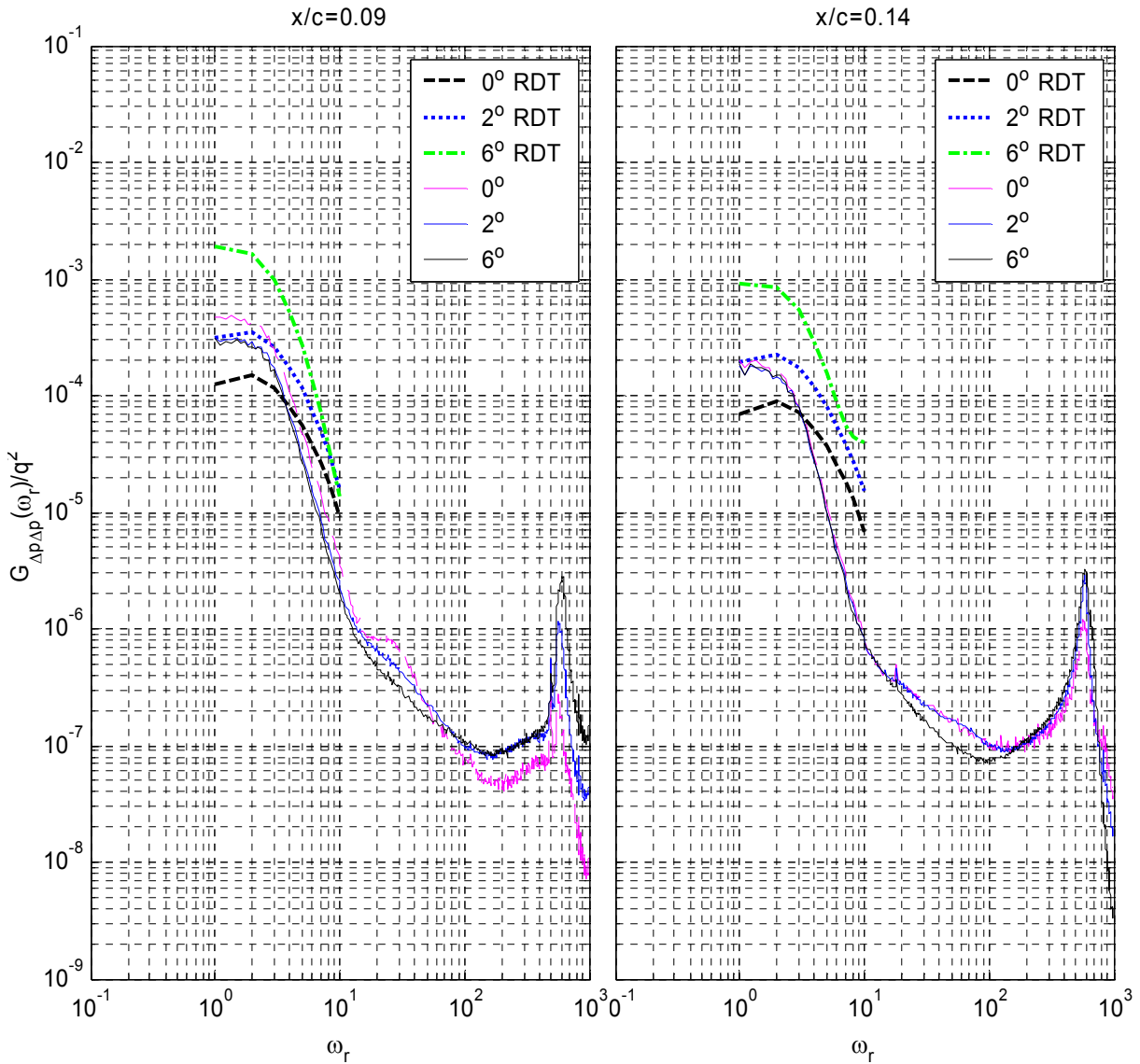


Figure 5.2 continued: Predictions of pressure difference spectra from the Rapid Distortion Theory of Reba and Kerschen (1996) plotted with measured data for $\alpha = 0^\circ, 2^\circ,$ and 6° at chordwise locations, $x/c = 1, 2.5, 4, 6, 9,$ and 14%

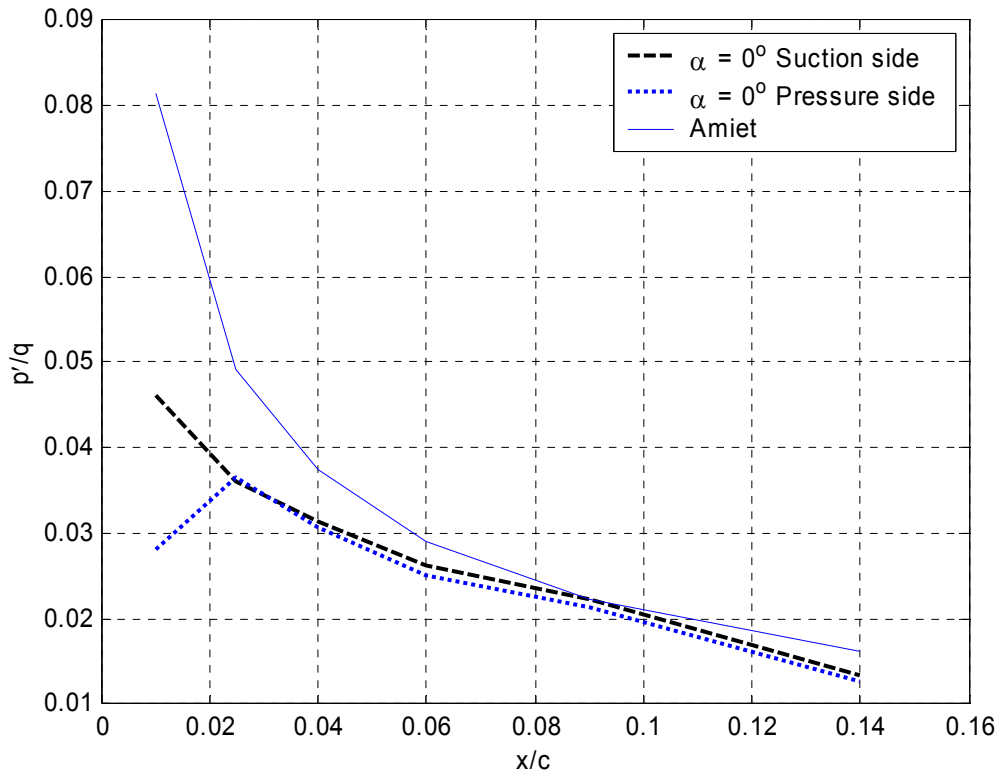


Figure 5.3: Pressure and suction side root mean squared of p as a function of x/c at $\alpha = 0^\circ$, formed from integrating pressure spectrum over $\omega_r = 0.4 - 100$. Comparison made with Amiet (1976a, b).

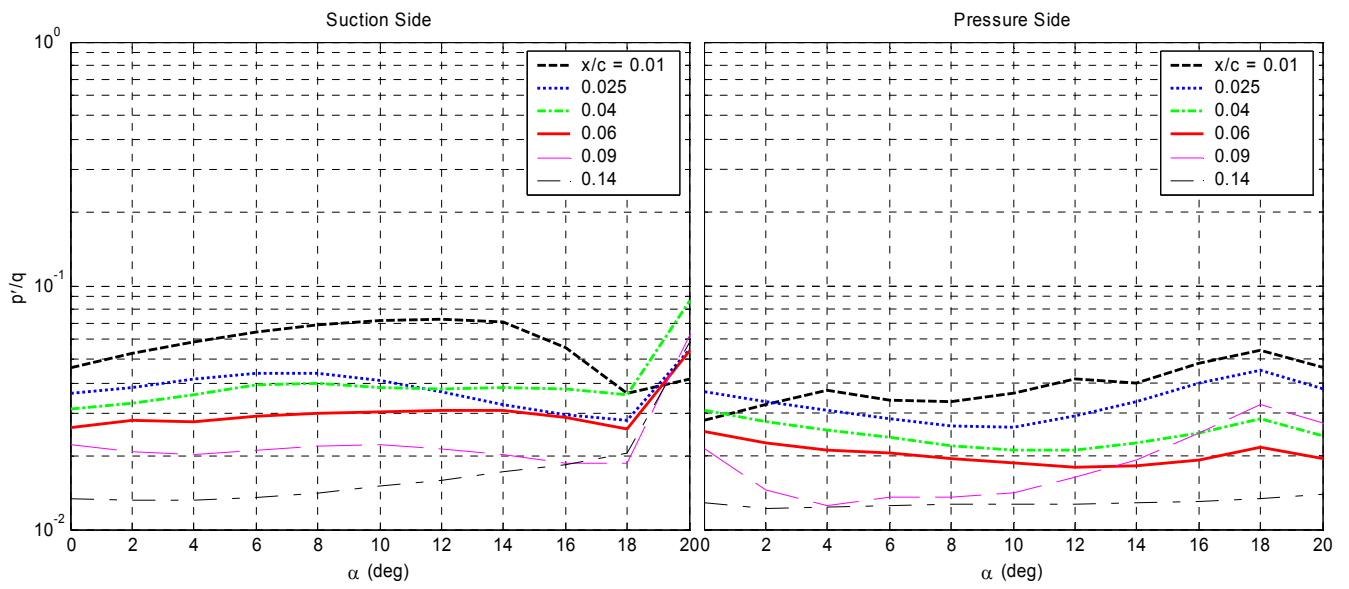


Figure 5.4: Pressure and suction side root mean squared of p as a function of angle of attack for $x/c = 0.01, 0.025, 0.04, 0.06, 0.09,$ and 0.14 .

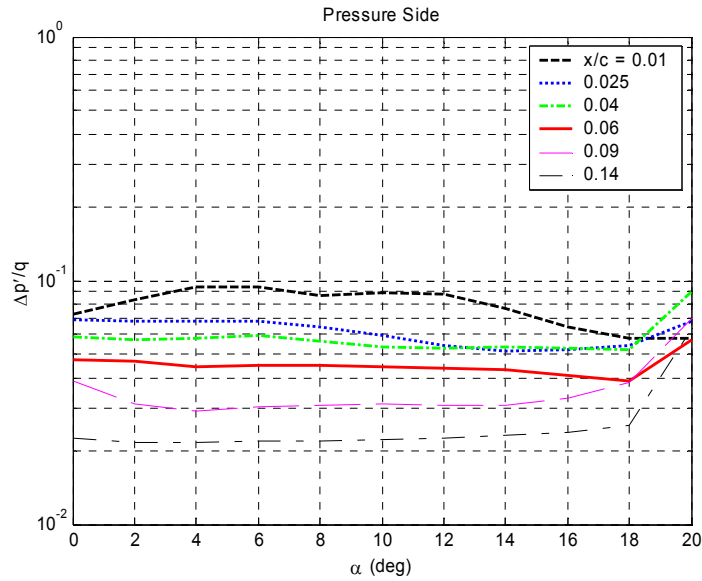


Figure 5.5: Large grid root mean square p computed from pressure difference spectra as a function of angle of attack for $x/c = 0.01, 0.025, 0.04, 0.06, 0.09,$ and 0.14

 = Microphones used in unsteady lift calculation

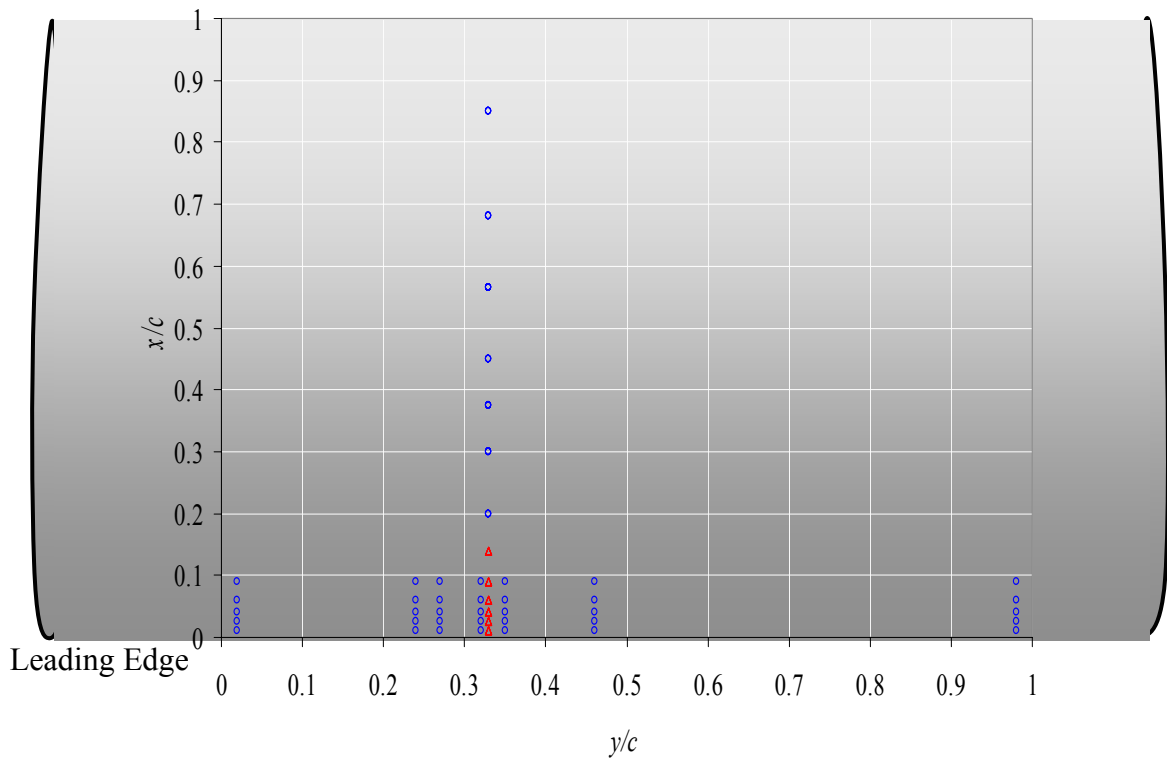


Figure 5.6: Microphones used in unsteady lift calculation indicated by triangle symbol

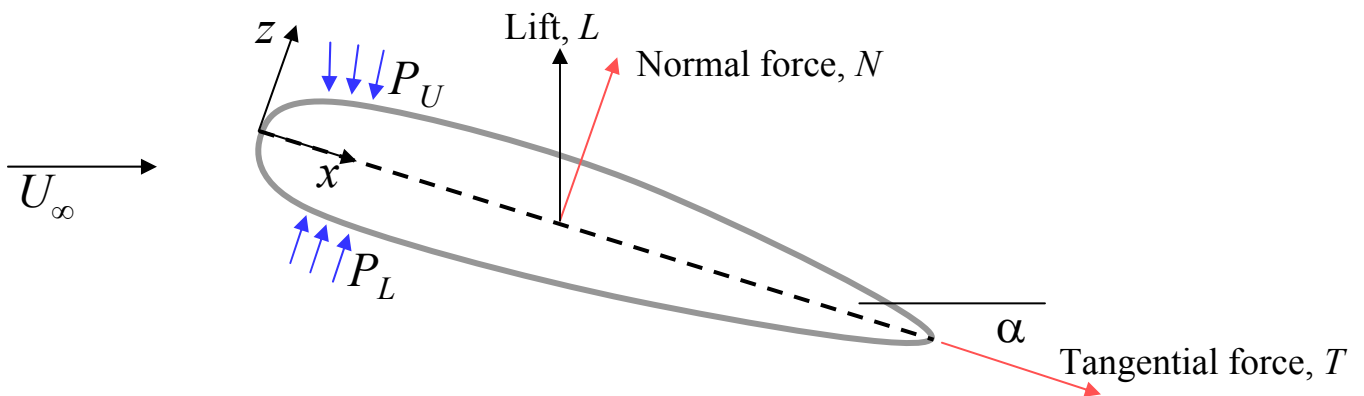


Figure 5.7: Resolving unsteady pressure into lift

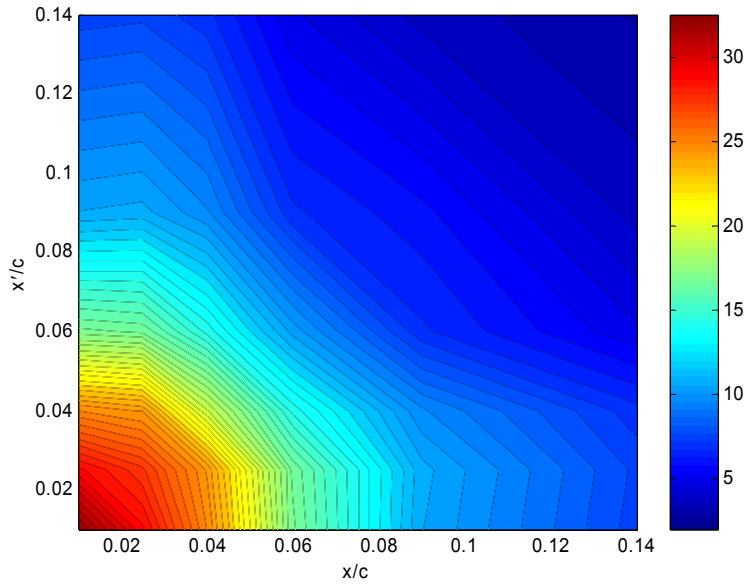


Figure 5.8: $G_{\Delta P \Delta P}(\omega, x, x') = G_{\Delta P \Delta P}(3, x, x')$ showing the variation of the pressure difference cross-spectra in x

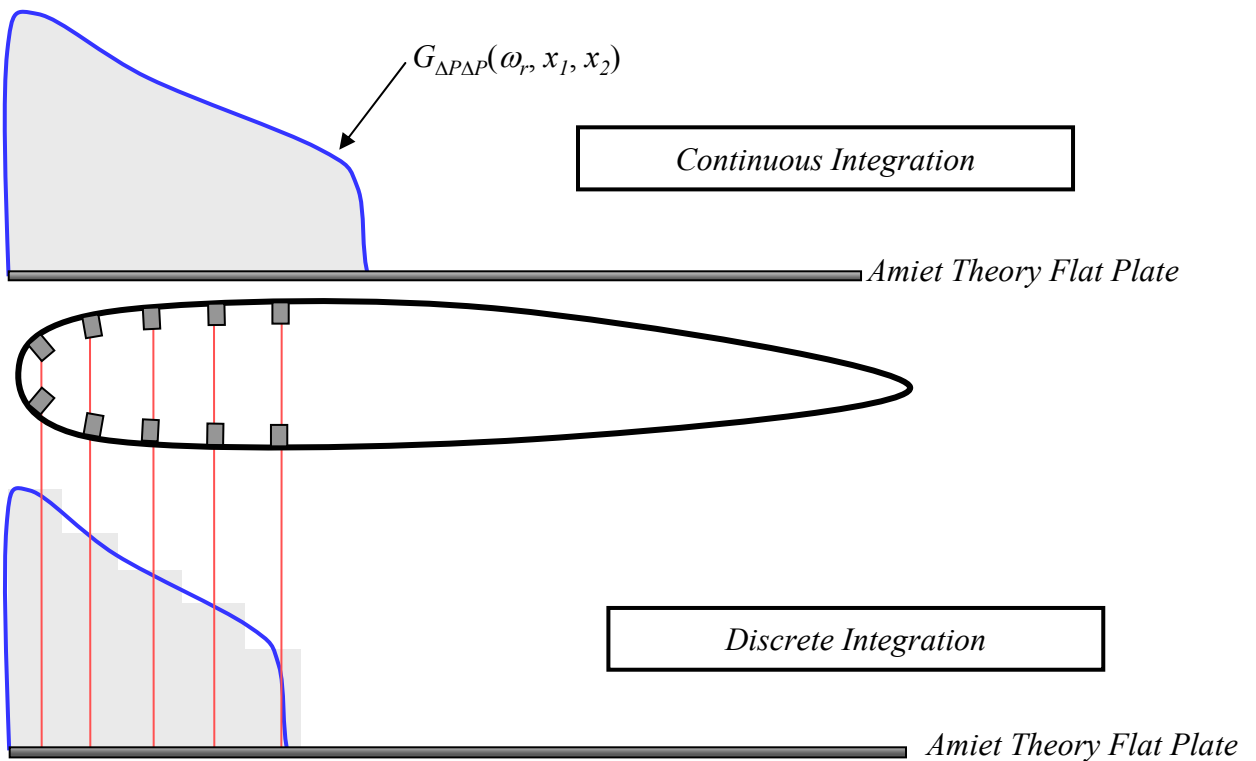


Figure 5.9: Depiction illustrating how Amiet's Thin Airfoil Theory is used to assess errors related to discretizing lift spectra equations

Large Grid Flow

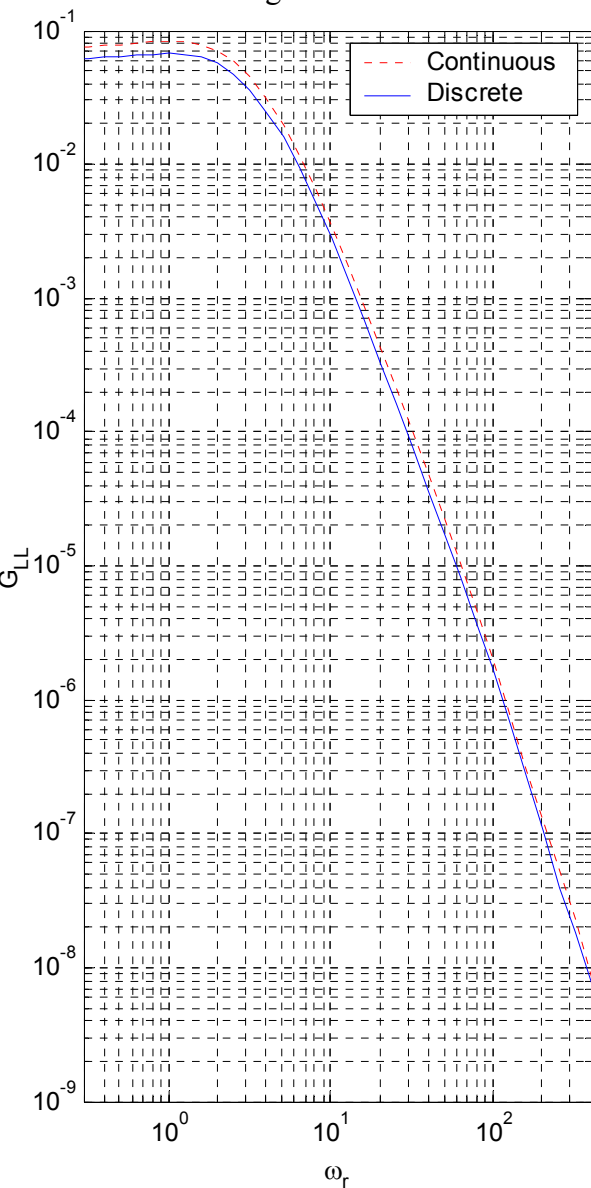


Figure 5.10: Continuous and discrete calculations of unsteady lift using Amiet's theory

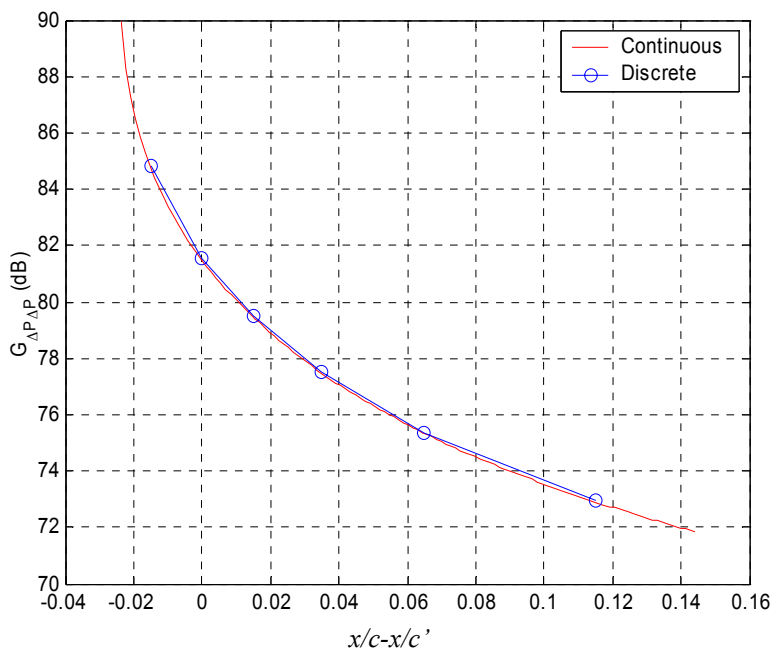


Figure 5.11: $G_{\Delta P \Delta P}$ at $x/c = 2.5\%$, $\omega_r = 10$ from Amiet's theory computed continuously and discretely, plotted against all other chordwise locations

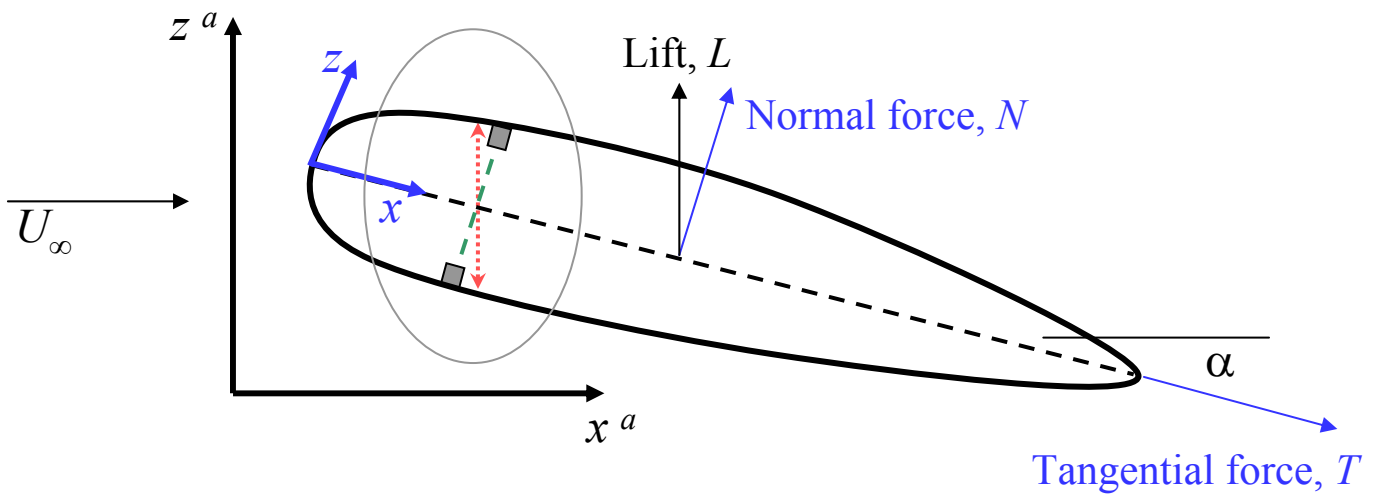


Figure 5.12a: Depiction of coordinate transformation used to form unsteady lift

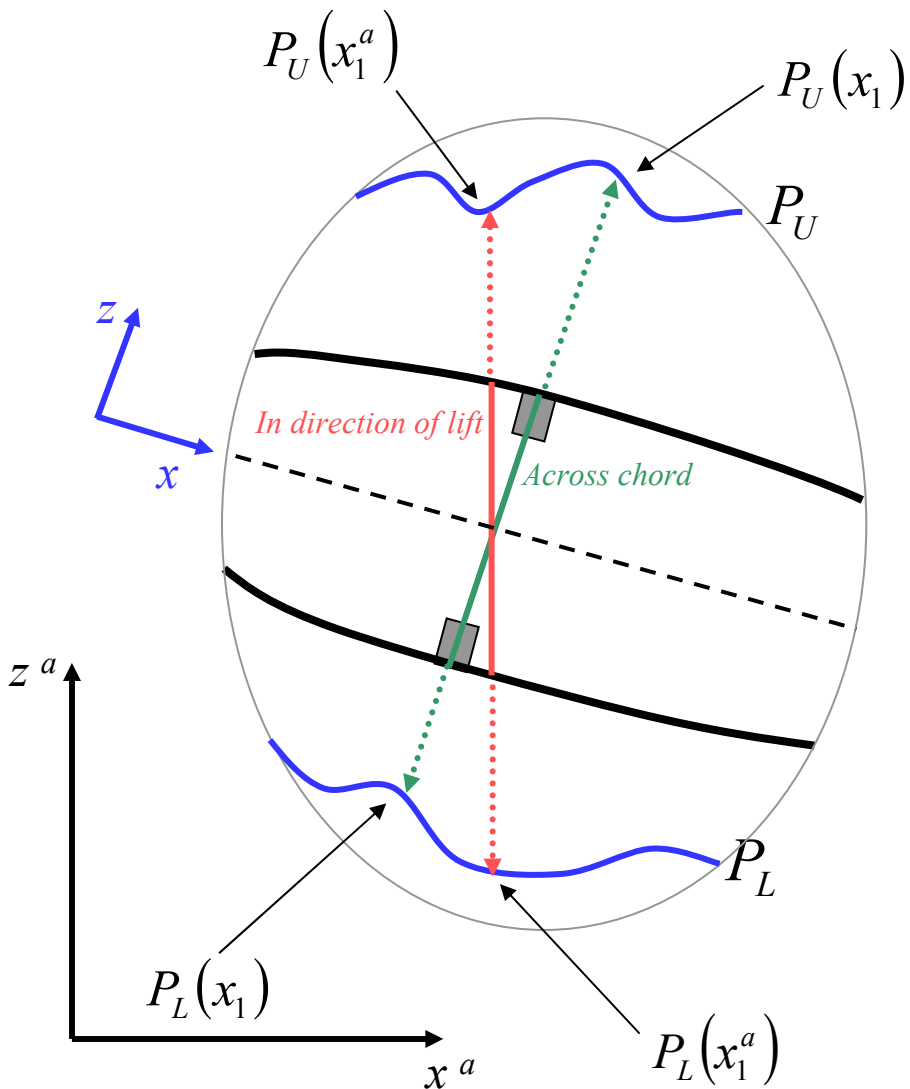


Figure 5.12b: Depiction of coordinate transformation used to form unsteady lift

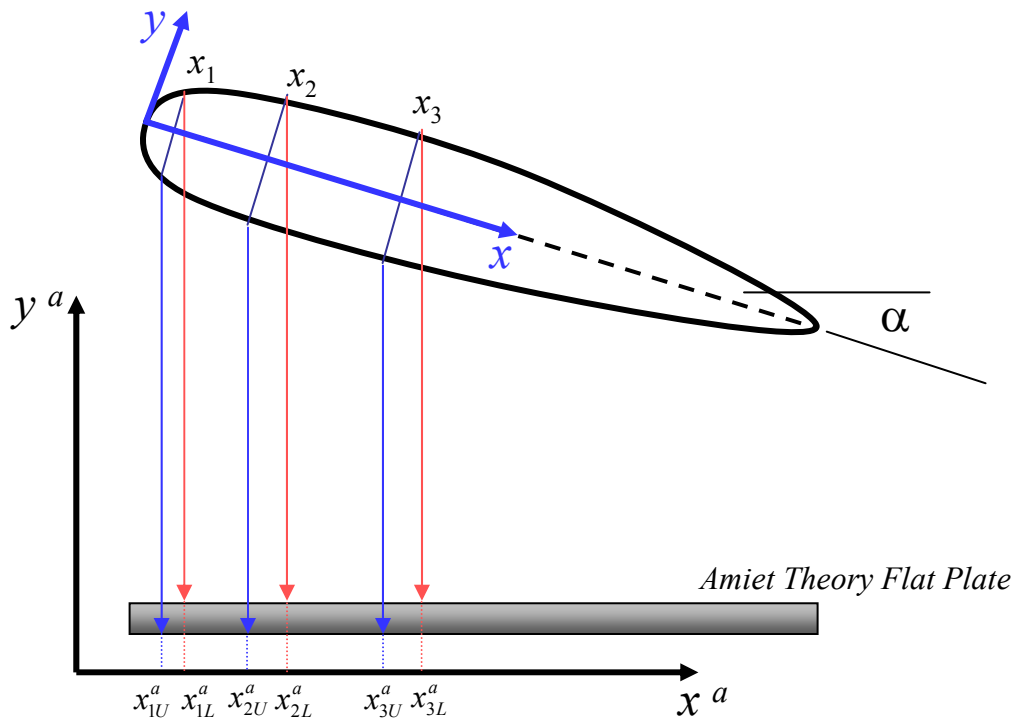


Figure 5.13: Projection of microphone locations into flow aligned coordinate system for Amiet thin airfoil theory simulation

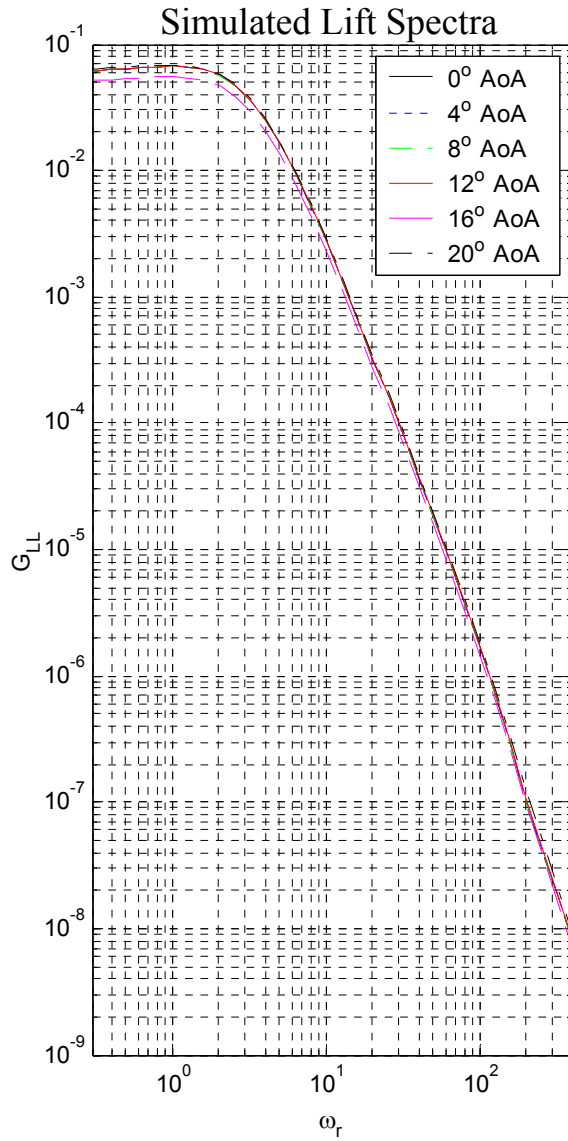


Figure 5.14: Unsteady lift computed from Amiet simulation shown for each angle of attack

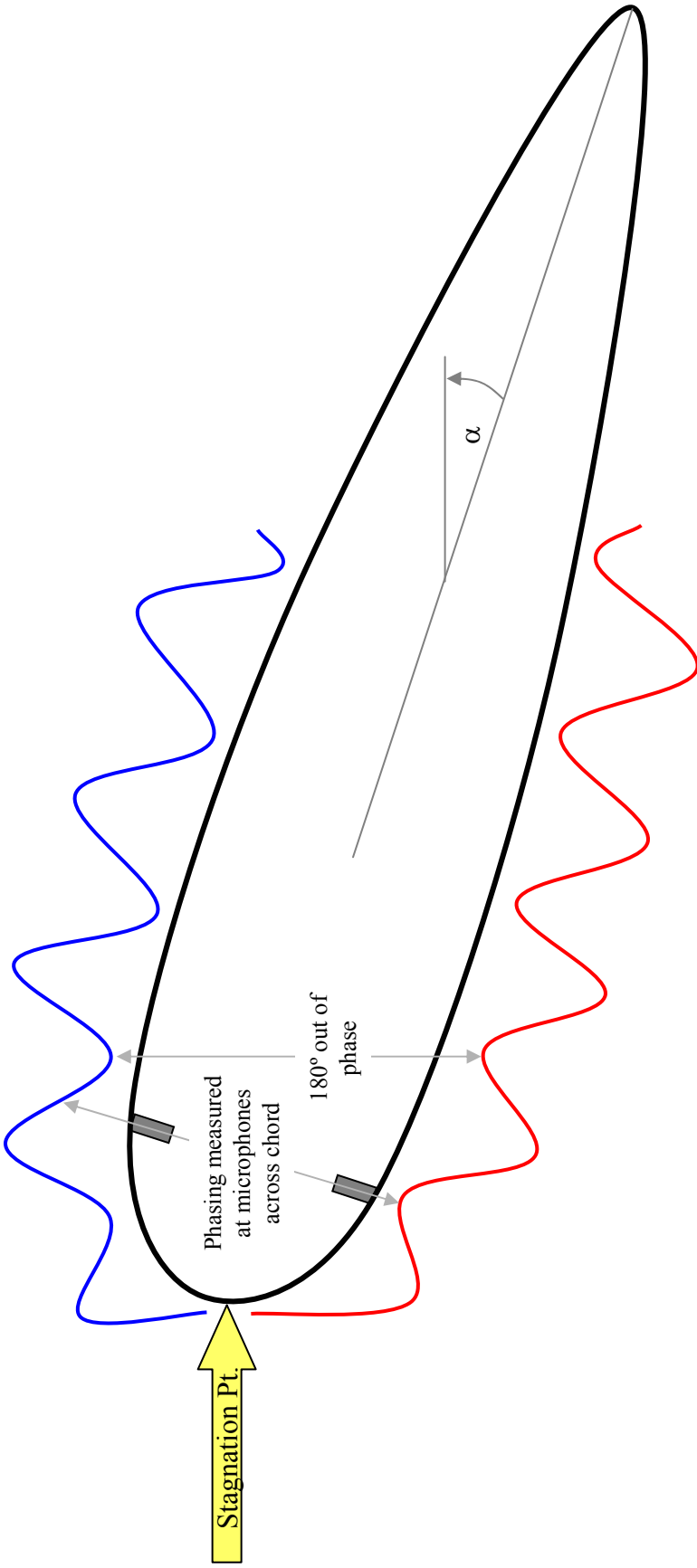


Figure 5.15: Drawing showing phase shift in pressure when airfoil is at non-zero angle of attack

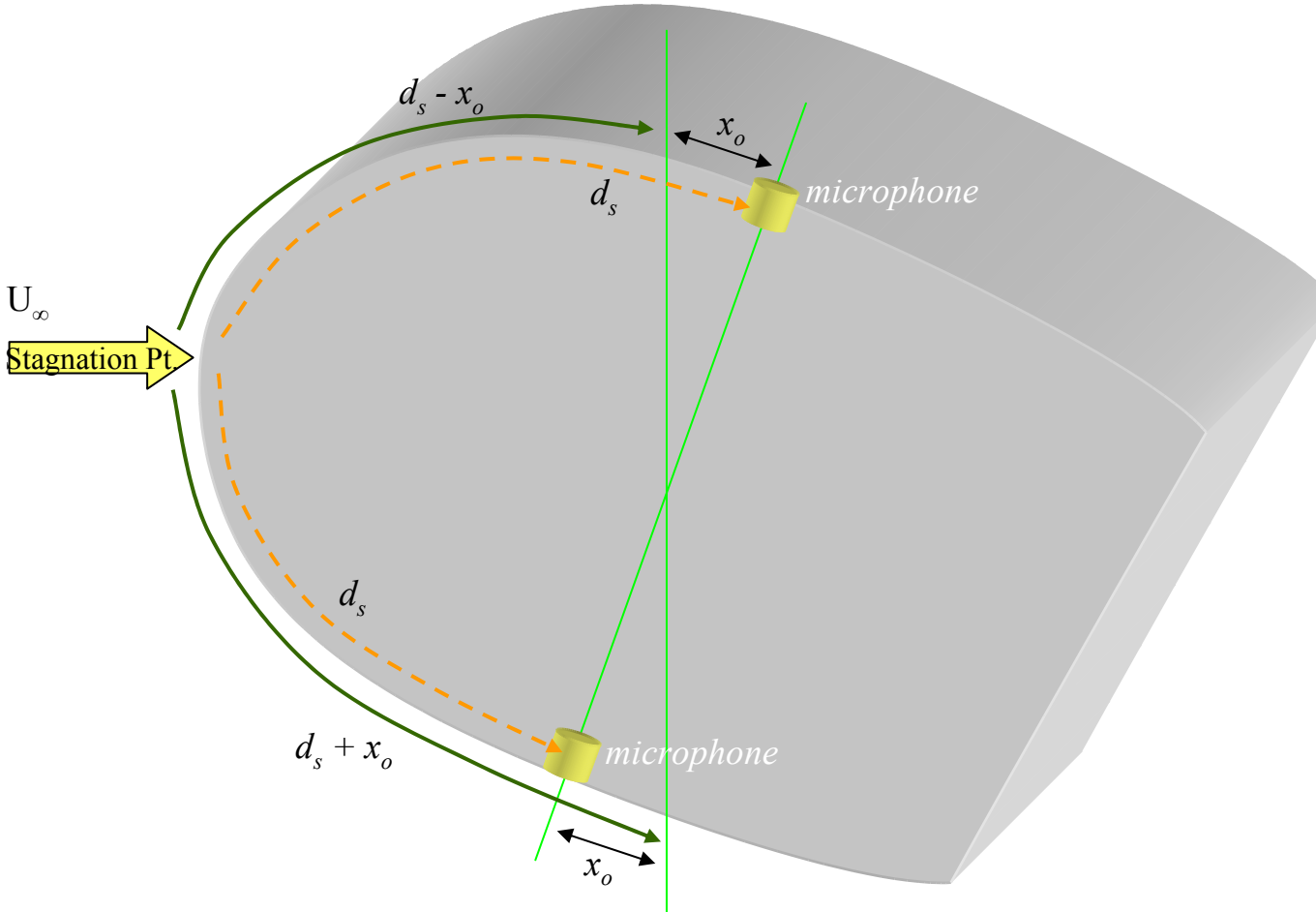


Figure 5.16: Geometry of phasing model

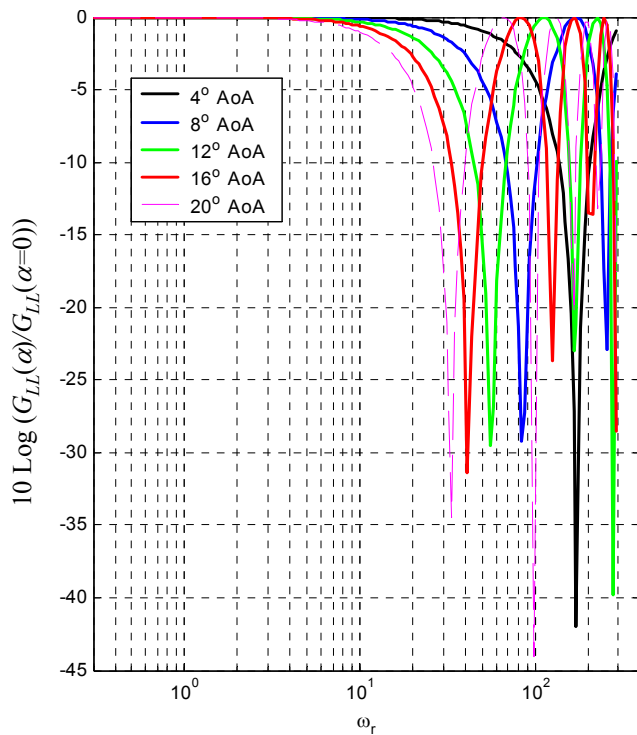


Figure 5.17: Ratio of unsteady lift at non-zero angle of attack to zero angle of attack unsteady lift based on phasing model

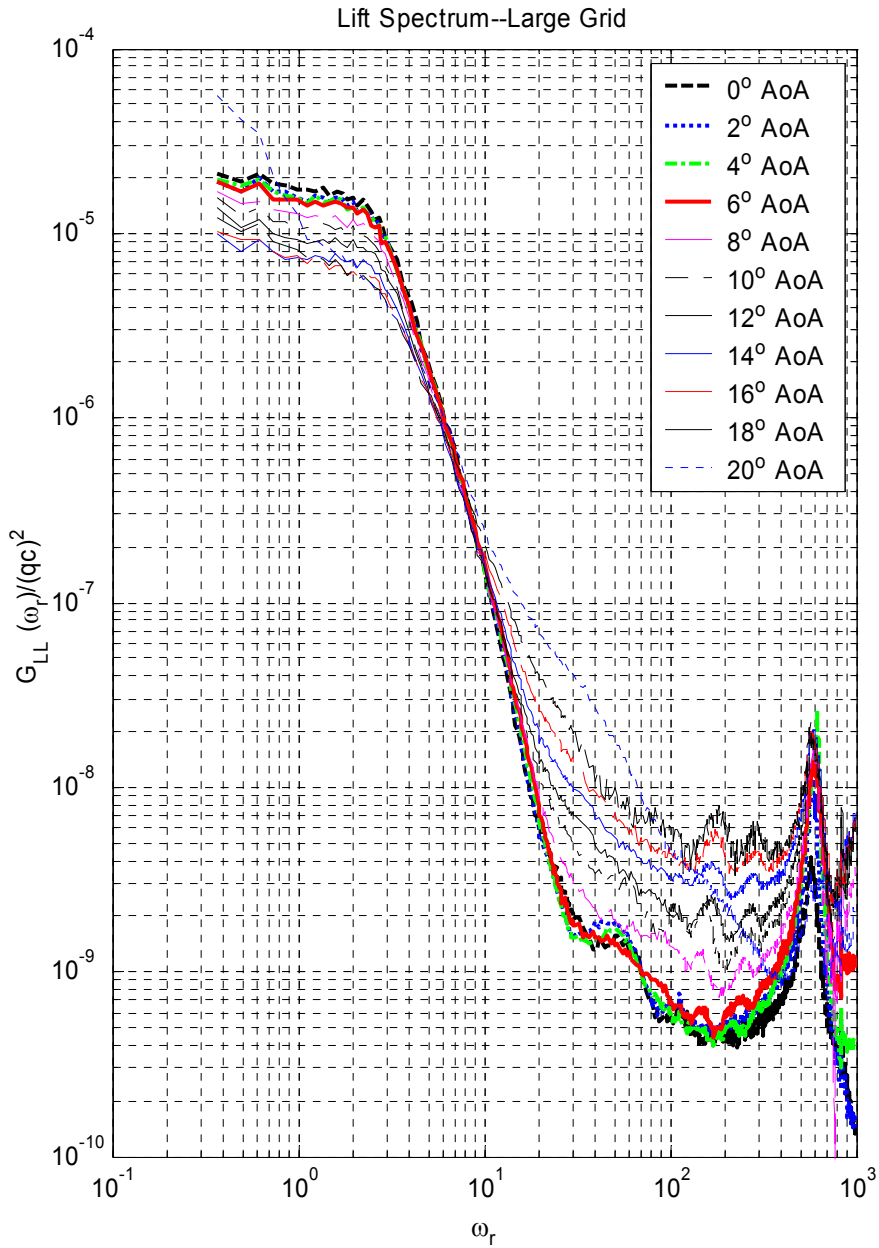


Figure 5.18: Unsteady lift calculate from measured unsteady pressure in large grid turbulence

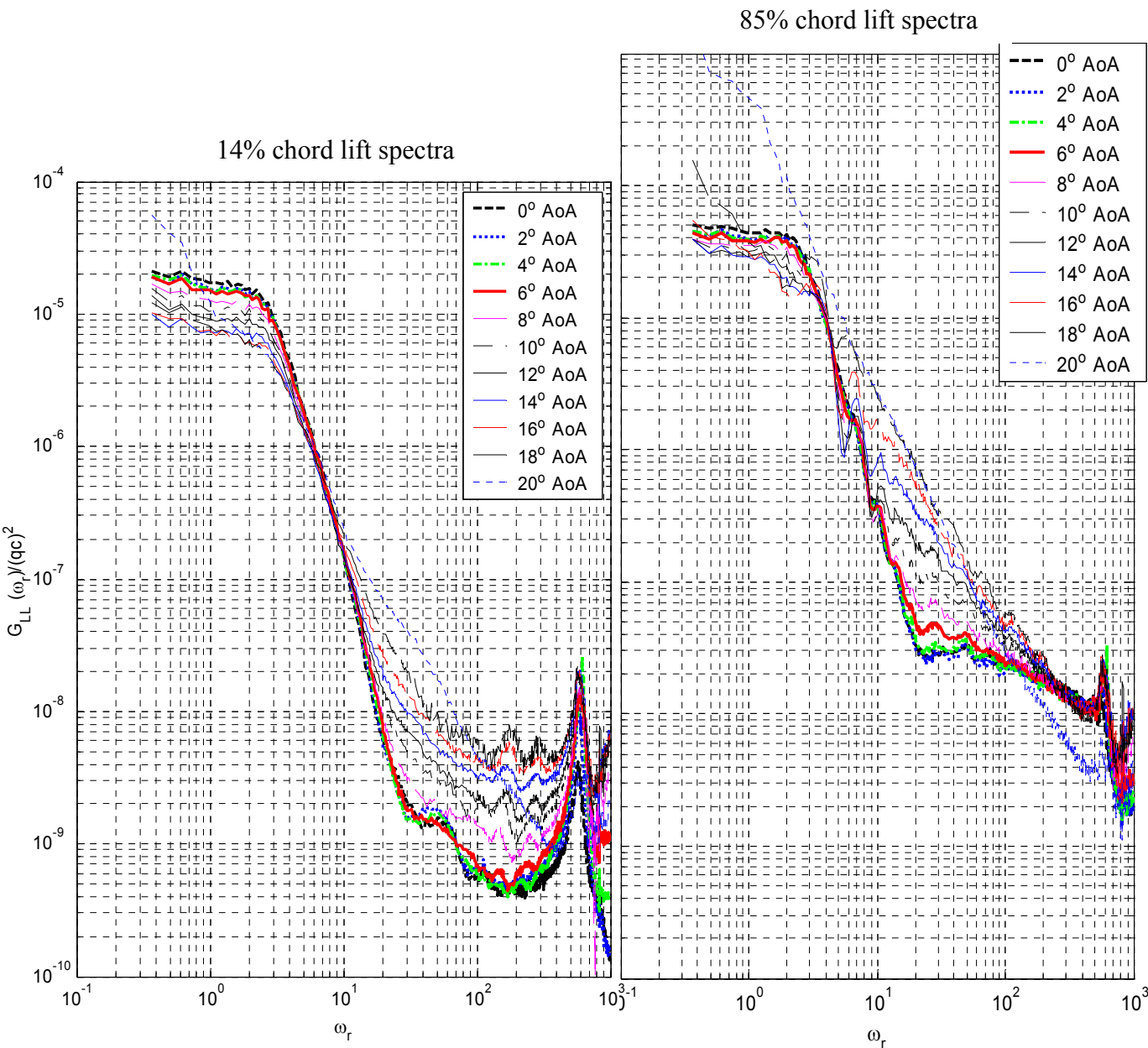


Figure 5.19: Large grid unsteady lift calculated using pressure measurements from the first 14% and the first 85% chord

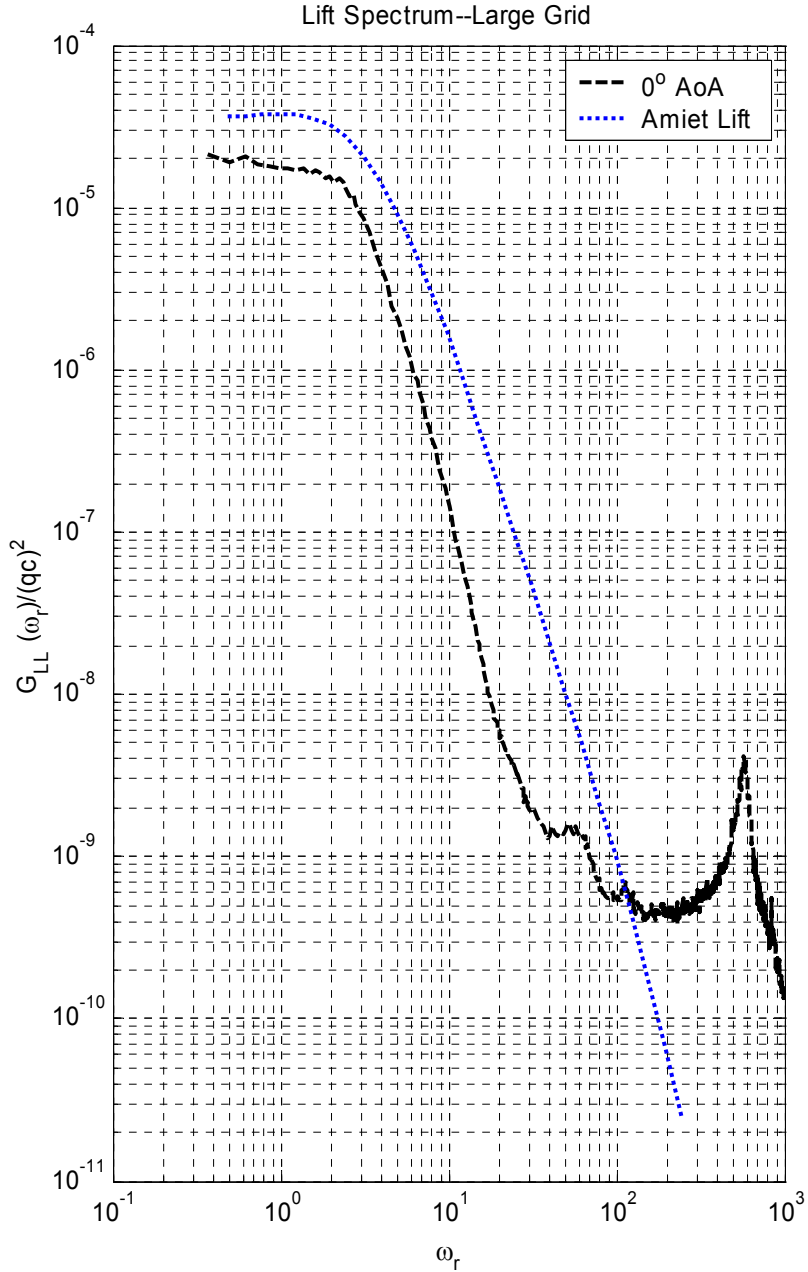


Figure 5.20: Unsteady lift calculated from high angle of attack resolution data for *large* grid turbulence at $\alpha = 0^\circ$ compared with that predicted from Amiet’s (1976a, b) theory.

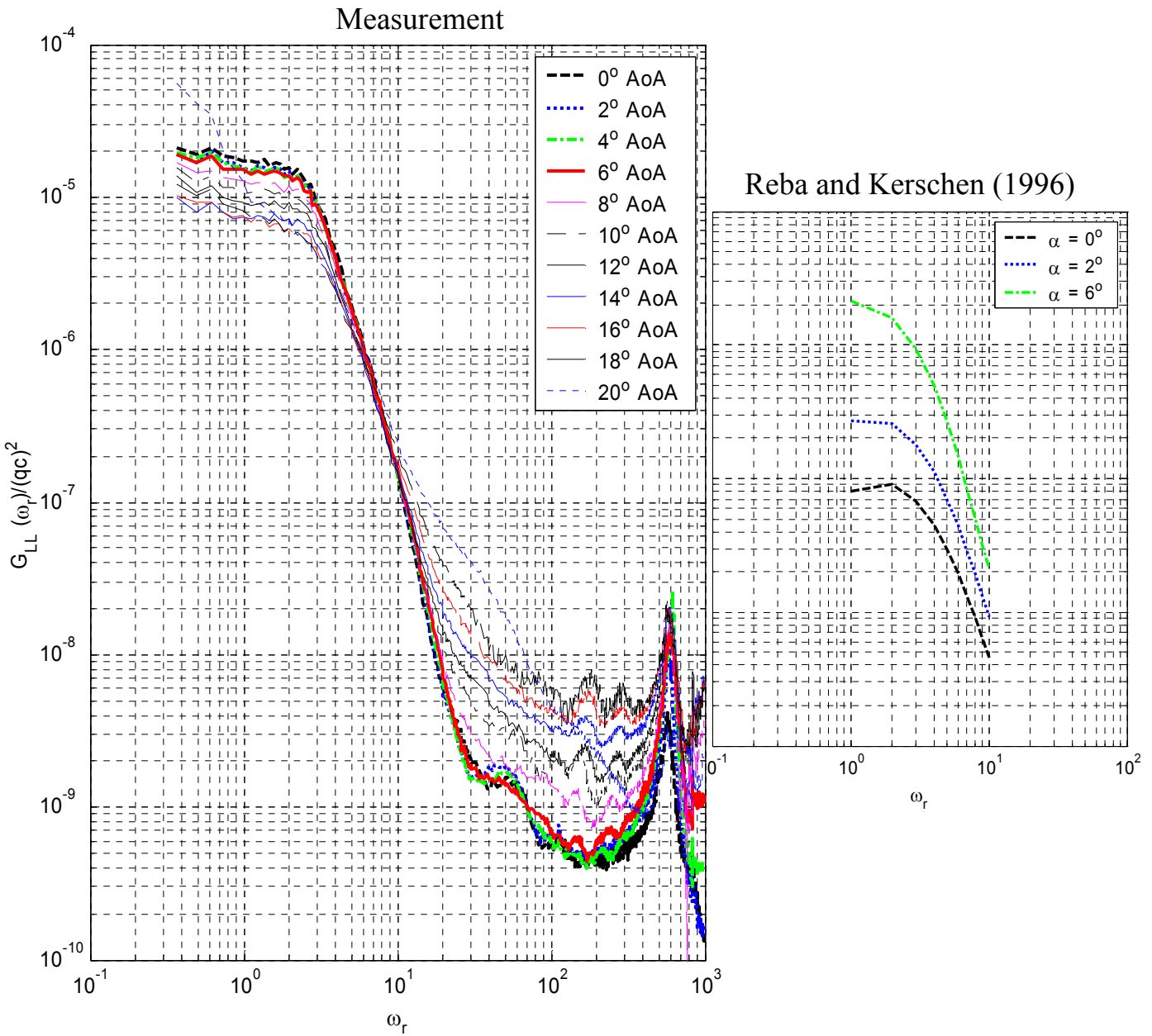


Figure 5.21: Unsteady lift calculated from pressure measurements compared with lift computed from Reba and Kerschens (1996) unsteady response theory.

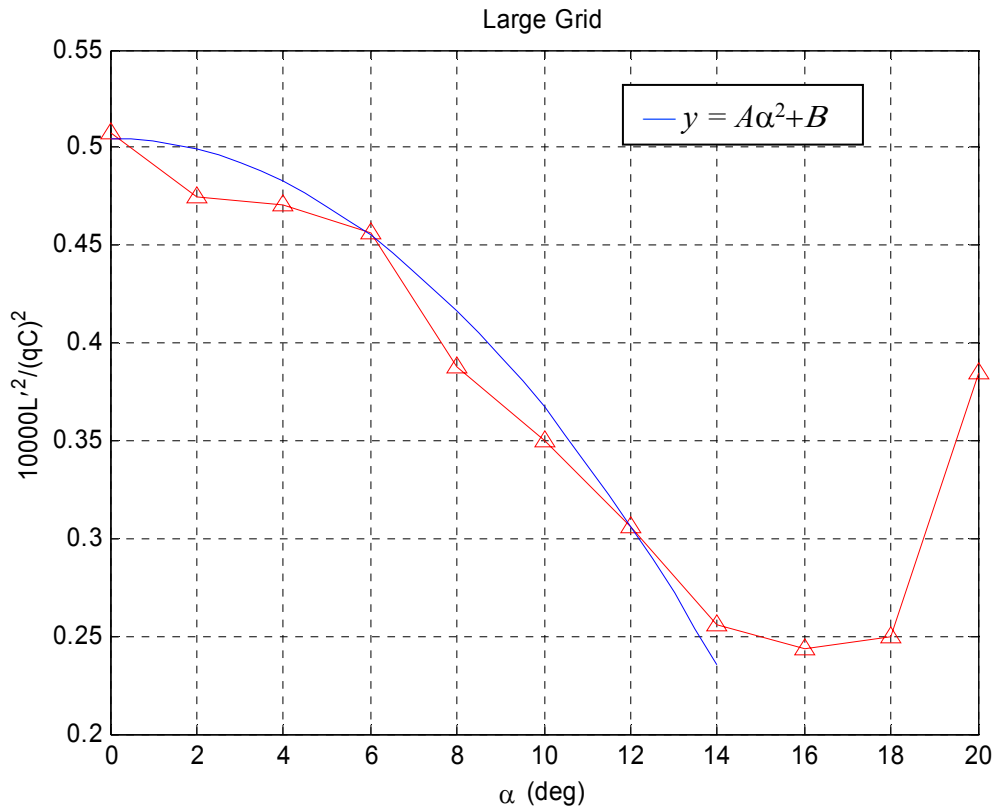


Figure 5.22: Measured L'^2 as a function of angle of attack compared with a curve representing α^2

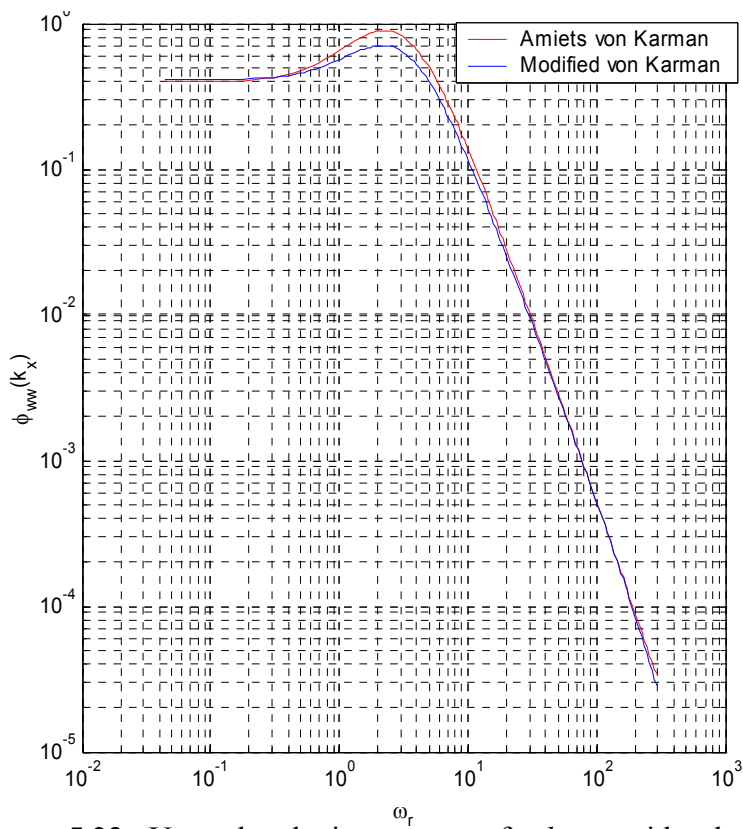


Figure 5.23: Upwash velocity spectrum for *large* grid turbulence

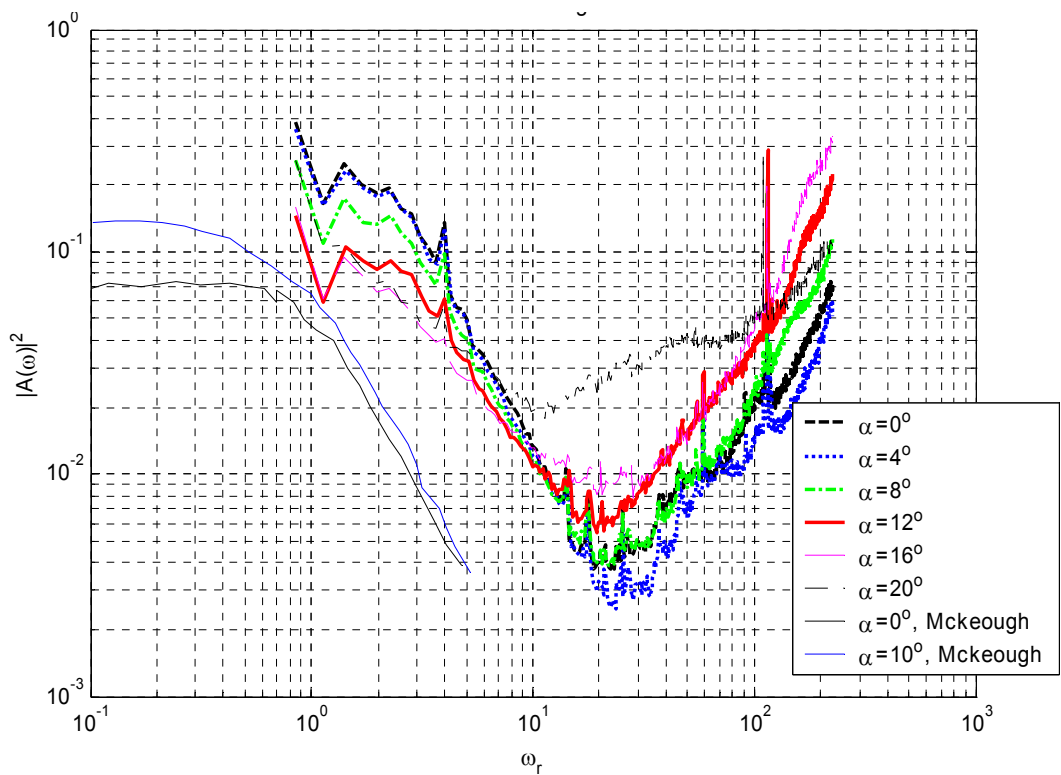


Figure 5.24: Admittance function calculated from unsteady pressure measurements compared with McKeough's (1976) measurements

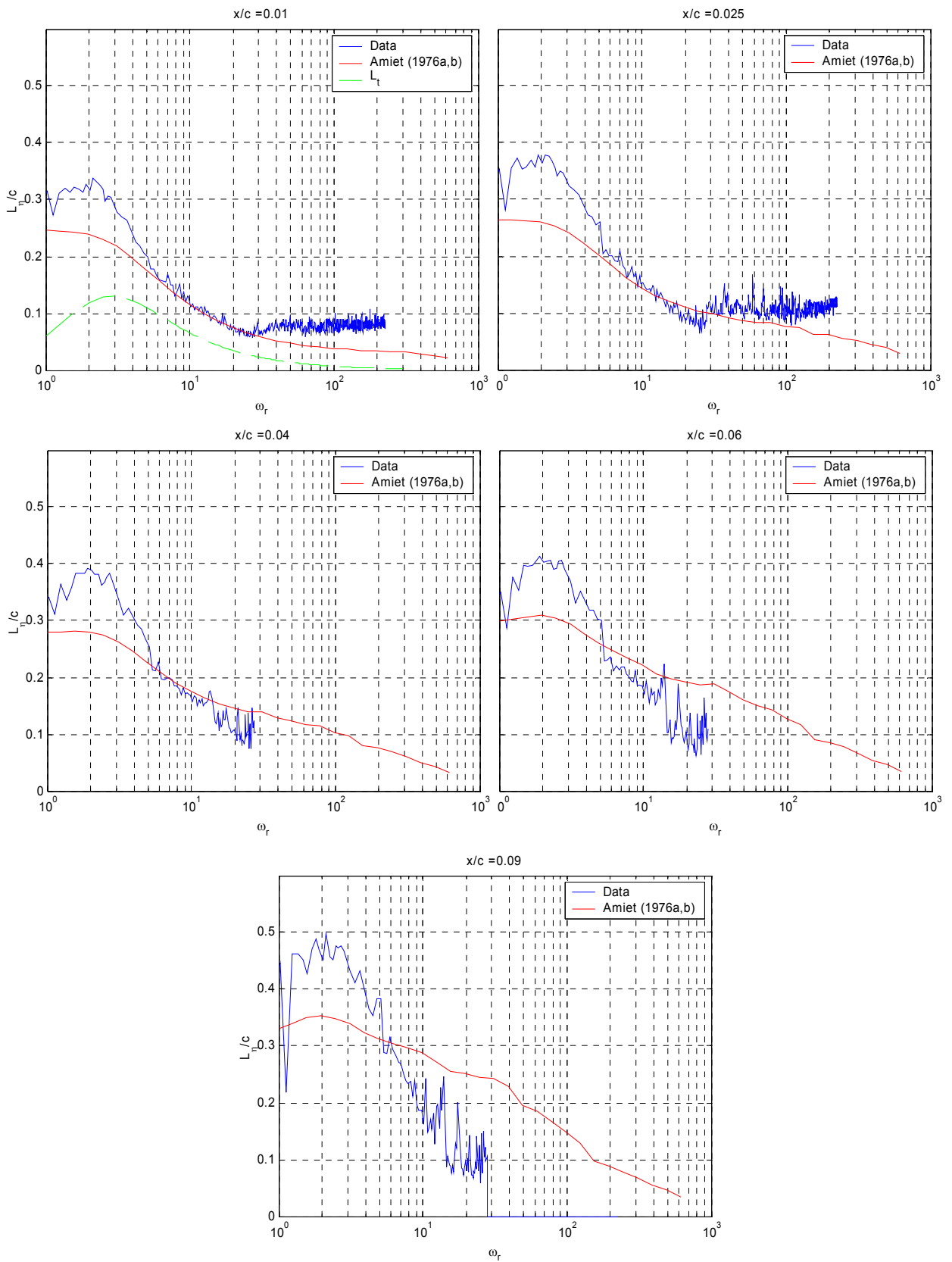


Figure 5.25: Comparison of measured and predicted *spanwise* correlation length scales, $\alpha = 0^\circ$

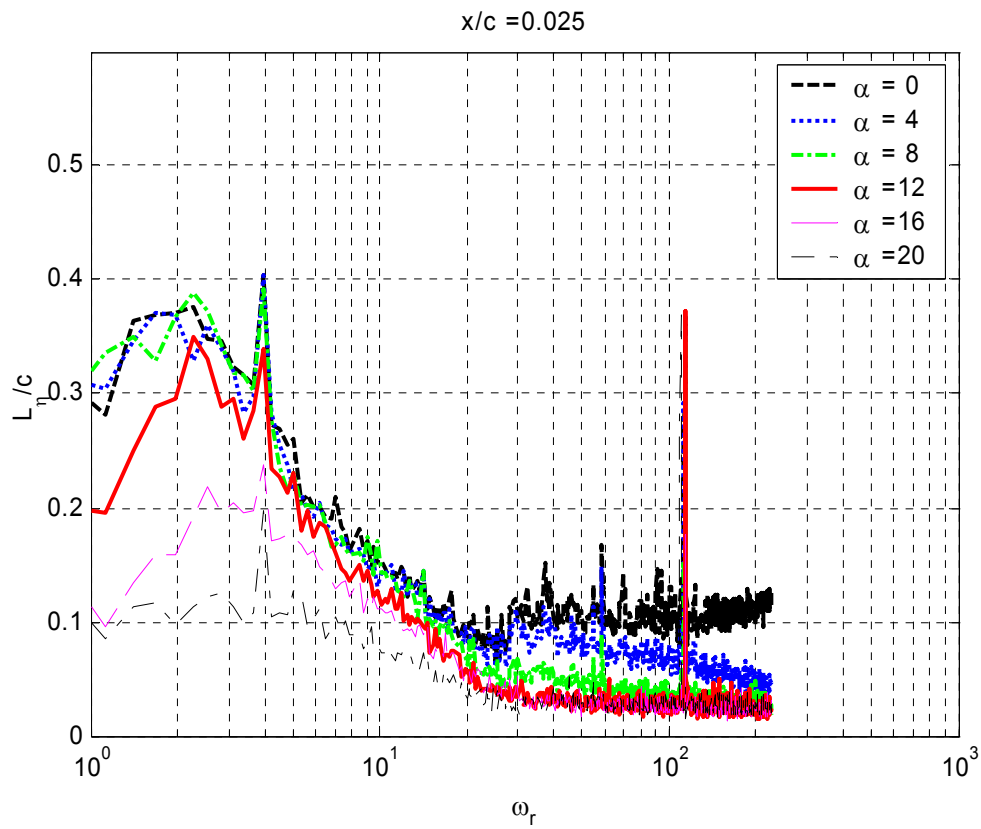
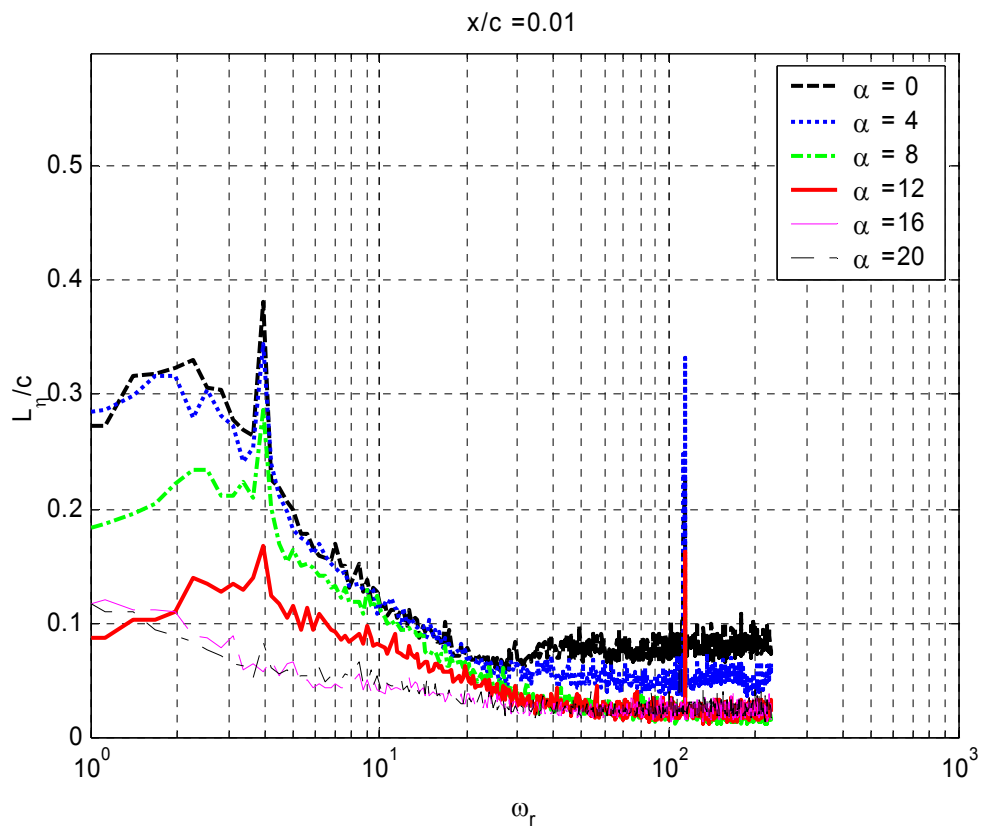


Figure 5.26: Effects of angle of attack on *spanwise* correlation length scales at $x/c = 1$ and 2.5% chord

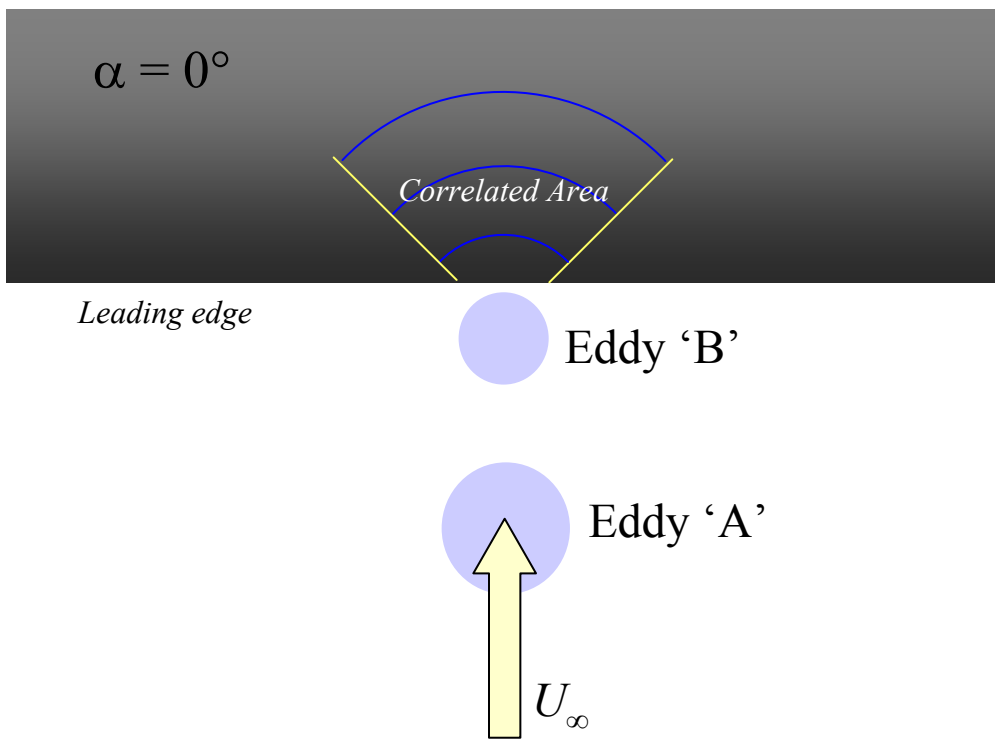


Figure 5.27a: Top down view of airfoil at $\alpha = 0^\circ$ showing the reduction in cross-sectional area of an eddy encountering an airfoil as a result of eddy stretching by the mean potential field.

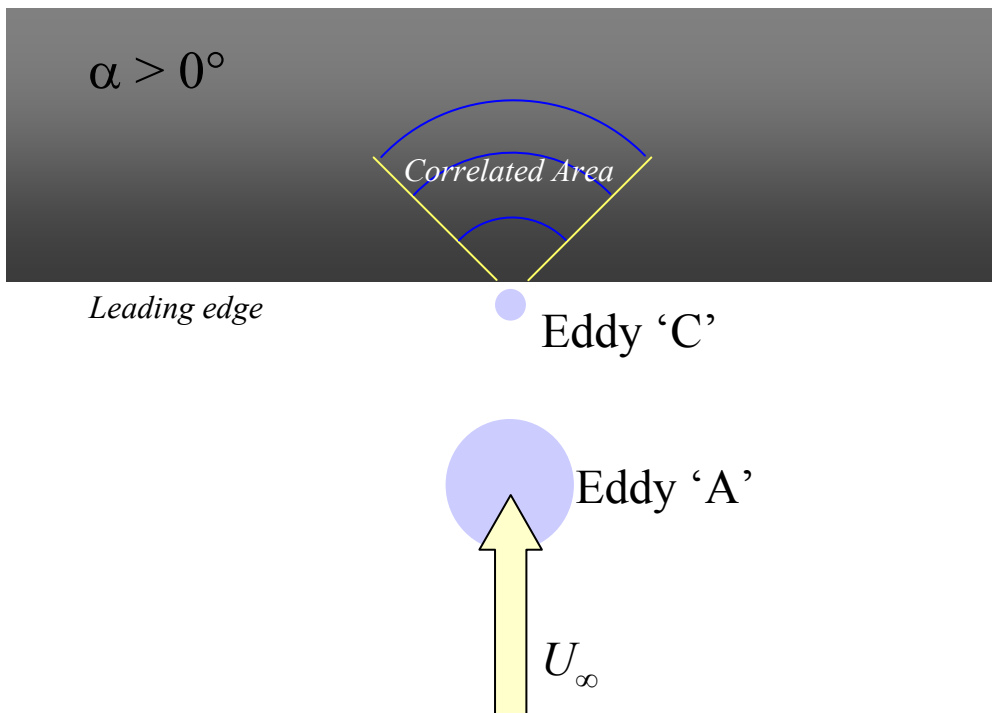


Figure 5.27b: Top down view of airfoil at $\alpha > 0^\circ$ showing the significant reduction in cross-sectional area of an eddy encountering an airfoil as a result of eddy stretching by the mean potential field.

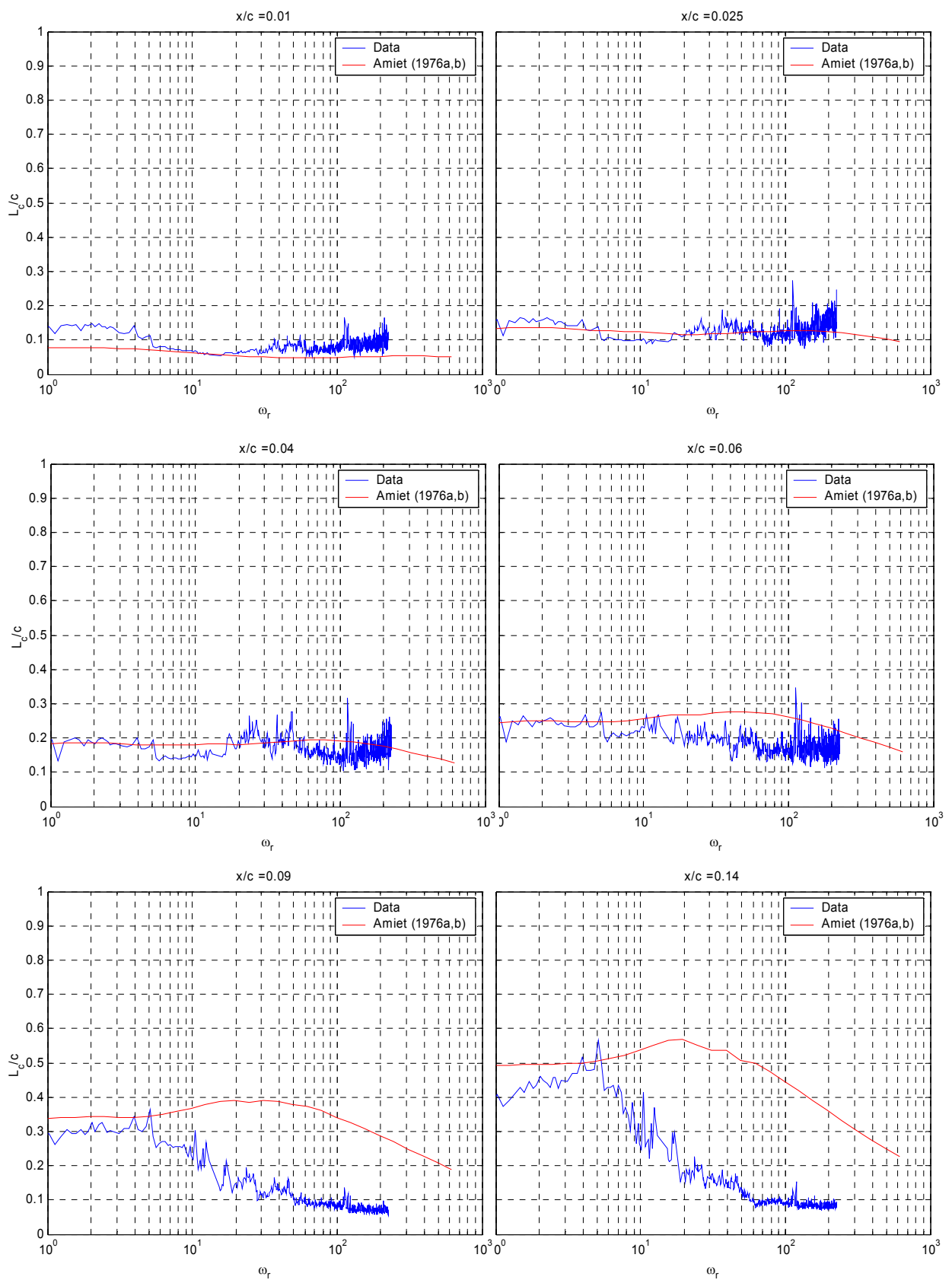


Figure 5.28: Comparison of measured and predicted *chordwise* correlation length scales, $\alpha = 0^\circ$

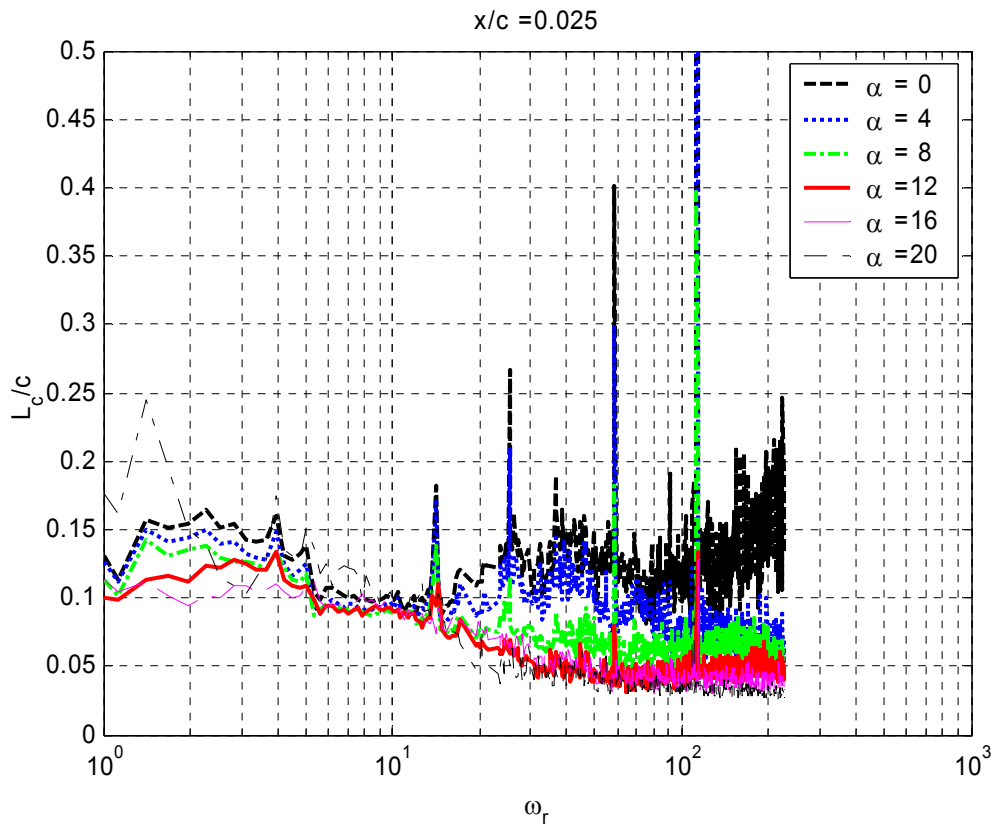
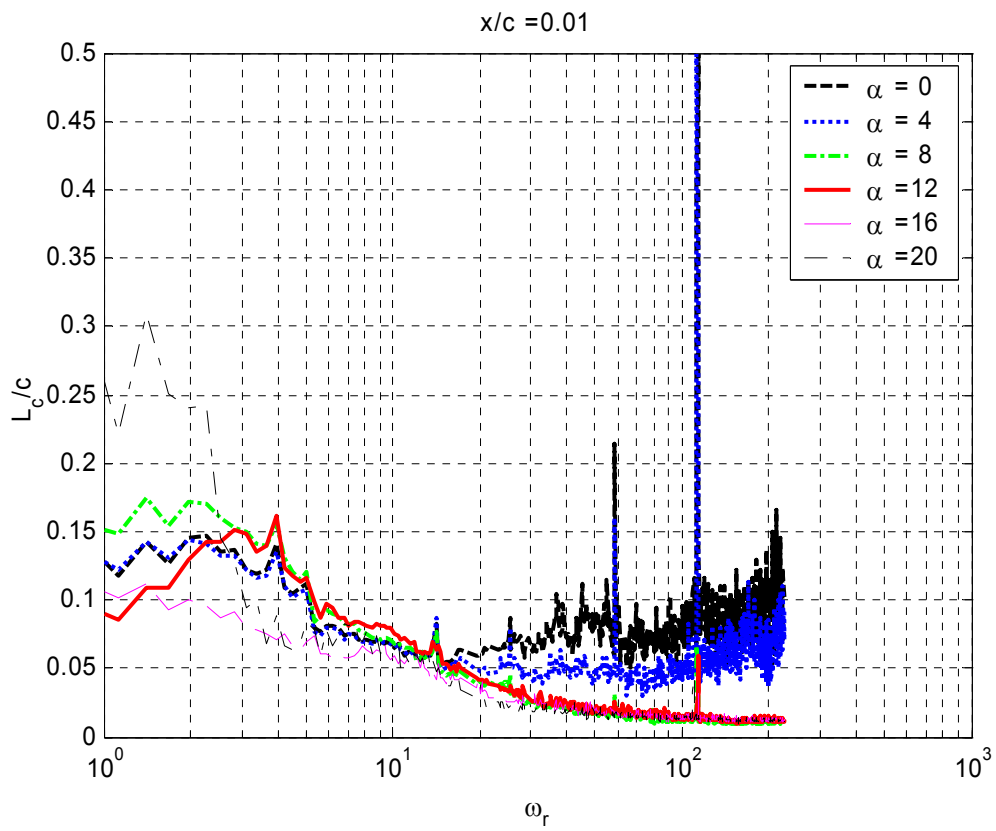


Figure 5.29: Effects of angle of attack on *chordwise* correlation length scales at $x/c = 1$ and 2.5% chord

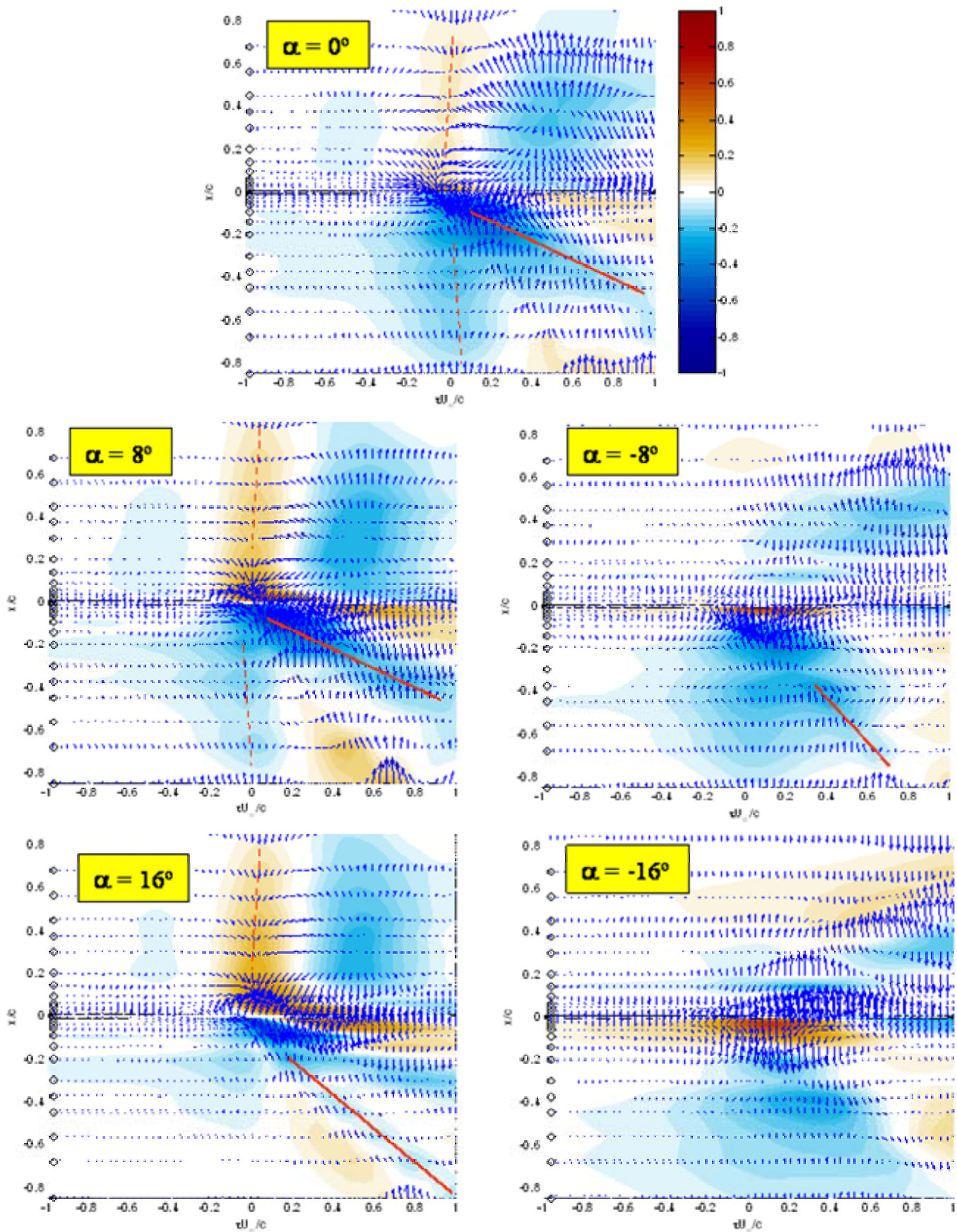


Figure 5.30: Contour plots of pressure-velocity correlation function, $R_{pv}(x=14\%, x', \tau)$

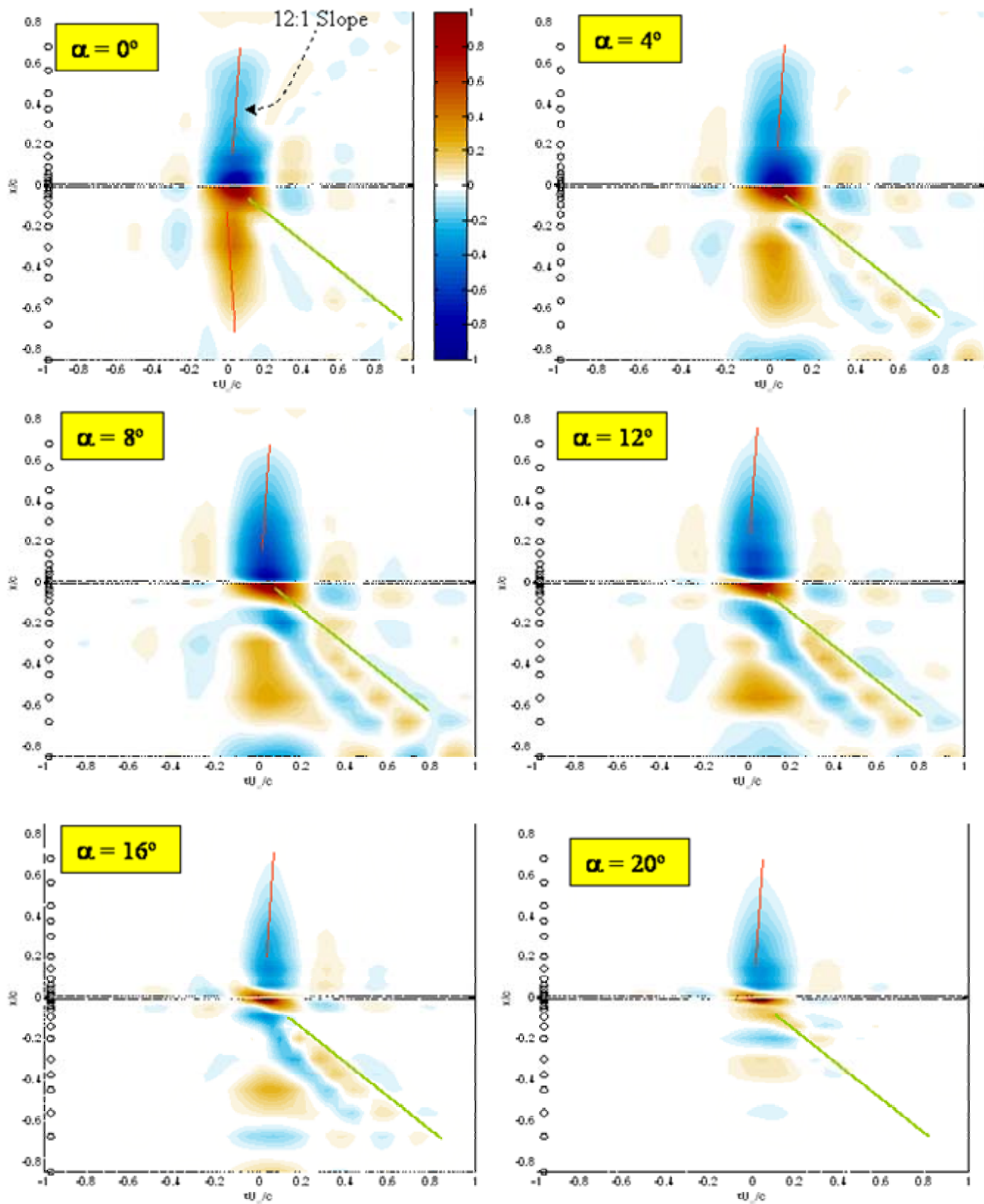


Figure 5.31: Contour plots of $R_{pp}(x=1\%, x', \tau)$ with trailing edge modification installed

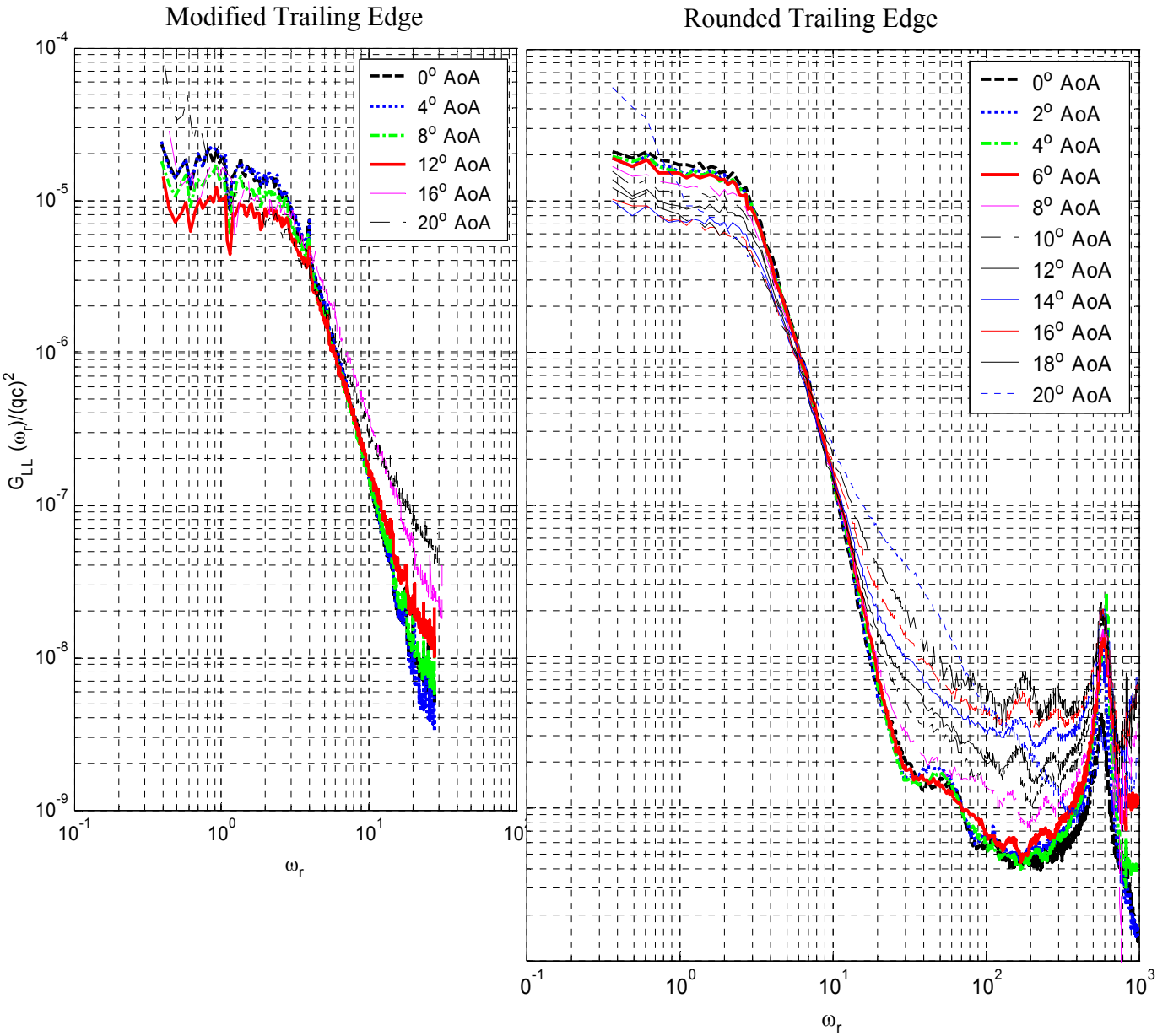


Figure 5.32: Unsteady lift calculate with and without the modified trailing edge

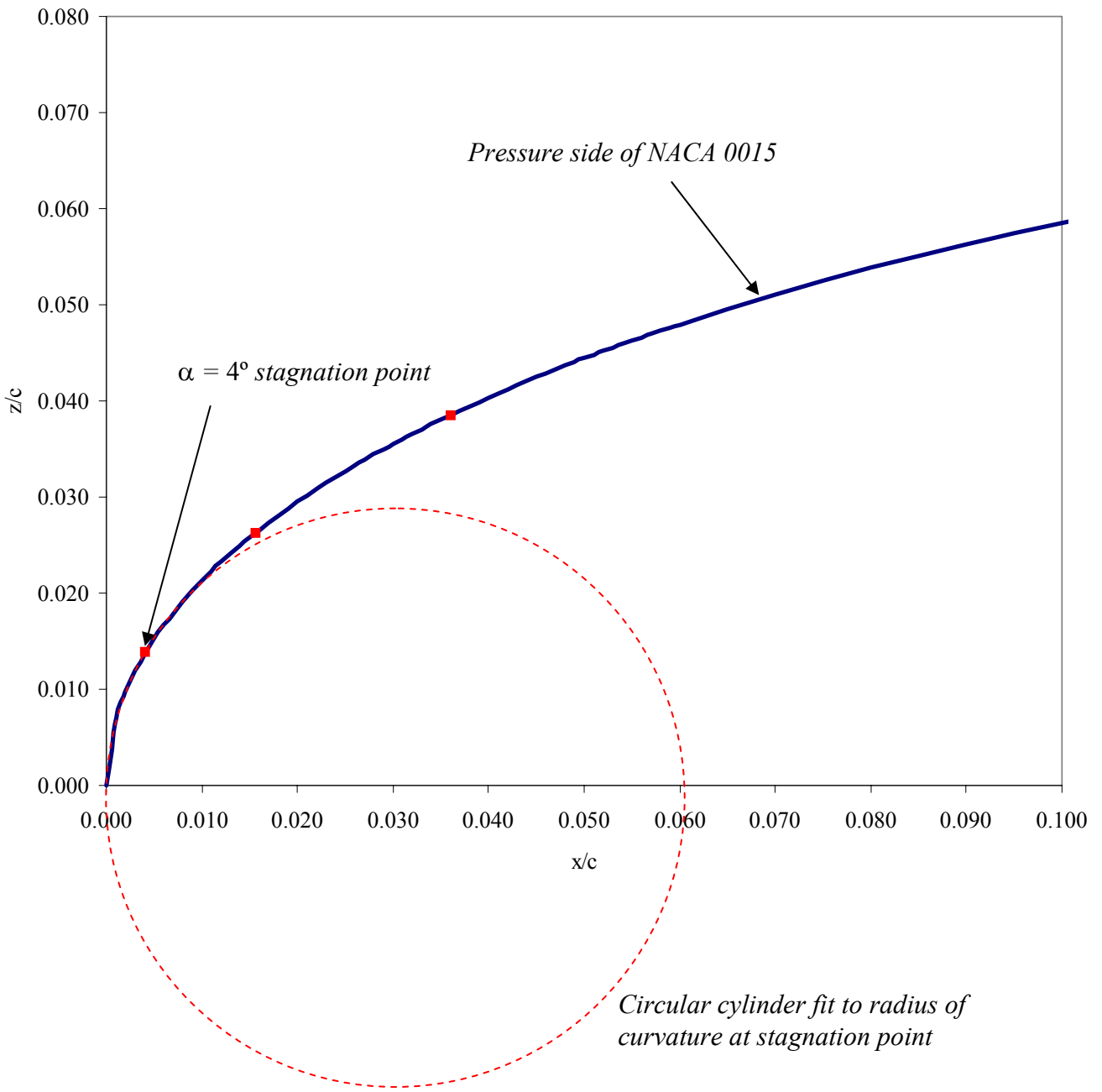


Figure 5.33: Diagram showing a circular cylinder fit to the airfoils radius of curvature at the $\alpha = 4^\circ$ stagnation point location

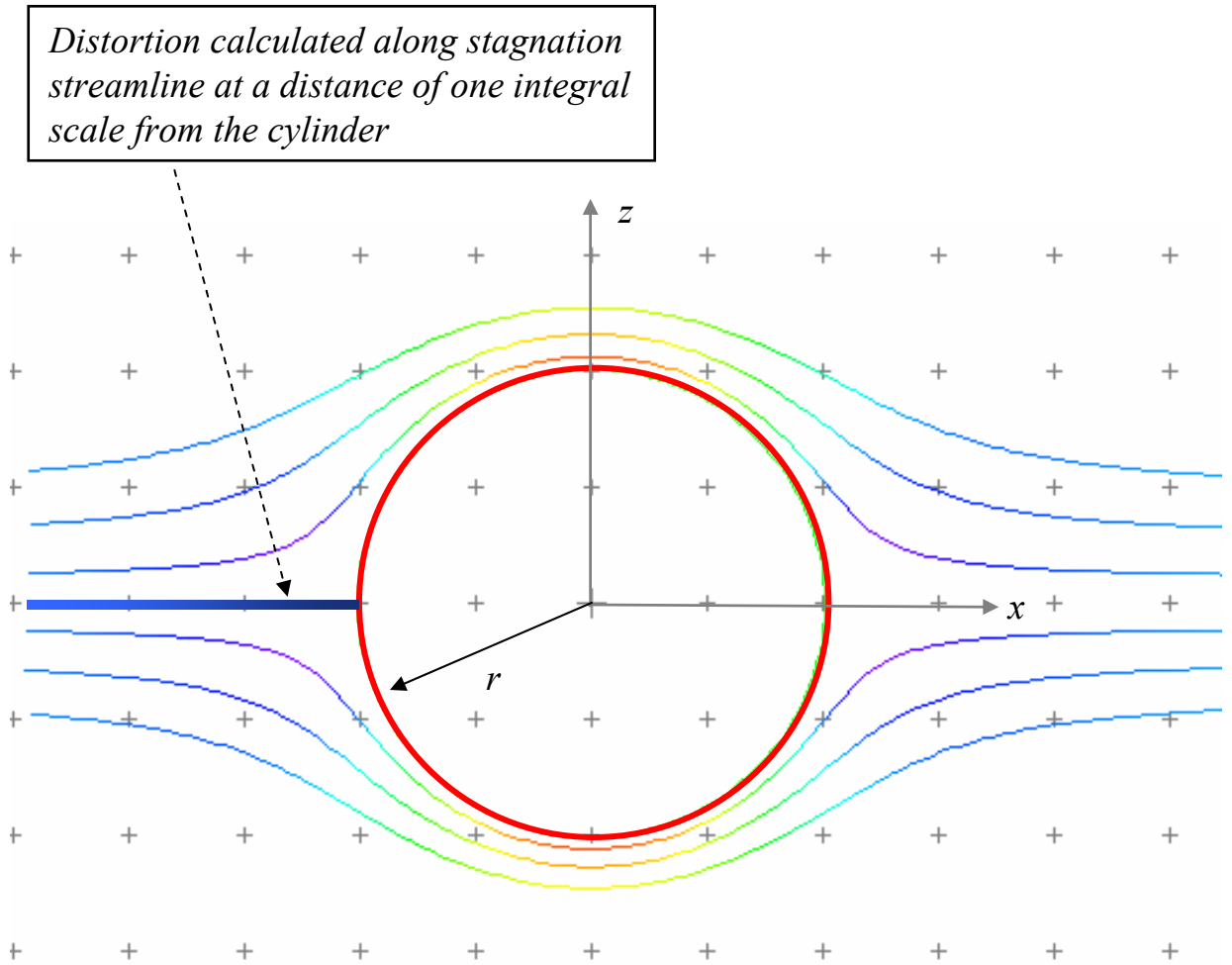


Figure 5.34: Diagram showing the streamline along which the turbulence distortion is calculated

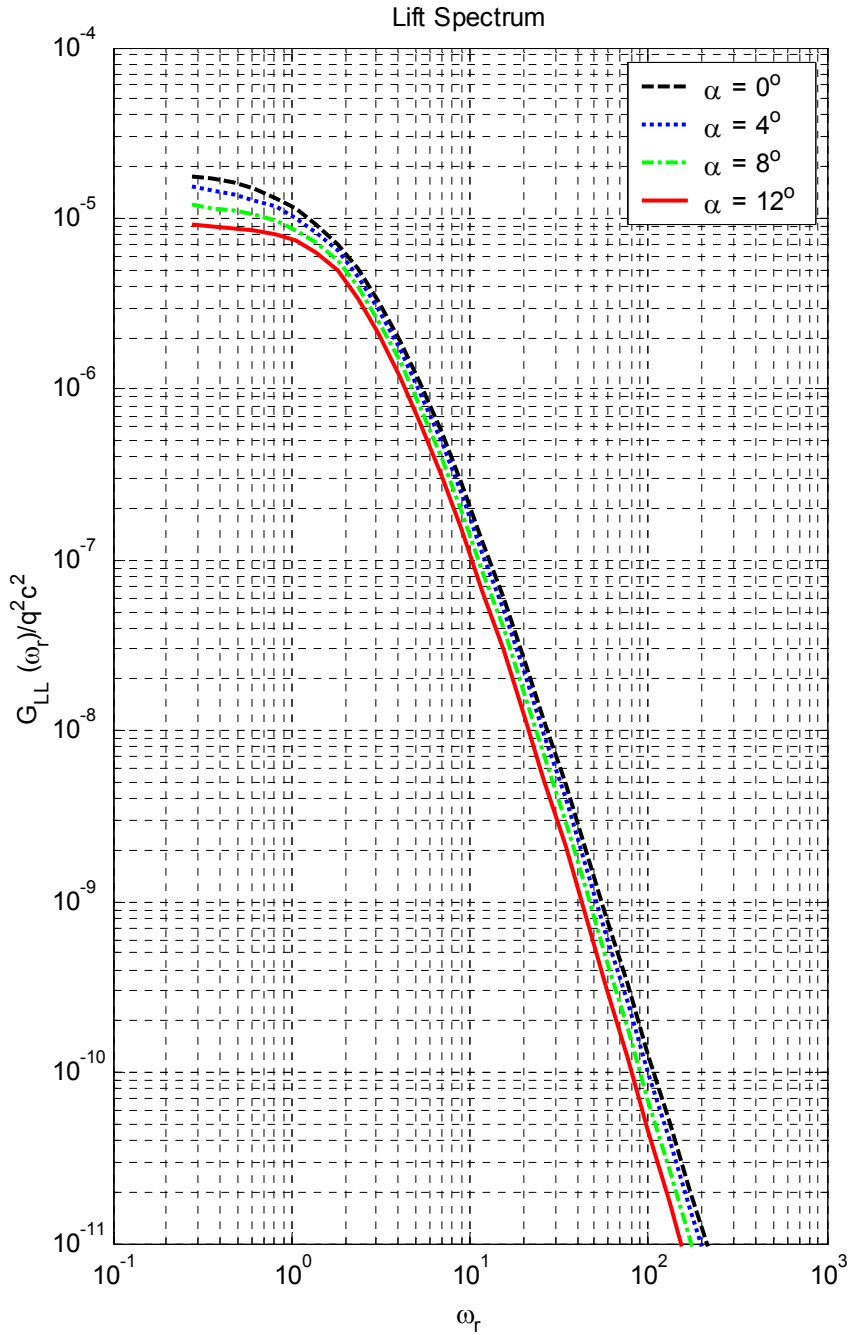


Figure 5.35: Unsteady lift spectra calculated using the distorted inflow turbulence energy spectra with Amiet's (1976a, b) solution. Distorted turbulence energy spectra are computed using the distortion tensor calculated along the stagnation streamline of a circular cylinder.

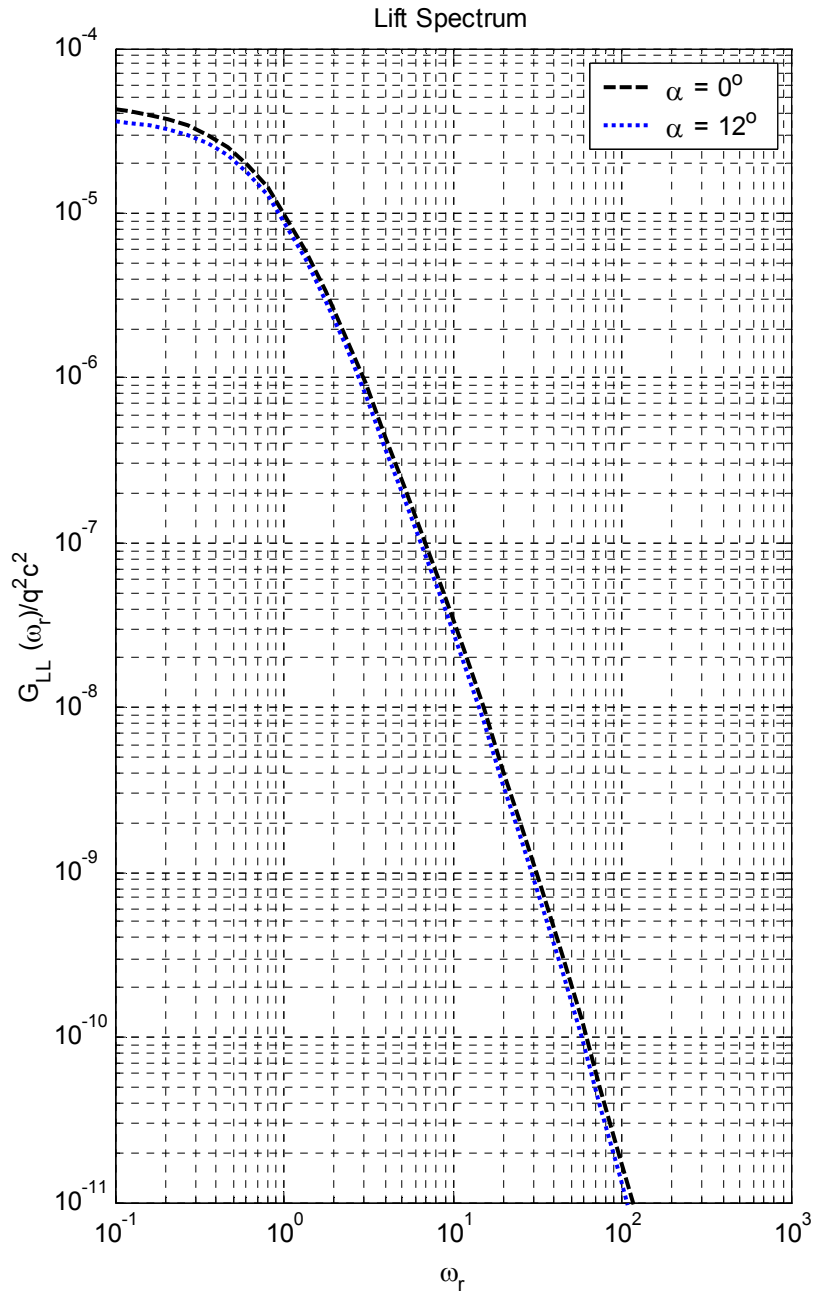


Figure 5.36: Unsteady lift spectra calculated using the distorted inflow turbulence energy spectra with Amiet’s (1976a, b) solution for McKeough’s (1976) flow conditions. Distorted turbulence energy spectra are computed using the distortion tensor calculated along the stagnation streamline of a circular cylinder.

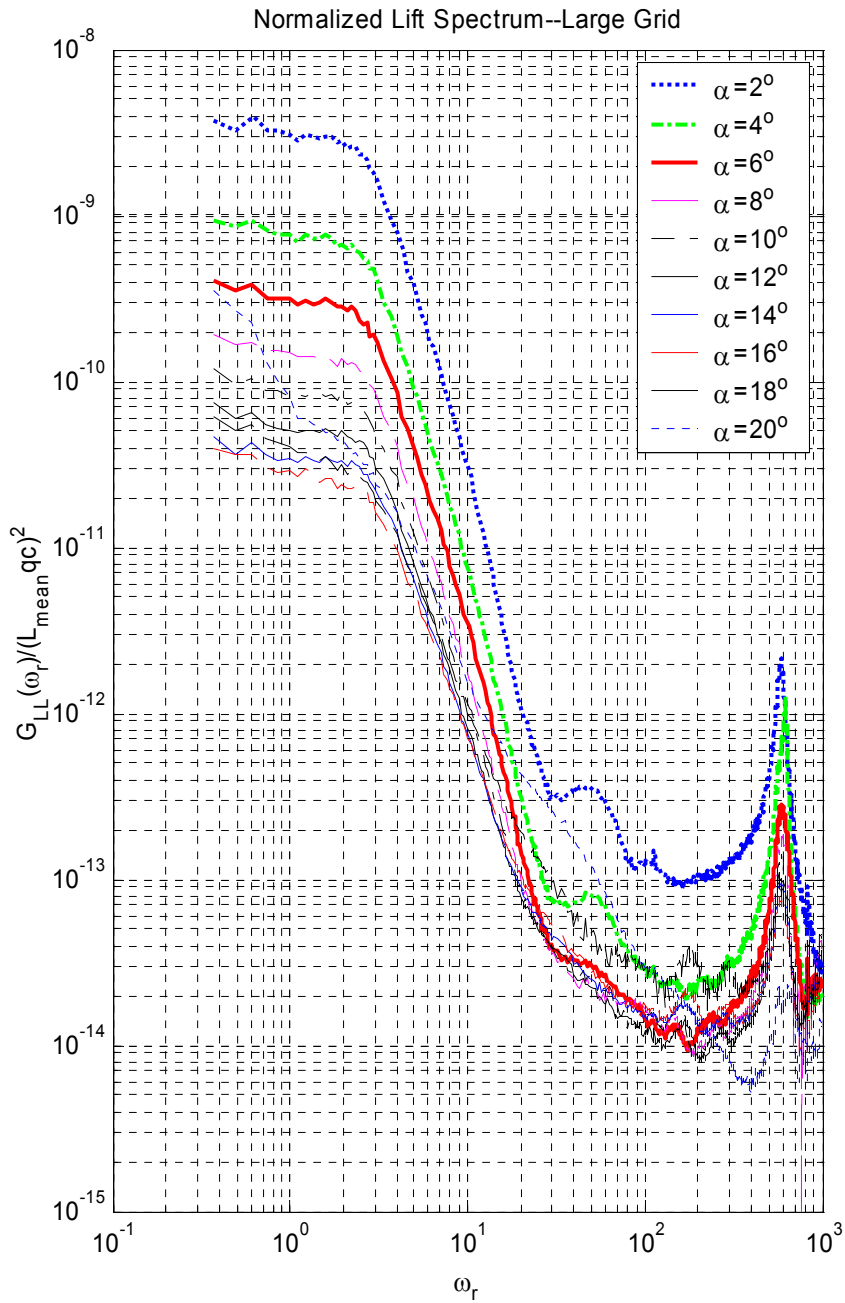


Figure 5.37: Lift spectra scaled on the mean lift squared

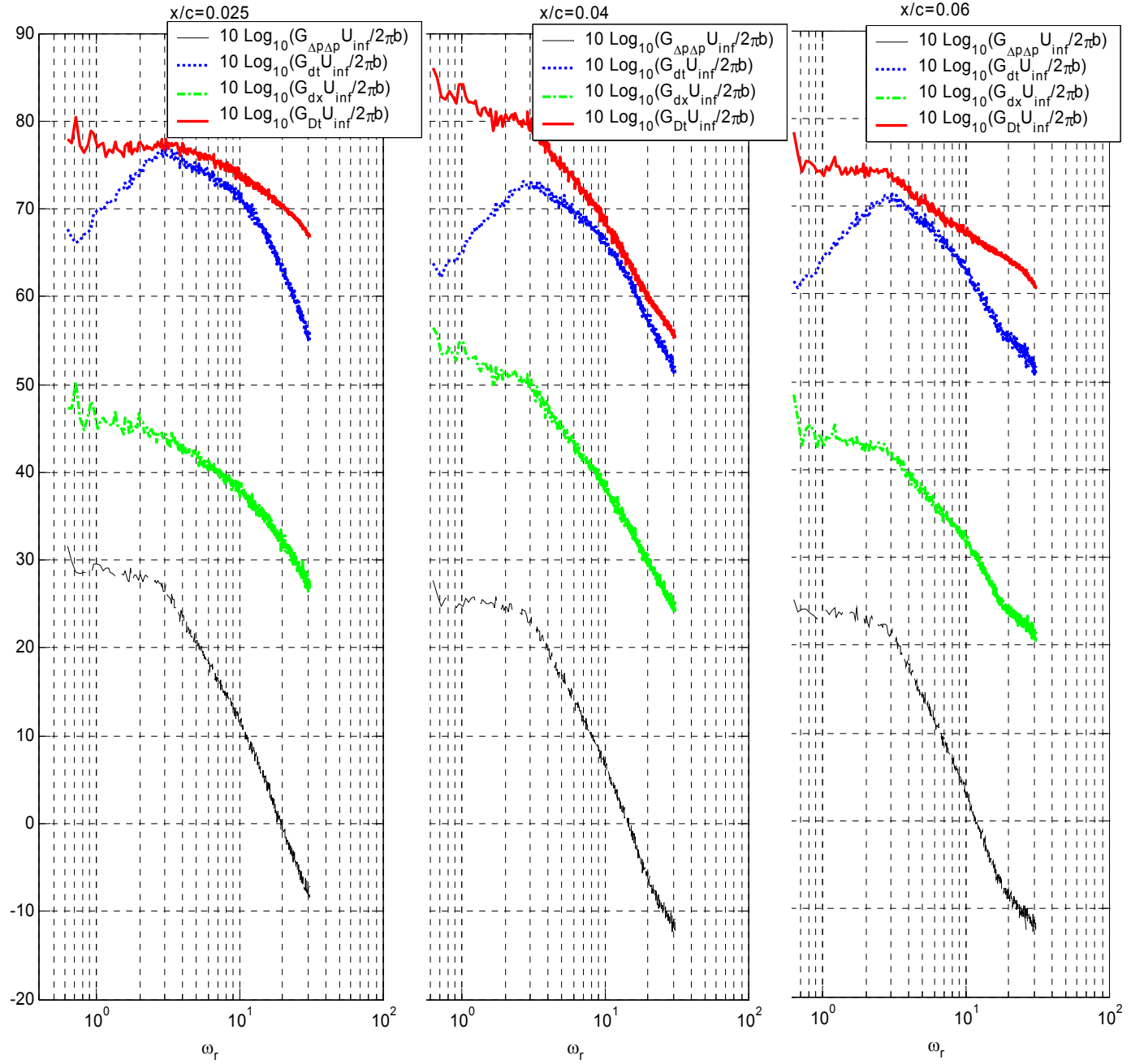


Figure 5.38: Convective derivative of *pressure difference* cross-spectral density for $\alpha = 0^\circ$ at chordwise locations, $x/c = 1, 2.5, 4, 6, 9,$ and 14%

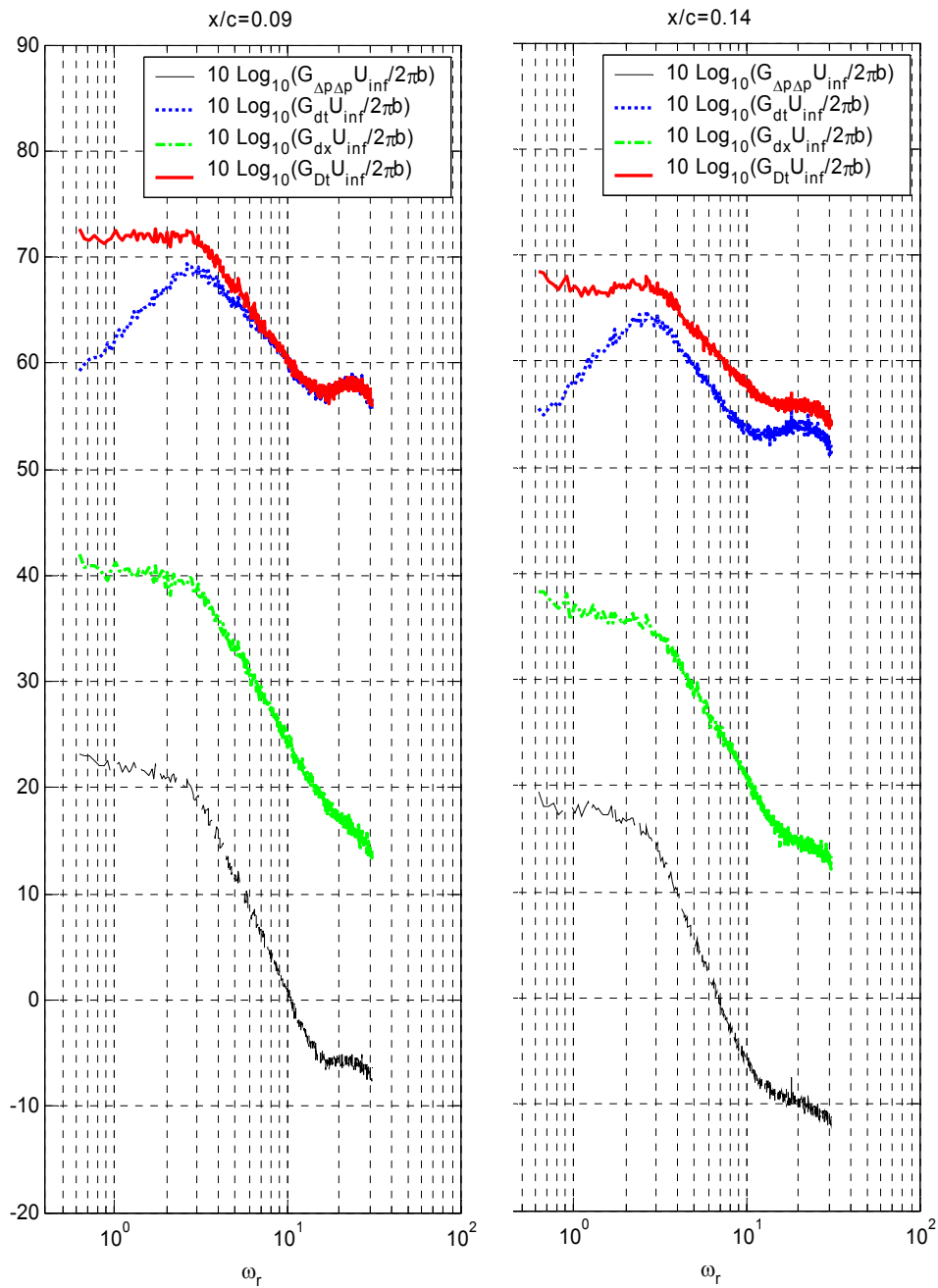


Figure 5.38 continued: Convective derivative of *pressure difference* cross-spectral density for $\alpha = 0^\circ$ at chordwise locations, $x/c = 1, 2.5, 4, 6, 9,$ and 14%

6. CASCADE IN PERIODIC DISTURBANCE

This dissertation has focused, up to this point, on the measurement and analysis of a single airfoils inviscid response when encountering turbulence. The measurement system, an array of small microphones mounted subsurface, was shown to be effective at measuring the airfoil's inviscid response when subject to the rigors of a random inflow. As such, attention is now turned to the inviscid response of a cascade of airfoils (multiple airfoils). The established measurement system is used to determine the inviscid response of a cascade blade encountering a periodic disturbance. Due to the deterministic inflow, the analysis of this data is somewhat simplified and its interpretation a bit more intuitive.

6.1 Background

Background is provided here which highlights the significance of understanding the inviscid response cascade subject to periodic inflow. The flow simulated is that from an axial propulsion pump rotor operating in the wakes of a set of inlet guide vanes. The work of Ma (2003) suggested that tip leakage vortex shedding in the presence of a periodic disturbance is heavily influenced by the inviscid response of the cascade blade. Ma (2003) performed three component turbulence and microphone measurements phase averaged with respect to the relative position of the blades and their vortical inflow in cross-sections downstream of the blade tips as a function of tip gap ($t_g/c = 0.00825, 0.0165, 0.022, 0.033$). His measurements showed the unsteady motions of the tip leakage vortex generated in response to the periodic vortical inflow in terms of phase-averaged mean velocities, stresses, triple products, and pressure fluctuations in the flow. Consequently, a number of crucial findings have resulted:

1. The inflow vortices are one to two orders of magnitude weaker than the tip leakage vortex; however, they produce substantial fluctuations in the size, strength (circulation), structure, and position of the tip leakage vortex
2. The effects of the inflow vortices increase in magnitude with increasing tip gap.
3. When the tip gap is small the effects appear to be produced largely by direct interaction (or superposition) between the inflow vortices and the tip leakage vortex.
4. At large tip gaps the effects appear to be primarily the result of the inflow vortices interfering with the shedding of circulation from the blade tip. As such, the inflow vortices are able to

interact with the tip gap flow producing fluctuations in the circulation strength of the tip leakage vortex that are many times the circulation strength of the inflow vortices.

These results provide evidence that indeed, the blade tip loading is possibly the result of the inviscid response of the blade row to the inflow disturbance. Additionally, these results indicate that the unsteady blade tip loading may be the primary mechanism for generating the tip leakage unsteadiness. Therefore, it is the goal of this work to characterize the extent of inviscid response occurring during blade-disturbance interaction using a similar measurement system discussed in chapter 2

The discussion and analysis of cascade blade unsteady pressure measurements is broken into three chapters. Chapter 7 provides background on the instrumentation and apparatus, including a review on the unsteady pressure measurement system. The cascade response theory developed by Glegg (1999) is discussed in chapter 8. This theory is used for comparisons with measured data that are presented in chapter 9.

7. CASCADE INSTRUMENTATION AND APPARATUS

7.1 Linear Cascade Wind Tunnel

The flow simulated is that from an axial propulsion pump rotor operating in the wakes of a set of inlet guide vanes. As such, the Virginia Tech Low Speed Linear Cascade Wind Tunnel was built by Muthanna (1998) and Wang (2000) for this purpose, by modifying the turbine cascade tunnel of Moore *et al.* (1994). A centrifugal fan powered by a 15 h.p. AC motor drives the tunnel. Air passes through a diffuser and a settling chamber and undergoes a contraction of 6.43:1 before entering the rectangular section of 762mm x 304.8mm, which drives the flow onto the blade row.

Figure 7.1 is a schematic of the test section.

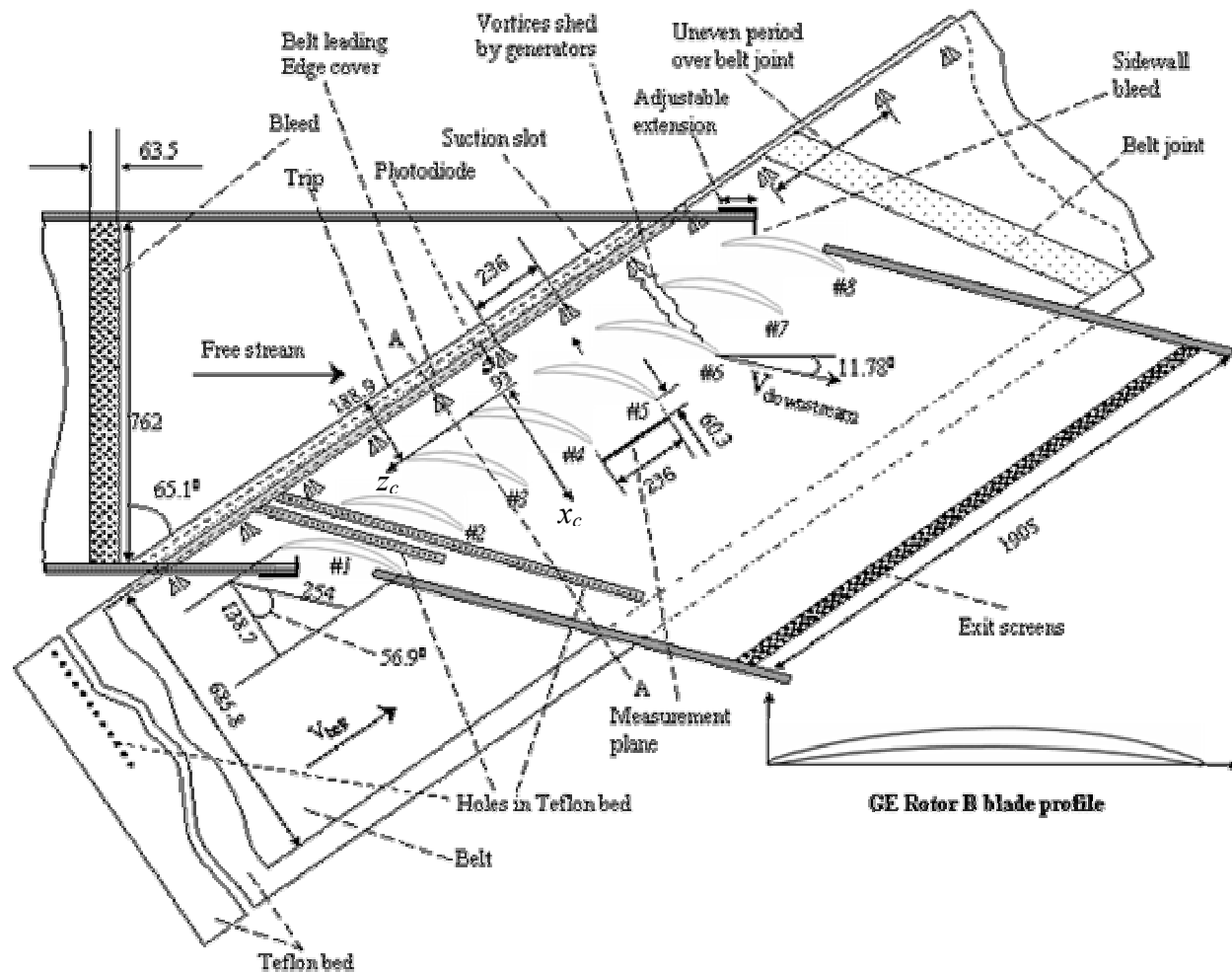


Figure 7.1: Linear Cascade Wind Tunnel (courtesy of Ma 2003)

Flow at the test section entrance is closely uniform and of low (0.12%) turbulence intensity. The blade row is at an angle of 24.9° (inlet angle 65.1°). The stagger angle of the cascade is 56.9° . The cascade consists of 8 cantilevered GE rotor B section blades mounted on a structure that allows individual adjustments for each tip gap and also the vertical and dihedral alignments. By shimming the structure the tip gaps of all the blades may also be adjusted simultaneously. The blades, machined of aluminum, have a chord length of 254mm and effective span of nearly the same depending on the size of the tip gap. The blade spacing is 236mm and tip gaps (to the lower end wall) used in this experiment were $t_g/c = 0.00825, 0.0165, 0.022, 0.033, 0.045, 0.057, 0.079,$ and 0.129 . Boundary layer trips, 6.4 mm wide (0.51mm diameter glass sanding beads spread in single layer), were attached on both sides of each blade at 25.4mm downstream of the blade leading edge to eliminate any undesirable effects caused by natural boundary layer transition.

The blade row is located 189mm axially downstream of the suction slot leading edge to allow room for the vortex generators. The tunnel inlet section floor includes a porous strip (63.5mm wide, spanning the section) to bleed 8% of the mass flow. The bleed ensures that the boundary layer on the floor can be completely removed at the pitchwise suction slots without imposing any pressure gradient on the flow here.

Ahead of the cascade, two 25.4mm high suction slots on the upper and lower end walls are used to remove the boundary layers growing in the inlet section as shown in figure 7.2. A boundary layer trip wire of rectangular cross section (2.4mm x 2.4mm) was introduced 7mm downstream of the lower-wall suction slot leading edge to increase the thickness of the lower end wall boundary layer entering the cascade.

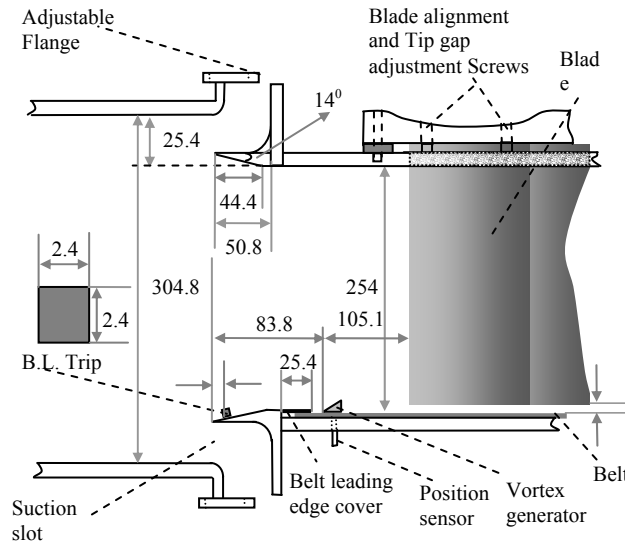


Figure 7.2: Cascade tunnel cross-section AA (courtesy of Ma 2003)

A new, pitchwise uniform, boundary layer flows over the lower end wall into the cascade. The suction slots reduce the height of the test section to 254mm at the blade row and downstream. Adjustable angle tailboards are used to guide the flow downstream of the cascade. Three screens fitted at the section exit raise the pressure at the cascade inlet to about 9mm of water above atmospheric so that the suction slots operate as designed. De la Riva (2001) and Muthanna (2002) give further details of the wind tunnel.

In the present measurements, the inlet free stream velocity (after the bleed) was 25.2m/s as measured by a Pitot-static probe mounted in the inlet section. The tailboards were adjusted to a turning angle of 11.8° at which the flow was free from any pitchwise pressure gradient (see Ma 2003).

To simulate relative motion between the blade tips and casing of a real turbo machine, a moving end wall was installed under the blade row. The moving wall consisted of a 0.254mm-thick Mylar belt that is driven using a 15HP AC synchronous motor over a Teflon bed flushed into the lower end wall underneath the blade row. The belt is 686mm wide and extends about 125mm axially upstream and 422mm axially downstream of the blade row. The belt is propelled and guided using two 200mm-diameter rollers located outside the tunnel. A 3mm gap at the bottom of the tailboards over the width of the belt allows the belt to pass in and out of the test section. With free stream velocity of 25.2m/s the belt speed required is $25.2 \times \cos(24.9^\circ) = 22.85$ m/s, i.e. the tangential component of the free stream. The belt speed was continually adjusted to

keep it within 1% of the correct fraction of the free-stream velocity. The belt speed stability was better than 0.24% RMS.

Two rows of perforations were cut on the Teflon bed near where the belt enters the tunnel as shown in figure 7.2. In addition 12 holes of 8mm diameter at 25.4mm interval were drilled through the bed on the outside of the tunnel. The perforations were necessary to remove any air from underneath the belt, the air being driven out by the higher pressure inside the tunnel and, in the case of the outside holes, by a vacuum pump connected to a plenum underneath the bed. With no air under the belt, vertical vibration is almost completely eliminated. The amplitude of the vibration was measured by Kuhl (2001) using an optical sensor embedded under the belt bed as $6.6\mu\text{m}$ RMS, which is lower than 0.2% of the design tip gap

The belt joint (a 7 cm-wide strip where the belt thickness is doubled) produced the fluctuations in instantaneous tip gap outside of this range. However, measurements made in the vicinity of the belt joint were easily eliminated in post processing, see below. The joint was skewed at an angle between 40° to 45° to improve the alignment and stability of the belt position. Axial drift of the belt was less than $\pm 6\text{mm}$ and at most times much less. The windward edge of the belt was covered by a 25.4mm-wide Mylar strip to prevent it from lifting inside of the tunnel. Electrically grounded anti-static brushes suspended just above the belt outside the wind tunnel were used to prevent a build up of static electricity (see Kuhl, 2001). Belt heating, previously measured by Wang *et al.*, (1999) was found to be negligible.

In order to simulate the casing junction wakes of an upstream row of stator blades (or inlet guide vanes), pairs of half delta wing vortex generators (figure 7.3) were glued to the belt with their leading edges $68.6\pm 4.2\text{mm}$ axially upstream of the blade row. The vortex generators produce an unsteady, periodic vortical inflow representative of an array of stator necklace vortices.

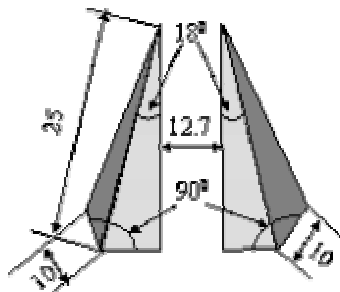


Figure 7.3: Delta wing vortex generator pair (courtesy of Ma 2003)

Note that, the uncertainty in location reflects the limits of the axial drift of the belt, not the positioning of the generators on the belt. The generators, based on the design of Pauley and Eaton (1989), were made of 0.5-mm thick sheet metal, have an axial chord length of 25 mm, height of 10 mm and angle of attack of $\pm 18^\circ$. They were placed 12.7mm apart at mid-chord in pairs so as to produce a 'common-flow down' counter-rotating vortex pair - an idealization of a necklace vortex wake. Except at the belt joint, the spacing between successive pairs of generators was set equal to the blade spacing (236mm) so that the unsteady boundary conditions of the flow would be periodic (an important consideration for processing and theoretical comparisons). Since the total belt length was not an integer multiple of the generator spacing, one uneven spacing interval was inevitable. This interval was arranged to coincide with the belt joint which provided a means for detecting the passage of the joint. Note that, the axes of the generator pairs were aligned perpendicular to the blade row since, in the frame of reference moving with the belt, this is the direction of the free stream. The counter-rotating vortices shed by the generators then grow in the axial direction as they are translated tangentially with the belt.

A photodetector was embedded in the Teflon bed underneath the belt at a location 80.5mm axially upstream of the center of the cascade leading edge line (i.e. directly in the path of the vortex generators; see figure 7.1). The detector was illuminated with a laser beam shone vertically downward from outside the tunnel through the clear Mylar belt, the beam being interrupted by the passage of the vortex generators. The detector signal was amplified and sampled simultaneously with unsteady pressure measurements. It was then post-processed to (a) identify and eliminate any measurements made during the passage of the belt joint (or when the belt joint or uneven generator spacing were upstream of the probe), (b) determine the time intervals between the passage of generator pairs, and thus the near-instantaneous belt speed, and (c) to construct a phasing signal by subdividing each time interval into 256 equal periods representing the instantaneous position of the vortex generator pairs relative to the blades. The resolution in the phasing signal corresponds to $236/256=0.92\text{mm}$ of vortex generator movement. As noted above, the RMS variation in belt speed inferred using this method was 0.24%. This is low enough that it may contain a significant contribution from the uncertainty in the placement of the generator pairs on the belt (0.24% in this case would correspond to a position uncertainty of 0.6mm).

7.2 Microphone System

Measurements of unsteady pressure were performed using Sennheiser microphones embedded in the tip region of two cascade blades. Ideally, one blade would have been instrumented with a set of microphones on both the pressure and suction sides. However, due to the size of the microphones and limited space available for mounting the two blades forming the pressure and suction sides of the central cascade passage were instrumented (blade 4 and 5). Each blade was equipped with a total of 12 microphones, 7 in a chordwise row 2.5% chord from the tip and 5 in a spanwise row.

The microphones are positioned in each blade such that the pressure difference is computed in the direction of the lift vector. Table 7.1 presents the spanwise and chordwise location of microphones on the two blades. The coordinate system is formed with the origin at the leading edge corner of the blade tip and leading edge with x pointing downstream, y pointing up the span of the blade (away from the tip), and z completing the right-hand rule.

Table 7.1: Locations of microphones in blade 4 and 5

<i>Microphone No.</i>	<i>x/c</i>	<i>y/c</i>
<i>Pressure side, blade 5</i>		
1	0.7625	0.025
2	0.55	0.025
3	0.39375	0.025
4	0.29375	0.025
5	0.23125	0.01875
6	0.175	0.025
7	0.23125	0.05
8	0.23125	0.075
9	0.23125	0.15
10	0.23125	0.25
11	0.23125	0.45
12	0.125	0.025
<i>Suction side, blade 4</i>		
13	0.75625	0.025
14	0.55625	0.025
15	0.40625	0.025
16	0.30625	0.025
17	0.24375	0.01875
18	0.1875	0.025
19	0.1375	0.025

20	0.24375	0.05
21	0.24375	0.075
22	0.24375	0.15
23	0.24375	0.25
24	0.24375	0.45

Note that microphone number 24 was not used in measurements due to the poor fit of this microphone. Figure 7.4 shows a planform view of a typical microphone layout.

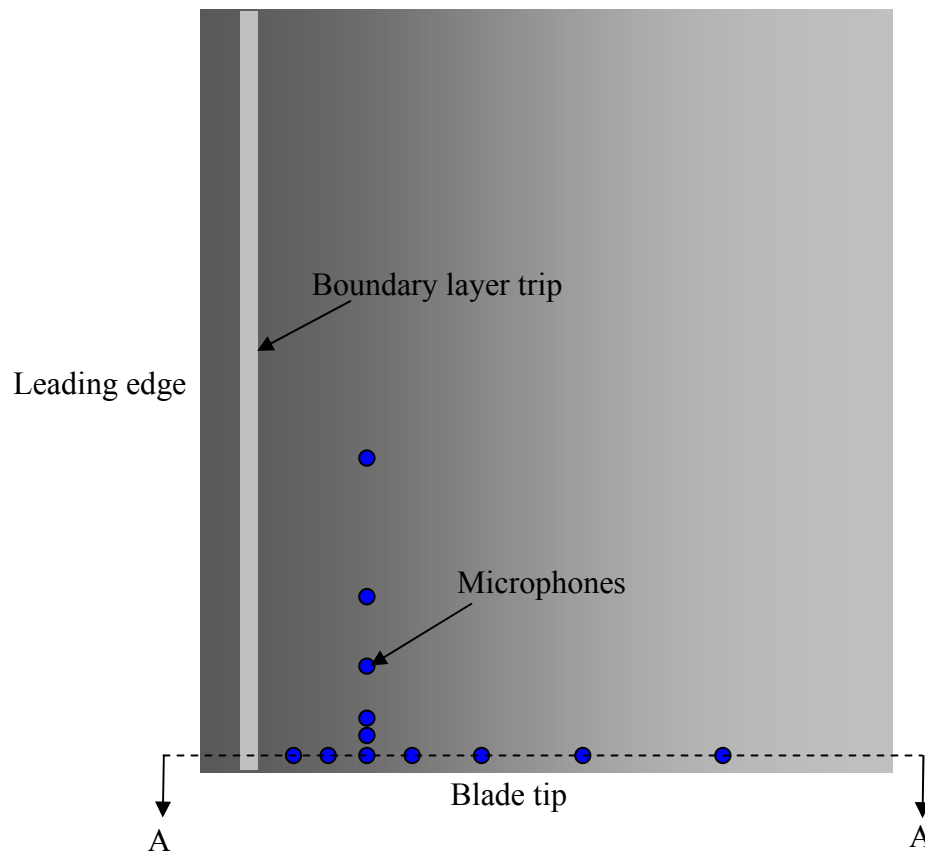


Figure 7.4: planform view of the microphone distribution

Figure 7.5 presents a cross-section (section AA of figure 7.4) through the blade detailing the microphone hole configuration for both blades.

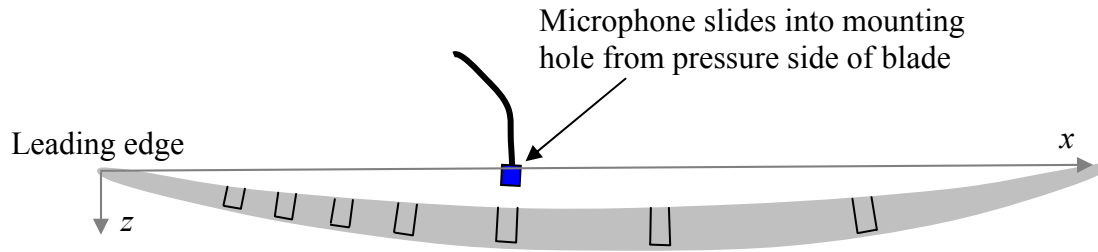


Figure 7.5a: Cross-section of blade measuring unsteady pressure on suction side (blade 5)

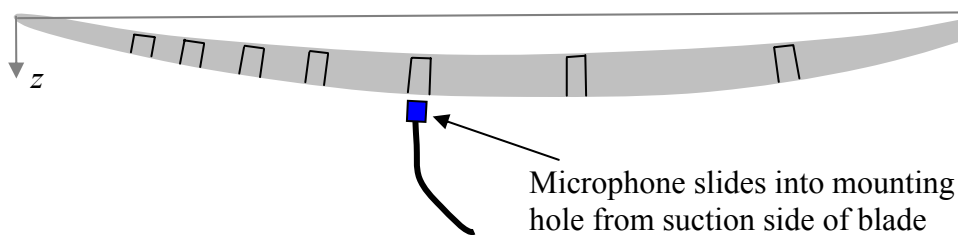


Figure 7.5b: Cross-section of blade measuring unsteady pressure on pressure side (blade 4)

The microphones slide into a slightly larger diameter hole and are separated from the exterior surface by approximately 1mm. A 1mm pinhole is drilled in the center of the mounting hole which aligns with the microphone pinhole (see chapter 2, figure 2.26).

The system is powered by 2 custom-built quiet power supplies. It was operated, and measurements were made using a Hewlett Packard E1432 based data acquisition system. This system provides simultaneous measurement of 64 channels with 16 bit accuracy at sampling rates up to 56kHz per channel, and has built in anti-alias filtering for each channel.

A central component of any such measurement system is a reliable means for calibrating the microphones. The same calibration scheme used for calibrating microphones in the single airfoil in turbulence measurement was used here (see chapter 2.1.5). Microphones were calibrated with a 25.6 kHz sampling rate using a 2048 point record length with 200 averages of data taken. This sampling scheme provided adequate resolution in frequency from 100Hz to 10kHz. One-hundred Hertz is considered an appropriate response lower limit due to the vortex generator passing frequency which is near 100Hz. Pressure fluctuations occurring below 100Hz are likely not related to the unsteady periodic disturbance produced by the vortex generators. The response of Sennheiser microphones was found to be flat over this frequency range and thus, one value, chosen from near 500Hz was used to describe the response of the microphone over the entire frequency range (100Hz to 10kHz).

8. CASCADE RESPONSE PREDICTION

The unsteady loading on a cascade of blades is theoretically predicted using Glegg's (1999) cascade response model. This theory is used to calculate the tip section lift coefficient as a function of phase number. Comparisons are then made with the unsteady lift calculated from surface pressure measurements.

8.1 Linear Cascade of Flat Plates

Glegg (1999) reconsiders the cascade response model developed by Envia and Kerschen (1986). He develops an analytical solution for a rectilinear cascade of flat plates subject to a three dimensional inflow gust. The model assumes the blade row is swept with finite chord and infinite span at zero angle of attack and includes coupling between blades.

The derivation of the unsteady lift coefficient for comparison with measurements is presented here based on Devenport (2002). The notation presented here Glegg (1999) develops an expression for the unsteady loading and presents the non-dimensionalized form of the unsteady lift amplitude, L as

$$C_p(\gamma_o, \alpha, \nu) = \frac{2i\omega D(0; \gamma_o, \alpha, \nu)}{U_o w_o c} \quad (8.1)$$

where C_p is defined as

$$C_p = \frac{L}{\pi \rho U_o w_o c} \quad (8.2)$$

and $D(0)$ is the mean velocity potential jump. The variables of eq. (8.1) are defined in table 8.1.

Table 8.1: Variable definitions for equation (8.1); see also figure 8.1

Variable	Definition
U_o	$\sqrt{U_\infty + W_\infty}$
U_∞	Free-stream velocity
W_∞	Cross flow velocity
w_o	Upwash component of gust amplitude
γ_o	Streamwise wavenumber
α_p	Normal to planform wavenumber
ν_s	Spanwise wavenumber
c	Blade chord
ρ	Density

The unsteady lift coefficient amplitude, C_L can be determined in terms of Glegg's C_p as

$$C_L = 2\pi \frac{w_o}{U_o} C_p \quad (8.3)$$

where C_L is defined as

$$C_L = \frac{L}{\frac{1}{2} \rho U_\infty^2 c} \quad (8.4)$$

Measurements of the upwash velocity produced by the vortex generator array at the entrance to the present cascade wind tunnel were made using phased-averaged single hot-wire anemometry by Ma (2003). These measurements, which effectively give the upwash field as a function of pitchwise and spanwise distance and time, and are related to the notation of Glegg's (1999) theory as shown in figure 8.1. The prime (') notation denotes the coordinate system used by Ma (2003).

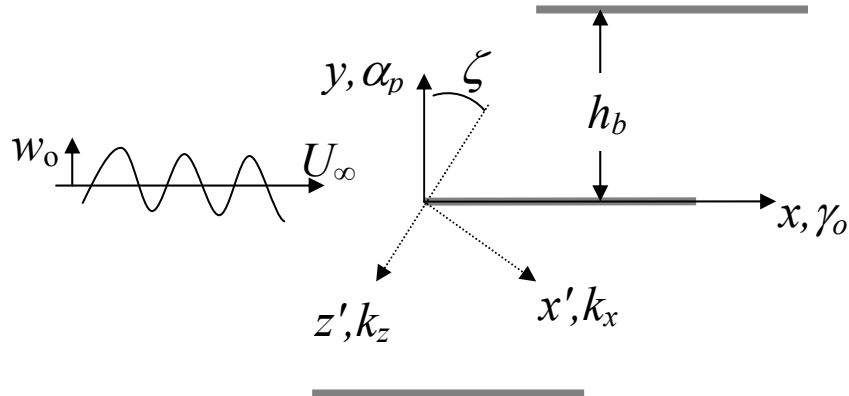


Figure 8.1: Geometry used in Glegg's (1999) cascade response theory

The notation of figure 8.1 is defined in table 8.2. Note that coordinate z points out of the paper and is aligned with coordinate y' with wavenumbers ν and k_y respectively.

Table 8.2: Definition of figure 8.1 notation

<i>Variable</i>	<i>Definition</i>
h_b	Blade separation
k_x	x' direction wavenumber as defined by velocity measurements of Ma (2003)
k_y	y' direction wavenumber as defined by velocity measurements of Ma (2003)
ζ	Coordinate rotation angle

The wavenumbers used by Glegg (1999) can be related to the velocity measurement coordinate system wavenumbers (noting that $k_x = 0$) by

$$\begin{aligned}
\alpha_p &= k_z \cos \zeta \\
\gamma_o &= -k_z \sin \zeta \\
\nu_s &= k_y
\end{aligned}
\tag{8.5}$$

As such, C_L can then be written in terms of the measurement wavenumbers

$$C_L(k_y, k_z) = \frac{-4\pi i k_z D(0; k_y, k_z) \sin \zeta}{U_o c} .
\tag{8.6}$$

For comparison with the measured unsteady lift equation (8.6) must be transformed from the wavenumber domain to the space and time domain. This is easily carried out by considering the double inverse Fourier transform of C_L

$$C_L(t, y) = \int_{-\infty}^{\infty} \int_{-\infty}^{\infty} C_L(k_y, k_z) e^{i(\omega t + k_y y)} dk_y d\omega
\tag{8.7}$$

with $\omega = \gamma_o U_o$ which, by eq. (8.5) is $\omega = -k_z U_o \sin \zeta$. Equation (8.7) is discretized and the calculation performed over the following wavenumber grid

$$k_y = (m-1) \Delta k_y
\tag{8.8}$$

where $m = 1, 2, 3 \dots 256$ and $\Delta k_y = 2\pi/s$ (s is the blade spacing) and

$$k_z = (n-1) \Delta k_z
\tag{8.9}$$

with $n = 1, 2, 3 \dots 256$ and $\Delta k_z = 2\pi/b$ (b is the blade double span).

Glegg's (1999) theory assumes the blades extend in the spanwise direction to infinity. As such, it is necessary to develop a method for incorporating tip gap effects which exist in the experiment. This is accomplished by taking the upwash to be zero over the tip gap region.

9. CASCADE IN PERIODIC DISTURBANCE: ANALYSIS OF UNSTEADY PRESSURE DATA

This chapter presents analysis of unsteady surface pressure measurements made on cascade blades encountering a periodic disturbance with the goal of characterizing the extent and dominance of the inviscid response. The phase average pressure coefficient is analyzed for several tip gaps. Additionally, unsteady pressure measurements are used to calculate the phase average lift and comparisons made with Glegg's (1999) cascade response theory.

9.1 Coordinate System, Test Configuration, and Data Sampling

The coordinate system is formed with the origin in the plane of the leading edge at the blade tip with x directed along the blade chord, y directed along the blade leading edge, and z completing the right hand rule (see figure 9.1).

The pressure side of blade #5 and suction side of blade #4 were instrumented with microphones. Both blades were instrumented with 12 microphones, 7 along the chord at roughly 2.5% chord from the blade tip and 5 along the span at a chordwise location of 23%. Unsteady pressure measurements were made at 8 tip gaps ($t_g/c = 0.00825, 0.0165, 0.022, 0.033, 0.045, 0.057, 0.079, 0.129$) with the cascade blade subject to a periodic disturbance. The speed of the vortex generators was monitored while simultaneously sampling unsteady pressure data on both blades. A sampling rate of 25.6kHz was used with a record length of 16384 and 200 averages of data. This sampling scheme ensures data is taken for one full revolution of the moving wall belt. The tunnel nominal velocity was $U_\infty = 24\text{m/s}$ producing a blade chord Reynolds number of 3.9×10^5 .

Unsteady surface pressure measurements were made with and without vortex generator present. The belt is running in both cases. No significant unsteady blade/disturbance interaction occurs with the wall running and no vortex generators present. As such, this case provides a baseline for contamination due to tunnel acoustics. Measurements with no vortex generators present were made at one tip gap only ($t_g/c = 3.3\%$). With no vortex generators present the unsteady pressure data, of course, cannot be phase averaged. As such, this data is averaged and examined in the frequency domain.

9.2 Formulation of Phase Averaged Data

9.2.1 Phased Averaged Data

Each microphone voltage time series is first converted to pressure through application of the microphone calibration. The microphone calibration is flat over the frequency range of interest and therefore can be applied in time as

$$p'(x, y, t) = \frac{v_m(x, y, t)}{M_s(m_n, f = 500\text{Hz})} \quad (9.1)$$

where p' [Pa] is the unsteady pressure, v_m [volts] is the microphone voltage time series. After application of the microphone calibration each time series is decomposed into 256 phases representing the passage of one vortex generator pair. The vortex generator signal is processed to determine the near-instantaneous belt speed and construct a phasing signal by subdividing each of the time intervals between successive vortex-pair passages into 256 equal periods representing the instantaneous position of the vortex generator pairs relative to the blades. Figure 9.2 indicates the relative blade/vortex generator pair position as the phase number advances from 0 to 256. At phase 0 generator pairs are positioned axially upstream of the center point of each blade passage entrance. At phase 128 generator pairs are located axially upstream of the blade leading edges. An increment in the phase number of 1 represents a tangential motion of the generators of $h_b/256$ (i.e. almost 1 mm) where h_b is the blade spacing of 0.236m.

The phase average mean is calculated for each phase, j as

$$\langle a \rangle_j = \frac{1}{N} \sum_{n=0}^{N-1} a(j+nT) \quad (9.2)$$

where $\langle \rangle$ indicates phase averaged, N is the number of averages, and T is the period time for a vortex generator pair passing through one passage. The phase average variance is calculated as

$$\begin{aligned} \langle a'^2 \rangle_j &= \frac{1}{N} \left(\sum_{n=0}^{N-1} (a(j+nT) - \langle a \rangle_j) (a(j+nT) - \langle a \rangle_j) \right) \\ &= \frac{1}{N} \sum_{n=0}^{N-1} (a(j+nT)a(j+nT)) - \langle a \rangle_j^2. \end{aligned} \quad (9.3)$$

9.3 Measurement Uncertainties

The uncertainty in unsteady pressure measurements was estimated based on repeated measurements during microphone calibration. Several sets of calibrations were taken for each microphone from which the uncertainty was estimated to be $\pm 1.2\text{dB}$ at 20 to 1 odds (95%). Microphones were typically calibrated using 200 averages of data; however, during phase averaged processing of unsteady pressure measurements the number of ensemble averages typically approaches 5000 and therefore, the uncertainty is expected to be reduced accordingly.

9.4 Basic Flow Definition

9.4.1 Contribution of Noise Sources

Unsteady pressure measurements were made without vortex generators attached to the moving wall to establish a baseline level for contamination. In the no vortex generator configuration the primary sources of pressure fluctuations are expected to be the ambient acoustic field and hydrodynamic pressure fluctuations (i.e. turbulent boundary layer and separation). The spectra from this measurement are compared with spectra measured with vortex generators to establish the likelihood and extent of contamination. All comparisons are made at a tip gap, $t_g/c = 3.3\%$.

Suction Side Comparisons: Figure 9.3 presents spectra from different spanwise stations on the suction side of blade #4. Curiously, the spectra from the no vortex generator measurement are as much as one order of magnitude higher in spectral level than those measured in the presence of vortex generators. This is a surprising result for several reasons. Reason 1; the ambient acoustic field is presumably the same in both measurements. The only difference between the measurements is the presence of vortex generators on the belt which will not significantly affect the ambient acoustic field. Reason 2; flow across the blade above 5% span will be largely unaffected by the presence of vortex generators. The turbulent boundary layer is expected to be similar in both measurement cases. In fact, pressure measurements in the presence of vortex generators are expected to contain additional unsteadiness associated with the inviscid response of the blade. And, indeed such fluctuations are visible in the spikes in these spectra, many of which occur at the vortex generator passing frequency, of 95Hz or harmonics thereof.

Looking now at the root mean square (RMS) pressure (figure 9.4) calculated from suction side spectra at different spanwise stations, the same trend is found to exist. The root mean square pressure is calculated from the mean square pressure which is found as

$$p'^2(x, y) = \int_{f_{\min}}^{f_{\max}} G_{pp}(f, x, y) df \quad (9.)$$

with $f_{\min} = 50\text{Hz}$ and $f_{\max} = 10\text{kHz}$. The RMS pressures are normalized on the free-stream dynamic pressure. The no vortex generator $\sqrt{p'^2}$ is nearly four times the $\sqrt{p'^2}$ measured with vortex generators present over much of the span. Again, this result is very surprising. For the RMS pressure levels to fall lower in the presence of a tip region inflow disturbance than when no disturbance is present is difficult to explain. As mentioned above, the flow over the blade away from the tip region is expected to be largely unchanged with or without vortex generators. Furthermore, the ambient acoustic field is not expected to vary between the two measurements.

It is interesting now to look at spectral levels at different chordwise station in the tip region on the suction side of the blade (figure 9.5). Again, the same trend is evident with the no vortex generators spectra 1 to 1.5 orders of magnitude above spectra measured with vortex generators present. The spectra measured with vortex generators present show several narrow band spikes occurring at nearly all chordwise locations which are likely related to the passage of the vortex generators. The difference in spectral levels becomes even more difficult to explain in the tip region. The inflow disturbance produced by the vortex generators is expected to produce pressure fluctuations many times those felt in the tip region with no vortex generators present. An argument could be made that the increased unsteadiness in the tip region with no vortex generators present results from flow separation on the suction side of the blade that is associated with the tip leakage vortex formation. However, such an argument is invalidated when recalling the difference in spectral levels at different spanwise stations presented above.

Looking now to the RMS pressures along the blade chord (figure 9.6), again, the $\sqrt{p'^2}$ values measured with no vortex generators present exceed those measured with vortex generators present with a difference of as much as 4 times occurring at some chordwise locations.

Pressure Side Comparisons: Looking to the pressure side of blade #5, spectra (figure 9.7) measured at different spanwise stations *with vortex generators present* tend to be 1 to 1.5 orders of magnitude *greater* than spectra measured *without vortex generators*. The comparison is well summarized by looking at $\sqrt{p'^2}$ levels in figure 9.8 which shows the RMS pressure levels with vortex generators to be 4 times greater than the no vortex generator measurement. This is nearly the exact opposite of what was shown on the suction side of the blade.

The results in the tip region are interesting as well, as shown in figure 9.9 which presents spectra from different chordwise stations on the pressure side of blade #5. Spectral levels from measurements of pressure with vortex generators present are one to two orders of magnitude below those taken without vortex generators present with exception to stations $x/c = 76.25\%$ and 55% . Again, this is a near reversal of what was shown to occur on the suction side of the blade. The results in the tip region are well summarized by the RMS pressure calculated at each chordwise location and presented in figure 9.10. This figure shows $\sqrt{p'^2}$ values measured with vortex generators present to be 4 to 6 times the $\sqrt{p'^2}$ values measured without vortex generators with exception to 55% chord.

Discussion of Inconsistencies: The differences in spectral levels shown between the two measurements and the variation from the pressure to the suction side of the blade are quite difficult to explain. One possible explanation was thought to be in the data acquisition and/or processing. The belt speed must be tracked and recorded when vortex generators are present which necessitates the usage of a data acquisition code different from that used when no vortex generators are present. Additionally, the processing of the output from both codes is performed using two slightly different MatLab codes. Therefore, it was thought that possibly one code could have an error which shifted the entire data set up or down in spectral level. Several checks were undertaken to ensure no such error occurred.

The first check involved calculating mean square pressures at each chordwise location from spectra and from phase average pressure. Phase average pressure is calculated from a processing code independent of those mentioned above. This serves as an independent verification that the processing code used to calculate spectra with vortex generators present is working correctly. Figure 9.11 presents a comparison of p'^2 calculated from spectra and from

phase average pressure on the suction and pressure side of the blade for a tip gap of 3.3%. Mean square pressure values are in excellent agreement along the chord on both sides of the blade. Such good agreement suggests the processing code used to calculate spectra with vortex generators present is functioning correctly.

Next, a check was performed to verify the application of microphone calibrations in each MatLab processing code. Each processing code reads voltage time series data saved from the data acquisition codes and then Fourier transforms the voltage time series and applies the microphone calibrations. A check of the application of microphone calibrations was accomplished by comparing the ratio of root mean square voltages from the two measurements

(without and with vortex generators), $\frac{\sqrt{V_{NVG}^{\prime 2}}}{\sqrt{V_{VG}^{\prime 2}}}$, to the ratio of root mean square pressures from the

two measurements, $\frac{\sqrt{P_{NVG}^{\prime 2}}}{\sqrt{P_{VG}^{\prime 2}}}$. Figure 9.12 presents the log of these ratios versus chordwise

location on the suction and pressure side of the blade. Figure 9.13 presents the data as a function of spanwise location. Agreement to within a factor of 1.5 is shown in all plots which suggest the microphone calibrations are being applied consistently in both processing codes.

With both processing codes likely working correctly one last check was performed of the entire system, from acquisition to processing. This test entailed acquiring a set of data with both acquisition codes using four microphones subject to an acoustic field formed from a radio tuned to static. Each acquisition code was run subject to this same acoustic field. Additionally, the same sampling rate, record length, and number of averages of data were used during this test as used during the actual measurement of blade surface pressures. After each set of data was acquired, they were each processed with the appropriate MatLab processing code and the results compared. Figure 9.14 presents a comparison of spectra measured during this test. The plot on the left is the processed output from the acquisition code used to acquire data when *no vortex generators* are present. The right-hand side plot is the processed output from the acquisition code used to acquire data when *vortex generators* are present. The two sets of data are nearly identically proving that both acquisition and processing codes work properly.

While it is difficult to accept, these checks have lead to the belief that the most likely source of differences in pressure spectral levels is one that is related to flow phenomena. A

possible source for the high spectral and RMS levels on the suction side of the blade with no vortex generators could be unsteady stall occurring over a significant extent of the blade span. However, velocity measurements in the blade passage and downstream of the blade do not support such a phenomenon. Surface oil flow visualization also tends to refute this explanation. An alternate explanation may be that the periodic inflow disturbance does indeed influence, through the inviscid response, the boundary layer formation on both sides of the blade. On the suction side, it is possible that the harmonic inflow is organizing the formation of eddies in such a manner as to suppress the unsteady surface pressure. While on the pressure side of the blade, the periodic inflow may be working to destabilize eddy formation which intensifies surface pressure fluctuations. This argument does admittedly ring of a manufactured nature; however, I am yet to find one related to flow phenomena, instrumentation, or analysis that does not. As such, these results remain somewhat enigmatic. Perhaps the most useful effort would be in a re-measurement of unsteady pressure at the 3.3% tip gap with and without vortex generators present.

While the differences observed in this data are difficult to reconcile, the analysis and discussion of phase averaged measurements made with vortex generators is presented below. It is felt that this data set is sound based on a number of internal and external consistency checks. Additionally, spectra measured along the span and across the chord are largely of consistent level between the suction and pressure side, and vary in a physically explainable way. Furthermore, as will be shown below, the general magnitude of phase averaged pressure fluctuations is also consistent with inviscid predictions and the phase-locked hot-wire results of Ma (2003).

9.5 Unsteady Loading

9.5.1 Chordwise Surface Pressure Distribution

The surface pressure distribution is investigated in terms of the phase averaged mean pressure coefficient, $\langle C_p \rangle$ which is defined as

$$\langle C_p(x, y, t) \rangle = \frac{\langle p'(x, y, t) \rangle}{\frac{1}{2} \rho U_\infty^2} \quad (9.5)$$

where p' is the unsteady pressure, ρ the density, and U_∞ the mean free-stream velocity. The phase averaged mean $\langle C_p \rangle$ is calculated according to eq. (9.2)

The suction side $\langle C_p \rangle$ is presented as a function of phase number plotted for each tip gap at all chordwise locations in figure 9.15. The fluctuations in $\langle C_p \rangle$ tend to be confined primarily to small tip gaps ($t_g/c < 4.5\%$) at the most leading edge locations ($x/c = 0.1375$ and 0.1875). As the chord is traversed from leading edge to trailing edge and the tip gap increased (up to $t_g/c = 5.7\%$) $\langle C_p \rangle$ tends to increase in magnitude. The fluctuations in $\langle C_p \rangle$ reach a peak at $x/c = 75.625\%$ for a tip gap $t_g/c = 5.7\%$. The rise in $\langle C_p \rangle$ as the trailing edge is approached is interesting and may result from the trailing edge singularity which occurs in unsteady response theory. The phasing location and extent of $\langle C_p \rangle$ fluctuations indicates that the blade is excited locally as the vortex generator pair move through the passage with exception to the $x/c = 75.625\%$ location. At this location the large tip gaps ($t_g/c > 3.3\%$) show the blade responding significantly at all phase numbers.

Figure 9.16 presents pressure side $\langle C_p \rangle$ as a function of phase number plotted for each tip gap at all chordwise locations. For tip gaps up to $t_g/c = 3.3\%$ slight fluctuations in $\langle C_p \rangle$ occur at the most leading edge positions ($x/c = 17.5, 23.125,$ and 29.375%). These fluctuations in $\langle C_p \rangle$ also tend to be limited to less than 100 phase numbers (i.e. vortex generator motion of $\sim 10\text{cm}$). Moving to $x/c = 39.375\%$ the $\langle C_p \rangle$ for larger tip gaps ($t_g/c > 2.2\%$) begins to fluctuate substantially. At $x/c = 55$ and 76.25% tip gaps between $3.3\% < t_g/c < 12.9\%$ show significant fluctuation of $\langle C_p \rangle$ and over the entire phase number extent. As shown on the suction side, $\langle C_p \rangle$ tends to increase moving away from the leading edge and as the tip gap is increased. Again, the rise moving down the chord may be related to the trailing edge singularity.

Figure 9.17 presents movies of $\langle C_p \rangle$ on the pressure and suction side as a function of chordwise location for each tip gap. The movies are embedded in each plot and can be played by double clicking the plot. The movies provide a qualitative feel for how the blade tip responds during passage of the vortex generator pair. Each movie has a small circular symbol which moves across the figure indicating the advancement in phase number from 0 to 256.

At the smallest tip gap, $t_g/c = 0.825\%$, $\langle C_p \rangle$ fluctuates significantly over the first 50% chord when the phase number is above 150 (i.e. as the vortex generator wakes moves past the blade leading edge). As the tip gap is increased the response becomes stronger (higher values of $\langle C_p \rangle$) and the blade is locally excited as the vortex generator wakes pass. The pressure and suction sides of the blade respond largely out of phase with each other. The increase in the pressure response is consistent with the increase shown by Ma (2003) to occur in the circulation of the tip leakage vortex with increasing tip gap (i.e. linear superposition is no longer valid at the larger tip gaps). For $t_g/c = 3.3, 4.5,$ and 5.7% the largest fluctuations in $\langle C_p \rangle$ begin to occur on the latter half of the blade ($x/c > 50\%$) with this entire portion of the blade responding as the generator wakes pass. As the tip gap is increased to $t_g/c = 7.9\%$ and 12.9% the pressure response becomes less dramatic with lower values of $\langle C_p \rangle$ achieved and less oscillation.

The increase in $\langle C_p \rangle$ level with increasing tip gap up to $t_g/c = 5.7\%$ shown in figures 9.15 – 9.17 agrees well with the findings of Ma (2003). Recall Ma (2003) showed the fluctuations in the tip leakage vortex circulation to increase as the tip gap is increased. As such, clearly, a linear superposition interaction of the vortex generator wake with the tip leakage vortex is not occurring. The fact that the blade is excited both locally and over a substantial portion of the chord (as shown in figure 9.17 for $t_g/c > 2.2\%$) indicates that a more complex interaction containing both inviscid response and viscous phenomena is underway. It is particularly interesting that the latter half of the blade ($x/c > 50\%$) is excited in magnitude of $\langle C_p \rangle$ much more than the leading edge region.

9.5.2 Spanwise Surface Pressure Distribution

Figure 9.18 presents suction side $\langle C_p \rangle$ as a function of phase number plotted for all tip gaps over the span of the blade ($y/c = 1.875, 5, 7.5, 15, 55, 25, 45\%$). The chordwise position of the spanwise row of microphones is $x/c = 23.125\%$. As expected, near the tip of the blade ($y/c = 1.875$ and 5%) significant fluctuation in $\langle C_p \rangle$ occurs over a phase number (150 – 200) corresponding to a location where the vortex generator wakes impinge on the blade at the $x/c = 23\%$ chord location. At $y/c = 1.875\%$ the largest fluctuations in $\langle C_p \rangle$ occur over $0.825\% < t_g/c$

$< 4.5\%$ with little variation in $\langle C_p \rangle$ occurring at the larger and smaller tip gaps. Moving up the span the magnitude of $\langle C_p \rangle$ begins to decrease; however, the higher phase numbers (> 150) continue to show variation in $\langle C_p \rangle$ consistent with the tonal contributions to the spectra. At the $y/c = 5\%$ location it is interesting to note that this location appears to respond (i.e. non-zero $\langle C_p \rangle$) over all phase numbers for tip gaps of $t_g/c = 1.65$ and 2.2% . Continuing to move up the span of the blade the pressure response expectedly continues to decrease. At $y/c = 45\%$ a very slight response occurs over the higher phase numbers primarily at $t_g/c = 1.65$ and 2.2% .

Pressure side $\langle C_p \rangle$ is plotted as a function of phase number for each tip gap along the span in figure 9.19. The chordwise location of the spanwise row of microphones is $x/c = 24.375\%$. As expected the tip region shows the largest response in level of $\langle C_p \rangle$ with the tip gaps between $0.825\% < t_g/c < 4.5\%$ being most affected. The largest fluctuations in $\langle C_p \rangle$ near the tip occur for phase number greater than 150. Again, this range of phase number corresponds to the $x/c \approx 23\%$ region where the vortex generator wakes impinge on the blade. It is interesting to see that the pressure side of the blade responds over much of the phase number range near the tip of the blade ($y/c = 1.875$ and 5%). Moving up the span, the pressure response begins to decrease with the larger tip gaps ($t_g/c = 7.9$ and 12.9%) showing a higher response than the smaller tip gaps. As with the suction side of the blade, the pressure side shows substantial pressure fluctuations occurring up to $y/c = 25\%$.

Clearly, the inviscid response has taken on a substantial role in forming the surface pressure field based on the spanwise extent of the measured pressure fluctuations on both sides of the blade. That is, the vortex generator wakes are on the order of 4% of the chord in height and therefore, the purely hydrodynamic pressure fluctuations associated with their passage along the blade will not be present at spanwise locations above $y/c = 5\%$. Thus, the source of pressure fluctuations at the larger spanwise locations must be related to the inviscid blade response.

Movies of $\langle C_p \rangle$ on the pressure and suction side of the blade as a function of spanwise location provide additional support for this conclusion. Figure 9.20 presents embedded movies of $\langle C_p \rangle$ versus y/c for each tip gap. These movies can be viewed by double clicking them. For

the smaller tip gaps ($t_g/c < 4.5\%$) significant fluctuations in $\langle C_p \rangle$ occur up to 45% span with the largest $\langle C_p \rangle$ fluctuations occurring, as expected near blade tip. Large fluctuations at the tip occur over a phase number range which corresponds to the passage of the vortex generator wakes at the $x/c = 23\%$ chord location. The spanwise extent of the pressure response, as mentioned above indicates that the inviscid response is contributing significantly to the overall response of the blade. For larger tip gaps ($3.3\% < t_g/c < 12.9\%$) the spanwise extent of the response is reduced; however, large fluctuations in $\langle C_p \rangle$ continue to occur near the tip and the response is significant up to $y/c = 30\%$. The fluctuations in magnitude of $\langle C_p \rangle$ rise with increasing tip gap to a maximum at $t_g/c = 4.5\%$. At the largest tip gap ($t_g/c = 12.9\%$) the response near the tip is substantially smaller in magnitude, although the blade responds significantly up to $y/c = 20\%$.

9.5.3 Tip Section Unsteady Lift

Phase averaged mean unsteady lift over the tip section of the blade is calculated from pressure measurements. The calculation of lift is performed as

$$\langle C_L(t) \rangle = \int_0^{x_{\max}/c} \langle C_{Pu}(x,t) \rangle dx/c - \int_0^{x_{\max}/c} \langle C_{Pl}(x,t) \rangle dx/c \quad (9.6)$$

which is discretized such that

$$\langle C_L(t) \rangle = \sum_{i=1}^{n_u} \langle C_{Pu_i}(x_{u_i}, t) \rangle \Delta \frac{x_{u_i}}{c} - \sum_{i=1}^{n_l} \langle C_{Pl_i}(x_{l_i}, t) \rangle \Delta \frac{x_{l_i}}{c} \quad (9.7)$$

where $\langle C_{Pu_i} \rangle$ and $\langle C_{Pl_i} \rangle$ are the pressure coefficients on the suction (upper) side and pressure (lower) side respectively at the i^{th} chordwise location, and $\Delta \frac{x_{u_i}}{c}$ and $\Delta \frac{x_{l_i}}{c}$ are the areas (unit width) over which the pressure at the i^{th} chordwise location is multiplied on the suction and pressure side of the blade respectively. The lift coefficient is defined as

$$\langle C_L(t) \rangle = \frac{\langle L \rangle}{\frac{1}{2} \rho U_\infty^2 c} \quad (9.8)$$

where $\langle L \rangle$ is the unsteady lift, ρ the density, U_∞ the mean free-stream velocity, and c the chord. The integration is performed from the leading edge of the blade to $x_{\max}/c = 75.625\%$ on the

suction side (blade 4) and 76.25% on the pressure side (blade 5). Figure 9.21 presents the incremental area's per unit span (Δx_i) used to calculate the unsteady loading on the blade. Blade #4 (measures unsteady pressure on suction side) is shown in this figure; however, blade #5 is discretized in a similar manner. Table 9.1 presents the microphone number, x/c location, and corresponding $\Delta x_i/c$ used to calculate the unsteady force.

Table 9.1: Microphones used in unsteady lift calculation and corresponding resolution

Mic No.	i	x/c	$\Delta x_i/c$
1	6	0.7625	0.2125
2	5	0.55	0.184375
3	4	0.39375	0.128125
4	3	0.29375	0.08125
5	2	0.23125	0.059375
6	1	0.175	0.203125
13	6	0.75625	0.2
14	5	0.55625	0.175
15	4	0.40625	0.125
16	3	0.30625	0.08125
17	2	0.24375	0.059375
18	1	0.1875	0.215625

Figure 9.22 and 9.23 presents the $\langle C_L \rangle$ as a function of phase number for tip gaps, $t_g/c = 0.825, 1.65, 2.2, 3.3\%$ and $t_g/c = 4.5, 5.7, 7.9, 12.9\%$, respectively. Figure 9.22 shows for tip gaps $t_g/c = 0.825, 1.65, 2.2\%$ little variation in $\langle C_L \rangle$ occurs over the first 150 phase numbers (i.e. as the vortex generator wakes pass over the first 60% chord). For phase numbers above 150 $\langle C_L \rangle$ increases and reaches a peak in the 175 to 225 phase number range. As the tip gap increases from 0.825% to 2.2% the magnitude of $\langle C_L \rangle$ falls slightly in this phase number range. The interaction of the vortex generator wakes and tip leakage vortex at these tip gaps appears to be a linear superposition of the two. That is to say, the inviscid response is not playing a large role in the overall blade response. When the tip gap is increased slightly more to $t_g/c = 3.3\%$ the unsteady lift response changes considerably. The largest fluctuations in $\langle C_L \rangle$ occur over the first 100 phase numbers corresponding to the vortex generator wakes passing the first 30% of the blade chord. Additionally, $\langle C_L \rangle$ oscillates more over the phase number range as compared to the first three tip gaps. The unsteady lift response continues to increase as the tip gap is increased (figure 9.23) up to and including $t_g/c = 7.9\%$. The lift oscillates significantly over the

entire phase number range reaching peak values in the first 150 phase numbers. The increase in the lift response with increasing tip gap is consistent with the large increase in tip leakage vortex circulation which occurs as the tip gap is increased uncovered by Ma (2003).

9.5.4 Tip Section Lift Compared with Inviscid Theory

The response at these larger tip gaps appears to be heavily influenced by the inviscid blade response, or at least a complex interaction of the inviscid and viscous response. To assess the extent of interaction response related to the inviscid response comparisons are made with the theory of Glegg (1999). Figure 9.24 presents a comparison of the measured and theoretical tip section lift at all tip gaps as a function of phase number. The unsteady lift has the same shape over the first 6 tip gaps, reaching its maximum value at the smallest tip gap. The theoretical $\langle C_L \rangle$ declines linearly from near zero at phase zero to a minimum near phase number 140. $\langle C_L \rangle$ then rises quickly over a very short phase number range to a peak. The lift then falls rapidly, rising briefly and then continuing to fall smoothly to zero at phase number 256. This variation in $\langle C_L \rangle$ suggested that the blade becomes heavily loaded as the vortex generator wakes pass the aft 40% of the blade chord. Poor agreement exists between the details of the theoretical and measured lift at $t_g/c = 0.825, 1.65, 2.2, 3.3\%$ with the measured lift fluctuating much more than predicted and in poor agreement with the shape of the predicted $\langle C_L \rangle$. The theory also tends to over predict the magnitude of $\langle C_L \rangle$. At larger tip gaps, $t_g/c = 4.5, 5.5, 7.9, 12.9\%$ the lift tends to be under predicted and the measured lift fluctuates much more than that predicted. However, it is interesting to note that in all cases the measured and predicted lift fluctuations are of the same order of magnitude.

Since the measured unsteady pressure is expected to contain some component related to hydrodynamic pressure fluctuations it is not surprising to see the poor agreement between the details of the measured and predicted $\langle C_L \rangle$. In fact, the involvement of significant hydrodynamic pressure fluctuations indicates the complex nature of the interaction between the blade and inflow vortices. Additionally, the integration limits and resolution used to compute unsteady lift from pressure measurements must be considered. Limiting the chordwise extent of integration cuts what would likely be a significant portion of the unsteady loading. Lastly, the tip treatment

used to account for the tip gap in Glegg's (1999) cascade response theory may influence the theoretical prediction of unsteady lift.

9.6 Comparison of Measured Lift with Tip Leakage Circulation

The phase averaged lift is compared with phase averaged circulation (measured and presented by Ma 2003) in the tip leakage vortex in figure 9.25 for $t_g/c = 0.825, 1.65, 2.2,$ and 3.3% . It is interesting to see that the magnitude of $\langle C_L \rangle$ is of the same order as the phase averaged circulation at each tip gap (however, a factor of $\frac{2h_b}{c} = 1.858$ must multiply the normalized phase averaged circulation to make an exact comparison). Also, the variation in phase number is similar, particularly at the 3.3% tip gap despite the slight relative phase lag between the two. The implication here is that the large fluctuations in the tip leakage vortex circulation appear to be closely related to the inviscid response of the blade.

9.7 Higher Order Moments and Spectra

The phase averaged variance of unsteady pressure, $\langle C_p'^2 \rangle$ is computed according to eq. (9.3) and presented in figure 9.26 and 9.27 on the suction and pressure side, respectively as a function of phase number for each chordwise location. Levels of $\langle C_p'^2 \rangle$ remain near zero over much of the leading edge portion of the blade, becoming non-zero beyond $x/c = 40\%$. Significant levels of $\langle C_p'^2 \rangle$ occur over the entire phase number range at the most trailing edge measurement location, $x/c = 75.625\%$.

Unsteady pressure power spectral densities, G_{pp} are presented as a function of frequency (Hz) on the suction side along the chord in figure 9.28 and along the span in figure 9.29. Chordwise and spanwise pressure side spectra are presented in figures 9.30 and 9.31 respectively.

9.8 Summary

Measurements of unsteady pressure were made on the suction and pressure side of blades in a linear cascade. Measurements were made with an array of 24 microphones mounted subsurface. The inflow disturbance was periodic and formed by a set of small vortex generators designed to model the horseshoe vortex which develops on the inlet guide vanes. The unsteady

pressure was measured at eight tip gaps ($t_g/c = 0.00825, 0.0165, 0.022, 0.033, 0.045, 0.057, 0.079, 0.129$). It is shown that the interaction of a cascade of blades with a periodic inflow disturbance is complex and involves both significant viscous and inviscid mechanisms.

The magnitude of fluctuations in the pressure response is shown to increase with increasing tip gap up to $t_g/c = 5.7\%$. This result agrees well with the findings of Ma (2003) which demonstrated an increase in magnitude of fluctuations in the tip leakage vortex circulation with increasing tip gap. Chordwise measurements of unsteady pressure are shown to increase moving towards the trailing edge possibly as a result of the trailing edge singularity which occurs in blade response theory.

The fact that the blade is excited both locally and over a substantial portion of the chord indicates that a more complex interaction containing both inviscid response and viscous phenomena is underway. However, although the theoretical prediction of unsteady tip loading does not match details of the measurement, the correct order of magnitude response is shown. Additionally, based on comparisons of phase averaged lift and circulation in the tip leakage vortex, a close relationship appears to exist between the two. This suggests that broadband noise calculations using inviscid theory could produce useful results. Furthermore, these results imply the fluctuation in tip leakage circulation and, perhaps pressure fluctuations in the tip leakage vortex could be estimated from inviscid theory.

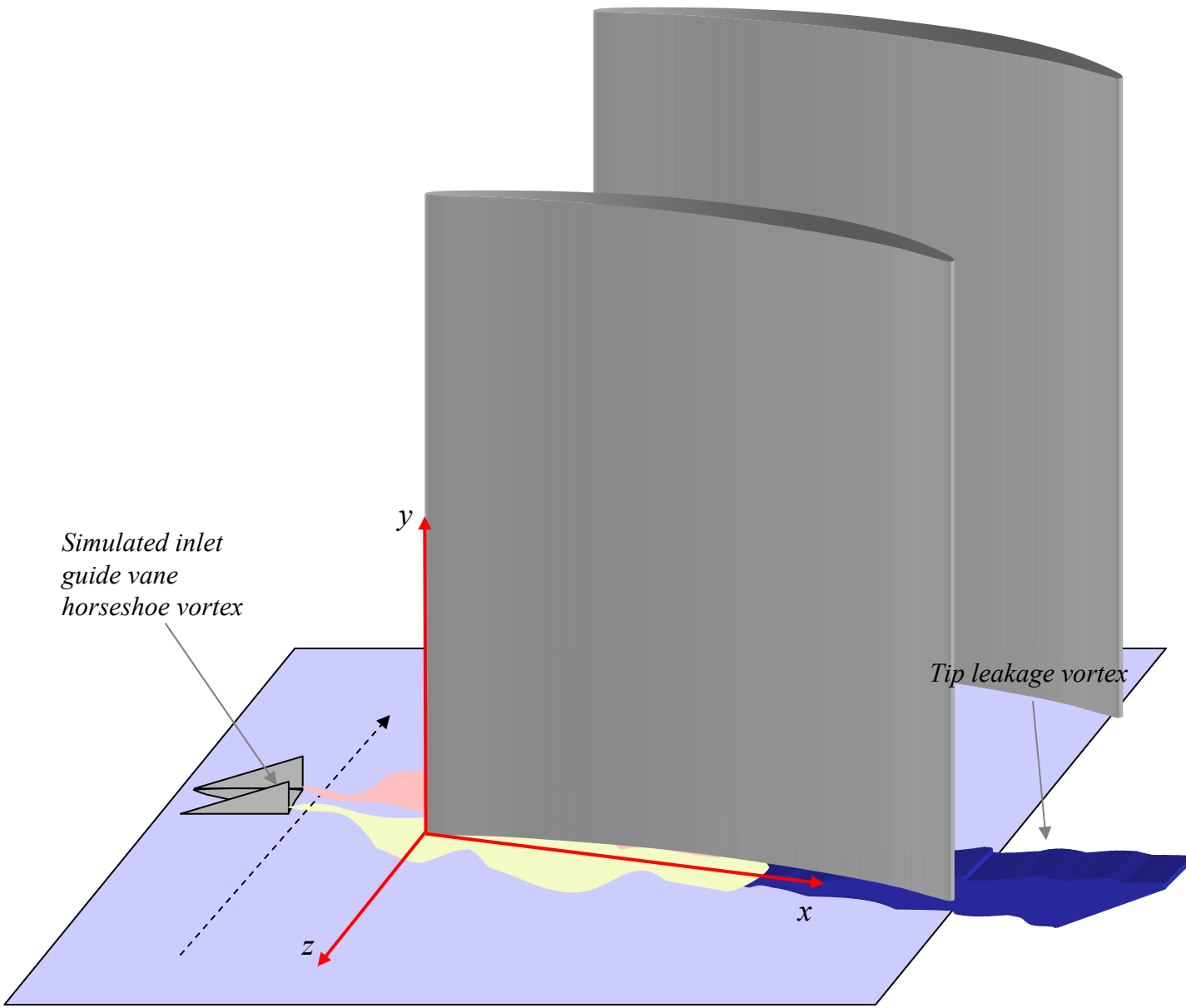


Figure 9.1: Schematic of blade/disturbance interaction showing coordinate system

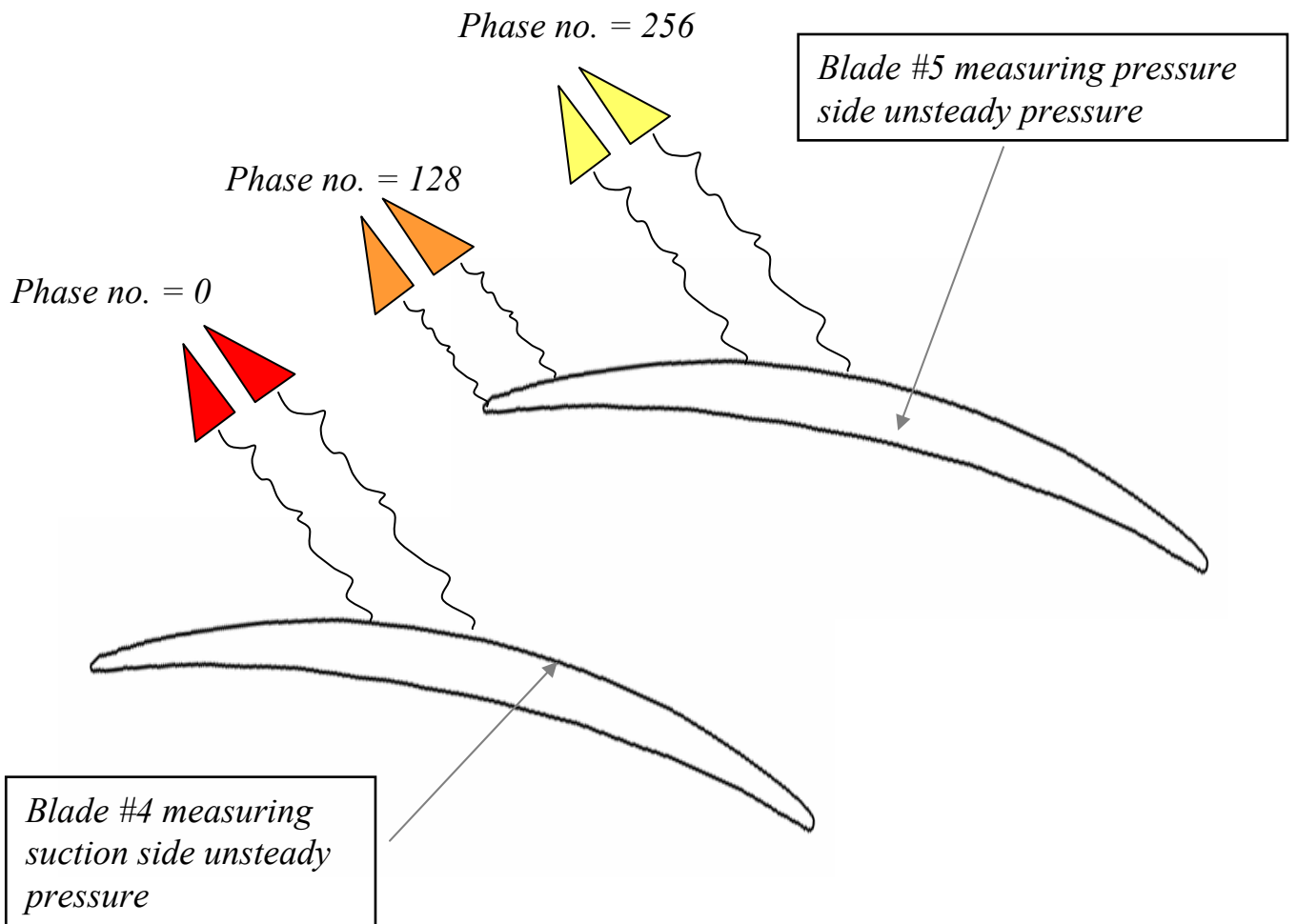


Figure 9.2: Schematic showing position of vortex generators relative to blades as phase number varies from 0 to 256

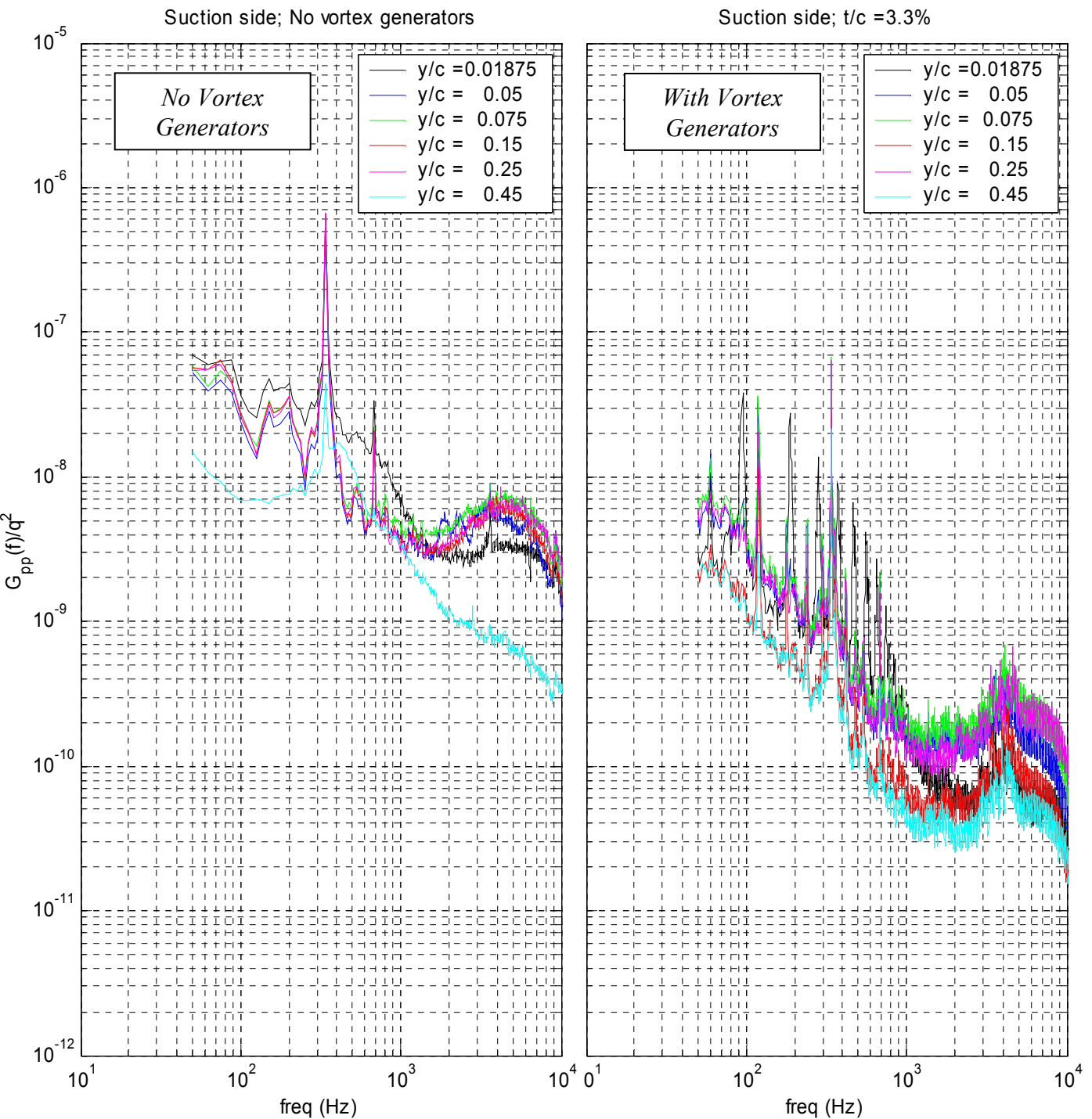


Figure 9.3: Time averaged pressure spectra on *suction* side of blade at different spanwise stations for $t_s/c = 3.3\%$. Comparison of spectra measured for belt in motion and no vortex generators attached with spectra measured with vortex generators attached.

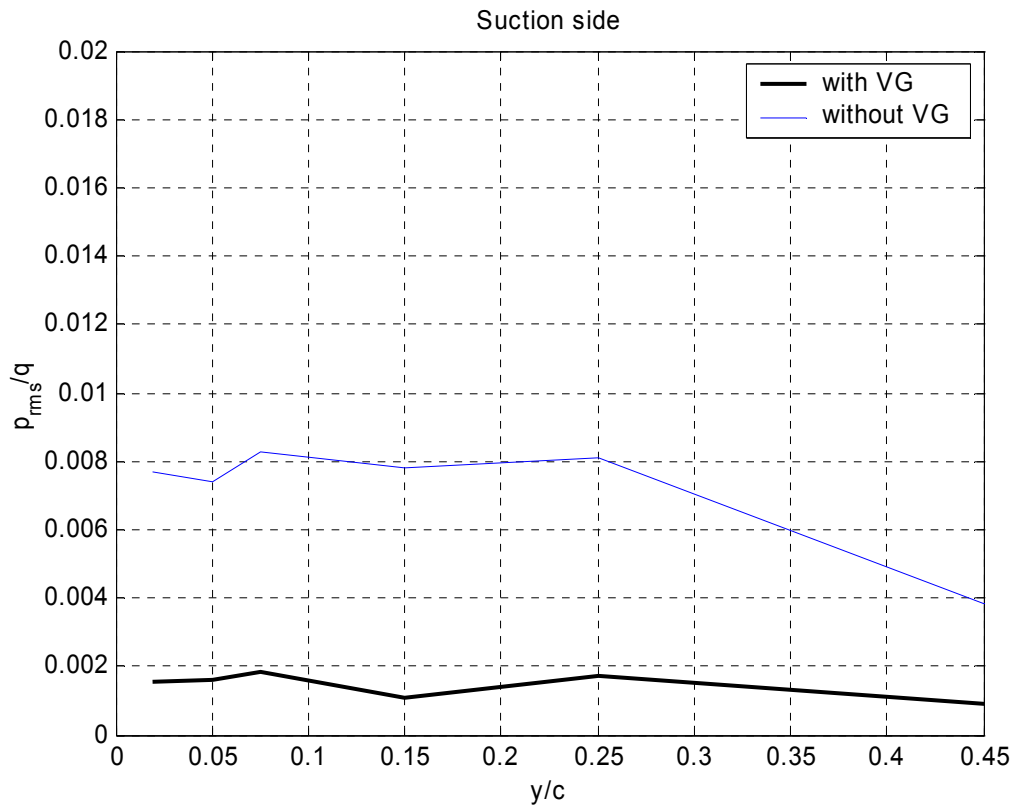


Figure 9.4: Spanwise RMS pressure on *suction* side of blade for $t_g/c = 3.3\%$ with belt in motion and no vortex generators attached compared with measurements made with vortex generators attached.

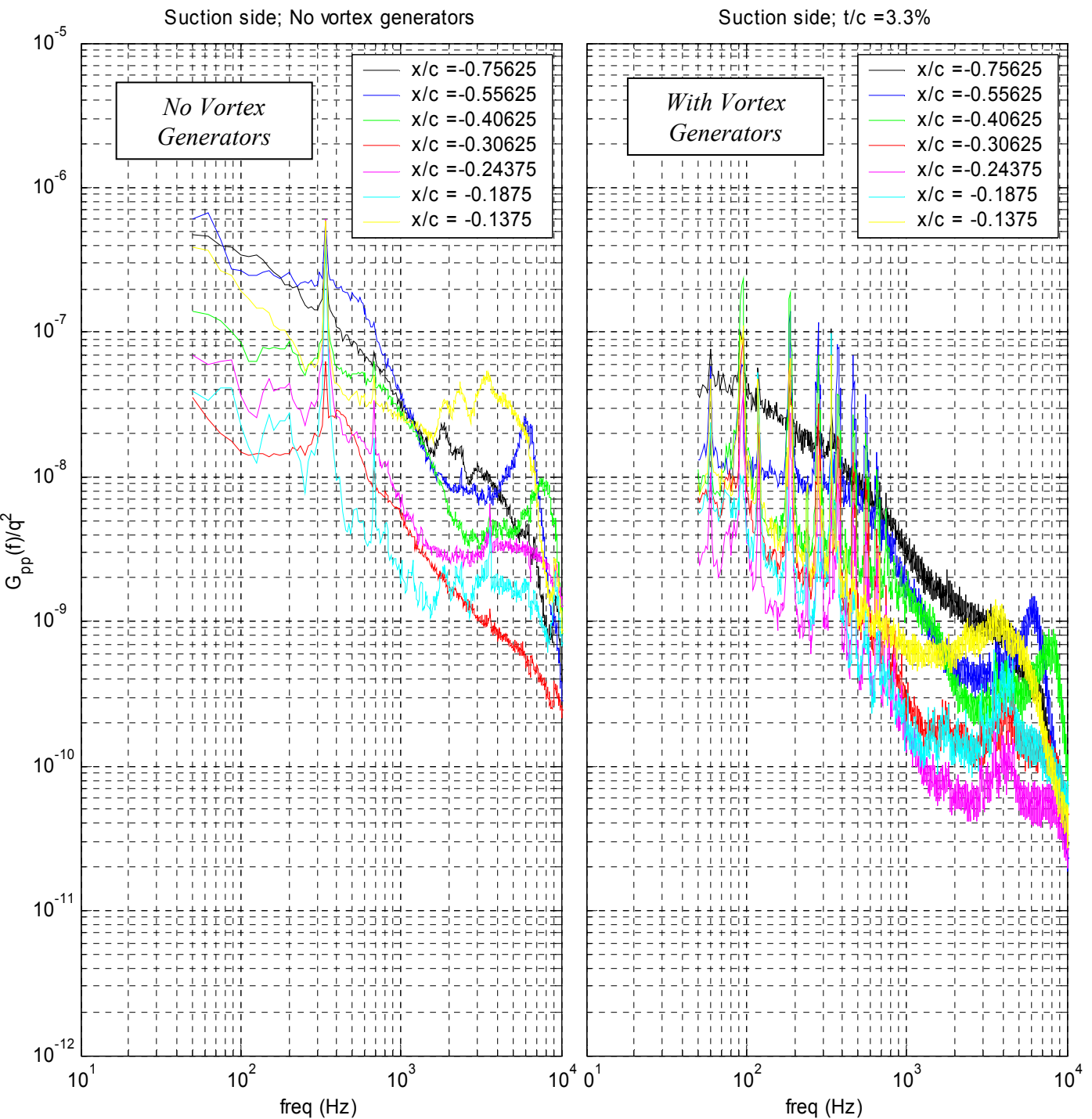


Figure 9.5: Time averaged pressure spectra on *suction* side of blade at different chordwise stations for $t_s/c = 3.3\%$. Comparison of spectra measured for belt in motion and no vortex generators attached with spectra measured with vortex generators attached.

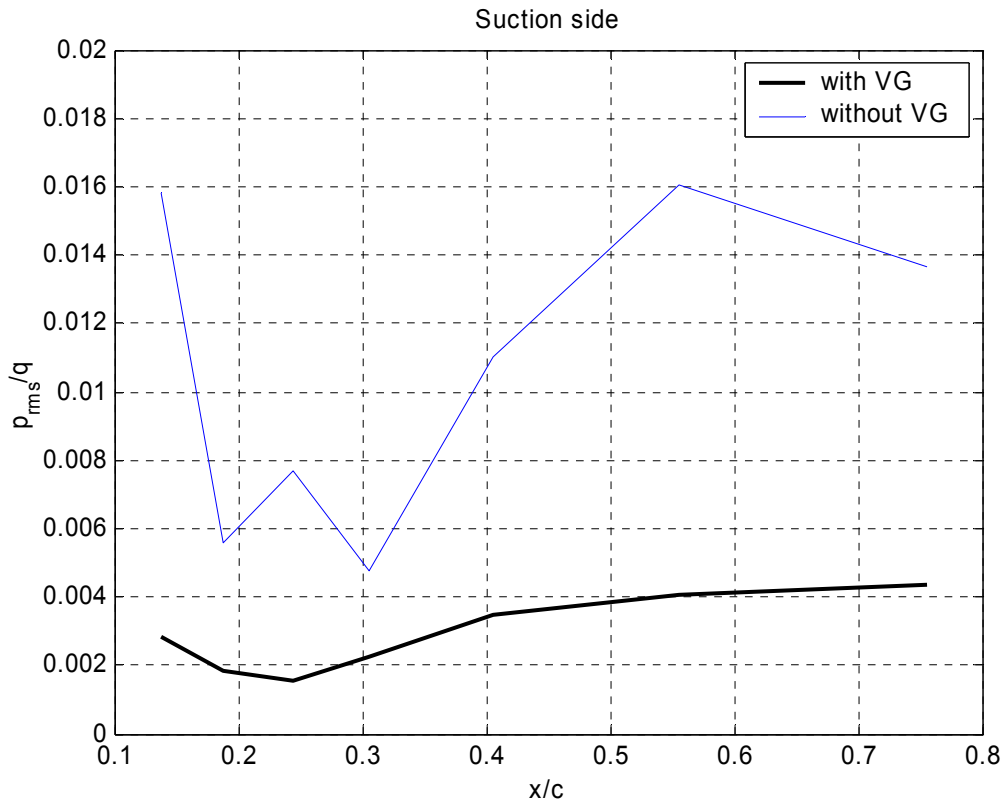


Figure 9.6: Chordwise RMS pressure on *pressure* side of blade for $t_g/c = 3.3\%$ with belt in motion and no vortex generators attached compared with measurements made with vortex generators attached.

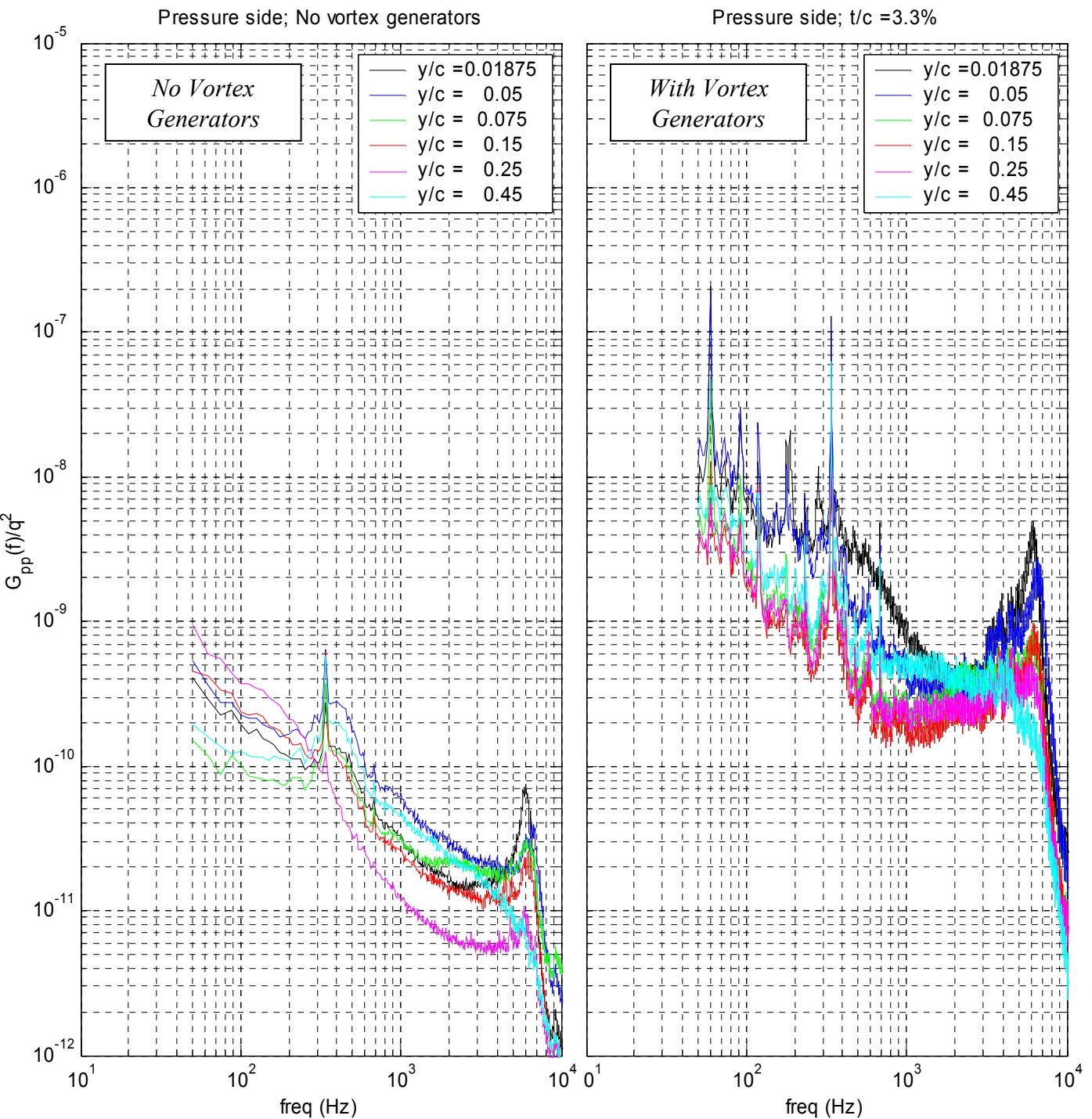


Figure 9.7: Time averaged pressure spectra on *pressure* side of blade at different spanwise stations for $t_g/c = 3.3\%$. Comparison of spectra measured for belt in motion and no vortex generators attached with spectra measured with vortex generators attached.

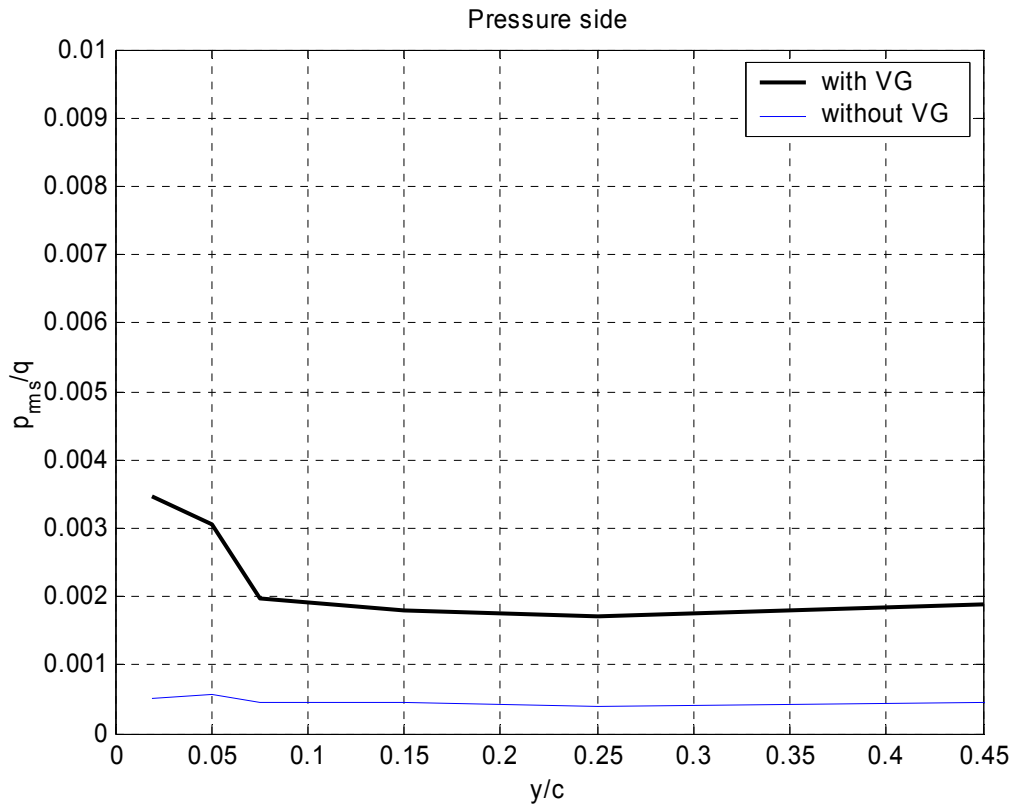


Figure 9.8: Spanwise RMS pressure on *pressure* side of blade for $t_g/c = 3.3\%$ with belt in motion and no vortex generators attached compared with measurements made with vortex generators attached.

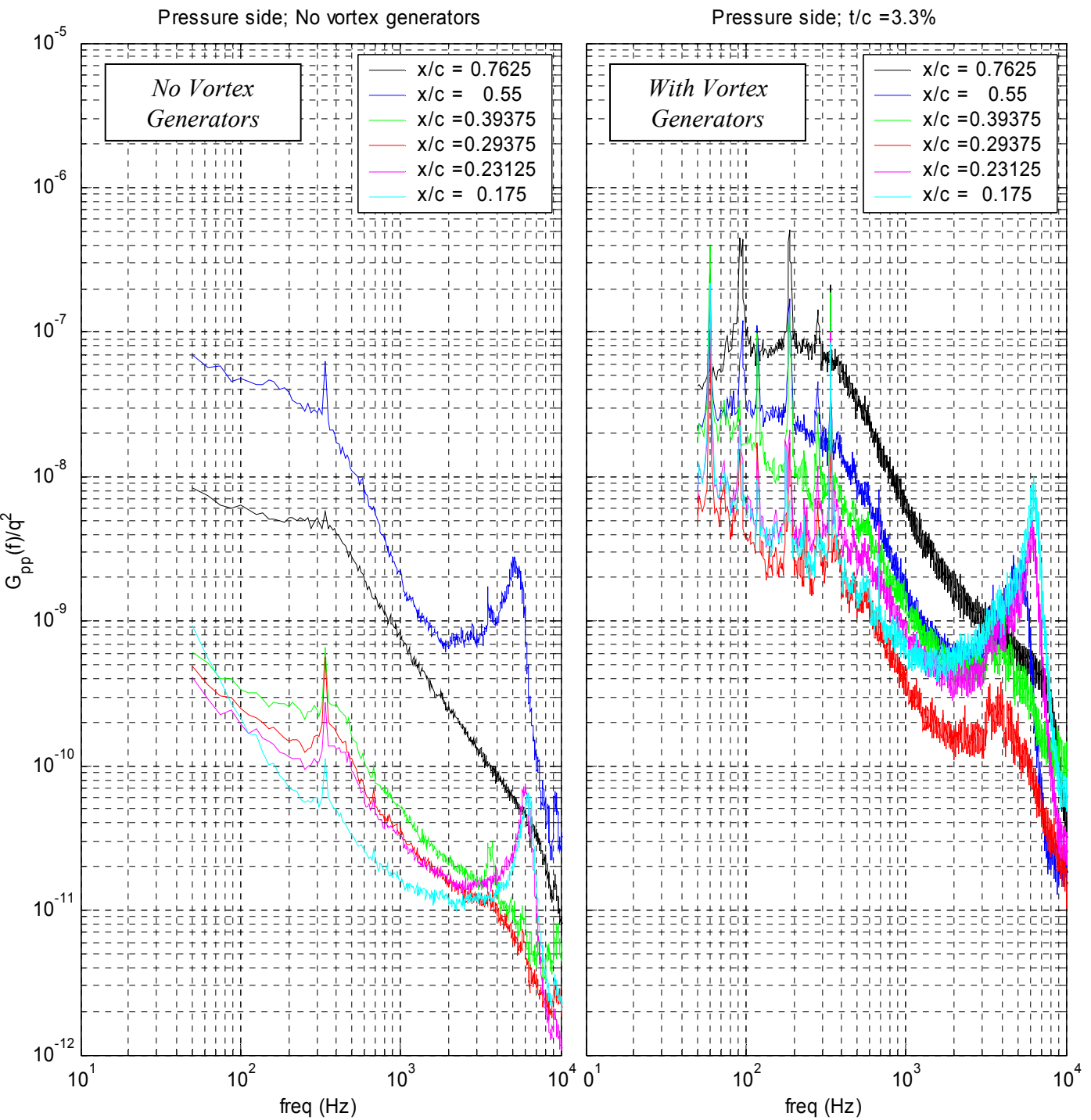


Figure 9.9: Time averaged pressure spectra on *pressure* side of blade at different chordwise stations for $t_g/c = 3.3\%$. Comparison of spectra measured for belt in motion and no vortex generators attached with spectra measured with vortex generators attached.

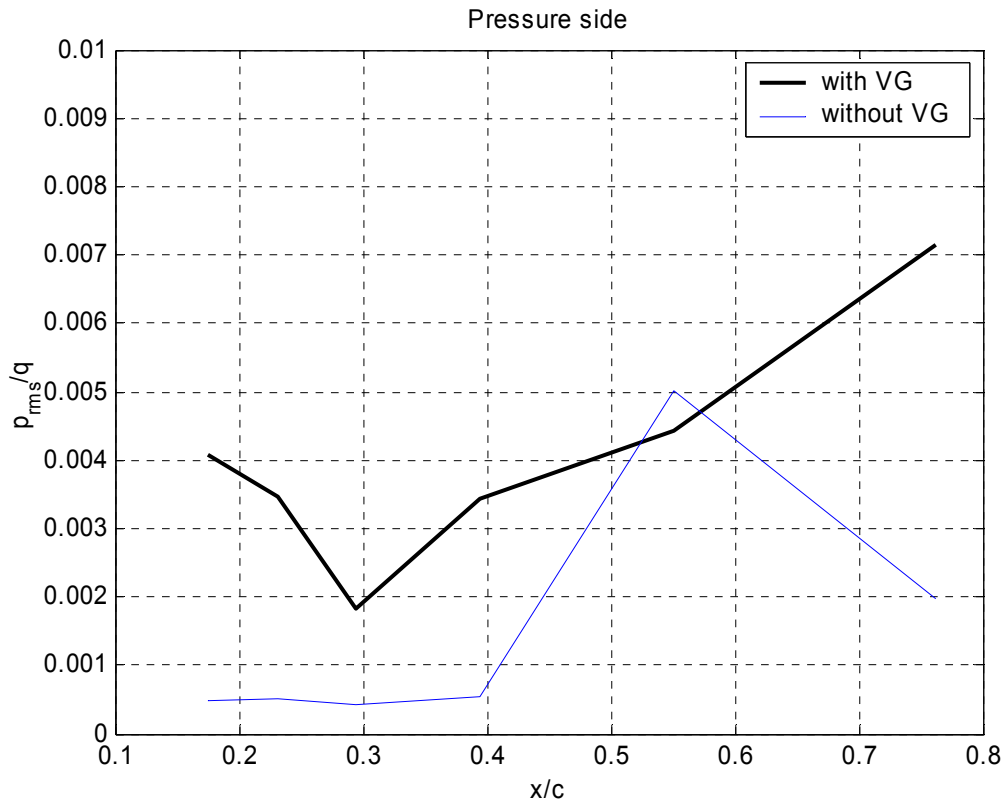


Figure 9.10: Chordwise RMS pressure on *pressure* side of blade for $t_g/c = 3.3\%$ with belt in motion and no vortex generators attached compared with measurements made with vortex generators attached.

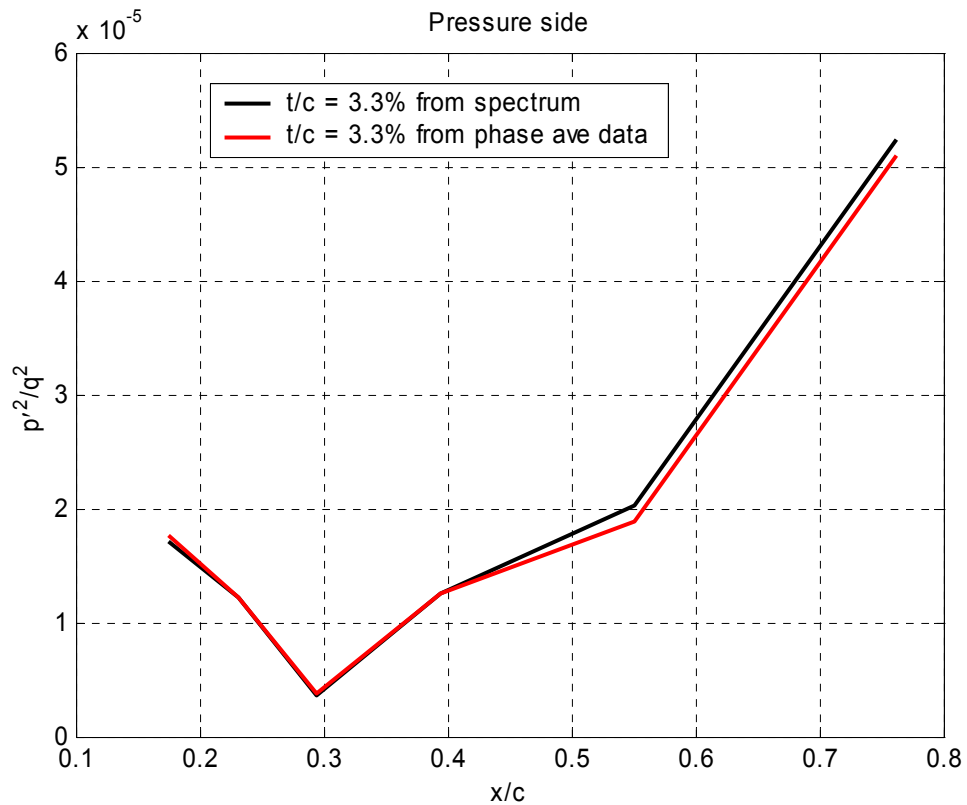
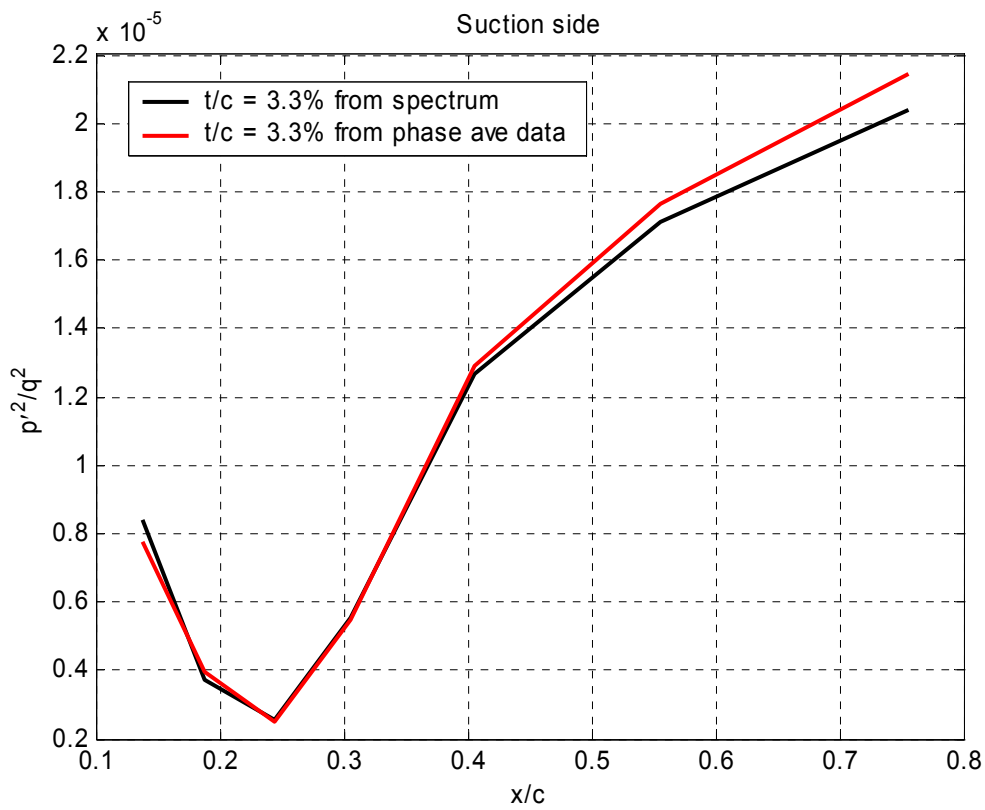


Figure 9.11: Comparison of chordwise p'^2 calculated from spectra and from phase averaged data. Such a comparison serves as an independent check of the two processing codes used. Plots presented for the suction and pressure side of blade for $t_g/c = 3.3\%$.

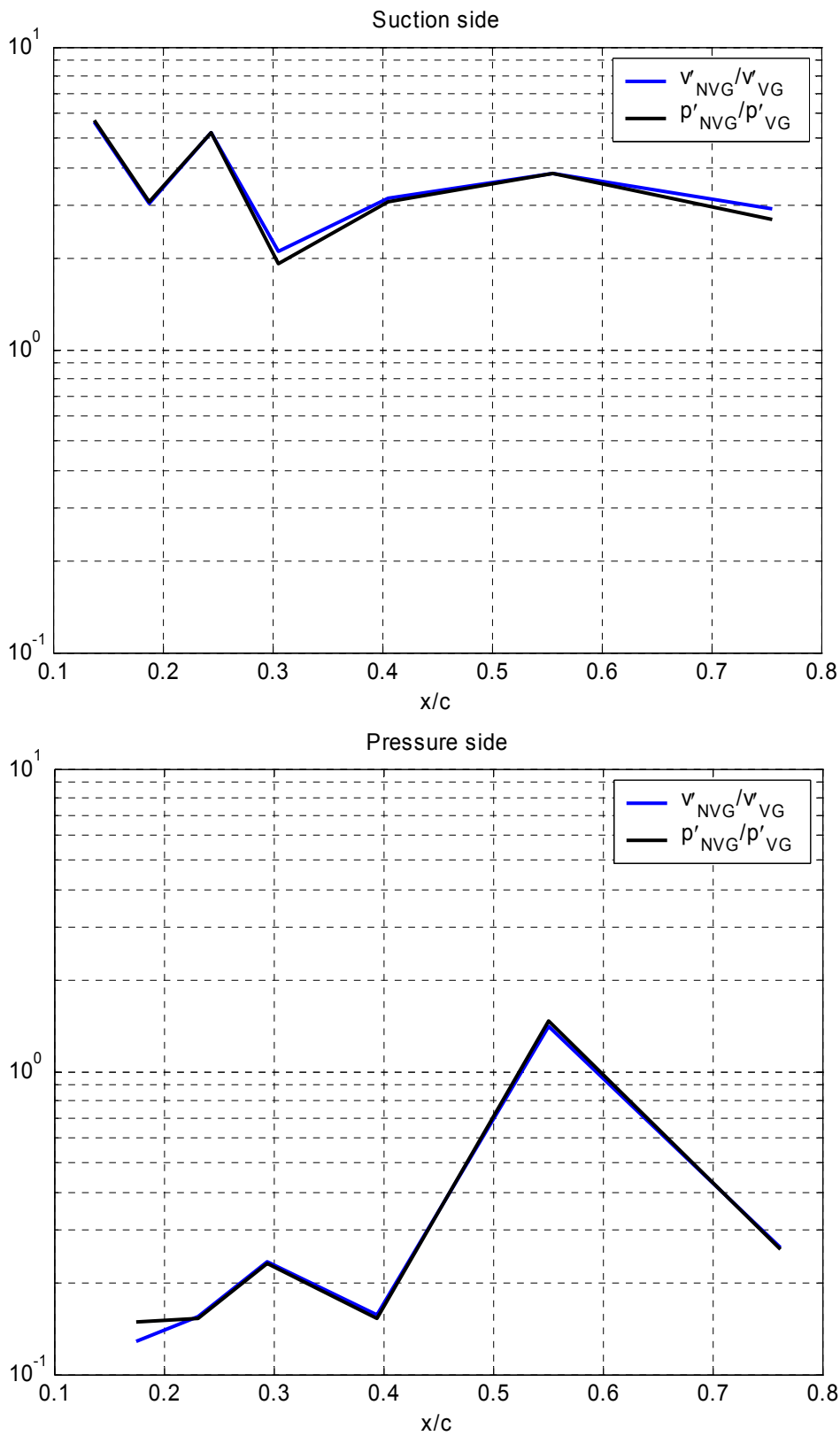


Figure 9.12: Ratio of RMS voltages calculated without and with vortex generators compared to ratio of RMS pressures calculated without and with vortex generators. Such comparisons ensure the proper application of microphone calibrations in both processing codes. Data presented for the pressure and suction side of blade as a function of chordwise location for $t_g/c = 3.3\%$.

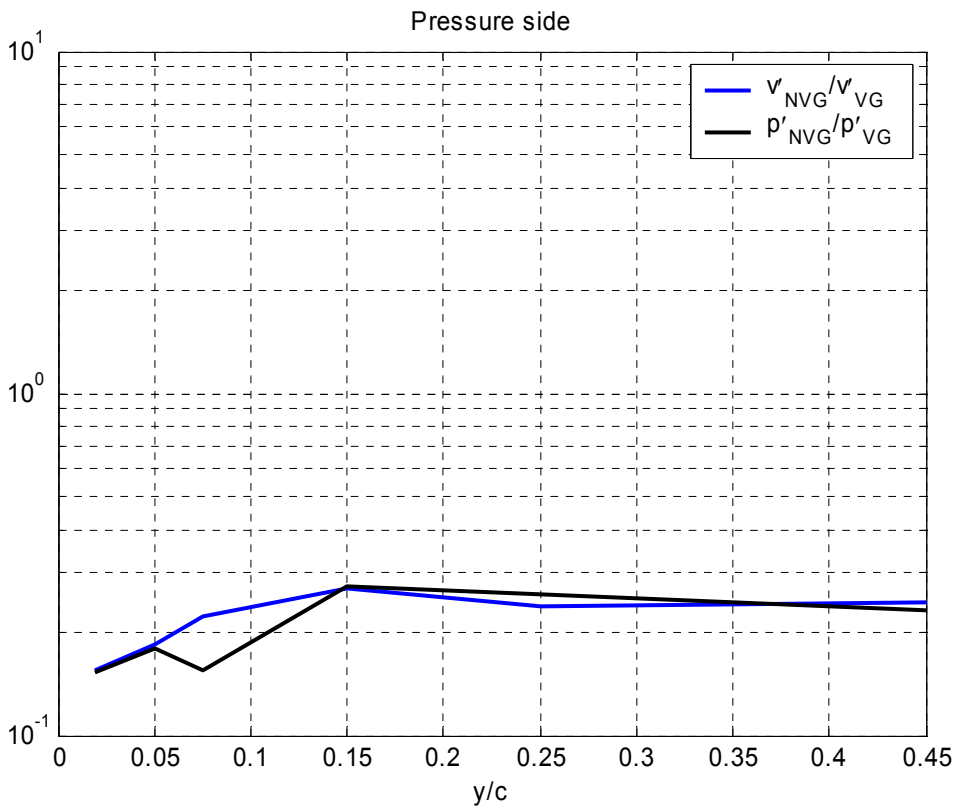
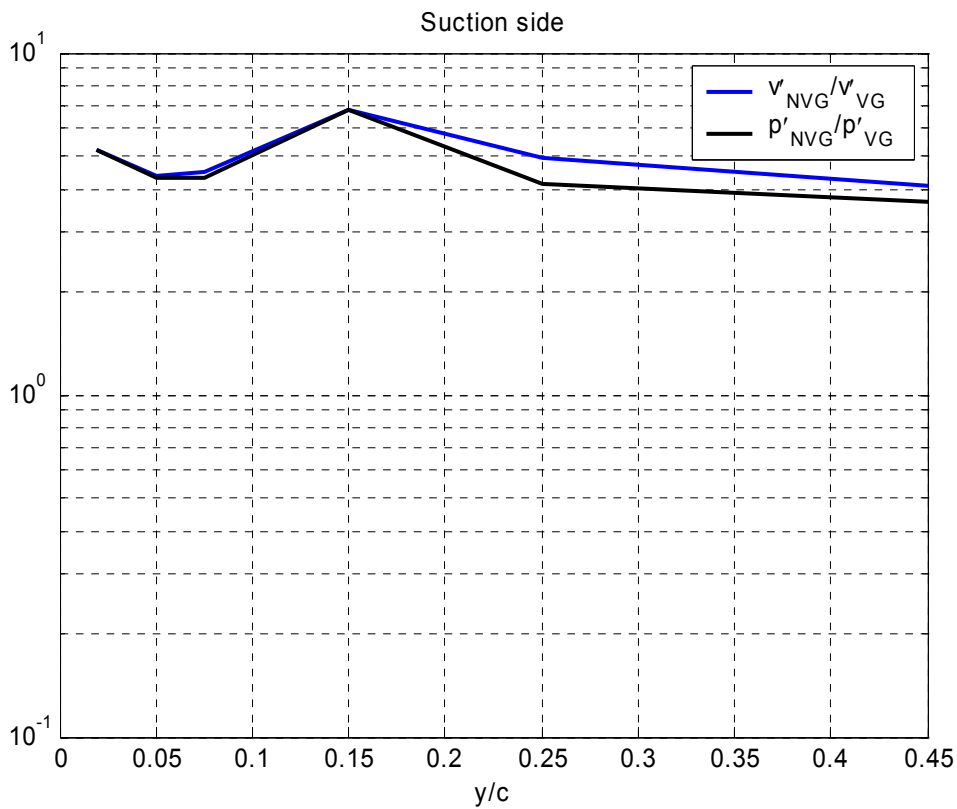


Figure 9.13: Ratio of RMS voltages calculated without and with vortex generators compared to ratio of RMS pressures calculated without and with vortex generators. Such comparisons ensure the proper application of microphone calibrations in both processing codes. Data presented for the pressure and suction side of blade as a function of spanwise location for $t_g/c = 3.3\%$.

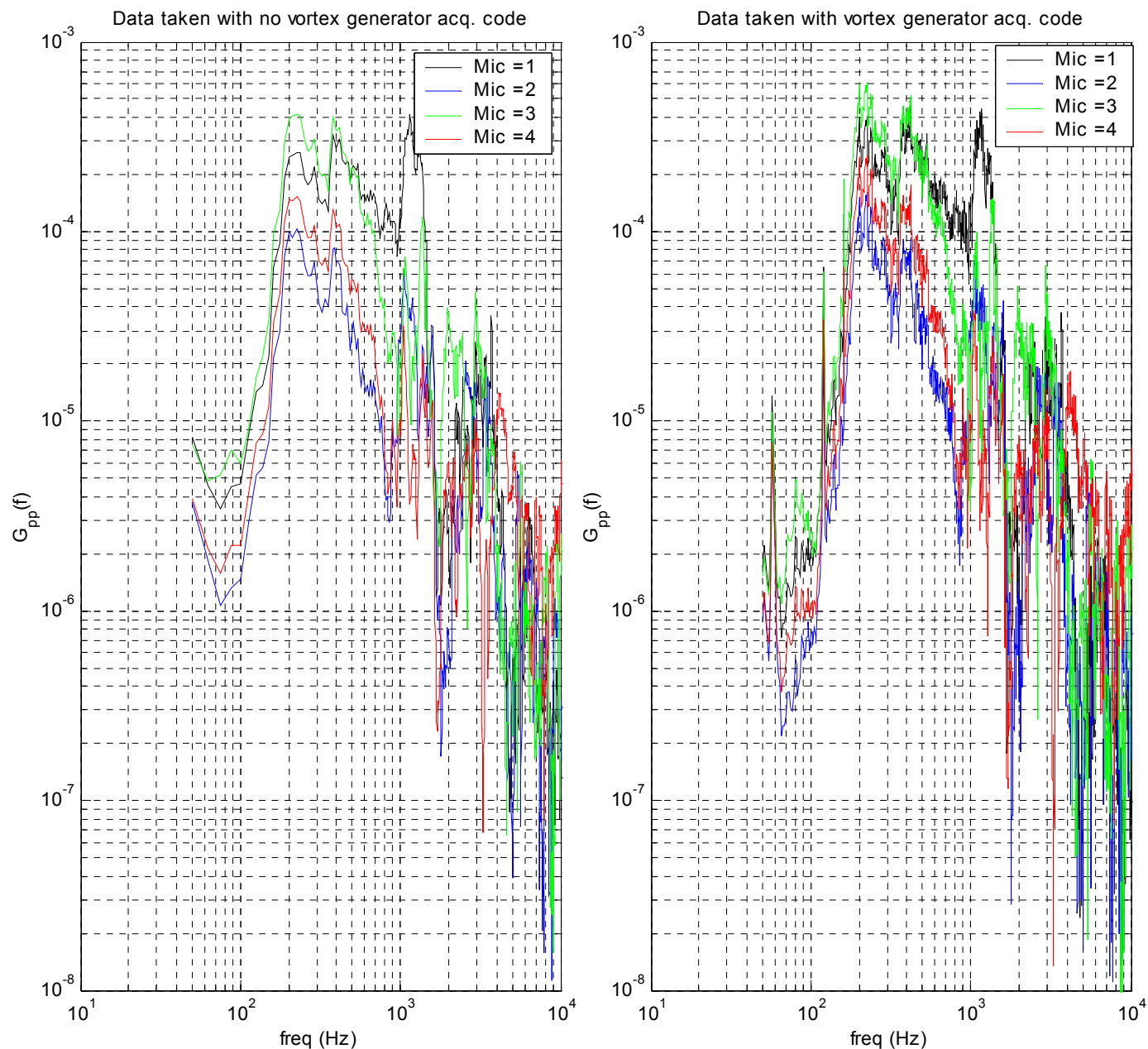


Figure 9.14: Measurement of acoustic field produced by radio tuned to static. Data on left was taken with the acquisition code used to make pressure measurements without vortex generators present. Data on right was taken with the acquisition code used to make pressure measurements when vortex generators are present. Comparison of both sets of data assists in ensuring data acquisition and processing is consistent between both measurements.

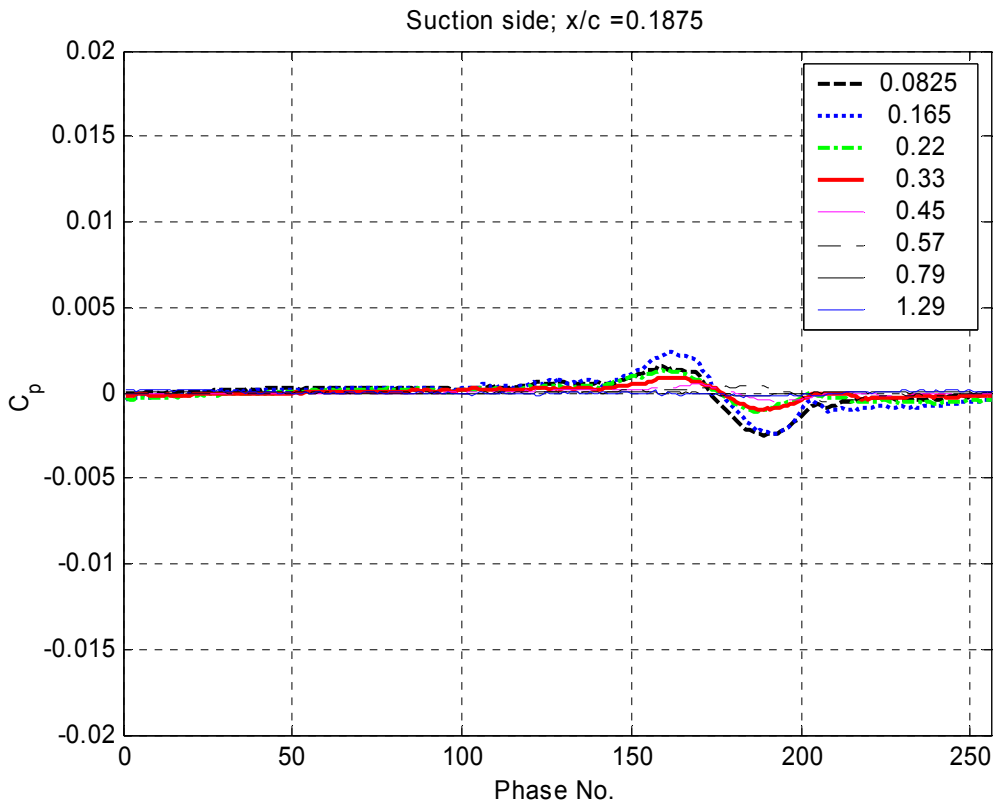
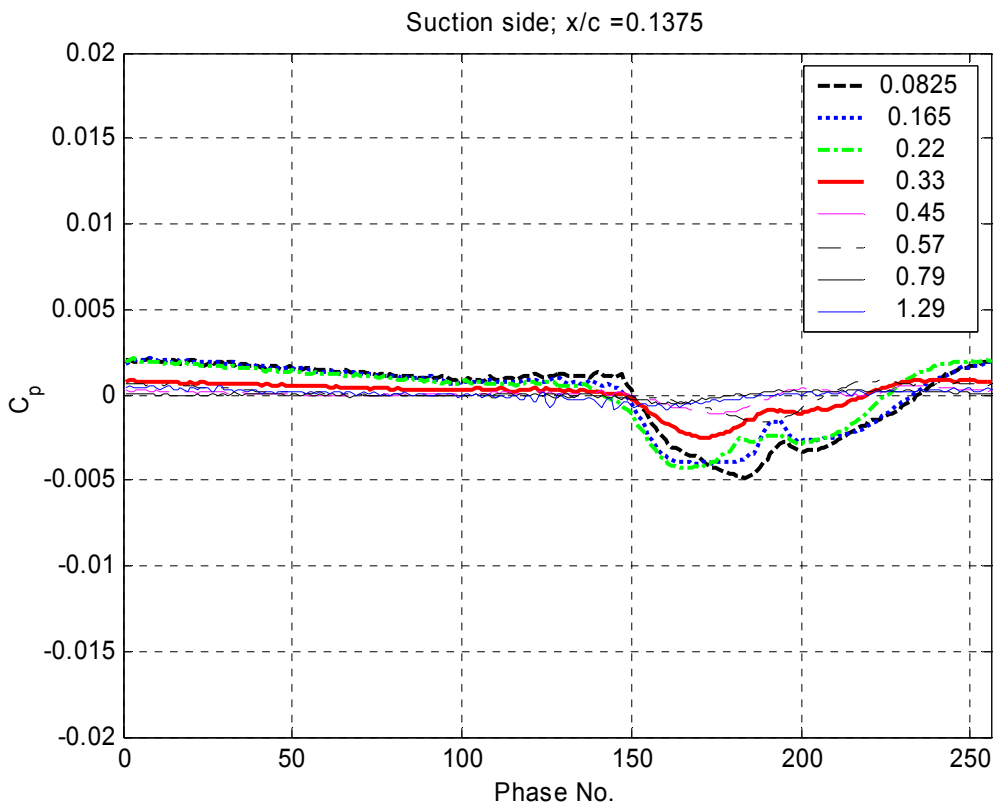


Figure 9.15: Suction side C_p as a function of phase number plotted for each tip gap along the chord at $x/c = 13, 18, 24, 30, 40, 55, 75$

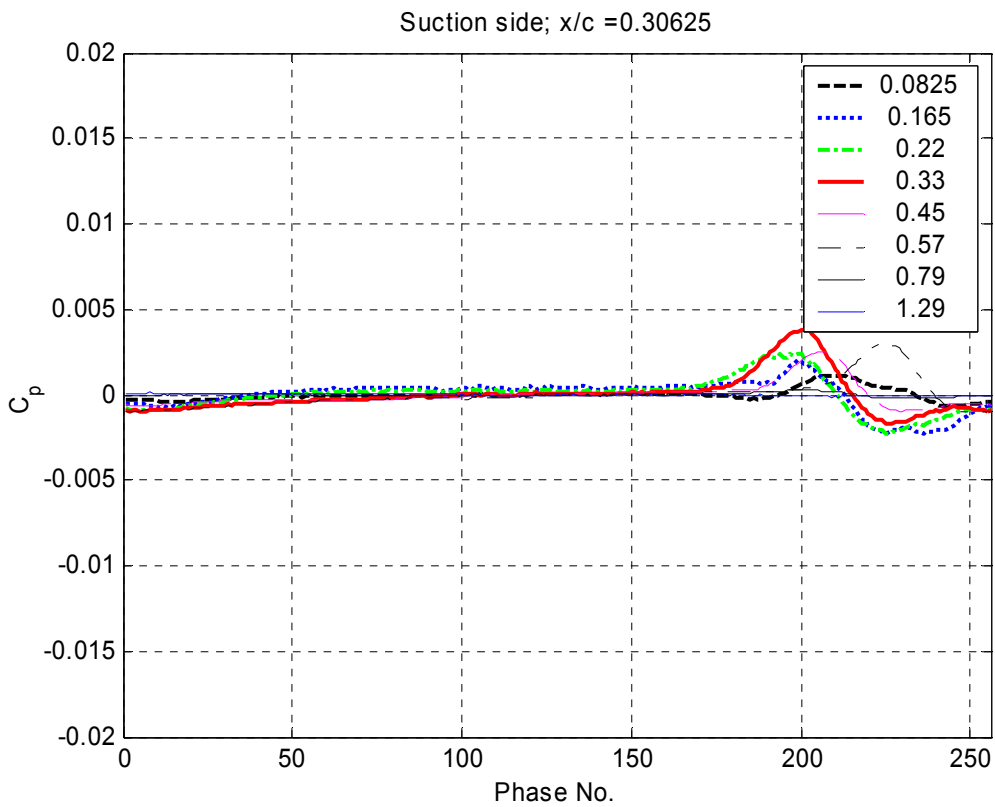
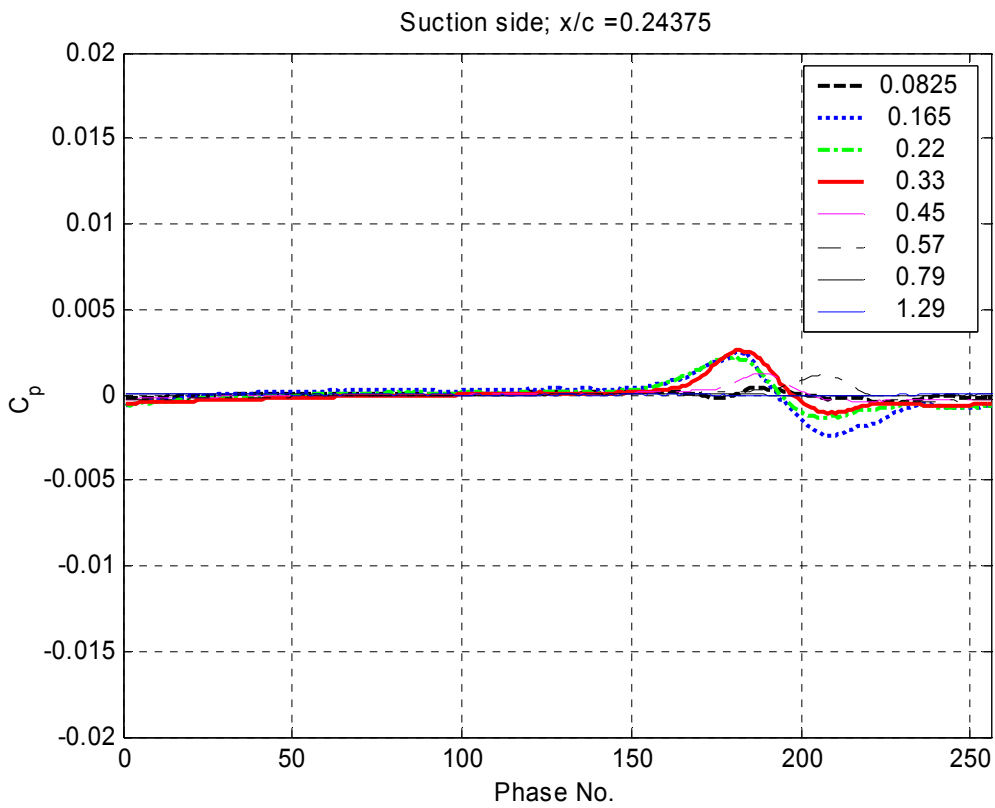


Figure 9.15 continued: Suction side C_p as a function of phase number plotted for each tip gap along the chord at $x/c = 13, 18, 24, 30, 40, 55, 75$

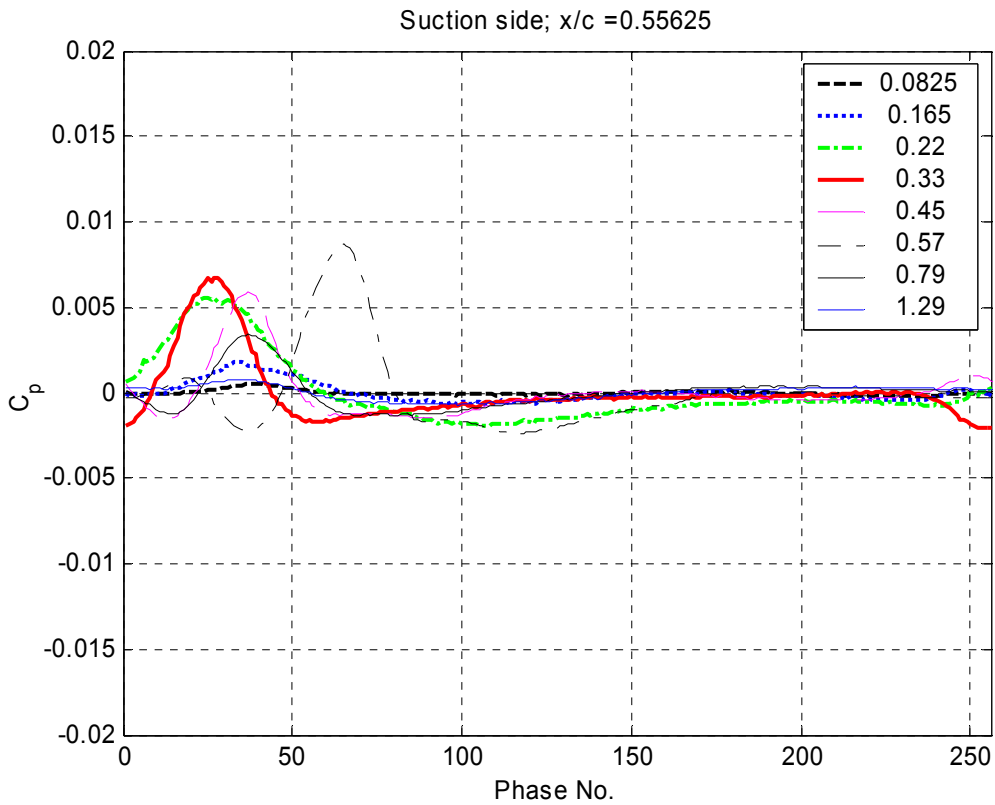
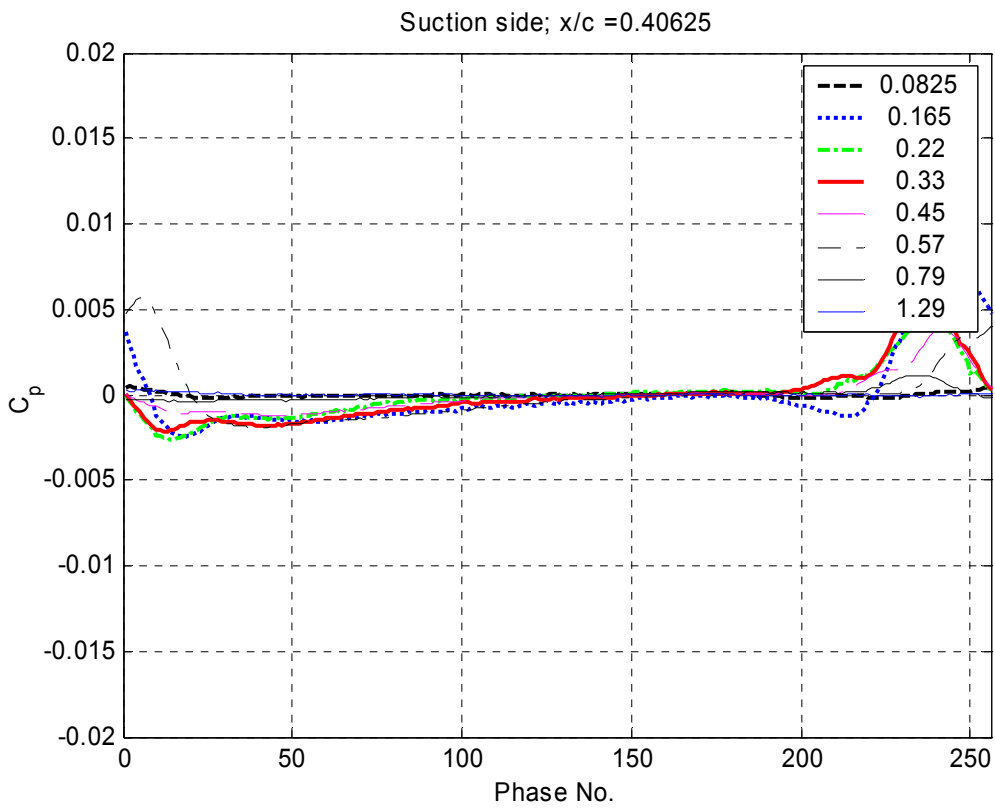


Figure 9.15 continued: Suction side C_p as a function of phase number plotted for each tip gap along the chord at $x/c = 13, 18, 24, 30, 40, 55, 75$

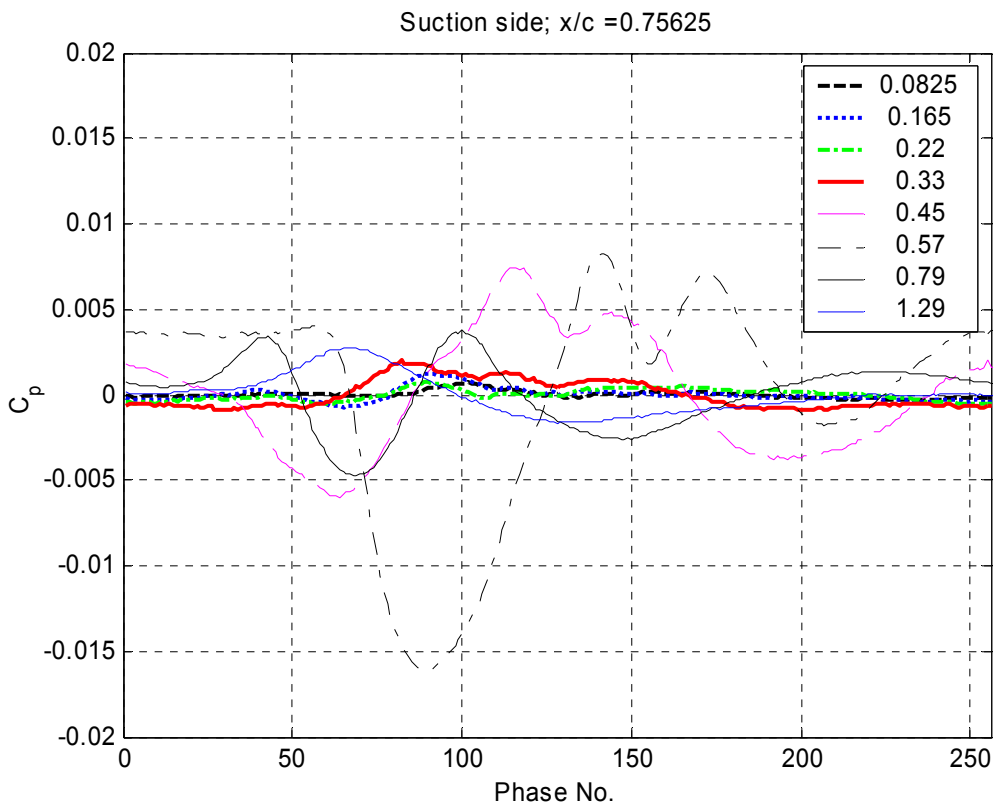


Figure 9.15 continued: Suction side C_p as a function of phase number plotted for each tip gap along the chord at $x/c = 13, 18, 24, 30, 40, 55, 75$

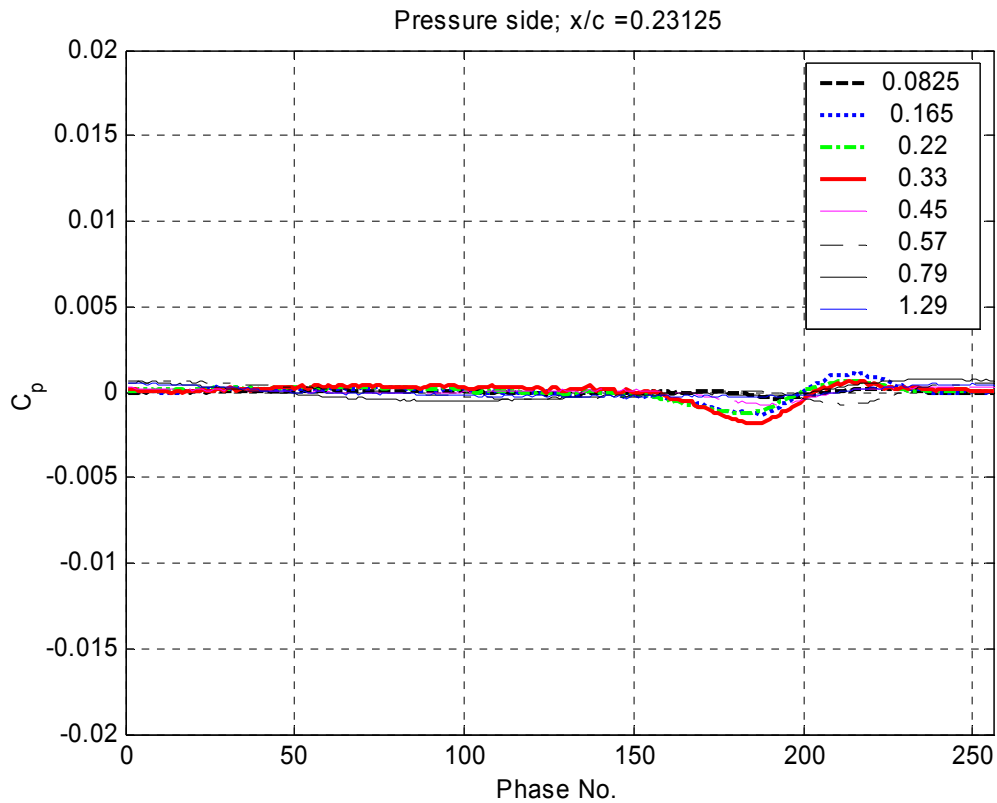
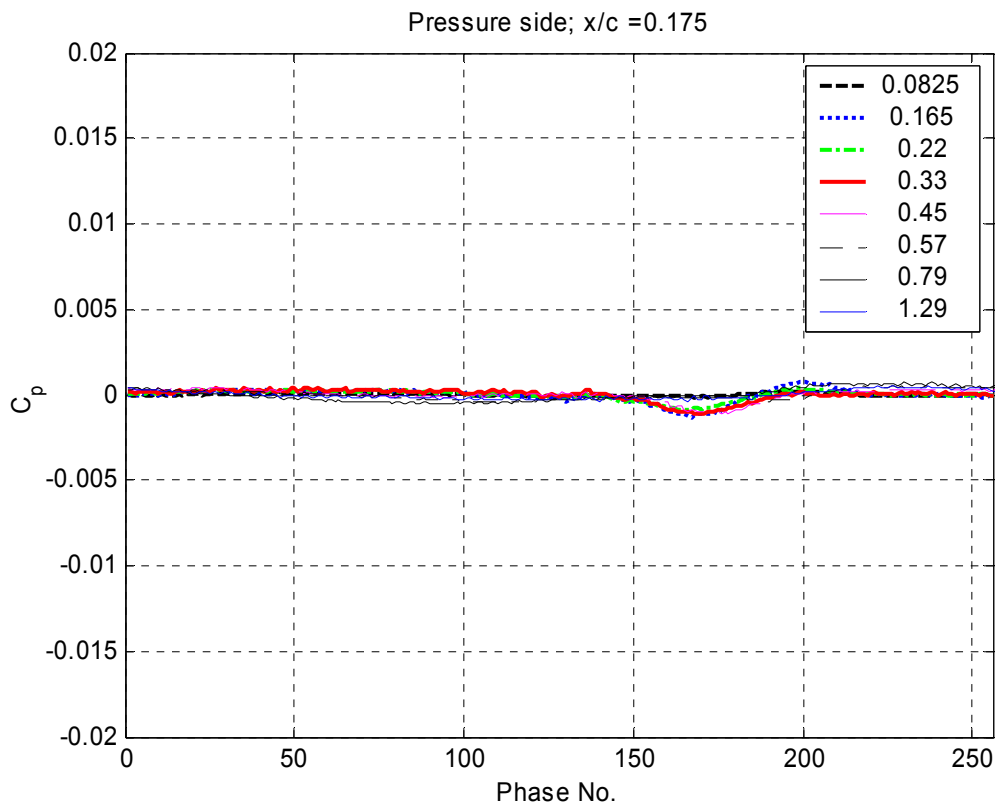


Figure 9.16: Pressure side C_p as a function of phase number plotted for each tip gap along the chord at $x/c = 17.5, 23.125, 29.375, 39.375, 55, 76.25\%$

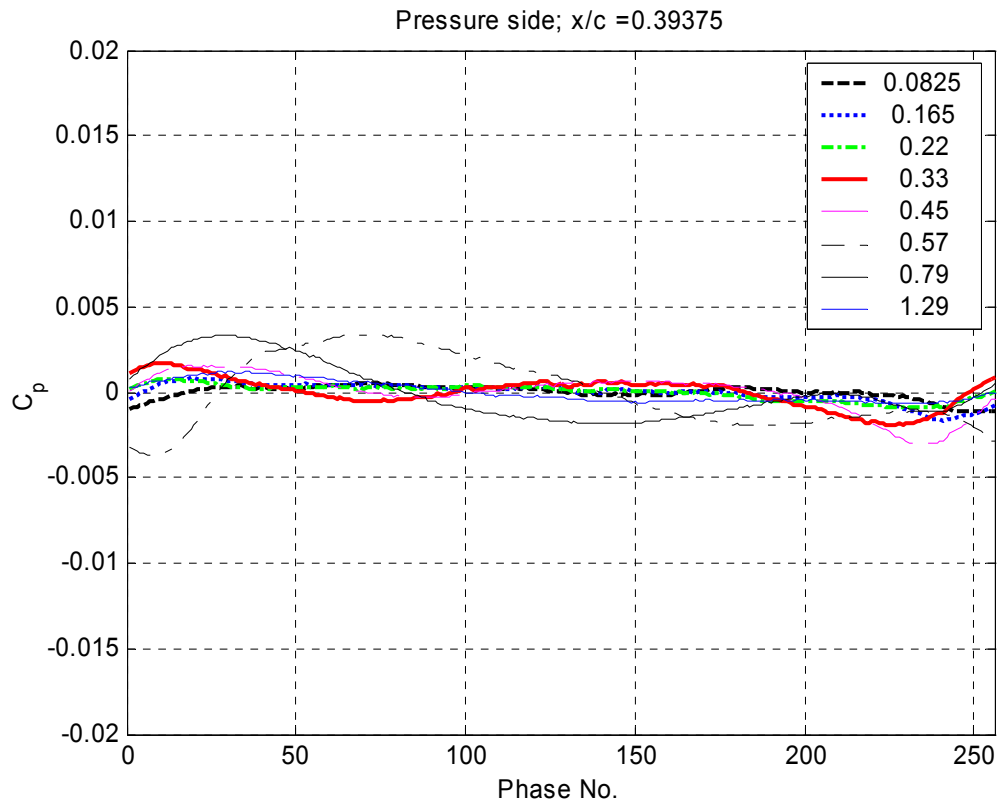
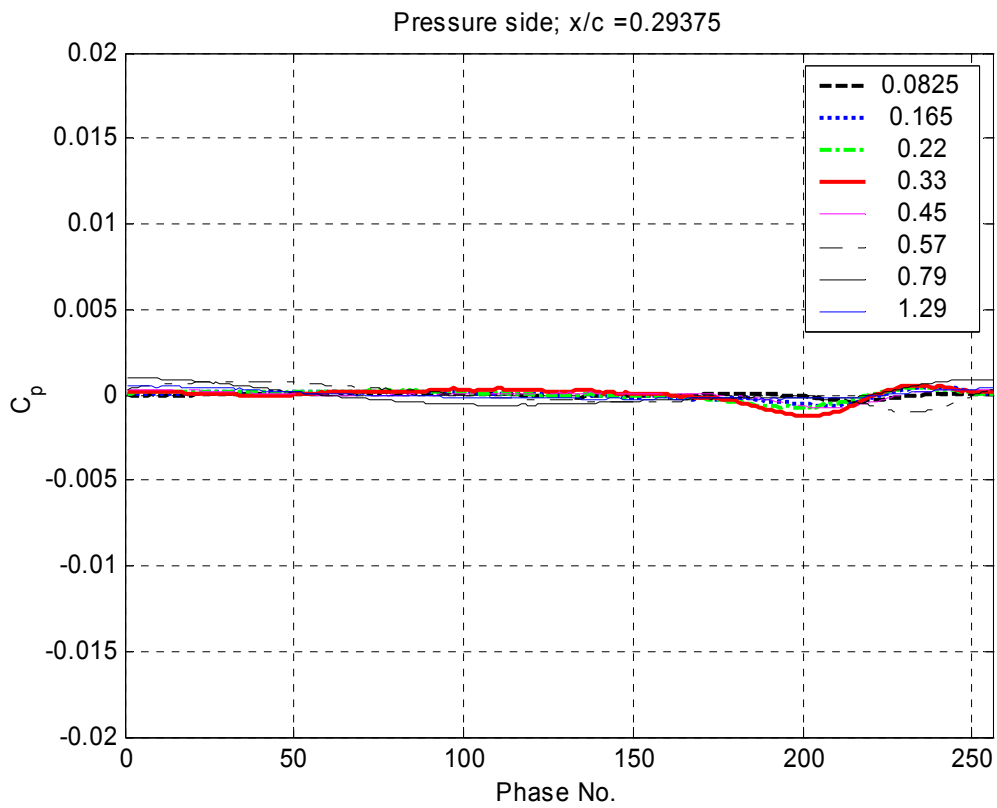


Figure 9.16 continued: Pressure side C_p as a function of phase number plotted for each tip gap along the chord at $x/c = 17.5, 23.125, 29.375, 39.375, 55, 76.25\%$

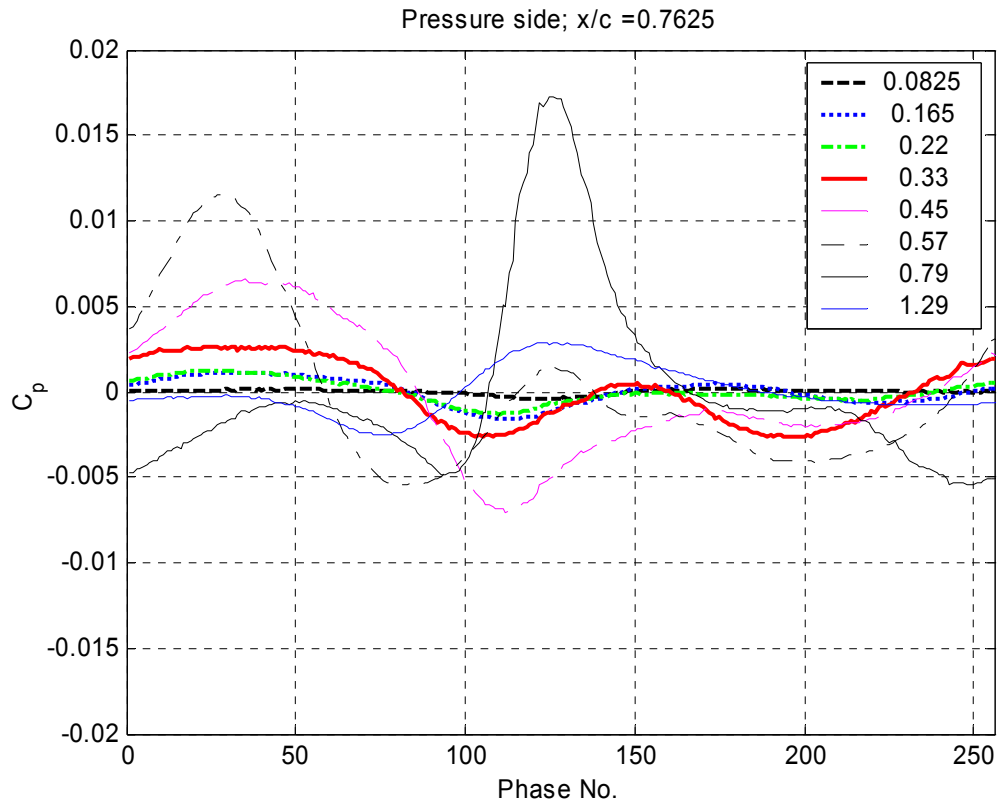
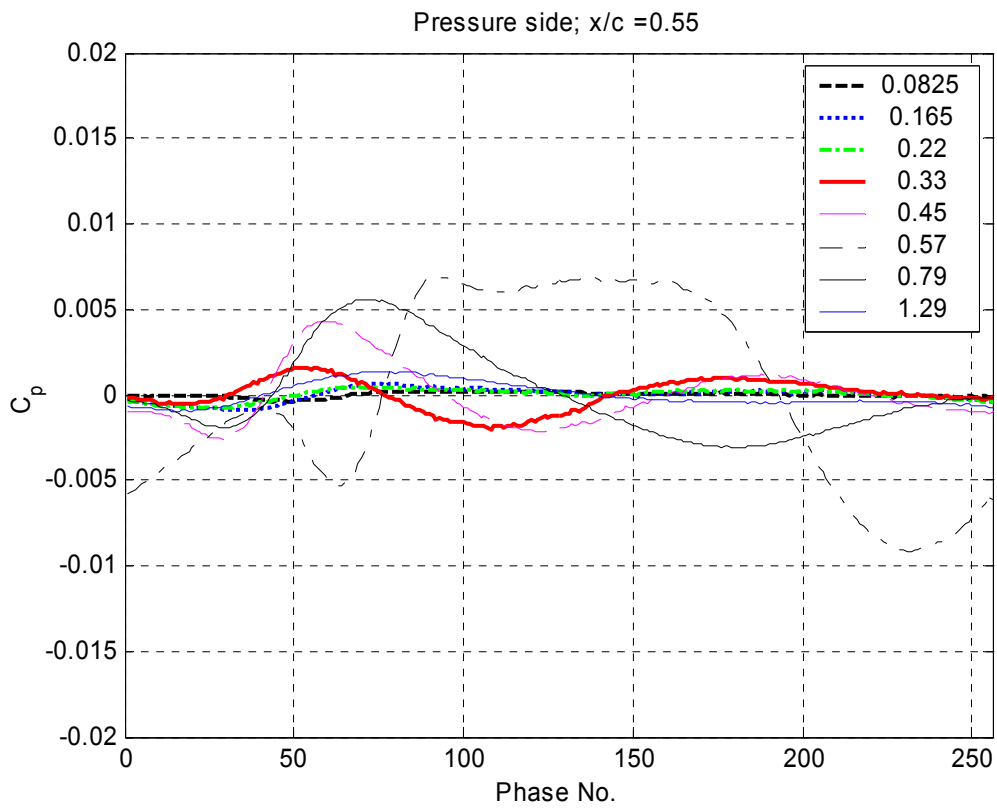


Figure 9.16 continued: Pressure side C_p as a function of phase number plotted for each tip gap along the chord at $x/c = 17.5, 23.125, 29.375, 39.375, 55, 76.25\%$

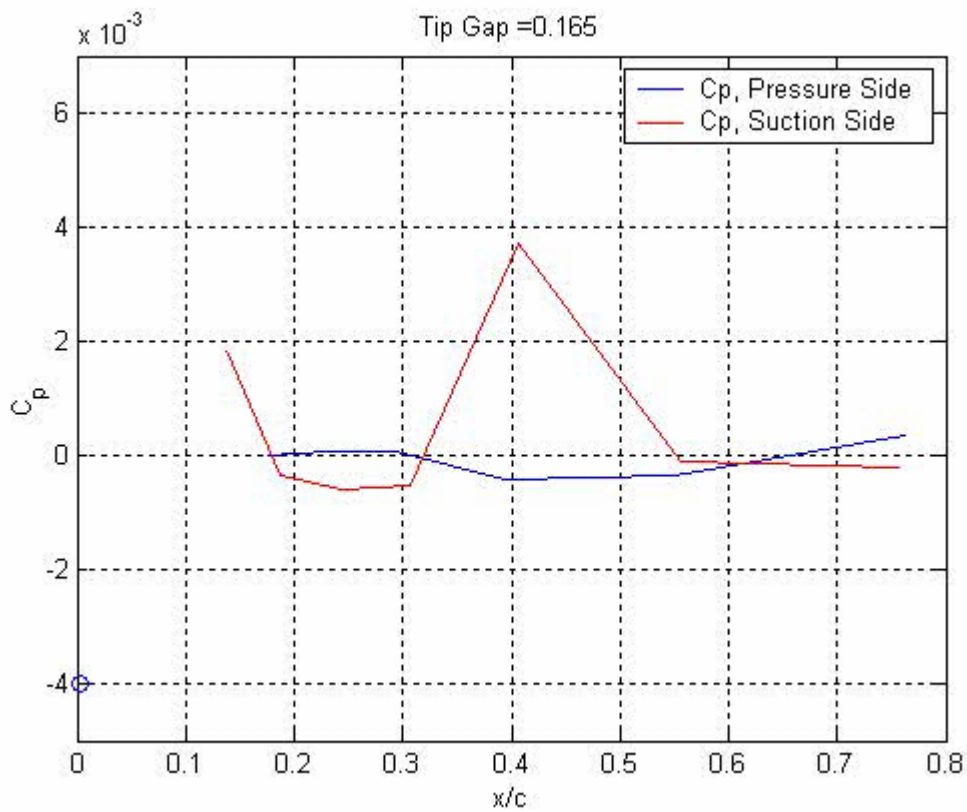
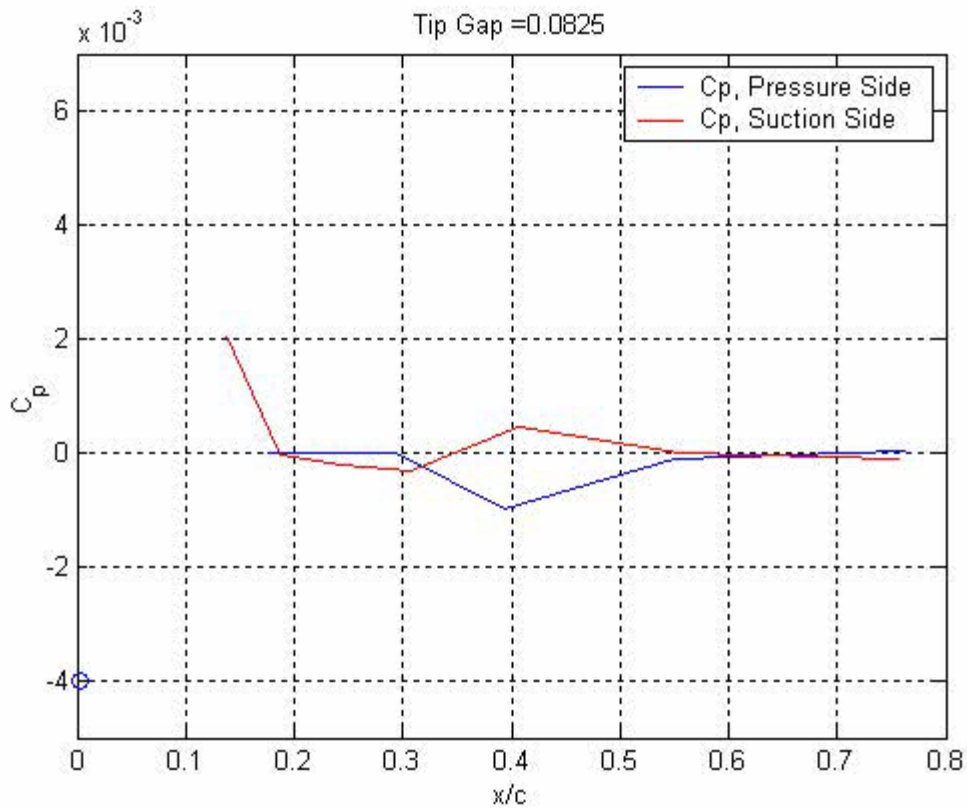


Figure 9.17: Pressure and suction side C_p movies as a function of chordwise location plotted for each tip gap, $t_g/c = 0.00825, 0.0165, 0.022, 0.033, 0.045, 0.057, 0.079, 0.129$

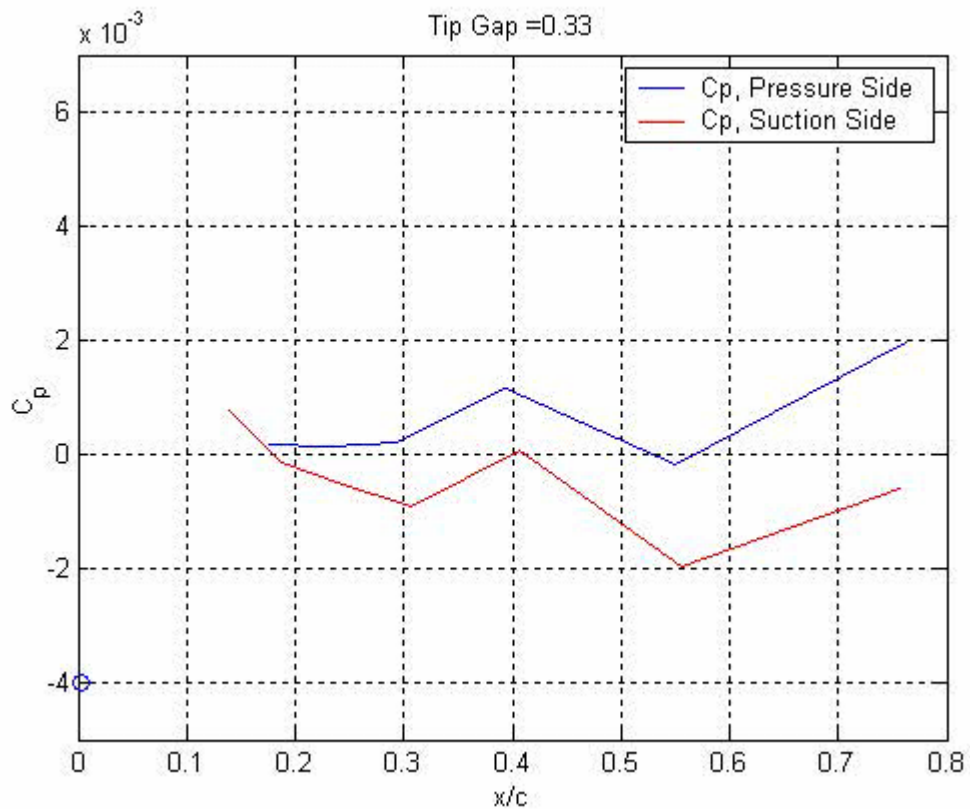
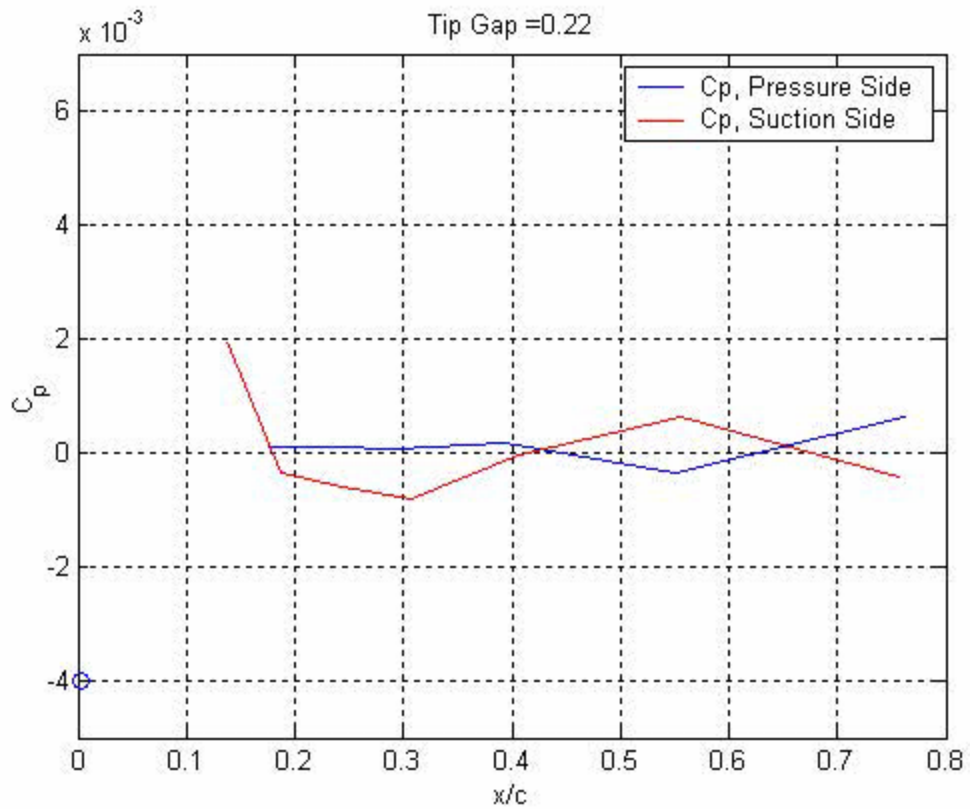


Figure 9.17 continued: Pressure and suction side C_p movies as a function of chordwise location plotted for each tip gap, $t_g/c = 0.00825, 0.0165, 0.022, 0.033, 0.045, 0.057, 0.079, 0.129$

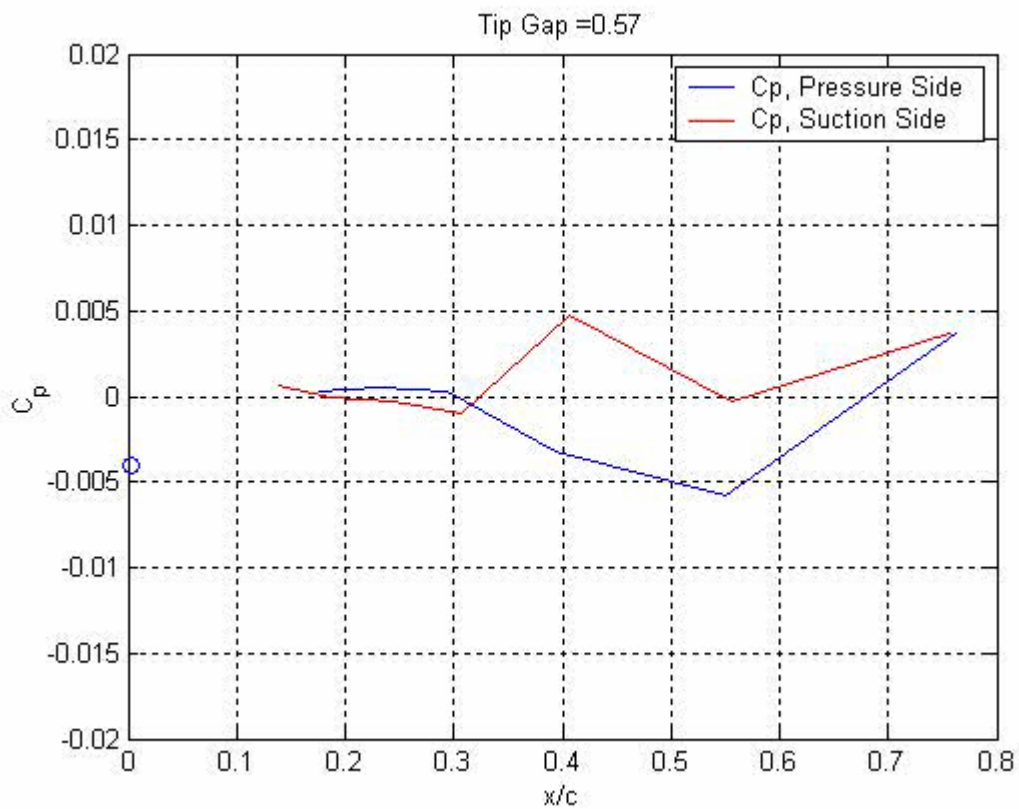
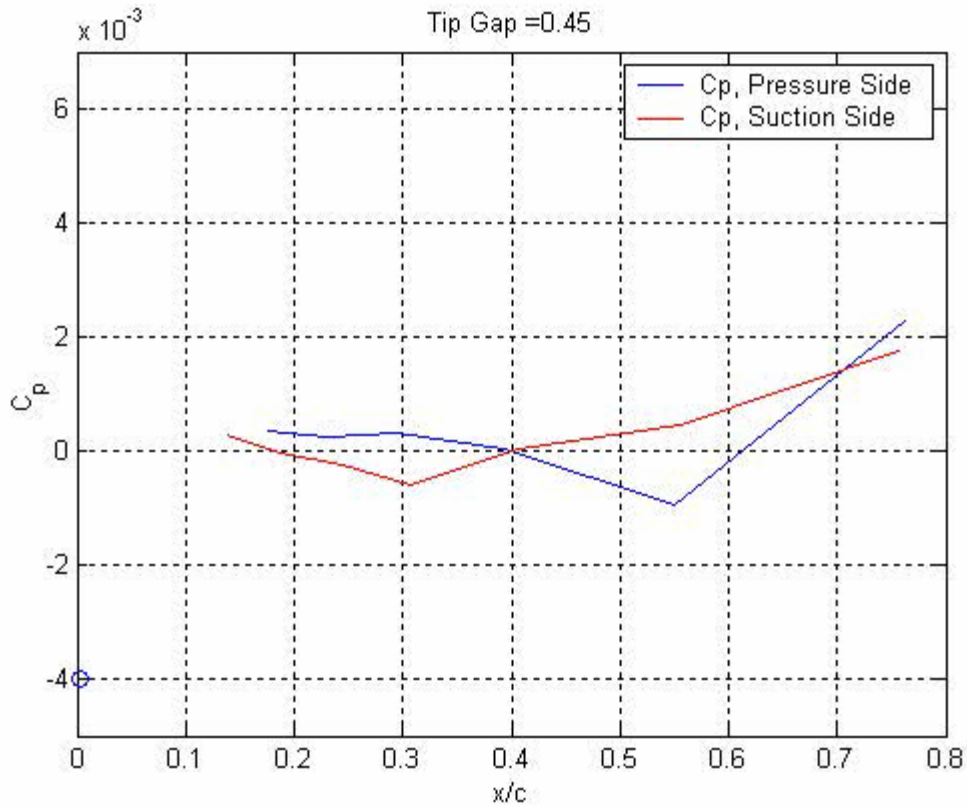


Figure 9.17 continued: Pressure and suction side C_p movies as a function of chordwise location plotted for each tip gap, $t_g/c = 0.00825, 0.0165, 0.022, 0.033, 0.045, 0.057, 0.079, 0.129$

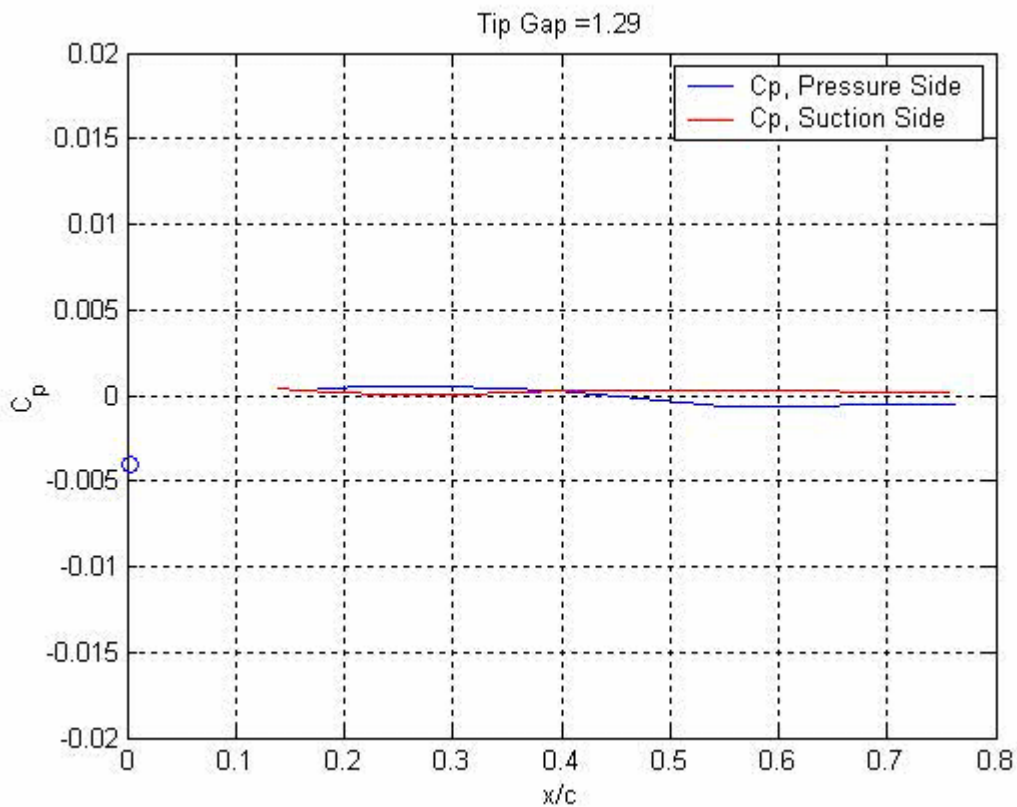
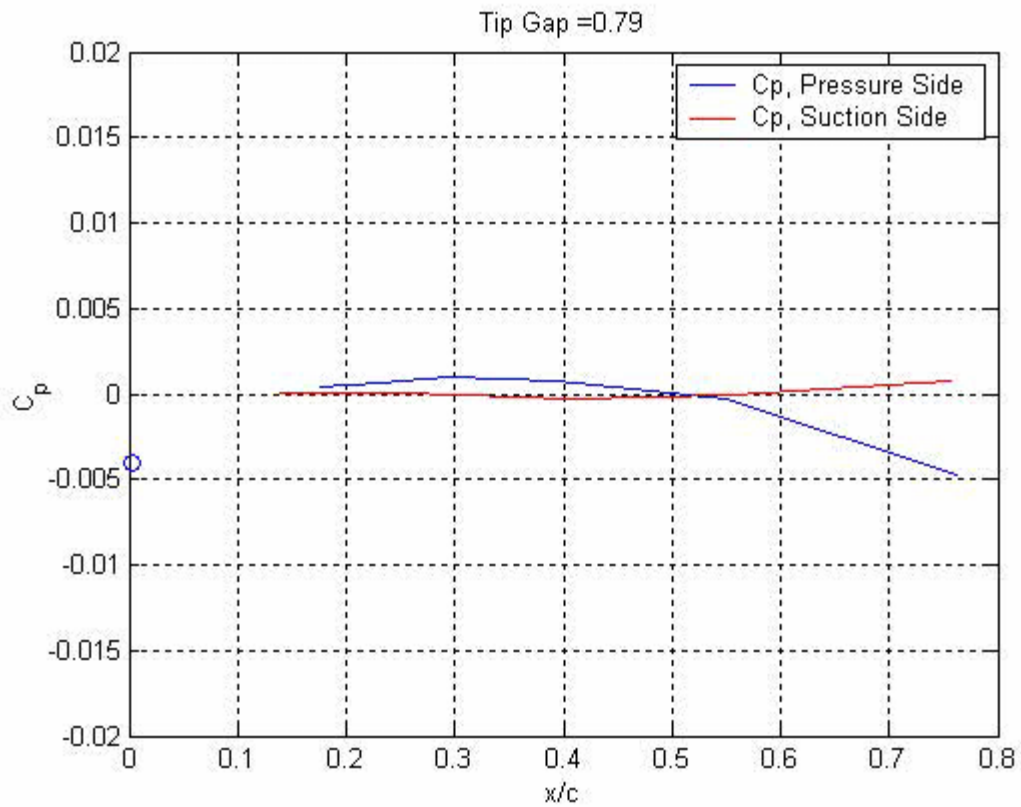


Figure 9.17 continued: Pressure and suction side C_p movies as a function of chordwise location plotted for each tip gap, $t_g/c = 0.00825, 0.0165, 0.022, 0.033, 0.045, 0.057, 0.079, 0.129$

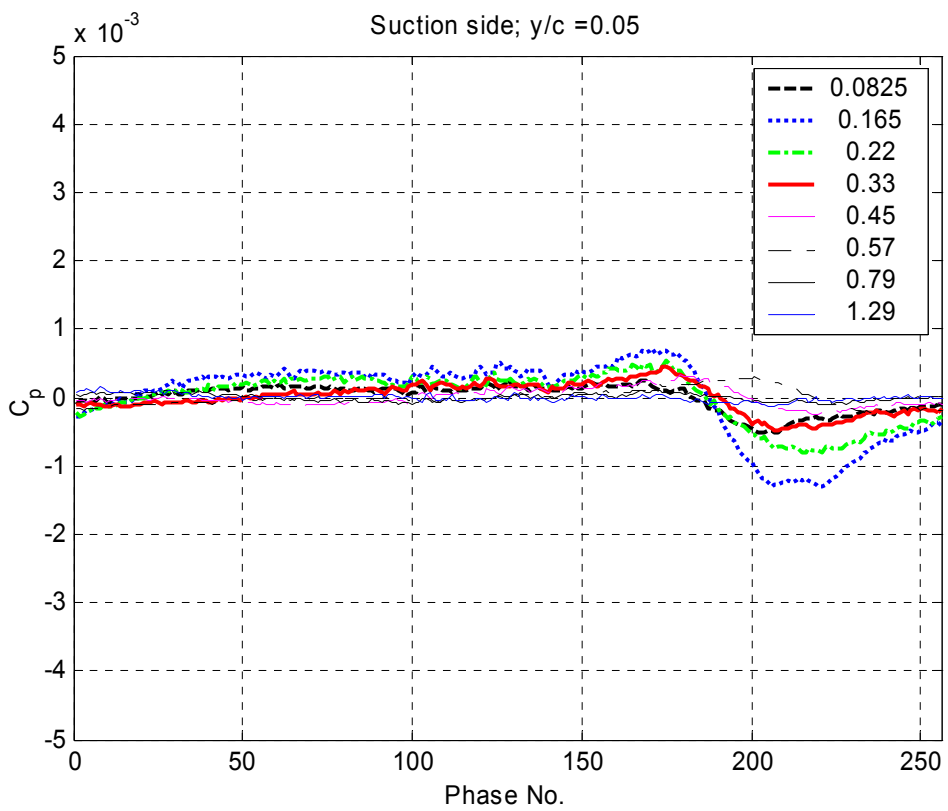
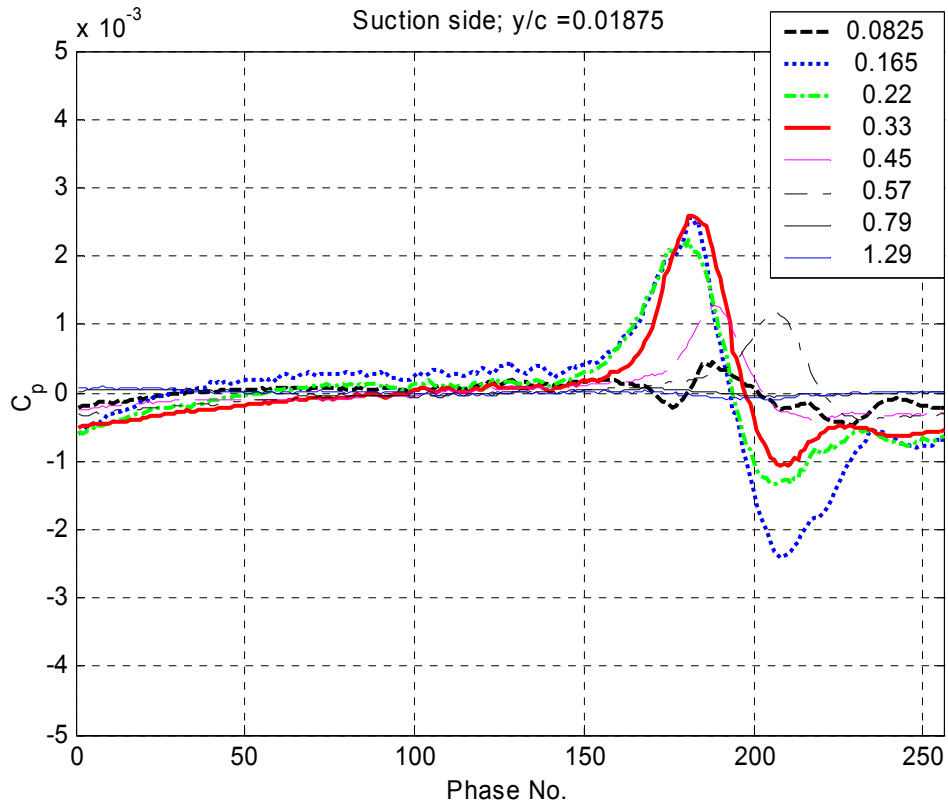


Figure 9.18: Suction side C_p as a function of phase number plotted for each tip gap along the span at $y/c = 1.875, 5, 7.5, 15, 55, 25, 45\%$

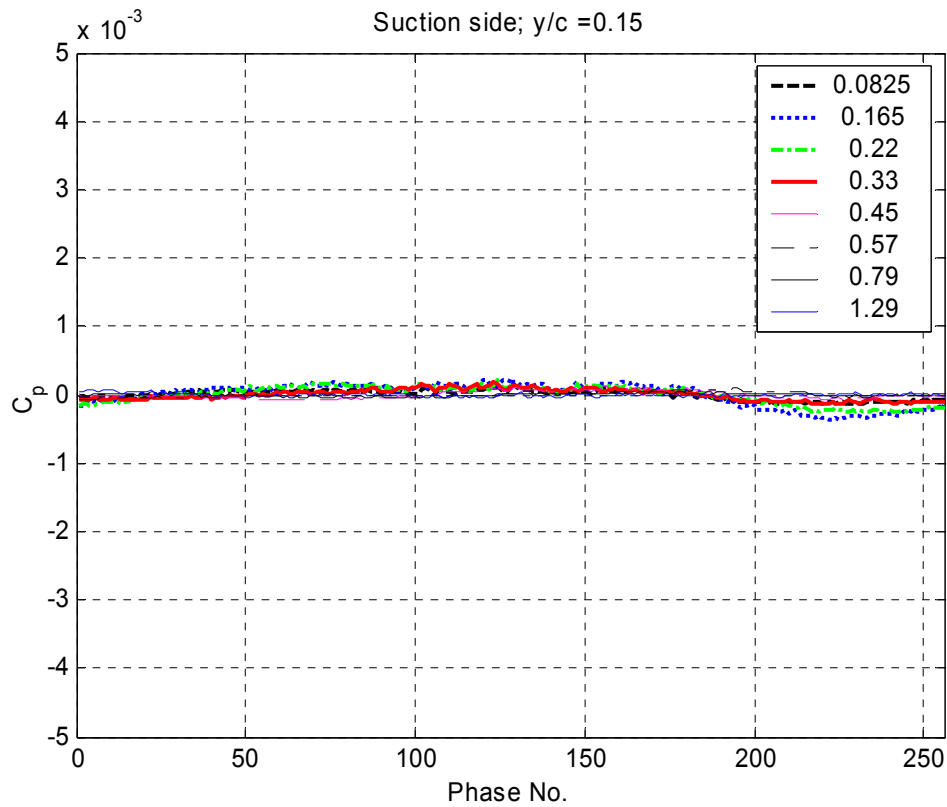
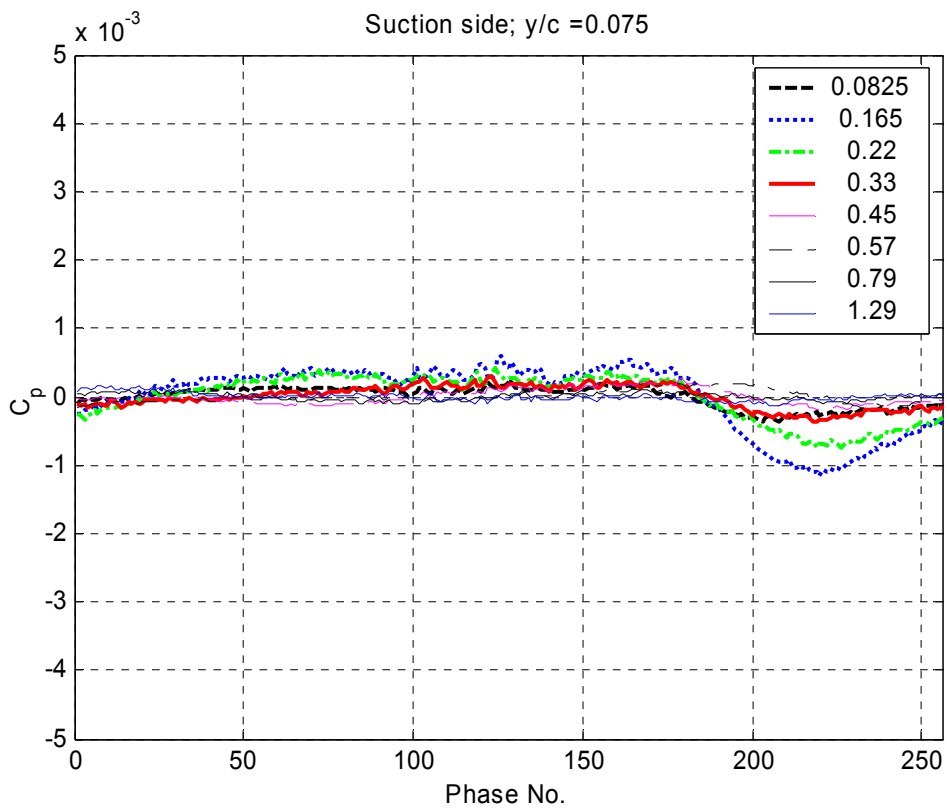


Figure 9.18 continued: Suction side C_p as a function of phase number plotted for each tip gap along the span at $y/c = 1.875, 5, 7.5, 15, 55, 25, 45\%$

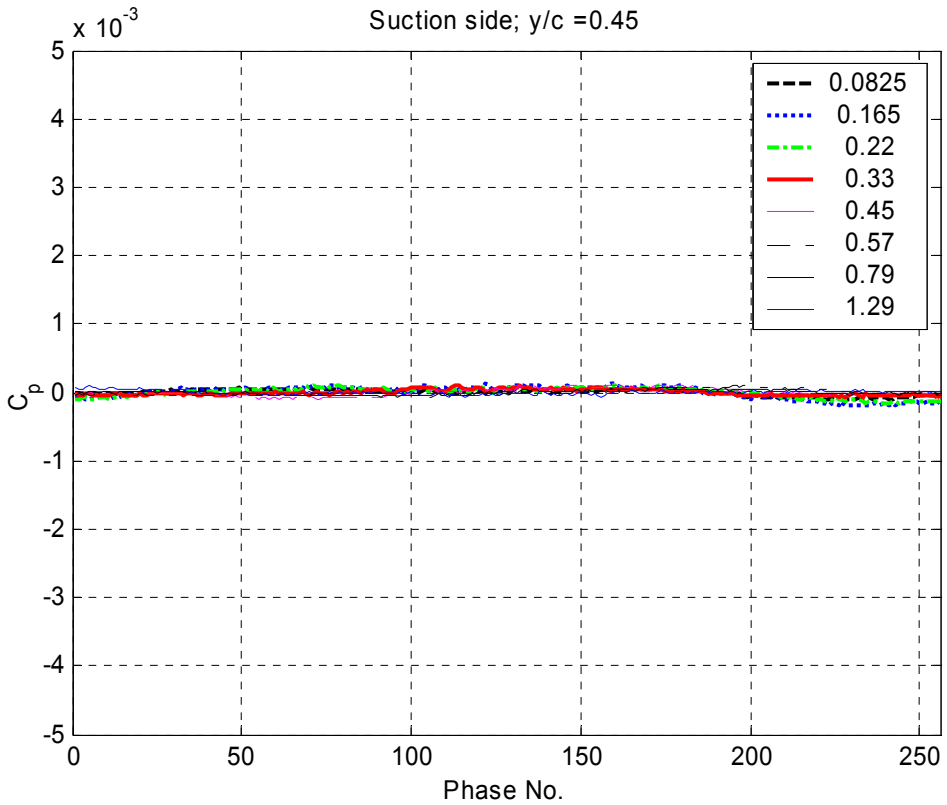
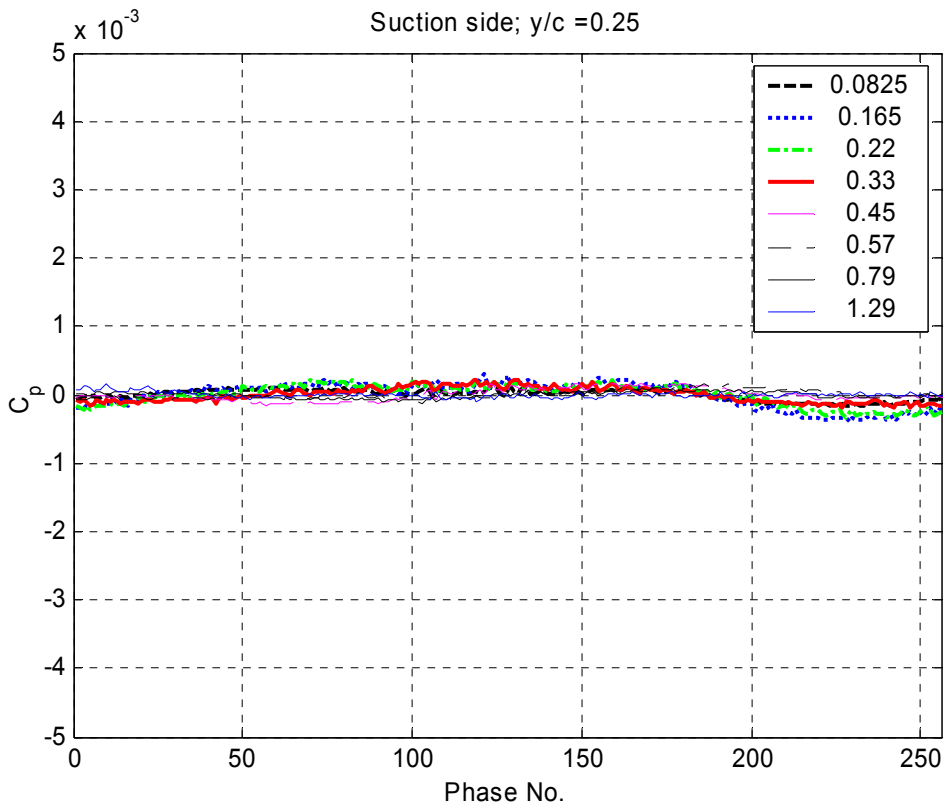


Figure 9.18 continued: Suction side C_p as a function of phase number plotted for each tip gap along the span at $y/c = 1.875, 5, 7.5, 15, 55, 25, 45\%$

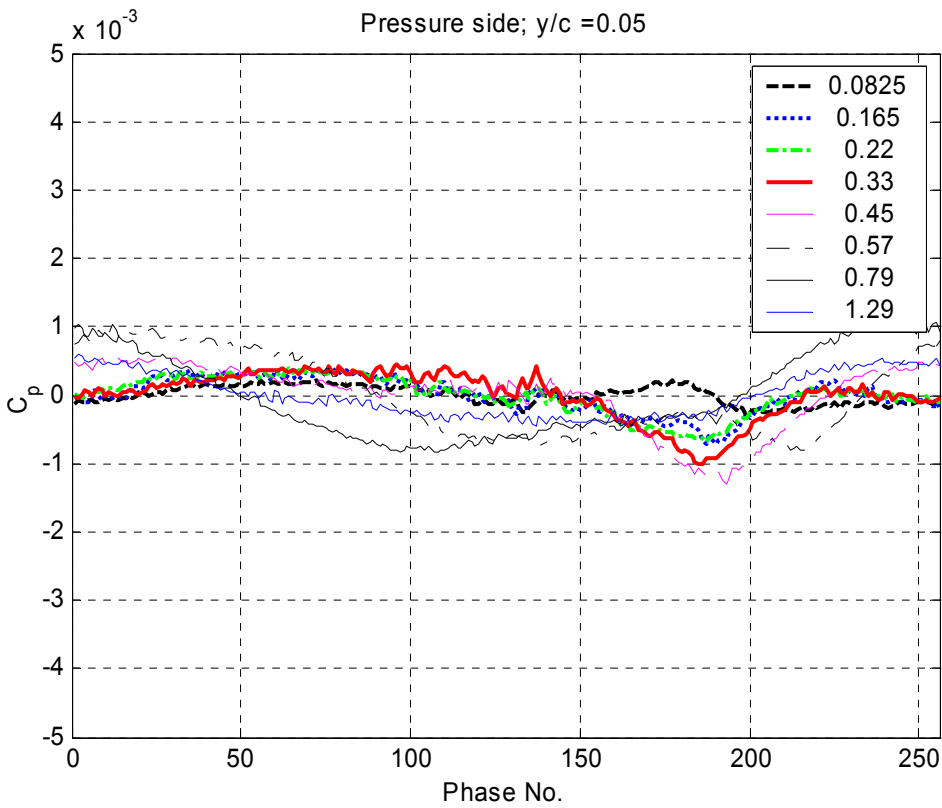
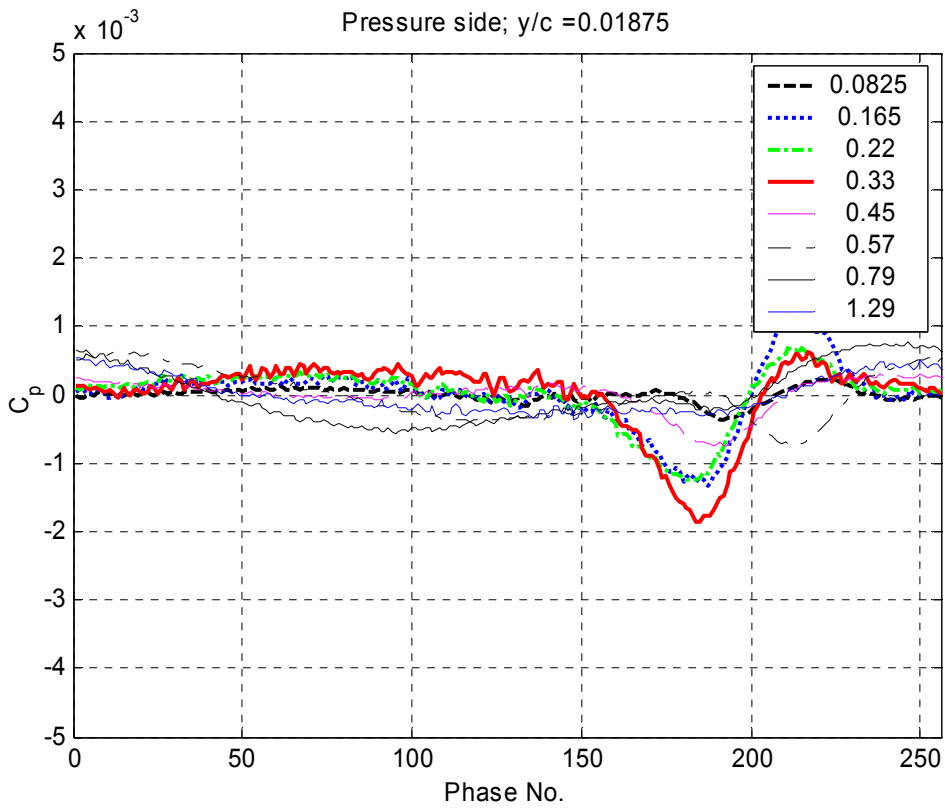


Figure 9.19: Pressure side C_p as a function of phase number plotted for each tip gap along the span at $y/c = 1.875, 5, 7.5, 15, 55, 25, 45\%$

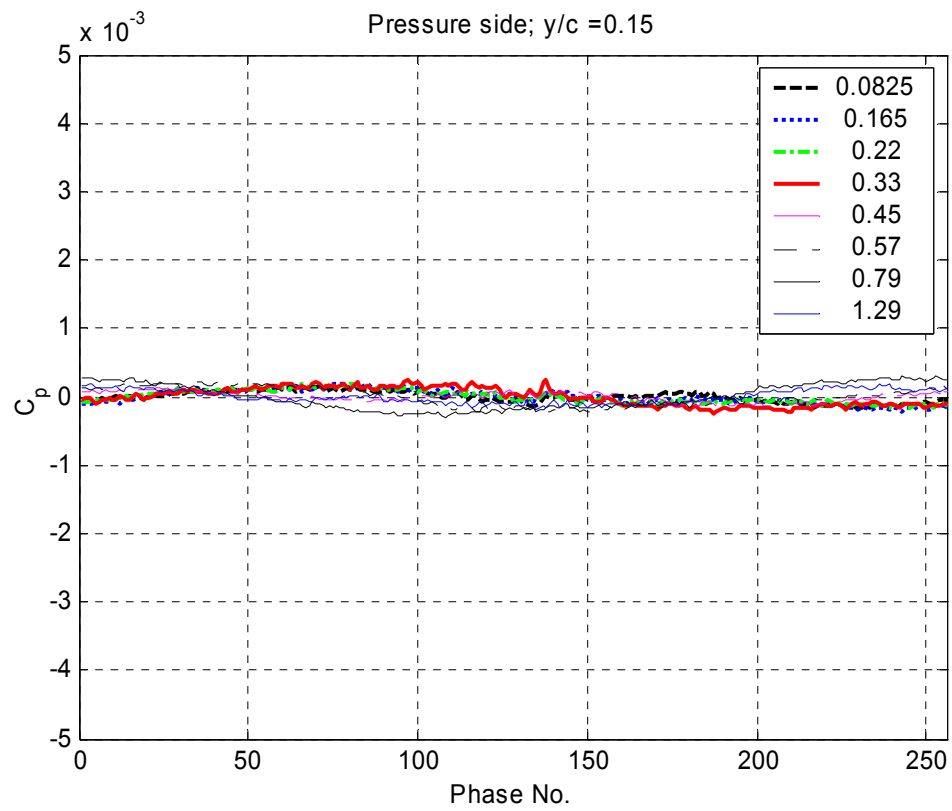
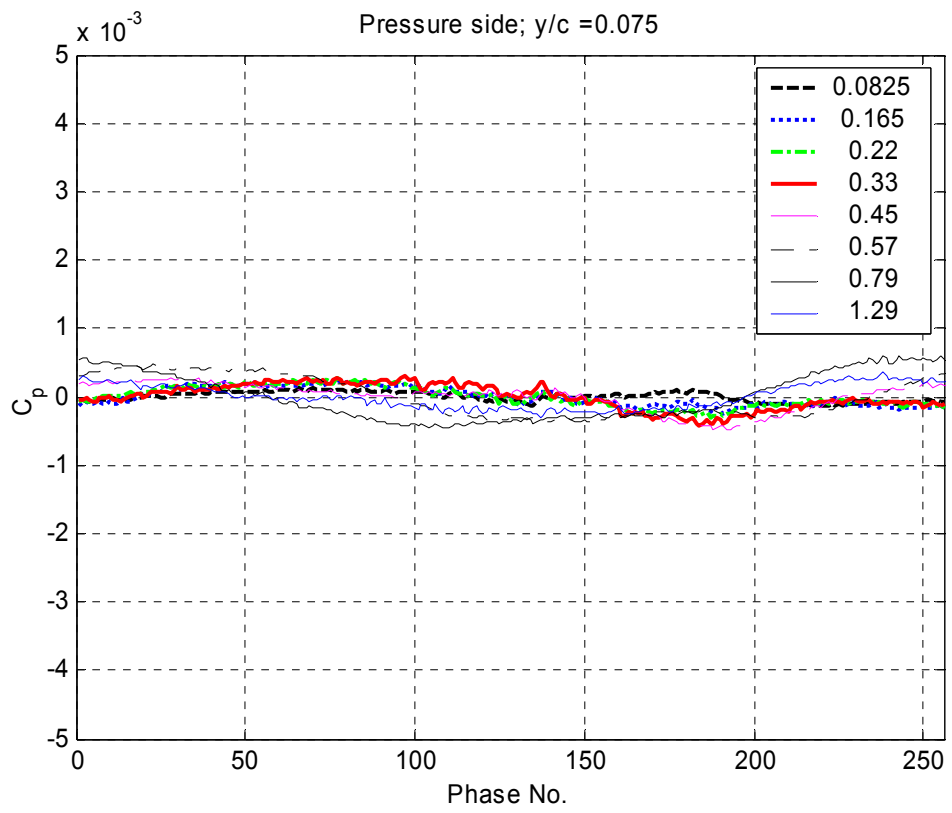


Figure 9.19 continued: Pressure side C_p as a function of phase number plotted for each tip gap along the span at $y/c = 1.875, 5, 7.5, 15, 55, 25, 45\%$

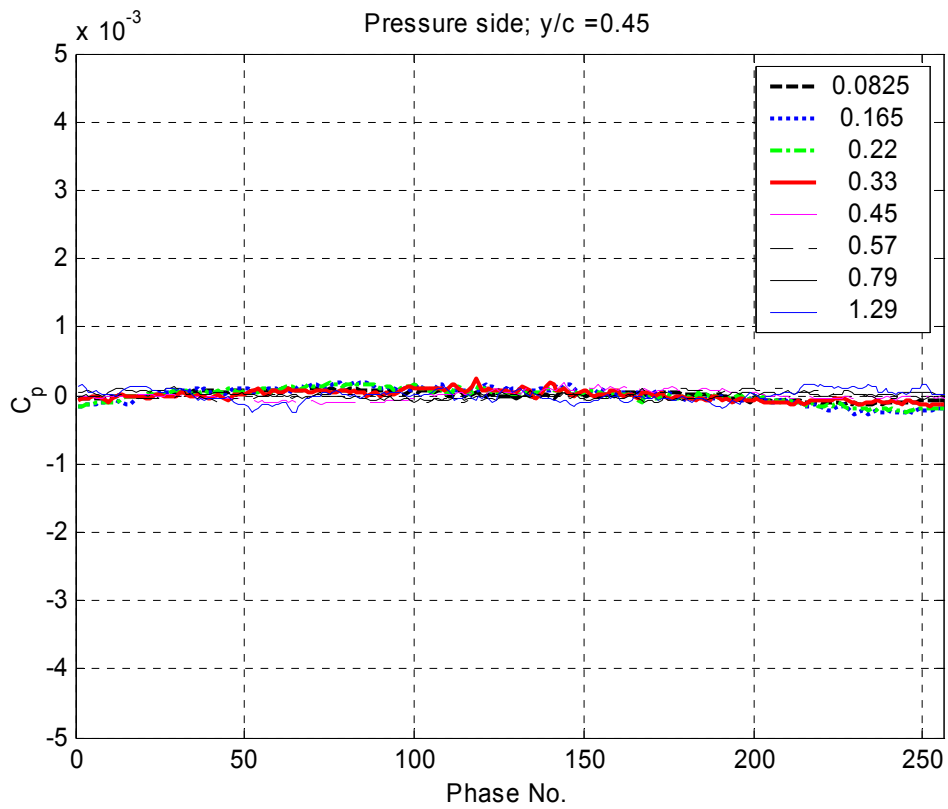
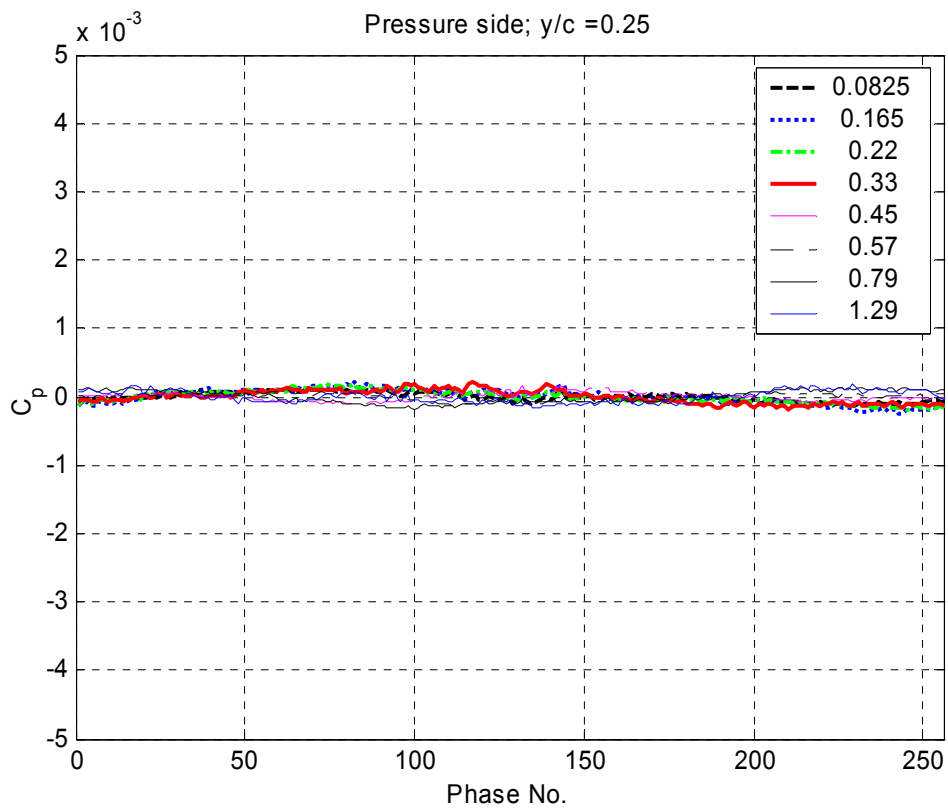


Figure 9.19 continued: Pressure side C_p as a function of phase number plotted for each tip gap along the span at $y/c = 1.875, 5, 7.5, 15, 55, 25, 45\%$

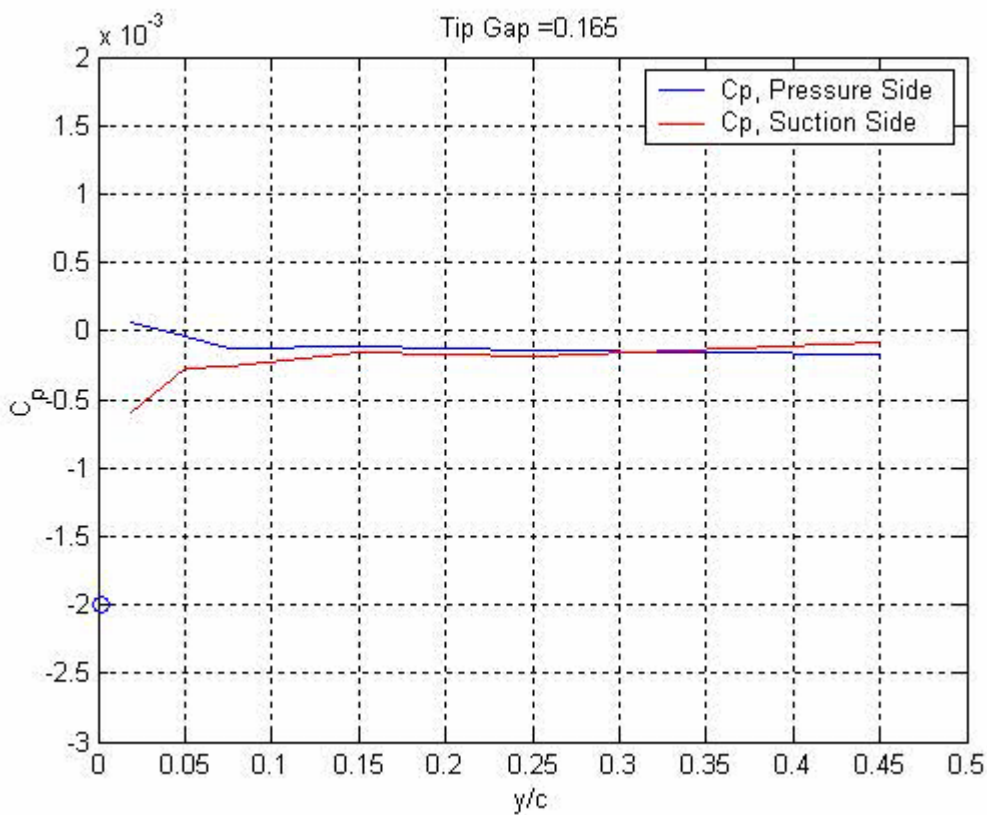
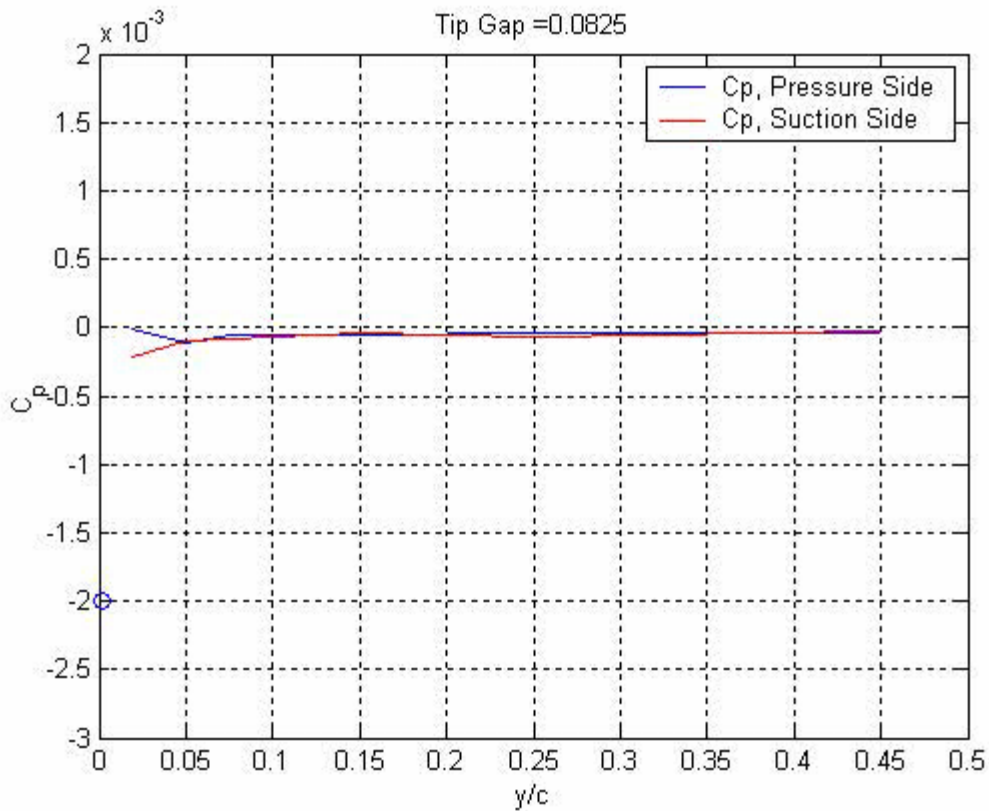


Figure 9.20: Pressure and suction side C_p movies as a function of spanwise location plotted for each tip gap, $t_g/c = 0.00825, 0.0165, 0.022, 0.033, 0.045, 0.057, 0.079, 0.129$

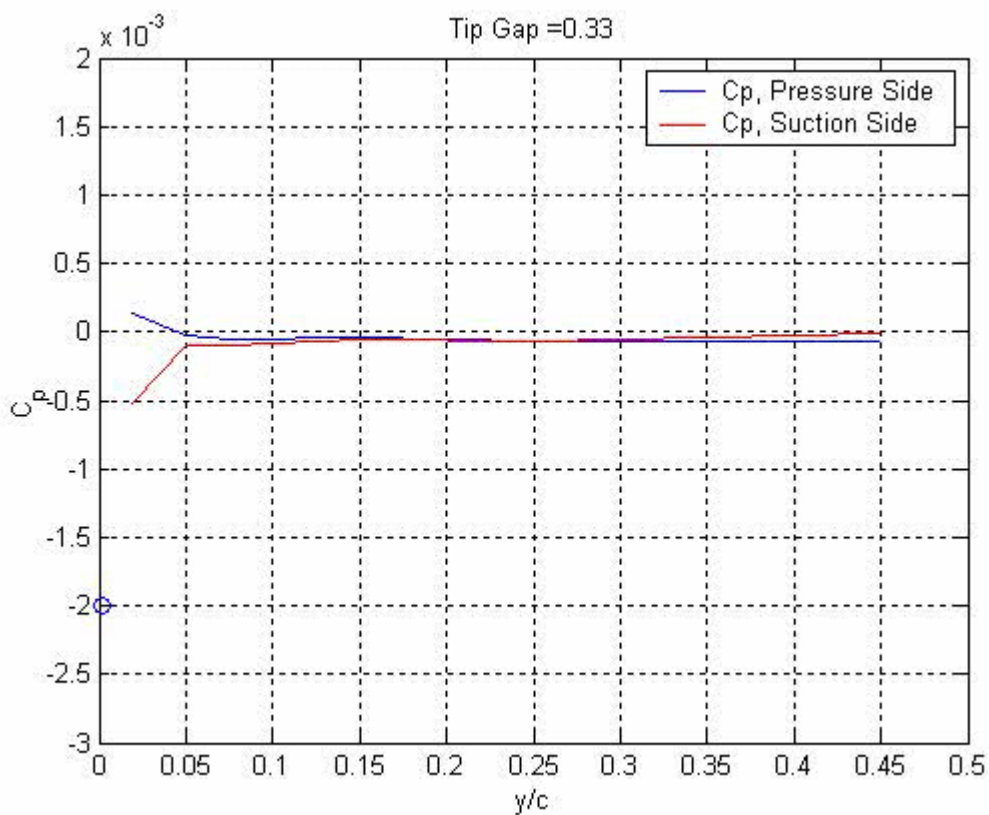
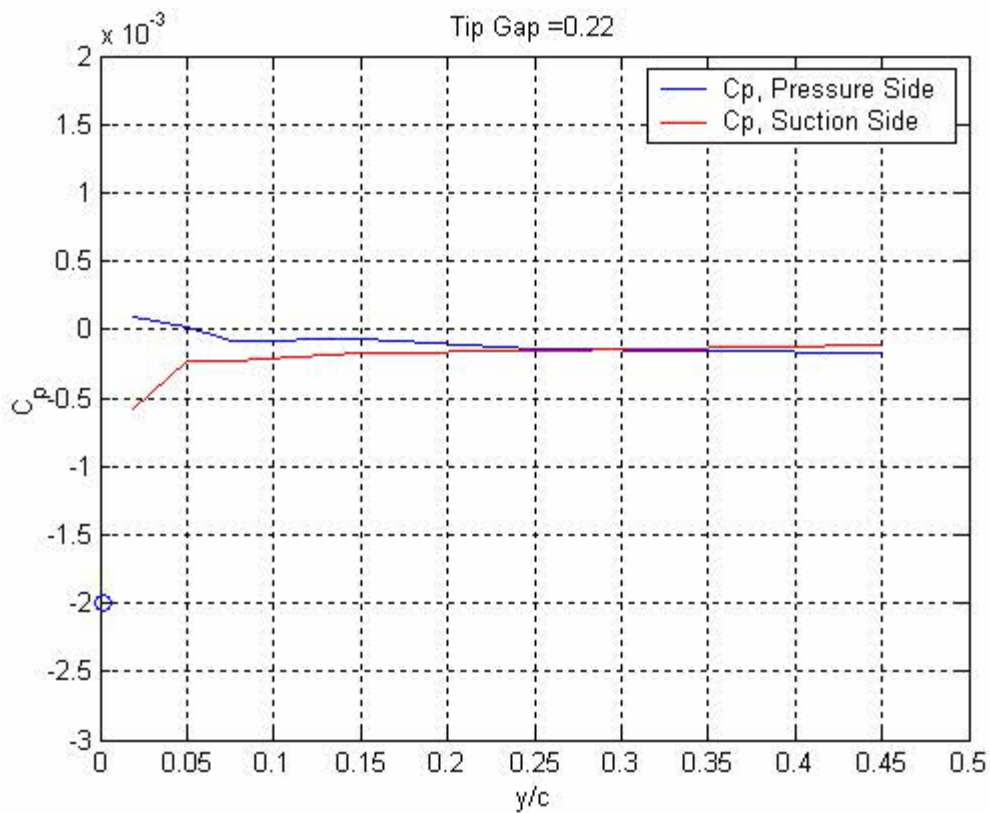


Figure 9.20 continued: Pressure and suction side C_p movies as a function of spanwise location plotted for each tip gap, $t_g/c = 0.00825, 0.0165, 0.022, 0.033, 0.045, 0.057, 0.079, 0.129$

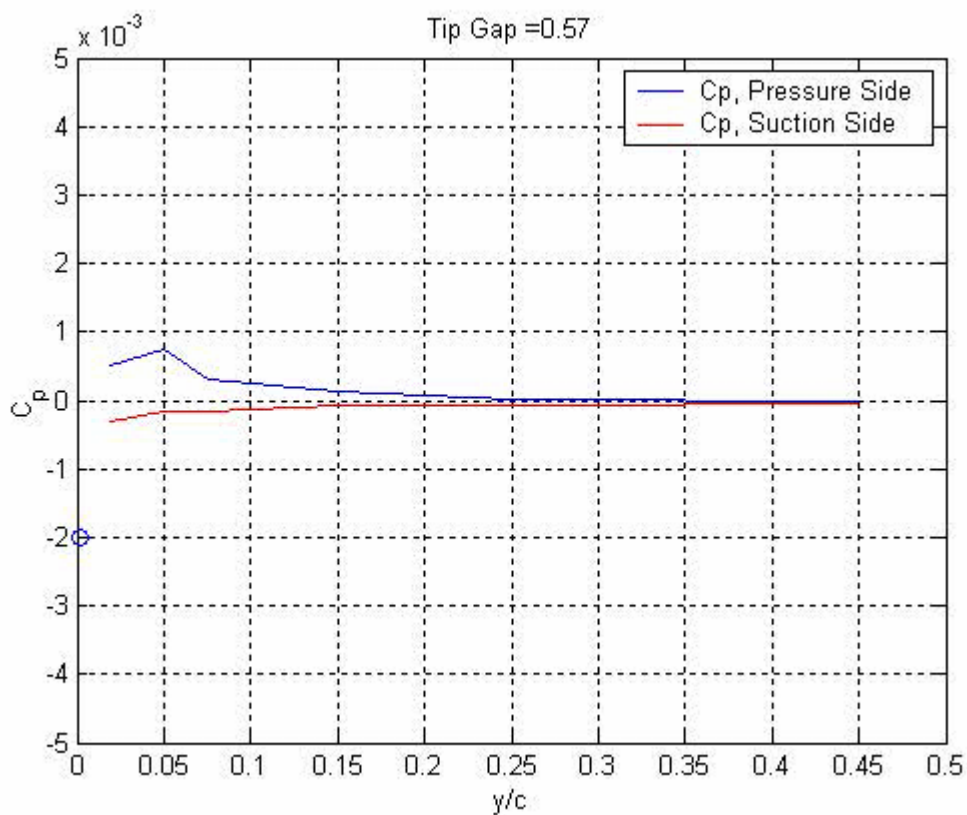
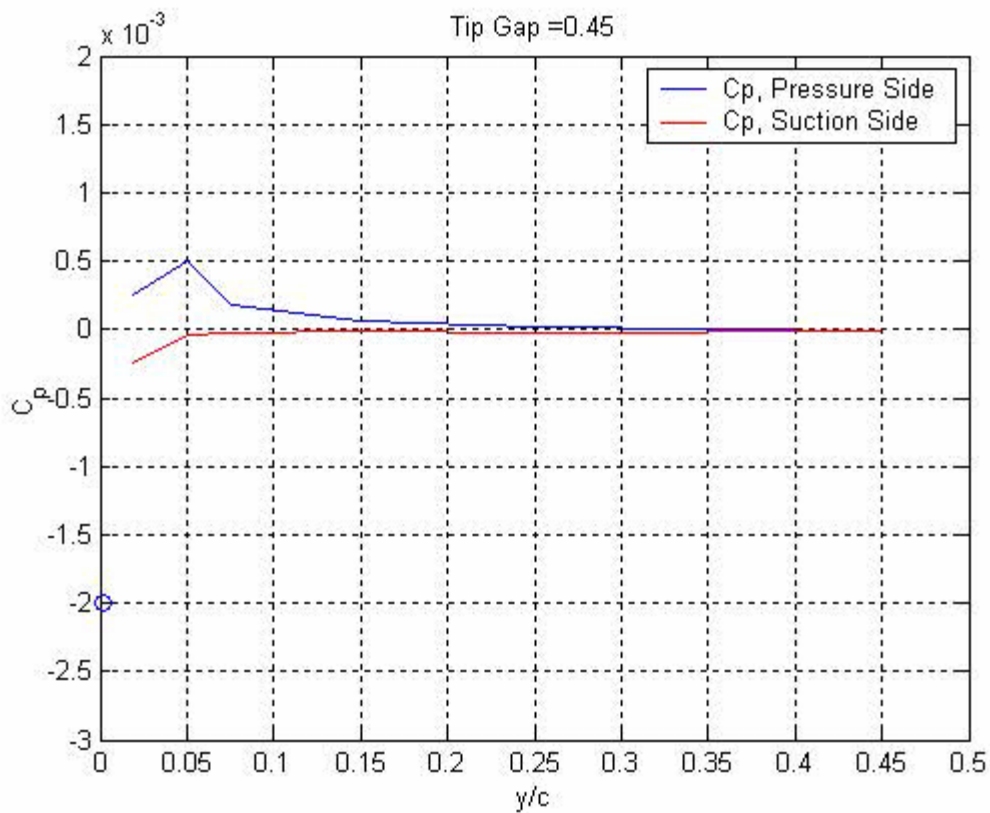


Figure 9.20 continued: Pressure and suction side C_p movies as a function of spanwise location plotted for each tip gap, $t_g/c = 0.00825, 0.0165, 0.022, 0.033, 0.045, 0.057, 0.079, 0.129$

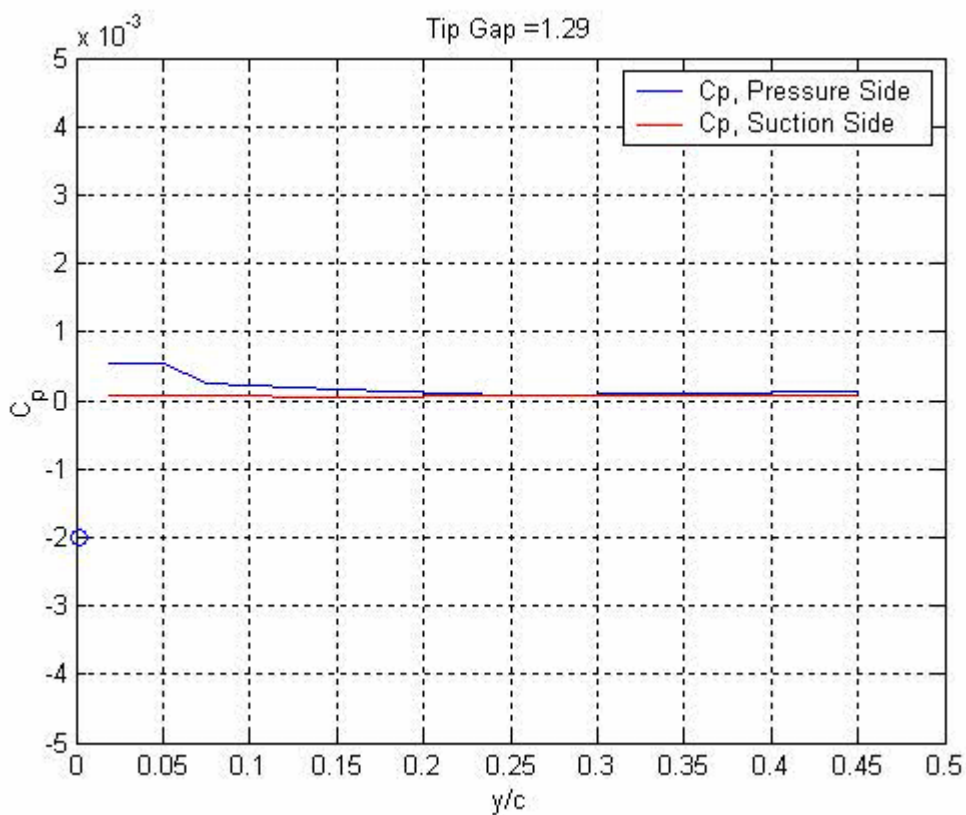
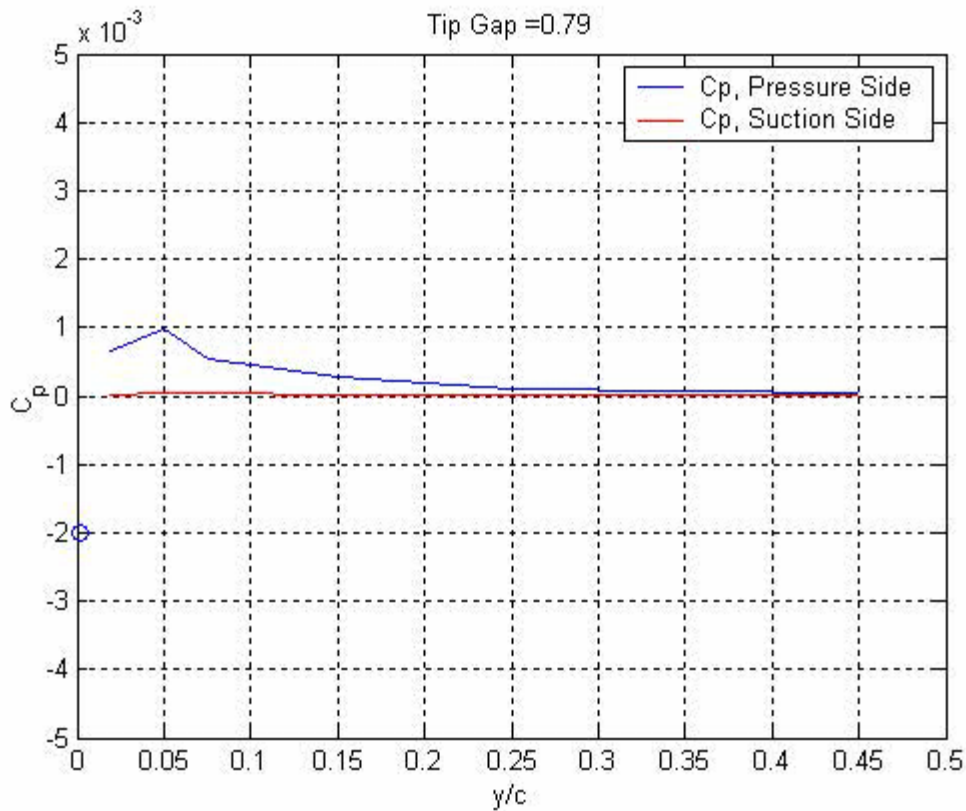


Figure 9.20 continued: Pressure and suction side C_p movies as a function of spanwise location plotted for each tip gap, $t_g/c = 0.00825, 0.0165, 0.022, 0.033, 0.045, 0.057, 0.079, 0.129$

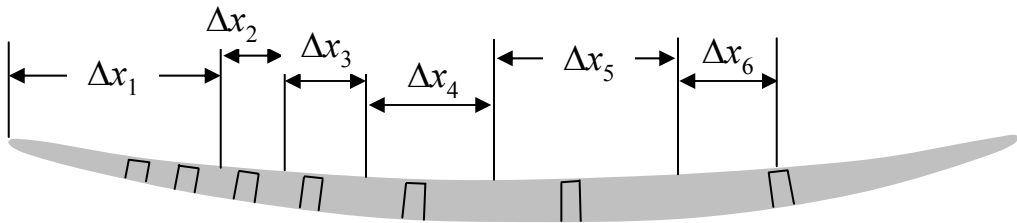


Figure 9.21: Schematic showing typical Δx 's used in unsteady lift calculation

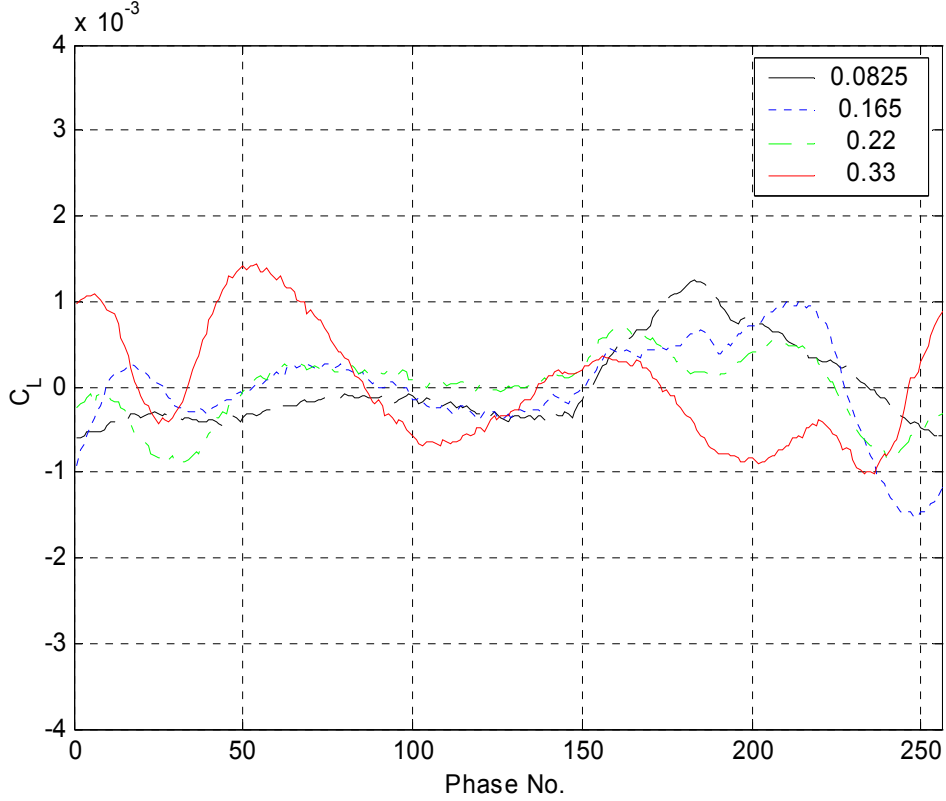


Figure 9.22: Unsteady Lift coefficient, C_L as a function of phase number plotted for tip gaps, $t_g/c = 0.00825, 0.0165, 0.022, 0.033$

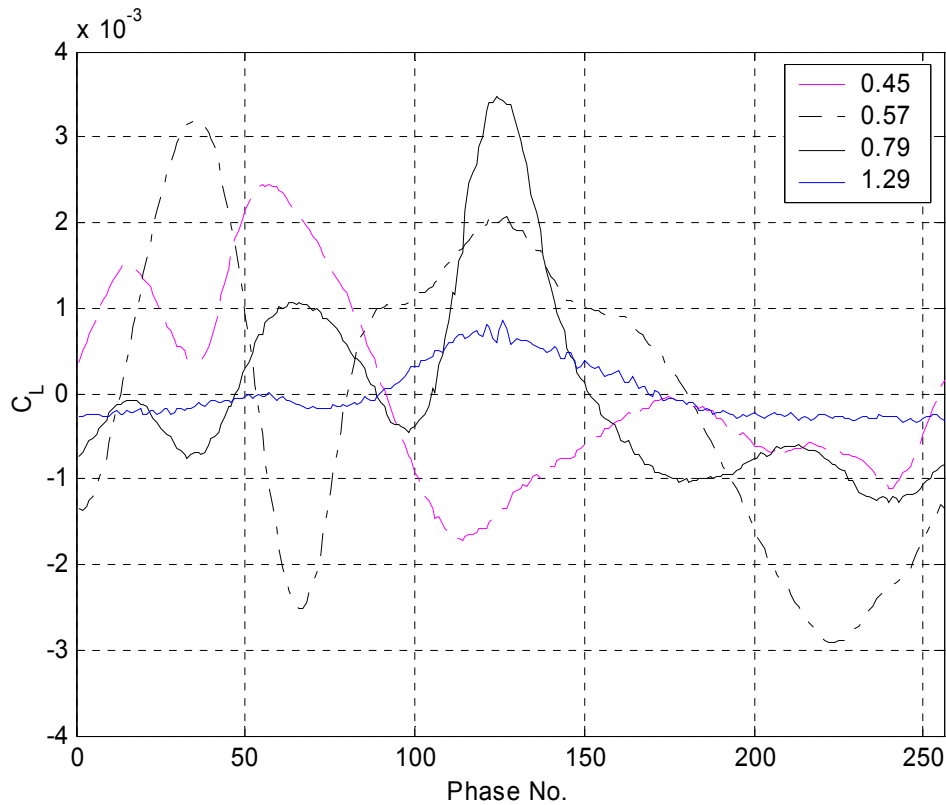


Figure 9.23: Unsteady Lift coefficient, C_L as a function of phase number plotted for each tip gap, $t_g/c = 0.045, 0.057, 0.079, 0.129$

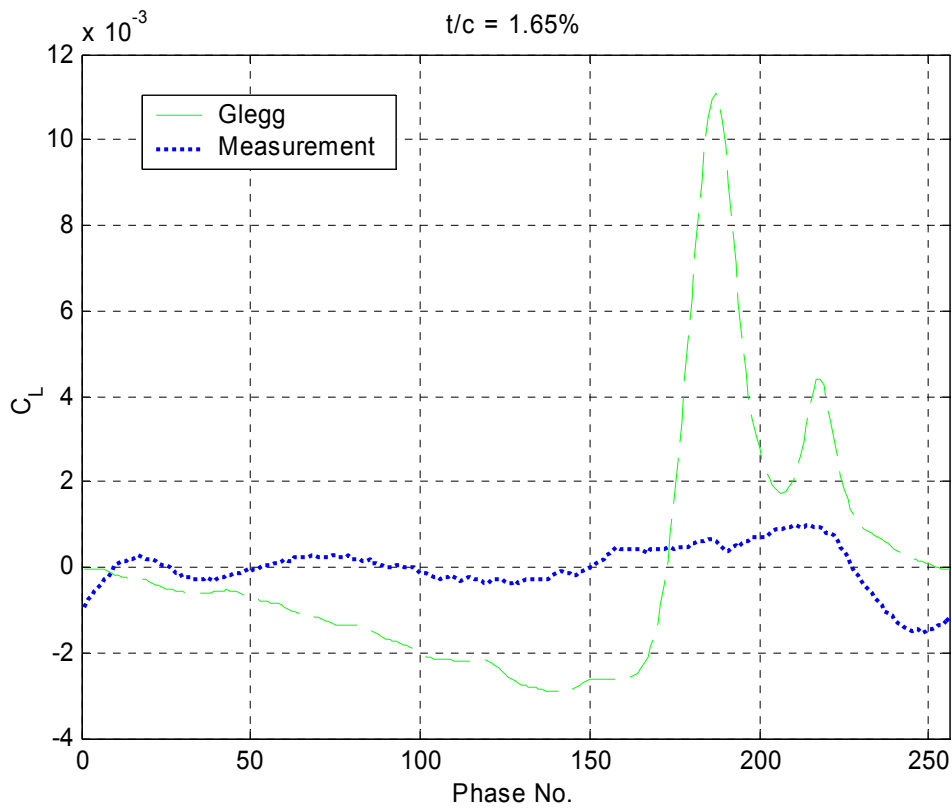
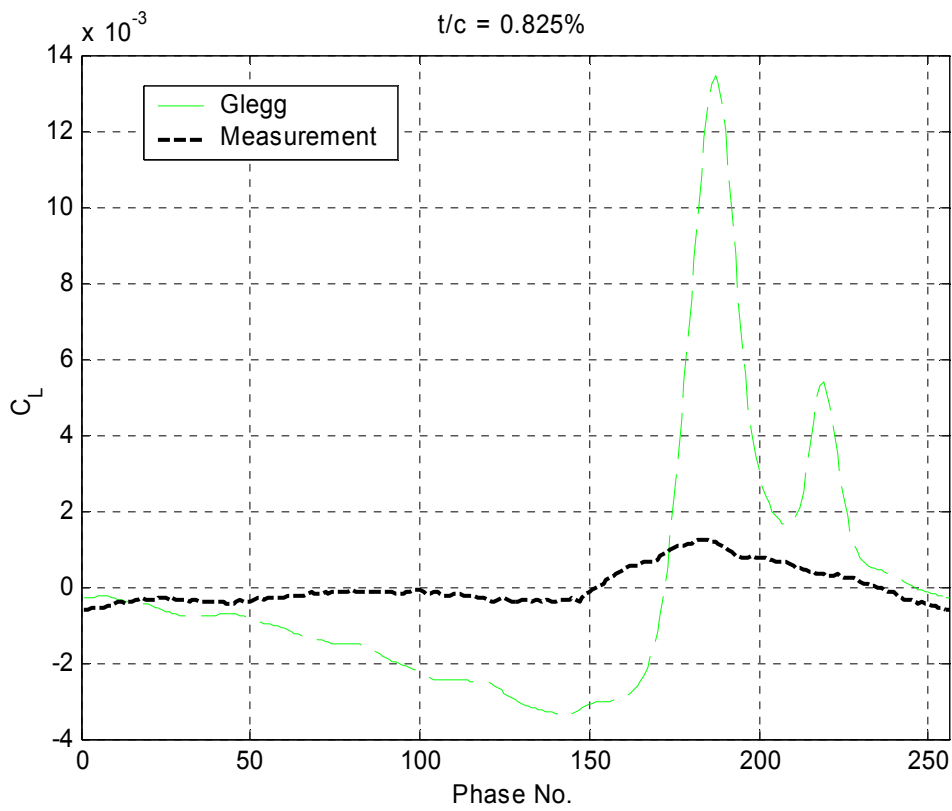


Figure 9.24: Theoretical and measured unsteady lift coefficient, C_L as a function of phase number plotted for $t_g/c = 0.00825, 0.0165, 0.022, 0.033, 0.045, 0.057, 0.079, 0.129$

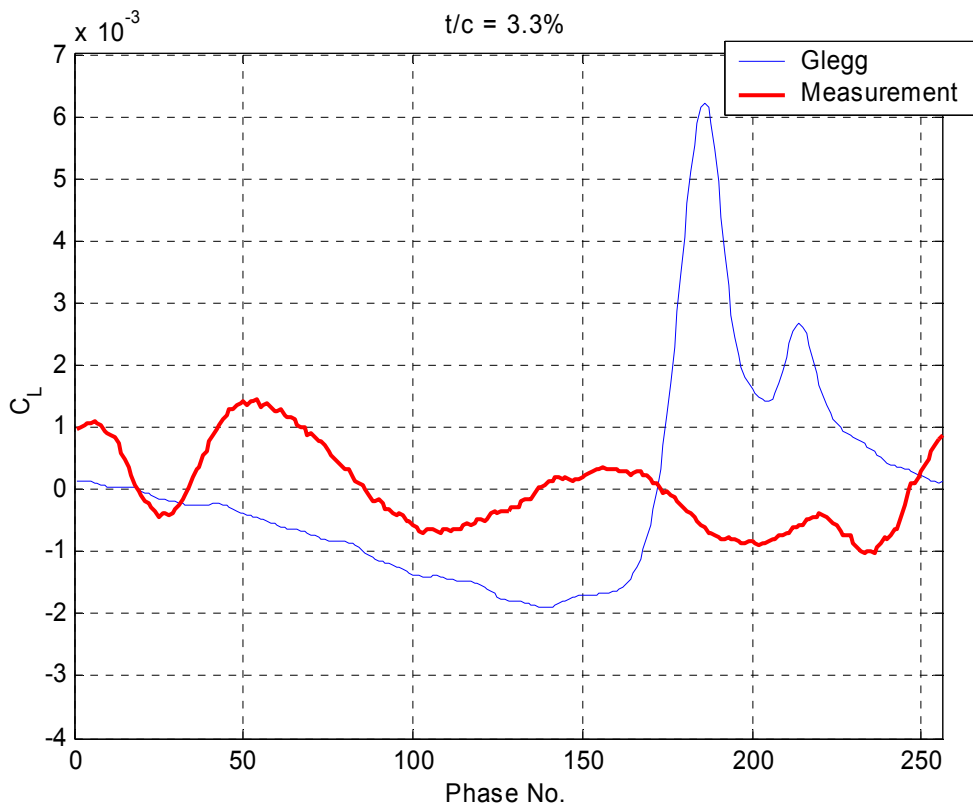
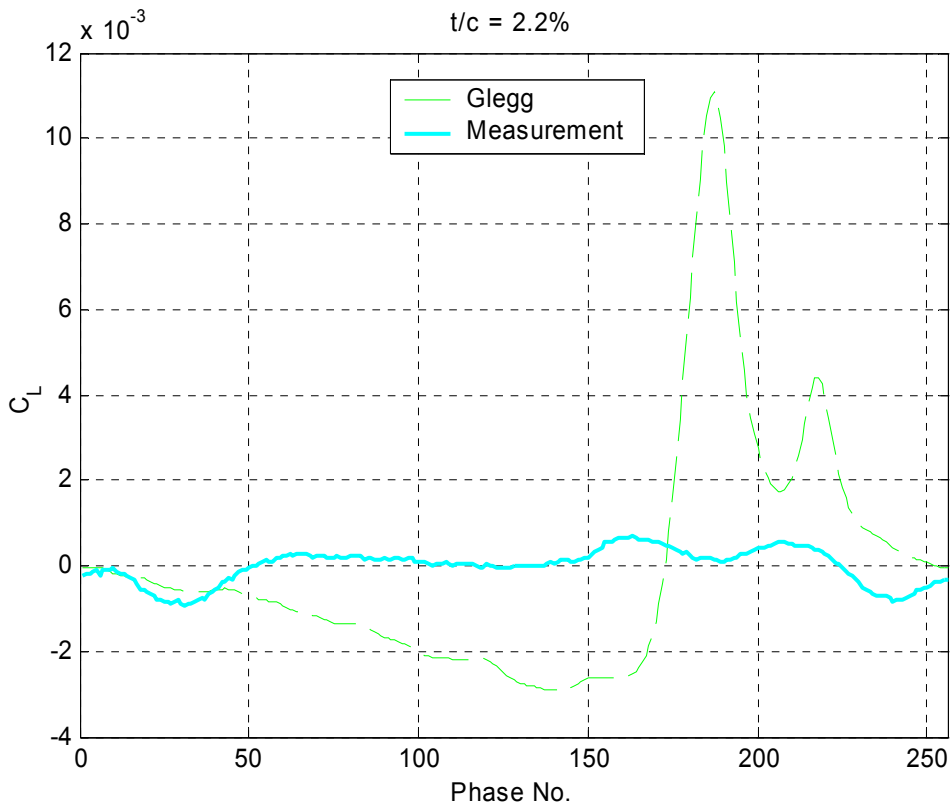


Figure 9.24 continued: Theoretical and measured unsteady lift coefficient, C_L as a function of phase number plotted for $t_g/c = 0.00825, 0.0165, 0.022, 0.033, 0.045, 0.057, 0.079, 0.129$

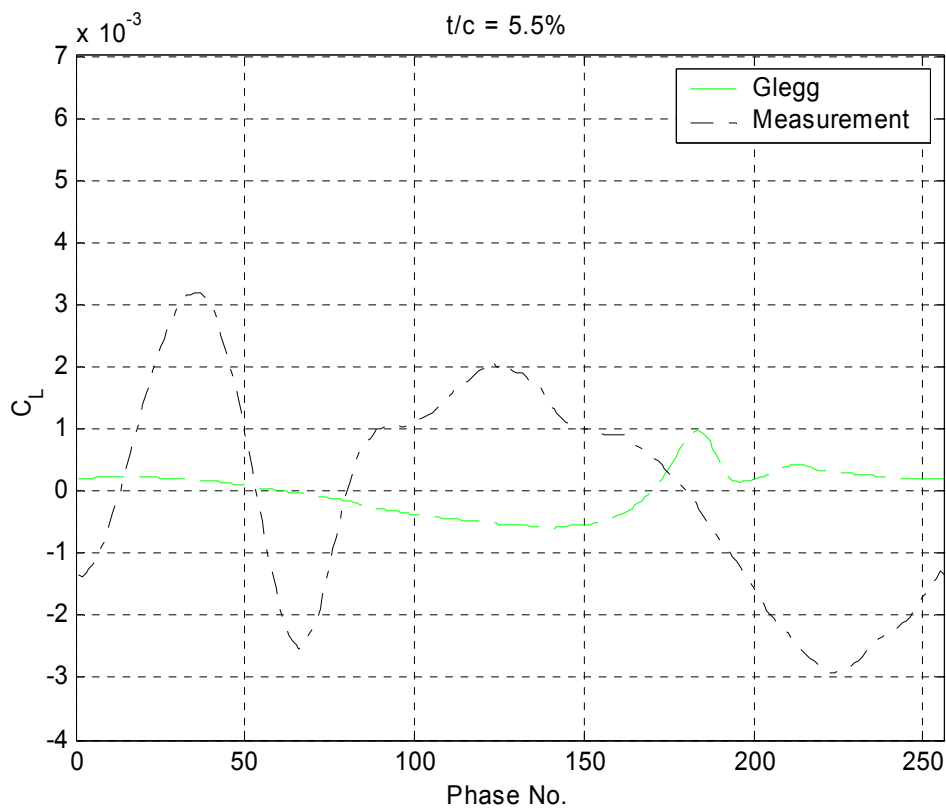
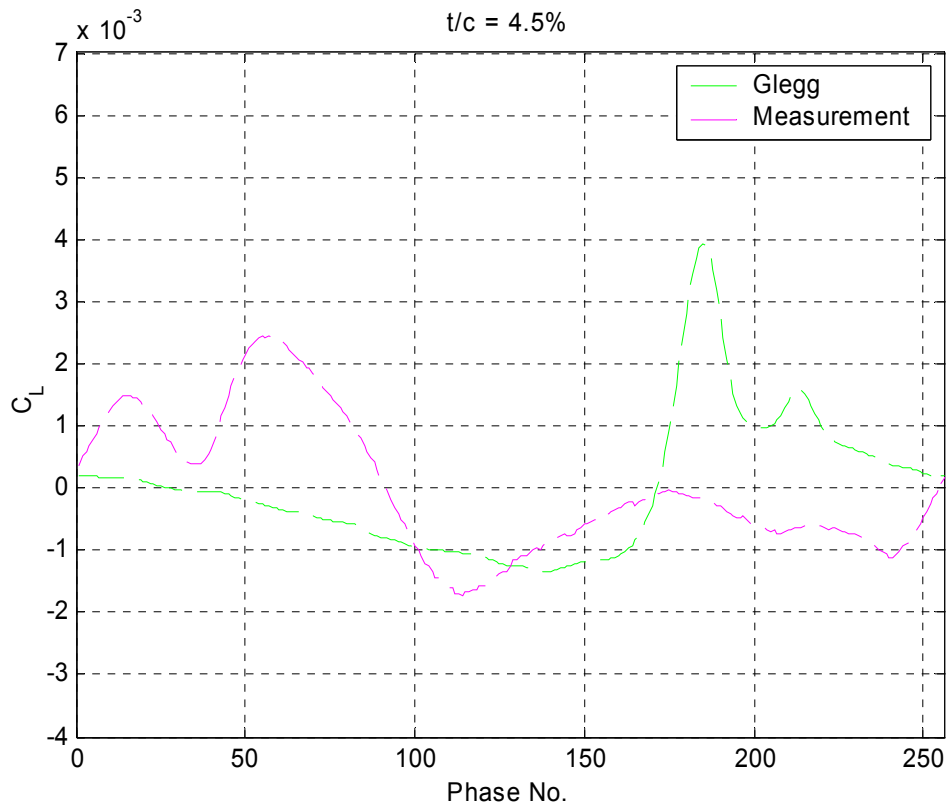


Figure 9.24 continued: Theoretical and measured unsteady lift coefficient, C_L as a function of phase number plotted for $t_g/c = 0.00825, 0.0165, 0.022, 0.033, 0.045, 0.057, 0.079, 0.129$

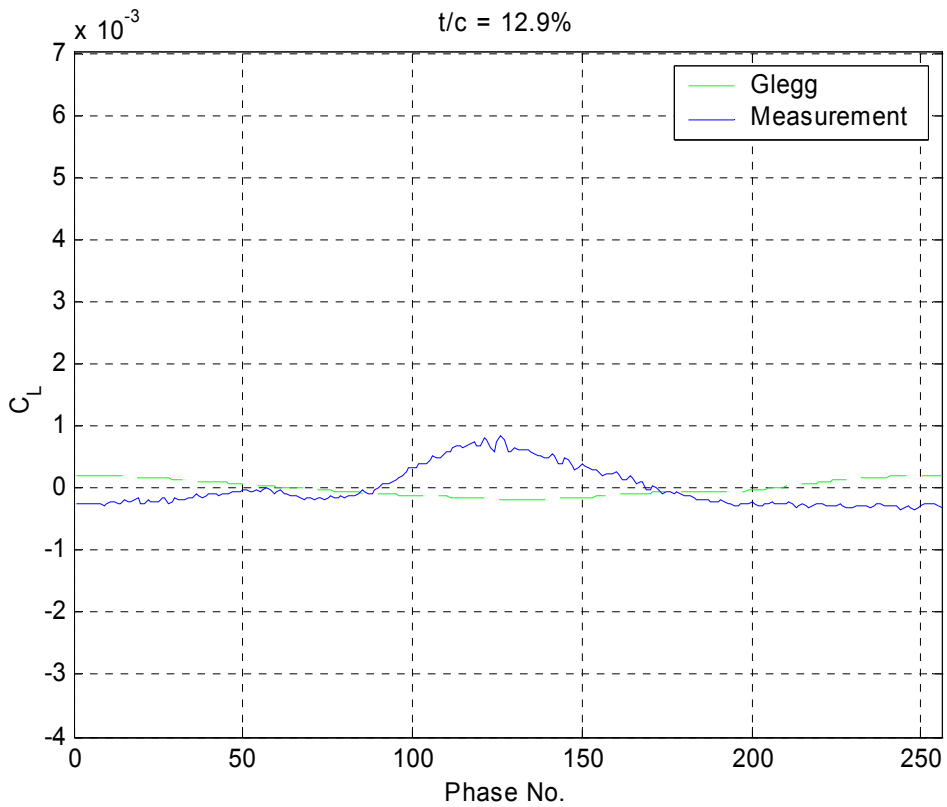
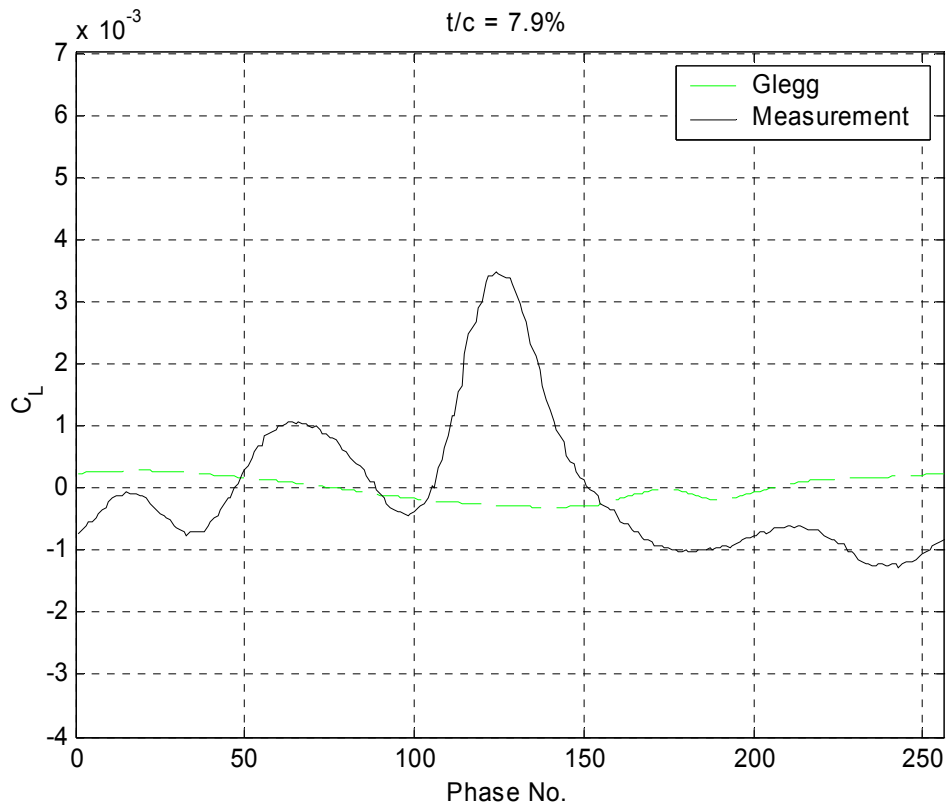


Figure 9.24 continued: Theoretical and measured unsteady lift coefficient, C_L as a function of phase number plotted for $t_g/c = 0.00825, 0.0165, 0.022, 0.033, 0.045, 0.057, 0.079, 0.129$

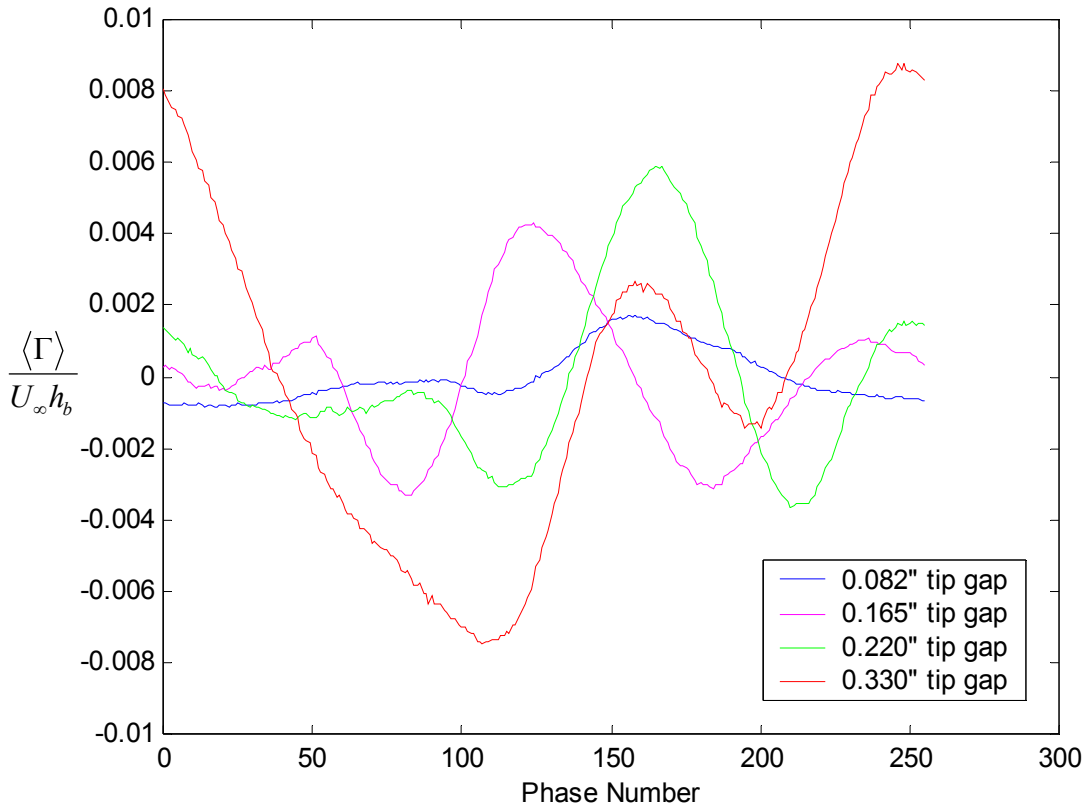
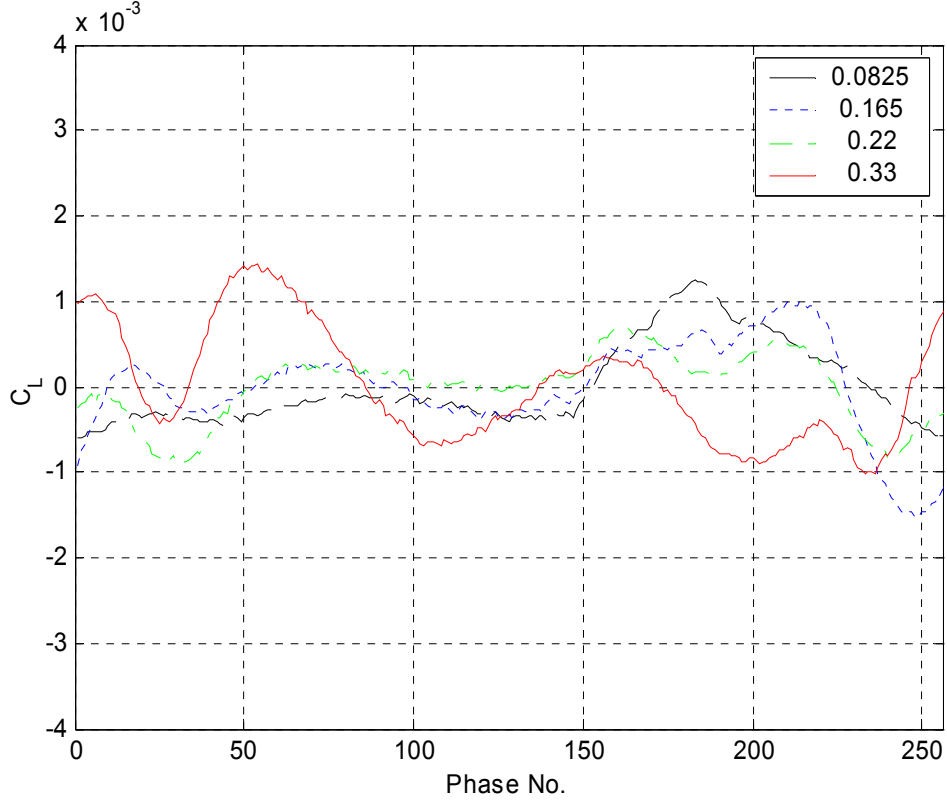


Figure 9.25: Comparison of phase averaged C_L (upper plot) with phased averaged circulation (lower plot—courtesy of Ma, 2003) measured in the tip leakage vortex by Ma (2003).

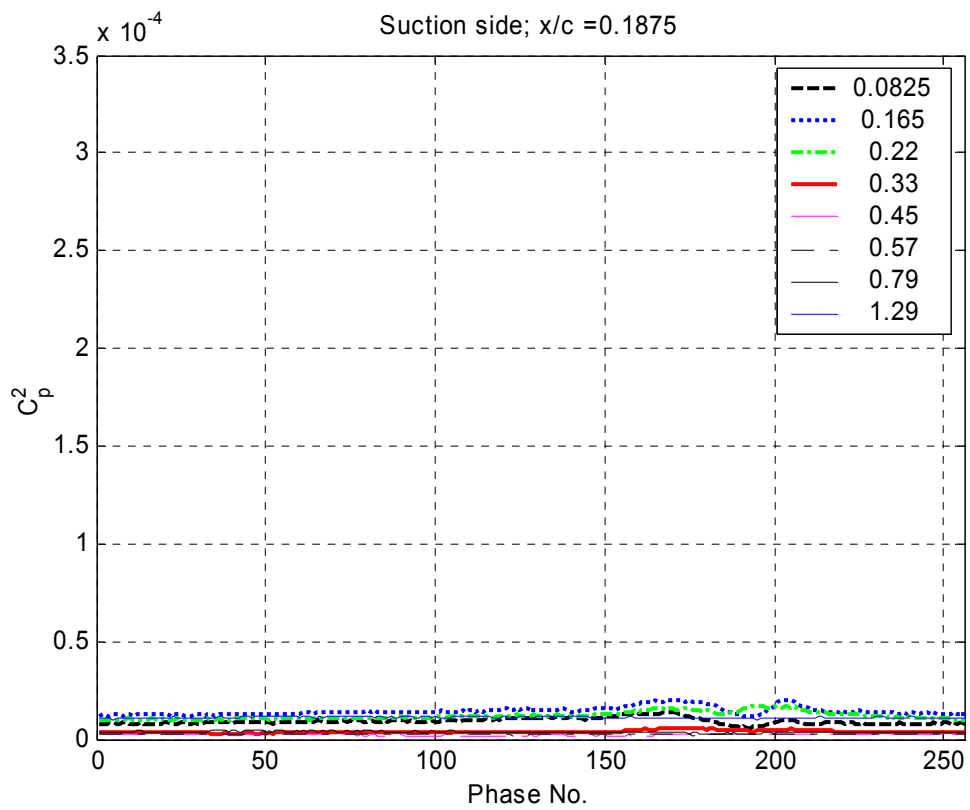
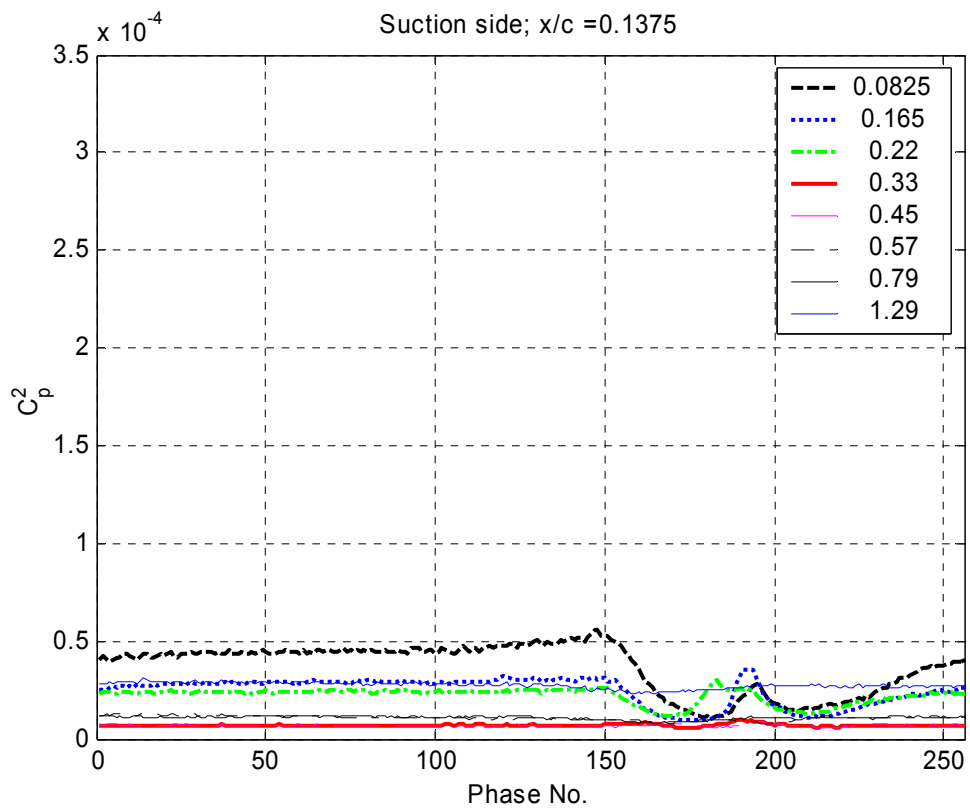


Figure 9.26: Suction side C_p^2 as a function of phase number plotted for each tip gap along the chord at $x/c = 13, 18, 24, 30, 40, 55, 75\%$

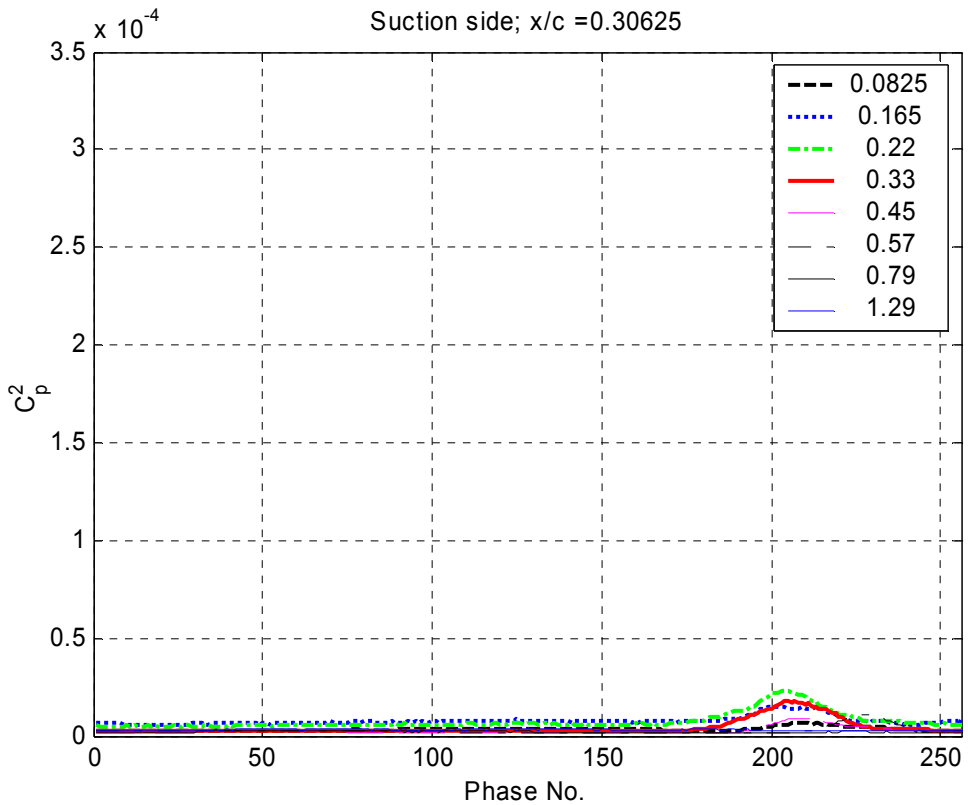
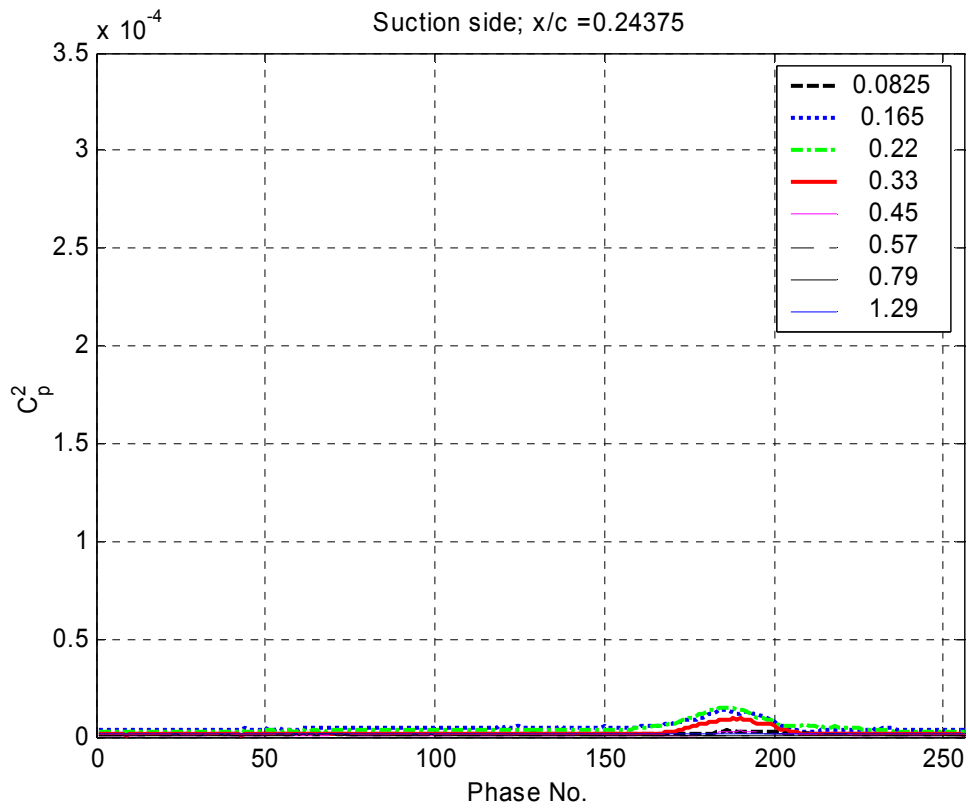


Figure 9.26 continued: Suction side C_p^2 as a function of phase number plotted for each tip gap along the chord at $x/c = 13, 18, 24, 30, 40, 55, 75\%$

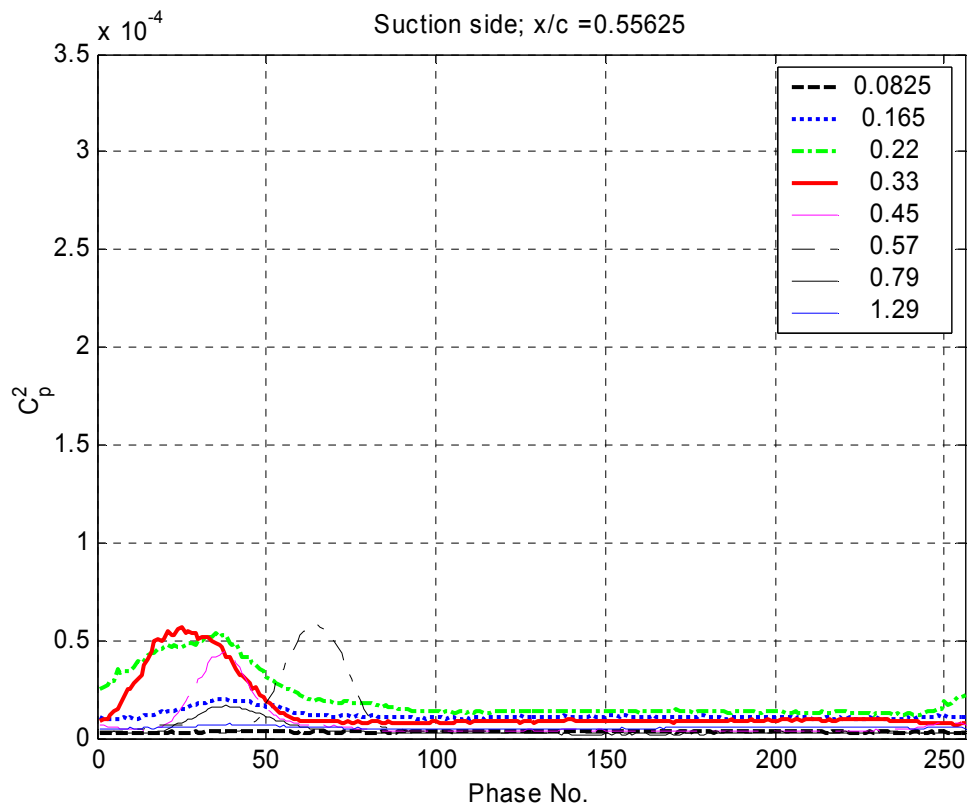
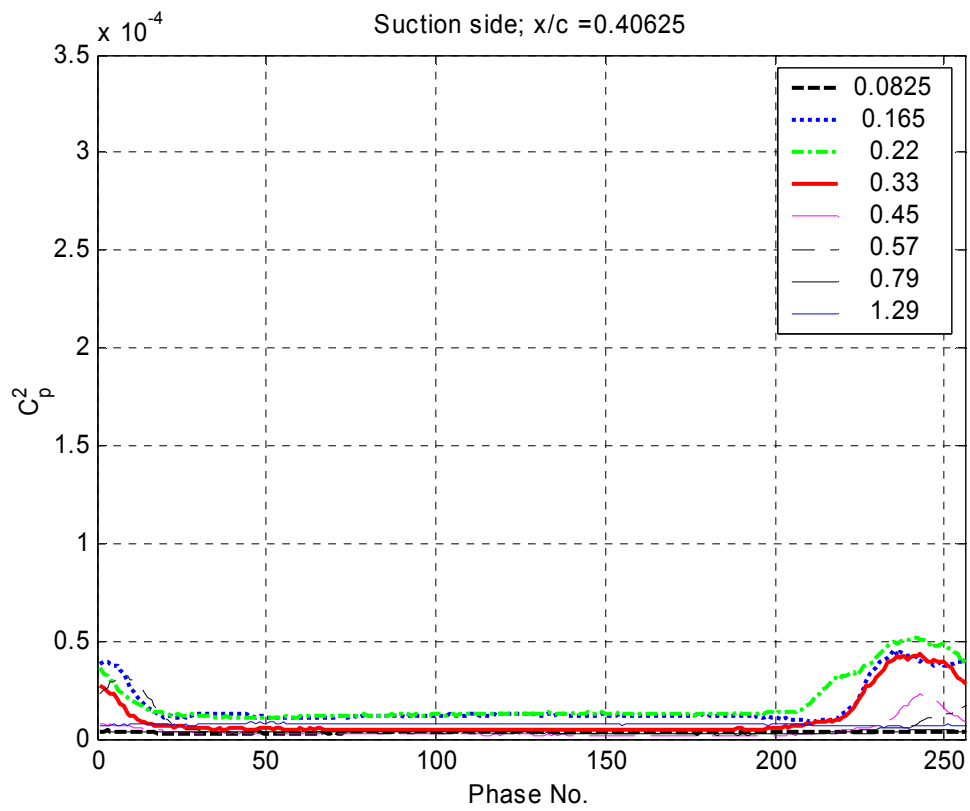


Figure 9.26 continued: Suction side C_p^2 as a function of phase number plotted for each tip gap along the chord at $x/c = 13, 18, 24, 30, 40, 55, 75\%$

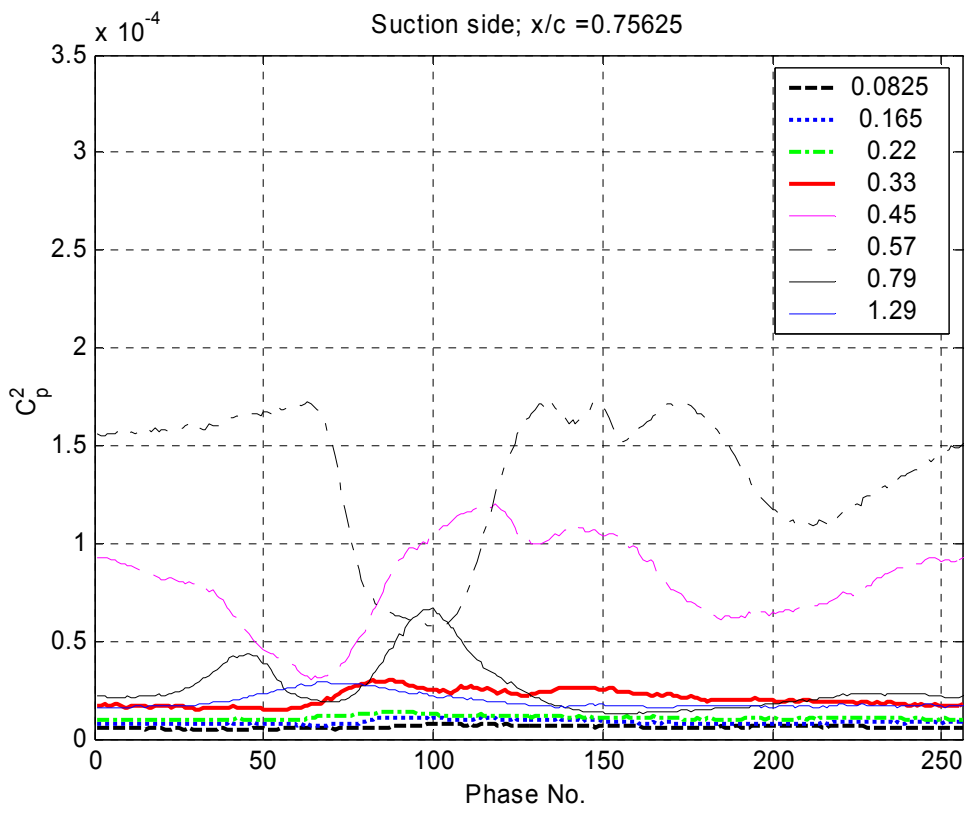


Figure 9.26 continued: Suction side C_p^2 as a function of phase number plotted for each tip gap along the chord at $x/c = 13, 18, 24, 30, 40, 55, 75\%$

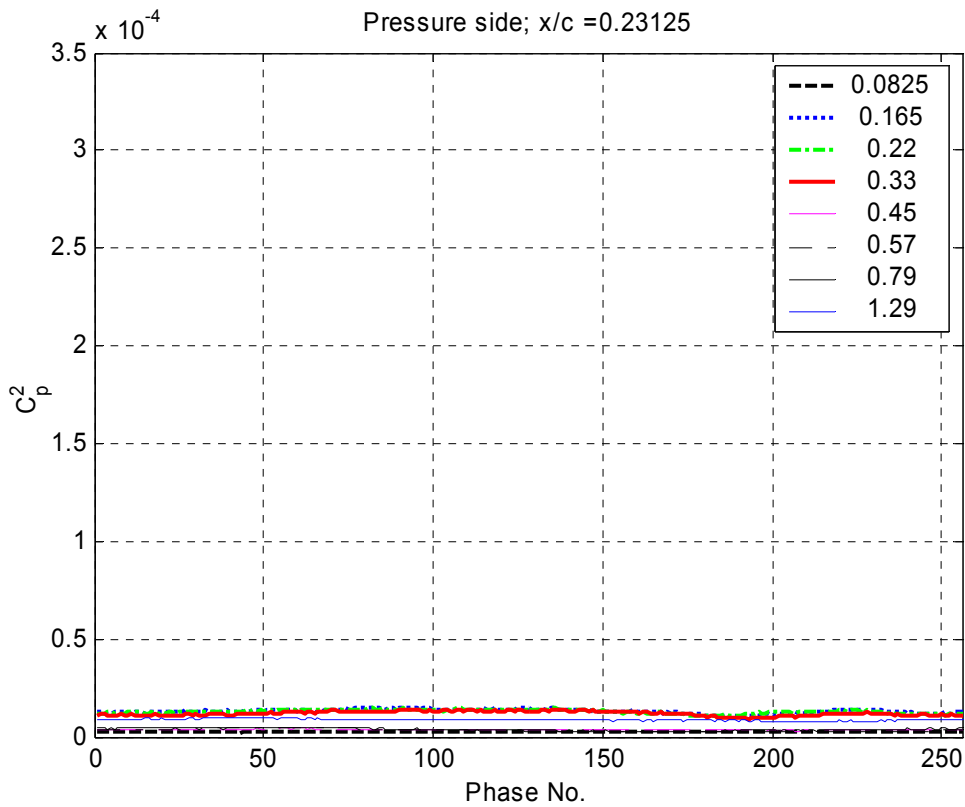
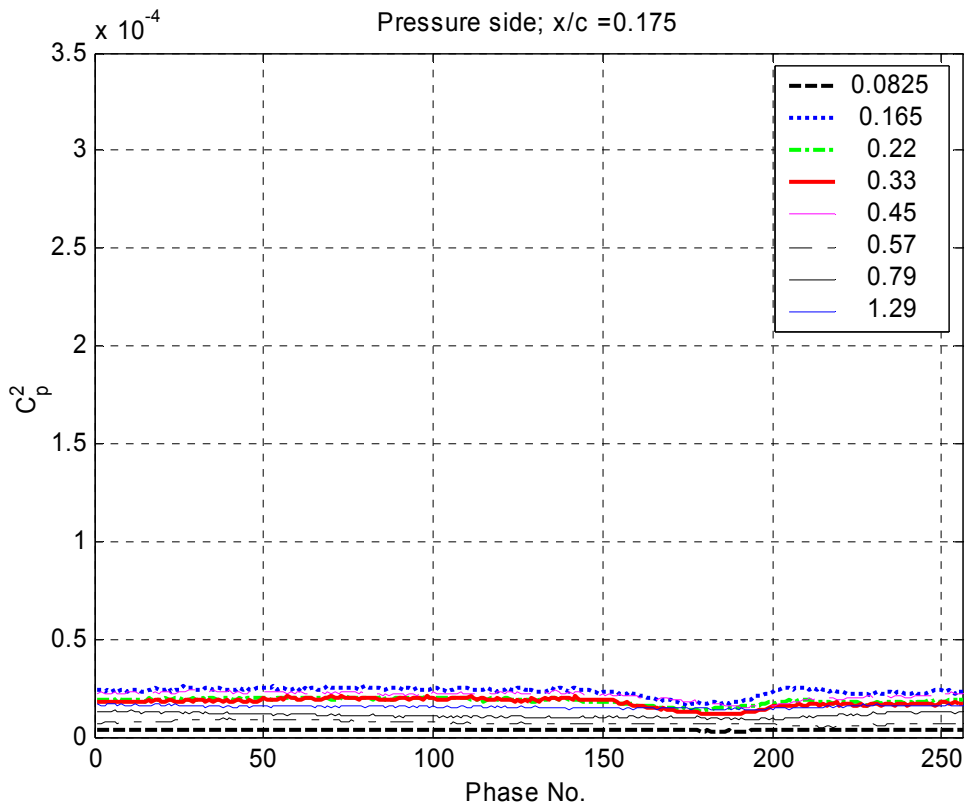


Figure 9.27: Pressure side C_p^2 as a function of phase number plotted for each tip gap along the chord at $x/c = 17.5, 23.125, 29.375, 39.375, 55, 76.25\%$

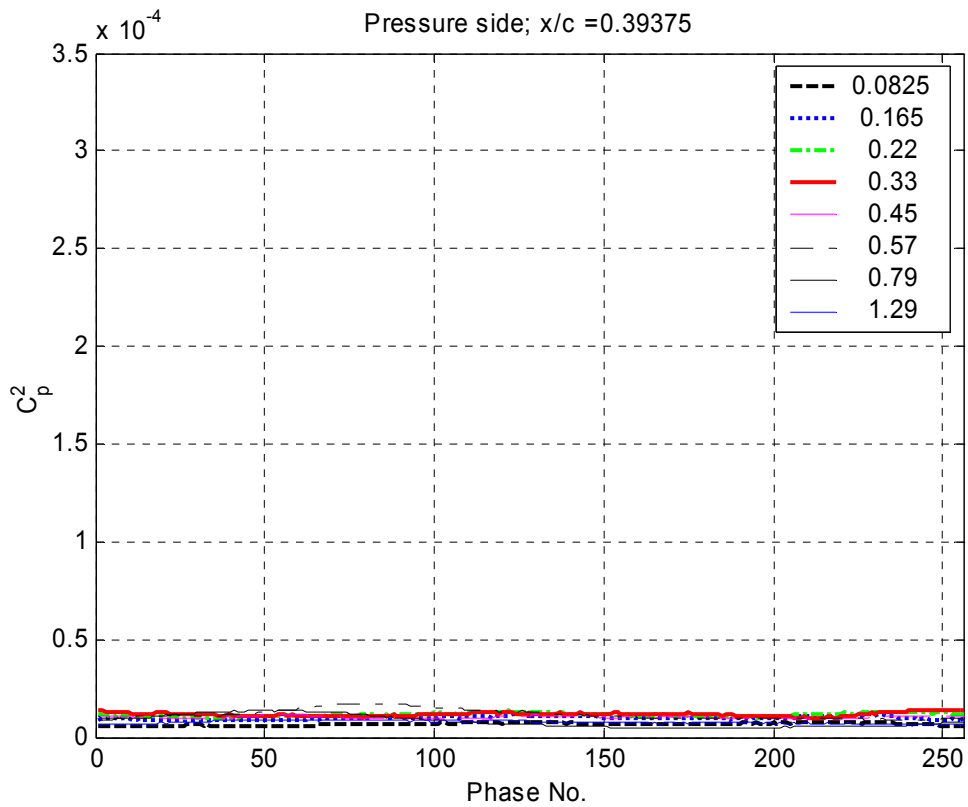
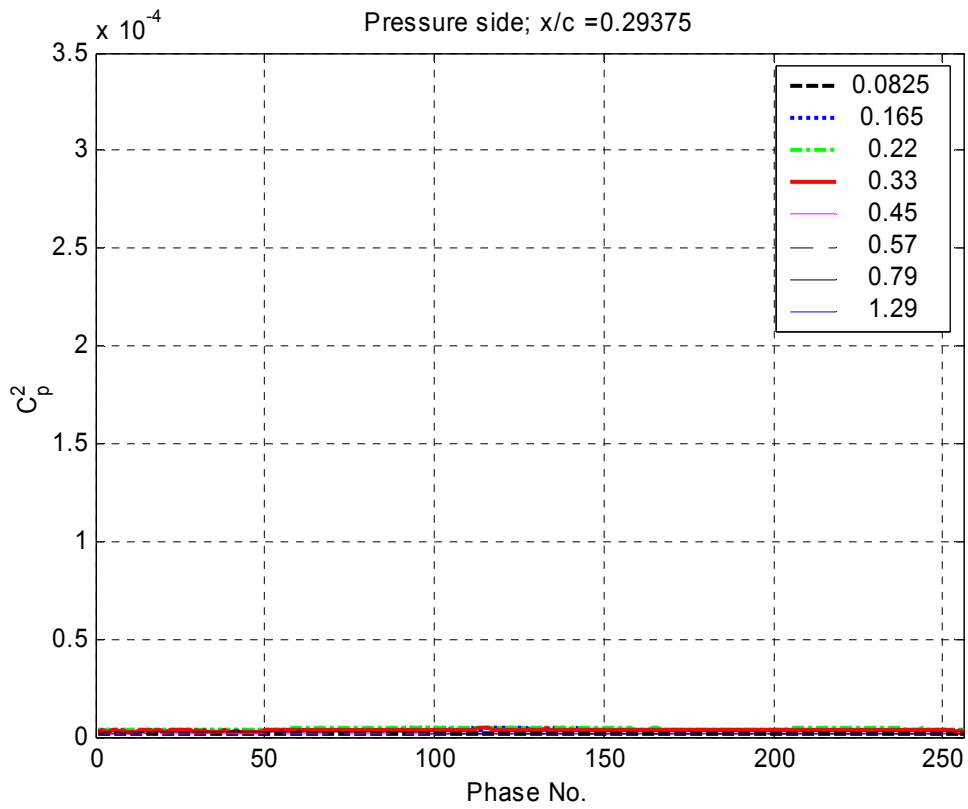


Figure 9.27 continued: Pressure side C_p^2 as a function of phase number plotted for each tip gap along the chord at $x/c = 17.5, 23.125, 29.375, 39.375, 55, 76.25\%$

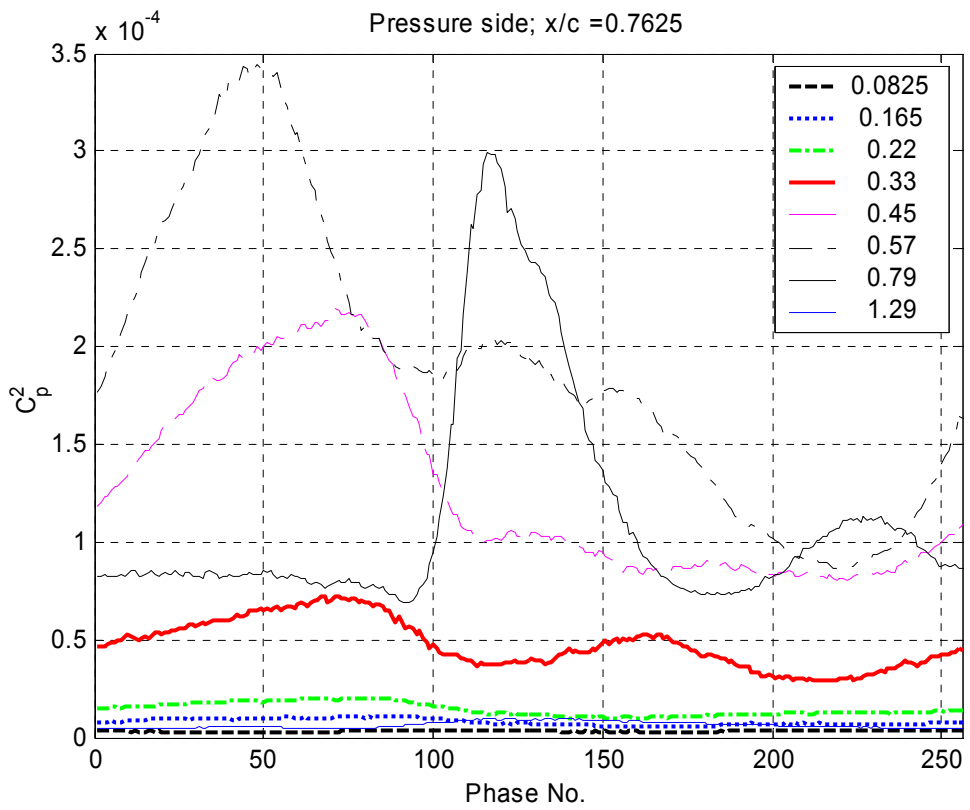
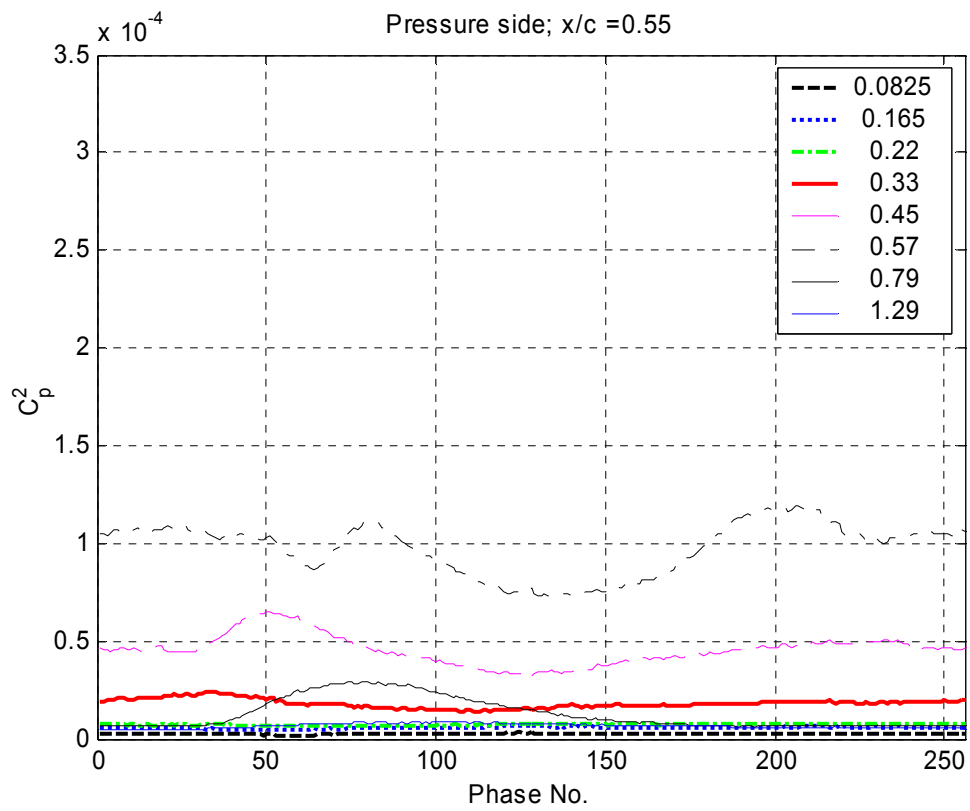


Figure 9.27 continued: Pressure side C_p^2 as a function of phase number plotted for each tip gap along the chord at $x/c = 17.5, 23.125, 29.375, 39.375, 55, 76.25\%$

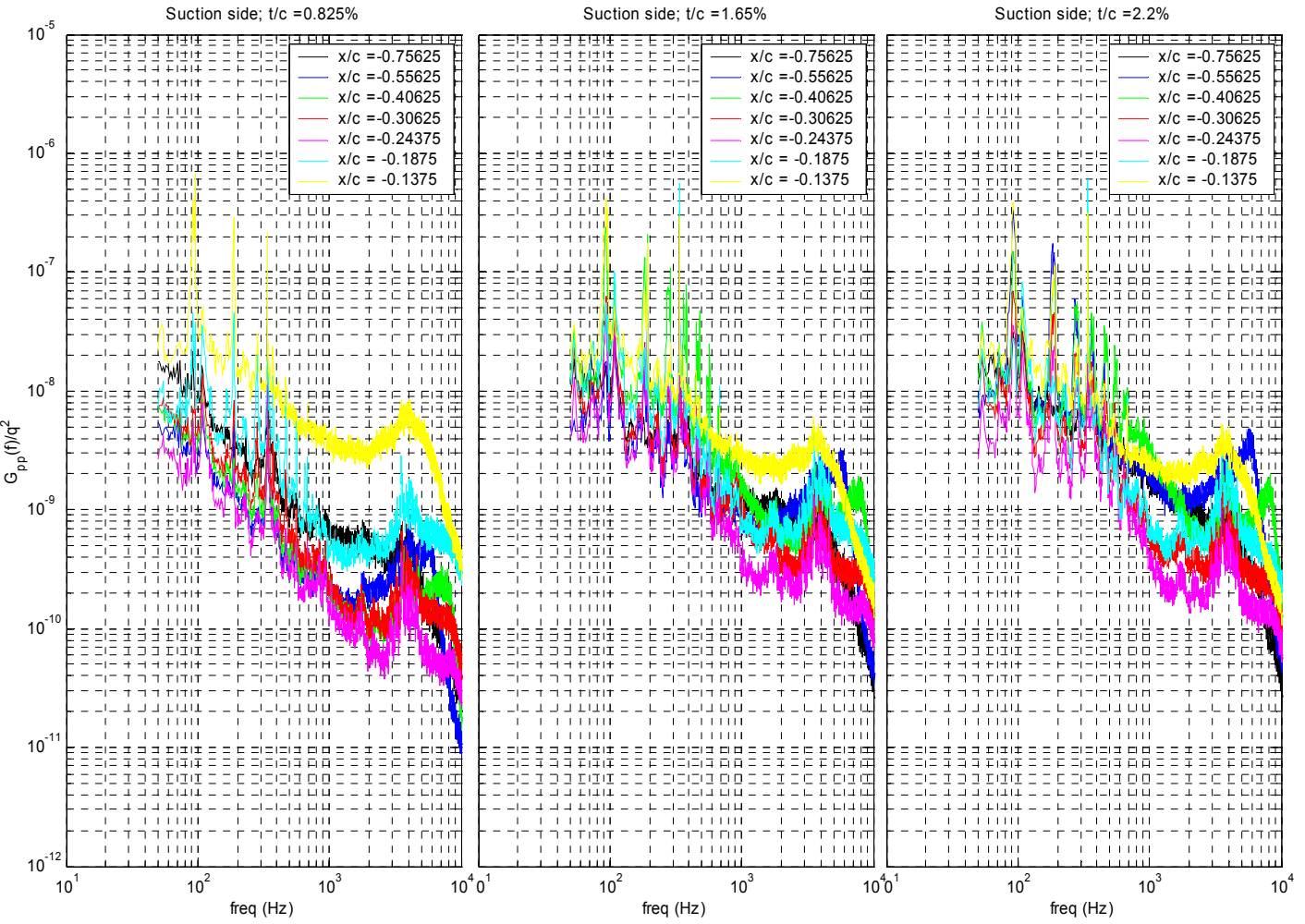


Figure 9.28: Chordwise unsteady pressure spectra on the *suction* side plotted for each tip gap, $t_g/c = 0.00825, 0.0165, 0.022, 0.033, 0.045, 0.057, 0.079, 0.129$.

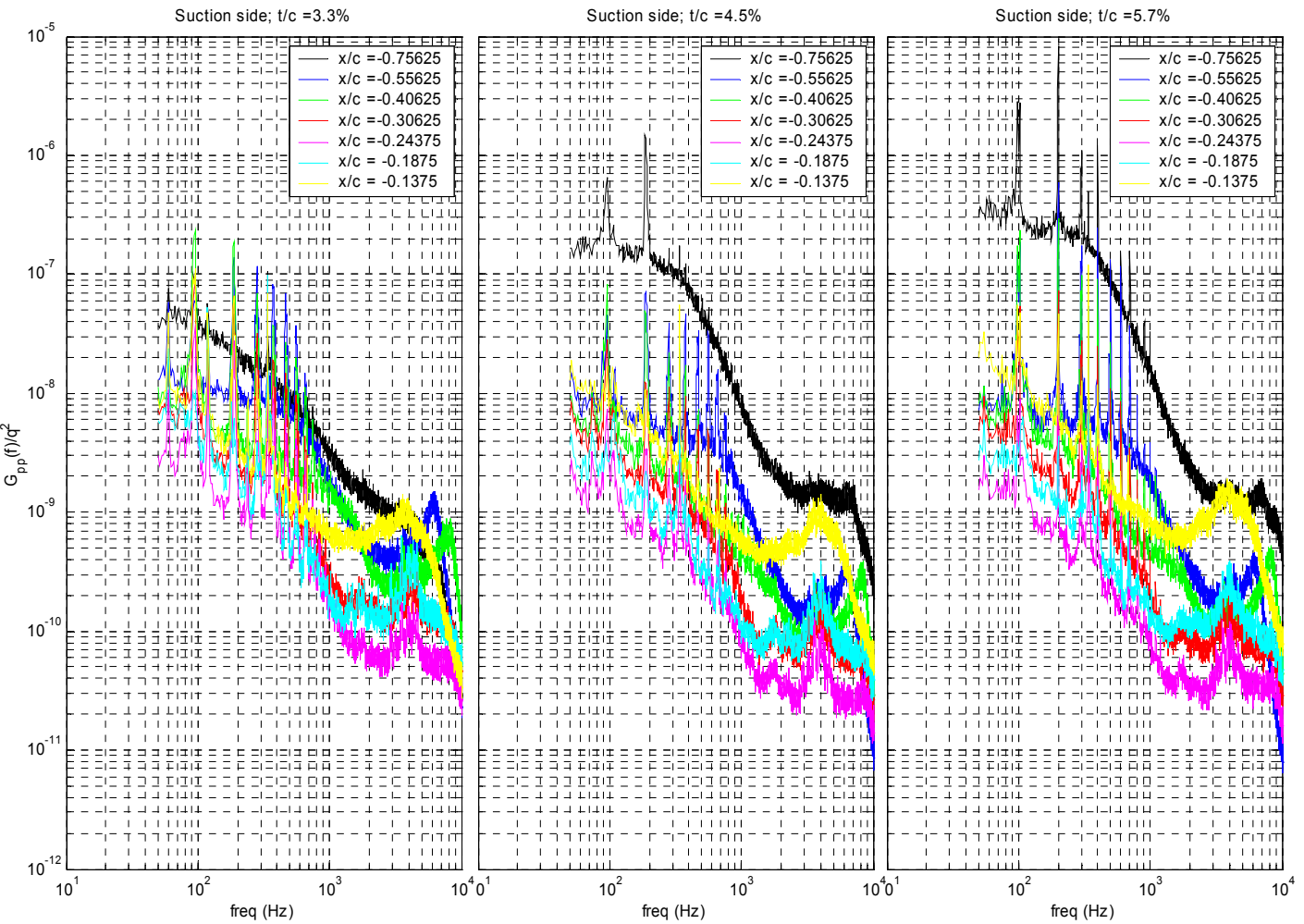


Figure 9.28 continued: Chordwise unsteady pressure spectra on the *suction* side plotted for each tip gap, $t_g/c = 0.00825, 0.0165, 0.022, 0.033, 0.045, 0.057, 0.079, 0.129$.

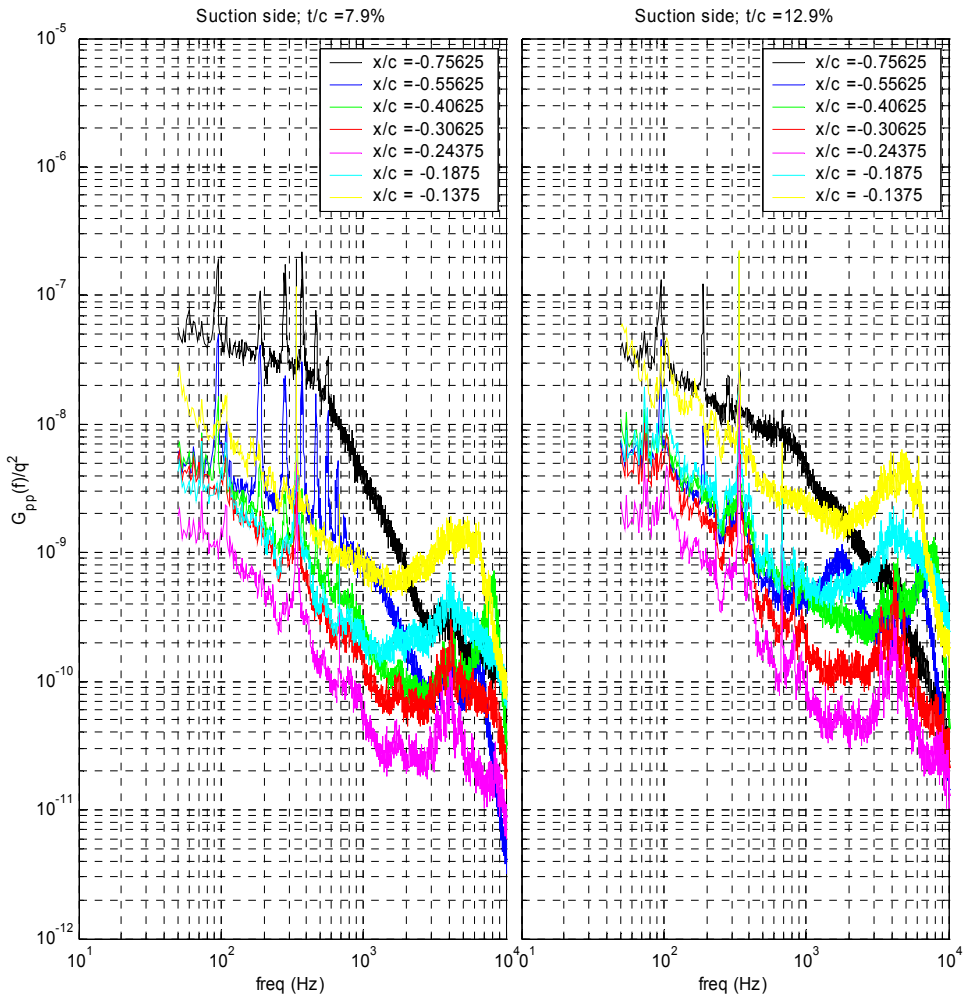


Figure 9.28 continued: Chordwise unsteady pressure spectra on the *suction* side plotted for each tip gap, $t_g/c = 0.00825, 0.0165, 0.022, 0.033, 0.045, 0.057, 0.079, 0.129$.

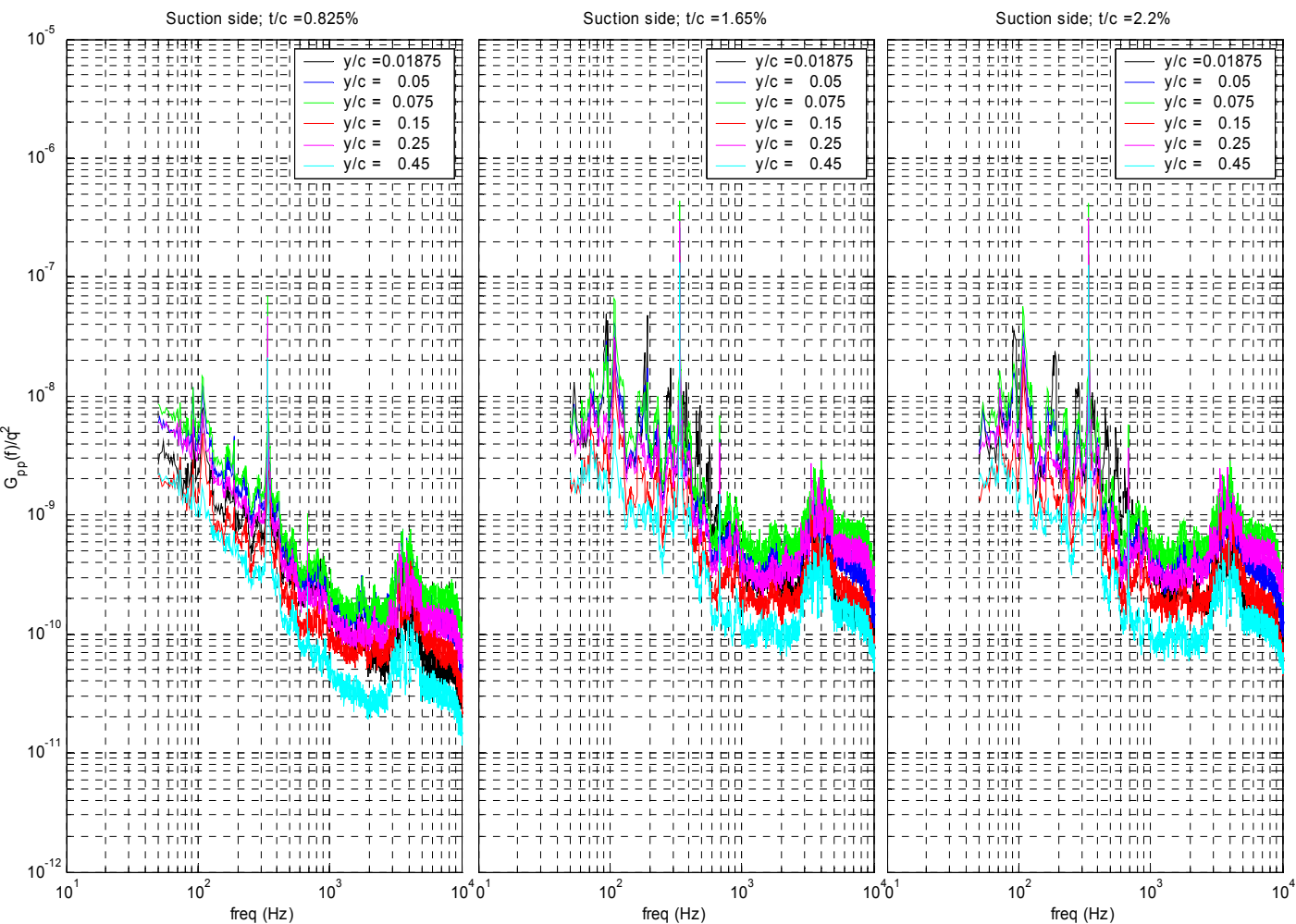


Figure 9.29: Spanwise unsteady pressure spectra on the *suction* side plotted for each tip gap, $t_g/c = 0.00825, 0.0165, 0.022, 0.033, 0.045, 0.057, 0.079, 0.129$.

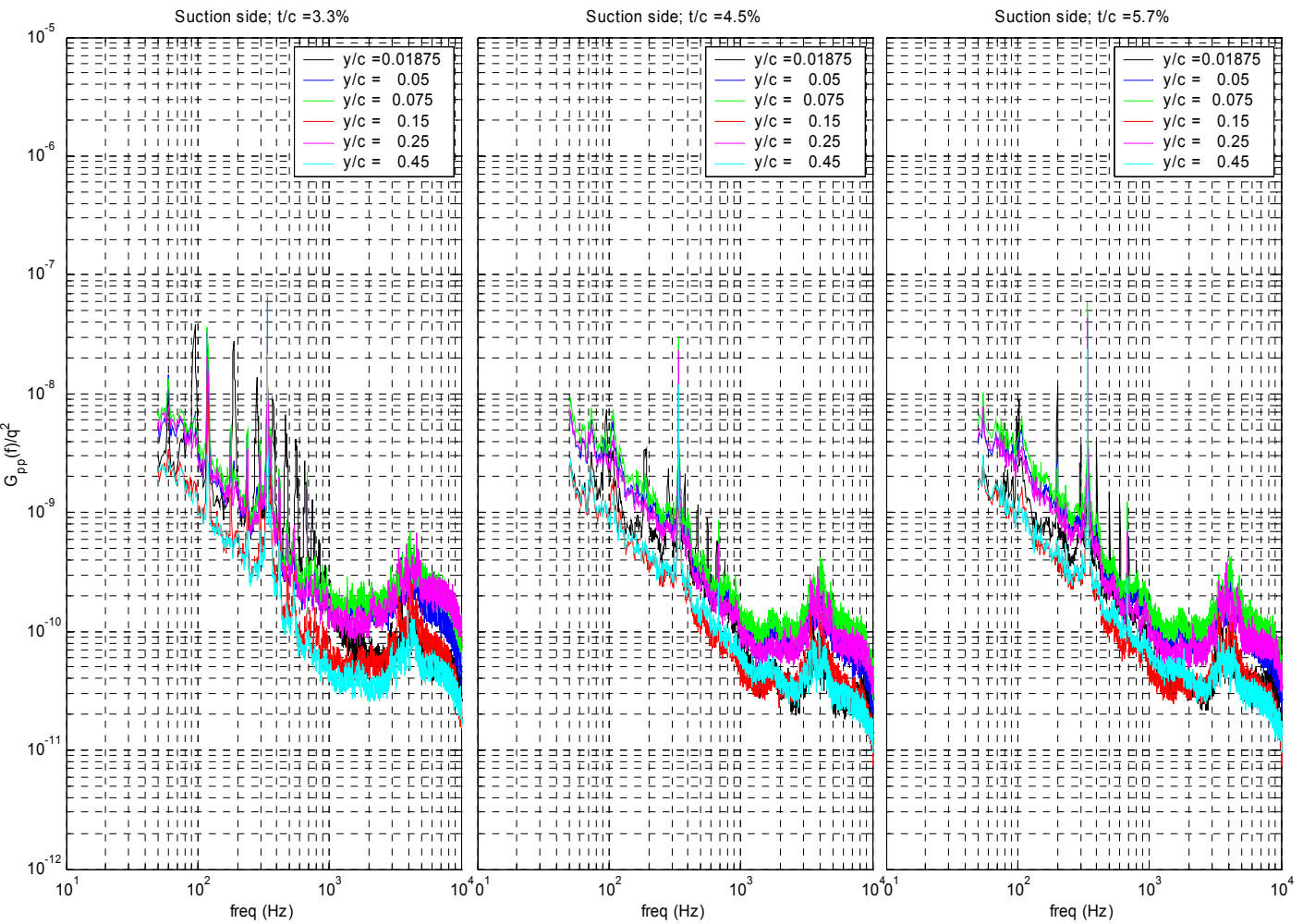


Figure 9.29 continued: Spanwise unsteady pressure spectra on the *suction* side plotted for each tip gap, $t_g/c = 0.00825, 0.0165, 0.022, 0.033, 0.045, 0.057, 0.079, 0.129$.

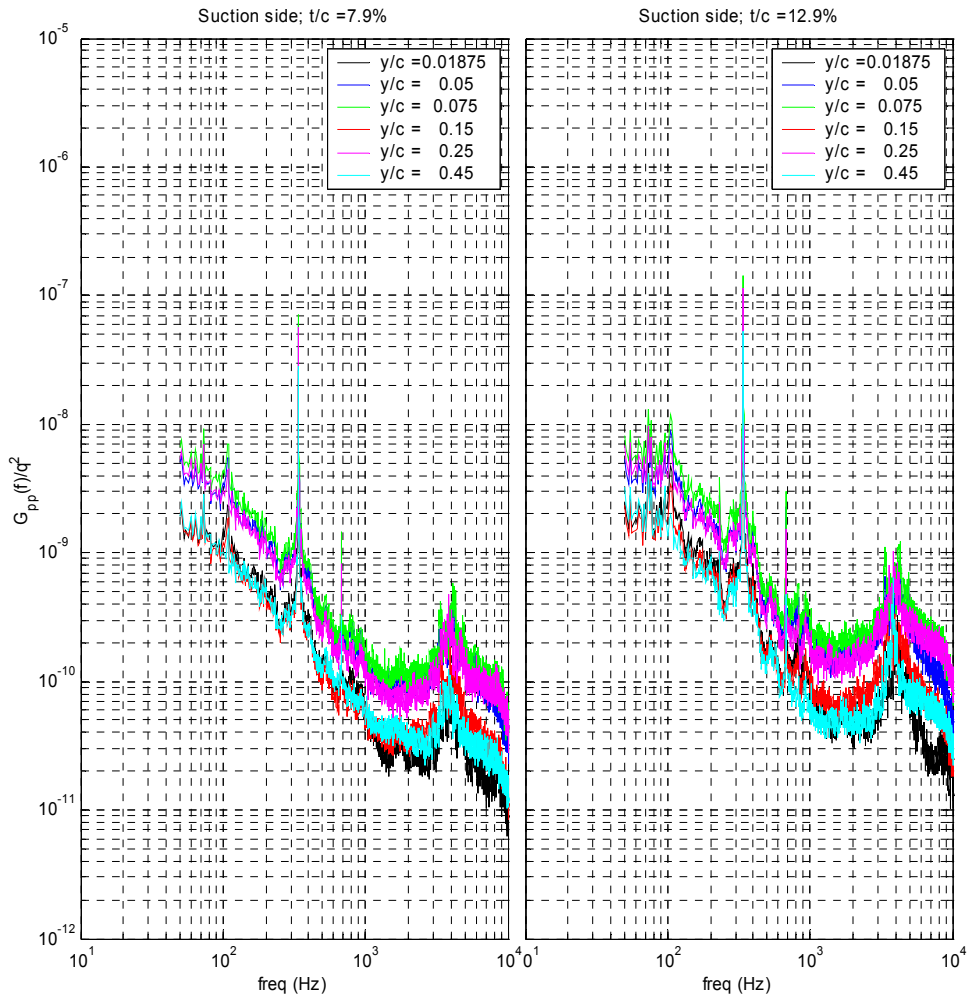


Figure 9.29 continued: Spanwise unsteady pressure spectra on the *suction* side plotted for each tip gap, $t_g/c = 0.00825, 0.0165, 0.022, 0.033, 0.045, 0.057, 0.079, 0.129$.

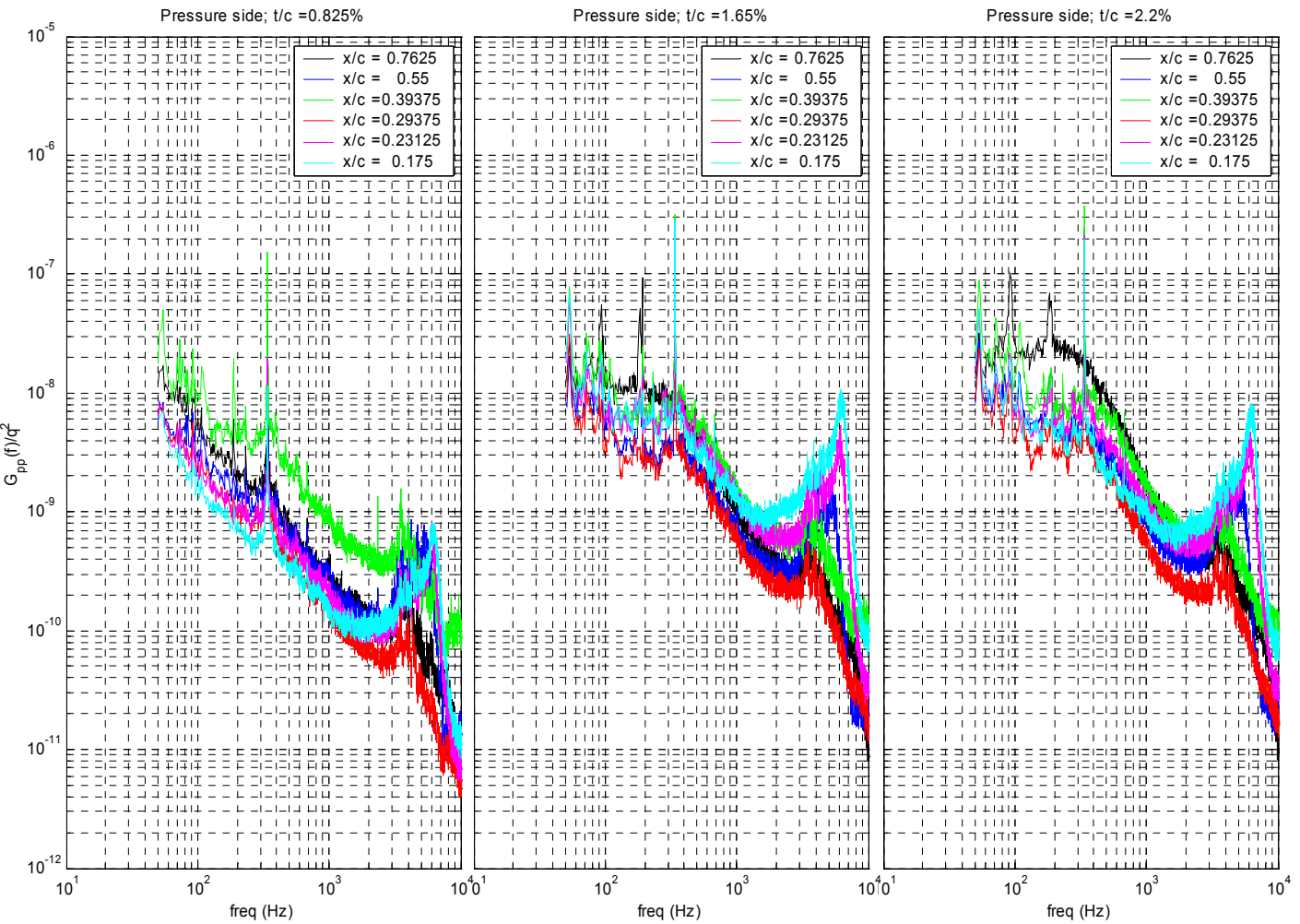


Figure 9.30: Pressure spectra on the *pressure* side at each chordwise station plotted for each tip gap, $t_g/c = 0.00825, 0.0165, 0.022, 0.033, 0.045, 0.057, 0.079, 0.129$.

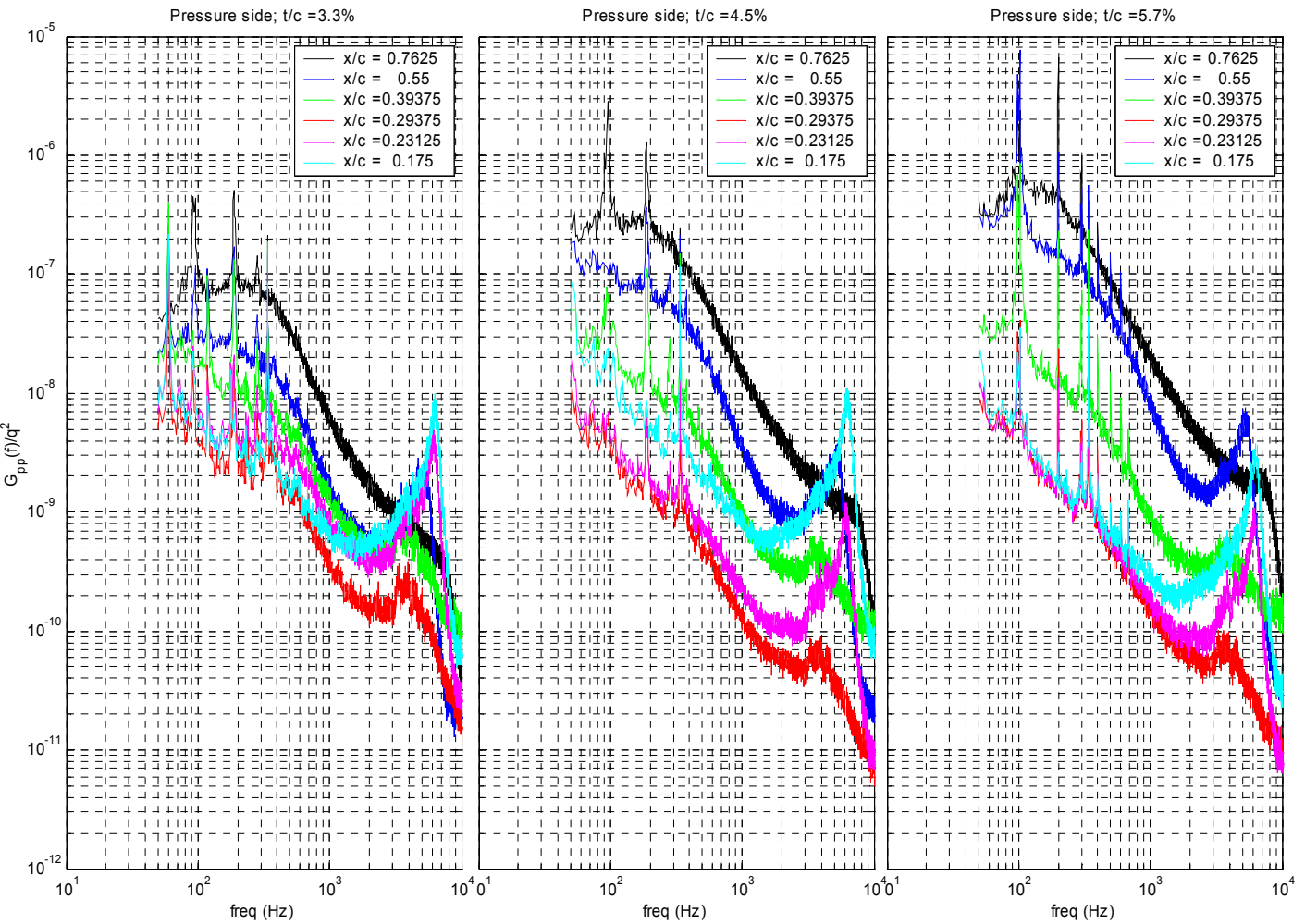


Figure 9.30 continued: Pressure spectra on the *pressure* side at each chordwise station plotted for each tip gap, $t_g/c = 0.00825, 0.0165, 0.022, 0.033, 0.045, 0.057, 0.079, 0.129$.

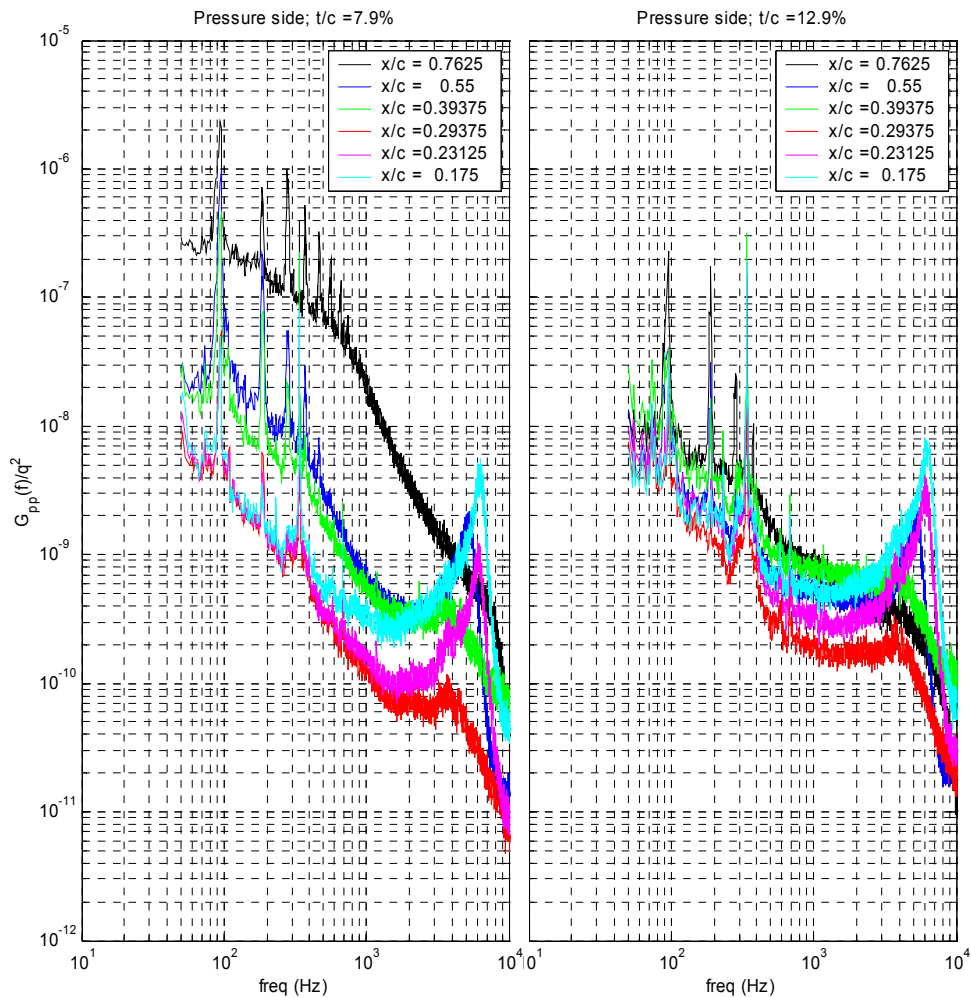


Figure 9.30 continued: Pressure spectra on the *pressure* side at each chordwise station plotted for each tip gap, $t_g/c = 0.00825, 0.0165, 0.022, 0.033, 0.045, 0.057, 0.079, 0.129$.

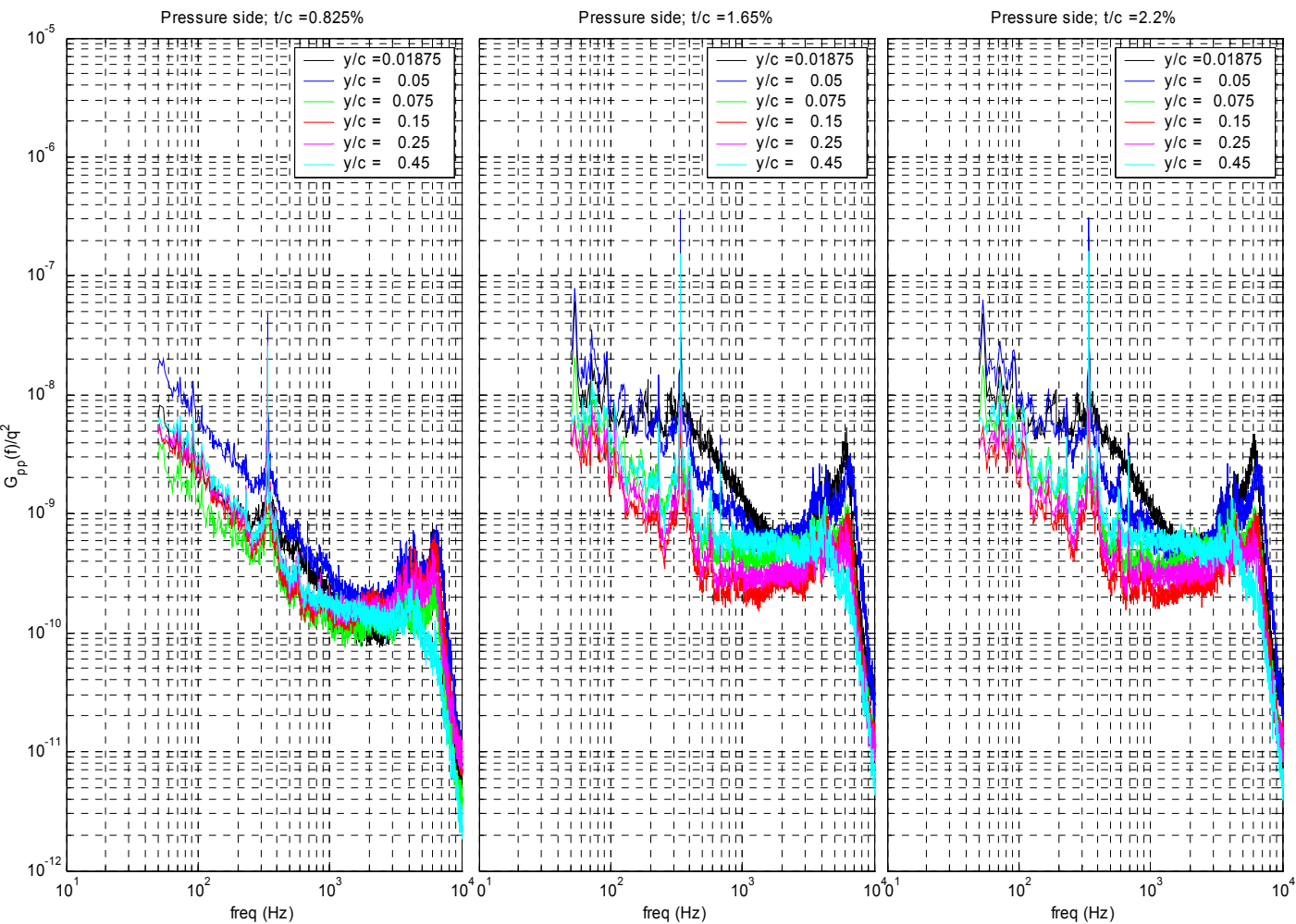


Figure 9.31: Spanwise unsteady pressure spectra on the *suction* side plotted for each tip gap, $t_g/c = 0.00825, 0.0165, 0.022, 0.033, 0.045, 0.057, 0.079, 0.129$.

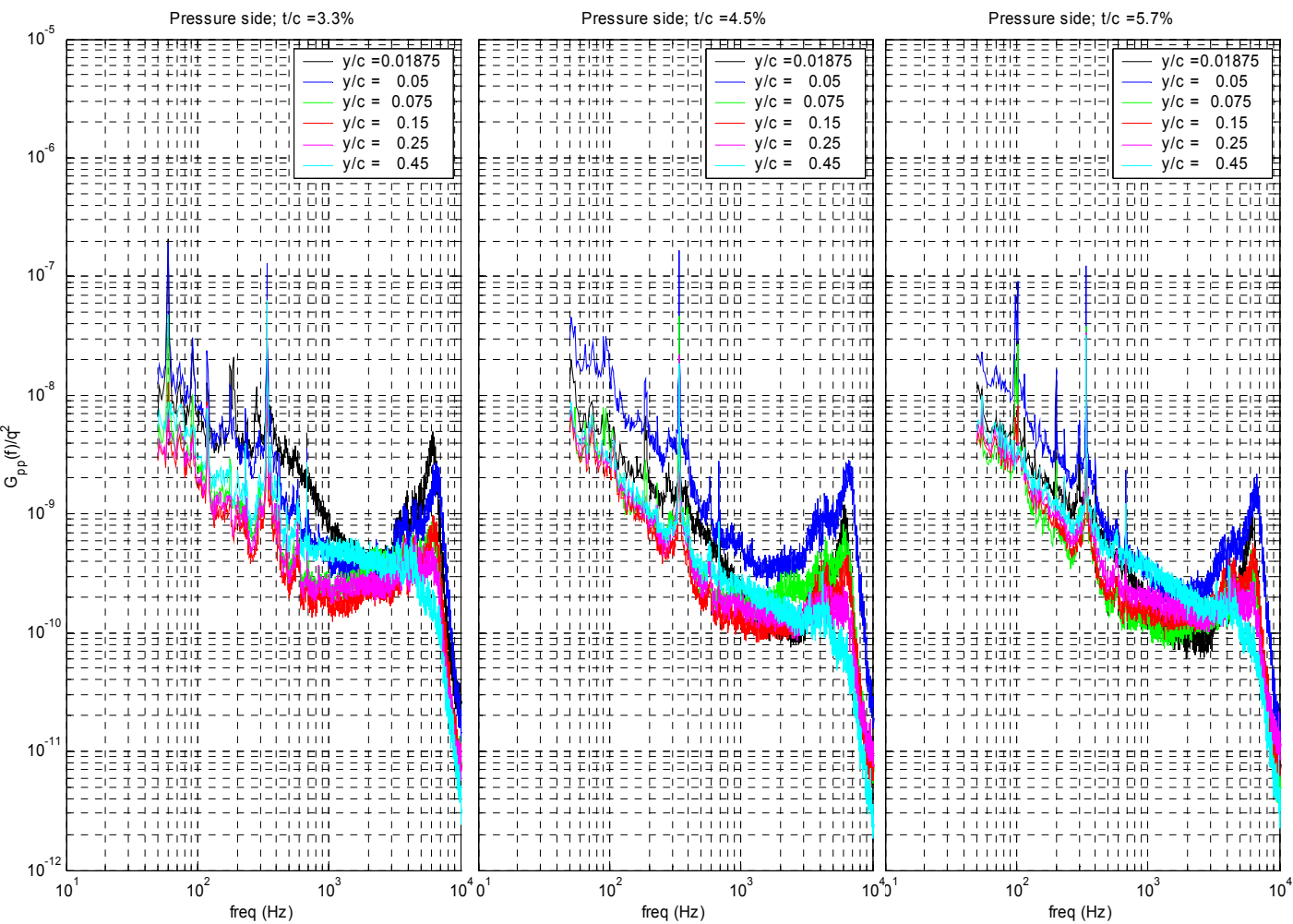


Figure 9.31 continued: Spanwise unsteady pressure spectra on the *suction* side plotted for each tip gap, $t_g/c = 0.00825, 0.0165, 0.022, 0.033, 0.045, 0.057, 0.079, 0.129$.

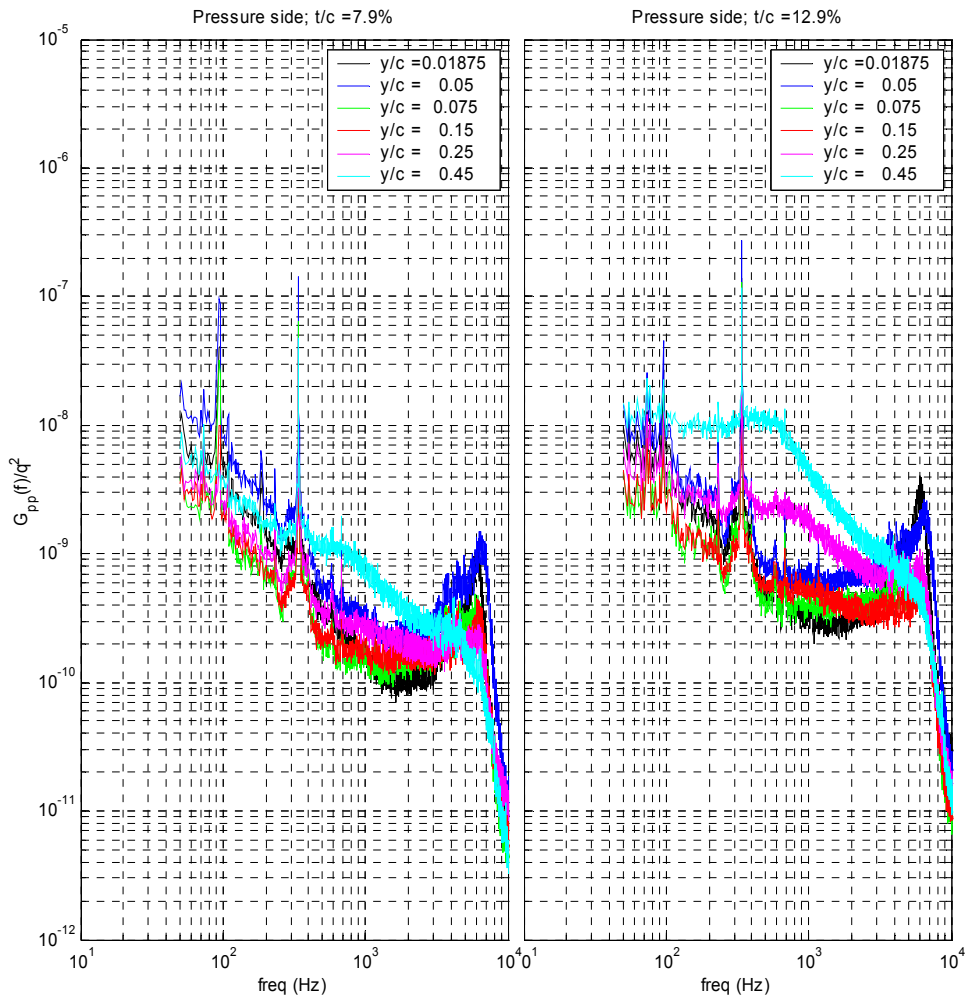


Figure 9.31 continued: Spanwise unsteady pressure spectra on the *suction* side plotted for each tip gap, $t_g/c = 0.00825, 0.0165, 0.022, 0.033, 0.045, 0.057, 0.079, 0.129$.

10. CONCLUSIONS

10.1 Single Airfoil in Turbulence

10.1.1 Primary Contributions

Measurements of fluctuating surface pressure were made on a NACA 0015 airfoil immersed in grid generated turbulence. The airfoil model has a 2' chord and spans the 6' Virginia Tech Stability Wind Tunnel test section. Two grids were used to investigate the effects of turbulence length scale on the surface pressure response. A large grid which produced turbulence with an integral scale 13% of the chord and a smaller grid which produced turbulence with an integral scale 1.3% of the chord. Measurements were performed at angles of attack, α from 0° to 20° . An array of microphones mounted subsurface was used to measure the unsteady surface pressure. The goal of this measurement was to characterize the effects of angle of attack on the surface pressure response. Three major contributions have resulted from this work.

The first significant result is shown in large grid lift spectra calculated from unsteady surface pressure measurements. Lift spectra were calculated for each angle of attack and comparisons made which revealed two distinct interaction regions; for $\omega_r < 10$ a reduction in unsteady lift of up to 7 decibels (dB) occurs while the unsteady lift increases for $\omega_r > 10$ as the angle of attack is increased. The reduction in unsteady lift at low ω_r with increasing angle of attack is a result that has never before been shown either experimentally or theoretically and as such, is a significant and new finding.

The source of the reduction in lift spectral level appears to be closely related to the distortion of inflow turbulence based on analysis of surface pressure spanwise correlation length scales. This result suggest eddies are stretched as they approach the airfoil thereby reducing their spanwise integral scale which in turn reduces the surface pressure spanwise correlations length scale. The effects of distortion are more pronounced as the angle of attack is increased due to the larger velocity gradients associated with the mean field which results in a reduction in spanwise correlation length scale with increasing angle of attack. The unsteady pressure therefore, has a smaller correlated area over which to act and thus, a reduction in unsteady lift occurs with increasing angle of attack. Furthermore, while the distortion of the inflow appears to be critical in this experiment, wherein the integral scale (λ/c) is 13% of the chord, this effect does not seem

to be significant in larger integral scale (relative to the chord) flows based on the previous experimental work of McKeough (1976). This leads to the second major result of this work; the airfoils size relative to the inflow integral scale is critical in defining how the airfoil will respond under variation of angle of attack.

The flat plat theoretical formulations developed by Reba and Kerschen (1996), Graham (1970a), and Atassi (1984) appear to accurately predict the airfoil response when the inflow integral scale is large relative to the airfoil chord. However, such flat plat predictions schemes are not appropriate for the case of smaller scale inflow because they do not model the distortion of the inflow correctly. The third major contribution of this work is the development of a prediction scheme which correctly accounts for the effects of distortion when the inflow integral scale is small relative to the airfoil chord. This scheme utilizes Rapid Distortion Theory to account for the distortion of the inflow with the distortion field modeled using a circular cylinder.

10.1.2 Suggestions for Future Work

The relative size of the airfoil to inflow integral scale appears to be a critical parameter in determining the airfoil response subject to variation of angle of attack. McKeough's (1976) measurements of unsteady lift showed an increase in lift spectral level with increasing angle of attack for an inflow integral scale 40% of the airfoil chord. The current experiment shows a reduction in unsteady lift when the angle of attack is increased for an inflow integral scale 13% of the airfoil chord. This finding suggests the existence of an integral scale to airfoil chord ratio which results in an unsteady loading that is independent of angle of attack. Therefore, examination of the airfoil response under variation of both angle of attack and λ/c will provide insight on how the dominant physics vary with λ/c . Such an experiment would offer valuable details necessary for developing a unified model of the airfoil response. With an instrumented airfoil this measurement could be carried out with an active grid for generation of turbulence of varying integral scale.

Analysis of oil flow visualization and unsteady surface pressure data suggests the presence of a transient laminar separation bubble in the airfoil leading edge region. It is not clear how this bubble, if in fact it really exists, affects the unsteady loading of the airfoil. This bubble, if present, may be coupled to the inflow and as such, shedding vorticity which provides means

for relaxing the unsteady loading on the airfoil. Careful examination of the flow field surrounding the airfoil through both velocity measurements and flow visualization together with surface pressure measurements could offer the evidence required to determine this bubbles presence and its effect on the airfoil response.

10.2 Cascade in Periodic Disturbance

10.2.1 Primary Contributions

The unsteady surface response of a linear cascade of blades subject to a periodic disturbance was measured using the multi-channel microphone measurement system employed in the single airfoil in turbulence experiment. Unsteady pressure was measured on the suction and pressure side of two cascade blades with an array of 24 microphones (12 per blade side) mounted subsurface. The periodic disturbance was generated using a pair of vortex generators attached to a moving end wall. Measurements were made for 8 tip gaps ($t_g/c = 0.00825, 0.0165, 0.022, 0.033, 0.045, 0.057, 0.079, 0.129$) and phased averaged with respect to the vortex generator pair position. This measurement was motivated by the results presented by Ma (2003). The work of Ma (2003) suggested that tip leakage vortex shedding in the presence of a periodic disturbance is heavily influenced by the inviscid response of the cascade blade. This conclusion was arrived at by Ma's (2003) observation that as the tip gap is increased the amount of fluctuation in the tip leakage vortex circulation increases dramatically, in fact, many times the circulation in the inflow vortices.

Unsteady pressure measurements reveal that the blade response involves a complex interaction of both inviscid response and viscous phenomena. However, a close relationship between unsteady tip loading and tip leakage vortex circulation is revealed. This leads to the next major contribution of this work; the inviscid response appears to be significant in determining the tip leakage vortex circulation. Additionally, predictions using inviscid theory, although not capturing the details of the unsteady tip loading, agree well with measured levels of unsteady tip loading. As such, inviscid theory may be useful for predicting the tip leakage circulation and perhaps, pressure fluctuations in the tip leakage vortex which is the final significant finding of this work.

10.2.2 Suggestions for Future Work

The most pressing issue with the cascade unsteady pressure data is the reconciling of differences between surface pressure measurements made with and without vortex generators. Resolving this matter will remove any doubt about the validity of unsteady pressure data measured with vortex generators present.

To better understand the role of the inviscid response in producing large scale tip leakage vortex circulation and pressure fluctuations, simultaneous velocity-surface pressure measurements could be undertaken. Such measurements would likely show precisely the extent of influence the inviscid response has on tip leakage vortex circulation. Furthermore, this information could aid in locating where, along both the chord and span, surface pressure fluctuations most heavily influence tip leakage vortex formation. Such information may offer improvements to inviscid unsteady loading prediction schemes in the presence of a blade tip gap. Furthermore, simultaneous surface pressure-tip leakage vortex pressure measurement would provide valuable information about the relationship between the blade response and formation of high intensity pressure fluctuations in the tip leakage vortex.

Additionally, measurement of the unsteady loading at several spanwise locations (outside of the inflow vortices wake region) and comparisons with inviscid theory may show the ability (or inability) of an inviscid to accurately predict the details of the blade response as a function of phase time.

REFERENCES

- Adamczyk J J, 1974, "Passage of a swept airfoil through an oblique gust", *Journal of Aircraft*, vol. 11, no. 5, pp. 281-287.
- Adamczyk J J, and Brand R S, 1972, "Scattering of sound by an airfoil of finite span in a compressible stream", *Journal of Sound and Vibration*, vol. 25, no. 1, pp. 139-156.
- Allen H J and Vincenti W G, 1944, "Wall Interference in a Two-Dimensional-Flow Wind Tunnel with Consideration of the Effects of Compressibility", NASA TR 782.
- Amiet R K, 1974, "Compressibility effects in unsteady thin airfoil theory", *AIAA Journal*, vol. 12, no. 2, pp 252-255
- Amiet R K, 1975, "Acoustic radiation from an airfoil in a turbulent stream", *Journal of Sound and Vibration*, vol. 41, no. 4, pp. 407-420.
- Amiet R K, 1976b, "Airfoil Response to an Incompressible Skewed Gust of Small Spanwise Wave-Number", *AIAA Journal*, vol. 14, no. 4, pp. 541-542.
- Amiet R K, 1976a, "High-frequency thin airfoil theory for subsonic flow", *AIAA Journal*, vol. 14, no. 8, pp. 1076-1082.
- Amiet R K and Sears W R, 1979, "The Aerodynamic Noise of Small Perturbation Subsonic Flow", *Journal of Fluid Mechanics*, vol. 44, pt. 2, pp. 227-235.
- Aravamudan K S and Harris W L, 1979, "Low frequency broadband noise generated by a model rotor", *Journal of the Acoustical Society of America*, vol. 66, no. 2, pp. 522-533.
- Atassi H M, 1984, "Sears problem for a lifting airfoil revisited-new results", *Journal of Fluid Mechanics*, vol. 141, pp. 109-122
- Atassi H M, Dusey M and Davis C, 1993a, "Acoustic radiation from a thin airfoil in non-uniform subsonic flows, *AIAA Journal*", vol. 31, pp. 12-19.
- Atassi H M, Fang J and Patrick S, 1993b, "Direct calculation of sound radiated from bodies in non-uniform flows, *Journal of Fluids Engineering*", vol. 115, pp. 573-579, December.
- Atassi H M and Grzedzinski J, "Unsteady disturbances of streaming motions around bodies", *Journal of Fluid Mechanics*, vol. 209, pp. 385-403, 1989.
- Barlow J B, Rae W H, and Pope A, 1999, *Low-Speed Wind Tunnel Testing*, John Wiley & Sons, 3rd edition, pp.353-361.
- Batchelor, G K and Proudman, 1954, "The effects of rapid distortion on a fluid in turbulent motion", *Quarterly Journal of Mechanics and Applied Mathematics*, vol. 7, part 1, pp. 83-103.

Bendat, J S and Piersol A G, 1986, *Random data: analysis and measurement procedures*, 2nd edition, New York, Wiley.

Bereketab S, Wang H, Mish P, and Devenport W J, 2000, "The Surface Pressure Response Of A NACA 0015 Airfoil Immersed In Grid Turbulence. Volume 1: Characteristics of the turbulence", Final report to NASA Langley under grant NAG 1-1942, AOE Dept., Virginia Tech.

Blake W K, 1986, *Mechanics of Flow Induced Vibrations*, vol. II, pp. 735-756, Academic Press, New York.

Bradshaw, P, 1967, "Inactive motion and pressure fluctuations in turbulent boundary layers", *Journal of Fluid Mechanics*, vol. 30, no.2, pp 241-258.

Burley C. L., Brooks T. F, Splettstoesser W. R., Schultz K. J., Kube R., Bucholtz H., Wagner W., and Weittemeyer W., 1997, "Blade Wake Interaction Noise For a BO-105 Model Main Rotor", AHS Technical Specialists' Meeting for Rotorcraft Acoustics and Aerodynamics, Williamsburg Virginia, October 28-30

Casper J, and Farassat F, 2002, "Broadband noise predictions based on a new aeroacoustic formulation", AIAA 2002-0802, 40th Aerospace Sciences Meeting and Exhibit, January 14-17, Reno, NV.

Casper J, Farassat F, Mish P F, and Devenport W J, 2003, "Broadband Noise Predictions for an Airfoil in a Turbulent Stream", AIAA paper no. 2003-0366, 41st Aerospace Sciences Meeting & Exhibit, January 6-9, 2003, Reno, Nevada.

Chase, D M, 1980, "Modeling the wave vector-frequency spectrum of turbulent boundary layer wall pressure", *Journal of Sound and Vibration*, vol. 70, no. 1, pp. 29-67.

Choi K and Simpson R L, 1987, "Some mean velocity, turbulence and unsteadiness characteristics of the Virginia Tech Stability Wind Tunnel", Report VPI-AOE-161, Virginia Tech, Blacksburg VA.

Commerford G. L. and Carta F. O., 1970, "An exploratory investigation of the unsteady aerodynamic response of a two-dimensional airfoil at high reduced frequency", United Aircraft Research Laboratories, East Hartford, Connecticut, Report UAR-J182.

Commerford G L and Carta F. O., 1973, "Unsteady Aerodynamic Response of a Two Dimensional Airfoil at High Reduced Frequency", *AIAA Journal*, Vol 12, No.1, pp. 43-48.

Corcos, G M, 1963, "Resolution of pressure in turbulence", *Journal of the Acoustical Society of America*, vol 35, no. 2, pp. 192-199.

Curle, N, 1955, "The influence of solid boundaries upon aerodynamic sound", *Proceedings of the Royal Society of London, Series A231*, pp. 505-514.

de la Riva, D H, 2001, "Turbulence Interaction in a Highly Sataggered Cascade-Propulsor Configuration", Masters thesis, Aerospace and Ocean Engineering, Virginia Tech, Blacksburg VA.

Devenport, W J, 2002, private communication.

Envia E and Kerschen E J, 1986, "Noise generated by convected gusts interacting with swept airfoil cascades", AIAA paper no. 86-1872, 10th Aeroacoustics Conference, Seattle, Washington.

Fang J and Attassi H M, 1993, "Numerical solutions for unsteady subsonic vortical flows around loaded cascades", *Journal of Turbomachinery*, vol. 115, pp. 810-816.

Filotas L T, 1969, "Response of an infinite wing to an oblique sinusoidal gust", *Basic Aerodynamic Noise Research*, pp. 231-246.

Fleeter S, Capece V, and Chiang H D, 1989, "Unsteady Aerodynamic Gust Response Including Steady Flow Separation", *AIAA Journal*, Vol 28, No. 6, pp 1024-1031.

Fujita H and Kovasznay L G, 1974, "Unsteady Lift and Radiated Sound from a Wake Cutting Airfoil", *AIAA Journal*, Vol 12, No. 9, pp. 1216-1221.

Gershfeld, J L, 2002, private communication, March.

Glegg S A L, 1999, "The response of a swept blade row to a three-dimensional gust", *Journal of Sound and Vibration*, vol. 227, no. 1, pp. 29-64.

Goldstein M E, 1979, "Turbulence generated by the interaction of entropy fluctuations with non-uniform mean flows", *Journal of Fluid Mechanics*, vol. 93, part 2, pp. 209-224.

Goldstein M E and Attassi H, 1976, "A complete second order theory for the unsteady flow about an airfoil due to a periodic gust", *Journal of Fluid Mechanics*, vol. 74, pt. 4, pp. 741-765.

Goody, M C and Simpson, R L, 2000, "Surface pressure fluctuations beneath two- and three-dimensional turbulent boundary layers", *AIAA Journal*, vol. 38, no. 10, pp. 1822-1831.

Goody, M C, 2002, "An empirical spectral model of surface pressure fluctuations that includes Reynolds number effects", 8th AIAA/CEAS Aeroacoustics Conference, 17-19, June, Breckenridge, Colorado.

Graham J M R, 1970a, "Lifting surface theory for the problem of an arbitrarily yawed sinusoidal gust incident on a thin airfoil in incompressible flow", *Aeronautical Quarterly*, May, pp. 182-198.

Graham J M R, 1970b, "Similarity rules for thin airfoils in non-stationary subsonic flows", *Journal of Fluid Mechanics*, vol. 43, pt. 4, pp. 753-766.

Graham J M R and Kullar I, 1977, "Small perturbation expansions in unsteady airfoil theory", *Journal of Fluid Mechanics*, vol. 83, part 2, pp. 209-224.

Hall K C and Verdon J M, 1991, "Gust response analysis for cascades operating in non-uniform mean flows", *AIAA Journal*, vol. 29, no. 9, pp. 1463-1471.

Henderson G H and Fleeter S, 1993a, "Forcing function effects on unsteady aerodynamic gust response. Part 2 - Low solidity airfoil response", *Journal of Turbomachinery*, vol. 115, pp. 751-759.

Henderson G H and Fleeter S, 1993b, "Airfoil wake and linear theory gust response including sub and super-resonant flow conditions", *Journal of Propulsion and Power*, vol. 9, no. 6 (Nov Dec), pp. 847-857.

Henderson G H and Fleeter S, 1997, "Vortical gust response of a low solidity vane row including steady loading and dynamic stall effects", *Journal of Turbomachinery*, vol. 119, July, pp. 482-490.

Hinze, J O, 1975, *Turbulence*, New York, McGraw-Hill

Horlock J H, 1968, "Fluctuating lift forces on airfoils moving through transverse and chordwise gusts", *Journal of Basic Engineering*, vol. 90, pp. 494-500.

Howe M S, 1998, *Acoustics of fluid-structures interactions*, Cambridge University Press.

Humbad N G and Harris W L, 1980, "Model rotor low-frequency broadband noise at moderate tip speeds", AIAA paper 80-1013.

Humbad N G and Harris W L, 1981, "Tip geometry effects on model helicopter rotor low frequency broadband noise", AIAA 7th Aeroacoustics conference, October 5-7, Palo Alto, CA, AIAA-81-2003.

Jackson R, Graham J M R and Maull D J, 1973, "The lift on a wing in a turbulent flow", *Aeronautical Quarterly*, vol. 24, pp. 155-166.

Kaji S and Okazaki, 1970, "Propagation of sound waves through a blade row", *Journal of Sound and Vibration*, vol. 11, pp. 355-375.

Kaji S and Okazaki, 1970a, "Generation of sound by a rotor stator interaction", *Journal of Sound and Vibration*, vol. 13, pp. 281-307.

Karasoy, S, 1990, "Pressure measurements directed to wall adaptation for two-dimensional unsteady flows", Masters Thesis, Aeronautical Engineering, Middle East Technical University.

Kemp N H, 1952, "On the lift and circulation of airfoils in some unsteady-flow problems", *Journal of the Aeronautical Sciences*, vol. 19, pp. 713-714.

Kerschen, E. J. and Myers, M. R., 1983, "Incident Angle Effects on Convected Gust Airfoil Noise", AIAA 8th Aeroacoustics Conference, April 11-13, Atlanta, GA, AIAA-83-0765

Kline, S J and McClintock, F A, 1953, "Describing uncertainties in single sample experiments", *Mechanical Engineer*, vol. 75, pp. 3-8.

Kuhl, D D, 2001, "Near Wall Investigation of Three Dimensional Turbulent Boundary Layers", Masters Thesis, Aerospace and Ocean Engineering Dept., Virginia Tech, Blacksburg VA.

Kullar I and Graham J M R, 1986, "Acoustic effects due to turbulence passing through cascades of thin aerofoils", *Journal of Sound and Vibration*, vol. 110, No. 1, pp. 143-160.

Landahl M, "Unsteady Transonic Flow", Pergamon Press, New York, 1961, pp. 27-30.

Larsen J V and Devenport W J, 1999, "Acoustic Properties of the Virginia Tech Stability Wind Tunnel", Rept. VPI-AOE-263, AOE Dept., Virginia Tech, avail.

<http://www.aoe.vt.edu/aoe/physical/vpi-aoe-263.pdf>

Liepman H W, 1955, "Extension of the statistical approach to buffeting and gust response of wings of finite span", *Journal of the Aeronautical Sciences*, vol. 22, pp. 197-200.

Lighthill, M J, 1952, "On sound generated aerodynamically: I. General theory", *Proceedings of the Royal Society of London, Series A*, vol. 222, 1-32.

Lighthill, M J, 1954, "On sound generated aerodynamically: II. Turbulence as a source of sound", *Proceedings of the Royal Society of London, Series A*, vol. 211, pp564-587.

Lorence C B and Hall K C, 1996, "Sensitivity analysis of the aeroacoustic response of turbomachinery blade rows", *AIAA Journal*, vol. 34, no. 8, August, pp. 1547-1554.

Ma R, 2003, "Unsteady periodic turbulence interaction in a tip leakage flow downstream of a simulated axial compressor rotor". Ph.D. dissertation, Aerospace and Ocean Engineering Dept., Virginia Tech, Blacksburg VA.

Manwaring S R and Fleeter S, 1993, "Rotor blade unsteady aerodynamic gust response to inlet guide vane wakes", *Journal of turbomachinery*, vol. 115, pp. 197-206.

Martinez R and Widnall A E, 1980, "Unified aerodynamic-acoustic theory for a thin rectangular wing encountering a gust", *AIAA Journal*, vol 18, no. 6, June, pp. 636-645.

Maskell E C, 1965, "A Theory of the Blockage Effects on Bluff Bodies and Stalled Wings in a Closed Wind Tunnel", *ARC R&M 3400*.

McGrath, B E and Simpson, R L, 1987, "Some features of surface pressure fluctuations in turbulent boundary layers with zero and favorable pressure gradients", *NASA CR-4051*.

McKeough P J, 1976, "Effects of turbulence on aerofoils at high incidence", Ph.D. Dissertation, University of London.

McKeough P J and Graham J M R, 1980, "The effect of mean loading on the fluctuating loads induced on aerofoils by a turbulent stream", *The Aeronautical Quarterly*, vol. 31, pp. 56-69.

Miles J W, 1950, "Quasi-Stationary Airfoil Theory in Subsonic Compressible Flow", *Quarterly of Applied Mathematics*, vol. 8, pp 181.

Mish P F, 2001, "Mean Loading and Turbulence Scale Effects on the Surface Pressure Fluctuations Occurring on a NACA 0015 Airfoil Immersed in Grid Generated Turbulence", Masters Thesis, Aerospace and Ocean Engineering Dept., Virginia Tech, Blacksburg VA.

Moore J G, Heckel S P and Ballesteros R, 1994, "Reynolds stresses and dissipation mechanisms in a turbine tip leakage vortex", *ASME paper 94-GT-267*.

Morfey P C, 1970, "Lift fluctuations associated with unsteady chordwise flow past an airfoil", *ASME Journal of Basic Engineering*, vol. 92, pp. 663-665.

Mugridge B D, 1970, "Sound radiation from airfoils in turbulent flow", *Journal of Sound and Vibration*, vol. 13, pp. 362-363.

Muthanna C, 1998, "Flowfield downstream of a compressor cascade with tip leakage", M.S. Thesis, Virginia Tech, Blacksburg VA.

Muthanna C, 2002, "The Effects of Free Stream Turbulence on the Flow Field through a Compressor Cascade", PhD dissertation, Aerospace and Ocean Engineering, Virginia Tech, Blacksburg VA.

Myers M and Kerschen E J, 1995, "Influence of incidence angle on sound generation by airfoils interacting with high frequency gusts", *Journal of Fluid Mechanics*, vol. 292, pp 271-304.

Newman J N, 1982, *Marine Hydrodynamics*, pp. 220-236, MIT Press, Cambridge Massachusetts.

Osborne C, 1971, "Compressibility Effects in the Unsteady Interaction Between Blade Rows", Ph.D. thesis, Graduate School of Aerospace Engineering, Cornell Univ, Ithaca, N.Y.

Osborne C, 1973, "Unsteady thin-airfoil theory for subsonic flow", *AIAA Journal*, vol. 11, no. 2, pp. 205-209.

Patterson R W and Amiet R K, 1976a, "Acoustic radiation and surface pressure characteristics of an airfoil due to incident turbulence", NASA CR 2733.

Patterson R W and Amiet R K, 1976b, "Acoustic radiation and surface pressure characteristics of an airfoil due to incident turbulence", 3rd AIAA Aero-Acoustics Conference, Palo Alto, CA, July 20-23, 1976, AIAA paper 76-571.

Pauley W R, Eaton J K, 1989, "Boundary layer turbulence structure in the presence of embedded streamwise vortex pairs", Seventh Symposium on Turbulent Shear Flows, Stanford University, Aug. 21-23, 1989.

Poling D R and Telionis D P, 1986, "The response of airfoils to periodic disturbances—the unsteady Kutta condition", *AIAA Journal*, vol. 24, no. 2, pp. 193-199.

Reba R A and Kerschen E J, 1996, "Influence of airfoil angle of attack on unsteady pressure distributions due to high-frequency gust interactions", report to NASA Langley Research Center.

Reba R A and Kerschen E J, 1997, "Influence of airfoil camber on unsteady pressure distributions due to high-frequency gust interactions", Final report to NASA Langley Research Center.

Reissner E, 1951, "On the application of Mathieu functions in the theory of subsonic compressible flow past oscillating airfoils", NACA TN 2363.

Ribner H S, 1956, "Statistical Theory of Buffeting and Gust Response: Unification and Extension", *Journal of Aeronautical Sciences*, vol. 23, pp 1075-1118.

Satyanarayana B, Henderson R E, Gostelow J P, 1974, "A Comparison Between Experimental and Theoretical Fluctuating Lift on Cascades at Low Frequency Parameters", ASME.

Schloemer, H H, 1967, "Effects of pressure gradient on turbulent boundary layer wall pressure fluctuations", *Journal of the Acoustical Society of America*, vol. 42, no. 1, pp. 93-113.

Schwartzschild K, "Die Beugung und Polarisation des Lichts durch einen Spalt-I", *Mathematische Annalen*, Vol. 55, 1902, pp. 177-247.

Scott J R, 1990, "Compressible flows with periodic vortical disturbances around lifting airfoils", Ph.D. dissertation, University of Notre Dame, April.

Scott J R and Atassi H M, 1995, "A finite-difference, frequency domain numerical scheme for the solution of the gust response problem", *Journal of Computational Physics*, vol. 119, pp75-93.

Sears W R, 1941, "Some aspects of non-stationary airfoil theory and its practical application", *Journal of the Aeronautical Sciences*, vol. 18, no. 3, pp. 104-108.

Simpson, R L, Ghodbane, M, and McGrath, B E, 1987, "Surface pressure fluctuations in a separating turbulent boundary layer", *Journal of Fluid Mechanics*, vol. 177, pp. 167-186.

Sing C and Widnall S, 1974, "Prediction of Unsteady Airloads for Oblique Blade-Gust Interaction in Compressible Flow", *AIAA Journal*, vol. 12, no. 9, pp. 1228-1235.

Smith S N, 1973, "Discrete frequency sound generation in axial flow machines", *Aeronautical Council R&M 3709*.

Stratton, J A, 1941, *Electromagnetic theory*, New York, McGraw Hill.

Townsend, A A, 1961, "Equilibrium layers and wall turbulence", *Journal of Fluid Mechanics*, vol. 11, pp. 97-120.

Van Driest E R and Blumer C B, 1963, "Boundary Layer Transition, Free Stream Turbulence, and Pressure Gradient Effects", *AIAA Journal*, Vol. 1, pp. 1303-1306.

von Karman T and Sears W R, 1938, "Airfoil theory for non-uniform motion", *Journal of the Aeronautical Sciences*, vol. 5, no. 10, pp. 379-390.

Wang Y, 2000, "Tip Leakage Flow Downstream a Compressor Cascade with Moving End Wall", M.S. Thesis, Virginia Tech, Blacksburg VA.

Wang Y, Muthanna C and Devenport W J, 1999, "The Design and Operation of a Moving Endwall System for a Compressor Cascade Wind Tunnel", 37th AIAA Aerospace Sciences Meeting and Exhibit, January 11-14, Reno NV, AIAA 99-0741.

Williams M and Harris W L, 1984, "Helicopter rotor broadband noise due to rotor-turbulence interaction", FDRL Report 84-1, Department of Aeronautics and Astronautics, MIT.

Willmarth, W W, and Woolridge, C E, 1962, "Measurements of the fluctuating pressure at the wall beneath a thick turbulent boundary layer", *Journal of Fluid Mechanics*, vol. 14.

APPENDIX A

A.1 Formulation of Pressure Cross-spectral Density from Measured Pressure

The first step in producing the *surface pressure* cross-spectral density from measured pressure data is the application of microphone calibrations. This begins by applying the Fourier transform to each microphone voltage time series, v_m such that

$$v_m(x, y, f) = \int_{-\infty}^{\infty} v_m(x, y, t) e^{-i2\pi ft} dt \quad (\text{A.1})$$

which is numerically implemented as

$$v_m(x, y, f_k) = \sum_{j=1}^{N_s} v_m(x, y, t_j) e^{\frac{2\pi i}{N_s}(j-1)(k-1)} \quad (\text{A.2})$$

where j and k are indices for each time and frequency increment, respectively and $N_s = 2048$ (i.e. the record length). The microphone calibration, M_s [volts/Pa] is applied to each microphone voltage spectrum to obtain pressure, p' [Pa] as

$$p'(x, y, f) = \frac{v_m(x, y, f)}{M_s(m_n, f)}. \quad (\text{A.3})$$

where m_n is a unique number assigned to each microphone. The *surface pressure* cross-spectral density is then formed as

$$S_{qq}(x_i, x_j, \eta, f) = \frac{2}{N_s \cdot S_R} E \left[p'(x_i, y_i, f)^* p'(x_j, y_j, f) \right] \quad (\text{A.4})$$

where $E[\]$ is the expected value, $*$ indicates the complex conjugate, S_R is the sampling rate, and $\eta = y' - y$. Also, i and j denote different measurement locations. The factor of two in equation (A.4) accounts for the fact that (A.1) is only evaluated over the positive time domain. The *pressure difference* cross-spectral density is calculated as

$$S_{qq}^{\Delta}(x_i, x_j, \eta, f) = \frac{2}{N_s \cdot S_R} E \left[\Delta P(x_i, y_i, f) \Delta P(x_j, y_j, f)^* \right] \quad (\text{A.5})$$

where ΔP is the difference between the lower and upper surface pressure measurements

$$\Delta P(x, y, f) = P_L(x, y, f) - P_U(x, y, f). \quad (\text{A.6})$$

Throughout this work S_{qq} is used in several different forms which are identified here. The *surface pressure* auto-spectrum, G_{pp} is related to S_{qq} as

$$G_{pp}(x, f) = S_{qq}(x_i, x_i, \eta = 0, f) \quad (\text{A.7})$$

The *pressure difference* auto-spectrum, $G_{\Delta P \Delta P}$ is related to the cross-spectral density as

$$G_{\Delta P \Delta P}(x, f) = S_{qq}^{\Delta}(x_i, x_i, \eta = 0, f). \quad (\text{A.8})$$

A.2 Formulation of Coherence and Pressure Phasing

The coherence of the unsteady pressure signal across the airfoil is chord is found as

$$\gamma_p^2 = \frac{|G_{P_U P_L}|}{G_{P_U P_U} G_{P_L P_L}} \quad (\text{A.9})$$

where $G_{P_U P_L}$ is the cross-spectrum between the upper and lower surface of the airfoil, $G_{P_U P_U}$ is the auto-spectrum on the upper surface, and $G_{P_L P_L}$ is the auto-spectrum on the lower surface. The corresponding phasing between pressure signals on the upper and lower surface of the airfoil is found as

$$\phi = \arctan \left(\frac{\text{Im}(G_{P_U P_L})}{\text{Re}(G_{P_U P_L})} \right). \quad (\text{A.10})$$

The author was born December 21st, 1975 in Washington DC just outside of his boyhood home in Gambrills, Maryland. Having spent much of his life on the coastal waters of the Atlantic Ocean and Chesapeake Bay the author thought it wise to pursue an education in Naval Architecture and thus, matriculated to Virginia Tech. After several years of combined course work in the Aerospace and Ocean Engineering Department at Virginia Tech and co-operative education at the Navy's small boat design office, the author yearned for a deeper understanding of fluid mechanics and an opportunity to impact the research in this field. As such, after the completion of his B.S in Ocean Engineering, the author began the second leg of his formal education studying experimental unsteady fluid mechanics in Aerospace Engineering at Virginia Tech. The author completed his Masters degree on this topic June 2001 and pressed on to complete this work March 2003.

Patrick F. Mish